UNIVERSITY OF SOUTHAMPTON

FACULTY OF NATURAL AND ENVIRONMENTAL SCIENCES

Ocean and Earth Science

A study of the South Atlantic Ocean: Circulation and Carbon Variability

by

Gavin Rex Evans

Thesis for the degree of Doctor of Philosophy

July 2013

UNIVERSITY OF SOUTHAMPTON

ABSTRACT

FACULTY OF NATURAL AND ENVIRONMENTAL SCIENCES

School of Ocean and Earth Science

Doctor of Philosophy

A Study of the South Atlantic Ocean: Circulation and Carbon Variability

by **Gavin Rex Evans**

This analysis indicates that the Southern Ocean provides a strong sink, yet low storage, for atmospheric CO_2. The South Atlantic Ocean, in particular, facilitates major inter-basin exchange through the interaction of the Antarctic Circumpolar Current (ACC), Atlantic Meridional Overturning Circulation (AMOC), Agulhas Current and Weddell Gyre systems. Hydrographic occupations from Drake Passage (WOCE section SR1) in 1990 and 2009, along 30°E from the African continent to Antarctica (WOCE section I6S) in 1996 and 2008 and across 24°S in the Atlantic in 2009 create a 'box' and enable comparison between repeat occupations on each box boundary. Calibration factors from GLODAP and CARINA cross-calibration projects were applied for salinity, oxygen and nutrients to 1990 and 1996 occupations.

Distributions of Dissolved Inorganic Carbon (DIC) and anthropogenic carbon (C^{ant}) from each hydrographic occupation support an average C^{ant} increase of $4.7\pm0.2\mu$mol kg^{-1} decade^{-1} at Drake Passage within recently ventilated Subantarctic Mode Water, increasing by $10.4\pm0.2\mu$mol kg^{-1} decade^{-1} at 30°E. Seasonal Winter Water ventilates Subantarctic Mode Water and Antarctic Intermediate Water, and further subduction ventilates the ocean interior. C^{ant} increase within Antarctic Bottom Water yields average sectionwide increases of 0.7 ± 0.4 and $1.4\pm0.2\mu$mol kg^{-1} decade^{-1} across Drake Passage and 30°E, respectively.

Large-scale circulation is estimated by constructing an inverse box model using boundary sections of the South Atlantic Ocean. The 24°S section supports an overturning of 20.2Sv and associated C^{ant} overturning of 0.18Mmol s^{-1}, thus the overturning circulation transports C^{ant} northward. Net meridional northward C^{ant} flux, opposes the southward 0.7Sv volume transport, southward DIC transport and southward overturning freshwater transport of 0.09Sv across 24°S. At 30°E, the net eastward ACC transport carries C^{ant} out of the South Atlantic, north of the 15.9 ± 2.3Sv westward flow of the Weddell Gyre southern limb, partly comprised of Antarctic Bottom Water recently ventilated east of 30°E.

Contents

List of Figures

List of Tables

DECLARATION OF AUTHORSHIP

I, Gavin Evans declare that the thesis entitled *A Study of the South Atlantic Ocean: Circulation and Carbon Variability*, and the work presented in the thesis are both my own, and have been generated by me as the result of my own original research. I confirm that: this work was done wholly or mainly while in candidature for a research degree at this University; where any part of this thesis has been previously submitted for a degree or any other qualification at this University or any other institution, this has been clearly stated; where I have consulted the published work of others, this is always clearly attributed; where I have quoted from the work of others, the source is always given. With the exception of such quotations, this thesis is entirely my own work; I have acknowledged all main sources of help; where the thesis is based on work done by myself jointly with others, I have made clear exactly what was done by others and what I have contributed myself.

ACKNOWLEDGEMENTS

Professionally, I would like to thank the kind contributions made to this thesis of my primary supervisor Elaine McDonagh, as well as my co-supervisors Brian King and Harry Bryden. Further discussions have contributed to this work, and in no particular order I would like to thank: Peter Brown, Dorothee Bakker, Takamasa Tsubouchi, Loïc Jullion, Eric Achterberg, Andrew Yool and Victoire Rerolle. I would also like to thank Ute Schuster, Andy Watson, Kevin Speer, Rik Wanninkhof, Esa Peltola and Mark Stinchcombe for supplying some of the data that I have used in this thesis. I would also like to thank the Natural Environment Research Council and National Oceanography Centre - Marine Physics and Climate Group for my funding.

Personally, I would like to thank Chongyuan (Yolanda) Mao who contributed both at a professional level, in terms of providing an outlet for scientific discussion, and also providing a friendly ear in times of crisis. I would also like to thank my parents, Janis and Clive Evans, my sister Vanessa, and my grandparents Sally and Emlyn, for their support during the ups and downs of my PhD. This PhD has been a real test of perseverance and commitment, and on many days I have battled with my confusions and misunderstandings of the academic world. And to quote the words of Nelson Mandela: "It always seems impossible until it's done."

Nomenclature

Acronyms

AABW: Antarctic Bottom Water

AAIW: Antarctic Intermediate Water

AASW: Antarctic Surface Water

ACC: Antarctic Circumpolar Current

AMOC: Atlantic Meridional Overturning Circulation

AOU: Apparent Oxygen Utilisation

ASC: Antarctic Slope Current

ASF: Antarctic Slope Front

AZ: Antarctic Zone

BCF: Brazil Current Front

BC: Brazil Current

BMC: Brazil Malvinas Confluence

CARINA: Carbon in the North Atlantic

CDW: Circumpolar Deep Water

CFC: Chlorofluorocarbon

CLIVAR: Climate Variability and Predictability

CO_2: Carbon Dioxide

CRM: Certified Reference Material

CTD: Conductivity-Temperature-Depth

DCL: Deepest Common Level

DIC: Dissolved Inorganic Carbon

DWBC: Deep Western Boundary Current

eMLR: Extended Multiple Linear Regression

ENSO: El Nino Southern Oscillation

GCM: Global Circulation Model

GLODAP: Global Ocean Data Analysis Project

LCDW: Lower Circumpolar Deep Water

LNM: Level of No Motion

MC: Malvinas Current

MLD: Mixed Layer Depth

MOC: Meridional Overturning Circulation

NADW: North Atlantic Deep Water

NERC: Natural Environment Research Council

NOC: National Oceanography Centre

O_2: Oxygen

pCO_2: Partial pressure of Carbon Dioxide

PFZ: Polar Frontal Zone

PF: Polar Front

RAPID: Rapid Climate Change programme

SACCF: Southern Antarctic Circumpolar Current Front

SAC: South Atlantic Current

SAF: Subantarctic Front

SAMW: Subantarctic Mode Water

SAZ: Subantarctic Zone

SB: Southern Boundary

SEC: South Equatorial Current

SF6: Sulfur hexafluoride

SST: Sea Surface Temperature

STF: Subtropical Front

STMW: Subtropical Mode Water

STZ: Subtropical Zone

SVD: Singular Value Decomposition

SW: Surface Water

TA: Total Alkalinity

TrOCA: Tracer combining Oxygen, inorganic Carbon, and total Alkalinity

UCDW: Upper Circumpolar Deep Water

WOCE: World Ocean Circulation Experiment

WSBW: Weddell Sea Bottom Water

WSDW: Weddell Sea Deep Water

WW: Winter Water

Symbols

$\triangle C^*$: Delta C star

γ^n: Neutral density

ρ: Density

φ: Geopotential height

Chapter 1

Introduction

1.1 Background

Climate Change, Global Warming, Fossil Fuels: each of these terms has become ubiquitous in representing the changing climate that the Earth has experienced since the industrial revolution, as a consequence of the interaction of humans with their environment. At the birth of heavy industry (∼1750), the societal benefits of industrialisation and the associated developments outweighed any thought regarding the degradation caused to the local environment. From deep shaft coal mines of the nineteenth century to North Sea gas fields of the twentieth, each use of fossil fuels has emitted CO_2 into the atmosphere. An atmospheric increase of CO_2 was first observed in the 1960s (Keeling, 1960), and quickly connected with the worldwide proliferation of economic development and fossil fuel burning. In recent years, the actions of the United Nations Framework Convention on Climate Change (UNFCCC), partially under the guise of the Kyoto Protocol has had limited success in imposing targets on reducing CO_2 emissions, particularly for industrialised countries. The task of adaptation for a changing climate is work in progress and represents a major challenge for present and future governments worldwide.

Between 2000 and 2010, global atmospheric CO_2 grew by $\sim 4\mathrm{Pg\,C\,yr^{-1}}$ (1 Petagram C = 1Pg C = 1×10^{15} g) (Friedlingstein et al. (2010, 2011)). Continued use of fossil fuels and cement production ensures the continued accumulation of CO_2 within the atmosphere reaching a globally averaged concentration of 395.09ppm for January 2013 (http://www.esrl.noaa.gov/gmd/ccgg/trends/global.html). Approximately 30% of anthropogenic CO_2 emissions are absorbed by the ocean (Sabine et al., 2004) assuming no change in ocean circulation or ocean biology. The ocean dominates the storage of natural carbon ($\sim$ 38000GtC (1 Gigaton C = 1Gt C = 1×10^{15} g)), compared to the

land and atmosphere combined (∼2900Gt C) (Denman et al., 2007) with anthropogenic CO_2 currently contributing ∼0.003% to the total ocean carbon content.

CO_2 accumulation is associated with the so-called 'greenhouse effect' for atmospheric warming. Average global surface temperatures have risen by 0.74±0.18°C for 1901-2000 (Trenberth et al., 2007) and is an unequivocal consequence of human activity from the use of fossil fuels and deforestation. Continued warming is predicted to have significant consequences for communities across the globe from the effects of rising sea levels (Church et al., 2004; Church and White, 2006), changes in hydrological cycle (Curry et al., 2003; Helm et al., 2010; Durack and Wijffels, 2010) and desertification (Schlesinger et al., 1990; Le Houérou, 1996; Lal, 2003). Global ocean warming of up to 0.15°C within the upper 700m is attributed to human influence from bias-corrected datasets (Domingues et al., 2008; Ishii and Kimoto, 2009; Levitus et al., 2009; Gleckler et al., 2012), and is evidence for the impact of the greenhouse effect on the ocean.

The Atlantic Ocean covers approximately 20% of the Earth's surface. Within the Atlantic, the Meridional Overturning Circulation (MOC) is the dominant circulation pathway with cold, deep water flowing southwards, and compensatory northward flow of upper ocean water. Within the South Atlantic, the MOC interacts with the Antarctic Circumpolar Current (ACC) (Marshall and Speer, 2012). The Meridional Overturning Circulation (MOC) is also a key driver of global climate (Kuhlbrodt et al., 2007), linking to the El Niño-Southern Oscillation (Timmermann et al., 2005, 2007), the position of the Intertropical Convergence Zone (Vellinga and Wood, 2002; Wu et al., 2008), South Asian monsoon (Chen et al., 2010), the North Atlantic marine ecosystem (Schmittner, 2005; Zickfeld et al., 2008), North Atlantic sea level (Levermann et al., 2005; Bingham and Hughes, 2009) and the Greenland Ice Sheet (Hu et al., 2009).

This thesis focuses on the South Atlantic and South Atlantic sector of the Southern Ocean, where the eastward ACC flow is crucial for connecting the Pacific and Indian Oceans and facilitating oceanic teleconnections between remote locations (White and Peterson, 1996; Rintoul et al., 2001; White and Annis, 2004). The ACC also separates warmer subtropical waters to the north from colder, Antarctic and Subantarctic water to the south (Orsi et al., 1995; Belkin and Gordon, 1996). Both the MOC and ACC are major contributors to ocean climate, and an understanding of the fluxes involved is vital for interpreting large-scale changes and identifying linkages to broader changes in the Earth's climate.

The remainder of Chapter 1 is separated into two sections. Firstly discussing the Physical Perspective, with respect to circulation within the South Atlantic at all depths, and secondly discussing the Chemical Perspective of this research for the assessment

of changes in ocean carbon content. Both perspectives will provide the focus for the following thesis Chapters.

1.2 Physical Perspective

1.2.1 Bathymetry of the South Atlantic

Discussion of South Atlantic circulation is incomplete without first reviewing the bathymetrical features that facilitate the observed circulation pattern (Figure 1.1). The South American and African continents are eastern and western boundaries, respectively. South of the South American continent, Drake Passage is a narrow passageway for Pacific Ocean water to flow initially into the Scotia Sea and then into the broader South Atlantic. The Scotia Sea is framed to the north, east and south by the Scotia Ridge. North of the North Scotia Ridge lies the Falkland Islands, the Falkland Plateau to the east and further east, Georgia Basin, north of South Georgia. North of ∼48°S marks the transition between the Argentine Basin and Brazil Basin, with Vema Channel and Hunter Channel restricting bottom water flow.

The Mid-Atlantic Ridge (MAR) is a clear indicator to separate eastern and western Atlantic basins, and rises to a depth of ∼2000m. The southern end of the MAR reaches ∼ 55°S, at which point it appears to join with the quasi-zonal path of the Southwest Indian Ridge (SWI). Between the SWI Ridge and Southern Africa lies the Agulhas Basin, with the Agulhas Ridge marking a northern boundary. North of the Agulhas Ridge, the Cape Basin is bounded to the north by Walvis Ridge with seamounts within the southeast Cape Basin. Walvis Ridge runs southwestwards from the African continent towards MAR. North of Walvis Ridge, the Angola Basin corresponds to the transition to the Tropical Zone with the Guinea Basin, predominantly north of the equator. East of ∼25°E on the East African coast, the Transkei Basin and Natal Valley are pinned between the African coastline and Mozambique Plateau. East of the Mozambique Plateau lies the Mozambique Basin.

1.2.2 Antarctic Circumpolar Current (ACC) flow structure

The South Atlantic sector of the Southern Ocean is dominated by the eastward-flowing Antarctic Circumpolar Current (ACC). The ACC is characterised by three ACC fronts: Southern Antarctic Circumpolar Current Front (SACCF), Polar Front (PF) and Subantarctic Front (SAF), with the Subtropical Front (STF) further northwards. South of the ACC, the Southern Boundary (Sievers and Emery, 1978; Sievers and Nowlin, 1984;

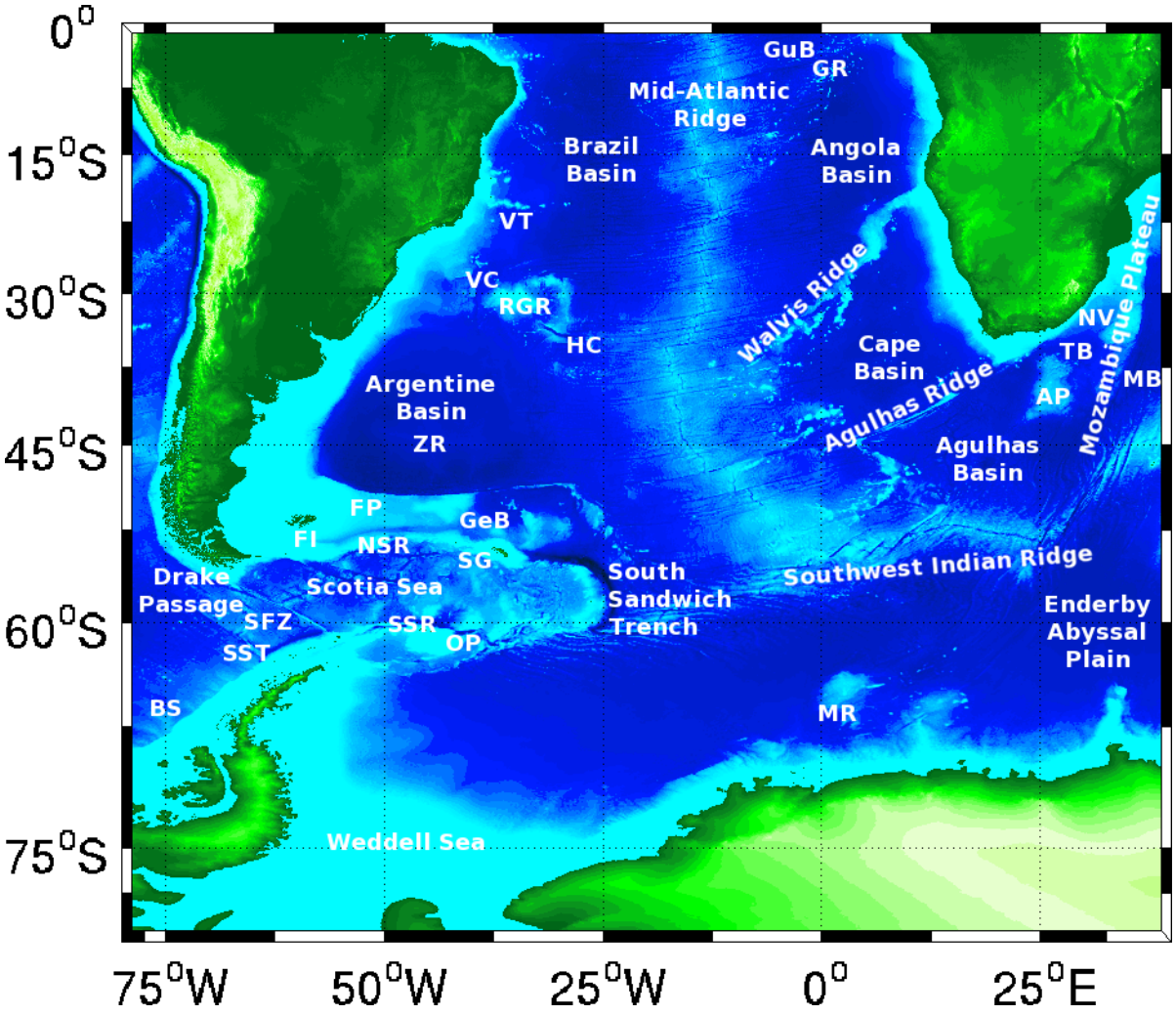

Figure 1.1: South Atlantic bathymetry (Smith and Sandwell, 1997). The major topographical features are labelled: Guinea Basin GuB, Guinea Rise GR, Vitoria-Trinidade seamounts VT, Vema Channel VC, Rio Grande Rise RGR, Hunter Channel HC, Zapiola Rise ZR, Falkland Islands FI, Falkland Plateau FP, North Scotia Ridge NSR, Georgia Basin GeB, South Georgia SB, South Scotia Ridge SSR, Orkney Passage OP, Shackleton Fracture Zone SFZ, South Shetland Trench SST, Bellinghausen Sea BS, Maud Rise MR, Agulhas Plateau AP, Transkei Basin TB, Natal Valley NV, Mozambique Basin MB.

Naveira Garabato et al., 2002b) and Antarctic Slope Front (Jacobs, 1991; Whitworth et al., 1998) lie between the ACC and the Antarctic continent, schematically represented in Figure 1.2. The fronts are narrow zones determined by sharp gradients in hydrographic properties, with a jet-like flow at each front (Cunningham et al., 2003; Sokolov and Rintoul, 2007; Swart et al., 2008). The fronts also define boundaries for hydrographical zones: Subtropical Zone (STZ), north of the Subtropical Front; Subantarctic Zone (SAZ), between Subtropical Front and Subantarctic Front; Polar Frontal Zone (PFZ), between Subantarctic Front and Polar Front; and Antarctic Zone (AZ), south of the Polar Front. The latitude of the fronts is indicated by isotherm and isopycnal definitions, for example, from Orsi et al. (1995) and Belkin and Gordon (1996).

1.2.3 Water mass description

The following water mass descriptions are intended to illuminate the reader in the prominent features of each water mass, namely typical thermohaline properties and formation mechanisms. These descriptions are by no means exhaustive, and further in-depth descriptions are available within the given references.

1.2.3.1 Antarctic Surface Water (AASW)

Antarctic Surface Water (AASW) extends southward from the PF to the continental margins of Antarctica as cold and fresh water, where shelf waters are found at near freezing temperatures. North of the PF, low salinity surface waters subduct northwards into the SAZ (Rintoul and Solokov, 2001; Gladyshev et al., 2008) as a result of Ekman transport, contributing towards Antarctic Intermediate Water formation (Sloyan and Rintoul, 2001a). AASW subduction causes an increase in surface ocean temperature of 2-3°C with a salinity increase of 0.5 from south to north (Emery, 1977). Further south within the AZ, AASW temperature is typically between -1.9 and 1°C in winter, and between -1 and 4°C in summer. Salinity is typically between 33 and 34.5 and is influenced by seasonal sea ice formation and melting (Talley et al., 2011).

1.2.3.2 Winter Water (WW)

South of the Polar Front and below the surface mixed layer, Winter Water (WW) of the Antarctic Zone is a subsurface, seasonal thermocline resulting in a temperature minimum (<2°C) at 150-200m depth (Orsi et al., 1995; Sallée et al., 2008). WW temperature decreases from 2°C at the Polar Front to less than -1.7°C near the Antarctic coast. Distribution of WW is not zonally uniform around Antarctica (Park et al., 1998).

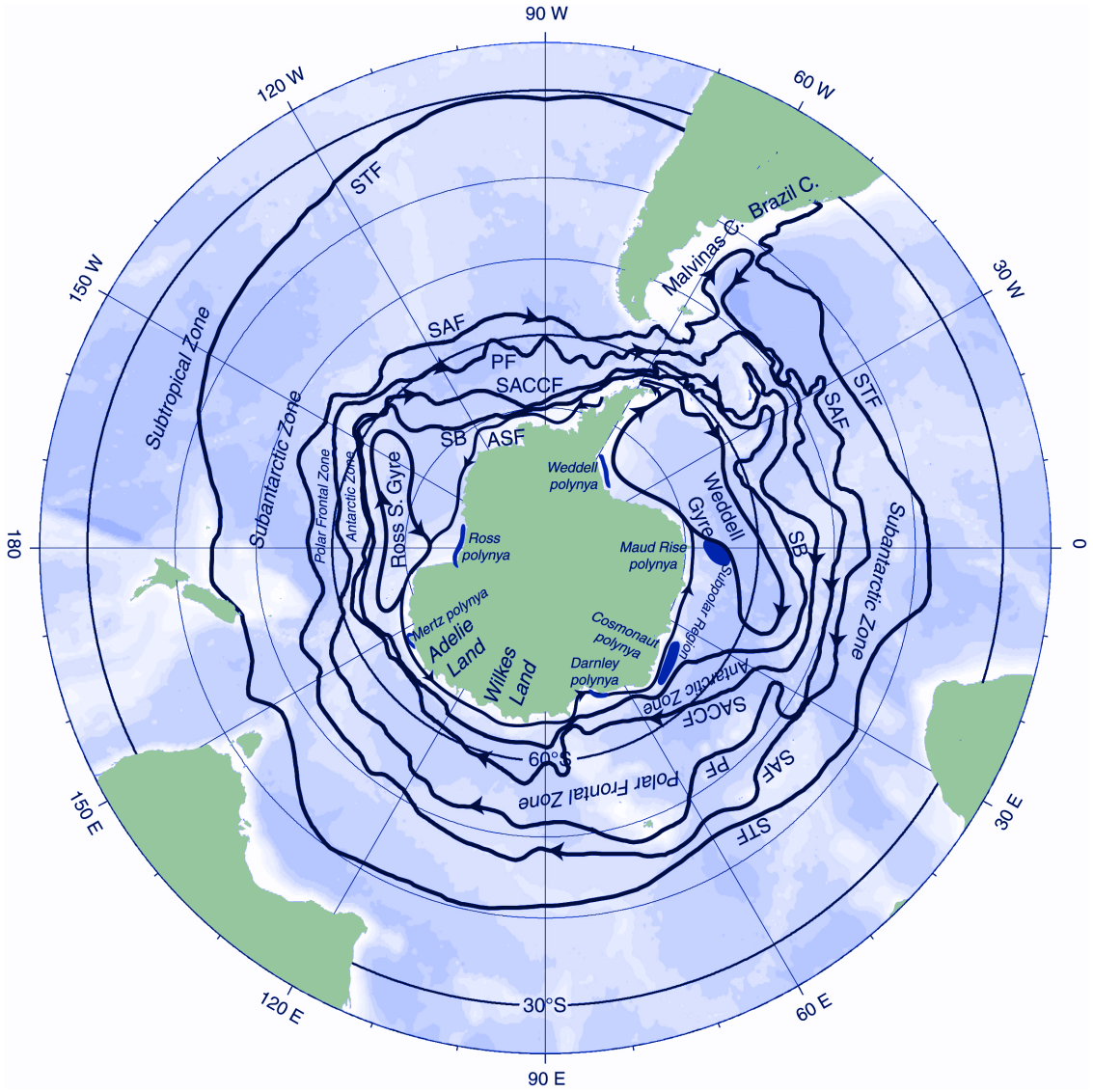

Figure 1.2: Southern Ocean geography from Talley et al. (2011). Frontal locations are marked for: Subtropical Front (STF), Subantarctic Front (SAF), Polar Front (PF), Southern Antarctic Circumpolar Current Front (SACCF), Southern Boundary (SB) and Antarctic Slope Front (ASF), in addition to hydrographic zones. This study considers the Antarctic Zone to consist of all the area south of the PF. The anticlockwise circulation of the Weddell Gyre and Ross Sea Gyre are labelled, as are major polynyas (dark blue patches) near the Antarctic continent.

Recent freshening of WW, formed in the Bellinghausen Sea, at Drake Passage, subsequently freshen deeper AAIW upon downwelling at the Polar Front (Naveira Garabato et al., 2009). The Bellinghausen Sea, west of the Antarctic Peninsula, has also experienced rapid warming both on the adjacent land (Turner et al., 2005), and at sea (Meredith and King, 2005). Bellinghausen Sea freshening has two possible sources, firstly an increase in precipitation (Thomas et al., 2008), and secondly an interdecadal retreat of the winter sea ice field (Meredith and King, 2005; Meredith et al., 2010). Northerly winds to the west of the Antarctic Peninsula are hypothesised to link these small-scale changes to global climate variations: El Niño-Southern Oscillation (ENSO) and the Southern Annular Mode (SAM) (Naveira Garabato et al., 2009).

1.2.3.3 Subantarctic Mode Water (SAMW)

A mode water is a homogeneous water mass that is characterised by a potential vorticity minimum and an oxygen maximum (McCartney, 1977; McDonagh et al., 2008). Subantarctic Mode Water (SAMW) is a type of mode water situated between Antarctic Intermediate Water and the surface water. In the South Atlantic although Subtropical Mode Water (STMW) is also present (Herraiz-Borreguero and Rintoul, 2010), mode waters are typically referred to as either SAMW or STMW, with SAMW assumed most prevalent for the remainder of this thesis. SAMW thermohaline properties range from the warmest (15°C, 35.8 psu) (Provost et al., 1999) to the coldest (4-5°C, 34.5 psu) (Hanawa and Talley, 2001). Salinities can freshen to $<$34.1 psu (Naveira Garabato et al., 2009), with summer ice melt contributing to salinities as low as 33 psu (Talley et al., 2011).

SAMW is formed on the northern side of the ACC during the winter period (McCartney, 1977) by a deep mixed layer, and vigorous convection drawing surface water down to $\sim$300m (Provost et al., 1999). In spring, a seasonal thermocline separates the deeply convected water from the surface. The isolated water contributes to ventilation of the thermocline with oxygen-rich waters. Newly-formed mode water is advected away from its source region and disperses within the ocean interior (McCartney, 1977; Sallée et al., 2006; Hartin et al., 2011). SAMW formation is not spatially uniform with preferential subduction at specific sites around the Antarctic continent (Sallée et al., 2010a; Herraiz-Borreguero and Rintoul, 2010). An example of a formation region is within the southeast Pacific (Figure 1.3) comprising deep mixed layers ($>$500dbar), and regarded as producing the coldest, freshest and densest SAMW variety in Southern Ocean waters (Aoki et al., 2007; Naveira Garabato et al., 2009).

Thermohaline properties of SAMW at formation are affected by major modes of

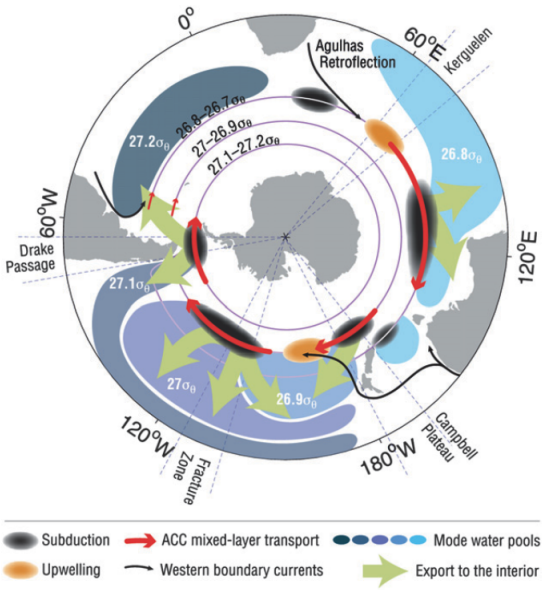

Figure 1.3: Schematic from Sallée et al. (2010a) indicating regions of intense subduction and significant export for Subantarctic Mode Water (SAMW) and Antarctic Intermediate Water (AAIW) in the Southern Ocean.

climate variability (e.g. Southern Annular Mode (SAM), interdecadal Pacific Oscillation (IPO) and El Niño Southern Oscillation (ENSO)), which influence subduction of both heat and carbon from the atmosphere (Sallée et al., 2010a). For example, during positive SAM, an increase in subpolar westerlies increases northward Ekman transports, and encourages globally asymmetric deepening of the mixed layer depth (Naveira Garabato et al., 2009; Sallée et al., 2010b; Hartin et al., 2011). Therefore, SAMW formed in the Pacific Ocean and measured at Drake Passage (Naveira Garabato et al., 2009) is partially dependent on large-scale climatic conditions.

1.2.3.4 Antarctic Intermediate Water (AAIW)

Antarctic Intermediate Water (AAIW) exists between SAMW and Circumpolar Deep Water, characterised by a salinity minimum centered within 27.23 $<\gamma^n<$ 27.40 kg m^{-3} (Naveira Garabato et al., 2009). At Drake Passage, AAIW is ventilated by northward subduction of Winter Water (WW). More generally, CDW upwells near the Antarctic continent, and subsequently contributes to northward surface flow. Upon reaching the Subantarctic Front, air-sea fluxes induce surface water subduction, and AAIW formation. Surface water salinities of 33.6-33.9 contribute to the AAIW salinity minimum (Naveira Garabato et al., 2009). Recent ventilation of AAIW also contributes to relatively high oxygen, CO_2 and CFC concentrations (Hartin et al., 2011).

Spatial uniformity of AAIW formation is uncertain with a number of creation sites suggested depending on the particular definition of AAIW applied: southeast Pacific (Taft, 1963), south Atlantic (Talley, 1996), and in the Indian Ocean near Kerguelen Islands (Molinelli, 1981). Typical AAIW temperatures and salinities are 2-7°C and 34.1-34.4, respectively with further warming and salinification as it advects equatorwards (Schmidtko and Johnson, 2012).

AAIW variability has seen a net freshening (Bindoff and McDougall, 2000) of ∼0.05 in the ∼1970-2000 period in the Indian Ocean (Bryden et al., 2003; McDonagh et al., 2005), although as noted by McCarthy et al. (2012), the Atlantic Ocean exhibits both freshening (Curry et al., 2003) and salinification (Arbic and Owens, 2001; McCarthy et al., 2011) signals depending on the timeframe of analysis. Freshening is linked to extreme climate change on the western portion of the Antarctic Peninsula causing enhanced summertime sea ice melt (Meredith and King, 2005; Bindoff et al., 2007). Winter Water ventilation within the Bellinghausen Sea, and freshening by increased precipitation and retreat of the sea-ice edge, contributes to the AAIW freshening. Teleconnection of this freshening to the subtropical South Atlantic is blurred by the observed salinification of AAIW at 24°S via increased Agulhas leakage, hence masking freshening caused by hydrological cycle intensification (McCarthy et al., 2011).

1.2.3.5 North Atlantic Deep Water (NADW)

North Atlantic Deep Water (NADW) is formed primarily in the Labrador Sea and Greenland Sea by freshwater loss to ice formation. Density increase (γ^n >27.6 kg m^{-3} Lumpkin and Speer (2007)) caused by cooling and salinification causes buoyancy loss and sinking of surface waters. NADW is distinctive for its high salinity signature (∼34.9), as well as high oxygen and low nutrient concentrations, reflecting water mass properties at formation. NADW penetrates into the South Atlantic as a Deep Western Boundary Current (DWBC) with a volume transport of 20.3±10.1Sv at 5°S, west of 31.5°S (Schott et al., 2005), 20Sv at 19°S (Zangenberg and Siedler, 1998) and an initial estimate of 17Sv (Meinen et al., 2012) from under one year of mooring data at 34°S.

Southward NADW progress is limited by interaction with the ACC. South of the ACC, isopycnals shoal steeply as deep water masses including NADW, modified through contact with Circumpolar Deep Water, upwell to the surface (Rintoul et al., 2001). Lighter upwelled deep waters subsequently return northward as Antarctic surface water masses (e.g. Speer et al. (2000)) prior to subducting below warm, equatorial surface water to contribute towards northward-flowing SAMW and AAIW.

1.2.3.6 Upper Circumpolar Deep Water (UCDW)

UCDW is distinguished by an oxygen minimum ($\sim$160μmol kg^{-1}) and a nutrient maximum layer, as a product of isopycnal and diapycnal mixing of deep water sourced from the Indian and Pacific Oceans (Callahan, 1972). Convergence of deep water from the eastern Pacific and western Indian Ocean (Callahan, 1972; Park et al., 1993; Orsi et al., 1995) within the ACC zone facilitates UCDW formation. At Drake Passage, UCDW volume transport is $\sim$69Sv (Sloyan and Rintoul, 2001b) and $\sim$54Sv across the WOCE A23 transect (Heywood and King, 2002). Net gain or loss of UCDW across the South Atlantic, as measured by outflow into the Indian Ocean of 71Sv (Sloyan and Rintoul, 2001b), is therefore small.

At the Antarctic Peninsula, UCDW is characterised by a potential temperature and salinity range of 1.55-2.10°C and 34.62-34.68, respectively (Moffat et al., 2009), whilst more generally within the Antarctic Zone, Talley et al. (2011) estimate θ $\sim$1.5-2.5°C. Recent trends suggest warming and salinification of UCDW south of the Polar Front, through warming and salinification at the base of the mixed layer (Aoki et al., 2005). South of the PF, UCDW is at >600dbar, before shoaling south of the ACC to the upper 300dbar (Orsi et al., 1995). Destruction of UCDW occurs south of the ACC by upwelling, for example, within the Scotia Sea (Naveira Garabato et al., 2002a), and contributes towards AABW formation. UCDW upwelling supplies nutrient-rich deep water to surface waters and encourages phytoplankton growth, as observed at the Antarctic Peninsula (Prezelin et al., 2000), as well as potentially influencing heat balance on the local continental shelf (Klinck, 1998; Reiss et al., 2009). Southward penetration of UCDW is limited by outcropping and entrainment of LCDW and the mixed layer.

1.2.3.7 Lower Circumpolar Deep Water (LCDW)

High salinity deep water south of the Polar Front is typically associated with LCDW (Sievers and Nowlin, 1984; Whitworth and Nowlin, 1987) whilst north of the Polar Front is indicative of NADW influence (Naveira Garabato et al., 2002a). LCDW salinity maximum is derived from NADW penetration into ACC deep water masses within the Southern Ocean (Callahan, 1972; Park et al., 1993). Along with modified NADW primarily within upper LCDW, lower LCDW also consists of modified AABW. For instance in the Scotia Sea, CDW interaction with underlying Weddell Sea Deep Water (WSDW) causes notable cooling and freshening. Along the Antarctic Peninsula, LCDW is characterised by a salinity maximum of 34.73 and a temperature range of 1.25-1.57°C

(Moffat et al., 2009), whilst Talley et al. (2011) estimate an Atlantic AZ salinity range of 34.8-34.9.

LCDW volume transport in Sloyan and Rintoul (2001b) yields 29Sv entering the South Atlantic through Drake Passage, and 41Sv exiting into the Indian Ocean sector. The increase in volume transport is primarily linked to the contribution of the southward flowing NADW to ACC deep water, and upward mixing of AABW to lower LCDW. The latter mechanism is a partly circular process as the interaction of salty LCDW with shelf waters forms AABW, that later upwells within the South Atlantic interior to LCDW.

1.2.3.8 Antarctic Bottom Water (AABW)

Antarctic Bottom Water (AABW) forms along the coast of the Weddell and Ross Seas (Jacobs et al., 1970; Foster and Carmack, 1976), along the Adélie coast of Antarctica south of Australia (Gordon and Tchernia, 1972; Rintoul, 1998; Williams et al., 2010a) and at Prydz Bay (Meredith et al., 2010; Yabuki et al., 2006; Meijers et al., 2010) when very dense, cold near-surface shelf waters, created by ocean-atmosphere and ocean-ice interactions mix with upwelling LCDW (Doney and Hecht, 2002). Ohshima et al. (2013) also suggest that AABW formation is linked to intensive sea ice formation at the Cape Darnley polynya (Tamura et al., 2008; Kusahara et al., 2010). After exposure to the atmosphere, the upwelled water has higher concentrations of atmospheric constituents such as CFCs, in comparison to low CFC Circumpolar Deep Water in the ocean interior (Orsi et al., 1999; Doney and Hecht, 2002), as well as a high silicate content (McDonagh and King, 2005). The shelf water and LCDW mixture then sinks down the continental slope, creating a fresher and colder deep water mass, denser than NADW and LCDW.

AABW flows northward from its formation sites below NADW/LCDW (Rhein et al., 1998; Orsi et al., 1999). In the Southern Ocean, AABW is defined as γ^n>28.27 ($\sigma_2 \gtrsim 37.16$, $\sigma_4 \gtrsim 46.04 - 46.06$) (Orsi et al., 1999), with a typical range for potential temperature and salinity of 0 to -0.8°C and 34.6-34.7. As AABW travels equatorwards from its source region, mixing with overlying water masses causes warming with AABW typically defined as colder than $\theta \sim 1.9$°C (Limeburner et al., 2005), or 2°C (Hogg et al., 1999) ($\sigma_4 < 45.87$ McDonagh et al. (2002)) and at depths below ∼4000m (Limeburner et al., 2005). Atlantic AABW flow is limited by bathymetry with bottom water transport estimates of 6.9Sv northward through Vema Channel and Hunter Channel (θ<2°C Hogg et al. (1999)) and 6.2Sv outflow from the Vema Channel Extension ($\sigma_4 < 45.87$ McDonagh et al. (2002)). North of Vema Channel, AABW eastward progression is

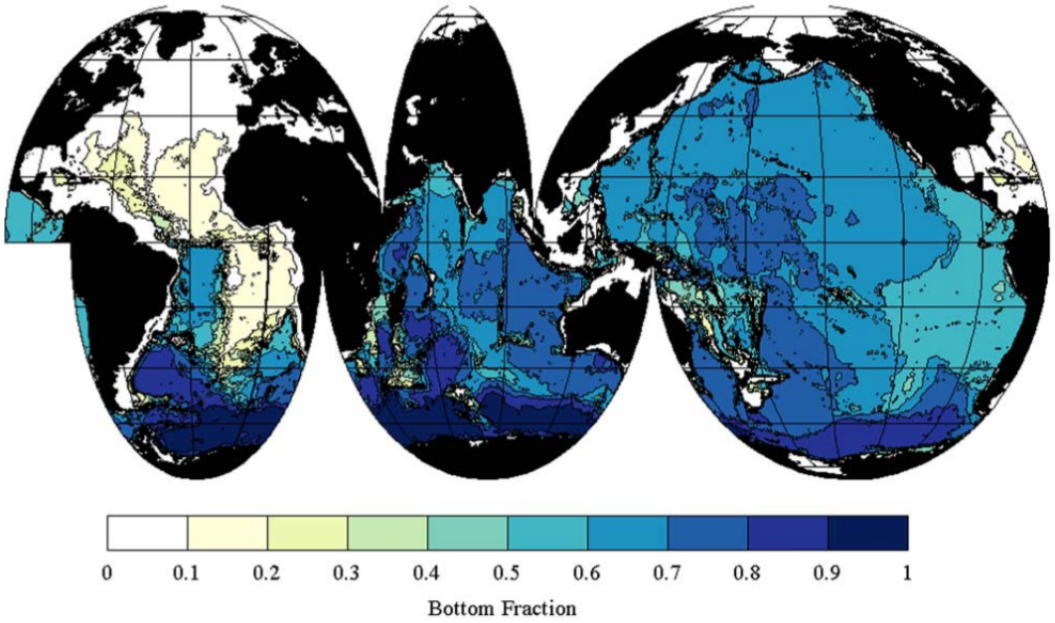

Figure 1.4: Fraction of AABW at the deepest sample in the WOCE Global Hydrographic Climatology (Gouretski and Koltermann, 2004) contoured at 0.1 intervals. From Johnson (2008).

restricted by the Mid-Atlantic Ridge. No significant transport into the eastern basin occurs until approximately at the equator, with 1.22±0.25Sv ($\theta < 1.9$°C) at the Romanche Fracture Zone and Chain Fracture Zone (Mercier and Morin, 1997; Mercier and Speer, 1998; Stephens and Marshall, 2000), and ∼2.2Sv (θ<2°C) at the Vema Fracture Zone at 11°N (McCartney et al., 1991; Fischer et al., 1996).

1.2.3.9 Weddell Sea Deep Water/Weddell Sea Bottom Water (WSDW/WSBW)

AABW flowing northwards from the Weddell Sea, is originally constructed from Weddell Sea Deep Water (WSDW) and Weddell Sea Bottom Water (WSBW). WSBW forms from interaction between recently upwelled LCDW, and shelf water. Shelf water derived from oceanic processes, termed High Salinity Shelf Water (HSSW) by Huhn et al. (2008), has high salinity through sea ice formation and subsequent brine rejection, with typical salinity >34.70, and potential temperature near the surface freezing point ($T_F \approx -1.9$°C) (Huhn et al., 2008). Cooling and freshening upon interaction with the ice shelf causes Ice Shelf Water (ISW) formation, defined as potential temperature below the surface freezing point ($T_F \sim -1.9$C) (Foldvik et al., 2004). Interaction of high density shelf water with Weddell Sea surface water creates a high density water mass that descends along the Antarctic continental slope to form WSBW. The contribution of ISW to WSBW and, more generally, AABW is significant for formation of AABW

with different properties.

WSDW and WSBW have potential temperatures θ of between 0 and -0.7°C, and <-0.7°C, respectively (Carmack and Foster, 1975). WSDW flows northward over South Scotia Ridge, and into the Scotia Sea (Locarnini et al., 1993; Naveira Garabato et al., 2002b). WSBW is, however, constrained poleward of South Scotia Ridge (Meredith et al., 2000). Therefore, the only escape option for WSBW from the Weddell Sea, is to gradually mix with overlying LCDW to form WSDW (Schroeder et al., 2004). Alternative exit pathways for WSDW are along the South Sandwich Abyssal Plain, or east of the Mid-Atlantic Ridge (Orsi et al., 1993, 1999). Export of WSDW is hypothesised as linking to wind-forcing on the Weddell Gyre (Jullion et al., 2010b; Gordon et al., 2010; Wang et al., 2012), and hence potentially to larger-scale climate phenomena, such as the Southern Annular Mode (SAM), and El Niño/Southern Oscillation (Gordon et al., 2010).

1.2.4 Large-scale circulation features

1.2.4.1 Meridional Overturning Circulation (MOC)

Atlantic Ocean circulation is governed by the effect of the Meridional Overturning Circulation (MOC). The MOC is commonly split into two limbs. For the upper limb in the North Atlantic, cooling and salinification by the removal of freshwater by evaporation and sea ice formation leads to surface water buoyancy loss, as described in section 1.2.3.5. Northward progression for newly formed deep water into the Arctic Ocean is limited (Tsubouchi et al., 2012), and hence the major pathway for NADW is southward towards the South Atlantic. The lower limb, or southern limb of the MOC corresponds to upwelling of deep water south of the ACC. Whilst the lighter deep water contributes towards northward surface water, denser deep water progresses southward to the Antarctic continent prior to upwelling. At the Antarctic continent, cooling and salinification of upwelled deep water causes buoyancy loss and AABW formation, as described in section 1.2.3.8. AABW subsequently spreads northward from the Antarctic continent, occupying the seafloor across the majority of the global ocean (Figure 1.4, Johnson, 2008).

Within the South Atlantic, MOC monitoring is part of the SAMOC (South Atlantic Meridional Overturning Circulation) project and is currently achieved using hydrographic surveys of the boundary current systems and transbasin occupations, and in situ instruments, namely pressure-equipped inverted echo-sounders (PIES), with a transbasin mooring array, a long-term goal (Baehr et al., 2009; Garzoli and Matano,

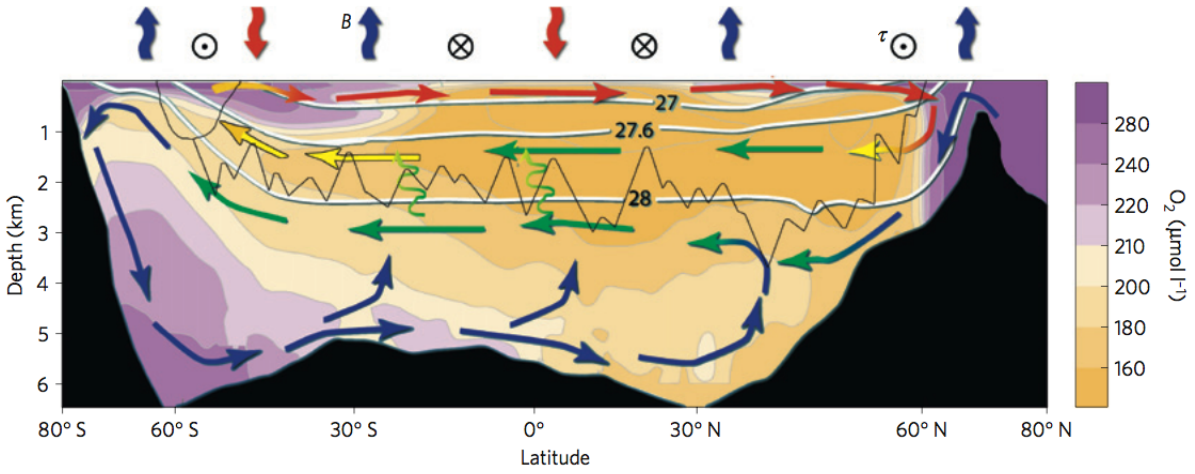

Figure 1.5: Schematic circulation of Upper and Lower limb of the global MOC from Marshall and Speer (2012). The distribution of zonally averaged oxygen indicates low values (yellow) for older water, and high values (purple) for recently ventilated water. White lines indicate density isopycnals that outcrop in the polar seas. The jagged thin black lines indicates bathymetry of the Mid-Atlantic Ridge and the Scotia Ridge in the Southern Ocean. Mixing processes associated with bathymetry are indicated by the vertical squiggly arrows. Air-sea surface density flux, indicates surface waters becoming less (red arrows), or more dense (blue arrows). The relative density of water masses is indicated by schematic coloured arrows for: lighter mode and thermocline waters (red), upper deep waters (yellow), deep waters including NADW (green) and bottom waters (blue).

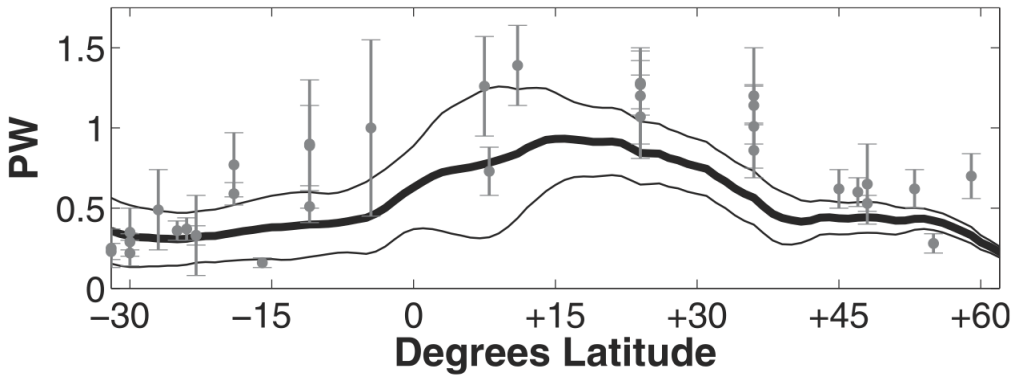

Figure 1.6: Meridional Atlantic heat transport from Piecuch and Ponte (2012). The black solid thick line represents their average time-mean ECCO estimate (mean state ocean estimates chosen as evolved and optimised solutions for the Massachusetts Institute of Technology general circulation model (MITgcm)), black solid thin lines represent the uncertainty interval as a standard deviation of the heat transport time series with the hydrographic estimates marked with the additional error bars (grey).

2011). Current estimates of South Atlantic MOC transport range from 16.5Sv/21.5Sv at 24°S (Bryden et al., 2011), 23±3Sv, 22.7Sv and 20±2Sv at 30°S (Ganachaud, 1999; Holfort and Siedler, 2001; McDonagh and King, 2005), 17.9Sv at 35°S (Dong et al., 2009) and 22Sv, 21±2Sv, 21.7Sv and 18±4Sv, nominally at 45°S (Saunders and King, 1995; Ganachaud, 1999; Holfort and Siedler, 2001; McDonagh and King, 2005).

Within the South Atlantic basin, meridional heat transport is equatorwards. This is counterintuitive to expectations for a gain of heat in the tropics and a loss of heat at higher latitudes. However, southward transport of cold deep water, formed in the North Atlantic dominates northward returnflow of warm upper ocean. The resulting difference in temperature between southward and northward flows yields a net equatorward heat transport in the South Atlantic. Meridional heat transport within the Atlantic Ocean for hydrographic occupations is shown in Figure 1.6 and fitted with a model estimate. Northward heat transport maximum appears at ∼15°N, however, the range of variability in the South Atlantic is extended by the inclusion of additional analyses of -0.23PW (de las Heras and Schlitzer, 1999) and 0.94PW (Saunders and King, 1995). Better establishing the range of variability for South Atlantic heat transport is a long-term goal of the SAMOC project.

1.2.4.2 Deep Western Boundary Current (DWBC)

Deep Western Boundary Currents (DWBC) are characterised by narrow, fast-flowing deep water pathways. In the Atlantic, the DWBC originates through dense overflow,

deep convection and subsequent southward flow along the western boundary (Schmitz and McCartney, 1993). Western intensification associated with DWBCs follows from Stommel (1948)'s explanation of the variation of the Coriolis parameter with latitude. Transport estimates in the North Atlantic yield 26.5Sv southward (Johns et al., 2008), which continues into the South Atlantic as a 25.5±8.3Sv flow at 5°S (Schott et al., 2005). At ∼8°S, however, Dengler et al. (2004) report from mooring and hydrographic cruise observations, a suggested breakdown of the DWBC into eddies north of 11°S. Further south at 34.5°S, a combination of inverted echo sounders and hydrographic observations yields a 25Sv transport estimate with the DWBC appearing to reconstitute between ∼11°S and 34.5°S.

In addition to the direct southward pathway, a NADW zonal pathway originating from the DWBC is thought to exist in the Atlantic (Speer et al., 1995; Zangenberg and Siedler, 1998; Arhan et al., 2003; Hogg and Thurnherr, 2005; van Sebille et al., 2012). The zonal pathway is estimated to constitute between 3-16Sv, from estimates of ∼5Sv (Hogg and Thurnherr, 2005), 3±5Sv through the Cape Basin at 22.5°S with a total of 11±7Sv at 35°S (Arhan et al., 2003), 3Sv at 15°W (Speer et al., 1995) and up to 16Sv (Zangenberg and Siedler, 1998). van Sebille et al. (2012) hypothesised that the zonal pathway is intermittent with associated transports determined remotely by the strength of Agulhas rings entering the Cape Basin. Agulhas rings create a depression of potential vorticity isolines that act to pull NADW along a compensatory zonal pathway towards the Cape Basin. From the limited information so far, further research is required to characterise meridional and zonal DWBC flows within the South Atlantic.

1.2.4.3 Agulhas Current and Return Current

The Agulhas Current is a WBC that flows southward along the East African continent, comprising the western limb of the South Indian Ocean subtropical gyre. South of the African continent, the Agulhas Current protrudes westward into the Atlantic Ocean with recent volume transport measurements of 69.7Sv using in-situ current meters (Bryden et al., 2005a). The majority of Agulhas Current westward flow is retroflected back, as the Agulhas Return Current, towards the Indian Ocean. The Return Current follows a quasi-permanent pathway, including a northward meander around the Agulhas Plateau (Lutjeharms and Ansorge, 2001; Boebel et al., 2003), closing the subtropical gyre of the South Indian Ocean (Lutjeharms and van Ballegooyen, 1988; Matano et al., 1998; Dencausse et al., 2010b). Both currents are associated with enhanced primary productivity through nutrient-rich deep water upwelling.

The residual between the Agulhas Current and the Agulhas Return Current is com-

monly described as Agulhas leakage. Recent observations using subsurface floats and surface drifters estimate an Agulhas leakage of 15Sv (Richardson, 2007). The leakage mechanism is hypothesised as anticyclonic eddies, or Agulhas 'rings' that shed from the main Agulhas flow, primarily within the upper ∼2000dbar (Byrne et al., 1995; McDonagh et al., 1999). Leakage brings warm, salty Indian Ocean water into the Atlantic and contributes towards the upper ocean northward flow of the MOC (Lutjeharms, 2007). Recent modelling studies (Biastoch et al., 2009) and observations (Backeberg et al., 2012) have suggested an intensification of Agulhas leakage into the Atlantic, as a compensatory mechanism for MOC deceleration. Further suggestions for warming of the Agulhas Current system (Rouault et al., 2009), therefore implies enhanced Agulhas leakage heat flux, in excess of heat flux implications from an Agulhas leakage volume flux increase alone. MOC stability relating to Agulhas variability is a topic of current research (Beal et al., 2011).

1.2.4.4 Agulhas Undercurrent

The Undercurrent is a flow of deep water from the Atlantic Ocean into the Indian Ocean hugging the continental shelf, thought to be primarily comprised of AAIW and NADW (Beal and Bryden, 1997, 1999; Bryden et al., 2005a; Beal, 2009). Previous volume transport estimates of 4.2±2.9Sv from a single current meter record (Bryden et al., 2005a) are in agreement with a more recent mooring estimate of 4.2±5.2Sv (Beal, 2009). Approximately 2.3±3.0Sv is eastward-flowing NADW, representing a NADW escape pathway from the Atlantic.

1.2.4.5 Brazil Current

North of the ACC, a strong poleward flow near the western boundary of the South Atlantic is the Brazil Current (BC). The Brazil Current is the western limb of the South Atlantic subtropical gyre that transports warm, salty ($\theta \gtrsim 15$°C, >35.5) upper ocean water southwards, schematically represented by Figure 1.7 (Stramma and England, 1999). Within the upper 500-600dbar (Peterson and Stramma, 1991), and predominately within the upper 300dbar (Bryden et al., 2011), the Brazil Current is fully formed north of the Vitoria-Trinidade Seamounts at ∼20°S with a weak transport of 3.8-6.8Sv (Evans et al., 1983), and intensifies southwards on an order of 5% per 100km (Gordon and Greengrove, 1986). Southward flow continues until ∼38°S (Gordon and Greengrove, 1986; Garzoli and Garraffo, 1989), where it meets the cold and fresh northward flowing Malvinas Current, and forms the highly energetic Brazil-Malvinas Confluence

(BMC; Reid et al. (1977); Gordon and Greengrove (1986); Oliveira et al. (2009); Jullion et al. (2010a)). The South American coastline forces the colliding currents offshore in a series of large-scale meanders (Gordon and Greengrove, 1986), creating the South Atlantic Current.

Compared to other Western Boundary Currents, the BC is notably weak with transport estimates at 24°S ranging between 4.1Sv and 13.2Sv (Signorini, 1978; Evans et al., 1983; Evans and Signorini, 1985; Stramma, 1989; Garfield, 1990; Zemba, 1991; Campos et al., 1995; Bryden et al., 2011) for historical estimates. Intensification is caused through a partial anticyclonic recirculation of the Brazil Current Front, after interaction with the BMC (Gordon and Greengrove, 1986). The recirculation cell is associated with a transport of 12Sv in the upper 1400m (Gordon and Greengrove, 1986), and 7.5Sv in the upper 800m (Stramma, 1989), approximately west of 35°W (Peterson and Stramma, 1991; Saraceno et al., 2004).

1.2.4.6 Vema Channel

Vema Channel near 39°30'W extends as a narrow trough 25-50 km wide with a sill depth of ∼4600m that enables northward bottom water progression from the Argentine Basin to the Brazil Basin (Johnson and Biscaye, 1976). Hunter Channel (∼4200m), farther to the east near 28°W, provides a smaller pathway for northward transport (Zenk et al., 1999). Hogg et al. (1999) estimate a deep Vema Channel transport of ∼4Sv for θ<2°C compared to 3.7±0.7Sv and 2.7±0.7Sv for $\sigma_4 < 45.87$ in McDonagh et al. (2002). Following McDonagh et al. (2002), northward flow is restricted to the deep Vema Channel with the eastern flank of the Vema Channel and the Santos Plateau to the west contributing a southward flow of bottom water and LCDW. Estimates of Hunter Channel northward transport are 2.9Sv (Hogg et al., 1999; Zenk et al., 1999) and 0.7Sv (Speer and Zenk, 1993). Vema Channel entrance pathways are thought to either feed from the DWBC to the west, or from the southeast along the Mid-Atlantic Ridge. Whereas McDonagh et al. (2002) observed little evidence for the westward flowing jet, Zenk and Visbeck (2012) found the existence of a westward flow plausible. Further work is needed to ascertain the significance of a westward flow towards the mouth of the Vema Channel.

1.2.4.7 Malvinas Current

The Brazil-Malvinas Confluence can not form without the northward flowing cold, fresh Malvinas Current (<7°C at the surface in winter (Saraceno et al., 2004), 14-16°C in

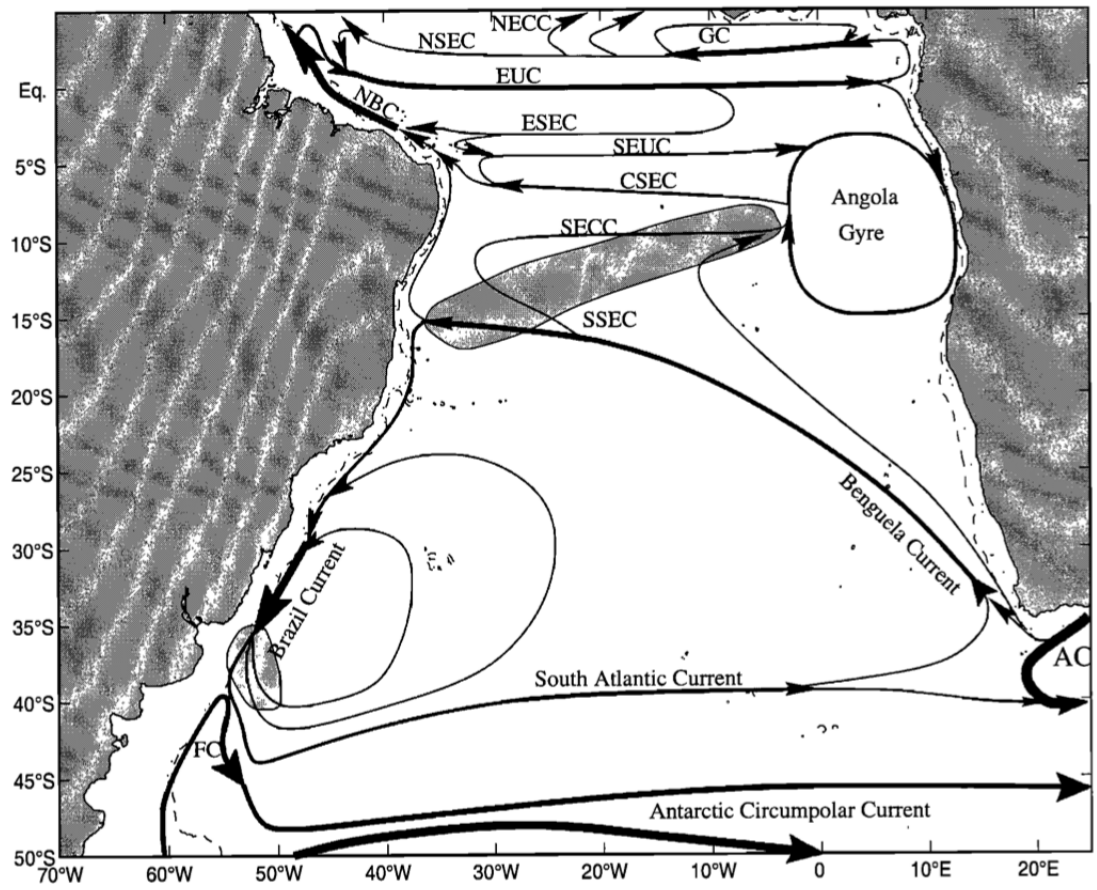

Figure 1.7: Schematic circulation from Stramma and England (1999) of the upper 100m for the South Atlantic between the equator and 50°S. Shown are the Falkland Current (FC); Brazil Current; South Atlantic Current; Agulhas Current (AC) and its retroflection; Benguela Current; South Equatorial Current (SEC), with northern (NSEC), equatorial (ESEC), central (CSEC), and southern (SSEC) branches; South Equatorial Countercurrent (SECC), South Equatorial Undercurrent (SEUC); Angola Gyre; Equatorial Undercurrent (EUC); North Brazil Current (NBC); North Equatorial Countercurrent (NECC); and Guinea Current (GC). A dashed line gives 1000m depth. Formation of some subsurface water: salinity maximum in the tropics and SAMW in the subtropics are shaded.

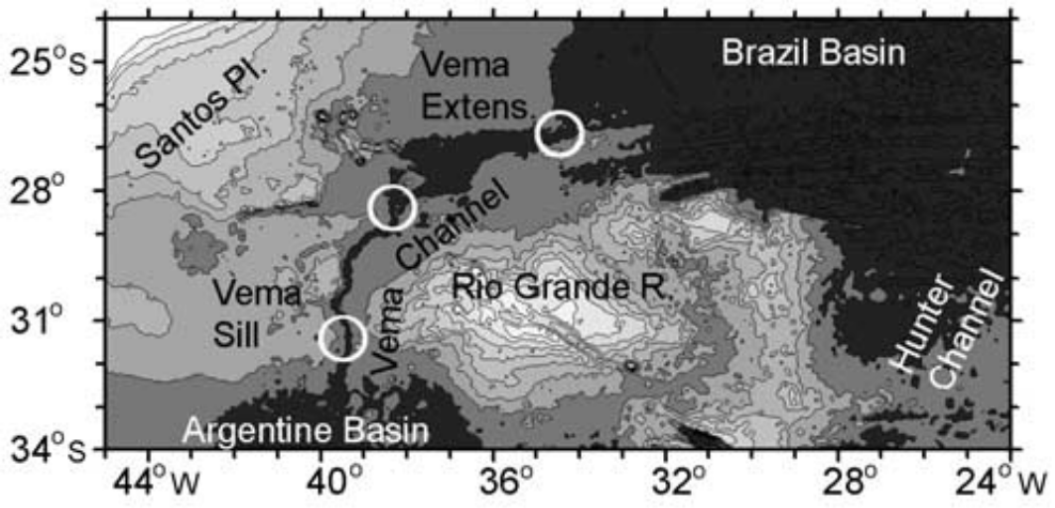

Figure 1.8: Topography of Vema Channel in the South Atlantic. White circles indicate from south to north, Vema Sill, Santos Plateau and Vema Extension. From Zenk and Morozov (2007).

summer (Gordon and Greengrove, 1986; Stramma and Peterson, 1990)). The Malvinas Current originates from the northern SAF branch of the ACC as it turns sharply northwards upon entering the South Atlantic basin (Piola and Gordon, 1989; Peterson and Whitworth, 1989), represented schematically in Figure 1.9. Historical estimates from hydrography of the Malvinas Current range from 10-70Sv, with individual estimates of 10Sv (Gordon and Greengrove, 1986), 70Sv (Peterson, 1992), 60Sv (Saunders and King, 1995) and 45Sv (Maamaatuaiahutapu and Garc, 1998). Comparatively, the first current-velocity time series from in situ moorings estimated the transport as ∼41.5Sv (Vivier and Provost, 1999; Spadone and Provost, 2009) and re-calculated as 32.8Sv for a December 1993 and June 1995 deployment. More recent current meter deployments between December 2001 - February 2003 estimate 33.3Sv, compared to transport derived from altimetry data between October 1992 and May 2007 of 34.3Sv (Spadone and Provost, 2009).

1.2.4.8 South Atlantic Current

The South Atlantic Current (SAC) is the southern limb of the South Atlantic subtropical gyre and constitutes the broad, meandering continuation of the Brazil Current Front from the BMC and a sharp decrease in the surface flow (Stramma and Peterson, 1990; Oliveira et al., 2009). The SAC is associated with the Subtropical Front across the Atlantic, and acts as a hydrographic boundary between warm, saline subtropical water and cold, fresh subpolar waters (Deacon, 1933, 1937). Separation of the Brazil

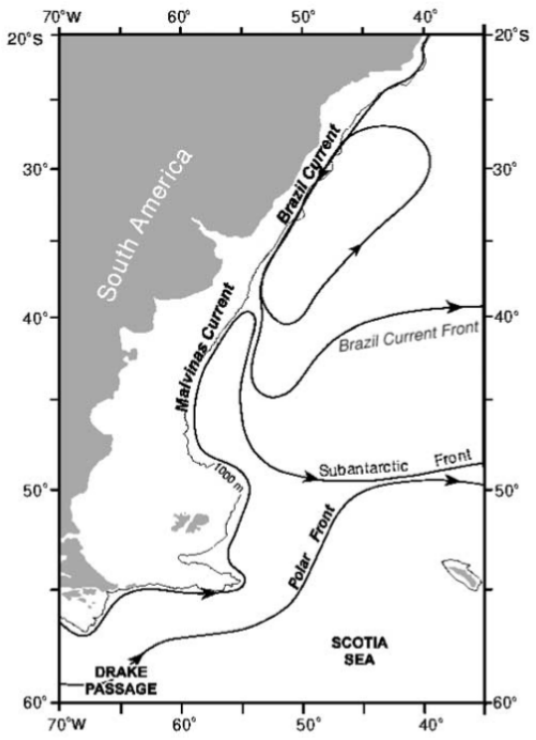

Figure 1.9: Schematic representation of upper ocean circulation in the Southwestern Atlantic. From Saraceno et al. (2004), based on Brandini et al. (2000) and Peterson and Stramma (1991).

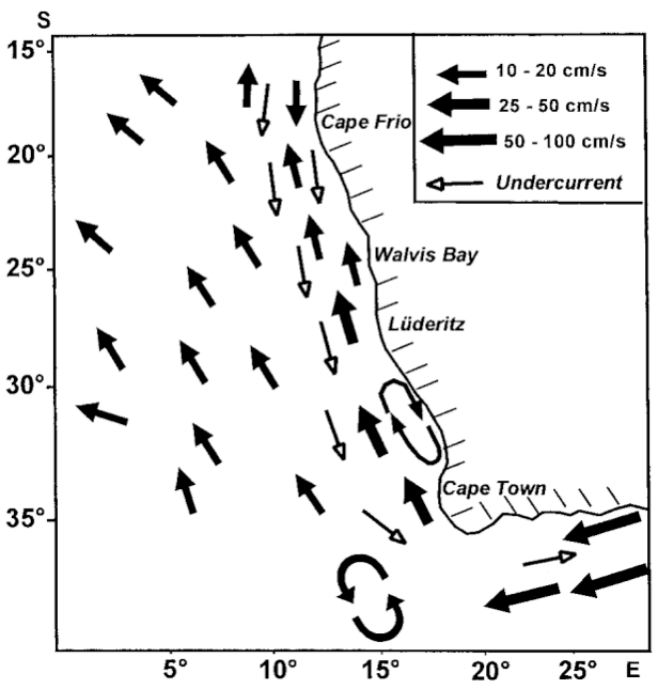

Figure 1.10: Schematic representation of surface and undercurrent flow in the Benguela Current System. Edited from Fennel (1999), in turn redrawn from Nelson and Hutchings (1983); Shannon (1985); Shannon and Nelson (1996).

Current Front/STF and SAF is observed west of 40°W (Roden, 1986), and subsequent flow of the SAC along the STF is predominately within the upper 1000m (Stramma and Peterson, 1990) with a typical volume transport of 30Sv in the Argentine Basin. Within the Cape Basin, the SAC turns northward to feed the Benguela Current with transport estimates of 15Sv, 6Sv, 11-28Sv and 9-12Sv, respectively (Stramma and Peterson, 1990; Garzoli and Gordon, 1996; Smythe-Wright et al., 1998; Mercier et al., 2003).

1.2.4.9 Benguela Current

The Benguela Current flows equatorwards from its inception within the Cape Basin between 14°S and 35°S (Shillington, 1998; Field and Shillington, 2006). Agulhas leakage variability impacts the downstream Benguela Current composition with for example, Garzoli and Gordon (1996) estimating from a 1993-1996 average of inverted echo sounder data, a 50% contribution from the South Atlantic, 25% from the Indian Ocean and 25% from the tropics whilst from an inverse box model, Mercier et al. (2003) estimated a 40% contribution from the South Atlantic, 50% from the Indian Ocean, and 10% from the tropics.

The Benguela Current System is associated with substantial coastal upwelling driven

by northward winds across the surface ocean, stimulating westward Ekman offshore transport. Offshore surface ocean transport (Figure 1.7 and 1.10) causes upwelling of cold, nutrient rich deep water, which facilitates phytoplankton growth and high biological activity (Andrews and Hutchings, 1980). The Benguela Current System is also associated with a band of hypoxia, known as an Oxygen Minimum Zone (OMZ) through weak ventilation of the subsurface layer, between ∼100-400m (Arntz et al., 2006; Karstensen et al., 2008). Only areas south of 20°S are typically affected by severe hypoxia (Helly and Levin, 2004; Arntz et al., 2006). Typically, the relatively low-oxygen Indian Ocean water gives a relative minimum ($<210\mu\mathrm{mol\,kg^{-1}}$) at intermediate levels (Mercier et al., 2003).

Benguela Current transport ranges between 16-32Sv, with individual estimates of 26Sv (upper 1000m, 30°S (Stramma, 1989)), 25Sv (upper 1500m, 30°S (Gordon et al., 1992)), 16±1Sv (upper 1000m, 30°S (Garzoli and Gordon, 1996)), 32±4Sv ($\sigma_1<32.1$ (upper 1000-1400m), east of 9°W (Mercier et al., 2003)) and 28±4Sv ($\sigma_1<32.1$ (upper 1000-1400m), east of 10°E (Mercier et al., 2003)). Transport appears to remain steady from its origin as it progresses northwards and eastwards towards the South American coast.

1.2.4.10 Weddell Gyre

Orsi et al. (1999) suggest that the Weddell Sea contributes more than 60% of global AABW, however estimates of the net Weddell Sea contribution has decreased over time (Jacobs, 2004; Meredith, 2013). Knowledge of circulation within the Weddell Sea stems from Svedrup (1953), Gill (1973) and Carmack and Foster (1975), who characterise the westward flowing southern limb of the Weddell Gyre and the Antarctic Slope Current (ASC) inflow along the Antarctic shelf from east of the Weddell Sea. ASC is predominately comprised of Circumpolar Deep Water and AABW, and hugs the coastline into the Weddell Sea. Within the Weddell Sea, additional AABW is ventilated and formed by interacting with the Filchner-Ronne (Whitworth et al., 1998) and Larsen (Fahrbach et al., 1995; Weppernig et al., 1996) ice shelves. The detailed nature of ice shelf interactions and potential for changes to the ice-mass loss is a topic of current research (Hellmer et al., 2012).

The westward-flowing southern limb closes the cyclonic Weddell Gyre circulation. The gyre effect causes Weddell Sea-formed deep water and bottom water to follow a northward pathway along the eastern coast of the Antarctic Peninsula, and subsequent eastward pathway, partially guided by the South Scotia Ridge. Some AABW escapes into the western South Atlantic basin (9.7±3.7Sv Naveira Garabato et al. (2002b))

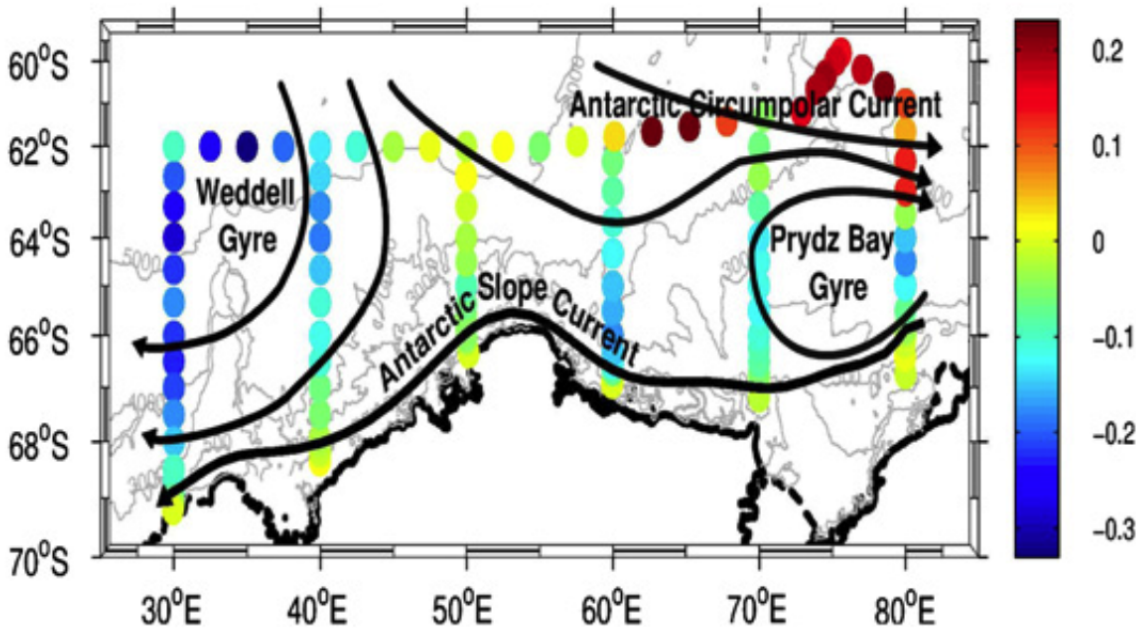

Figure 1.11: Sea Surface Height (SSH) from a CTD survey along the Antarctic coast. Each coloured circle represents a station. Heights are relative to the stations closest to the coastline, which have 0m. Major circulation patterns are added based on approximate SSH streamlines. From Meijers et al. (2010).

whilst the remainder characterises the eastward flowing limb of the Weddell Gyre. Weddell Gyre closure occurs east of 30°E (Park et al., 2001), with the westward-flowing Weddell Gyre return flow merging with the ASC (Figure 1.11 from Meijers et al., 2010).

1.2.5 Water mass transformation mechanisms

1.2.5.1 Diapycnal Mixing

Along isopycnal flow is vital for the modification of upwelled deep water through atmospheric interaction as part of closing the MOC (section 1.2.4.1, Toole and McDougall (2001)). Diapycnal processes provide an alternative pathway for deep ocean waters to reach the upper ocean. The contribution of diapycnal fluxes to the large-scale circulation was tackled in the pioneering work of Munk (1966) giving a diapycnal diffusivity of $K \sim 10^{-4}\mathrm{m}^2\mathrm{s}^{-1}$. Observational analysis since Munk (1966)'s estimate has sought to prove/disprove the reliability of Munk (1966)'s diapycnal diffusivity estimate. Analysis has included inverse box models (e.g. Ganachaud (1999); Sloyan and Rintoul (2000, 2001a); Naveira Garabato et al. (2003); Jullion et al. (2010a)), general circulation models (Toggweiler and Samuels, 1997) and increasingly in situ observations (Webb and Suginohara, 2001; Ledwell et al., 2011), and typically indicate a lower diapycnal diffus-

ivity ($K \sim 10^{-5}\mathrm{m}^2\mathrm{s}^{-1}$) than calculated by Munk (1966). Marshall and Speer (2012) suggested that low diapycnal diffusivities are consistent with a plausible circulation (Zika et al., 2009). Higher diapycnal diffusivities are limited, both spatially to areas of rough topography (Toole et al., 1994; Polzin et al., 1997; Ledwell et al., 2000; Heywood et al., 2002; Naveira Garabato et al., 2009), and temporally by the seasonal cycle of surface wind stress (Wu et al., 2011).

1.2.5.2 Air-sea interaction

Outcropping of isopycnals provides an opportunity for water mass heating or cooling at the surface (Walin, 1982). Changes in temperature facilitates changes in density and transformation of water masses across isopycnals (Speer and Tziperman, 1992; Tziperman and Speer, 1994). Diapycnal flux from light to dense, demands density supply from either the convergence of diapycnal density fluxes, or from air-sea interaction. At the surface, densification corresponds with ocean cooling and evaporation. Air-sea interaction driven transformation potentially occurs anywhere with isopycnal outcropping whether within the North Atlantic (Speer and Tziperman, 1992), Mediterranean Sea (Tziperman and Speer, 1994), North Pacific (Ladd and Thompson, 2001), or South Indian (Karstensen and Quadfasel, 2002). For a Southern Ocean inverse box model, Sloyan and Rintoul (2001a,b) estimate a 8Sv transformation of Surface water to Antarctic Intermediate Water across the Atlantic sector of the Southern Ocean.

1.2.5.3 Freshwater Cycle (Evaporation-Precipitation)

The freshwater or hydrological cycle unites land, ocean and atmospheric processes. For the ocean, input is by precipitation, river runoff or ice melt, and output by evaporation. These processes cause freshening and salinification of ocean surface waters. Precipitation and evaporation typically dominate at the large scale, with river runoff accounting for ∼10% (Dai and Trenberth, 2002). Upon assuming a steady state salinity distribution, freshwater input establishes a gradient of freshwater from a region of net precipitation to a region of net evaporation. Historical observations of precipitation over the ocean are understandably sparse and rely on ship-borne, in situ measurements. Only with the proliferation of oceanographic satellites that measure: sea surface temperature (SST), sea surface roughness, ocean colour and sea surface height (Robinson, 2004), has the large-scale observation of the oceanic hydrological cycle been possible (Schanze et al., 2010).

Over a long-term average, the global freshwater transport must balance to nearly

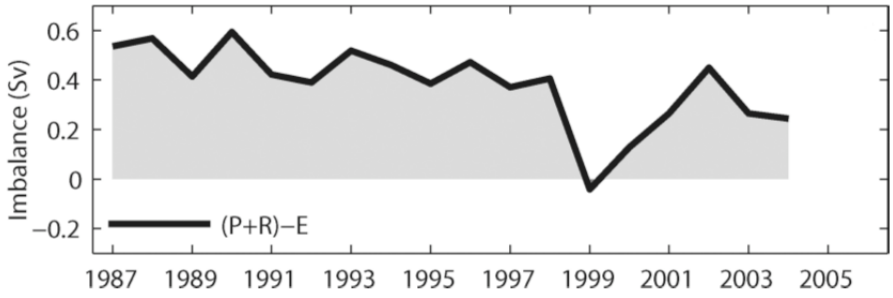

Figure 1.12: Global oceanic freshwater imbalance between (Precipitation + River run-off) - Evaporation, (P+R)-E (solid black line) from Schanze et al. (2010) for GPCP (Global Precipitation Climatology Project) and OAFlux (Objectively-Analyzed Ocean-Atmosphere Fluxes) climatologies from 1987-2006. Positive regions are shaded in light gray, and indicate net gain of freshwater. From Schanze et al. (2010).

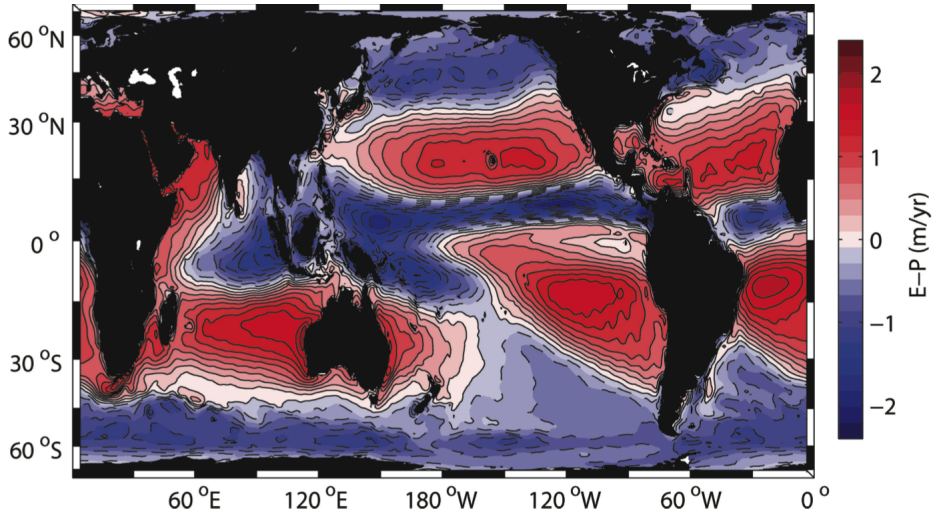

Figure 1.13: Global annual average Evaporation - Precipitation (E-P) map for 1987-2006 from Schanze et al. (2010).

zero. Currently available datasets, as observed by Schanze et al. (2010) (Figure 1.12), give a net imbalance associated with measurement uncertainty, particularly within the polar regions (Talley et al., 2011) through spatial and temporal undersampling, with an associated accuracy of 5-10% (Quartly et al., 2007; Yu et al., 2008; Schanze et al., 2010). The analysis by Schanze et al. (2010) gives the global net E-P distribution of Figure 1.13. Precipitation dominates the South Atlantic sector of the Southern Ocean whilst evaporation dominates for the region south of the equator in the subtropical gyre.

1.3 Chemical Perspective: Oceanic Carbon System

1.3.1 Introduction to carbon system

The global carbon system is comprised of interaction between ocean, atmosphere and land reservoirs. Variability of each reservoir on a variety of temporal and spatial scales adds to the complexity of the system. Short-term fluxes are controlled predominately by photosynthesis and respiration within plants and soil (e.g. Chapin et al., 2009; Dorrepaal et al., 2009). Long-term fluxes are associated with weathering processes related to events on geological timescales of 10-100 million years (Berner, 1990), and glacial-interglacial timescales of 10000-100000 years (Jansen et al., 2007). Spatial scales for investigation range from the global scale to ocean basin scale, for example within the Southern Ocean (Swart et al., 2012), to small biological scales for plankton and particulate organic matter (Falkowski, 2012; Wilson et al., 2012).

Exchange between each reservoir is facilitated by CO_2 gas exchange, flow of DIC in rivers and burial of inorganic forms, such as calcium carbonate ($CaCO_3$) (Emerson and Hodges, 2008). Continuous interaction between the atmosphere and ocean allows CO_2 to be readily absorbed into the surface ocean. CO_2 immediately reacts with water to form bicarbonate (HCO_{3^-}) and carbonate (CO_3^{2-}) ions. Collectively, CO_2, HCO_{3^-} and CO_3^{2-} are known as Dissolved Inorganic Carbon (DIC). Within the ocean, DIC is distributed according to both the solubility pump and biological pump (Raven and Falkowski, 1999; Emerson and Hodges, 2008). The solubility pump is dependent on the MOC (Denman et al., 2007) through enhanced CO_2 solubility in the cold, high latitude oceans. NADW formation occurs for cold, dense surface water that is therefore comparatively rich in CO_2, and contributes towards enrichment of the deep ocean CO_2. Elsewhere, for example in the equatorial Pacific, water is upwelled and heated, facilitating degassing to the atmosphere.

The biological pump in contrast relies upon absorption of CO_2 by phytoplankton for photosynthesis. Organic particulate matter sinks, and below the surface ocean bacterial respiration facilitates remineralisation, returning organic carbon to dissolved inorganic CO_2. Approximately 90% of particulate matter follows this pathway, with hence 5-10% escaping to the deep ocean (Martin et al., 1987; Wakeham and Lee, 1993; Wakeham, 2000). Only $<$1% of primary production reaches the seafloor. An additional component of the biological pump relies on the dissolution of calcium carbonate, which makes a $\sim$20% contribution to the vertical CO_2 gradient, compared to $\sim$70% for organic particulate matter sinking and $\sim$10% for the solubility pump (Figure 1.14, Sarmiento and Gruber (2006)).

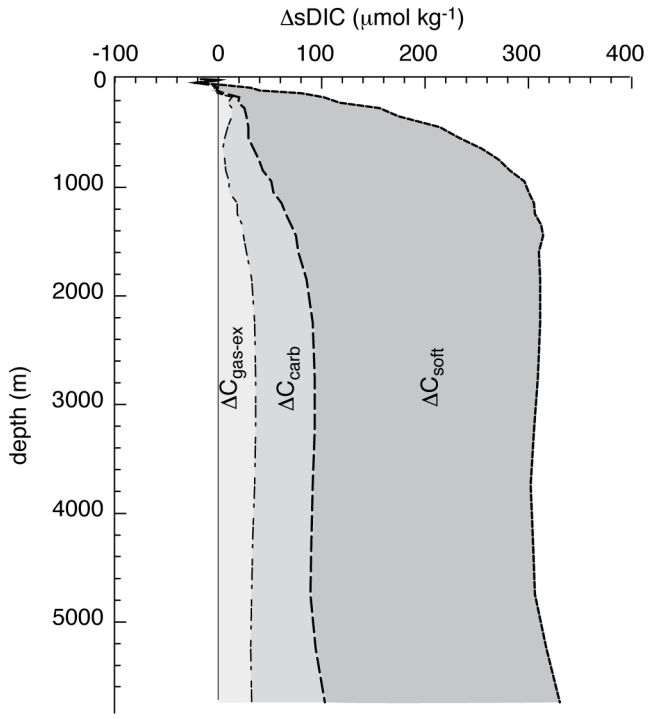

Figure 1.14: From Sarmiento and Gruber (2006), global mean profiles for the contribution of organic particulate matter sinking (ΔC_{soft}), dissolution of calcium carbonate ($\triangle C_{carb}$) and the solubility pump ($\triangle C_{gas-ex}$). $\triangle$sDIC is the change in DIC, when DIC is normalised to constant salinity.

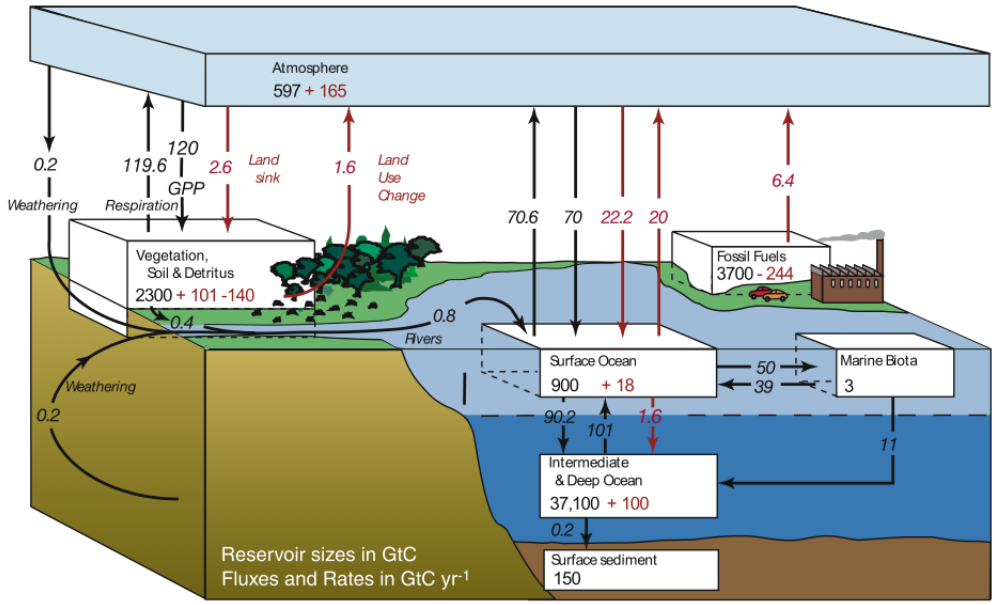

Figure 1.15: Schematic of the global carbon cycle from Denman et al. (2007), modified from Sarmiento and Gruber (2006). The pre-industrial reservoir and associated fluxes are in black, and anthropogenic fluxes are in red.

Both land and ocean reservoirs naturally acts as both source, adding carbon to the atmosphere, and sink, removing carbon from the atmosphere. Schematically, the source/sink for each reservoir is included in the representation by Denman et al. (2007). The reservoir of pre-industrial CO_2 within the intermediate and deep ocean (37100GtC) clearly exceeds all other storage sites, and emphasises the magnitude of the contribution that the ocean makes to the carbon cycle. Given the present day increases in atmospheric CO_2 ($\sim$ 165GtC), the ocean acts as an important buffer by absorbing $\sim$ 118GtC. The buffering capacity of the ocean, given that atmospheric CO_2 is predicted to continue to rise in the near future (Friedlingstein et al., 2011) is suggested to be finite (e.g. Thomas et al. (2007)). A side-effect of ocean buffering is that additional acidic CO_2 consumes carbonate ions and lowers ocean pH. The prospect of ocean acidification, and its affect on a plethora of ocean species, has been the subject of intense research (Caldeira and Wickett, 2003; Orr et al., 2005; Hoegh-Guldberg et al., 2008; Doney et al., 2009a).

1.3.2 Changing ocean properties

The following section reviews the variability in ocean properties with particular focus on the Southern Ocean and South Atlantic, which are the focus of this study. Further information is available within the references provided.

1.3.2.1 Dissolved Inorganic Carbon (DIC)

Since the industrial revolution, global atmospheric CO_2 levels have risen by 38% from 281ppm (Canadell et al., 2007) to 395.09ppm in January 2013 (http://www.esrl.noaa.gov/gmd/ccgg/trends/global.html). Atmospheric CO_2 increase is mediated by absorption into the ocean's upper layers with recent estimates of 2.2±0.4 Pg C yr^{-1} for the global ocean sink (Le Quéré et al., 2009). Increases in ocean DIC concentration have the potential to affect how the ocean carbon cycle copes with enhanced atmospheric CO_2, impacting the ocean's ability to act as a CO_2 sink both now (Gruber et al., 2009) and in the future (Le Quéré et al., 2007; Lovenduski and Ito, 2009). The rate of absorption for CO_2 from the atmosphere is dependent on oceanic CO_2 saturation (Le Quéré et al., 2010; Keeling et al., 2011; Barbero et al., 2011), with forward simulations suggesting enhanced ocean saturation acts as a positive feedback for further increases in atmospheric CO_2 concentration (Crueger et al., 2008; Roy et al., 2011).

The first direct observation of ocean DIC increase was in the late 1970s (Brewer, 1978; Chen and Millero, 1979). DIC variability is comprised of both natural and anthropogenic DIC variability (Etheridge et al., 1996; Gloor et al., 2010). Separating the anthropogenic component from the total DIC concentration is achieved using a number of available methods. As the anthropogenic component is not chemically different, estimates often rely upon separating out a pre-industrial DIC estimate (e.g. Gruber et al., 1996; Touratier and Goyet, 2004b). Alternative estimates for anthropogenic DIC typically rely upon calculating changes between two occupations of the same cruise track (e.g. Wallace, 1995; Friis et al., 2005), or using alternative tracer methods (e.g. Hall et al., 2002). Recent changes in content associated with trends and variability of total DIC have been calculated in Kawakami et al. (2007); Wakita et al. (2010), in addition to anthropogenic CO_2 calculations using ocean models (Le Quéré et al., 2007; Cao et al., 2009; Lovenduski and Ito, 2009), ocean observations of anthropogenic CO_2 (Lo Monaco et al., 2005b; Mikaloff Fletcher et al., 2006; Murata et al., 2007, 2008, 2010; Vázquez-Rodríguez et al., 2009b; Sabine and Tanhua, 2010; Wanninkhof et al., 2010) and atmospheric inversions (Patra et al., 2005).

The Southern Ocean is suggested by Sabine et al. (2004) to store only 9% of the global ocean's anthropogenic CO_2 inventory, whilst Gruber et al. (2009) suggests that the Southern Ocean across all latitudes is the largest oceanic sink region for atmospheric CO_2. Estimates for the Southern Ocean CO_2 sink include 0.34±0.20 Pg C yr^{-1} (ocean inversion)/ 0.30±0.17 Pg C yr^{-1} (pCO_2 climatology) (Gruber et al., 2009), and 0.4±0.25Pg C yr^{-1} (oceanic DIC/alkalinity climatology, McNeil et al., 2007), compared to ∼0.75 Pg C yr^{-1} for anthropogenic carbon only (Mikaloff Fletcher et al., 2006; Gru-

ber et al., 2009). Difference between the location of atmospheric CO_2 uptake, and the location of storage suggests that oceanic DIC is transported out of the uptake region by ocean circulation (Broecker and Peng, 1992), in addition to the air/sea exchange of CO_2 (Barbero et al., 2011).

Surface ocean waters are the most directly affected by CO_2 absorption from global (Takahashi et al., 2009), and regional observations (Bates, 2001; Murata et al., 2007, 2008, 2010). The surface ocean provides surface area for CO_2 absorption, whilst the deep ocean contains a huge volume of water able to store both natural and anthropogenic CO_2. In the Southern Ocean, outcropping NADW rich in DIC and nutrients from accumulation of remineralised organic matter, outgasses natural CO_2 (McNeil et al., 2007) and uptakes anthropogenic CO_2. This partially contributes to AABW upon formation, and allows recently ventilated AABW to inject anthropogenic CO_2 into the deep ocean (Klatt et al., 2005; van Heuven et al., 2011). Northward flow of recently ventilated waters facilitate anthropogenic CO_2 influence within the subtropical South Atlantic (Murata et al., 2008; Peng and Wanninkhof, 2010; Ríos et al., 2010; Wanninkhof et al., 2010) as well as the South Atlantic sector of the Southern Ocean (Arrigo et al., 2008; Hauck et al., 2010; van Heuven et al., 2011).

Within the ACC, hydrographic fronts experience meridional variability in their position, on interannual to decadal timescales (Sokolov and Rintoul, 2009a,b). In the vicinity of the ACC fronts, atmospheric CO_2 follows a pathway down outcropped isopycnals into the ocean interior with front variability affecting outcropping (Caldeira and Duffy, 2000; Sabine et al., 2004). The latitude of the ACC fronts impacts Mode Water formation on the equatorward side of the SAF, surface water subduction on the poleward side of the PF, and hence, impacts AAIW ventilation (Naveira Garabato et al., 2009; Meredith et al., 2011b). Ventilation of intermediate water masses, allows subduction of higher anthropogenic CO_2 waters into the ocean interior.

The ability of the ocean to absorb atmospheric CO_2 is inherently linked to ocean circulation and will be further explored later in this thesis. In addition, other ocean properties can be used to indicate the anthropogenic component and are discussed in the following subsections.

1.3.2.2 Nutrients

The Southern Ocean is well-known for high nutrient concentrations (e.g. nitrate and phosphate). However, despite apparent nutrient availability, chlorophyll concentrations within the upper ocean remain low (Tréguer and Jacques, 1992; Comiso et al., 1993; Sullivan et al., 1993; Banse, 1996). The Southern Ocean is therefore, an example of a

high nutrient-low chlorophyll (HNLC) zone (Martin et al., 1990; Moore and Abbott, 2000).

Remineralisation of organic matter into inorganic components is typically represented as the reverse of the process of organic matter synthesis at the surface (Sarmiento and Gruber, 2006) according to :

$$\underbrace{C_{106}H_{175}O_{42}N_{16}P}_{\text{organic}} + 150\text{O}_2 \rightleftharpoons \underbrace{106CO_2 + 16HNO_3 + H_3PO_4 + 78H_2O}_{\text{inorganic}} \tag{1.1}$$

Remineralisation stoichiometries below 400m are slightly different with $\text{P/N/C/O}_2 = 1/16/117/-170$ (Anderson and Sarmiento, 1994) and these stoichiometries will be used later in the thesis. Average nutrient stoichiometries, similar both in inorganic form in ocean waters, and in organic form within plankton (Redfield et al., 1963; Falkowski, 2000), are commonly termed 'Redfield ratios' following Redfield et al. (1963). Organic matter nutrient ratios are typically also dependent on the phytoplankton species responsible for export from the surface layers (Arrigo et al., 1999; Ho et al., 2003; Quigg et al., 2003). Southern Ocean Spring blooms, typically between October to December in the Southern Ocean, may cause stoichiometries that exceed Redfield ratios, with nutrient depletion of the surrounding ocean water (Figure 1.1, Rubin (2003); Green and Sambrotto (2006)). By January-February, enhanced remineralisation causes additional inorganic nutrient production to compensate for excess inorganic nutrient loss during phytoplankton growth.

Period	Biological Carbon Pump Stage
October-December	Phytoplankton growth stage
January-February	Enhanced remineralisation
March onwards	Vertical mixing of inorganic nutrients to surface

Table 1.1: Southern Hemisphere seasonal variation of the biological carbon pump, within the Antarctic Circumpolar Current zone, south of the Subtropical Front. (Rubin, 2003; Green and Sambrotto, 2006)

Alternatively, Redfield ratios are affected through processes of denitrification (Gruber and Sarmiento, 1997; Sarmiento and Gruber, 2006), and nitrogen-fixing (Karl and Letelier, 2008; Mills and Arrigo, 2010; Koeve and Kähler, 2010). Denitrification refers to remineralisation of organic matter by bacteria where nitrate replaces oxygen as the oxidant. At the surface, nitrogen fixation refers to the use of relatively inert, gaseous nitrogen N_2 from the atmosphere for organic matter production and typically occurs in

regions of nitrate depletion.

1.3.2.3 Silica

A typical ocean residence time of 15000 years (Tréguer et al., 1995) to 17000 years (Laruelle et al., 2009), requires the origin of silica to be discussed in a palaeo-context. Silica enters the ocean through the break down of the Earth's crust via a variety of mechanisms, with rivers an important source. Within the water column, high AABW silica concentration ($120 \mu\text{mol}\,\text{kg}^{-1}$) reflects the high rate of biogenic silica production, deposition and recycling, near the Antarctic continent (Mantyla and Reid, 1983; Hsu and Weissert, 1985). Estimates of silica production within the Southern Ocean range from approximately 50 $\text{Tmol}\,\text{Si}\,\text{year}^{-1}$ (Tréguer and Van Bennekom, 1991) to 80 ± 18 $\text{Tmol}\,\text{Si}\,\text{year}^{-1}$ (Pondaven et al., 2000), and approximately one-third of the total marine production of biogenic silica (Tréguer and De La Rocha, 2012). Significant alteration of the silica cycle through anthropogenic influence is likely to affect both carbon sequestration and primary production in the coastal zone (Bernard et al., 2010, 2011).

1.3.2.4 Alkalinity

According to the definition by Millero (2007), total alkalinity is defined as the concentration of all hydrogen ion acceptors (base) that can accept a hydrogen ion (H^+) during the titration of hydrochloric acid (HCl) to the carbonic acid end point. For most waters, alkalinity is reasonably given by bicarbonate $\left(HCO_3^-\right)$, carbonate $\left(CO_3^{2-}\right)$ and boric acid $\left(B\left(OH\right)_4^-\right)$:

$$TAlk = [HCO_3^-] + 2[CO_3^{2-}] + [B\left(OH\right)_4^-]$$

with other bases generally displaying a minor influence. Seawater alkalinity is predominately controlled by precipitation, evaporation, water mass mixing and carbonate dissolution (Cai et al., 2010b). Recent observed alkalinity variability, linked to changes in atmospheric CO_2 (e.g. Raymond and Cole (2003)) are poorly spatially resolved, with alkalinity commonly treated as a conservative parameter (Cai et al., 2010b). The future response of alkalinity to the changing climate is unknown, however, based on the hypothesis of Kheshgi (1995), increased alkalinity would cause enhanced carbon sequestration.

1.3.2.5 Chlorofluorocarbon (CFC)

CFC release into the atmosphere is an unintended side-effect of industrial development with CFCs commonly used as industrial coolants in refrigerators, aerosol spray propellants, foaming agents, cleaning agents, etc since the 1930s (Fine, 2011). Gradual uptake of CFCs from the atmosphere by the ocean helps identify water masses with higher ventilation rates (Hammer and Hayes, 1978; Hahne et al., 1978). A common application of CFC concentration is therefore, as an age estimate, if the CFC concentration measured for a particular water mass corresponds to the year of last atmospheric contact for the water mass. Prinn et al. (2000) and Walker et al. (2000)'s estimate of atmospheric time histories connect CFC concentration and water mass age. Stronger industrial regulation since Montreal Protocol means that the relationship between CFC and age is no longer strictly monotonic (Wanninkhof et al., 2010), reducing the value of oceanic CFC concentrations as age estimates.

1.4 A study of the South Atlantic sector of the Southern Ocean: Aim of the PhD

The aim of this PhD thesis is two-fold for the purposes of answering challenging questions related to the South Atlantic Ocean system. Firstly the aim is to investigate both natural and anthropogenic CO_2 distributions, and secondly, inverse box model-derived general circulation, within the South Atlantic Ocean. The originality within this work consists of the synthesis of the CO_2 data into an inverse box model within the South Atlantic, which is a key conduit for the ACC and MOC. Inverse box methodology has been previously applied to the South Atlantic by Fu (1981) and Rintoul (1991). This work will seek to build on Rintoul (1991)'s methodology by including synoptic hydrographic data, diapycnal and air-sea interaction terms and by solving for additional property fluxes.

Examples of the interesting questions that this study is aimed at addressing are: whether there are significant and robust increases in DIC and anthropogenic CO_2 in the South Atlantic, with this study able to update Chen (1982) to calculate Drake Passage anthropogenic CO_2 distribution. Also, does the inverse box model provide a reasonable circulation for the South Atlantic, compared to previous observations, and what is the MOC volume transport and the freshwater transport associated with the overturning? What is the outflow of NADW underneath the Agulhas Current, that corresponds to the zonal pathway of the DWBC across the Atlantic? And, is the South Atlantic a net

source or sink of CO_2 to the atmosphere? These are examples of questions that will be posed in the later Chapters of this thesis.

Chapter 2

Data

2.1 Introduction

This Chapter reviews the datasets from a series of hydrographic cruises within the South Atlantic Ocean. Each dataset contributes towards creating a boundary at the north, east and west of the South Atlantic, in preparation for studying changes in ocean CO_2, and South Atlantic interbasin exchange using inverse box methodology, in later Chapters. The boundaries are marked in Figure 2.1. Drake Passage is the western boundary, occupied along the A21 WOCE cruise line in 1990 (Roether et al., 1990), and repeated in 2009 (McDonagh, 2009). The eastern boundary is created using the I6S WOCE cruise line occupation south of Africa in 1996 (Poisson et al., 1996), and repeat occupation in 2008 (Speer and Dittmar, 2008). The 24°S transatlantic occupation in 2009 (King, 2010) provides a South Atlantic northern boundary.

This Chapter describes the CTD datasets from each occupation, including physical and biogeochemical data, such as Dissolved Inorganic Carbon (DIC). The latter part of this Chapter discusses some initial data processing and additional datasets that will be used in the remainder of the thesis.

2.2 Hydrographic Cruise Descriptions

2.2.1 Drake Passage (A21 1990)

The 1990 Meteor cruise (expedition designation: 06MT11_5, METEOR No11 leg5) occupied both the A21 (Western Drake Passage) and SR02 (passage south of Africa) WOCE sections. In total, 79 CTD stations were completed after departing from Ushuaia, Chile on 23 January and arriving in Cape Town, South Africa on 8 March.

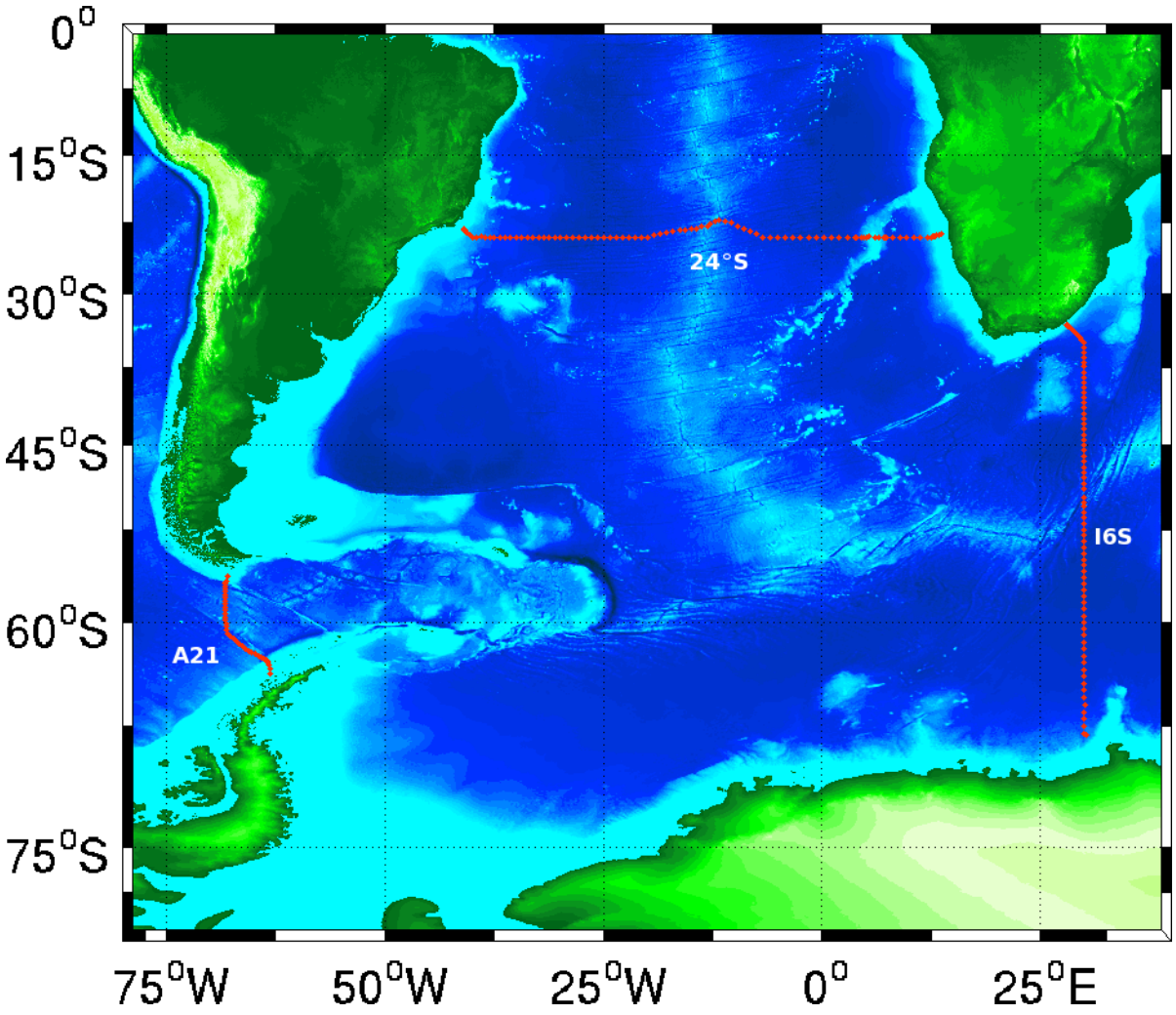

Figure 2.1: South Atlantic bathymetry (Smith and Sandwell, 1997) with hydrographic sections along South Atlantic boundaries, designated by either a WOCE code or a latitude marker for: Drake Passage (A21), 30°E (I6S) and along 24°S. Red markers indicate CTD stations from hydrographic occupations along Drake Passage, 30°E and 24°S in 2009, 2008 and 2009, respectively.

Wolfgang Roether was principal scientist. The A21 portion of the cruise was completed between 23 January and 30 January occupying 16 CTD stations with 9 stations regarded as full-depth for DIC measurements (Figure 2.2a)). From the 7 non-full-depth stations, 6 had a surface measurement only, whilst 1 station recorded DIC to ∼1500dbar.

Each CTD station collected water samples at up to 24 discrete depths. Coulometric analysis of nutrient concentrations used a Technicon auto-analyser, whilst dissolved oxygen measurements used a modified Winkler titration system. Coulometric DIC measurements were by D. Breger and D.W. Chipman with an estimated precision of $1\mu\text{mol}\,\text{kg}^{-1}$. CFC samples were taken using a glass syringe and measured using a gas chromatograph. CFC sampling gave a total error of ∼3%. Total alkalinity was not a measured parameter. Previous analyses using the A21 1990 dataset found minimal difference between hydrographic and nutrient distributions with those of earlier measurements (Roether et al., 1993). More recently, Sudre et al. (2011)'s investigation finds little evidence for Weddell Sea Deep Water at Drake Passage, which is prevented from extending westwards by the Shackleton Ridge at ∼60°W. Further details are available from Roether et al. (1990) and Chipman et al. (1991).

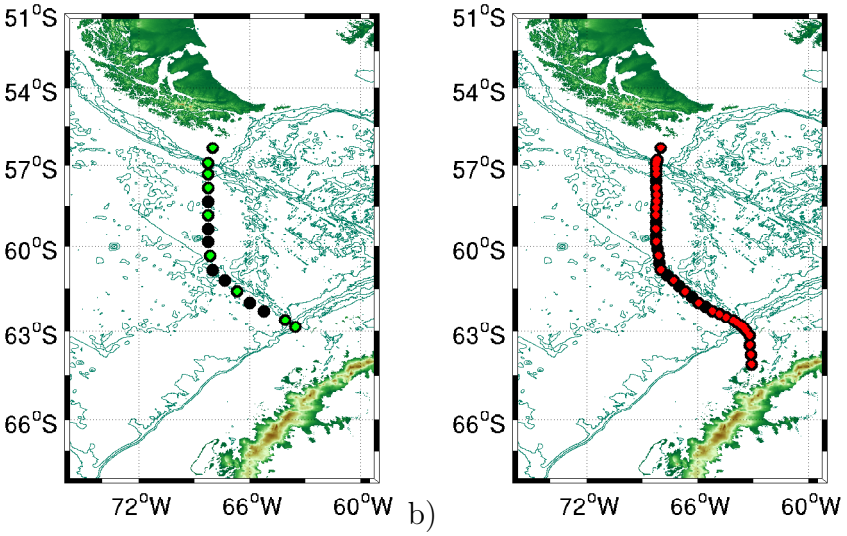

Figure 2.2: Transect of A21 WOCE section occupied in a) 1990 and b) 2009. Black dots represent a CTD station whilst a coloured dot indicates a CTD station with a full-depth DIC profile. The land is shaded, whilst the bathymetry from GEBCO (General Bathymetric Chart of the Oceans) is in 1000dbar intervals.

2.2.2 Drake Passage (A21 2009)

The 2009 James Cook cruise (JC031) was a repeat occupation of the A21/SR1 (western Drake Passage) and SR1b (eastern Drake Passage) WOCE transects as part of the

Oceans2025 Drake Passage sustained measurement program. This program enables an annual hydrographic cruise across eastern Drake Passage, with the 2009 cruise extended to include a repeat of the A21 WOCE cruise line. A total of 84 stations were sampled during the two legs of the cruise, with stations 1-49 along A21/SR1, and stations 50-84 along SR1b. The section was occupied by the James Cook research vessel departing from Punta Arenas, Chile on 3 February and arriving in Montevideo, Uruguay on 3 March, with the A21 leg completed between 3 February and 18 February. Elaine McDonagh was principal scientist.

Salinity, oxygen, nutrients, carbon, total alkalinity and chlorofluorocarbons (CFCs) were measured using a 24 Niskin bottle rosette per station. Nutrient concentrations (phosphate and nitrate) were determined with a Skalar San Plus Autoanalyser following Kirkwood (1996). Analysis commenced within 12 hours of the sample being drawn. The oxygen sensor on-board the CTD rosette was calibrated by Winkler titration following Culberson and Huang (1987) and Holley and Hydes (1994). DIC analysis by coulometry used both a CO_2 extraction unit, and a Versatile Instrument for the Detection of Titration Alkalinity (VINDTA) combined DIC/alkalinity instrument following Johnson et al. (1987) with Dorothee Bakker the team leader. Total alkalinity measurements were by potentiometric titration using two VINDTA instruments (Mintrop, 2004). At least two CRMs (Certified Reference Materials: Batches #90 and #92) were run per station for DIC and alkalinity with DIC sampled for 35 out of the 49 stations along A21, with full-depth profiles available for 31 stations (Figure 2.2b). Both DIC and TA accuracy is estimated as $3\mu\mathrm{mol\,kg^{-1}}$. CFC sampling involved collection in a 500ml glass stopper sealed bottle and maintained at $<5°$C prior to analysis. CFC and SF6 analysis was based on W. Smethie, E. Gorman, pers. com (McDonagh, 2009) and the use of a gas chromatograph. Further details are available from McDonagh (2009).

2.2.3 30°E (I6S 1996)

In 1996, the I6S section south of Africa was occupied between 1 February and 31 March, departing from and returning to Durban, South Africa on-board the R/V Marion Dufresne research vessel. This was the second occupation of the section following an aborted 1993 cruise, aboard the same ship. In total, 98 casts were sampled, with the cruise sampling occurring north to south along the section. Two casts were sampled for each station with the first cast from the surface to 1350 dbar, and a second cast from 1350 dbar to the bottom to obtain greater vertical resolution. Combining 98 separate casts, 58 stations sampled DIC with 51 regarded as full-depth station profiles, shown in Figure 2.3. The principal scientists on-board were Alain Poisson, Nicolas Metzl and

Christian Brunet.

Salinity, oxygen, nutrients, carbon, total alkalinity and chlorofluorocarbons (CFCs) were all measured using a 24-bottle rosette. From Lo Monaco et al. (2005b), a Guildline salinometer in a constant temperature laboratory measured salinity, an automatic Winkler potentiometric titration system measured oxygen and two automatic Technicon analysers measured nitrate, silicate and phosphate. DIC was measured using a potentiometric system with certified reference materials simultaneously measured as standards for TA and DIC concentrations. DIC yields uncertainties of $1.9\mu\text{mol}\,\text{kg}^{-1}$ with a DIC and TA accuracy of $\pm 3.1\mu\text{mol}\,\text{kg}^{-1}$ and $\pm 2.4\mu\text{mol}\,\text{kg}^{-1}$, respectively (Lo Monaco et al., 2005b). CFC samples were collected in a 100mL syringe directly from Niskin bottles prior to gas chromatograph analysis. Further details are available in Poisson et al. (1996), Park et al. (2001) and Lo Monaco et al. (2005b). Previous examinations of the I6S 1996 dataset revealed abrupt gradients throughout the water column to characterise the Polar Front, and concluded that the Weddell Gyre extends east of 30°E (Park et al., 2001). A further study by Lo Monaco et al. (2005b) exclusively using the I6S 1996 dataset calculated larger anthropogenic CO_2 storage in the Antarctic Zone (south of 51°S), compared with midlatitude regions.

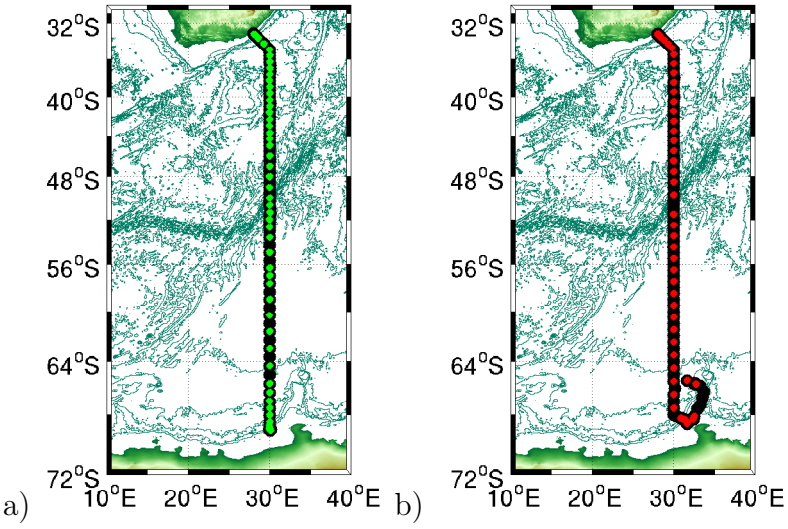

Figure 2.3: Transect of the I6S WOCE section occupied in a) 1996 and b) 2008. Black dots represent a CTD station whilst a coloured dot indicates a station with a full-depth DIC profile. The land is shaded, whilst the bathymetry from GEBCO (General Bathymetric Chart of the Oceans) is in 1000dbar intervals.

2.2.4 30°E (I6S 2008)

The I6S hydrographic section was repeated in 2008 departing from Durban, South Africa on 4 February and arriving at Cape Town, South Africa on 17 March on-board the R/V Revelle research vessel as part of the World Climate Research Programme (WCRP)'s Climate Variability and Predictability (CLIVAR) project. As the result of a large storm to the south, the cruise diverted eastward from the 30°E line, before progressing further southward to the ice edge. The missing part of the 30°E section was completed on the northward return. The principal scientist on-board was Kevin Speer. Out of 106 stations, 55 were full-depth DIC profiles (Figure 2.3b), with a 36-bottle rosette. Additionally, 22 stations are sampled within the upper 200-2000dbar only. The team leader for the DIC measurements was Rik Wanninkhof.

A ODF-modified Technicon AutoAnalyzer II determined nutrient concentrations following the methods of Gordon et al. (1993). Nitrate and phosphate analysis followed a modification of Armstrong et al. (1967) and Bernhardt and Wilhelms (1967), respectively. Calibration of the oxygen sensor followed the modified-Winkler titration of Carpenter (1965) and Culberson et al. (1991). DIC analysis by coulometry consisted of a coulometer coupled to DIC Extractor (DICE) inlet system, as an in-house modernisation of the SOMMA (Single Operator Multiparameter Metabolic Analyzer) system (Johnson et al., 1985, 1987; Johnson, 1992; Johnson et al., 1993). Total alkalinity analysis was performed using potentiometric titration (Dickson et al., 2003). CFC sampling involved ∼100mL glass syringe flushed several times to avoid air bubbles, prior to using a gas chromatograph (Speer and Dittmar, 2008). Sampling accuracy was monitored using CRMs Batch #85 for DIC and Batch #86 for alkalinity, supplied by Andrew Dickson of Scripps Institution of Oceanography. Further information is available in Speer and Dittmar (2008).

2.2.5 24°S (2009)

In 2009, the James Cook research vessel occupied a South Atlantic Ocean section (JC032) departing from Montevideo, Uruguay on 7 March and arriving at Walvis Bay, Namibia on 21 April, funded under the Oceans2025 program to measure standard CLIVAR physical, chemical and biological parameters. The Brazil Current was intersected three times prior to beginning the main transatlantic section at 24°S. In total, 118 stations were sampled with 96 stations along 24°S and 88 stations with full-depth DIC profiles, shown in Figure 2.4. The principal scientist was Brian King.

A 24-bottle rosette was used for salinity, oxygen, nutrients, carbon, total alkalinity

and chlorofluorocarbons (CFCs) measurements. Nutrient samples were stored below 4°C, prior to analysis, usually within 4 hours of collection. Analysis by a continuous-flow Skalar San Plus Autoanalyser follows a slightly modified version of Kirkwood (1996). Dissolved Oxygen calibration used a Winkler Ω-Metrohm titration unit and followed Culberson and Huang (1987). DIC water sample collection followed Dickson et al. (2007) with samples kept in the dark and cold prior to analysis. Ute Schuster was the DIC team leader. DIC analysis used two instruments: SOMMA and VINDTA, whilst two VINDTA instruments measured total alkalinity (Mintrop, 2004; Dickson et al., 2007). CRMs (Batch #90) varied by $\pm 3.3 \mu\text{mol kg}^{-1}$ and $\pm 3.4 \mu\text{mol kg}^{-1}$ for each instrument respectively. Preparation of chemical reagents followed Dickson (1994), and recommendations by Dickson (1994) and Holley and Hydes (1994) were adopted. CFC samples were collected in 500mL glass stopper sealed bottles and stored below 5°C. A gas chromatograph was used for analysis. Further details are available in King (2010).

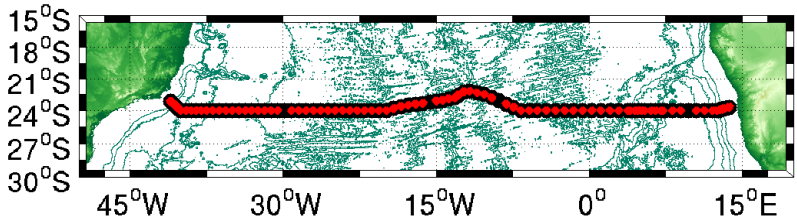

Figure 2.4: Transect of the transatlantic section at 24°S occupied in 2009. Black dots represent a CTD station whilst a coloured dot indicates a station with a full-depth DIC profile. The land is shaded, whilst the bathymetry from GEBCO (General Bathymetric Chart of the Oceans) is in 1000dbar intervals.

2.2.6 GLODAP/CARINA calibration factors

Differences between measurements from separate occupations of the same cruise track are subject to uncertainties as to whether the observed changes are real, or generated from biases within the dataset. In this instance, all hydrographic cruises are quasi-seasonal, occurring between late January and mid-April in austral summer, hence seasonal variability is assumed negligible. To eliminate systematic measurement biases, A21 1990 and I6S 1996 parameters were adjusted with GLODAP/CARINA calibration factors (Gouretski and Jancke, 2000; Wanninkhof et al., 2003; Key et al., 2004; Hoppema et al., 2009). For I6S 1996, these calibration factors are discussed further in Hoppema et al. (2009) and Lo Monaco et al. (2010). These databases are constructed using rigorous quality control, including cruise crossover analysis of high-quality historical cruise datasets. No specified adjustments are necessary for DIC for either cruise.

	Salinity	Nitrate	Phosphate	Oxygen	Silicate
A21 (Drake Passage 1990)	+1.1	+0.04	-0.06	+0.03	+4.9
I6S (30°E 1996)	×1.0	×0.96	×0.97	×1.0	×0.9

Table 2.1: GLODAP/CARINA correction factors. Drake Passage adjustments are additive with units μmol kg^{-1}, whilst adjustments along 30°E are multiplicative. Salinity listed as additions in parts per million, and oxygen listed in units of ml/l requiring multiplication by a factor of 43.55 to convert to μmol kg^{-1}.

2.3 Data processing

2.3.1 Neutral density

Large-scale ocean circulation is driven by density gradients created by changes in temperature and salinity. Density is therefore a function of temperature, salinity and pressure across the global ocean. As density changes with pressure, oceanographers developed the potential density term to express density for each water parcel if adiabatically brought to a reference pressure. In practice in the deep ocean, multiple reference pressures are typically applied requiring multiple potential densities to be defined. As a simplification, neutral density (γ^n) developed by Jackett and McDougall (1997) is preferred.

For both Drake Passage, 30°E and 24°S hydrographic properties are vertically interpolated using least squares fitting from their native 2dbar grid, or bottle data pressures, across a $\pm 0.04\gamma^n$ vertical range onto a $0.01\gamma^n$ grid. For visualisation in pressure coordinates, hydrographic properties on γ^n coordinates are linearly interpolated onto a 20dbar pressure grid. Neutral density allows the definition of water masses based on neutral density interfaces (Table 2.2) following definitions for the Southern Ocean from Orsi et al. (1999); Heywood and King (2002); Naveira Garabato et al. (2002b) and Naveira Garabato et al. (2009). NADW is not included as a separate water mass but is chosen to comprise lower UCDW and upper LCDW within a $27.90 \leq \gamma^n \leq 28.10$ range. These water mass definitions will remain valid for the entire remainder of the thesis.

2.3.2 Geopotential height

ACC fronts vary in latitude primarily on annual and decadal timescales (Thorpe et al., 2002; Yuan et al., 2004; Sokolov and Rintoul, 2007, 2009a,b) with any long-term shifts currently unclear (Böning et al., 2008; Graham et al., 2012). To account for northward/southward shifts associated with ACC front variability, geopotential height is applied as the respective x-coordinate. Geopotential height φ is calculated by first

Water Masses	Upper limit	Lower limit
Surface Water	surface	26.80
SAMW	26.80	27.23
AAIW	27.23	27.50
UCDW	27.50	28.00
LCDW	28.00	28.26
AABW	28.26	bottom

Table 2.2: Neutral density interfaces for major water masses within the Southern Ocean: Surface Water, Subantarctic Mode Water (SAMW), Antarctic Intermediate Water (AAIW), Upper Circumpolar Deep Water (UCDW), Lower Circumpolar Deep Water (LCDW) and Antarctic Bottom Water (AABW).

estimating the geopotential Φ for each station:

$$\Phi = \int_0^z g\left(\phi, z\right)\, dz = \int_0^p -\alpha\, dp \tag{2.1}$$

and represents the variability of gravity, $g\left(\phi, z\right)$ over a given depth z, for latitude ϕ , or alternatively the integral of the specific volume, $\alpha\,(= {}^1/_\rho)$ over a given pressure (Figure 2.5). For a given isobar pair, geopotential differs between isobars by $\Phi\left(P_1\right) - \Phi\left(P_2\right)$ (Figure 2.5). Geopotential height in this study is given by the geopotential difference divided by gravity:

$$\varphi = \frac{\left(\Phi\left(P_1\right) - \Phi\left(P_2\right)\right)}{g_o} \tag{2.2}$$

where $g_o = 9.8\mathrm{ms}^{-2}$. In this study, geopotential height is calculated at 500dbar (P_2) relative to 1500dbar (P_1), similar to Naveira Garabato et al. (2009), giving a x-coordinate with units of geometric metres, that includes the dominant thermohaline variability (Rintoul et al., 1997; Yuan et al., 2004; Swart et al., 2008; Böning et al., 2008).

φ is favoured as an x-coordinate due to its quasi-monotonic relationship with latitude, and ability to represent cross-passage water mass fluctuations associated with ACC front variability. Hydrographic properties are horizontally interpolated by selecting a central station, and applying least squares fitting across a ± 2 station range and subsequent linear interpolation onto a 0.02 φ grid. North of 35°S along I6S, the geopotential height/latitude monotonicity breaks down (Figure 2.6b), hence only south of 35°S φ is substituted for latitude. A 0.02 φ grid is applied between 35°S and 58°S whilst in the slightly stratified waters south of the 58°S, a 0.002 φ grid is applied. The result is for both the more recent and historical dataset along Drake Passage and 30°E

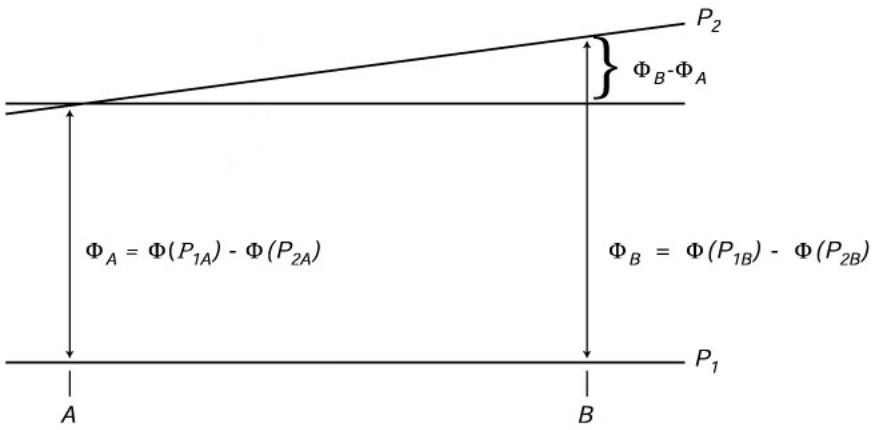

Figure 2.5: Schematic diagram of geopotential Φ, geopotential anomaly ($\Phi_B - \Phi_A$) and geopotential height definition. A and B are hydrographic stations, and P_1 and P_2 are along section isobars. Adapted from Stewart (2008).

respectively, to occupy the same geopotential height range. For visualisation, geopotential height is re-converted to latitude using the best fit line in Figure 2.6 a) and b). The best fit line is constructed by interpolating the station latitudes to match the 0.02φ grid intervals and fitting with a polynomial. This polynomial gives a latitude coordinate for every φ grid point for latitude/φ conversion. For 24°S, vertical gridding is the same as Drake Passage and 30°E, however, the dataset is interpolated in the horizontal onto a 0.2° longitude grid.

2.4 Alkalinity

For the Drake Passage 1990 occupation, alkalinity was not measured. This study therefore creates a pseudo-alkalinity field based on the assumption that alkalinity has changed little in the ocean over the period between 1990 and 2009 (Ilyina et al., 2009; Doney et al., 2009a), and differently to DIC, due to differing responses to pelagic calcification, remineralisation of organic matter and the freshwater cycle. The 2009 alkalinity field is therefore linearly interpolated in the vertical and horizontal in neutral density space onto CTD coordinates from the 1990 occupation. Nearest neighbour extrapolation extends the data to the seafloor. The 1990 alkalinity field therefore has an additional uncertainty of $\pm 10 \mu\text{mol}\,\text{kg}^{-1}$.

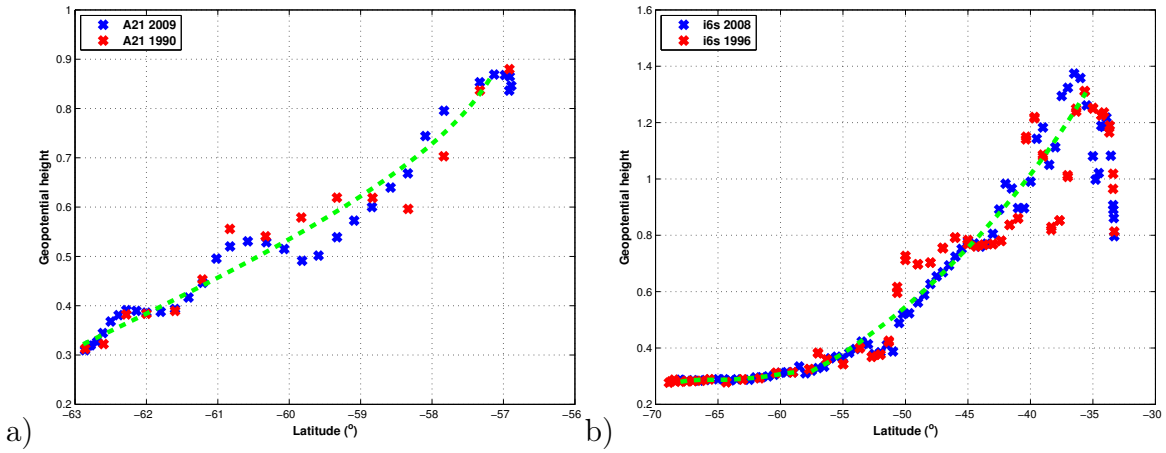

Figure 2.6: Distribution of geopotential height φ a) across Drake Passage for both A21 1990 (red x) and A21 2009 (blue x), and b) along I6S (30°E) for both I6S 1996 (red x) and I6S 2008 (blue x). The best fit line (green dashed line) is fitted through both latitude datasets along A21 and I6S respectively, and linearly interpolated to match the size of the 0.02 φ grid. Note a 0.002φ grid is applied south of 58°S along I6S. All stations for all cruises use a geopotential anomaly ($\Phi_B - \Phi_A$) at 500dbar relative to 1500dbar.

2.5 Atmospheric chlorofluorocarbon-12 (CFC-12)

In this study, CFC-12 is used as a tracer. Atmospheric CFC-12 data from the Carbon Dioxide Information Analysis Center (CDIAC) in units of parts-per-trillion (ppt) gives a single estimate per year from 1910 to 2011 (Bullister, 2011). The estimates derived since the late 1970's and early 1980's use the available CFC data from a global monitoring program. Estimates prior to this period rely on the estimation of annual industrial production and subsequent compound release into the atmosphere, accounting for atmospheric lifetime (Bullister, 2011). The available time period of the CDIAC dataset therefore limits the maximum calculated water mass age. A Northern Hemisphere and Southern Hemisphere estimate are available, with the Southern Hemisphere estimate used in this study.

2.6 World Ocean Atlas

Separation of the water column into water masses is common practice in oceanography, with differences in water mass composition at different locations depending on thermohaline fields. World Ocean Atlas 2009 (WOA09) contains statistically-derived fields for a range of in-situ oceanographic properties (temperature, salinity, phosphate, nitrate, silicate, dissolved oxygen, Apparent Oxygen Utilisation (AOU), and percent

oxygen saturation) on a 1° grid, interpolated to standard depth levels (Boyer et al., 2005; Antonov et al., 2010; Locarini et al., 2010). Estimates are for monthly, seasonal and annual periods. In this study, an austral summer period from WOA09 (January, February, March) is selected for temperature and salinity fields only (Antonov et al., 2010; Locarini et al., 2010). Seasonally-averaged temperature and salinity fields enable an estimate of seasonally-averaged isopycnal surfaces and water mass interfaces.

2.7 Air- sea heat flux

In this study, air-sea heat flux is represented using NOC (v2.0) climatology, derived from in situ weather reports from Voluntary Observing Ships (VOS) for the period 1973-2009, and optimally interpolated onto a 1° grid. Daily fields are calculated for each grid point and averaged to yield monthly fields with associated uncertainties. In this study, the dataset is restricted to recent years 2002-2009. Seasonally averaged observations are calculated, for austral summer (January, February, March) for each component of the heat flux: latent heat (Q_H), sensible heat flux (Q_E), longwave (Q_{LW}) and shortwave (Q_{SW}) (Grist and Josey, 2003). For the surface of the South Atlantic box, the austral summer average of each heat flux component is summed to give an estimate for the average net heat flux in austral summer. Alternative available heat flux datasets include: NCEP/NCAR Global Reanalysis Project 2 (Kanamitsu et al., 2002), ECMWF Re-Analysis 40 (Uppala et al., 2005) and the Hamburg Ocean Atmosphere Parameters and Fluxes from Satellite Data (HOAPS-3), are reviewed for the Southern Ocean by Liu et al. (2011). In this study, only a single averaged-estimate of net heat flux is required for austral summer, and therefore, likely to be broadly representative.

2.8 Air-sea freshwater flux (Evaporation - Precipitation)

Freshwater flux is commonly represented as evaporation E minus precipitation P, or E-P. Positive freshwater flux at the air-sea interface, equates to loss of freshwater to the atmosphere. A number of products estimate net evaporation minus precipitation, such as NCEP/NCAR Global Reanalysis Project 1, NCEP/NCAR Global Reanalysis Project 2, Modern Era Retrospective-Analysis for Research and Applications, the ECMWF Re-Analysis 40 (Kistler et al., 2001; Kanamitsu et al., 2002; Rienecker et al., 2011; Uppala et al., 2005), as well, as evaporation (Objectively Analyzed Air-Sea Heat

Flux (OAFlux); Yu and Weller (2007); Yu et al. (2008)) and precipitation individually (Global Precipitation Climatology Project (GPCP); CPC Merged Analysis of Precipitation; Xie and Arkin (1997); Adler et al. (2003)) .

Following Schanze et al. (2010), a combination of OAFlux for Evaporation and GPCP for Precipitation is used in this study. OAFlux incorporates objective analysis of remotely sensed satellite data and atmospheric reanalysis products to reduce the error estimate of each data source to obtain minimum error variance on a 1° grid. Estimates exist from 1958 to present for monthly and annual periods. The GPCP dataset consists of the merger of geosynchronous satellite observations with surface rain gauges to create monthly satellite-rain gauge data and associated precipitation error estimates on a 2.5° grid for annual and monthly periods since 1979. In this analysis, mean OAFlux and GPCP for January, February and March for 2008 and 2009 estimates only are applied. Precipitation is linearly interpolated onto a 1° grid to match evaporation. From the $1° \times 1°$ grid for precipitation and evaporation, evaporation-precipitation (E-P) is created to represent freshwater flux at each grid point, with a mean value of E-P taken to represent freshwater flux at the South Atlantic Ocean surface.

Chapter 3

South Atlantic hydrographic section analysis

3.1 Introduction

The previous Chapters have familiarised the reader with the key water masses that will be referred to throughout this study and introduced the datasets involved in this analysis. The following Chapters 4 and 5 focus on analysing oceanic DIC and calculating the anthropogenic CO_2 component. Chapter 6 constructs and applies an inverse box model to the South Atlantic. All three Chapters make use of a range of measured properties. This Chapter seeks to describe thermohaline and biogeochemical properties of the South Atlantic sector of the Southern Ocean from the transects described in Chapter 2 to provide an overview of the key hydrographic features.

For the hydrographic cruise tracks across Drake Passage and from South Africa to Antarctica along 30°E, and separately across 24°S, the ACC and MOC can be monitored. The long-term trend in ACC front position is of significant interest due to its suspected link to wind stress and temperature. Sokolov and Rintoul (2009b) reported an increase in wind stress, potentially driven by SAM (Cai et al. (2005); Fyfe et al. (2007); Cai et al. (2010a)). Wind stress increase causes a southward shift in ACC fronts, resulting in an apparent increase in temperature, as warmer waters from the north penetrate further southward. Monitoring of ACC fronts using hydrographic data is most readily achieved at Drake Passage given the high frequency of repeat occupations, with a subset of two cruises used in this analysis to give an indication of ACC variability.

3.2 Thermohaline distributions

ACC fronts are most readily defined using potential temperature θ and salinity transitions following Orsi et al. (1995) and Belkin and Gordon (1996). The following section describes θ and salinity distributions, vertically interpolated onto a 20dbar grid, for each transect as a first point of analysis, with the Drake Passage 1990 transect previously described by Roether et al. (1993). The water masses described correspond with the neutral density interface definitions in Table 2.2 and qualitatively introduced in Chapter 1. As a reminder, NADW ($27.9<\gamma^n<28.1$) is not marked on the following figures within this Chapter, and the remainder of the thesis, and is found at the UCDW/LCDW boundary. Bathymetry for all following distributions is from GEBCO (General Bathymetric Chart of the Oceans).

Firstly focussing on Drake Passage occupations in 1990 and 2009, the warmest θ (> 7°C) along the 2009 section is within the upper 100dbar surface waters near the South American coast, with waters > 3°C predominately north of 58°S within the upper 1000dbar. South of 58°S, waters are uniformly <3°C beneath the upper 100dbar. North of 58°S, the 4.5°C isotherm marks the vertical SAMW extent at ∼600dbar, whilst south of 58°S, SAMW is limited to the upper 100dbar, before outcropping, south of 62.5°S. For deep water masses, the AAIW/UCDW interface passes through two cores of colder water, with a minimum θ core south of ∼61°S. Subsurface temperature minima, corresponds with Winter Water (WW), and with salinity dominating local density stratification. Winter Water, as described in Park et al. (1998) and Naveira Garabato et al. (2009), is consistent with the remnant of the mixed layer from the previous winter, that has developed a cap of warmer water in austral summer. For the main bulk of WW within the Antarctic Zone, the temperature minimum reaches $\theta_{min} < -0.5$°C in 2009 compared to $\theta_{min} < -1$°C in 1990. The UCDW/LCDW interface closely follows the 2°C isotherm, north of ∼61°S, whilst further south the 2°C isotherm shallows to ∼400dbar. AABW is exclusively south of ∼61.5°S, approximately below the 0.5°C isotherm.

Variations in the subsurface WW cores between 1990 and 2009 are associated with mesoscale eddy activity. The primary WW core south of 61.5°S remains, whilst annual variability in the northward extent of the WW signature is dependent on global teleconnections (ENSO, SAM), as suggested in Naveira Garabato et al. (2009). In 1990, two additional cores are observed, firstly at ∼60.5°S, and a more northerly core at ∼58.5°S, and provides evidence for the potential erosion of WW by interaction with surrounding warmer water masses, as it flows northward and deepens.

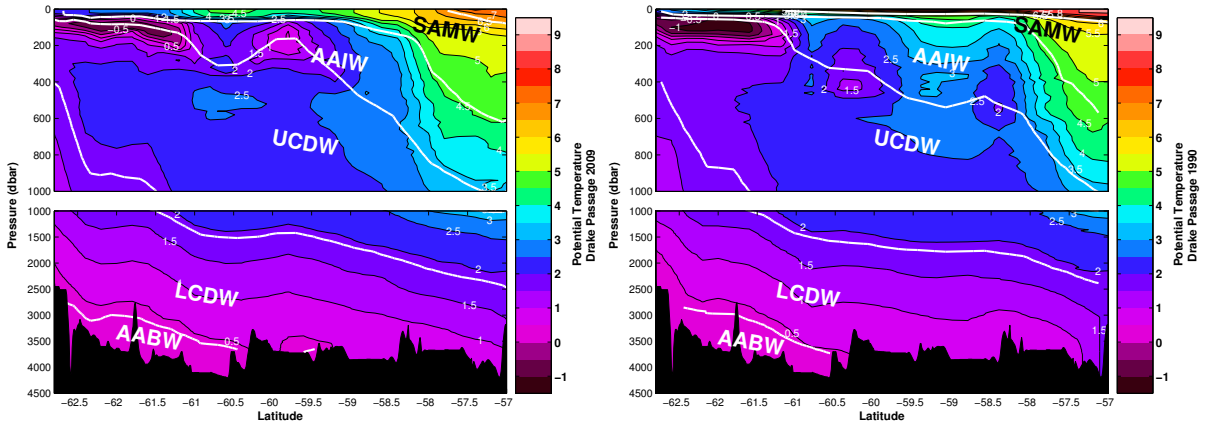

Figure 3.1: Potential temperature (θ) distribution across Drake Passage for a) 2009 and b) 1990. White lines are neutral density water mass interfaces. Water masses are labelled. Units of °C. Bathymetry from GEBCO.

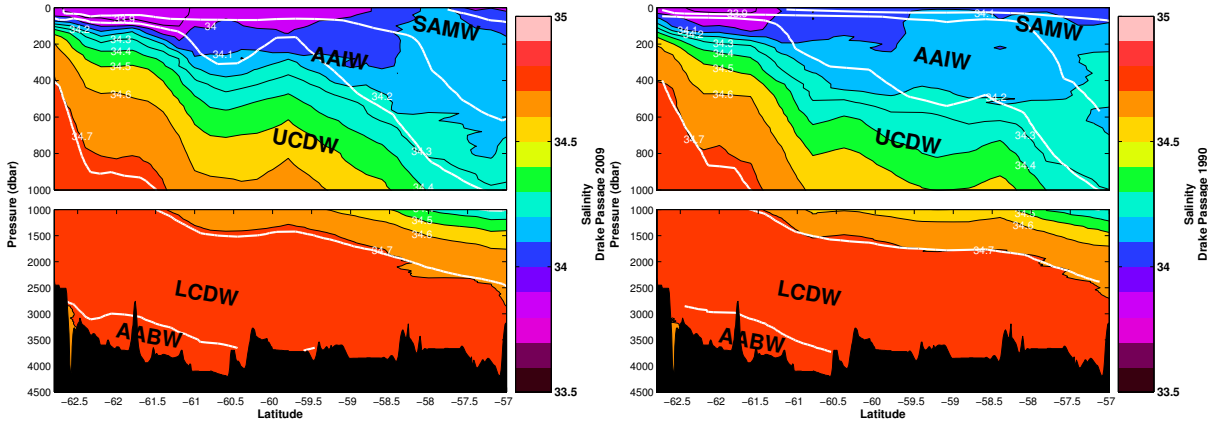

Figure 3.2: Salinity distribution across Drake Passage for a) 2009 and b) 1990. White lines are neutral density water mass interfaces. Water masses are labelled. Units of psu. Bathymetry from GEBCO.

Across Drake Passage in 2009 (Figure 3.2), salinity follows the general pattern of increasing with depth. As observed in Park et al. (1998), warm, fresh (<33.9) water acts as a surface cap on the WW temperature minimum causing it to remain below the surface. From north to south, isohalines shoal as colder, saltier deep water occupies a greater proportion of the water column, remaining below 34.8 across the transect. Isopycnals show little direct dependence on isohalines, apart from for cold, deep water masses e.g. the UCDW/LCDW interface, which closely follows the 34.7 isohaline, highlighting the importance of salinity variations on density at low temperatures. For the 1990 occupation, the Winter Water cores, north of 61.5°S, are predominately within

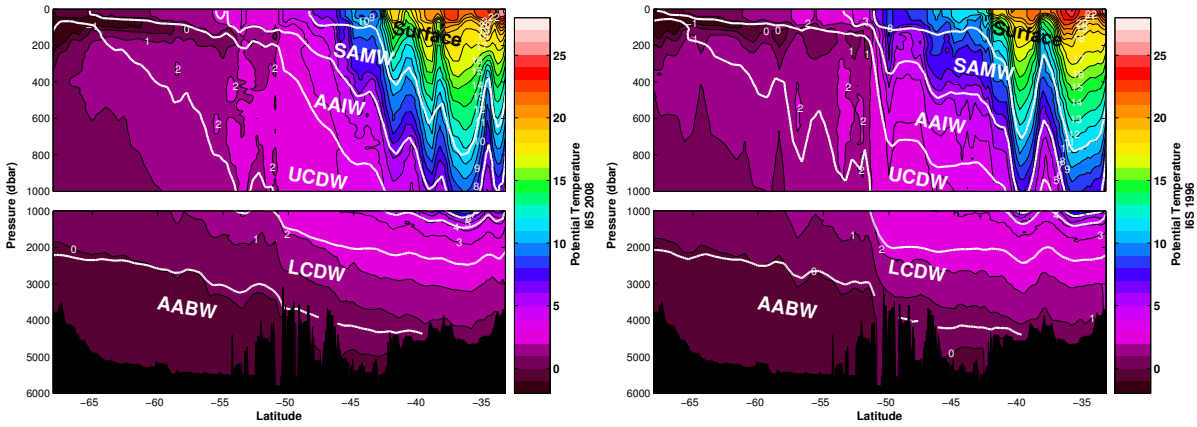

Figure 3.3: Potential temperature (θ) distribution along 30°E for a) 2008 and b) 1996. White lines are neutral density water mass interfaces. Water masses are labelled. Units of °C.

the 34.1-34.2 range, and therefore slightly warmer and saltier, than 2009 WW.

For the I6S 2008 transect (Figure 3.3), warmer water θ>11°C is restricted to the upper 1000dbar of the Agulhas regime, north of ∼42.5°S. Within the Agulhas regime, eddies cause isopycnal heave and subsequent draw of colder water to shallower depths. The sharp gradient of the 11-16°C isotherms at ∼42.5°S marks the transition from Agulhas regime to ACC. South of 42.5°S, surface waters outcrop at ∼47.5°S matching the 5°C isotherm. The SAMW/AAIW interface acts as a vertical bound to the warm water signature of the Agulhas regime. AAIW has a small layer thickness within the Agulhas regime, where the AAIW/UCDW interface follows the 4°C isotherm prior to eventually outcropping, co-incident with the 0°C isotherm at the the south of the section. WW similar to that observed at Drake Passage is evident within the upper 200dbar by a tongue of <0°C water protruding from the Antarctic continent. WW is partly within LCDW as the UCDW/LCDW interface shallows from ∼2000dbar within the Agulhas regime to ∼100dbar at the Antarctic continent. AABW is predominantly south of 50°S and exclusively below 2000dbar, with the LCDW/AABW interface approximately given by the 0°C isotherm.

The I6S 1996 transect is distinguished by a strong eddy within the Agulhas regime, as previously described by Park et al. (2001), with this eddy observed by the heave of multiple isotherms throughout the water column. Transition from Agulhas to ACC regime is accompanied by strong gradients of the 12-16°C isotherms, north of surface water mass outcrop at ∼50°S. Within the deeper ocean at ∼50°S, the 2°C isotherm shows a strong gradient extending from ∼100-2000dbar. AAIW layer thickness follows a similar trend as for 2008, with ∼100dbar within the Agulhas regime, before expanding

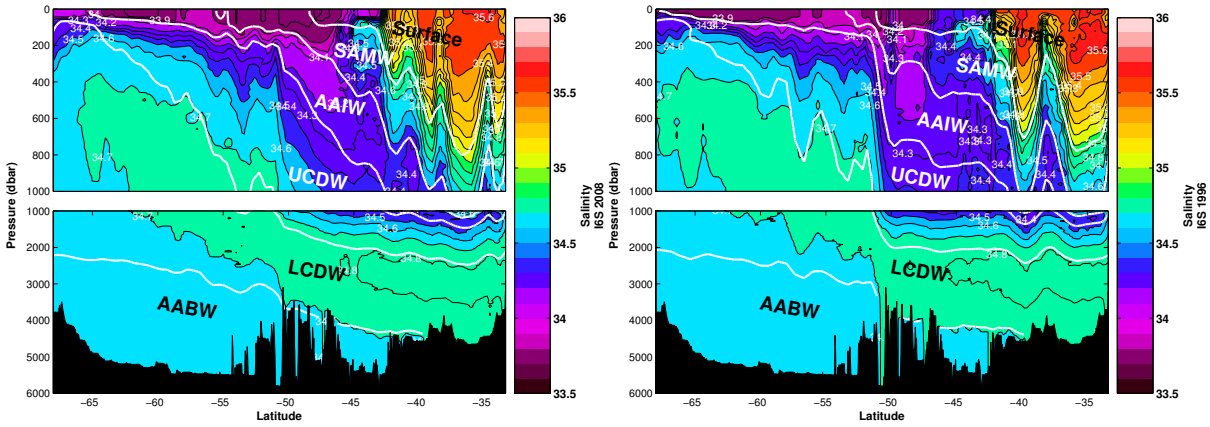

Figure 3.4: Salinity distribution along 30°E for a) 2008 and b) 1996. White lines are neutral density water mass interfaces. Water masses are labelled. Units of psu.

to up to ∼400dbar between 41°S and 50°S before collapsing as the SAMW/AAIW isotherm outcrops. Similar to I6S 2008, a Winter Water core is evident with patches of <1°C water extending northwards within the upper 200dbar towards the 2°C isotherm. LCDW and AABW display similar patterns to 2008, with the 0°C isotherm, a guide for defining AABW.

In 2008, the Agulhas Current brings warm, salty Indian Ocean water across 30°E with a salinity maximum (>35.5) within the upper 400dbar (Figure 3.4). Beneath the Agulhas Current-driven salinity maximum, a salinity minimum of 34.4-34.5 is within the AAIW, and further beneath, a secondary salinity maximum (>34.80) is a signature of the NADW transport around the African continent towards the Indian Ocean. Transition from the Agulhas to ACC regime is marked by fresher water, for example, <33.9 in the upper 100dbar yielding a strong salinity gradient. The fresh signature covers the entire ACC range, and is too fresh and buoyant to sink. The sharp salinity gradient of 34.4-34.6 isohalines at 50°S corresponds with shallower isohaline gradients, north of the Polar Front in 2008. South of ∼50°S, a sharp salinity gradient exists within the upper 400dbar along with an ocean interior salinity maximum (>34.7) between ∼400-2000dbar, predominately within LCDW. Salinity distribution across 30°E, for both occupations is therefore broadly similar, with major differences firstly due to variations in cold, fresh eddies within the Agulhas regime, and secondly through sharper salinity gradients of the 34.4-34.6 isohalines that help to demarcate the PF in 1996.

For the zonal transect across 24°S (Figure 3.5), the θ range extends from >27°C within the upper 100dbar west of ∼27.5°W, to <1°C at the seafloor. From west to east, isotherms uniformly shallow with θ<20°C at the surface, east of 10°E. The Surface/SAMW interface closely follows the 11°C isotherm with the surface layer thickness

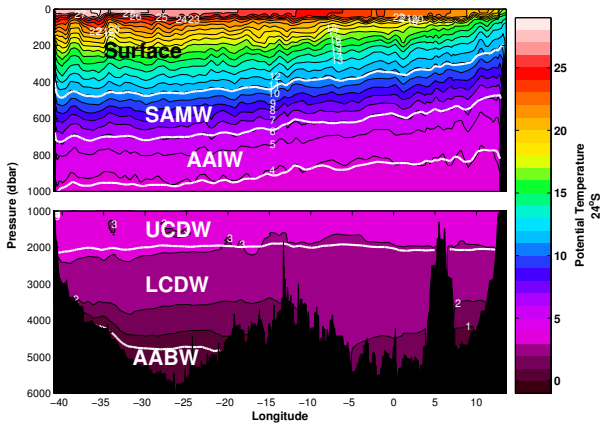

Figure 3.5: Potential temperature (θ) distribution across 24°S for 2008. White lines are neutral density water mass interfaces. Water masses are labelled. Units of °C.

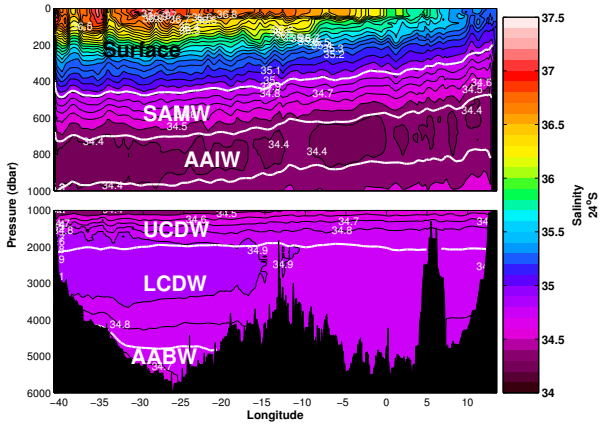

Figure 3.6: Salinity distribution across 24°S for 2008. White lines are neutral density water mass interfaces. Water masses are labelled. Units of psu.

reducing by ∼100dbar from west to east across the basin. SAMW and AAIW both uniformly shoal from west to east with SAMW/AAIW and AAIW/UCDW interfaces closely following 6°C and 4°C isotherms, respectively. For deeper water masses, isopycnals remain flat across the section with the UCDW/LCDW interface most closely resembling the 3°C isotherm. No <0°C water mass exists across the section, with the LCDW/AABW interface best matching the 1°C isotherm and AABW restricted to west of the Mid-Atlantic Ridge.

Within the upper 200dbar and west of 25°W, a salinity maximum is observed (>37), co-incident with the θ maximum corresponding with the warm, salty southward flowing Brazil Current (Figure 3.6). Similar to the θ distribution, isohalines shoal from west to east along the transect, with salinities exceeding 36 predominately located in the upper 200dbar, west of 5°E. The Surface/SAMW interface closely follows the 34.9 isohaline,

whilst SAMW/AAIW and AAIW/UCDW do not follow any particular isohaline. The vertical salinity minimum is constrained to patches of AAIW with S<34.4. A secondary salinity maximum shows S>34.9 extending from lower UCDW into mid-LCDW, consistent with NADW, exclusively within the western basin at 24°S. AABW has salinity 34.7-34.8. The slight increase in salinity between the AABW at 24°S, and at Drake Passage and 30°E supports the salinification of AABW as it travels northwards and interacts with saltier overlying waters.

3.3 Property distributions: Oxygen(O_2), Nitrate (N), Phosphate (P), Silicate (Si), Total Alkalinity (TA), CFC-12

In addition to thermohaline properties, the inclusion of further property distributions provides information regarding the source of water masses and the location of biological activity. The following section details observations from the comparison of property distributions along Drake Passage, 30°E and for the single 24°S occupation. The first three properties (O_2, N, P) represent those included within the stoichiometrically averaged Redfield ratios. The distribution of the biologically-derived components gives a first impression of sectionwide biological activity. Silicate, total alkalinity and CFC-12 distributions are also discussed.

3.3.1 Drake Passage

Oxygen distribution shows distinct similarities for both Drake Passage occupations. For 2009 within the upper 200dbar, the high oxygen concentration ($>320\mu$mol kg^{-1}), particularly south of ∼60.5°S, corresponds with recently ventilated Winter Water formed in the Bellinghausen Sea (Naveira Garabato et al., 2009). Additional high oxygen concentrations $>300\mu$mol kg^{-1} are restricted to south of ∼58°S. Oxygen-poor water is primarily within old, poorly-ventilated UCDW and reaches shallower depths at the south of the transect with $<180\mu$mol kg^{-1} observed at ∼200dbar at the southern end of the transect. Within AABW, oxygen concentrations lie in the 200-220μmol kg^{-1} range. In 1990, UCDW comparatively shows greater oxygen concentrations ($>180\mu$mol kg^{-1}), particularly south of ∼61.5°S. North of 61.5°S, the $<180\mu$mol kg^{-1} water mass also occupies a smaller area within the water column. Reduced ventilation of UCDW south of ∼61.5°S in 2009 implies comparatively 'older' UCDW in 2009. Shallowing of the lower

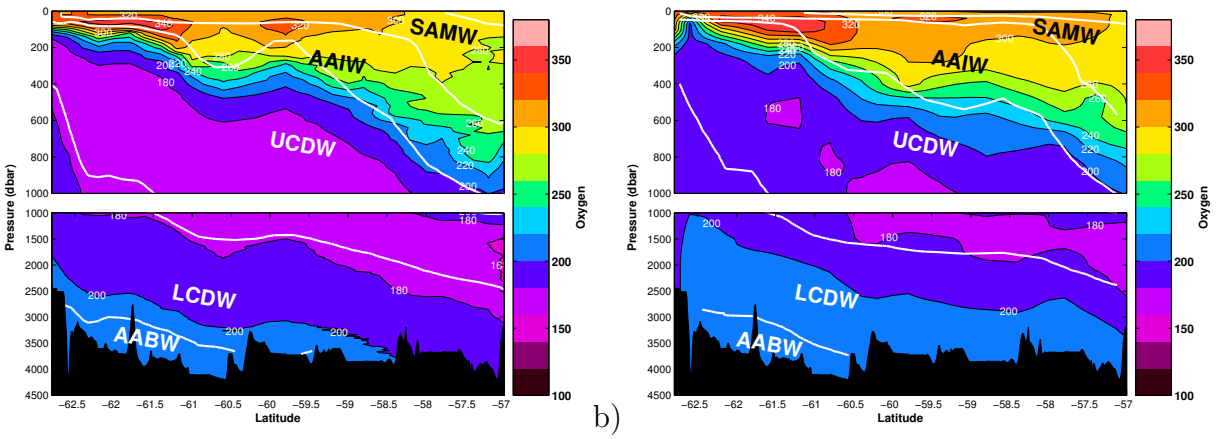

Figure 3.7: Oxygen (O_2) distribution across Drake Passage for a) 2009 and b) 1990. White lines are neutral density water mass interfaces. Water masses are labelled. Units of μmol kg^{-1}.

200μmol kg^{-1} isopleth within LCDW, further supports systematically more oxygenated water masses in 1990 compared to 2009. Biases in source data, given that for 1990 only GLODAP-adjusted bottle oxygen measurements were available, may contribute towards the difference.

The upper 200dbar of the 2009 and 1990 nitrate distribution shows no Winter Water signature. Nitrate concentration reaches a minimum (<18μmol kg^{-1}) for the 1990 surface ocean, north of ~58°S with SAMW and AAIW acting as a transition between the surface water minimum and relative UCDW maximum (>34μmol kg^{-1}). Below 200dbar, the greatest difference between 1990 and 2009 is a maxima in the 34-36μmol kg^{-1} range in 1990, in comparison to small patches of >36μmol kg^{-1} nitrate concentration in 2009, and enhancement of >34μmol kg^{-1} concentration waters south of 62°S. Nitrate greater than 34μmol kg^{-1} is limited to UCDW in both occupations with a majority of LCDW and AABW nitrate within the 32-34μmol kg^{-1} range.

Given Redfield (16:1) stoichiometry, phosphate distribution is uniformly linked to nitrate distribution. In 2009 and 1990, a phosphate minimum (<1.6μmol kg^{-1}) within the upper 200dbar, north of ~58.5°S is co-located with the nitrate minimum. Phosphate isopleths within SAMW and AAIW markedly shallow towards the south of the transect. Phosphate maxima (>2.2μmol kg^{-1}) are co-located with UCDW nitrate maxima supporting a nitrate:phosphate uniformity, with N/P for the high concentration areas estimated as N/P $\approx 34/2.2 = 15.5$ in 2009, compared to a higher phosphate concentration (>2.4μmol kg^{-1}) in 1990 yielding N/P $\approx 34/2.4 = 14.2$. Fewer LCDW minima (<2.2μmol kg^{-1}) are in 1990, with larger patches exceeding 2.4μmol kg^{-1} within 1990 UCDW.

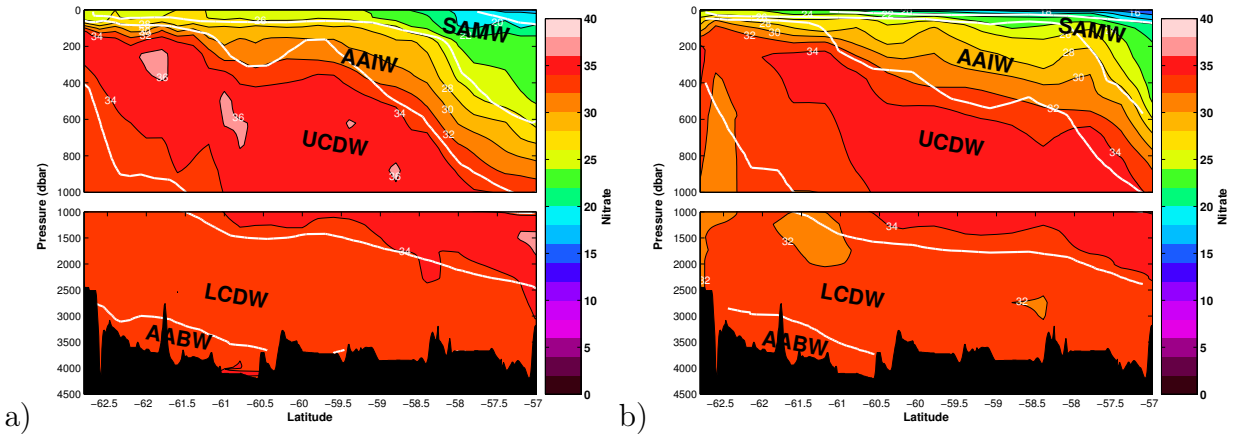

Figure 3.8: Nitrate (N) distribution across Drake Passage for a) 2009 and b) 1990. White lines are neutral density water mass interfaces. Water masses are labelled. Units of μmol kg^{-1}.

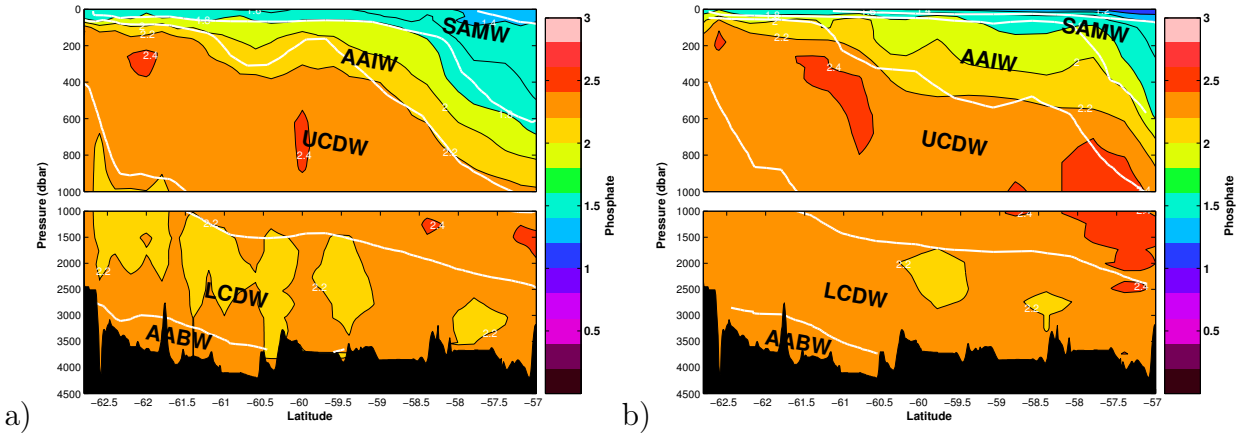

Figure 3.9: Phosphate (P) distribution across Drake Passage for a) 2009 and b) 1990. White lines are neutral density water mass interfaces. Water masses are labelled. Units of μmol kg^{-1}.

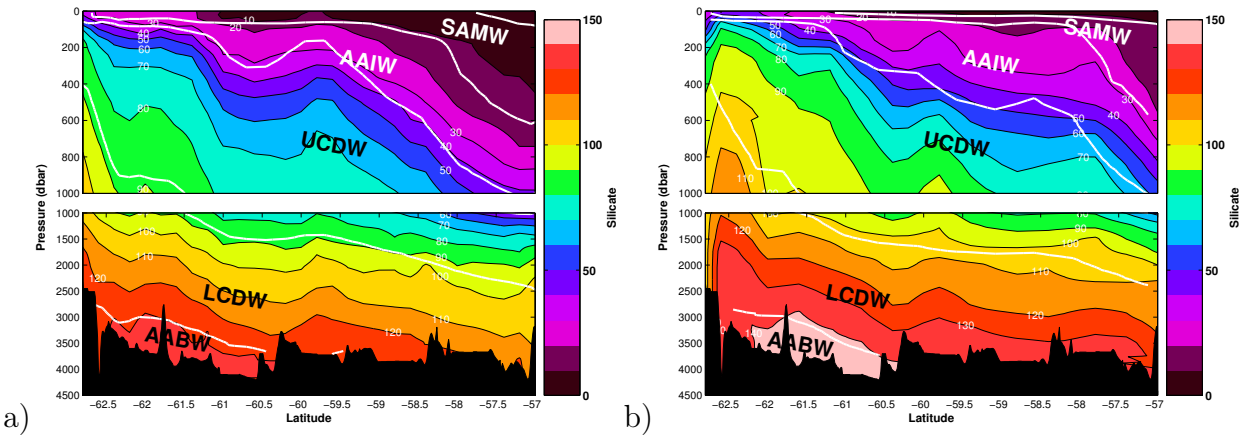

Figure 3.10: Silicate (Si) distribution across Drake Passage for a) 2009 and b) 1990. White lines are neutral density water mass interfaces. Water masses are labelled. Units of μmol kg^{-1}.

Silicate distribution is defined by the biological consumption of silicate. The death of organisms in the upper ocean, dissolution of siliceous material and subsequent downward trajectory, enriches the deep ocean. In 2009 and 1990, silicate reaches a minimum within the surface water and SAMW, particularly north of ~58.5°S. Silicate isopleths closely follow isopycnals as evident south of ~62°S by a sharp shallowing of higher silicate concentrations (>90μmol kg^{-1}). The along transect maxima (>130μmol kg^{-1}) within AABW and lower LCDW is a result of deep ocean enrichment. In 1990, the deep ocean maximum displays a greater proportion of >140μmol kg^{-1} water mass within AABW than observed for 2009 with silicate concentrations in 1990 significantly influenced by the GLODAP calibration factor of +4.9μmol kg^{-1} (Gouretski and Jancke, 2000).

The absence of alkalinity measurements from the 1990 occupation led to the creation of a pseudo alkalinity dataset from the 2009 measurements. Differences between distributions are therefore generated by interpolation with fewer gridpoints along the 1990 transect reflected in a similar general pattern with local features generated by interpolation onto a sparser grid, as well as variation of the γ^n isopycnals. Both 1990 and 2009 show alkalinity less than 2280μmol kg^{-1} restricted to the upper ~500dbar, north of 58°S. The alkalinity maximum (>2360μmol kg^{-1}) is within LCDW and AABW.

Whereas O_2, N, P, Si and TA property distributions represent naturally occurring properties, CFC-12 is anthropogenically sourced. CFC-12 within the ocean provides an indication of the timescale for ventilation of water masses, with younger, more recently ventilated water masses containing higher CFC-12 concentrations. Across Drake Passage in 2009 is a clear Winter Water CFC-12 signature of >3pmol kg^{-1}, primar-

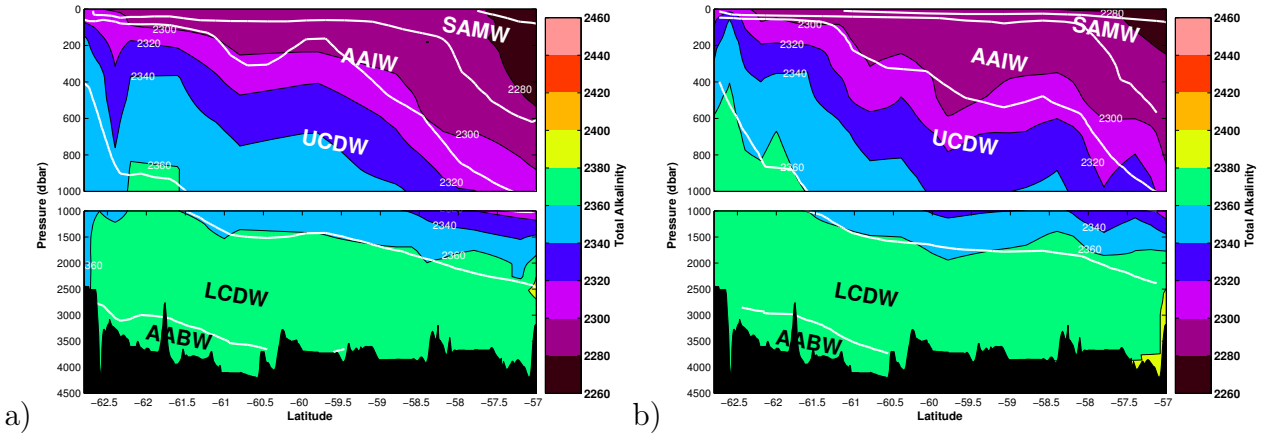

Figure 3.11: Total Alkalinity (TA) distribution across Drake Passage for a) 2009 and b) 1990. White lines are neutral density water mass interfaces. Water masses are labelled. Units of μmol kg^{-1}.

ily south of 61.5°S with >2pmol kg^{-1} within the upper 100dbar across the transect. CFC-12 (>0.5pmol kg^{-1}) invades to shallower depths at the southern end of the transect (200dbar) compared with the northern end (1200dbar) reflecting along isopycnal penetration of recently ventilated surface waters into SAMW and AAIW at the north of the transect. LCDW and AABW CFC-12 concentration is uniformly within the 0-0.5pmol kg^{-1} range. AABW at Drake Passage is predominately blocked by the Shackleton Ridge, and hence poorly ventilated with little CFC-12 signature.

Enhanced WW CFC-12 concentration (>2.5pmol kg^{-1}) in 1990 further represents recent WW ventilation. The >2pmol kg^{-1} concentration does not extend across the section, restricted to south of 57.5°S. The 2009 distribution comparatively sees a deepening of the 0.5pmol kg^{-1} isopleth, enhanced WW concentration and an expansion of higher concentration areas across the section.

3.3.2 30°E

Oxygen across 30°E reaches a maximum (>320μmol kg^{-1}) within the upper 200dbar, south of 50°S in 2008 and 1996, corresponding to recent ventilation of the outcropping water masses. However, unlike at Drake Passage this maxima mostly extends between the surface and 200dbar without the cap of warmer, fresher water found at Drake Passage. Upper 200dbar oxygen concentrations are more noticeably depleted within the Agulhas regime with typical concentrations in the 180-240μmol kg^{-1} range. The water column minima (<180μmol kg^{-1}) within UCDW, sits above NADW. In comparison to 2008, the 1996 oxygen minimum (<180μmol kg^{-1}) appears partially eroded. Low

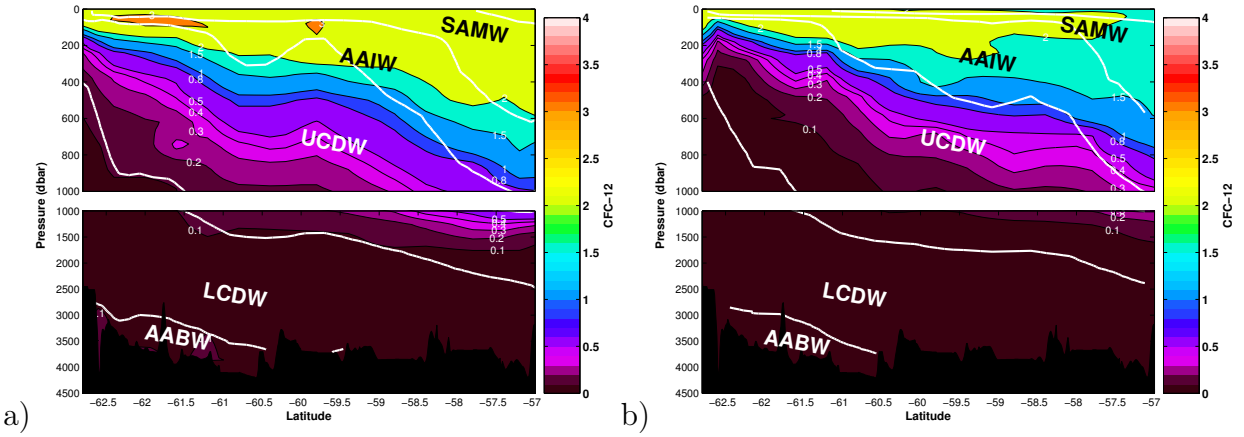

Figure 3.12: CFC-12 distribution across Drake Passage for a) 2009 and b) 1990. White lines are neutral density water mass interfaces. Water masses are labelled. Units of pmol kg^{-1}.

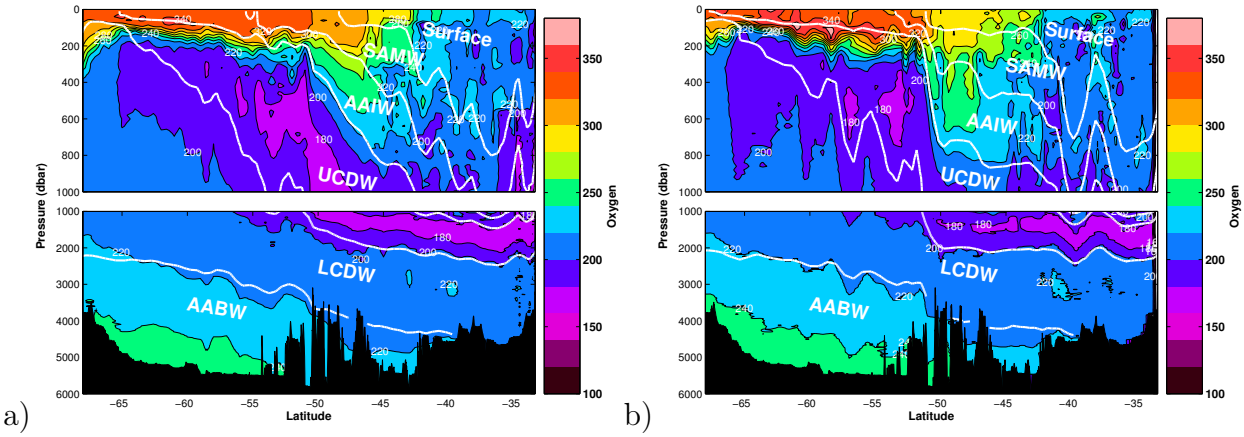

Figure 3.13: Oxygen (O_2) distribution along 30°E for a) 2008 and b) 1996. White lines are neutral density water mass interfaces. Water masses are labelled. Units of μmol kg^{-1}.

oxygen concentrations indicate a water mass with little direct connection to the surface, with AABW reaching >240μmol kg^{-1}. The increased area for the oxygen minimum zone in 2008 suggests older water masses that have experienced further oxygen depletion, as similarly observed at Drake Passage in 2009.

Nitrate concentrations clearly demarcate the biologically active Agulhas regime with notable nitrate-deficiency (<2μmol kg^{-1}) in the upper 200dbar, north of ~43°S in 2008 and 1996. The minima within the Agulhas regime extends to ~1000dbar. No nitrate Winter Water signature is observed. Deeper in the water column, maxima (>32μmol kg^{-1}) are observed firstly within UCDW matching the oxygen minimum layer (Redfield et al., 1963; Broecker, 1974), as well as primarily within AABW. Nitrate

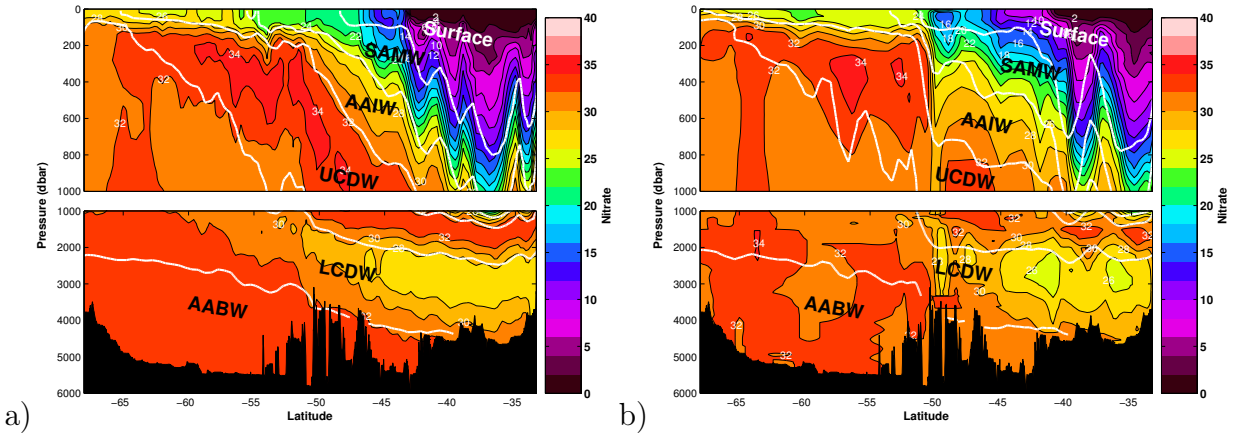

Figure 3.14: Nitrate (N) distribution along 30°E for a) 2008 and b) 1996. White lines are neutral density water mass interfaces. Water masses are labelled. Units of μmol kg^{-1}.

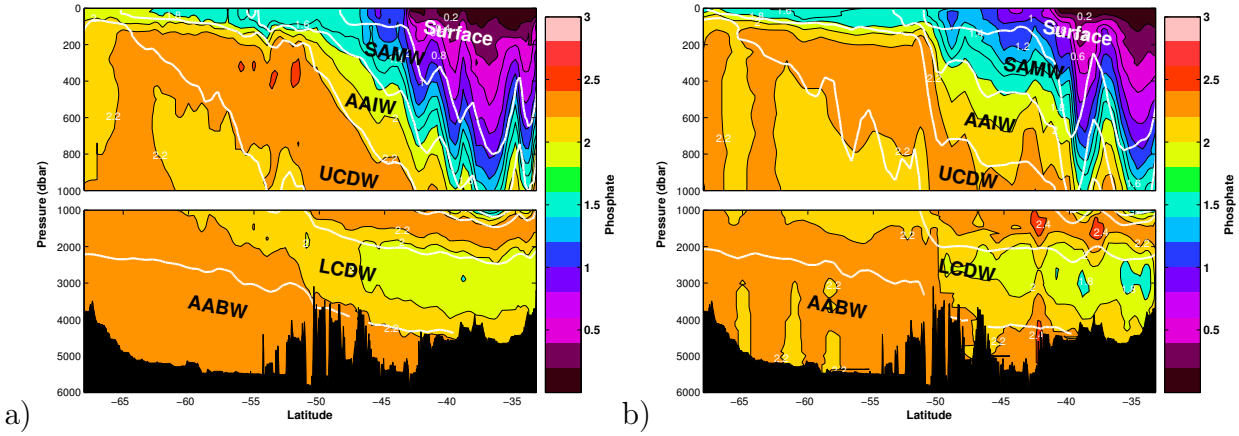

Figure 3.15: Phosphate (P) distribution along 30°E for a) 2008 and b) 1996. White lines are neutral density water mass interfaces. Water masses are labelled. Units of μmol kg^{-1}.

minima within LCDW, reaching $<26\mu$mol kg^{-1} in 1996 is a nutrient minima signature of NADW that reflects nutrient-deficient source waters.

Phosphate distribution closely matches nitrate distribution. Within the Agulhas regime upper ocean, phosphate is severely depleted by phytoplankton nutrient consumption, with the Agulhas phosphate signature extending to ~1000dbar. A secondary NADW minima below ~1000dbar in the Agulhas regime gives a phosphate concentration below 2μmol kg^{-1}. NADW within the Agulhas regime is hypothesised to have followed a more direct pathway from the Deep Western Boundary Current towards the Indian Ocean. Lower phosphate concentration, therefore reflects NADW found at source. This pattern is replicated for the 1996 transect with both upper 200dbar and NADW minima north of ~50°S.

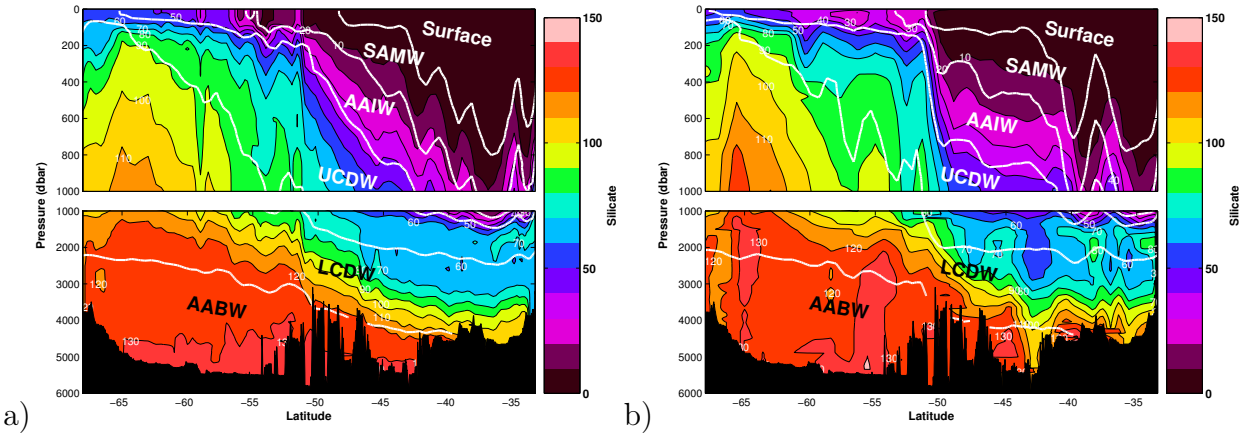

Figure 3.16: Silicate (Si) distribution along 30°E for a) 2008 and b) 1996. White lines are neutral density water mass interfaces. Water masses are labelled. Units of μmol kg^{-1}.

At Drake Passage, silicate is strongly dependent on depth, and this profile also exists at 30°E. In 2008, silicate concentrations broadly follow isopycnals with shallowing of isopycnals consistent with shallowing of silicate isopleths. A silicate minimum of $<10\mu$mol kg^{-1} within the upper 1000dbar, north of 50°S is not restricted by the Agulhas/ACC transition. South of 50°S, silicate concentrations of $>90\mu$mol kg^{-1} reach 200dbar, with $>90\mu$mol kg^{-1} concentrations occupying the majority of the water column. A silicate maximum of $>130\mu$mol kg^{-1} is within AABW. In 1996, a silicate minimum is similarly restricted to the upper 1000dbar, north of 50°S. The AABW maxima ($>130\mu$mol kg^{-1}) is lower than the Drake Passage maxima ($>140\mu$mol kg^{-1}).

Alkalinity, particularly within the surface ocean has a known co-dependency with salinity (Lee et al., 2006; Cai et al., 2010b). In 2008, low alkalinity concentrations ($<2300\mu$mol kg^{-1}) exist as a band, primarily within SAMW and AAIW. Concentration minima ($<2280\mu$mol kg^{-1}) are within the upper 400dbar, south of the Agulhas regime, in the vicinity of SAMW and AAIW outcrop. The water column maxima is within the AABW and lower LCDW, north of 50°S. South of 50°S, the majority of the water column is $>2340\mu$mol kg^{-1}. In 1996, alkalinity minimum is similarly restricted to the Surface, SAMW and AAIW with a sharp alkalinity gradient at ~50°S approximately corresponding to the Polar Front. In 1996, alkalinity maximum ($>2360\mu$mol kg^{-1}) remains within lower LCDW and AABW, similar to 2008, with additional patches within lower LCDW south of 50°S.

Recent ventilation of the near-surface ocean, south of 50°S is evident from the CFC-12 maxima (>3pmol kg^{-1}) in 2008. CFC-12 signature of >0.5pmol kg^{-1} is evident within the upper 1000dbar, predominantly north of 50°S and within the upper 400dbar

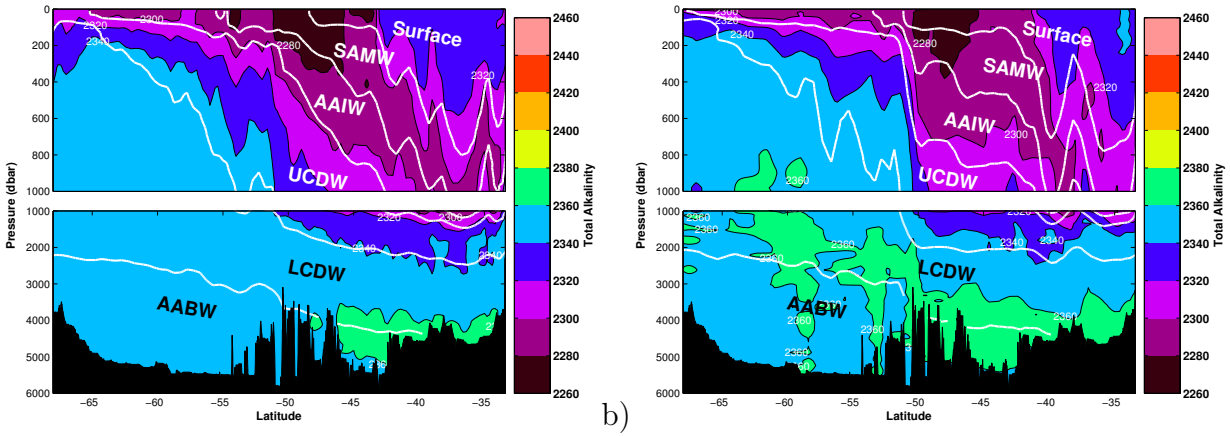

Figure 3.17: Total Alkalinity (TA) distribution along 30°E for a) 2008 and b) 1996. White lines are neutral density water mass interfaces. Water masses are labelled. Units of μmol kg^{-1}.

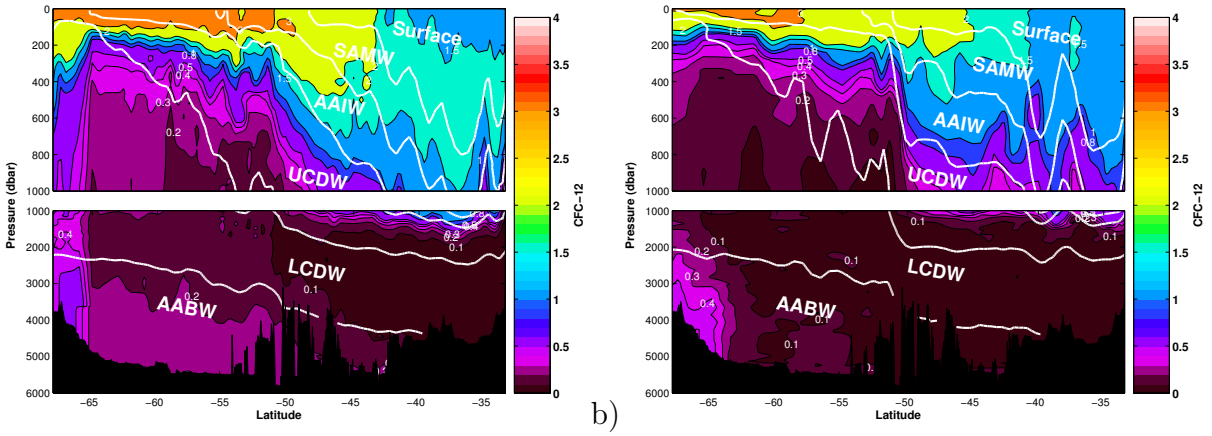

Figure 3.18: CFC-12 distribution along 30°E for a) 2008 and b) 1996. White lines are neutral density water mass interfaces. Water masses are labelled. Units of pmol kg^{-1}.

south of 50°S. This supports the along isopycnal penetration of CFC-12 from the surface ocean south of 50°S, to the subsurface within the Agulhas regime. An exception to this is the presence of enhanced CFC-12 adjacent to the Antarctic continent, which is a signature of recent AABW formation. The majority of AABW, however, displays CFC-12 <0.5pmol kg^{-1} supporting the longer renewal rate required compared to the upper ocean. Lower CFC-12 in the upper 200dbar within the Agulhas regime is primarily a temperature effect with CFC solubilities increasing with decreasing temperature at approximately 1% per degree Celsius (Fine, 2011). In 1996, a lower (<0.5pmol kg^{-1}) signature of AABW formation is found adjacent to the Antarctic continental margin. CFC-12 maxima (2.5pmol kg^{-1}) is restricted to the upper 200dbar, south of 50°S. Penetration of CFC-12 (>1.5pmol kg^{-1}) into the Agulhas regime subsurface ocean is absent.

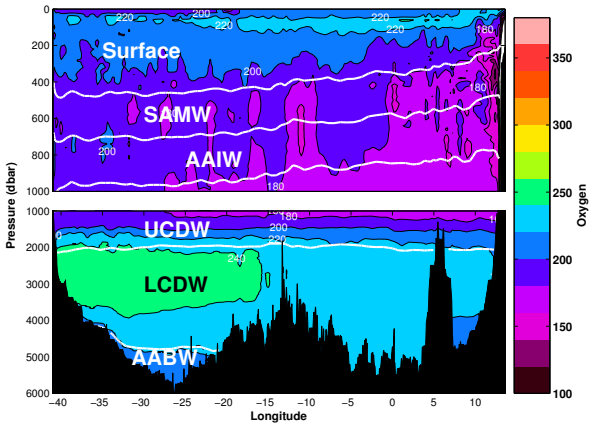

Figure 3.19: Oxygen (O_2) distribution along 24°S in 2009. White lines are neutral density water mass interfaces. Water masses are labelled. Units of μmol kg^{-1}.

3.3.3 24°S

Along 24°S, the 2009 occupation is discussed individually. Oxygen concentration minima are adjacent to the African continent, dominating between 200dbar and 1000dbar. Close to the African continent, offshore Ekman transport brings nutrient-rich deep water to the surface, as part of the Benguela Current System. However beneath this surface layer, exists a hypoxic area with limited ocean-atmosphere exchange (De Decker, 1970; Andrews and Hutchings, 1980; Bailey and Chapman, 1991; Arntz et al., 2006). This hypoxic area is heavily restricted to the continental margin, east of ∼11°E. Other areas of low oxygen (<180μmol kg^{-1}) appear as a westward expansion of this hypoxic area with a deep boundary at ∼1200dbar, and upper boundary deepening from ∼400dbar at the eastern edge to ∼900dbar at 26°W. Upper ocean maxima (>220μmol kg^{-1}) are firstly within a subsurface layer (50-150dbar) extending westward from the outcrop of the oxygen maximum layer within the Benguela Current System. This subsurface layer is slowly eroded in the western basin. A surface layer oxygen maximum and hypoxic layer underneath is caused by intense vertical mixing and oxygen consumption within the productive Benguela upwelling zone. A further maximum (>240μmol kg^{-1}) is primarily within the deep western basin, corresponding to NADW, close to the UCDW/LCDW boundary.

In the subtropical gyres, Ekman convergence (downwelling) forces nitrate-rich waters away from the surface as shown by the near complete depletion in the upper 200dbar. A further nitrate minimum (<22μmol kg^{-1}) in the western basin clearly demarcates NADW and reflects NADW nutrient depletion at source. Enhanced nitrate concentrations (>32μmol kg^{-1}) correspond to hypoxic areas in Figure 3.19, caused by

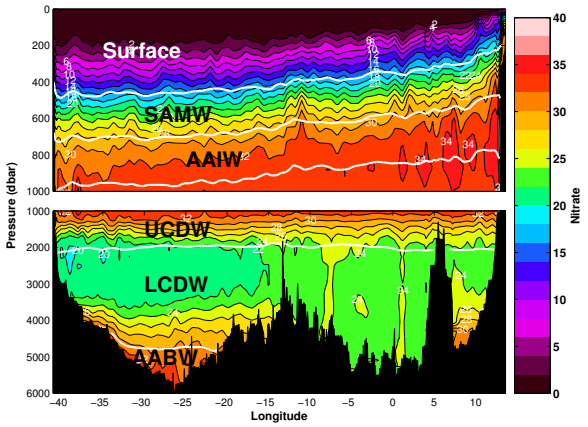

Figure 3.20: Nitrate (N) distribution along 24°S in 2009. White lines are neutral density water mass interfaces. Water masses are labelled. Units of μmol kg^{-1}.

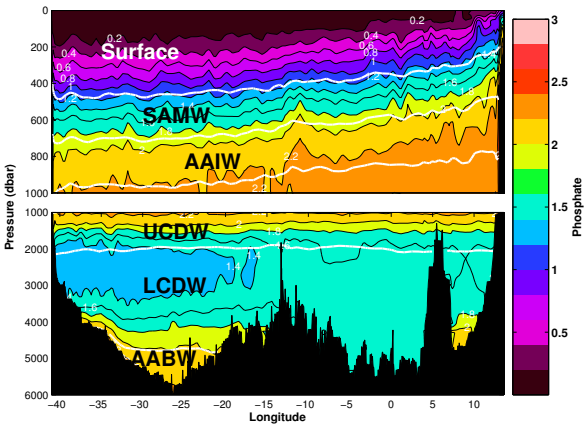

Figure 3.21: Phosphate (P) distribution along 24°S in 2009. White lines are neutral density water mass interfaces. Water masses are labelled. Units of μmol kg^{-1}.

detritus falling from the highly productive Benguela Current upper ocean. Enhanced nitrate at depth suggests either significant deeper remineralisation, or a significant contribution from the African shelf (Hansell and Follows, 2008). Isopycnal deepening from the eastern to the western boundary is matched by nitrate isopleths deepening with, for example, an east to west deepening of the 32μmol kg^{-1} isopleth from 400dbar to 900dbar.

Phosphate distributions are similar to nitrate with clear depletion in the upper 200dbar and deep ocean minima ($<$1.4μmol kg^{-1}) for NADW in the western basin. Enhanced phosphate concentration ($>$2.2μmol kg^{-1}) is evident between 500dbar and 1000dbar with shallowing of phosphate isopleths from the western to eastern boundary. Sharp isopleth shallowing onto the African shelf is supportive of Ekman pumping and subsequent upwelling of nutrient-rich deep water.

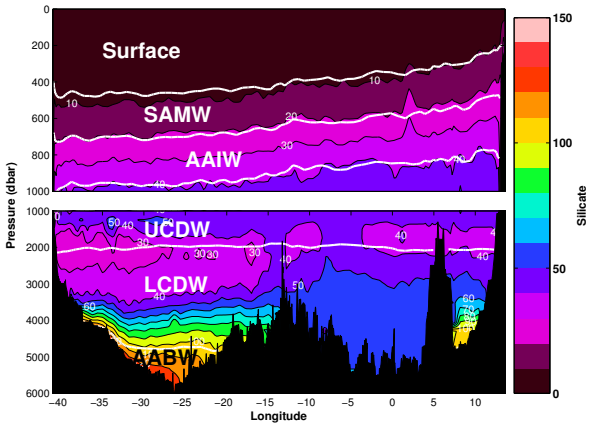

Figure 3.22: Silicate (Si) distribution along 24°S in 2009. White lines are neutral density water mass interfaces. Water masses are labelled. Units of μmol kg^{-1}.

Silicate is almost entirely absent from the upper 400dbar across 24°S. Unlike nitrate and phosphate, silicate remineralises at far greater depths, and explains the general increase in silicate with depth (Tréguer et al., 1995; Nelson et al., 1995). Secondary minima within UCDW and LCDW ($<40\mu$mol kg^{-1}) correspond both to NADW in the western basin, as well as additional deep water masses of circumpolar origin. Across 24°S, silicate distributions show a much smaller proportion of the water column containing higher concentrations of silicate ($>50\mu$mol kg^{-1}) compared to Drake Passage and 30°E. These higher concentrations are limited to the lower LCDW and AABW with high silicate concentrations ($>110\mu$mol kg^{-1}), a signature of AABW.

Alkalinity distribution is marked by a minima spanning SAMW and AAIW across the transect, between ~300dbar-900dbar at the western boundary and ~500dbar-1000dbar at the eastern boundary. This band of minimum alkalinity is enveloped by high alkalinity concentration water masses. The transect maximum ($>2420\mu$mol kg^{-1}) is within the upper 200dbar west of the Mid-Atlantic Ridge. Higher temperature and salinity are within this region, and as a simple test, total alkalinity is estimated from sea surface temperature (SST) and salinity (SSS) using the relationship from Lee et al. (2006) for the subtropical region. This gives a 2420-2430μmol kg^{-1} estimate for alkalinity, similar to Figure 3.23 observations. Deep water maxima occur along the seafloor outside AABW defined regions, and displays a greater dependence on temperature (<2°C) than on water mass source.

Subsurface CFC-12 maximum (>1.5pmol kg^{-1}) extends between 0-300dbar at the eastern boundary and 200-500dbar at the western boundary. Upwelling of deep water within the Southern Ocean exposes poorly ventilated deep water masses to the atmosphere. Downwelling of these newly ventilated water masses into the subsurface, as part

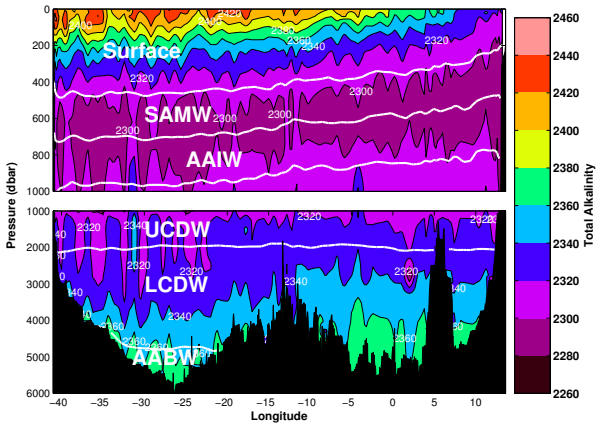

Figure 3.23: Total alkalinity (TA) distribution along 24°S in 2009. White lines are neutral density water mass interfaces. Water masses are labelled. Units of μmol kg^{-1}.

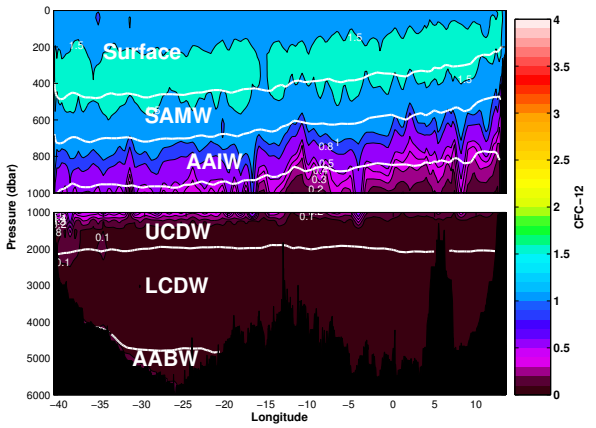

Figure 3.24: CFC-12 distribution along 24°S in 2009. White lines are neutral density water mass interfaces. Water masses are labelled. Units of pmol kg^{-1}.

of the Meridional Overturning Circulation, creates a core of enhanced CFC-12 concentration. CFC-12 concentrations across 24°S are notably lower than for Drake Passage and 30°E, as the high CFC-12 water masses move further from regions of substantial ventilation, for example Winter Water formation in the Bellinghausen Sea. Below the subsurface core, SAMW contains typically 1-1.5pmol kg^{-1} and AAIW has typically 0.5-1pmol kg^{-1}. UCDW is within the 0-0.5pmol kg^{-1} range whilst LCDW and AABW are predominantly $<$0.1pmol kg^{-1}.

Thermohaline, biogeochemical and tracer distributions (O_2, N, P, Si, alkalinity, CFC-12) discussed in this section are each affected by horizontal fluctuations of water masses. These large scale fluctuations within the Southern Ocean are commonly represented by the variability in the position of Antarctic Circumpolar Current (ACC) fronts, and this topic will be the focus of the following section.

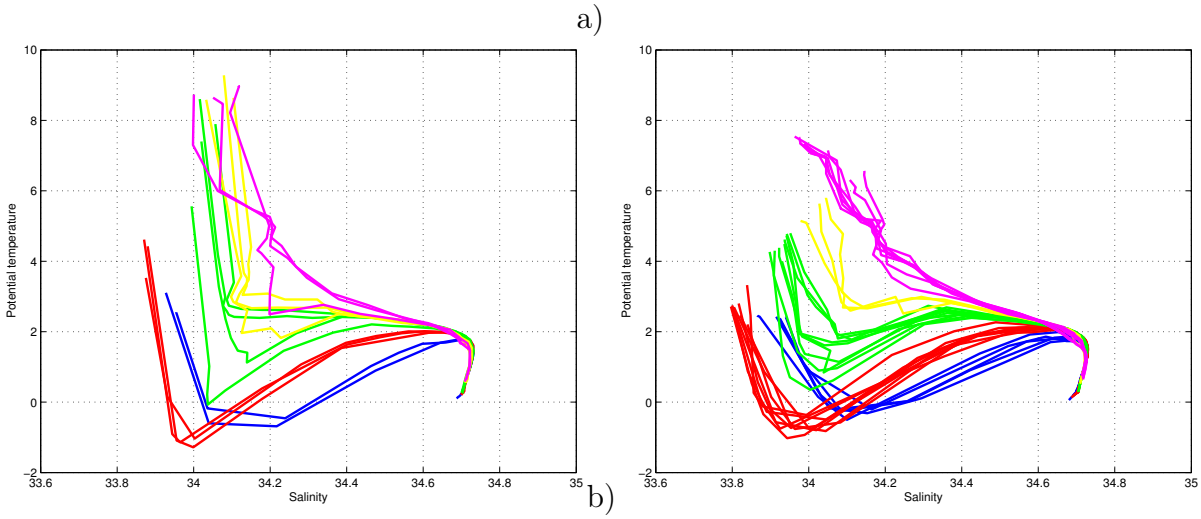

Figure 3.25: θ-S profiles for a) A21 1990 and b) A21 2009. Fronts mark the transition between station groups: SACCF - Blue-Red, SPF - Red-Green, NPF - Green-Yellow, SAF - Yellow-Pink.

3.4 Variability of Antarctic Circumpolar Current (ACC) Fronts

This section aims to define the latitude for ACC fronts and review interesting features. Sharp thermohaline gradients marking ACC fronts are typically the location for preferential outcropping of isopycnals, and therefore provides a pathway for atmospheric CO_2 along-isopycnal absorption into the surface ocean with the resultant distribution of Dissolved Inorganic Carbon reviewed in Chapters 4 and 5.

3.4.1 Drake Passage

The narrow opening at Drake Passage between the southern tip of South America (56°S) and the northern tip of the Antarctic Peninsula (62°S) is the entry point for the ACC into the South Atlantic. In this study, ACC fronts at Drake Passage are selected in θ-S space (Figure 3.25), similar to Cunningham et al. (2003), from all available stations, with a single θ-S profile for each station. Zones with homogeneous hydrographic properties have multiple stations tightly bunched, with an ACC front characterised by a gap between station groups in θ-S space. A gap represents a gradient in the hydrographic properties, and therefore a transition from one frontal zone to another. This method follows the principles of Orsi et al. (1995) and Belkin and Gordon (1996), where the SAF and PF are characterised by strong thermohaline gradients, whilst the Antarctic Zone south of the PF is characterised by colder and fresher water.

Zone	Colour grouping
Subtropical Zone	Pink
Polar Frontal Zone	Yellow, green
Antarctic Zone	Red, blue

Table 3.1: Colour groupings from Figure 3.25, corresponding to zones of similar water mass properties between ACC fronts.

Front	Colour grouping transition
Southern Antarctic Circumpolar Current Front (SACCF)	Blue-Red
Southern Polar Front (SPF)	Red-Green
Northern Polar Front (NPF)	Green-Yellow
Subantarctic Front (SAF)	Yellow-Pink

Table 3.2: Colour grouping transitions from Figure 3.25, corresponding to an ACC front.

Transitions of station groupings shown in Figure 3.25 correspond to the latitudes of ACC fronts (Tables 3.1-3.2). Figure 3.26 for the upper 500dbar, gives a best estimate for ACC front position by using additional information for the distribution of θ and S from Orsi et al. (1995). Northerly stations have higher temperatures with a general trend of salinification from south to north across the section from the northern Antarctic Zone - Polar Frontal Zone - Subtropical Zone. The Antarctic Zone upper 100dbar is the freshest water compared to cold and salty LCDW deeper in the Antarctic Zone shallowing towards the surface.

Across Drake Passage, the Polar Front is split into a Northern (NPF) and Southern Polar Front (SPF) (Table 3.3) as previously observed by Sievers and Nowlin (1984), as well as both upstream (Rintoul and Bullister, 1999; Rintoul and Solokov, 2001; Sokolov and Rintoul, 2002, 2007) and downstream (Sparrow et al., 1996; Gladyshev et al., 2008; Luis and Pednekar, 2010) of Drake Passage and is further discussed in section 3.4.1.1. SACCF is in a marginally more southerly position in 2009, whilst SPF is shifted slightly northward. NPF shows a greater northward shift suggestive of colder water within the upper ocean occupying a more northerly position in 2009, whilst SAF is slightly southward. The largest transition appears for NPF with variability arising from the northward limit of the Winter Water and southward penetration of the 3°C isotherm.

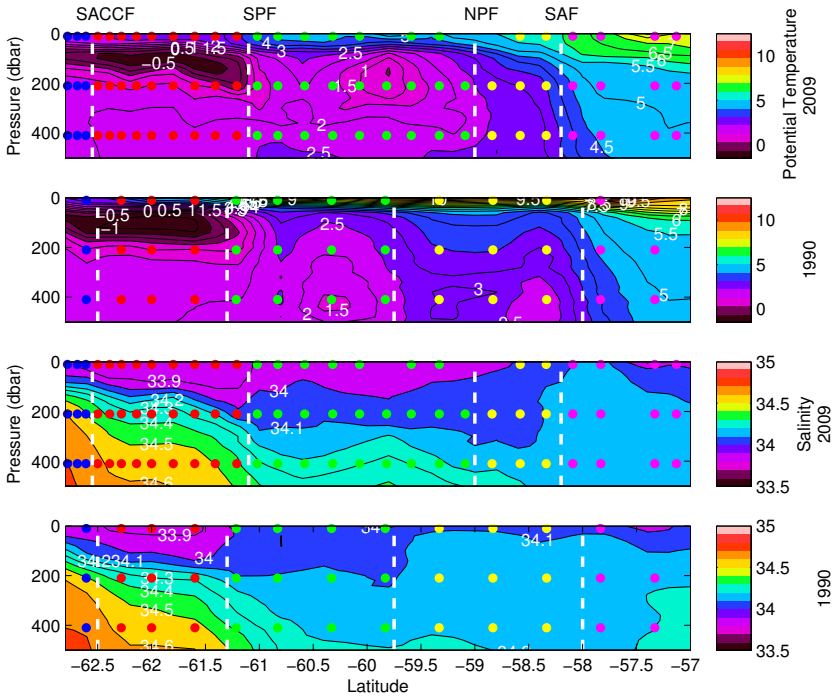

Figure 3.26: Potential temperature (θ) and salinity (S) distributions for A21 2009 and A21 1990 showing station positions, grouped in different colours according to the $\theta - \mathrm{S}$ plots in Figure 3.25 and Table 3.1. Dots are plotted at 200dbar intervals in the vertical.

	A21 2009 (°S)	A21 1990 (°S)
SACCF	62.55	62.5
SPF	61.1	61.3
NPF	59	59.75
SAF	58.2	58

Table 3.3: Latitudes for the Drake Passage ACC fronts: Southern Antarctic Circumpolar Current Front (SACCF), Southern Polar Front (SPF), Northern Polar Front (NPF) and Subantarctic Front (SAF) for the A21 Drake Passage cruises, deduced using θ-S station profiles.

	Polar Front criteria
(1)	$\theta < 2$°C at Z<200m
(2)	$\theta > 2.2$°C at Z>800m

Table 3.4: Potential temperature definitions of the Polar Front transition from Orsi et al. (1995).

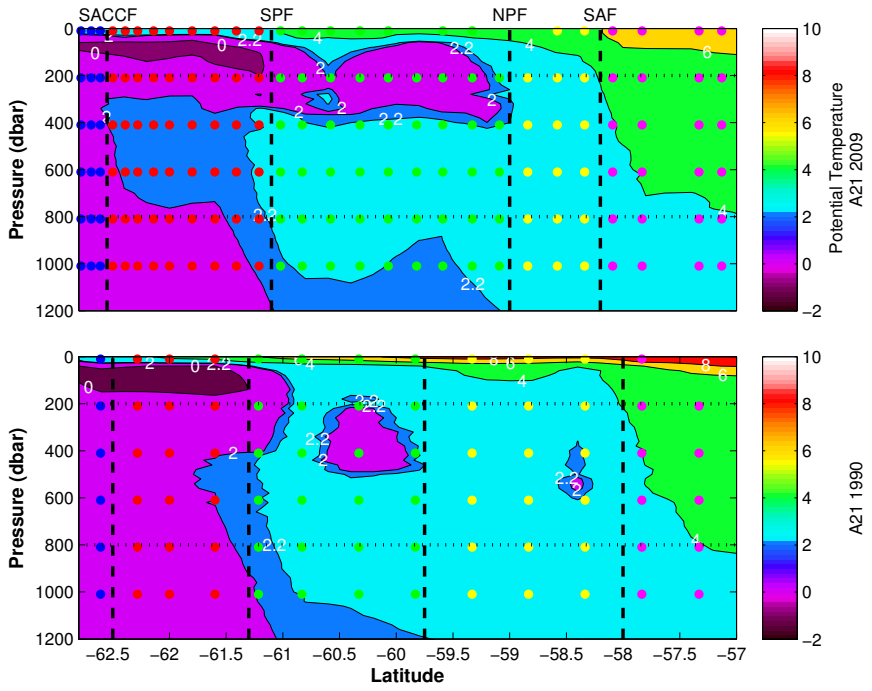

Figure 3.27: Potential temperature distribution across Drake Passage within the upper 1200dbar demarcating frontal transitions from Orsi et al. (1995) (Table 3.4) at $\theta < 2$°C (blue-green transition) and at $\theta > 2.2$°C (green-orange transition). Vertical dashed lines show ACC front positions whilst the horizontal dotted lines are at Z = 200m and Z = 800m to match the criteria.

3.4.1.1 Northern and Southern Polar Front

The existence of two distinguishable Polar Front features, classified as 'Northern' and 'Southern', is a known ACC feature at Drake Passage (Sievers and Nowlin, 1984). As a means of corroborating the presence of a Northern and Southern Polar Front, Polar Front definitions from Orsi et al. (1995) are applied (Table 3.4). Criteria from Orsi et al. (1995) refer to (1) upper ocean expression and (2) deeper expression of the Polar Front. Application of the Table 3.4 criteria is shown in Figure 3.27.

Focussing on criterion (1), northward penetration of the 2°C isotherm above 200dbar gives the near-surface expression of the Polar Front from Orsi et al. (1995) and thus the position of the Northern Polar Front. In 2009, both 2°C and 2.2°C isotherms

penetrate northward between 50dbar and 400dbar with deeper penetration of both isotherms abruptly limited at 400dbar. The 2°C isotherm approximately follows the near-400dbar isobar southward until deepening at the SACCF. The 1990 occupation differs through the separation of a cold patch (<2.2°C) between approximately 59.8°S and 60.8°S, from the main bulk of the colder water (< 2.2°C) south of ∼61°S. Separation is likely a consequence of a warm eddy from a more northerly latitude dissecting the 2.2°C isotherm between 200dbar and 500dbar. This feature is also seen in Roether et al. (1993), which links the warm eddy feature to a negative geostrophic velocity, and a secondary Polar Front.

Applying criterion (2) to Figure 3.27 in 2009, the position of the 2.2°C isotherm coincides with the 800dbar isobar giving a deeper expression of the Polar Front. For 1990, intersection of the 800dbar isobar and the 2.2°C isotherm is not as closely matching, but still only displays a 0.2° latitude difference. Between 300dbar and 800dbar, the 2.2°C isotherm remains close to the SPF, rather than shifting southward to the SACCF. Colder water is restricted close to the Antarctic continent for both occupations with the gradient of the 2.2°C isotherm shallowing below 1000dbar. In 2009, the 2.2°C isotherm shallows at ∼ 60°S but does not peak above the 800dbar isobar.

3.4.1.2 Winter Water

The northward limit of the cold Winter Water (WW) core (subsurface temperature minimum at ∼100m), coincides with the Polar Front (Orsi et al., 1995; Sallée et al., 2008), or specifically to the Southern Polar Front (SPF) in this study. The WW core is associated with both fresher water within the temperature minimum zone and within the WW surface cap (Naveira Garabato et al., 2009). Further northward progression of WW (< 2.2°C), cools the neighbouring water masses and subsequently subducts (Naveira Garabato et al., 2009). In 1990, the northern core (θ < 2°C) is completely separated, whilst some continuity of the isotherms remain across the SPF in 2009. WW northward progress is linked to fresher water (S < 34.1) in the upper 250dbar extending until close to the SAF in 2009, compared to ∼59.5°S in 1990, just beyond the NPF.

NPF position is given by the northward limit of the cold WW extension (θ < 2°C), or alternatively, the NPF corresponds to the shallowing of the 3°C isotherm to the 100dbar level. In 2009, this isotherm shallows between the SAF and NPF. In contrast in 1990, there is a deepening of the 3°C isotherm between 58.5°S and 59.5°S, before shallowing above the WW to give NPF position. Further to the north in the upper 200dbar near the South American continent, warmer (θ > 6°C) and fresher (S < 34.1) water results from interaction with the shelf water surrounding Tierra del Fuego, north

of the SAF.

Following Naveira Garabato et al. (2009), the northward shift in the position of the NPF between 1990 and 2009 may relate to changes in larger scale climate (ENSO, SAM). Frontal positions vary according to wind forcing, both directly as zonal winds drive the eastward ACC, or indirectly as meridional winds in the Bellinghausen Sea influence Winter Water formation and its subsequent northward extent at Drake Passage (Naveira Garabato et al., 2009). By comparing only two cruise datasets, it is not possible to draw any conclusions of the meridional trend in the frontal position, only the difference between the 1990 and 2009 hydrographic cruises specifically. Annual variability is expected, which is influenced by westerly wind stress (Allison et al., 2010). Southward shift in SAF and SACCF broadly corresponds with the model in Spence et al. (2010), identifying the overall poleward movement of ACC winds and fronts, whereas NPF and SPF both show contrasting equatorward movement.

The effect of WW and ACC front variability is significant both at Drake Passage within short timescales, but also across the rest of the Southern Ocean, including 30°E.

3.4.2 30°E I6S

The I6S section along 30°E between South Africa and Antarctica is dominated by two current systems: ACC and Agulhas. For I6S, the θ-S relationship gives inconclusive inter-frontal station groupings with no observed transition to indicate the ACC fronts. Orsi et al. (1995) front definitions are therefore applied.

3.4.2.1 Orsi et al. (1995) definitions

The definitions for isotherms and isohalines from Orsi et al. (1995) are shown in Table 3.5 and applied to Figure 3.28. Firstly for θ, the SACCF position is given by the northward extent of the subsurface minimum and 0°C isotherm. The 2.2°C isotherm below 100dbar has a very sharp gradient, particularly in 1996 (Figure 3.1, 3.28, Park et al. (2001)), with both Polar Front criteria satisfied at the same latitude (Table 3.5), rather than the double frontal structure seen at Drake Passage in section 3.4.1.1. South of SAF, surface/SAMW, SAMW/AAIW and AAIW/UCDW outcrop, whilst at the SAF, 4°C and 5°C isotherms descend sharply from south to north matching the SAF criterion at 400dbar. The STF similarly shows only a narrow band between 10°C and 12°C isotherms, helping to define the STF latitude within a narrow temperature band.

North of the STF in the Agulhas regime, isotherms rise and fall depending on the local eddy field. For example, the shallowing of the 10°C isotherm from 800dbar at 40°S

Front	Indicator
STF	10°C<θ<12°C at Z<100m
	34.6<S<35.0 at Z<100m
SAF	S<34.20 at Z<300m
	θ >4-5°C at 400m
PF	θ<2°C at Z<200m
	θ>2.2°C at Z>800m
SACCF	θ>1.8°C at Z>500m
	θ<0°C at Z<150m
	S>34.73 at Z>800m

Table 3.5: Definitions for ACC fronts taken from Orsi et al. (1995).

to 300dbar at 38°S is evidence for a cold eddy passing through the Agulhas regime. Alternatively, the 10°C isotherm shallowing could equally be interpreted as a warm eddy at 40°S, or a meandering current. For a warm eddy interpretation, the southern boundary of the Agulhas regime would be ∼38°S, and therefore a 4° southward movement of the STF between 1996 and 2008. It is not possible to rule out a meandering current, however, in accordance with previous observations of a similar feature (Lutjeharms and van Ballegooyen, 1984; Park et al., 2001), the cold eddy nomenclature is preferred. Therefore, as the position of the STF, is not assumed to deviate significantly between 1996 and 2008, the cold eddy hypothesis, which gives only a 0.4° difference in STF latitude between 1996 and 2008 is preferred.

For salinity, the SACCF in 2008 (Figure 3.28 d)) shows a tongue of S>34.73, restricted to a small area at ∼950dbar to the north of SACCF. The Polar Front has no salinity definition in Orsi et al. (1995) with possible suggestions listed in Table 3.4. SAF is clearly marked by the 34.2 isohaline extending vertically from 100dbar to approximately 600dbar. In I6S 1996, the 34.2-34.6 band is absent from the surface in I6S 2008 with the 34.2 isohaline marking the SAF, and separating fresher water to the south from saltier water to the north. The 34.2-34.6 band at 300dbar extends from SAF until STF. For the STF, the tight grouping of the 34.6-35.0 isohalines at 100dbar defines the transition from the fresher ACC regime, and saltier Agulhas regime. The cold eddy in 1996 is observed for salinity (Figure 3.28d) with, for example, the 34.73 isohaline ascending from 900dbar to 300dbar at ∼38°S. A cold and fresh eddy indicates a Subantarctic source.

	I6S 2008 (°S)	I6S 1996 (°S)
SACCF	58.75	57.75
PF	50.75	51.1
SAF	46.25	47.4
STF	42.9	42.5

Table 3.6: Latitudes for the ACC fronts at 30°E: Southern Antarctic Circumpolar Current Front (SACCF), Southern Polar Front (SPF), Northern Polar Front (NPF) and Subantarctic Front (SAF) for the I6S cruises, identified using Orsi et al. (1995) definitions.

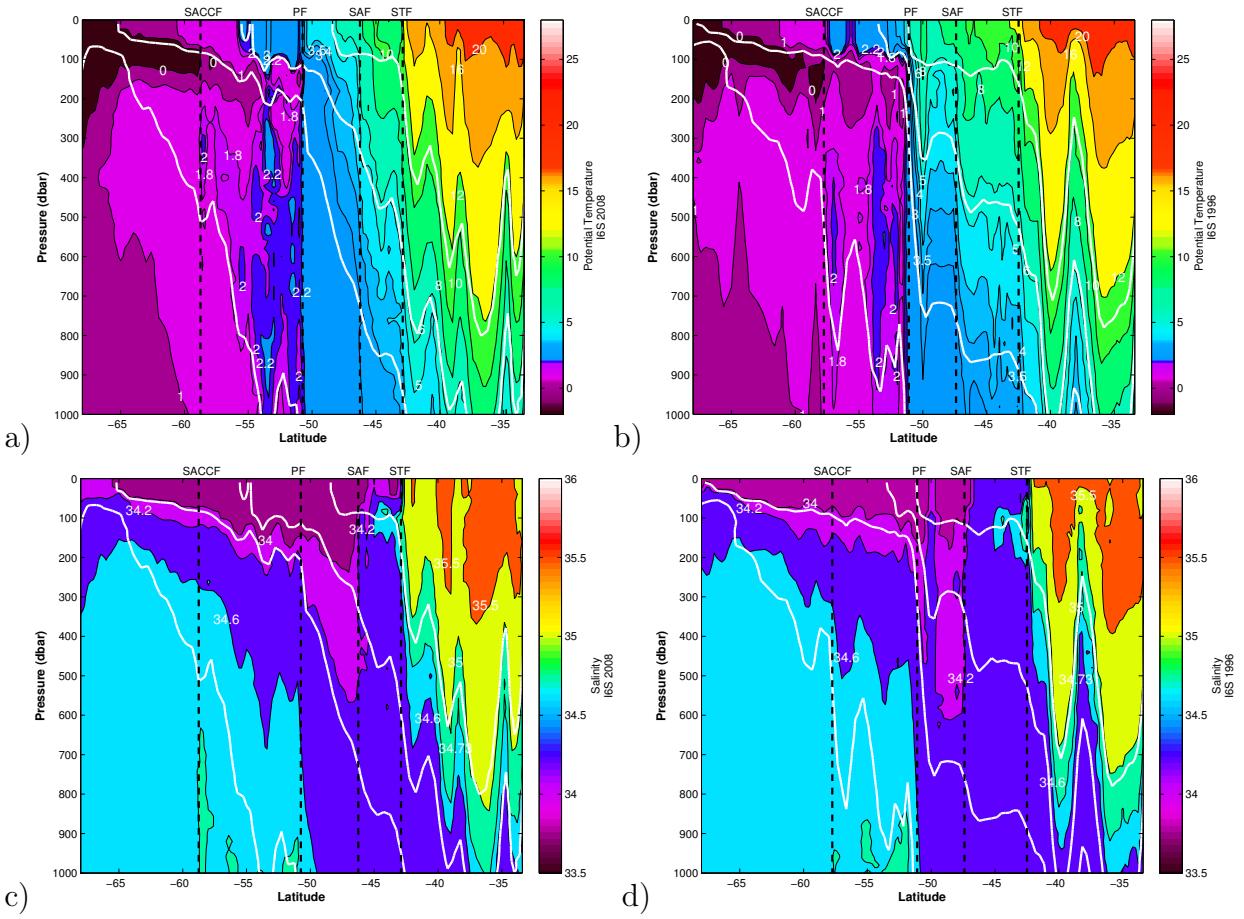

Figure 3.28: Potential temperature (θ) distributions (a, b) and Salinity (S) distributions (c, d) for the upper 1000dbar along 30°E with labelled isotherms and isohalines used for ACC front definitions. Neutral density contours in white are also added.

Front	Indicator
Polar Front	S>34.2 at Z<300dbar
	S>34.6 at Z>700dbar

Table 3.7: Suggested salinity criteria for the Polar Front at 30°E estimated from Figure 3.28.

3.5 Thermohaline property summary

Thermohaline properties are fundamental ocean properties that have been measured with increasing frequency in recent history. The connection between the gradients of these properties and large-scale Southern Ocean circulation is also a 20th century discovery (Deacon, 1937; Nowlin and Clifford, 1982; Sievers and Nowlin, 1984; Orsi et al., 1995; Belkin and Gordon, 1996). From the analysis of two hydrographic cruises across Drake Passage and 30°E, it is not possible to discuss a trend in the dataset, but rather only the decadal variability. At Drake Passage, the greatest variability relates to the position of the NPF. This front is generated by erosion of the Winter Water extension, which is evident in both 1990 and 2009 as a θ<2°C water mass core within the upper 400dbar consistent with subduction of Winter Water into the interior. As Winter Water is formed on an annual basis, fluctuations in the local atmospheric and oceanic conditions at formation, leave signatures that remain within the Winter Water for the remainder of the annual cycle.

At 30°E, the northward migration of the PF and SAF is observed in 2008. Along with variability in the frontal position, the 30°E transect suggests variability in the abruptness of the transition from one zone to another. This is particularly notable at the PF based on a marked steepening of e.g. θ and S in 1996 and has the potential to affect the strength of the associated volume transport. Interannual variability of the total volume transport across the ACC is observed across Drake Passage (King & Jullion, in prep.) with large frontal transport variability previously observed at Drake Passage in Renault et al. (2011).

Variability in frontal positions is indicative of variability of Southern Ocean circulation. The Southern Ocean is an area of strong ventilation from the atmosphere due to the upwelling of deep water (Speer et al. (2000), Crueger et al., 2008 and Sallée et al., 2010a), and specifically as to be discussed in Chapters 4 and 5, is responsible for strong DIC uptake and variability in DIC distribution (Marinov et al., 2006; Le Quéré et al., 2007; Lovenduski et al., 2008; Gruber et al., 2009). Methods and results from assessing variations in natural and anthropogenic carbon distribution will be discussed in Chapters 4 and 5.

Chapter 4

Dissolved Inorganic Carbon and Anthropogenic Carbon Calculation Methodology for the South Atlantic sector of the Southern Ocean

4.1 Introduction

Le Quéré et al. (2007) in a model-based study estimated a weakening of the Southern Ocean anthropogenic carbon (C^{ant}) sink in recent decades. Observational studies of a decreased sink are limited, and typically only indicative of local climate processes (Metzl, 2009) with a continued observed increase in the anthropogenic CO_2 uptake rate in the South Pacific ($1.0\pm0.4 \mathrm{mol\,m^{-2}\,a^{-1}}$, Murata et al. (2007)) , South Indian Ocean ($1.0\pm0.1 \mathrm{mol\,m^{-2}\,a^{-1}}$, Murata et al. (2010)) and South Atlantic Ocean ($0.6\pm0.1 \mathrm{mol\,m^{-2}\,a^{-1}}$, Murata et al. (2008)). Changes in uptake affects the CO_2 distribution initially at the surface, until surface water subducts into the deep ocean. Many previous studies have observed DIC change (Macdonald et al., 2003; Kawakami et al., 2007; Metzl, 2009; Wakita et al., 2010) with increased focus on the anthropogenic carbon contribution (Gruber et al., 1996; Perez et al., 2002; Lee et al., 2003; Peng et al., 2003; Brown et al., 2010; Peng and Wanninkhof, 2010; Ríos et al., 2010; Wanninkhof et al., 2010; van Heuven et al., 2011; Vázquez-Rodríguez et al., 2012).

Changes in Dissolved Inorganic Carbon (DIC) and anthropogenic CO_2 distribution are affected by the ventilation time of water masses that are dependent on larger-scale oceanic circulation and climate variability (e.g. Park and Wanninkhof, 2012). Anthro-

pogenic CO_2 changes within the ocean interior indicate the timescale that atmospheric CO_2 concentration increases are transmitted to the ocean system. Increased observations of the Southern Ocean carbon system help to monitor anthropogenic CO_2 increase as well as to validate Southern Ocean models (e.g. Le Quéré et al., 2007; Lovenduski et al., 2008) both for predicting future, and simulating past ocean CO_2 changes. In the present-day Atlantic Ocean, the importance of the strong, meridional overturning and deep water formation is connected to the ocean's ability to deal with increased CO_2 absorption (Keeling, 1960; Sabine et al., 2004; Wanninkhof et al., 2010; Keeling et al., 2011).

In this study, DIC and anthropogenic CO_2 distributions are calculated using hydrographic data from Drake Passage, 30°E and 24°S in the South Atlantic Ocean and changes in DIC and anthropogenic CO_2 are calculated for Drake Passage and 30°E. GLODAP/CARINA calibration factors are applied to each transect, as appropriate. This Chapter focusses on the methodology for calculating changes in the distributions of C^{ant} and $\triangle C^{ant}$. For the anthropogenic component, the three methods chosen: TrOCA, ΔC^* and eMLR are discussed in this Chapter.

4.2 Changes in Dissolved Inorganic Carbon (DIC)

4.2.1 Direct comparison

For each hydrographic cruise described in Chapter 2, DIC distributions are constructed from measured DIC concentrations. Temporal changes along a specific transect are most simply calculated by finding the difference in the measured concentrations between each hydrographic occupation, using a method similar to Macdonald et al. (2003), and given in this study as:

$$\triangle C = C_A - C_B \tag{4.1}$$

where the subscript A refers to the most recent hydrographic cruise, and B refers to the older hydrographic cruise, for either Drake Passage or 30°E. C is short-hand for Dissolved Inorganic Carbon (DIC).

Along each transect, thermohaline variability leads to the vertical displacement of isopycnals within the water column, and the horizontal displacement of thermohaline markers for the ACC fronts. Vertical variability of thermohaline properties is accounted for by using neutral density (γ^n, Chapter 2 for further details) and φ for horizontal variability as described in section 2.3.1 and 2.3.2. For visualisation in Chapter 5, γ^n vs. φ is converted to latitude vs. pressure with thermohaline variability removed to a

reasonable approximation.

For Drake Passage and 30°E, the difference (equation 4.1) is calculated at each grid point, with positive (negative) change indicating an increase (decrease) in DIC since 1990, or 1996 respectively. Uncertainties of $\sim 3\mu\text{mol}\,\text{kg}^{-1}$ in DIC are assumed based on the available literature (Roether et al., 1990; Poisson et al., 1996; Speer and Dittmar, 2008; McDonagh, 2009; King, 2010), and therefore results for the Chapter 5 must exceed $\sim 3\mu\text{mol}\,\text{kg}^{-1}$ to be significant.

Additionally, the single transect across 24°S is included. The monotonic relationship between latitude and φ noted by Rintoul et al. (1997) is not applicable for a zonal transect. DIC distribution is therefore generated using least squares fitting (section 2.3.1) of neutral density vs. longitude coordinates, and subsequent linear interpolation in the vertical onto a 20dbar grid.

4.2.2 DIC residual

Direct comparisons are vulnerable to anomalously high or low values in either C_A or C_B (equation 4.1), which would bias the results. To avoid this issue, an alternative method involving the calculation of residuals is applied. Residuals are calculated by fitting a best fit line to all datapoints along a section (e.g. 1990 and 2009 Drake Passage datasets) with the residuals equal to the differences between the best fit line and the datapoints.

In this section, DIC residuals are created for Drake Passage and 30°E individually. All DIC datapoints from Drake Passage and 30°E are linearly interpolated onto a $0.01\gamma^n$ grid, and fitted with a best fit polynomial, fifth order for Drake Passage (Figure 4.1) and second order for 30°E (Figure 4.2). Any best fit line that provides a reasonable fit to the dataset could have been chosen. The choice of best fit has implications only for the details of the solution, whilst the broader pattern would remain constant. A single best fit line is calculated for each section, and displayed in Figure 4.1 and 4.2 in separate hydrographic zones. A positive residual for a specific datapoint indicates a higher DIC concentration than expected from the best fit line, helping to guide estimates of DIC change.

Hydrographic zones are created using the fronts from Tables 3.3 and 3.6 as boundaries. For each zone, DIC concentrations (Figures 4.1 and 4.2) are lower in the lower γ^n surface ocean. For $\gamma^n < 28$, DIC profiles are monotonic for each zone across Drake Passage (Figure 4.1). For the Subantarctic Zone, DIC decreases almost linearly towards the surface for above the CDW $\gamma^n = 28$ maxima. For $\gamma^n < 28$ within the PFZ, the steepest increase occurs between γ^n=27.5 and 27.8 whilst for the AZ, few datapoints

exist above $\gamma^n = 27.5$. Steeper DIC concentration increase between γ^n=27.5 and 27.8 compared to only gradual change below $\gamma^n = 27.8$ is caused by enhanced stratification within the Antarctic Zone water column, with a more homogeneous deep water mass.

In Figure 4.2, the 30°E section is split into four hydrographic zones (AZ, PFZ, SAZ, STZ). STZ lighter water ($\gamma^n < 27.8$) corresponds with relatively uniform DIC increases, whilst denser water ($\gamma^n > 27.8$) displays two DIC concentration maxima at $\gamma^n \sim 27.9$ and 28.1. An intermediary decrease of $\sim 50 \mu\text{mol}\,\text{kg}^{-1}$ is a signature of NADW and causes a kink in the DIC profile that is not captured by the polynomial. A similar kink is observed for SAZ and PFZ. For lighter water, the linear relationship within SAZ is similar to Drake Passage with no light water masses $\gamma^n < 26.5$ present within the PFZ or AZ (note change of y-axis in Figure 4.2). The Antarctic Zone profile is far more dispersed around the best fit polynomial, and weakly splits into two further zones determined by the transition between the Weddell Gyre northern and southern limb. The absence of NADW signature from near the Antarctic continent helps give the mixed profile. DIC maxima occurs at $\gamma^n \sim 28.2$.

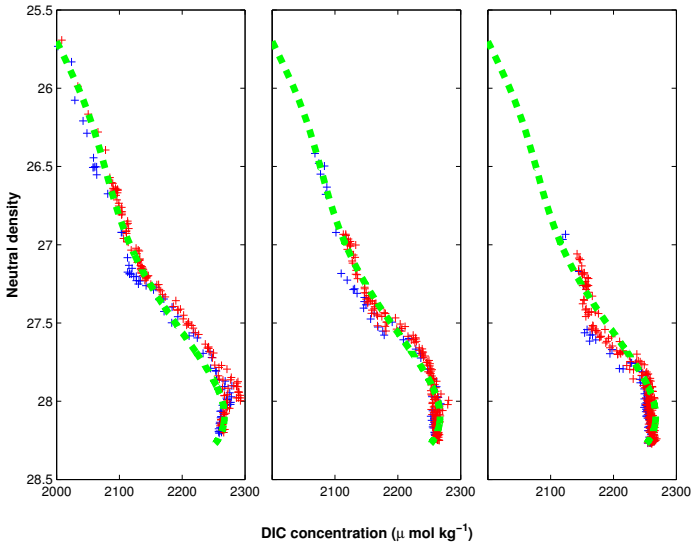

Figure 4.1: Drake Passage profiles of DIC versus neutral density (γ^n) for all bottle concentrations across the section, fitted with a best fit polynomial (fifth order) to calculate the residual. L-R: Subantarctic Zone, Polar Frontal Zone, Antarctic Zone. Bottle datapoints marked for: A21 1990 - blue, A21 2009 - red. The dashed green curve is the best fit polynomial and is the same for each zone.

Residuals from each hydrographic zone are merged to create a sectionwide distribution across Drake Passage and 30°E for each transect. This distribution is created in $\gamma^n : \varphi$ space, and plotted in pressure vs. latitude coordinates using the method described in sections 2.3.1 and 2.3.2.

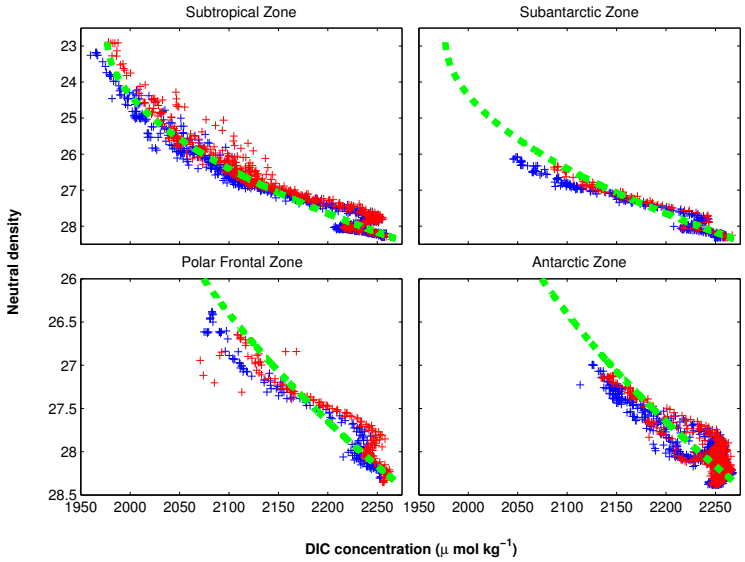

Figure 4.2: 30°E profiles of DIC versus neutral density (γ^n) for all bottle concentrations across the section, fitted with a best fit polynomial (second order) to calculate the residual. Upper L-R: Subtropical Zone, Subantarctic Zone with γ^n between 22.5-28.5. Lower L-R: Polar Frontal Zone, Antarctic Zone with γ^n between 26-28.5. Bottle datapoints marked for: A21 1990 - blue, A21 2009 - red. The dashed green curve is the best fit polynomial and is the same for each zone.

4.2.3 Changes in Redfield Ratio

Redfield ratios give average stoichiometries for N, P, C and O within the global ocean. In this study, unless otherwise stated, stoichiometric ratios of P:N:C:O are 1:16:117:170 following Anderson and Sarmiento (1994). Ratios are calculated by measuring inorganic nutrients within the seawater which are released during remineralisation. Care should be taken when comparing with literature values for the Redfield ratio in plankton as found in De Baar et al. (1997) and Weber and Deutsch (2010).

Redfield ratios naturally vary from these global averages within the ocean, caused by the preference for nitrate uptake in some organisms and phosphate uptake in others. Any difference in the N:P ratio over time is therefore not linked to anthropogenic forcings (Doney et al., 2009b). In this study, to assess any biological differences between each occupation, N:P ratios calculated for each bottle datapoint, are compared within each hydrographic zone along Drake Passage and 30°E. The full depth water column is separated into above and below the mixed layer depth (MLD), defined by the $\triangle$T>0.2°C definition, where $\triangle$T is the temperature difference (Stephenson et al., 2012). Within the mixed layer, greater turbulence occurs due to a range of processes e.g. wind forcing, evaporation, sea ice formation, as well as higher biological activity and

seasonal variability, and naturally separates from the more stable deep ocean. Variability for alternative stoichiometric ratios ($R_{C:O_2}$, $R_{O_2:N}$ and $R_{O_2:P}$) are briefly mentioned (Williams and Follows, 2011). $R_{C:O_2}$ estimates are later used in section 4.3.2.

Differences between the $R_{N:P}$ ratio for each occupation along Drake Passage and 30°E indicate biological differences at the time of sampling. $NO_3^- : PO_4^{3-}$ (herein N:P) ratio increases according to one of the following hypotheses:

1. Absolute increase of the nitrate concentration, compared with phosphate concentration within the seawater (Hypothesis 1)

2. Absolute decrease of the phosphate concentration, compared with nitrate concentration within the seawater (Hypothesis 2)

3. Both 1. and 2. (Hypothesis 3)

$R_{N:P}$ stoichiometry is monitored by using a Type-2 regression (two dependent variables, (Glover et al., 2002)) for nitrate vs. phosphate. A Type-2 regression refers to a regression calculated between two dependent variables that minimises the perpendicular distance between datapoints and the regression line. The gradient of the regression is the $R_{N:P}$ stoichiometry.

$\triangle$N, $\triangle$P and $\triangle$C are calculated within each hydrographic zone. Changes in nutrient concentration e.g. nitrate (NO_3^-), are assumed biologically-caused and calculated by the simple subtraction:

$$\triangle(NO_3^-) = (NO_3^-)_A - (NO_3^-)_B$$

where the subscript A refers to the most recent hydrographic cruise, and B refers to the older hydrographic cruise, for either Drake Passage or 30°E. Changes between recent and historical transects are only calculated for each 0.05 γ^n isopycnal for stations within a ± 0.02 φ range. Modification of $\triangle$C through anticipated anthropogenic changes may cause changes in the $\triangle C : \triangle N$ stoichiometry, calculated using a Type-2 regression, that are suggestive of non-biological influence. If DIC concentration has changed in accordance with nitrate change, then $\triangle C : \triangle N$ should be approximately equal to the Redfield 6.6:1 ratio. Strong increase in $\triangle C : \triangle N$, far above the Redfield ratio provides evidence for the influence of atmospheric, anthropogenic CO_2.

4.3 Changes in Anthropogenic Carbon (C^{ant})

4.3.1 TrOCA (Tracer combining Oxygen, inorganic Carbon and total Alkalinity)

The TrOCA (Tracer combining Oxygen, inorganic Carbon and total Alkalinity) method builds on the work by Touratier and Goyet (2004a,b) and Touratier et al. (2007) to quantify anthropogenic CO_2 (C^{ant}). In comparison to other estimates of C^{ant}, TrOCA is simple to apply, requiring potential temperature (θ), salinity (S), pressure, total alkalinity (TA), DIC and oxygen (O_2). TrOCA is an example of back-calculation, and has been applied in a number of studies (e.g. Lo Monaco et al. (2005a,b); Vázquez-Rodríguez et al. (2009b); Brown et al. (2010); Ríos et al. (2010); Sabine and Tanhua (2010); van Heuven et al. (2011)). DIC concentration (C^{DIC}) is separated into several components to represent:

- Addition of DIC from organic remineralisation and alkalinity change (C^{bio})
- Preindustrial DIC concentration, when atmospheric-ocean equilibrium is assumed, and pre-industrial atmospheric CO_2 is assumed to be 280μatm (C^{eqm})
- Disequilibrium between the atmospheric and ocean DIC concentration when the water left the surface (C^{diseq})
- Anthropogenic CO_2 absorbed into the ocean from the atmosphere (C^{ant})

Hence, C^{DIC} is written as:

$$C^{DIC} = C^{bio} + C^{eqm} + C^{diseq} + C^{ant} \tag{4.2}$$

C^{bio} is calculated from co-incident nutrient observations and Redfield ratios. Uncertainty exists within the calculation for C^{eqm} and C^{diseq}, particularly with the necessity for estimating water mass age, based on CFC, or alternative tracer estimates. For ΔC^{ant} from TrOCA, the C^{eqm} and C^{diseq} terms are assumed to display constant behaviour along isopycnal surfaces. Following Brown et al. (2010), ΔC^{ant} is written as:

$$\Delta C^{ant} = \left(C_2^{obs} - C_2^{bio}\right) - \left(C_1^{obs} - C_1^{bio}\right) \tag{4.3}$$

where the "1" and "2" subscripts represent separate time periods, and therefore only C^{bio} must be calculated. For the TrOCA method, this involves defining a conservative tracer combining DIC, oxygen and alkalinity in the form:

$$\mathrm{TrOCA} = \mathrm{O_2} + \frac{\mathrm{DIC} - 0.5\mathrm{TA}}{\mathrm{R_{C:O_2}} + 0.5\mathrm{R_{N:O_2}}} \tag{4.4}$$

where $\mathrm{R_{C:O_2}}$ and $\mathrm{R_{N:O_2}}$ are Redfield ratios and following Touratier et al. (2007), $\frac{1}{R_{C:O_2}+0.5R_{N:O_2}} = 1.279$. The TrOCA variable is calculated for each time step (A, B) to yield:

$$\Delta\mathrm{C^{ant}} = \mathrm{TrOCA_A} - \mathrm{TrOCA_B} \tag{4.5}$$

$\Delta\mathrm{C^{ant}}$ calculated for each CTD datapoint is interpolated according to the methodologies described in section 2.3.1 and 2.3.2 to create a $\Delta\mathrm{C^{ant}}$ distribution across Drake Passage and 30°E. Following the work of previous authors in assessing the decadal variability of carbon parameters (van Heuven et al., 2011), changes in $\mathrm{C^{ant}}$ are calculated per decade for each neutral density-defined water mass.

Yool et al. (2010) report TrOCA estimates of a single section give an over simplification of extrapolation to the surface (Brown et al., 2010). In this study, TrOCA is limited to the calculation of the change of $\mathrm{C^{ant}}$ ($\triangle\mathrm{C^{ant}}$) with biases caused by the pre-industrial, preformed value of TrOCA from a single section cancelling out for calculation of $\triangle\mathrm{C^{ant}}$. Therefore, this study focusses on the change in $\mathrm{C^{ant}}$ ($\triangle\mathrm{C^{ant}}$) between hydrographic occupations of the same transect at different periods, as recommended by Yool et al. (2010). Published uncertainty in the $\mathrm{C^{ant}}$ TrOCA method from Touratier et al. (2007) is $\pm 6.2 \mu\mathrm{mol\,kg^{-1}}$, assuming input parameter error is random, with a reduction in uncertainty for $\triangle\mathrm{C^{ant}}$ through the cancellation of some of the errors.

4.3.2 $\Delta\mathrm{C^*}$ (Delta C star)

Anthropogenic $\mathrm{CO_2}$ ($\mathrm{C^{ant}}$) calculations originally stemmed from the work of Brewer (1978) and Chen and Millero (1979). These methods 'back-calculate' $\mathrm{C^{ant}}$, as previously mentioned in section 4.3.1, by decomposing measured DIC into various components to account for alterations to DIC concentration over time. Following Gruber et al. (1996), a quasi-conservative tracer, $\Delta\mathrm{C^*}$, is created:

$$\Delta\mathrm{C^*} = \mathrm{C^{DIC}} - \mathrm{C^{bio}} - \mathrm{C^{eqm}} \tag{4.6}$$

with $\mathrm{C^{DIC}}$ referring to DIC concentration from observation. The biological component comprises the terms (Sabine et al., 2002):

$$C^{bio} = \overbrace{R_{C:O_2}AOU}^{\text{organic matter remineralisation}} + \overbrace{\frac{1}{2}(TA - TA^{o} - R_{N:O_2}AOU)}^{\text{dissolution of solid calcium carbonate}} + \overbrace{\frac{106}{104}N^{*}}^{\text{denitrification}} \tag{4.7}$$

where AOU (Apparent Oxygen Utilisation) is the difference between observed and saturation oxygen concentration; TA is total alkalinity, whilst TA^{o} is preformed TA, the TA that the water mass had when it was last at the surface; and N^{*} refers to the denitrification signal: $N^{*} = N - 16P + 2.90$ (Gruber and Sarmiento, 1997; Sabine et al., 2002). $R_{C:O_2}$ and $R_{N:O_2}$ are Redfield stoichiometries of 117/170 and 16/170 following Anderson and Sarmiento (1994).

The first component of C^{bio} represents organic to inorganic matter transformation (remineralisation), as part of the biological pump. Remineralisation is assumed to obey constant stoichiometries ($R_{C:O_2}$) (Gruber et al., 1996). The second component representing calcium carbonate dissolution ($CaCO_3$) may be alternatively written as a function of potential alkalinity (pTA), defined by $pTA = TA + NO_3 + PO_4$ (Brewer et al., 1975). Organic matter remineralisation has no effect on pTA, and therefore $1/2\,(pTA - pTA^{\circ})$ is a simplified version of the second component in this study, where pTA° is preformed pTA (section 4.3.2.1). The third component refers to denitrification (Gruber and Sarmiento, 1997). From the N^{*} calculation, the value of 2.90 is included only to make the global value of N^{*} equal to zero. Excess production of N without P caused by nitrogen fixation gives a positive N^{*}. Consumption of N without P consumption, typically in an oxygen-depleted environment, indicates denitrification and negative N^{*} . Under these conditions, nitrate (NO_3^-) is reduced towards ultimately forming molecular nitrate through a series of intermediary steps (Millero, 2000). Hence, C^{bio} is re-written as:

$$C^{bio} = R_{C:O_2}AOU + \frac{1}{2}(pTA - pTA^{o}) + \frac{106}{104}N^{*} \tag{4.8}$$

The equation 4.8 version of C^{bio} is preferred in this study, where $R_{C:O_2}$ follows the constant stoichiometries given by Anderson and Sarmiento (1994). For comparison in Chapter 5, C^{bio} is calculated for $R_{C:O_2}$ above and below the Mixed Layer Depth (MLD) for each hydrographic zone across Drake Passage and 30°E (section 4.2.3). The use of variable stoichiometric ratios adds additional uncertainty to the solution.

C^{eqm} is calculated from preindustrial atmospheric CO_2 fugacity, preformed TA, and present-day θ, S, silicate and phosphate using "CO2SYS.m" (Lewis and Wallace, 1998) (available at http://cdiac.ornl.gov/ftp/co2sys/CO2SYS_calc _MATLAB_v1.1/) and

equilibrium constants of Mehrbach et al. (1973), redetermined by Dickson and Millero (1987). Following equation 4.6, C^{bio} and C^{eqm} are represented more completely by:

$$\Delta C^{*} = C^{DIC} - R_{C:O_2}AOU - \frac{1}{2}(pTA - pTA^{o}) + \frac{106}{104}N^{*} \qquad (4.9)$$

$$-C^{eqm}(fCO_2 = 280\mu atm,\ TA^{o},\ \theta,\ S)$$

with the three central terms on the RHS comprising the biological component, C^{bio}. C^{eqm} is specific for pre-industrial fugacity ($fCO_2 = 280\mu atm$) and discussed further in section 4.3.2.2.

4.3.2.1 Preformed Alkalinity (TA^{o})

Both C^{bio} and C^{eqm} components of equation 4.9 rely on the estimation of TA^{o}. In the study of Gruber et al. (1996), preformed alkalinity is estimated using a multiple linear regression for conservative tracers with examples of previous tracers used e.g. θ, S , PO ($= O_2 + R_{O_2:P}P$) and NO ($= O_2 - R_{O_2:N}N$) (Gruber et al., 1996; Sabine et al., 2002; Lee et al., 2003). PO and NO follow the historical definition (Broecker, 1974) with $R_{O_2:P} = 135/1$, $R_{O_2:N}N = 9/1$.

This study follows the work of Vázquez-Rodríguez et al. (2009a) and Vázquez-Rodríguez et al. (2012) and their φC^{o}_{T} adaptation of the $\triangle C^{*}$ method by defining potential alkalinity pTA $=TA+NO_3+PO_4$ (Brewer et al., 1975; Fraga and Álvarez Salgado, 2005). Vázquez-Rodríguez et al. (2012)'s subsurface (100-200dbar) parameterisation of potential alkalinity (pTA^{SSL}) is constructed from hydrographic sections throughout the Atlantic including the 30°E section, south of Africa. pTA^{SSL} parameterisation is preferred as it is a conservative chemical parameter compared to TA, which varies according to phytoplankton photosynthesis (Fraga and Álvarez Salgado, 2005), whilst pTA^{SSL} is sensitive to $CaCO_3$ dissolution. The pTA^{SSL} subsurface layer parameterisation from Vázquez-Rodríguez et al. (2012) is applied:

$$pTA^{SSL} \pm 4.6 = 585.7 \pm 13 + (46.2 \pm 0.4)\,S + (3.27 \pm 0.07)\,\theta + (0.240 \pm 0.005)\,NO + (0.73 \pm 0.01)\,Si \qquad (4.10)$$

Preformed potential alkalinity is therefore calculated under the assumption that potential alkalinity in the subsurface is representative of water formation conditions, and hence $pTA^{SSL} \approx pTA^{o}$. Preformed alkalinity is calculated according to $TA^{o} = pTA^{SSL} - NO_3^{o} - PO_4^{o}$ (Brewer et al., 1975; Fraga and Álvarez Salgado, 2005) with NO_3^{o}

and PO_4^o referring to preformed nitrate and preformed phosphate, respectively, given by $NO_3^o = NO_3 - {}^{AOU}/_{9}$ and $PO_4^o = PO_4 - {}^{AOU}/_{135}$. The relationship is designed to hold for the Atlantic Ocean surface area, and is reasonably applied to the ocean interior given that the water masses observed at depth are likely to also have been largely formed within the Atlantic Ocean. The composition of water masses at depth is further discussed in section 4.3.2.5 and further analysis of TA^o is found in Vázquez-Rodríguez (2008) and Vázquez-Rodríguez et al. (2012).

4.3.2.2 C^{eqm} Equilibrium

From the recommendations of Vázquez-Rodríguez et al. (2012), it is decided not to use the surface-defined C^{eqm} parameterisation from Lee et al. (2003) due to discrepancies between the surface vs. subsurface parameterisation of TA^o in Lee et al. (2003) and Vázquez-Rodríguez et al. (2012). C^{eqm} is firstly calculated using the "CO2SYS.m" program (Lewis and Wallace, 1998), given θ, S, TA° and pre-industrial fugacity ($fCO_2 = 280\mu$atm). Secondly, C^{eqm} is parameterised, to feed into equation 4.9, from subsurface (100-200dbar) data only (Equation 4.11).

$$C^{eqm} = 2068 - 7.922\,(\theta - 10) - 7.728\,(S - 35) + 0.8089\,(TA^o - 2320) \tag{4.11}$$

This parameterisation therefore neglects the surface ocean, which as suggested by Vázquez-Rodríguez et al. (2012) and other authors (Broecker and Peng, 1992; Perez et al., 2002) yields systematic negative values for $\Delta TA = TA - TA^o$. This parameterisation, created from South Atlantic only sections, is limited in spatial accuracy, particularly with regards to the exclusion of the source of NADW; however, it is favoured due to the inclusion of the sections within the Atlantic sector of the Southern Ocean.

4.3.2.3 Water Mass Age

As a brief aside, water mass age is calculated for comparison to previous $\triangle C^*$ studies. Observational (Karstensen and Tomczak, 1998; Hall et al., 2002; Gebbie and Huybers, 2012) and modelling studies (England, 1995) generally rely upon the use of a tracer, i.e. a substance that will not react with the seawater, such as CFC-11, CFC-12, CFC-11/CFC-12 (Smethie, 1993), $^3H - ^3He$ (Jenkins, 1987), Carbon-14 (Stuiver et al., 1983) or SF6 (Sulfur hexafluoride), to calculate 'water mass age'. In this study, CFC-12 is available for all cruises and water mass age is estimated based on the assumption of ocean-atmosphere CFC-12 equilibrium during water mass formation and the monotonic

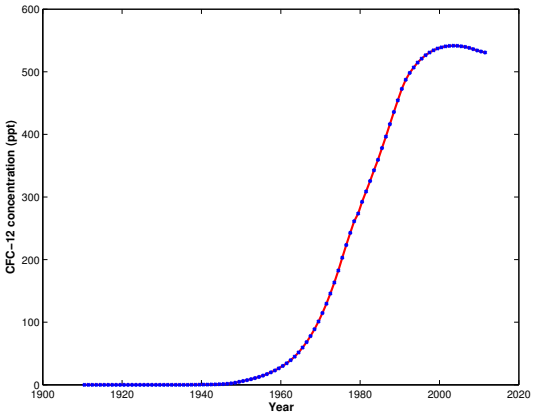

Figure 4.3: CFC-12 variability in the atmosphere since 1900 (Bullister (2011)).

relationship between atmospheric CFC-12 and the year of last atmospheric contact (Figure 4.3a)), until a stabilisation and slight decrease in recent years (Wanninkhof et al., 2010; Bullister, 2011). A non-monotonic, unimodal solution, suggests CFC-12's applicability as a reliable tracer for water mass age calculations is finite, similar to the CFC-11/CFC-12 ratio, which has remained unchanged since the mid-1970's.

For estimating water mass age, CFC-12 concentrations are converted into an average partial pressure of CFC (pCFC-12) following Warner and Weiss (1985) for each water mass. The year of formation is given by the average pCFC-12 for each water mass following Figure 4.3a. Water mass ages in Table 4.1 support recent atmospheric interaction of surface waters compared to older, deep waters. None of the water mass ages are after the CFC-12 stabilisation. For comparison, the years of last atmospheric contact calculated from a hydrographic occupation along 30°S are shown in Table 4.1b) from Murata et al. (2008). LCDW is older compared to AABW, and due to recent AABW formation. In this study, water mass age is only calculated for comparison to existing studies, with C^{diseq} alternatively parameterised (section 4.3.2.5).

4.3.2.4 Inclusion of C^{diseq}

Gruber et al. (1996) extended the work of Brewer (1978) and Chen and Millero (1979) by introducing a disequilibrium term (C^{diseq}) to account for the difference between C^{eqm} ($fCO_2 = 280\mu atm$) and the DIC concentration when the water mass lost contact with the atmosphere. Classically, C^{diseq} is calculated from knowledge of water mass age, or alternatively by calculating C^{ant} using an alternative method (e.g. TrOCA or Transit Time Distributions TTD (Hall et al., 2002, 2004; Pardo et al., 2011)). C^{diseq} is calculated separately for a selected number of water masses in the form (Lee et al.,

a)

Water Mass	Year of last atmospheric contact
Surface	1995.6
SAMW	1987.0
AAIW	1981.2
UCDW	1969.4
LCDW	1957.4
AABW	1961.0

b)

Water Mass	Year of last atmospheric contact
SAMW	1985±3
AAIW	1975±3
UCDW	1953±4

Table 4.1: a) Last contact between the neutral density-defined water mass and the atmosphere with an analytical uncertainty of order ±1 year, with a ∼10% bias in the water mass ages, through bias towards young water masses (Matsumoto and Gruber, 2005). b) Year of last contact with the atmosphere from Murata et al. (2008). Water masses defined using isopycnal surfaces: SAMW (26.6-27.0), AAIW (27.1-27.3) and UCDW (27.5-27.7).

2003):

$$C^{ant} = \Delta C^{*} - C^{diseq} \tag{4.12}$$

C^{diseq} is referred to using different nomenclature in the literature e.g. Sabine et al. (2002); Lee et al. (2003) and Vázquez-Rodríguez et al. (2012), with the formulation following that of ΔC^{*} in equation 4.9:

$$C^{diseq} = C^{DIC} - R_{C:O_2}AOU - \frac{1}{2}(pTA - pTA^{o}) + \frac{106}{104}N^{*} \tag{4.13}$$

$$-C^{eqm}(fCO_2(t),\ TA^{o},\ \theta,\ S)$$

with $fCO_2(t)$ representing the fugacity at the time, t, when the water mass was last at the surface and potentially calculated using historical estimates of global pCO_2 values obtained from direct observations or ice cores (Keeling and Whorf, 1994; Etheridge et al., 1996).

As reviewed by Matsumoto and Gruber (2005) and van Heuven et al. (2011), the C^{diseq} term is a key source of uncertainty within the $\triangle C^{*}$ calculation although a number of potential sources of uncertainties approximately cancel out, for example the effect of pO_2 disequilibrium, and inaccuracy in the Redfield remineralisation ratios on C^{bio}. Further uncertainties are discussed in Matsumoto and Gruber (2005), particularly focussing on the effects of the natural carbon cycle on C^{diseq}, and along with van Heuven et al. (2011) query the applicability of a single water mass age estimate, given that in

reality, a water mass is composed of an age spectrum of water masses.

4.3.2.5 C^{diseq} parameterisation

In this study, parameterisations from Pardo et al. (2011) (Indian/Pacific Ocean) and Vázquez-Rodríguez et al. (2012) (Atlantic Ocean) are applied to calculate C^{diseq}, as required for the φC_T^o adaptation of the $\triangle C^*$ method, and follow studies suggesting the limited applicability of the classical $\triangle C^*$ method of Gruber et al. (1996) in the Southern Ocean (Vázquez-Rodríguez et al., 2009b; van Heuven et al., 2011). This study therefore acts as an independent test of the φC_T^o adaptation within the Southern Ocean, outside of its application in previous studies (e.g. Vázquez-Rodríguez et al., 2009a,b; Pardo et al., 2011; Vázquez-Rodríguez et al., 2012). Vázquez-Rodríguez et al. (2012)'s Atlantic Ocean study includes a single age estimate, derived from CFC analysis, and is considered adequate in association with mixing estimates. In contrast, Pardo et al. (2011) estimate C^{diseq} by firstly calculating C^{ant} using the TTD method, and rearranging equation 4.12. The TTD method is preferable for its inclusion of more realistic mixing to reduce associated uncertainties and concerns, particularly for the Southern Ocean (van Heuven et al., 2011).

Following Vázquez-Rodríguez et al. (2012), the ocean is separated into potential temperature intervals: $-2 \leq \theta \leq 5$, $5 \leq \theta \leq 8$, $8 \leq \theta \leq 18$ and $18 \leq \theta \leq 25$ with separate C^{diseq} parameterisations for each θ interval (Pardo et al., 2011). Linearised regression fits represent the relationship between C^{diseq} and conservative tracers for each θ interval. After testing each parameterisation, the most appropriate regression fit from either Pardo et al. (2011) or Vázquez-Rodríguez et al. (2012) is applied to each transect, or θ interval, to best characterise local water mass properties. The parametric coefficients of equations 4.14 (Vázquez-Rodríguez et al., 2012) and 4.15 (Pardo et al., 2011) are listed in Table 4.2, with NO and PO defined as conservative tracers, given alternative definitions in Vázquez-Rodríguez et al. (2012) and Pardo et al. (2011) following Broecker (1974) ($NO = 9NO_3 + O_2$, $PO = 135PO_4 + O_2$, herein NO_A, PO_A) and Anderson and Sarmiento (1994) ($NO = 10.625NO_3 + O_2$, $PO = 170PO_4 + O_2$, herein NO_B, PO_B), respectively.

$$C^{diseq} = a + b\,(\theta - 10) + c\,(S - 35) + d\,(NO_A - 300) + e\,(PO_A - 300) + f(Si) \quad (4.14)$$

$$C^{diseq} = a + b\,(\theta) + c\,(S - 35) + d\,(PO_B - 300) \quad (4.15)$$

Linearised parameterisations from Table 4.2a) and b), above the 5°C isotherm are directly applied to calculate C^{diseq}. Following sensitivity testing, application of Table 4.2a) and Table 4.2b) parameterisations to all transects is preferable for comparison of the results in this study along 30°E with Lo Monaco et al. (2005a). Below the 5°C isotherm, non-linear mixing processes contribute towards deep and bottom water formation in the polar regions. C^{diseq} for a given water parcel is intuitively viewed as a mixture of C^{diseq} from definable water masses, as discussed in Sabine et al. (2002). Each water mass therefore, contributes a mixing proportion (x_i) of its properties to the water parcel with x_i determined using the OMP technique.

Optimum Multiparameter Analysis (OMP) method for deep ocean C^{diseq}

For deep ocean C^{diseq}, this work attempts to optimise C^{diseq} by following Sabine et al. (2002) and Lo Monaco et al. (2005b)'s usage of extended Optimum Multiparameter Analysis (eOMP) (Tomczak, 1981; Tomczak and Large, 1989; You and Tomczak, 1993; Karstensen and Tomczak, 1998; Poole and Tomczak, 1999), and making use of the software available at: http://www.ldeo.columbia.edu/~jkarsten/omp_std/. eOMP calculates mixing proportions for each measured property (θ, S, O_2, P, N, Si) from a set of pre-defined water masses or Source Water Types (SWT) with pre-defined SWT properties. SWT properties are intended to represent a body of water with a common formation history. A series of linear equations is constructed for each property for both conservative and non-conservative tracers, as well as overall mass conservation, and the system is solved by minimising the residuals. Nonconservative behaviour of biological parameters is accounted for using stoichiometric ratios. An example of the formulation of the OMP analysis for three SWTs is shown in:

$$x_1T_1 + x_2T_2 + x_3T_3 = T_{obs} + r_T \tag{4.16}$$

$$x_1S_1 + x_2S_2 + x_3S_3 = S_{obs} + r_S \tag{4.17}$$

$$x_1O_1 + x_2O_2 + x_3O_3 - R_{O_2:P}\Delta P = O_{obs} + r_O \tag{4.18}$$

$$x_1P_1 + x_2P_2 + x_3P_3 + \Delta P = P_{obs} + r_P \tag{4.19}$$

$$x_1N_1 + x_2N_2 + x_3N_3 + R_{N:P}\Delta P = N_{obs} + r_N \tag{4.20}$$

a)

Transect	θ interval	a	b $(\theta - 10)$	c $(S - 35)$	d $(NO_A - 300)$	e $(PO_A - 300)$	f Si	n	R^2	RMS
24°S	$18 \leq \theta \leq 25$	-38.6±3.0	1.67±0.39	16.3±1.4	-0.32±0.07	0.52±0.05	*	272	0.55	6.7
24°S	$8 \leq \theta \leq 18$	-10.7±2.6	-1.82±0.65	9.7±2.4	-0.12±0.04	-0.13±0.04	*	232	0.31	4.0
24°S	$5 \leq \theta \leq 8$	-7.1±1.0	1.29±0.32	11.1±1.0	*	*	*	138	0.62	4.1
24°S/All	$-2 \leq \theta \leq 5$	-15±2.0	3.45±0.25	20±3.0	0.11±0.03	0.14±0.03	-0.405±0.02	325	0.77	5.8

b)

Transect	θ interval	a	b (θ)	c $(S - 35)$	d $(PO_B - 300)$	n	RMS
30°E	$18 \leq \theta \leq 25$	-80.2	4.34	*	0.35	108	4.3
Drake Passage/30°E	$5 \leq \theta \leq 18$	a_1	2.31	*	0.16	185	6.4
Drake Passage/30°E	$-2 \leq \theta \leq 5$	-84.3	5.75	-12.95	0.17	131	4.9

Table 4.2: Coefficients and statistics from the multiple linear regression of equation 4.14 from Vázquez-Rodríguez et al. (2012) and equation 4.15 from Pardo et al. (2011) as applied in this study, parameterising C^{diseq} using conservative tracers. $\theta > 5$°C parameterisations are applied to each labelled transect with coefficient $a_1 = -51.3$ or -47.9 for 30°E or Drake Passage, respectively. For $\theta < 5$°C, both parameterisations are calculated and refined by Optimum Multiparameter Analysis (OMP). Units of °C (θ), psu (S) and μmol kg^{-1} (NO, PO and Si) are used for the coefficients and available associated standard errors. The correlation coefficient (R^2), RMS of the fit and number of data points (n) are shown, if available.

$$x_1Si_1 + x_2Si_2 + x_3Si_3 + R_{Si:P}\Delta Si = Si_{obs} + r_{Si} \tag{4.21}$$

$$x_1 + x_2 + x_3 = 1 + r_\Sigma \tag{4.22}$$

with x_i representing non-negative mixing coefficients for each SWT, $R_{O_2:P}$ (= 170 : 1), $R_{N:P}$ (= 16 : 1) and $R_{Si:P}$ (= 40 : 1) the respective Redfield ratios and r representing the respective residual for each parameter. Equation 4.22 expresses the condition for mass conservation. Each equation is normalised to ensure comparable units and weighted to account for differences in the observed range of a particular property. Weightings follow Tomczak and Large (1989):

$$W_j = \frac{\sigma_j^2}{\delta_{j_{MAX}}} \tag{4.23}$$

where in this study σ_j is the variance of the given parameter j within the $-2 \leq \theta \leq 5$ interval, and $\delta_{j_{MAX}}$ is the maximum variance for each parameter j from each of the SWTs. As equation 4.23 is not applicable for mass conservation (equation 4.22), a weight of 100 is assigned to ensure mixing coefficients x_i sum to 1, and hence mass is accurately conserved.

Characterisation of Source Water Types For selecting SWTs, both a potential temperature-salinity (θ-S) and a potential temperature-oxygen (θ-O_2) diagram are used. Dominant South Atlantic water masses are observed with a high salinity and nutrient minima NADW signature, and AABW with salinity of ∼34.65 and θ<O°C. Additional water masses are chosen to include a variety of other water masses at a range of θ, S and O_2 values following Sabine et al. (2002), Lee et al. (2003) and Lo Monaco et al. (2005a). $\theta - O_2$ defined SWT are included, in order to better represent low oxygen water masses. For eOMP, eight SWTs are determined with SWT properties given by the mean and standard deviation within a chosen property range.

SWTs in Table 4.3 are listed in approximate order of depth. In the upper ocean, cold and fresh, recently ventilated Winter Water (WW) is found at Drake Passage and 30°E. SAMW is warm, fresh and recently ventilated predominantly along 30°E, outcropping within the SAZ and acts as a barrier to a tongue of fresher Antarctic Surface Water (<34.2) extending from the Antarctic continent along 30°E. For intermediate SWTs, AAIW1 is a warm, salty Indian Ocean water and brought into the South Atlantic Ocean, as part of the Agulhas Current. AAIW2 is cooler, yet of the same salinity and represents a cluster of datapoints, particularly along 24°S.

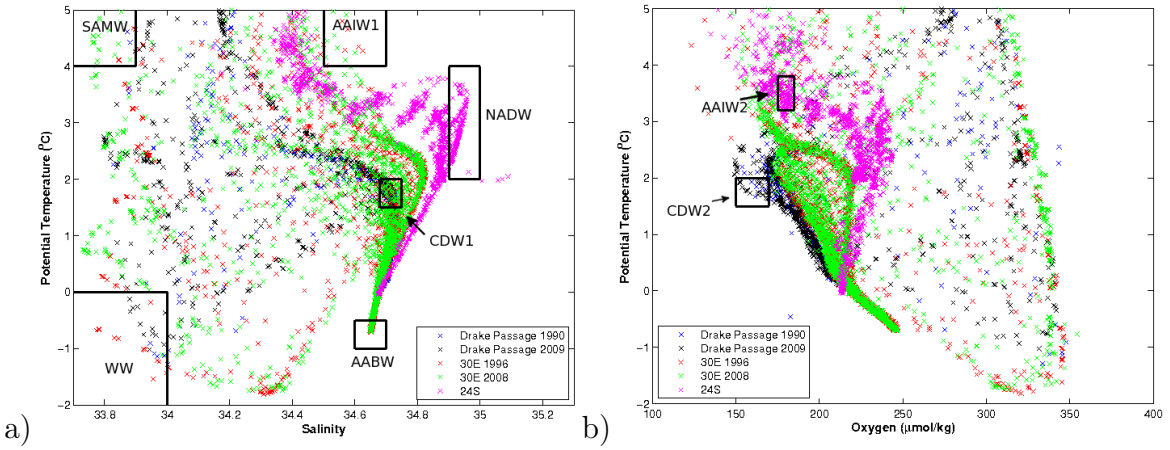

Figure 4.4: a) θ-S and b) $\theta - O_2$ for all datapoints for each hydrographic cruise section (Drake Passage, 30°E and 24°S). Each plot is labelled with the chosen Source Water Types (SWT) for analysis from Table 4.3.

Deep water masses include NADW, along with two types of CDW. CDW salinities are within ± 0.03. CDW1 is defined by a cluster of datapoints in $\theta - S$ space, whereas CDW2 is designed to capture an oxygen minima only observed at $\sim$1500dbar at the northern edge of Drake Passage, with elevated nutrient concentrations. AABW occupies a narrow salinity range, relatively high oxygen from its recent ventilation and a silicate maxima. High AABW silicate reflects the high rate of biogenic silica production, deposition and recycling in the water column around the Antarctic continent (Mantyla and Reid, 1983).

A variety of combinations of SWTs are tested in this study, prior to the final choice. The final choice is chosen partially to maximise the correlation coefficients (R^2) observed for each property. However in this study, R^2 estimates are notably lower than previous estimates from Brea et al. (2004), Álvarez et al. (2004) and Vázquez-Rodríguez (2008). Neither Lee et al. (2003) nor Sabine et al. (2002) provide R^2 estimates. However, both Brea et al. (2004) and Álvarez et al. (2004) conduct OMP along a single hydrographic section, compared with multiple transects in this study. Further uncertainties may result from the choice of SWTs given that, for example, the South Atlantic Ocean is not actually the source region for NADW. Including hydrographic sections from a temporal range of up to 19 years, may also be problematic given observed decadal ocean variability.

Application of eOMP to deep ocean C^{diseq} eOMP is applied to C^{diseq} for the deep ocean only ($-2 \leq \theta \leq 5$). The net disequilibrium from each observation (C^{diseq}) is calculated by multiplying the mixing coefficients, x_i, by the disequilibrium for each

Source Water Type	θ (°C)	Salinity (psu)	Oxygen (μmol kg^{-1})	Phosphate (μmol kg^{-1})	Nitrate (μmol kg^{-1})	Silicate (μmol kg^{-1})
WW	-0.8±0.38	33.91±0.07	340.1±7.79	1.84±0.12	26.5±1.27	45.5±12.0
SAMW	4.4±0.26	33.81±0.05	314.7±3.95	1.51±0.07	21.7±1.22	4.1±4.7
AAIW1	4.4±0.30	34.56±0.04	153.4±13.87	2.33±0.07	32.4±0.87	56.6±4.6
AAIW2	3.5±0.16	34.57±0.11	180.0±2.57	2.13±0.10	31.5±1.50	45.2±5.1
NADW	2.8±0.37	34.93±0.02	235.5±5.07	1.38±0.05	20.9±0.76	31.3±5.6
CDW1	1.7±0.15	34.71±0.02	182.4±9.28	2.21±0.07	32.3±1.27	94.0±8.2
CDW2	1.8±0.11	34.68±0.3	163.9±5.76	2.34±0.06	34.5±0.70	99.3±10.8
AABW	-0.6±0.06	34.65±0.01	242.8±2.17	2.24±0.03	32.3±0.38	135.8±7.0
W	15	5	9	4	6	10
R^2	0.9943	0.9724	0.9048	0.8620	0.8203	0.9787
std. err. of the estimated parameter	±0.01	±0.003	±0.53	±0.004	±0.05	±0.49
n	6225	6225	6132	5855	5825	5802

Table 4.3: Matrix of the thermohaline and chemical properties used to define a given source water type (SWT): Winter Water (WW), Subantarctic Mode Water (SAMW), Antarctic Intermediate Water (AAIW), North Atlantic Deep Water (NADW), Circumpolar Deep Water (CDW) and Antarctic Bottom Water (AABW). The SWT average with associated standard deviation is shown. The weighting (W), correlation coefficient (R^2), standard error of the estimate, and number of data points (n) are shown.

SWT C^{diseq_i}:

$$C^{diseq} = \sum_{i=1}^{n} x_i C^{diseq_i} \tag{4.24}$$

with n representing the total number of SWTs included. Both $-2 \leq \theta \leq 5$ parameterisations from Table 4.2a) and b) are calculated. Vázquez-Rodríguez et al. (2012)'s and Pardo et al. (2011)'s deep ocean parameterisation are hypothesised as being valid for the Atlantic, and Indian/Pacific Oceans, respectively. As Drake Passage and 30°E lie at the boundary of the range of applicability for each parameterisation, both parameterisations are applied during sensitivity testing. Firstly Vázquez-Rodríguez et al. (2012)'s parameterisation (Table 4.2a) was applied to all transects, and secondly to 24°S only, with Pardo et al. (2011)'s (Table 4.2b) parameterisation applied to Drake Passage and 30°E. Inclusion of Pardo et al. (2011)'s Indian/Pacific Ocean parameterisation (i.e. C_P^{diseq}) resulted in negative C^{ant} values along Drake Passage/30°E, whilst the application of Vázquez-Rodríguez et al. (2012)'s parameterisation (i.e. C_{VR}^{diseq}) to all transects, resulted in high deep ocean C^{ant}, particularly at 30°E in comparison to Lo Monaco et al. (2005a) and Vázquez-Rodríguez et al. (2009b) (their Figure 4). As a compromise, the mean of C_P^{diseq} and C_{VR}^{diseq} for each deep ocean SWT is applied for C^{ant} calculation (Table 4.4). The range in C^{diseq} between each parameterisation, greater than the associated standard error of the mean (SEM) for each SWT, gives a sense that the uncertainty associated with C^{diseq} and therefore C^{ant} is of order $\sim 10 \mu mol\, kg^{-1}$, similar to the deep ocean C^{ant} range estimated by Vázquez-Rodríguez et al. (2009b) (their Figure 4). Low SEM helps to justify that each SWT has a relatively uniform composition, in comparison to the differences in composition between each SWT.

Deep Ocean C^{bio} Lower C^{bio} for WW and SAMW correspond to high oxygen concentrations and cold, well-mixed and ventilated water masses (Table 4.3). Although a 5°C temperature difference exists between WW and SAMW, both are relatively fresh, caused by outcropping and subsequent freshening by precipitation or ice melting. The highest $\overline{C^{bio}}$ values are reserved for SWTs with an oxygen concentration below $200 \mu mol\, kg^{-1}$ (AAIW1, AAIW2, CDW1 and CDW2). These lower oxygen concentrations correspond with higher nutrient concentrations and salinities occupying a relatively small 34.56-34.71 range. These SWTs therefore relate to ocean interior nutrient depletion in the upper ocean leading to high nutrient/low oxygen values for intermediate and deep waters. Lower NADW $\overline{C^{bio}}$ corresponds with nutrient depleted surface waters at formation. Both NADW and AABW display similar values of oxygen,

and this explains the similarity of the $\overline{C^{bio}}$ estimates.

Deep Ocean C^{eqm} Pre-industrialisation DIC concentration is given by $\overline{C^{eqm}}$. Generally, $\overline{C^{eqm}}$ increases with depth. SAMW $\overline{C^{eqm}}$ is lowest, largely reflecting low DIC and $\overline{TA^{\circ}}$ (equation 4.10) and relatively low salinity, nutrient and silicate. $\overline{C^{eqm}}$ AABW maximum is enhanced by low temperature and high $\overline{TA^{\circ}}$ (equation 4.11) caused by pronounced $CaCO_3$ dissolution (Wust, 1935), matching the results shown here.

Deep Ocean C^{diseq} OMP analysis is only applied to the $-2 \leq \theta \leq 5$ interval to account for non-linear mixing. Calculation of C^{DIC}, C^{bio}, C^{eqm} and C^{diseq} for θ intervals above the 5°C isotherm is directly from the parameterisations from equations 4.10, 4.11 and 4.14 and Table 4.2a)-b).

$\overline{C^{diseq}}$ for each SWT is listed in Table 4.4. Differences between C^{diseq} parameterisations from Vázquez-Rodríguez et al. (2012) and Pardo et al. (2011) result in a clear deviation between $\overline{C^{diseq}_{VR}}$ and $\overline{C^{diseq}_{P}}$, influencing the resulting C^{ant}. Deviations are particularly significant for deep water masses, either formed or substantially modified within the Southern Ocean. Negative C^{ant} for $\overline{C^{diseq}_{P}}$ and high C^{ant} compared to Lo Monaco et al. (2005a) and Vázquez-Rodríguez et al. (2009b) for $\overline{C^{diseq}_{VR}}$ are calculated for Drake Passage and 30°E situated on the boundaries of the regions of applicability for each parameterisation. The mean of $\overline{C^{diseq}_{VR}}$ and $\overline{C^{diseq}_{P}}$ is a compromise to generate a C^{ant} field within the range of Vázquez-Rodríguez et al. (2009b) (their Figure 4).

Uncertainty within C^{diseq}, particularly for the Southern Ocean, is evident from the inter-comparison of both Pardo et al. (2011) (their Figure 6) and Vázquez-Rodríguez et al. (2012) (their Figure 4) with alternative C^{diseq} estimates (Lee et al., 2003; Takahashi et al., 2009), yielding discrepancies of up to $20\mu mol\,kg^{-1}$, south of 60°S (Lee et al., 2003) and gives a sense of the limitations of the method, compared to published estimates of uncertainty for the φC^{o}_{T} and $\triangle C^{*}$ methods in the Atlantic Ocean of $\pm 5.2\mu mol\,kg^{-1}$ and $\pm 7.9\mu mol\,kg^{-1}$ (Vázquez-Rodríguez et al., 2009b,a; Lee et al., 2003; Khatiwala et al., 2012), respectively. In this Chapter and Chapter 5, the focus is ΔC^{ant}, rather than C^{ant}, and in this instance uncertainties in C^{diseq} will cancel. Error propagation of the $-2 \leq \theta \leq 5$ interval in Table 4.4, therefore gives a C^{ant} uncertainty of up to $\pm 5\mu mol\,kg^{-1}$, which given the discrepancies in C^{diseq} is a lower bound on uncertainty whereas $\pm 5\mu mol\,kg^{-1}$ is a more reasonable uncertainty estimate for ΔC^{ant}.

ΔC^{*} Anthropogenic Carbon (C^{ant}) Following the calculation ΔC^{*} and C^{diseq}, C^{ant} is given by:

a)

SWT	$\overline{C^{DIC}}$	$\overline{C^{bio}}$	$\overline{C^{eqm}}$	$\overline{TA^{\circ}}$
WW	2162.9±1.9	14.0±1.0	2139.5±1.3	2293.0±1.4
SAMW	2121.7±4.6	5.8±0.5	2075.7±0.8	2264.3±1.0
AAIW1	2234.9±2.5	112.0±2.3	2123.0±1.5	2329.3±1.4
AAIW2	2217.1±1.0	103.9±0.6	2123.8±0.4	2321.3±0.4
NADW	2179.1±0.6	71.5±0.5	2126.4±0.4	2321.6±0.3
CDW1	2256.7±0.9	110.1±0.7	2168.6±0.4	2361.0±0.4
CDW2	2275.7±2.3	130.9±2.3	2170.4±1.4	2363.8±1.7
AABW	2251.5±0.3	66.3±0.2	2211.4±0.3	2390.5±0.3

b)

SWT	$\overline{C_{VR}^{diseq}}$	$\overline{C_{P}^{diseq}}$	$\overline{C^{diseq}}$	$\overline{C^{ant}}$
WW	-19.5±1.4	-13.6±0.5	-16.6±1.5	25.9±2.6
SAMW	-6.3±0.2	2.6±0.2	-1.9±0.3	42.1±4.7
AAIW1	-25.8±0.9	-10.6±0.6	-18.3±1.1	18.2±3.8
AAIW2	-23.0±0.2	-21.6±0.4	-21.6±0.4	11.1±1.2
NADW	-23.2±0.2	-23.2±0.2	-23.2±0.3	4.6±0.9
CDW1	-42.9±0.2	-26.7±0.1	-34.8±0.2	12.8±1.2
CDW2	-45.6±0.9	-25.1±0.3	-35.4±0.9	9.8±3.6
AABW	-53.3±0.2	-28.3±0.1	-40.9±0.2	14.7±0.4

Table 4.4: Mean values and standard error of the mean for each component of the C^{diseq} formulation, as well as $\overline{TA^{\circ}}$, after eOMP mixing coefficients are applied. $\overline{C_{VR}^{diseq}}$ is C^{diseq} calculated only using the Vázquez-Rodríguez et al. (2012) parameterisation for the $-2 \leq \theta \leq 5$ interval, whilst $\overline{C_{P}^{diseq}}$ is calculated upon inclusion of the Pardo et al. (2011) parameterisation. $\overline{C^{ant}}$ is calculated for each SWT from $\overline{C^{DIC}} - \overline{C^{bio}} - \overline{C^{eqm}} - \overline{C^{diseq}}$. Each property has units: μmol kg^{-1}.

$$C^{ant} = \Delta C^{*} - C^{diseq} \tag{4.25}$$

where C^{ant} represents anthropogenic carbon accumulation since pre-industrial levels. The change in C^{ant} between two timesteps is given by:

$$\triangle C^{ant} = C^{ant}_{A} - C^{ant}_{B} \tag{4.26}$$

with separate timesteps represented by "A" and "B".

4.3.3 eMLR (extended Multiple Linear Regression)

The MLR, and later eMLR, techniques are developed from the work of Wallace (1995) for comparing DIC changes from two hydrographic occupations along the same transect and have been applied in a number of Atlantic Ocean studies e.g. Brown et al. (2010); Peng and Wanninkhof (2010); Wanninkhof et al. (2010); van Heuven et al. (2011). The MLR method uses all the observed DIC data independent of location along the transect, to create a predictive equation for DIC from the available hydrographic and chemical parameters. Assumptions are made that the relationship between predictors e.g. N, P, Si and predictand, in this case DIC, remain unchanged over time. The assumption is therefore invalid for significant changes in e.g. ocean temperature, limiting the temporal applicability of this method (Wanninkhof et al., 2010; Goodkin et al., 2011). C^{ant} input causes DIC change without affecting predictor variable concentrations. Creating a predictor equation from a first transect and applying the predictor equation to a second, more recent transect produces a predicted DIC. The residual between the predicted DIC and the observed DIC along a transect is interpreted as anthropogenic CO_2 input.

The eMLR approach, prescribed by Friis et al. (2005) extends the approach of Wallace (1995) by creating a second predictor equation for the more recent cruise dataset. By applying both predictor equations to the latter dataset, assumed to be of higher quality, a difference is calculated at one time, and an increase over time is interpreted as anthropogenic. eMLR is favoured for minimising error propagation and providing a smoother spatial structure, eliminating the effect of water mass motion on the predictor variables. However, not all of the DIC variability will have mapped successfully to the regression equation. Non-Gaussian residual distributions suggests that part of the real DIC signal will be left in the residuals (Brown et al., 2010) and hence, the smoother spatial structure is at the expense of real information (Levine et al., 2008).

As described in Brown et al. (2010), the value of an eMLR generated anthropogenic CO_2 signal relies on the ability of the chosen parameters to estimate the observed DIC

measurements from a regression equation of the form:

$$\mathrm{DIC} = y_o + ax_1 + bx_2 + cx_3 \tag{4.27}$$

where a, b, c etc. represent predictor coefficients, whilst y_o is the y-intercept and $x_{i=1,2,3...}$ represents any number of parameters e.g. N, P, Si. In this study, the chosen predictor parameters are oxygen (O_2), potential temperature (θ), silicate (Si), total alkalinity (TA) and phosphate (P), for a predictive equation taking the form:

$$\mathrm{DIC} = y_o + a\mathrm{O}_2 + b\theta + c\mathrm{Si} + d\mathrm{TA} + e\mathrm{PO}_4^- \tag{4.28}$$

The inclusion of TA, given that TA was not a measured parameter in 1990, fits with the more general assumption for no change in the predictors over time, with no assumed anthropogenic influence on TA distribution (van Heuven et al., 2011). Predictor coefficients are calculated for two temporally separate hydrographic cruises and then differenced, and the difference is applied to the more recent dataset (designated by a subscript "2", compared to "1" for the earlier occupation) to create the predictive equation:

$$\Delta\mathrm{C}^{\mathrm{ant}} = \left(y_o^2 - y_o^1\right) + (a_2 - a_1)\,\mathrm{O}_2 + (b_2 - b_1)\,\theta + (c_2 - c_1)\,\mathrm{Si} + (d_2 - d_1)\,\mathrm{TA} + (e_2 - e_1)\,\mathrm{PO}_4^- \tag{4.29}$$

This combination of predictor parameters has the lowest cumulative standard deviation for the datasets analysed, and high correlation coefficients (Table 4.5). Additional coefficients are also shown in Table 4.5.

Similarly to $\Delta\mathrm{C}^{\mathrm{ant}}$ derived from TrOCA, $\Delta\mathrm{C}^{\mathrm{ant}}$ is interpolated using section 2.3.1 and 2.3.2 methodologies. In this analysis, all cruises are synoptic and gridded using γ^n isopycnals to minimise seasonal heave. Information up to the surface is preserved within the solution, with estimates within the upper 150dbar treated with greatest caution (Brown et al., 2010; Wanninkhof et al., 2010).

4.3.3.1 Sensitivity of corrections to eMLR $\Delta\mathrm{C}^{\mathrm{ant}}$

eMLR captures the dominant trend in the $\Delta\mathrm{C}^{\mathrm{ant}}$ distribution, however residuals remain between the measured DIC $\left(\mathrm{DIC}^{\mathrm{measured}}\right)$ and DIC predicted using the eMLR regression $\left(\mathrm{DIC}^{\mathrm{predicted}}\right)$. In this section, residuals (δDIC) are calculated for each transect following Brown et al. (2010):

Transect	$O_2 a$	θb	Sic	TAd	$PO_4^- e$	y_o	R^2	RMS (μmol kg^{-1})	n
Drake Passage 1990	-0.600	-11.424	-0.020	0.350	8.403	1538.946	0.995	3.9	210
Drake Passage 2009	-0.370	-7.112	-0.052	0.573	39.079	901.948	0.991	3.3	580
30°E 1996	-0.429	-8.587	0.034	0.514	21.044	1086.216	0.993	5.6	1923
30°E 2008	-0.367	-6.998	-0.073	0.612	30.634	835.341	0.990	6.5	1556

Table 4.5: Multiple Linear Regression Coefficients from equation 4.28 along with the correlation coefficient (R^2), RMS and number of data points per transect (n).

$$\delta\mathrm{DIC} = \mathrm{DIC}^{\mathrm{measured}} - \mathrm{DIC}^{\mathrm{predicted}} \tag{4.30}$$

The resultant residuals indicate data biases, and provide clues for potential data issues (Friis et al., 2005; Brown et al., 2010). In pressure space (Figure 4.5), the resultant residuals are distributed around zero with little structure below the upper 500dbar whilst along 30°E, some structure remains with a slight drift towards negative residuals above 200dbar and a slight positive residual bias between 200dbar and 500dbar. Published estimates for uncertainty from Friis et al. (2005) give $\pm 7\mu$mol kg^{-1} above 300dbar and $\pm 3\mu$mol kg^{-1} below 300dbar. In this study, uncertainties estimated from the standard deviation of the pressure residuals give $\pm 5.5/\pm 8.4\mu$mol kg^{-1} above 300dbar and $\pm 3.7/\pm 5.2\mu$mol kg^{-1} below 300dbar for Drake Passage and 30°E, respectively.

In γ^n space, the resultant residuals are generally centred around zero, with some structure observable, particularly within the lower γ^n upper ocean (Figure 4.6). Additionally in γ^n, differences between each occupation of a transect is calculated as the mean of the MLR residuals within γ^n intervals $\left(\overline{\delta\mathrm{DIC}_1(\gamma^n)} - \overline{\delta\mathrm{DIC}_2(\gamma^n)}\right)$, similar to Brown et al. (2010) (Figure 4.7, Table 4.6). Drake Passage and 30°E residuals deviate from positive to negative throughout the water column. Small residuals generally within $\pm 5\mu$mol kg^{-1} reflect both a representative regression fit, with the regression acting to smooth the $\mathrm{DIC}^{\mathrm{measured}}$, and the limit of the eMLR method to define $\triangle C^{ant}$. The reduced latitudinal/longitudinal range of the hydrographic section in this study, compared to Brown et al. (2010), also helps to maintain the regression fit as representative sectionwide.

To test the sensitivity of the regression fit, two sets of corrections are applied to the

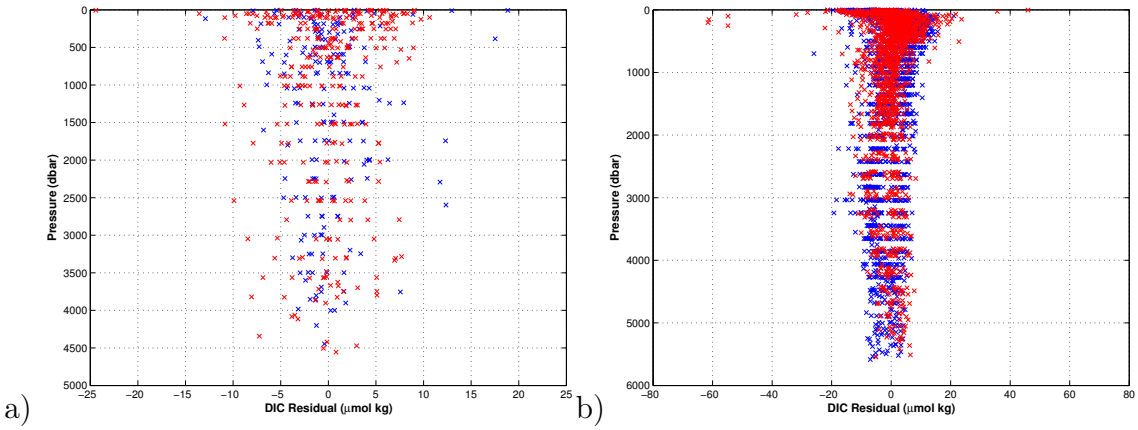

Figure 4.5: Sectionwide MLR $DIC^{measured} - DIC^{predicted}$ residuals for each transect in pressure space. $DIC^{measured}$ is directly from CTD data for a) Drake Passage for both 1990 (blue) and 2009 (red), and b) 30°E for both 1996 (red) and 2008 (blue).

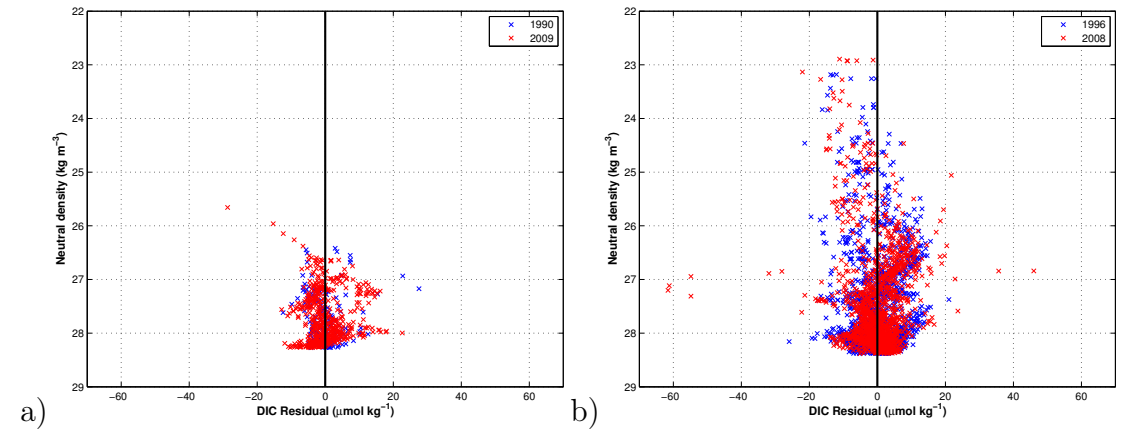

Figure 4.6: Similar to Figure 4.5, sectionwide MLR $DIC^{measured} - DIC^{predicted}$ residuals for each transect in neutral density space. a) Drake Passage for both 1990 (blue) and 2009 (red), and b) 30°E for both 1996 (red) and 2008 (blue).

Neutral density interval	Drake Passage (μmol kg^{-1})	30°E (μmol kg^{-1})
<24	*	-3.0
24-25	*	-1.4
25-26	*	-2.4
26-26.80	0.8	2.8
26.80-26.90	*	0.3
26.90-27.00	-2.9	-0.8
27.00-27.10	3.2	-1.0
27.10-27.23	0.7	-2.5
27.23-27.30	-0.2	-5.4
27.30-27.40	0.6	0.5
27.40-27.50	0.6	-1.3
27.50-27.60	-0.9	-1.6
27.60-27.70	-0.1	-1.6
27.70-27.80	1.3	0.2
27.80-27.90	1.5	-0.5
27.90-28.00	0.5	1.7
28.00-28.10	0.4	0.4
28.10-28.20	-0.3	0.4
28.20-28.27	-2.1	-0.6
28.27-27.35	*	0.6
>27.35	*	1.5

Table 4.6: Difference in the means of the MLR residuals ($\overline{\delta \mathrm{DIC}\,(\gamma^n)}$, equation 4.30) calculated for each transect across Drake Passage and 30°E for the defined neutral density intervals.

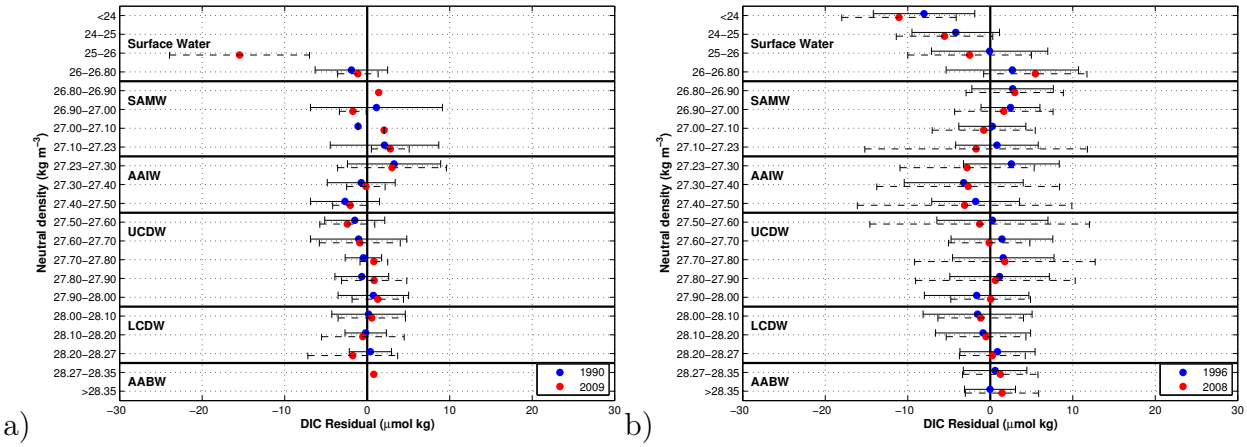

Figure 4.7: Mean and standard deviation for the sectionwide MLR DIC residual ($\mathrm{DIC^{measured}} - \mathrm{DIC^{predicted}}$) within the specified neutral density intervals. A dot defines the mean residual for the neutral density interval for a) Drake Passage: 1990 (red) and 2009 (blue), and b) 30°E: 1996 (red) and 2008 (blue). Water mass boundaries are shown for each water mass: surface, SAMW, AAIW, UCDW, LCDW and AABW.

eMLR estimate. Firstly, following Brown et al. (2010), γ^n interval mean residuals are applied as a sectionwide correction in Figure 4.7 and Table 4.6 using:

$$\triangle \mathrm{C}^{\mathrm{ant}}_{\mathrm{corrected}} = \triangle \mathrm{C}^{\mathrm{ant}}_{\mathrm{uncorrected}} + \left(\overline{\delta \mathrm{DIC}_1 \left(\gamma^n \right)} - \overline{\delta \mathrm{DIC}_2 \left(\gamma^n \right)} \right) \tag{4.31}$$

where "1" and "2" are the most recent and historical cruises, respectively. δDIC is the residual between measured DIC and predicted DIC (equation 4.30), whilst $\overline{\delta \mathrm{DIC} \left(\gamma^n \right)}$ is the mean DIC residual for each neutral density interval. Secondly following Peng and Wanninkhof (2010), a correction is calculated independently for each hydrographic zone along each transect, with three correction zones along Drake Passage (SAZ, PFZ, AZ), and four correction zones along 30°E (STZ, SAZ, PFZ, AZ). Corrections for each zone are shown in Figure 4.8 for Drake Passage, and Figure 4.9 for 30°E. Along Drake Passage and 30°E, DIC residuals are typically within $\pm 5 \mu \mathrm{mol\,kg^{-1}}$ with larger residuals generally within the Surface, SAMW or AAIW. At 30°E, DIC residuals extend throughout the water column in γ^n space. Small standard deviations observed for a number of the interval means, reflect the limited number of datapoints within each neutral density interval of each hydrographic zone.

Each mean DIC residual $\left(\overline{\delta \mathrm{DIC} \left(\gamma^n \right)} \right)$ acts as a correction factor and is added to every DIC measurement within the chosen neutral density interval (equation 4.31). eMLR sectionwide correction provides negligible effect to eMLR uncertainties calculated above and below 300dbar, calculated by adjusting the DIC residual from the earliest cruise by the γ^n interval mean residual. Uncertainties for sectionwide correction are

		STZ		SAZ		PFZ		AZ	
		Orig.	Adj.	Orig.	Adj.	Orig.	Adj.	Orig.	Adj.
Drake Passage	Above 300 dbar	*	*	±5.5	±5.4	±3.0	±2.7	±5.9	±5.5
	Below 300 dbar	*	*	±4.1	±4.0	±2.7	±2.7	±3.6	±3.7
30°E	Above 300 dbar	±8.3	±8.4	±6.5	±5.2	±15.0	±15.9	±6.5	±6.3
	Below 300 dbar	±5.9	±5.9	±4.2	±4.0	±4.4	±4.0	±4.2	±4.0

Table 4.7: Uncertainties for eMLR calculated as the standard deviation of the pressure residuals, above 300dbar and below 300dbar, for each hydrographic zone across Drake Passage and 30°E: Subtropical Zone STZ, Subantarctic Zone SAZ, Polar Frontal Zone PFZ, Antarctic Zone AZ. The 'Orig.' refers to the uncorrected pressure residual within each zone, whilst the 'Adj.' refers to the pressure residuals within each zone, when the pressure residuals for a single cruise are adjusted by the mean DIC residual $\left(\overline{\delta \mathrm{DIC}\left(\gamma^n\right)}\right)$ for each γ^n interval. Units of $\mu\mathrm{mol\,kg^{-1}}$.

thus, $\pm 5.5/\pm 8.4 \mu\mathrm{mol\,kg^{-1}}$ above 300dbar and $\pm 3.7/\pm 5.2 \mu\mathrm{mol\,kg^{-1}}$ below 300dbar for Drake Passage and 30°E, respectively. Uncertainties for each zone are shown in Table 4.7, with reduced uncertainty for the adjusted values in some zones. The resulting corrected and uncorrected eMLRs, both give ΔC^{ant} distributions across Drake Passage and 30°E that are interpolated following the methodology described in section 4.2.1 and are shown in Chapter 5. For comparison to TrOCA, changes in C^{ant} are also calculated per decade for each γ^n-defined water mass, and will be further discussed in Chapter 5.

A further correction was tested following Wanninkhof et al. (2010) to create an eMLR estimate by constructing separate regression equations for each potential density layer. The applicability of the Wanninkhof et al. (2010) method in this study was investigated for both A21 and 30°E, using both potential density layers and γ^n defined surface, SAMW, AAIW, UCDW, LCDW and AABW water masses, however, difficulties were encountered. Firstly, creating a reliable regression equation relies on a minimum number of datapoints within each potential density layer, as shown in Wanninkhof et al. (2010) (their Table 3). For A21 1990 in particular, the density of datapoints is not high enough to be able to generate realistic regression equations for ΔC^{ant}, and hence it is suggested that the Wanninkhof et al. (2010) method is primarily only applicable for

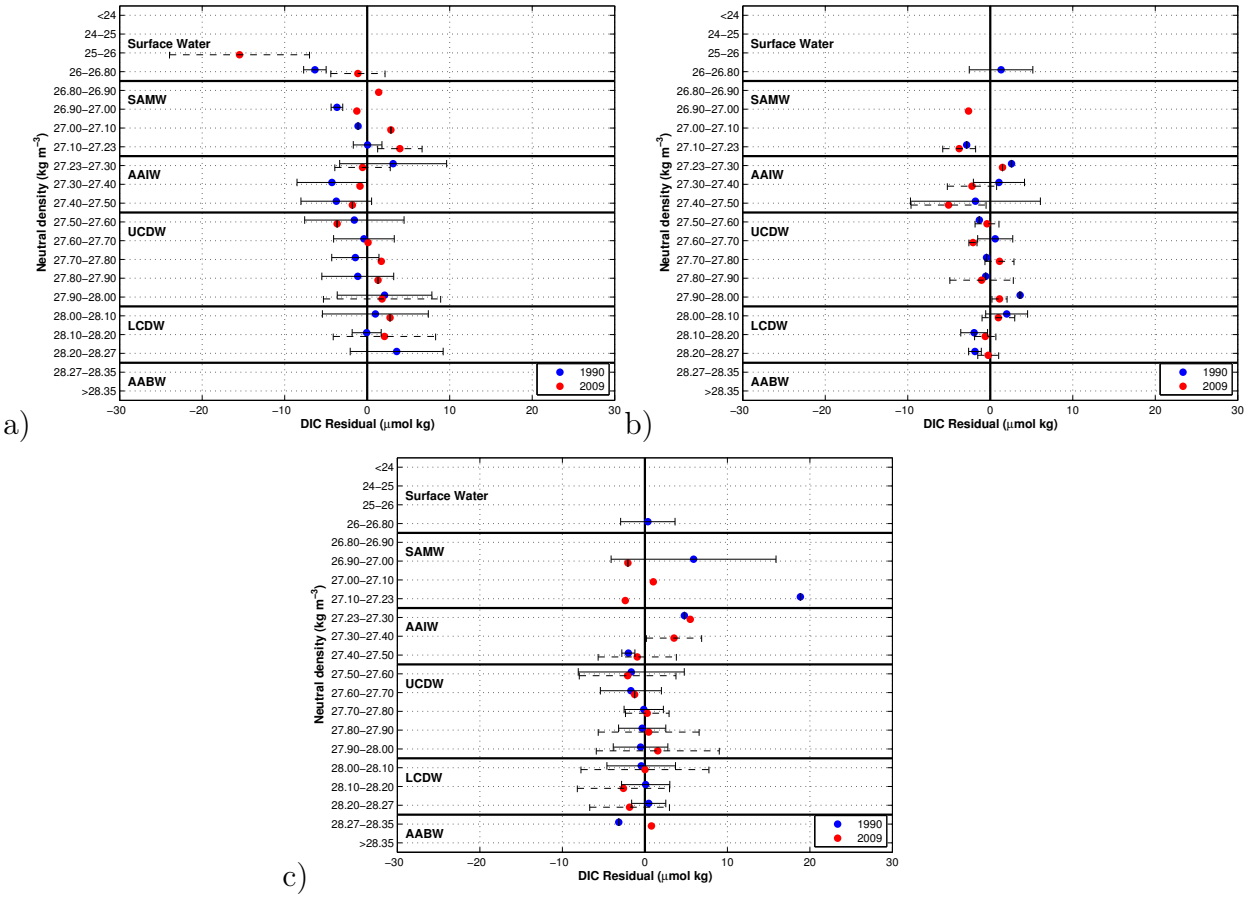

Figure 4.8: Mean and standard deviation for the DIC residual ($DIC^{measured} - DIC^{predicted}$) within the specified neutral density intervals. A dot defines the mean residual for the neutral density interval for Drake Passage: 1990 (red) and 2009 (blue) for a) Subantarctic Zone, b) Polar Frontal Zone, c) Antarctic Zone. Water mass boundaries are shown for each water mass: surface, SAMW, AAIW, UCDW, LCDW and AABW.

larger datasets.

4.3.3.2 Anomalous DIC differences

As a brief aside, anomalous DIC differences discovered via the methodology of section 4.2.1 are investigated using a version of the MLR technique following van Heuven et al. (2011) by creating a predicted DIC from a single MLR between DIC and additional variables (θ, salinity, pressure, oxygen, phosphate, TA, silicate) from all occupations of a particular transect. Variation in predicted DIC caused by co-incident variability in the predictor fields, is attributed to natural variability. Residuals between the predicted DIC and initial DIC field are attributed to C^{ant}.

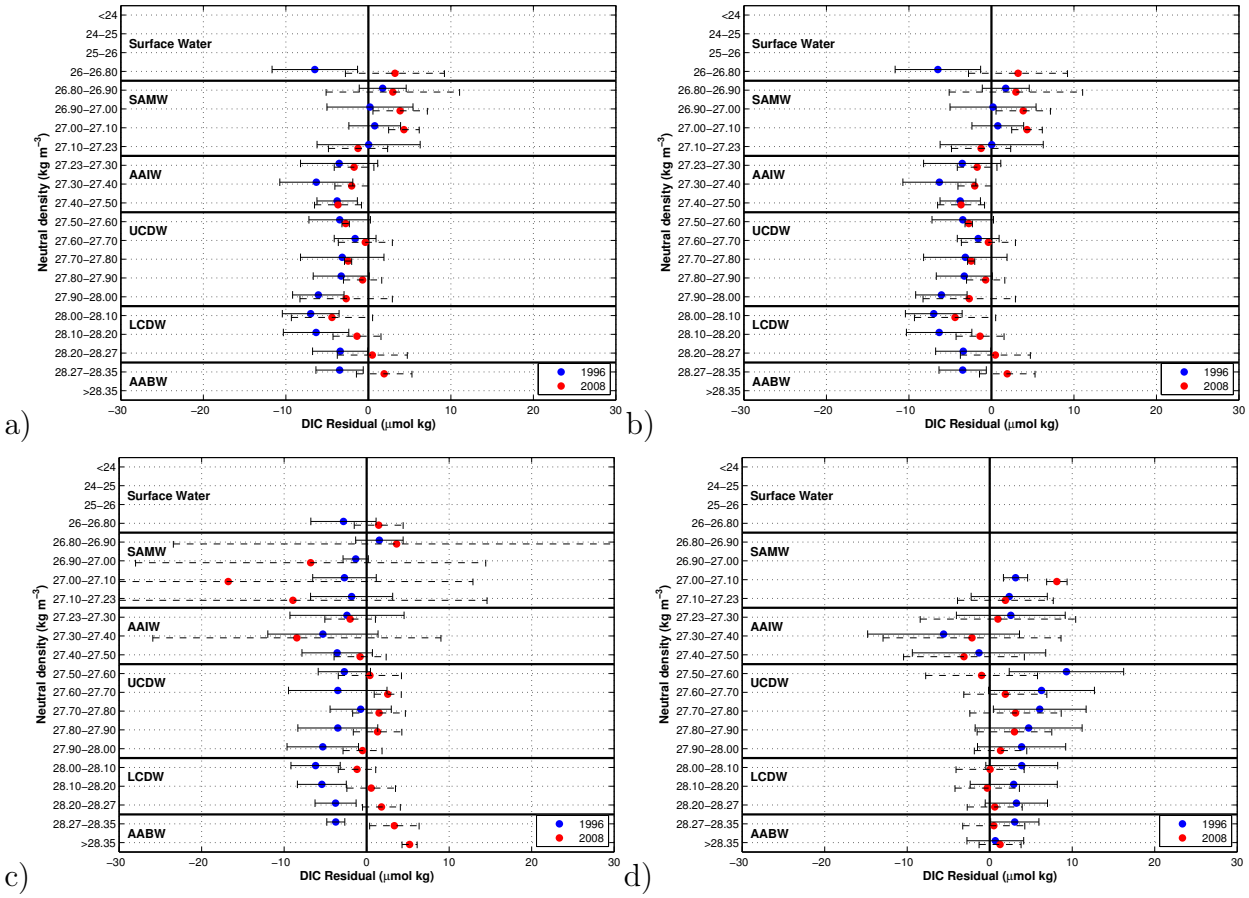

Figure 4.9: Mean and standard deviation for the DIC residual ($DIC^{measured} - DIC^{predicted}$). A dot defines the mean residual for the neutral density interval for 30°E: 1996 (red) and 2008 (blue) a) Subtropical Zone, b) Subantarctic Zone, c) Polar Frontal Zone, d) Antarctic Zone. Water mass boundaries are shown for each water mass: surface, SAMW, AAIW, UCDW, LCDW and AABW.

4.4 Summary

TrOCA Equation 4.4 displays the conservative TrOCA tracer combining DIC, oxygen and alkalinity. ΔC^{ant} is calculated by defining a TrOCA tracer for each transect, and finding the difference (equation 4.5).

$\triangle C^*$ $\triangle C^*$ is broken down into components (equation 4.6 and 4.9), making use of the potential alkalinity (pTA) parameterisation (equation 4.10) and the DIC, upon assumption of atmosphere-ocean equilibrium at pre-industrial fugacity (C^{eqm}, equation 4.11). C^{ant} is calculated for each transect using equation 4.12 as the difference between $\triangle C^*$ and C^{diseq}. C^{diseq} is parameterised according to equations 4.14 and 4.15, and Table 4.2a)-b). To better represent the well-mixed deep ocean, eOMP is applied to the deep ocean defined by the $-2 \leq \theta \leq 5$ interval. Once C^{ant} is calculated, ΔC^{ant} is calculated (equation 4.26). Value added by using the φC_T^o adaptation of the $\triangle C^*$ method is for subsurface parameterisations to better represent water mass formation and a reduction of the reliance upon the linear CFC-estimated water mass age (Matsumoto and Gruber, 2005).

eMLR A regression equation is calculated for each transect (equation 4.28) with resultant coefficients in Table 4.5. To calculate ΔC^{ant}, predictor coefficients from separate occupations of the same cruise track are differenced (equation 4.29). To try to improve the representativeness of the ΔC^{ant} regression relationship, two forms of post-regression correction are suggested. Corrections are calculated based on the residuals between measured DIC and the DIC predicted from the regression equations from each transect, with the mean difference between the residuals calculated for selected neutral density intervals (equations 4.30 and 4.31). The mean residual is applied as firstly, a sectionwide correction, and secondly, as a correction for each hydrographic zone.

Method comparison A simple comparison of the three methods applied in this study is shown in Table 4.8. All methods assume that the natural carbon system is in steady state, and variations in biological processes are adequately represented by Redfield ratios, or changes in biological parameters e.g. AOU. The TrOCA method assumes that the TrOCA tracer is a conservative parameter within the ocean, however, Yool et al. (2010) using model data, conclude that in the upper 200dbar the uncertainty associated with this assumption grows to up to 50%. For a study of ΔC^{ant}, the uncertainties reduce and likely fall close to the addition of Touratier et al. (2007)'s C^{ant} uncertainty of $\pm 6.2 \mu mol\,kg^{-1}$ in quadrature, yielding $8.8 \mu mol\,kg^{-1}$ for ΔC^{ant}. This

	Strengths	Weaknesses
TrOCA	Simple to apply using commonly measured parameters, for assumption of constant pre-industrial and disequilibrium behaviour no need to calculate C^{eqm} and C^{diseq} for ΔC^{ant}	Assumption of TrOCA conservation breaks down in the upper ocean
$\triangle C^*$	Well used in the literature, founded on biological/chemical processes	Calculation of ventilation of water masses and C^{diseq} uncertain, with uncertainties propagating to C^{ant}
eMLR	Simple to apply using commonly measured parameters, smooth resulting distribution making interpretation easier	Assumption of constancy of other ocean parameters, part of real signal lost by non-Gaussian residuals

Table 4.8: Comparison of the major strengths and weaknesses of TrOCA, $\triangle C^*$ and eMLR.

study estimates, based on DIC, TA and oxygen uncertainties, a TrOCA ΔC^{ant} uncertainty of $\pm 7.3 \mu mol\,kg^{-1}$ at Drake Passage, and $\pm 5.8 \mu mol\,kg^{-1}$ at 30°E.

Gruber et al. (1996) and Khatiwala et al. (2012) estimate an uncertainty for $\triangle C^*$ for C^{ant} of $\pm 9 \mu mol\,kg^{-1}$, however, this study estimates an uncertainty for $\triangle C^*$ C^{ant} of $\pm 6.6 \mu mol\,kg^{-1}$, based on DIC, TA, oxygen and nutrient uncertainties, whereas the inclusion of a maximum C^{diseq} uncertainty estimate of $\pm 12.5 \mu mol\,kg^{-1}$, based on the spread of C^{diseq} estimates in Table 4.4, indicates a maximum C^{ant} uncertainty of up to $\pm 13.4 \mu mol\,kg^{-1}$. For ΔC^{ant}, the assumption of constant pre-industrial conditions causes C^{eqm} to drop out, whilst part of the C^{diseq} uncertainty will cancel given that the same C^{diseq} parameterisation is applied to all datasets along a transect, leading to ΔC^{ant} uncertainty of $\pm 8.5 \mu mol\,kg^{-1}$, if uncertainties are assumed to be measurement uncertainties, rather than caused by the C^{diseq} parameterisation. The limitations of the $\triangle C^*$ approach relate to our knowledge of water mass ventilation and the efficiency with which atmospheric CO_2 is absorbed.

Uncertainties for eMLR from section 4.3.3, are up to $8.4 \mu mol\,kg^{-1}$ for ΔC^{ant} in the upper 300dbar, and up to $5.2 \mu mol\,kg^{-1}$ below 300dbar with the cause of uncertainty, as noted in Table 4.8, being the assumption for constancy of other ocean parameters that are used for predicting C^{ant}. eMLR corrections contibute a small to negligible reduction in the uncertainties.

Key points In this Chapter, the methodology for testing changes in DIC, both using direct differencing and by creating a DIC residual, in order to remove any anomalous data points, are described. Changes in Redfield ratio are discussed for the assessment of whether any changes in DIC are attributable to variations in biological cycling, or whether an external input of DIC is implied. Three anthropogenic CO_2 methodologies are described, including the relative merits of each.

The following Chapter will discuss the results from reviewing changes in DIC using the direct comparison of DIC from separate occupations, DIC residual methods and changes in Redfield ratio (sections 4.2.1, 4.2.2 and 4.2.3). Anthropogenic CO_2 distributions are calculated using TrOCA, eMLR and $\triangle C^*$ methods (section 4.3.1, 4.3.3 and 4.3.2), in addition to reviewing the inferred change per decade.

Chapter 5

Distribution of Dissolved Inorganic Carbon and Anthropogenic Carbon in the South Atlantic sector of the Southern Ocean

5.1 Introduction

Since the observation of an increasing trend in atmospheric CO_2 in 1958 (Keeling, 1960), ocean monitoring for a simultaneous increase in carbon content has been a major international effort. The inorganic component, referred to as Dissolved Inorganic Carbon (DIC), is naturally present in all the world's oceans, however, an increase in DIC above that of natural biological variability is indicative of anthropogenic carbon.

This Chapter analyses five hydrographic cruises from the South Atlantic sector of the Southern Ocean following the detailed methodology in Chapter 4. Results provide an indication of DIC and anthropogenic carbon variability. The 19- and 12-year timeframes between re-occupations along Drake Passage and 30°E respectively, are adequate to detect DIC concentration changes. Occupations separated by <5 years may produce a DIC signal, that is difficult to separate from natural variability, whilst occupations separated by longer timeframes are subject to additional uncertainty caused by changes in both ocean properties and ocean circulation.

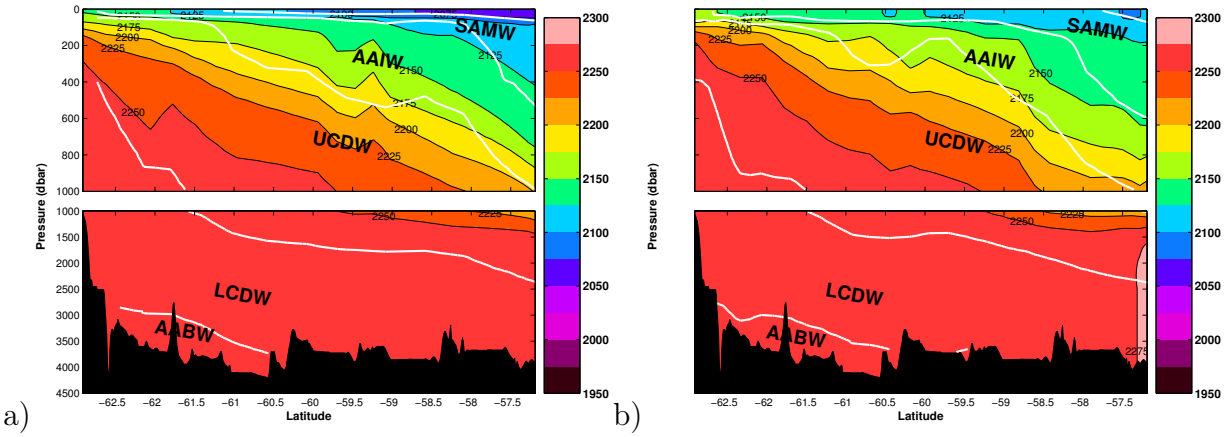

Figure 5.1: Drake Passage DIC distribution of a) A21 1990 and b) A21 2009. The white lines are neutral density water mass interfaces defined in Table 2.2 with, for example, the deepest white line representing the LCDW/AABW interface. Units of μmol kg^{-1}.

5.2 Changes in Dissolved Inorganic Carbon (DIC)

The following section contains the results for the methodologies, discussed in Chapter 4, for identifying changes in DIC.

5.2.1 DIC distributions

5.2.1.1 Drake Passage DIC distributions

For Drake Passage DIC distributions, Figure 5.1a)-b) for 1990 and 2009 respectively, surface/SAMW and SAMW/AAIW interfaces outcrop, providing a pathway for subsurface absorption. The minimum concentrations in 1990 ($<$2075μmol kg^{-1}) have increased in 2009 ($<$2100μmol kg^{-1}) within the upper 100dbar, north of 58.5°S. In 1990, surface/SAMW interface outcrops at close to the SPF at 61°S, compared to close to the SAF, north of 58°S, in 2009, contributing to subsurface ventilation. Near the Antarctic continent higher DIC concentrations ($>$2250μmol kg^{-1}) penetrate to $\sim$300dbar in 2009, compared to $\sim$400dbar in 1990, as UCDW, LCDW and AABW shallow from north to south.

5.2.1.2 30°E DIC distributions

For 1996 and 2008 (Figure 5.2a-b), the DIC minima is in the upper 400dbar, north of the Polar Front (50.75-51.1°S). The presence of a cold and fresh eddy in 1996, between 38°S and 40°S, distinguishable by isopleth shallowing is consistent with the eddy originating from a more southerly latitude. DIC concentrations lower than 2200μmol kg^{-1} are

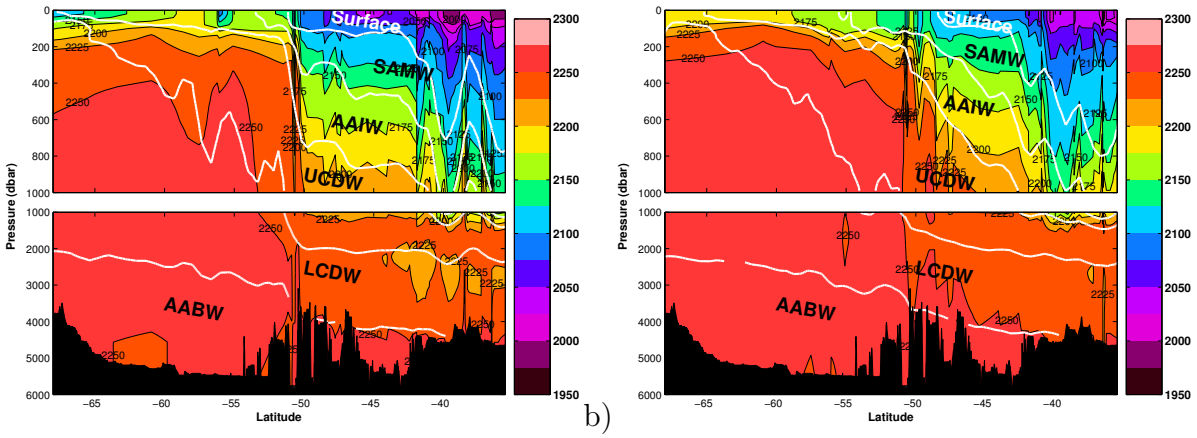

Figure 5.2: 30°E DIC sectionwide distributions for a) I6S 1996 and b) I6S 2008. Neutral density interfaces are shown for the major South Atlantic water masses (Table 2.2). Units of μmol kg^{-1}.

within the upper 1200dbar, north of the Polar Front, and the upper 200dbar south of the Polar Front only.

The most striking difference between Figure 5.2a) and b) is the change in the 2200-2250μmol kg^{-1} isopleths at the PF. For 1996, the 2000μmol kg^{-1} and 2225μmol kg^{-1} isopleths have a sharp gradient within the 200-1000dbar range, at the approximate position of the PF (~50.75°S). The gradient is ~800dbar per degree latitude for the 2225μmol kg^{-1} isopleth between 300dbar and 1000dbar, with nearly flat isopleths between the PF and the STF (~42.5°S). Sharp thermohaline PF gradients in 1996 of the 2°C isotherm and 34.5-34.7 isohalines (Figure 3.3b and Figure 3.4b) result in a stronger, more distinctive feature (Park et al., 2001) than in 2008.

In Figure 3.3a), 3.4a) and Figure 5.2b) for 2008, the Polar Front is less distinct, and indicated by the 2250μmol kg^{-1} isopleth, with a greater volume of higher DIC concentration water north of the PF. The 90dbar per degree latitude gradient of the 2225μmol kg^{-1} isopleth between 300dbar and 1000dbar, reflects gradual isopleth shallowing south of the STF (42.9°S). As the dominant method of mixing in the ocean is along isopycnals, sharp thermohaline gradients in 1996 restrict the advection and mixing of higher DIC concentration water masses from the south to latitudes north of the PF. Northward and upward expansion of the <2250μmol kg^{-1} water masses, as well as for the 2225-2250μmol kg^{-1} water mass between ~800-1100dbar at 45-50°S cause differing DIC compositions of the UCDW and LCDW in 2008 and 1996 in the PF to STF band. South of the PF, the DIC maxima (>2250μmol kg^{-1}) is predominantly within LCDW and AABW, between ~400-500dbar and the seafloor.

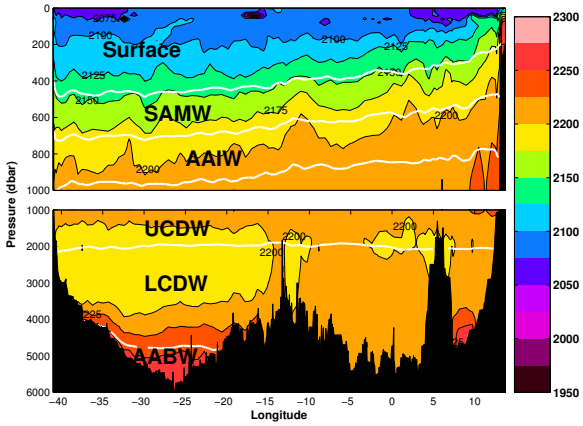

Figure 5.3: DIC distribution along 24°S. White lines are neutral density interfaces between water masses. Units of μmol kg^{-1}.

5.2.1.3 24°S DIC distribution

The hydrographic cruise along 24°S, completed in 2009, is the only occupation at this latitude with DIC measurements (King, 2010), hence no previous DIC data exists along this section to provide comparison. Across 24°S, AABW DIC concentrations are the highest (>2250μmol kg^{-1}) along the transect (Figure 5.3) similar to A21 (Figure 5.1) and I6S (Figure 5.2). AABW is confined to below 4000dbar within the Brazil Basin. The absence of high concentrations (> 2225μmol kg^{-1}), except east of Walvis Ridge at ~4-7°E, matches the absence of AABW within this region. Note that as described in Chapter 2, NADW is composed of lower UCDW and upper LCDW, and is identifiable in Figure 5.3 by a large patch of lower DIC concentration (<2200μmol kg^{-1}) spanning ~1500-3500dbar from 15°W to 40°W. East of the Mid-Atlantic ridge, lower deep ocean DIC concentrations (<2200μmol kg^{-1}) are limited to between 5°W and Walvis Ridge between ~1500dbar and 2500dbar. Above AAIW, DIC isopleths gradually shoal on eastward progression across 24°S. In the upper 200dbar, DIC concentrations are below 2100μmol kg^{-1}, with a section minima of <2075μmol kg^{-1} within the upper 100dbar, predominately within 5° longitude of the continents.

5.2.2 DIC residuals

Negative (positive) residuals in Figures 5.4 and 5.5 indicate that DIC concentrations are lower (higher) than the chosen best fit line (Figure 4.1 and 4.2) are not independently meaningful. For Figure 5.4a) for 1990, the majority of the distribution is negative whilst for 2009 (Figure 5.4b), there is a very similar distribution with slightly more positive values.

Along 30°E in 2008 (Figure 5.5b), a greater volume of positive residuals are observed compared to 1996 (Figure 5.5a) both north and south of the PF, with the $>30\mu$mol kg^{-1} maxima predominantly within UCDW and LCDW above ~2500dbar. Relatively recent ventilation of UCDW in 2008 both at source in the Indian and Pacific Oceans (Callahan, 1972) and subsequent modification in the Atlantic provide a mechanism for DIC accumulation. Positive residuals within the STZ surface waters indicates direct atmospheric CO_2 uptake by the ocean.

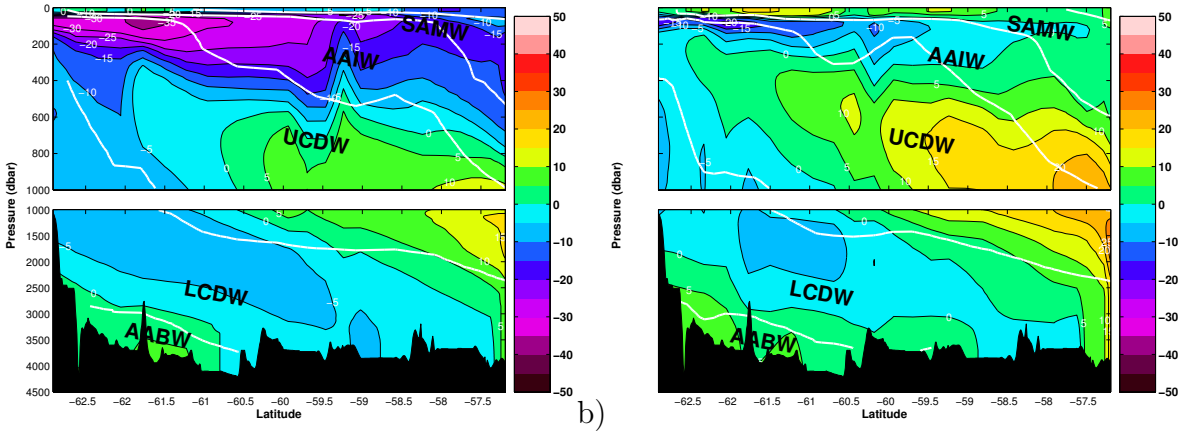

Figure 5.4: DIC residual distribution for Drake Passage (A21) calculated by merging the residuals from each hydrographic section. a) A21 1990, b) A21 2009. Solid white lines are neutral density interfaces between water masses from Table 2.2, water masses labelled. Blue - negative residual, red - positive residual. Units of μmol kg^{-1}.

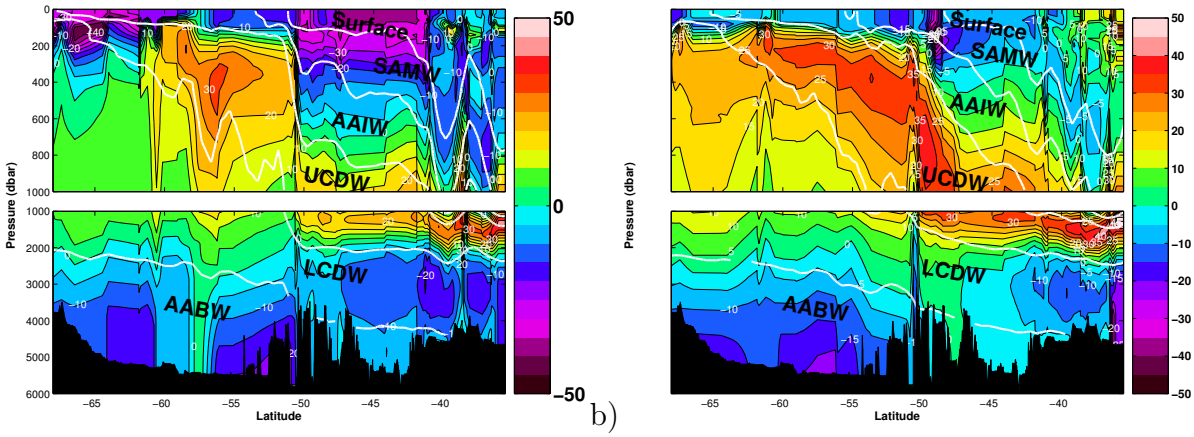

Figure 5.5: DIC residual distribution for I6S calculated by merging the residuals from each hydrographic section. a) I6S 1996, b) I6S 2008. Solid white lines are neutral density interfaces between water masses from Table 2.2, water masses labelled. Blue - negative residual, red - positive residual. Units of μmol kg^{-1}.

5.2.3 DIC and DIC residual difference distributions

5.2.3.1 Drake Passage

Positive DIC change in Figures 5.6a)-b) suggests a DIC increase over a 19-year interval since 1990, with a similar DIC distribution for DIC difference and DIC residual difference. DIC increases for the majority of the upper and deep ocean with the greatest increase reaching $\sim 30 \mu\text{mol kg}^{-1}$, within the upper 50dbar, as a direct consequence of mixed layer ventilation by recently absorbed CO_2. Between 100-600dbar, DIC changes are within the 0-25μmol kg^{-1} range. Subduction of high DIC surface waters contributes towards enhanced SAMW DIC ($>10 \mu\text{mol kg}^{-1}$) close to the South American continent within the upper 600dbar. Local formation of SAMW within the Southeast Pacific contributes to the recent subsurface SAMW ventilation. Further patches of positive change ($>20 \mu\text{mol kg}^{-1}$) are observed near the NPF in the upper 600dbar, as well as within the upper 500dbar, centered at $\sim$61.25°S. Positive patches of $>20 \mu\text{mol kg}^{-1}$ are generally below the recently ventilated Winter Water (Figures 3.1 and 3.26), and are likely affected by interannual front variability. Uniformly positive deeper ocean water mass (LCDW/AABW) changes in the 0-10μmol kg^{-1} range support slower deep ocean ventilation.

5.2.3.2 30°E

In comparison to Figures 5.6a)-b), deep ocean changes for 30°E are less uniform. For 30°E, positive DIC change dominates (Figure 5.7a-b), particularly north of the PF throughout the water column. The greatest positive differences ($>20 \mu\text{mol kg}^{-1}$) are in the upper 400dbar between the SAF and STF with additional patches within the STZ and PFZ. Positive DIC change exceeds $10 \mu\text{mol kg}^{-1}$ down to $\sim$3000dbar within the PFZ and SAZ. South of the SACCF, the greatest positive change $>10 \mu\text{mol kg}^{-1}$ is limited to the more recently ventilated upper 400dbar, with greater change for the DIC residual difference particularly at the WW/deep ocean transition. Negative residual differences are close to the SACCF, predominately limited to 54°S to 63°S.

Anomalous deep ocean DIC change The $>10 \mu\text{mol kg}^{-1}$ increase within the UCDW and LCDW between the PF and STF is further examined in Figure 5.8 and 5.7a)-b) by restricting DIC concentrations to the 2200-2270μmol kg^{-1} range. In 1996, a significant proportion of UCDW and LCDW in the PFZ/SAZ are within the 2230-2240μmol kg^{-1}, whilst in 2008, a greater UCDW/LCDW proportion is in the 2240-2250μmol kg^{-1} range, as confirmed by the original bottle data (Figure 5.9a-b). This offset is surprising for

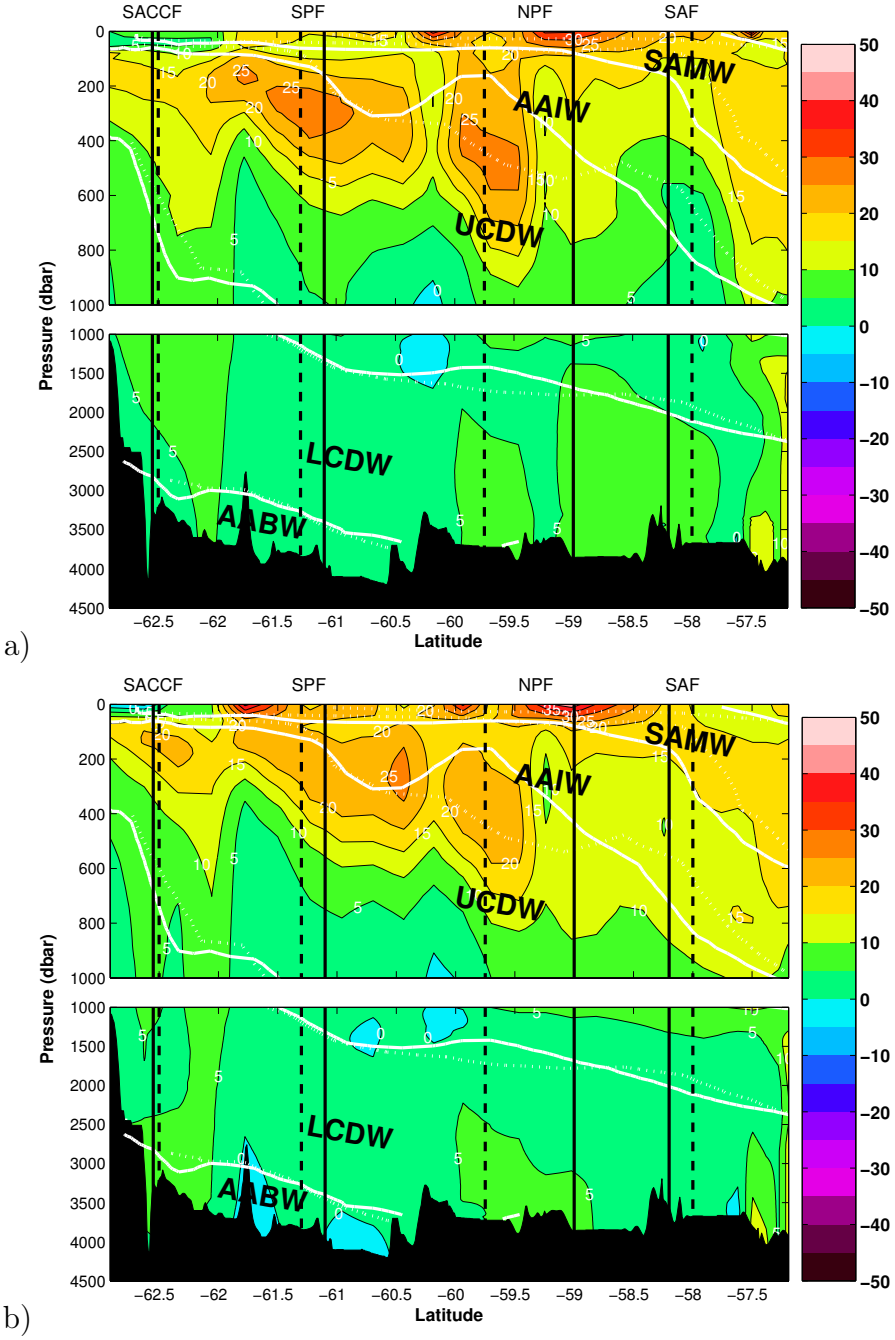

Figure 5.6: Distribution of a) DIC difference of $DIC_{(A21\ 2009)}$ -$DIC_{(A21\ 1990)}$ and b) residual DIC difference of residual $DIC_{(A21\ 2009)}$ -residual $DIC_{(A21\ 1990)}$, both gridded using geopotential height and neutral density. Neutral density levels are marked by white lines: continuous white lines - A21 2009; dotted white lines - A21 1990 for the dominant water masses. SACCF, SPF, NPF and SAF fronts are indicated by vertical lines: solid - A21 2009; dashed - A21 1990.

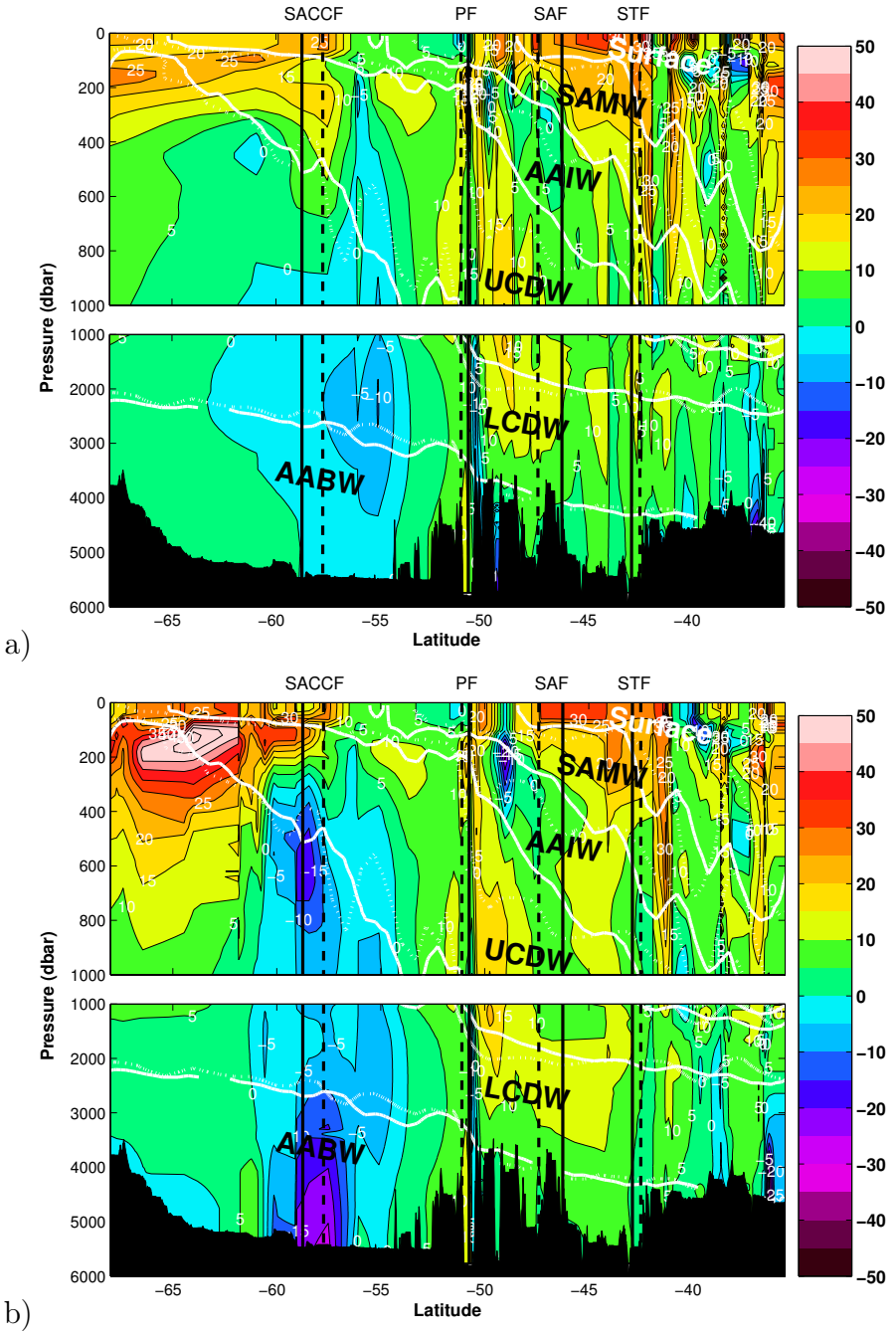

Figure 5.7: Distribution of a) DIC difference of $DIC_{(I6S\ 2008)}$ -$DIC_{(I6S\ 1996)}$ and b) residual DIC difference of residual $DIC_{(I6S\ 2008)}$ -residual $DIC_{(I6S\ 1996)}$, both gridded using geopotential height and neutral density. Neutral density interfaces are marked by white lines: continuous white lines - I6S 2008; dotted white lines - I6S 1996 for the major water masses. SACCF, PF, SAF and STF fronts are indicated by vertical lines: solid - I6S 2008; dashed - I6S 1996. Units of μmol kg^{-1}.

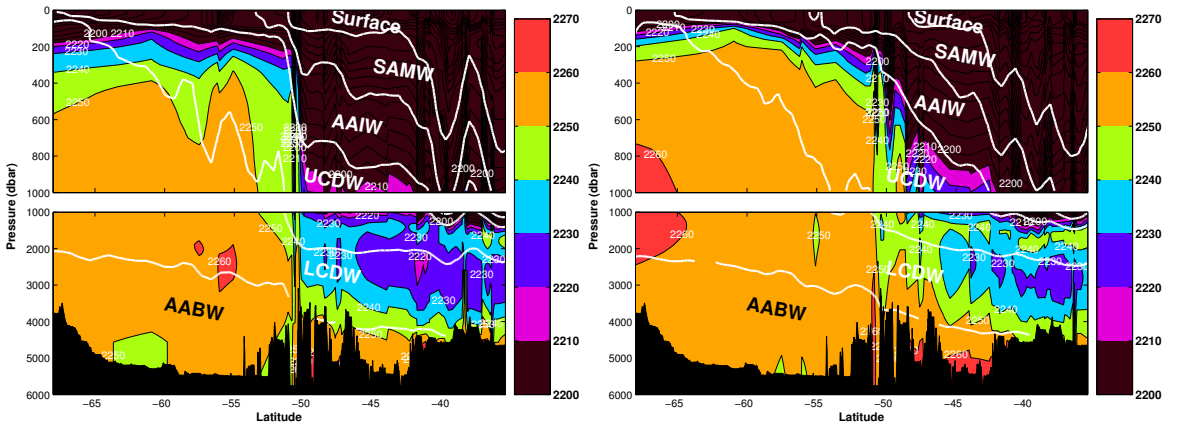

Figure 5.8: DIC sectionwide distributions for a) I6S 1996 and b) I6S 2008 with the DIC concentrations restricted to within the 2200-2270μmol kg^{-1} range. Neutral density interfaces are shown for the major South Atlantic water masses (Table 2.2). Units of μmol kg^{-1}.

relatively poorly ventilated deep water masses.

Natural DIC variability (Figure 5.9c) is estimated according to section 4.3.3.2 and van Heuven et al. (2011), by constructing a multiple linear regression equation for UCDW and LCDW independently for the combined 1996 and 2008 occupations, between the STF and PF. The resulting profile of predicted DIC is similar to the original bottle data (Figure 5.9c). The differences between predicted DIC estimates are attributed to natural variability. Differences between the mean UCDW and mean LCDW residual of 5.3$\pm$0.6μmol kg^{-1} and 3.6$\pm$0.6μmol kg^{-1} suggest that part of the DIC change can be attributed to natural variability, rather than anthropogenic change.

Natural variability is attributed to marked differences between the sharpness of the PF gradient between the two occupations. Sharp isopycnal, isotherm, isohaline and DIC isopleth gradients in the PF to STF band in 1996, attributed to a sharp meander of the mean flow by Naveira Garabato et al. (2011), has allowed lower DIC concentration water masses beneath the Agulhas regime to protrude southwards. Conversely in 2008, greater along isopycnal mixing within UCDW/LCDW from south of the PF has brought higher DIC concentration water into the PF/STF band. This analysis does not preclude the existence of a PF to STF measurement offset in the deep ocean DIC data, however, no particular issues are reported in the relevant cruise reports (Speer and Dittmar, 2008; Poisson et al., 1996), or Lo Monaco et al. (2005a,b)'s previous analysis of the I6S 1996 dataset. Hoppema et al. (2009)'s result that DIC along I6S 1996 could be up to 2μmol kg^{-1} too low, only partially accounts for the difference observed here.

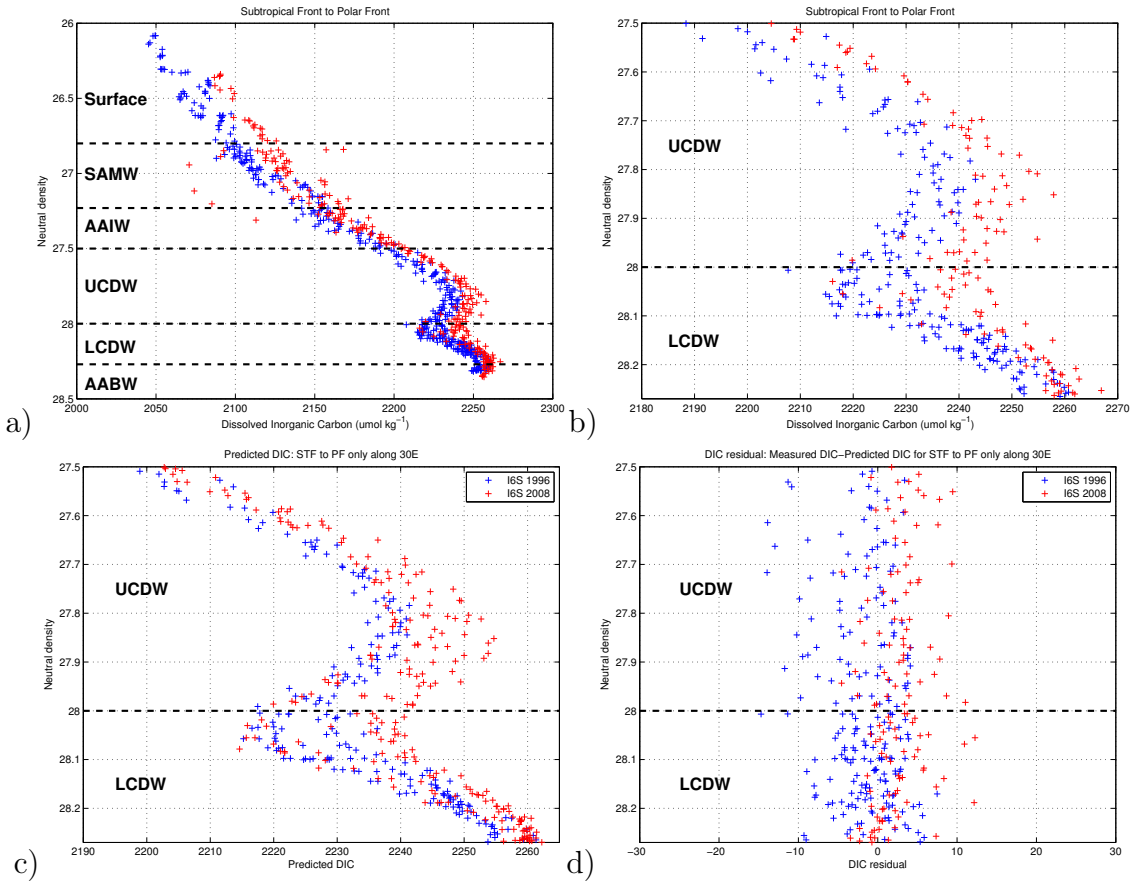

Figure 5.9: DIC profiles for I6S 1996 (blue) and I6S 2008 (red) between the Subtropical Front and Polar Front for the a) full depth water column and b) UCDW and LCDW only. c) Predicted DIC profiles for I6S 1996 (blue) and I6S 2008 (red) from a multiple linear regression equation using predictor variables θ, salinity, pressure, oxygen, phosphate, TA, silicate, and d) residual between predicted DIC field and initial DIC field. Neutral density interfaces are shown for the major South Atlantic water masses (Table 2.2). DIC units of μmol kg^{-1}.

5.2.3.3 Summary

Creating residuals of measured DIC is a preliminary method for establishing changes in oceanic carbon concentration. Using data directly from hydrographic CTD casts in γ^n space limits inaccuracies that develop from excessive interpolation, and takes into account water mass heave between transects and therefore DIC residual difference distributions are preferable to the direct comparison technique. Uncertainty within DIC residuals is therefore dependent on initial measurement uncertainty, estimated as $\pm 3 \mu\text{mol kg}^{-1}$ for the post-2000 transect, and $\pm 5 \mu\text{mol kg}^{-1}$ for the pre-2000 transects, or $\sim 6 \mu\text{mol kg}^{-1}$ for residual differences. Given that the majority of residual differences are in excess of the $\pm 6 \mu\text{mol kg}^{-1}$ range, the increasing DIC signal appears significant.

For further comparison of the DIC difference and DIC residual difference techniques, an area-weighted mean for DIC decadal change is calculated for each water mass, both sectionwide, and per zone. For Drake Passage, decadal variations for both methods follow a pattern of greater upper ocean change particularly within the surface and SAMW. Mixed layer ventilation and subsequent drawdown is accomplished at a sectionwide rate for SAMW of $9.5 \pm 0.1 / 9.7 \pm 0.1 \mu\text{mol kg}^{-1}$ decade^{-1}, respectively. Mechanisms for enhanced subsurface ventilation include: subduction of SAMW at Drake Passage after formation in the Southeast Pacific (Aoki et al., 2007; Herraiz-Borreguero and Rintoul, 2010); annual ventilation and subduction of Winter Water formed in Bellinghausen Sea (Naveira Garabato et al., 2009) and interannual variability of the frontal positions affecting isopycnal outcropping and the pathways for atmospheric CO_2 absorption (Sabine et al., 2004).

At 30°E, further evidence for WW ventilation south of the SACCF, and direct ventilation of the active STZ surface ocean are observed. In the deep ocean, DIC difference exceeding $10 \mu\text{mol kg}^{-1}$ at the UCDW/LCDW interface is associated with variable water mass composition in this region overlying the north side of the Southwest Indian Ridge (section 5.2.1.2), or possibly partially due to measurement uncertainty.

DIC decadal changes along 30°E in Table 5.2a) for both methods generally follows a pattern of higher DIC differences within the upper ocean, up to $22.5 \pm 0.8 / 23.3 \pm 0.3 \mu\text{mol kg}^{-1}$ decade^{-1} for the few datapoints in the SAZ surface ocean, decreasing towards the deep ocean. AABW shows a majority of weak DIC accumulation within the -2.2 ± 0.3 to $6.3 \pm 0.2 \mu\text{mol kg}^{-1}$ decade^{-1} range. For both methods, negative SAMW within the AZ is based on very few datapoints, and atypical of the upper ocean.

Although these simple methods, give an insight into the extent of the DIC increase within the ocean, natural and anthropogenic-sourced DIC are not separated. Separating the anthropogenic signal from the background DIC is the focus of a number of studies

		All	SAZ	PFZ	AZ
a)	Surface	8.3±0.4	8.3±0.4	*	*
	SAMW	9.5±0.1	8.9±0.1	12.2±0.2	8.8±0.3
	AAIW	7.6±0.2	6.7±0.2	7.3±0.2	8.8±0.1
	UCDW	4.5±0.1	2.8±0.1	3.5±0.1	5.6±0.2
	LCDW	2.5±0.1	3.2±0.1	3.1±0.1	2.2±0.1
	AABW	1.7±0.2	*	*	1.7±0.2
		All	SAZ	PFZ	AZ
b)	Surface	7.0±0.1	7.0±0.1	*	*
	SAMW	9.7±0.1	8.3±0.1	12.8±0.2	10.8±0.3
	AAIW	8.2±0.1	7.2±0.1	6.9±0.1	10.3±0.1
	UCDW	3.8±0.1	3.0±0.1	3.3±0.1	4.3±0.2
	LCDW	1.8±0.1	1.8±0.1	1.7±0.1	1.8±0.1
	AABW	1.5±0.5	*	*	1.5±0.5

Table 5.1: Drake Passage DIC decadal variations, calculated as an area-weighted mean, from a) DIC difference distribution (section 5.2.1) and b) DIC residual distribution within each water mass: Surface, SAMW, AAIW, UCDW, LCDW and AABW along Drake Passage for all zones and each hydrographic zone: SAZ, PFZ and AZ. Standard error of the mean is also shown. Units of μmol kg^{-1} decade^{-1} .

		All	STZ	SAZ	PFZ	AZ
a)	Surface	12.9±0.3	11.7±0.3	22.5±0.8	17.9±1.0	*
	SAMW	10.8±0.2	10.7±0.2	12.7±0.7	10.9±0.7	1.6±1.3
	AAIW	7.7±0.1	7.9±0.2	5.7±0.3	6.8±0.4	10.8±0.8
	UCDW	7.4±0.1	5.7±0.1	7.1±0.1	9.6±0.1	8.1±0.3
	LCDW	2.0±0.1	0.8±0.2	5.9±0.1	5.2±0.1	0.8±0.2
	AABW	0.1±0.1	0.1±0.3	3.9±0.1	0.8±0.3	-0.3±0.1
		All	STZ	SAZ	PFZ	AZ
b)	Surface	12.3±0.1	10.9±0.1	23.3±0.3	19.0±0.2	*
	SAMW	8.9±0.2	8.8±0.1	13.0±0.4	5.9±0.4	-0.9±0.8
	AAIW	8.1±0.1	6.4±0.2	9.1±0.3	7.5±0.3	11.0±0.4
	UCDW	8.0±0.1	5.4±0.1	8.5±0.1	10.2±0.1	9.3±0.3
	LCDW	3.5±0.2	2.3±0.2	8.2±0.2	5.7±0.2	2.3±0.5
	AABW	-1.1±0.3	3.9±0.2	5.6±0.1	6.3±0.2	-2.2±0.3

Table 5.2: 30°E DIC decadal variations, calculated as an area-weighted mean, from a) DIC difference distribution (section 5.2.1) and b) DIC residual distribution within each water mass: Surface, SAMW, AAIW, UCDW, LCDW and AABW along 30°E for all zones and each hydrographic zone: SAZ, PFZ and AZ. Standard error of the mean is also shown. Units of μmol kg^{-1} decade^{-1} .

(e.g. Brewer (1978); Chen and Millero (1979); Wallace (1995); Gruber et al. (1996); Touratier and Goyet (2004b); Lo Monaco et al. (2005b,a)) using a variety of methods (Sabine and Tanhua, 2010). Three of the methods for calculating anthropogenic CO_2 for the bounding South Atlantic hydrographic sections will be applied later in this Chapter, however, beforehand in the next section, biological influence on the DIC component is assessed.

5.2.4 Change in 'Redfield'-type stoichiometries

Redfield ratios are a global average, and small deviations from this average reflects natural variability, with Deutsch and Weber (2012) estimating an average $NO_3^- : PO_4^{3-}$ (herein N:P) from GLODAP data of 14.5:1 (c.f. Redfield 16:1). The following section examines nitrate, phosphate and DIC ratios for hints at whether changes between hydrographic cruises are solely biological, or whether an anthropogenic signal can be inferred, broadly following Takahashi et al. (1985) and Körtzinger et al. (2001). For section 5.2.4 only, the usage of the term 'upper ocean' and 'deep ocean' will be restricted to above, and below the mixed layer depth (MLD), respectively.

5.2.4.1 Change in N:P stoichiometry ($R_{N:P}$)

N : P ratios are generally kept steady through the compensatory behaviour of denitrification in high nutrient areas and subsequent nitrate remineralisation by N-fixers in low nutrient areas (Deutsch and Weber, 2012). Differences in N : P (Figure 5.10, Table 5.3) between each occupation is most clearly observed within the AZ for both Drake Passage and 30°E, caused by lower N : P within both the upper and deep ocean along A21 1990 and I6S 1996. Several mechanisms exist for causing this apparent nitrate depletion, such as, insufficient nitrate remineralisation at the time of sampling to compensate for the October-December growth phase (Table 1.1), insufficient physical mixing across biogeographic provinces (Weber and Deutsch, 2010) to enable the return of N : P to Redfield 16:1, evidence for a remnant of distant denitrification (Sigman et al., 2000) or variability of the dominant phytoplankton species (Goeyens et al., 1995; De Baar et al., 1997; Arrigo et al., 1999; Hoppema and Goeyens, 1999; Weber and Deutsch, 2010).

The A21 upper ocean generally supports northward increase of N : P (Figure 5.10, Table 5.3) resulting from enhanced nitrate remineralisation, reduced denitrification, or variability of the phytoplankton species in low nutrient, warmer waters, specifically within the recently ventilated surface layer, as AAIW subducts below (Whitworth and Nowlin, 1987; Pollard et al., 2006). For the A21 deep ocean sections (Figure 5.10

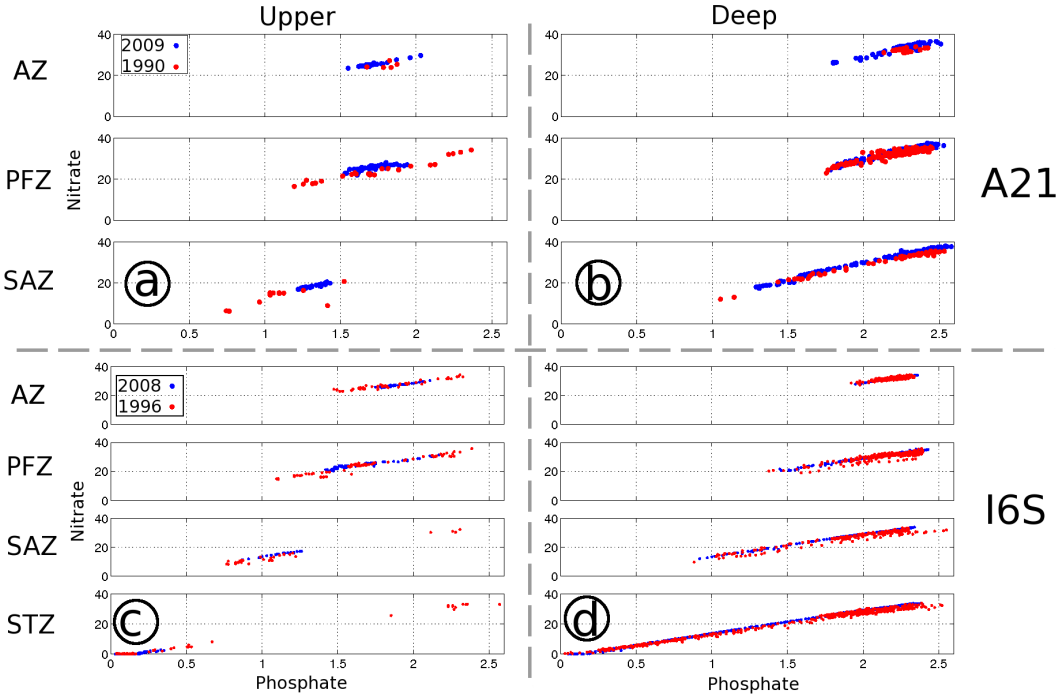

Figure 5.10: Nitrate vs. phosphate concentration for Drake Passage (A21) (a, b) and 30°E (I6S) (c, d) above and below the Mixed Layer Depth. For a) A21 1990 and 2009 upper ocean, b) A21 1990 and 2009 deep ocean, each plot consists of Upper Panel: Antarctic Zone, Central Panel: Polar Frontal Zone (PFZ), Lower Panel: Subantarctic Zone. For c) I6S 1996 and 2008 upper ocean, d) I6S 1996 and 2008 deep ocean, each plot consists of Upper Panel: Antarctic Zone, Upper Central Panel: Polar Frontal Zone (PFZ), Lower Central Panel: Subantarctic Zone and Lower Panel: Subtropical Zone. A21 2009 and I6S 2008 stations are blue, and A21 1990 and I6S 1996 stations are red. The gradient of each line is in Table 5.3.

b) and Table 5.3b)), only A21 2009 PFZ is within uncertainty of the Redfield ratio with all other regions below 16:1 with no clear trend along the A21 2009 section. Between 1990 and 2009, AZ and SAZ upper ocean N : P ratio (Table 5.3) increases by $5.2\pm10.1\mu\text{mol kg}^{-1}$ and $2\pm4.6\mu\text{mol kg}^{-1}$ and decreases by $3\pm1.6\mu\text{mol kg}^{-1}$ in the PFZ, whilst for the deep ocean (Table 5.3), N : P ratio increases by $10.7\pm1.9\mu\text{mol kg}^{-1}$, $1.9\pm0.4\mu\text{mol kg}^{-1}$ and $0.8\pm0.2\mu\text{mol kg}^{-1}$ for AZ, PFZ and SAZ respectively. Given the large uncertainties, upper ocean N : P changes are inconclusive, whilst the deep ocean is broadly supportive of N : P increase between 1990 and 2009.

From south to north along the I6S upper ocean section (Figure 5.10c), enhanced depletion of nitrate and phosphate in the warmer, saltier waters, particularly north of the SAF, contribute towards lower STZ ratios, whilst an increasing trend is observable from south to north for AZ-SAZ. I6S 1996 deep ocean results (Figure 5.10d) show

a)

	Above MLD		
	AZ	PFZ	SAZ
A21 1990	7.5±10.1	13.9±0.7	12.6±4.5
A21 2009	12.7±0.7	10.9±1.4	14.6±0.9

b)

	Below MLD		
	AZ	PFZ	SAZ
A21 1990	4.6±1.8	14.0±0.4	15.0±0.2
A21 2009	15.3±0.5	15.9±0.2	15.8±0.1

c)

	Above MLD			
	AZ	PFZ	SAZ	STZ
I6S 1996	11.7±0.4	15.4±0.5	15.2±0.4	14.4±0.1
I6S 2008	13.0±0.4	13.7±0.4	15.3±0.5	7.7±0.4

d)

	Below MLD			
	AZ	PFZ	SAZ	STZ
I6S 1996	10.3±0.5	13.4±0.4	14.0±0.3	14.6±0.1
I6S 2008	14.9±0.1	14.7±0.1	15.2±0.1	15.2±0.1

Table 5.3: Nitrate:Phosphate (N : P) ratio with their associated standard errors for the A21 section in 2009 and 1990, split in the vertical according to the Mixed Layer Depth into a) upper and b) deep ocean components, and for the I6S section in 2008 and 1996, split into c) upper and d) deep ocean components. Type 2 regression is applied for the two dependent variables (Glover et al., 2002). In the horizontal, N : P is given for each hydrographic zones: Antarctic, Polar Frontal Zone (PFZ), Subantarctic and Subtropical. Standard Redfield ratio stoichiometry gives N:P of 16:1.

slightly greater uncertainties than I6S 2008. A south to north trend is observed in 1996 (Table 5.3d) and much more weakly in 2008, with ratios in 2008 comparatively higher, closer to the Antarctic continent. Lower deep water ratios near the Antarctic continent in 1996 follow the mechanisms mentioned above, and are more supportive of a N : P increase across the section than the upper ocean.

5.2.4.2 ΔC : ΔN Redfield ratio

To reiterate, differences in the N : P ratio are only indicative of differences in the biological system along each transect at the time of sampling. An increase in the N : P ratios between occupations provides evidence for increased nitrate availability potentially due to either increased remineralisation, reduced denitrification or changes in the dominant phytoplankton species. In general, N : P ratios below the Redfield 16:1 ratio indicate nitrate limitation and therefore, this section investigates $\triangle$C : $\triangle$N, $\overline{\triangle \mathrm{C}}$, $\overline{\triangle \mathrm{N}}$ and $\overline{\triangle \mathrm{P}}$ for each upper/deep zone to identify whether DIC change is simultaneous with the hypothesised nitrate increase and caused by natural, biological variability. $\triangle$C : $\triangle$N is

chosen, as opposed to $\triangle C : \triangle P$, given that upon initial inspection $\overline{\triangle P}$ values appear small (Table 5.4-5.5). Excess DIC change, above the biologically-attributed nitrate change, is supportive of anthropogenic influence.

Across Drake Passage above the MLD, a trend (Figure 5.11) for more positive changes in DIC and N is observed within the PFZ ($\triangle C \approx 4.3$ to $29.2 \mu mol\,kg^{-1}$, $\triangle N \approx -1.0$ to $3.9\ \mu mol\,kg^{-1}$), compared to the AZ ($\triangle C \approx -6.4$ to $9.5 \mu mol\,kg^{-1}$, $\triangle N \approx -1.4$ to $2.3 \mu mol\,kg^{-1}$). $\triangle C$ and $\triangle N$ are greater than $0 \mu mol\,kg^{-1}$ for a majority of datapoints. For near-surface waters, the affect of temperature on CO_2 solubility is substantial, and contributes to a $\triangle C$ increase from south to north (Figure 5.6). Below the MLD, a clear trend in $\triangle C$ between SAZ and AZ is not observed, although the most positive $\triangle C$ ($\sim 15 \mu mol\,kg^{-1}$) is within the SAZ.

Upper ocean $\triangle C : \triangle N$ gradients for AZ and PFZ are above Redfield 6.6:1 ratio for each hydrographic zone for Figure 5.11 and Table 5.4 with SAZ biased by too few datapoints above the MLD. High stoichiometries suggest either enhanced DIC increase, or a comparatively lower increase in N. The y-intercept is by definition calculated for $\triangle N = 0$, however opposite to expectations, AZ and PFZ give negative $\triangle C$. The PFZ and SAZ yield the greatest $\overline{\triangle N}$ and $\overline{\triangle C}$, respectively with the greatest $\overline{\triangle C}$:$\overline{\triangle N}$ ratio equal to 17.5 for SAZ.

Below the MLD (Figure 5.11b, Table 5.4b), gradients are above the Redfield 6.6:1 ratio for each hydrographic zone with correlation coefficients in the 0.49-0.54 range. y-intercepts are negative across the transect. For mean datapoints, $\overline{\triangle C}$ is greatest within SAZ, whilst $\overline{\triangle N}$ decreases slightly between the AZ and SAZ leading to an increased $\triangle C : \triangle N$ gradient. The SAZ is also influenced by some datapoints with a high $\triangle C$ ($>40 \mu mol\,kg^{-1}$) causing gradient estimates above the Redfield ratio.

For 30°E upper ocean, $\Delta C : \Delta N$ gradients (Figure 5.12a, Table 5.5a) are above the Redfield 6.6:1 ratio for each zone except the SAZ. Correlation coefficients are highest for SAZ, whereas the more southerly zones contain a greater number of bunched datapoints causing a lower correlation coefficient. y-intercepts are positive for each PFZ to STZ hydrographic zone. $\overline{\triangle N}$ decreases in the STZ, whilst $\overline{\triangle C}$ is highest within the warmer SAZ and STZ mixed layer.

For the deep ocean, the $\Delta C : \Delta N$ gradient for each zone is above the Redfield 6.6:1 ratio, however, y-intercepts are negative for AZ-SAZ. Correlation coefficients are also generally quite low for the PFZ and SAZ corresponding with the anomalous deep ocean DIC change discussed in section 5.2.3.2, with outliers around a tight cluster of datapoints helping to set the gradient. Higher $\overline{\triangle N}$ is generally matched by higher $\overline{\triangle C}$ within PFZ-STZ, supporting a $\triangle C$ driven gradient above the Redfield ratio.

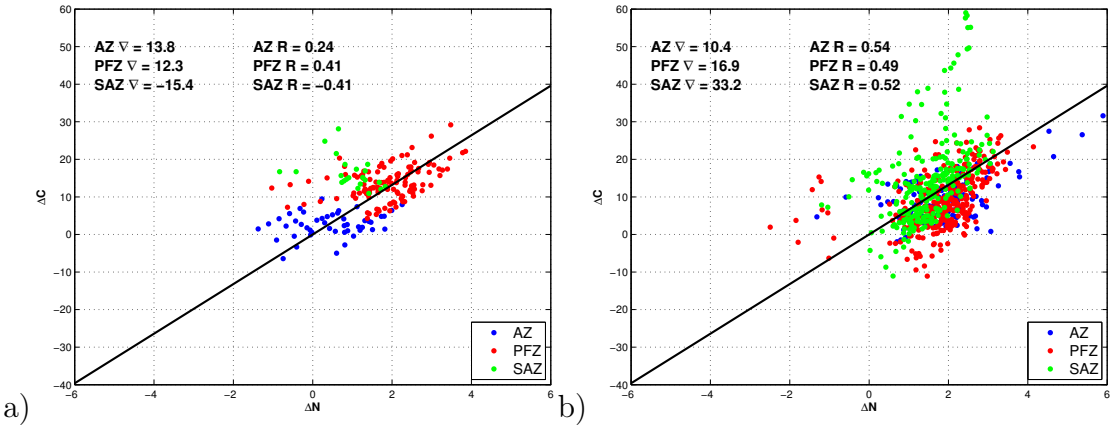

Figure 5.11: Ratio for the change in DIC vs. change in nitrate (ΔC : ΔN) for the Drake Passage transect for a) above Mixed Layer Depth (ΔT > 0.2°C), b) below Mixed Layer Depth. Gradient (∇) and correlation coefficient (R) for each hydrographic zone are also shown. Hydrographic zones are labelled: Antarctic Zone (AZ), Polar Frontal Zone (PFZ) and Subantarctic Zone (SAZ). The solid black line represents $R_{C:N}$ (= 6.6 : 1).

a)

Above MLD	AZ	PFZ	SAZ
Gradient	13.8±7.9	12.3±2.5	-15.4±7.2
y-intercept	-3.9±5.7	-9.4±3.5	30.60±7.2
Correlation coefficient	0.24	0.41	-0.41
$\overline{\triangle N}$	0.47±0.45	1.88±0.40	0.93±0.89
$\overline{\triangle C}$	2.57±0.13	13.65±0.08	16.28±0.14
$\overline{\triangle P}$	-0.033±0.010	-0.018±0.007	0.017±0.005

b)

Below MLD	AZ	PFZ	SAZ
Gradient	10.4±1.5	16.9±1.7	33.2±3.5
y-intercept	-10.2±2.2	-22.2±2.5	-35.4±4.5
Correlation coefficient	0.54	0.49	0.52
$\overline{\triangle N}$	1.91±0.50	1.84±0.43	1.52±0.85
$\overline{\triangle C}$	9.71±0.09	8.89±0.05	14.98±0.05
$\overline{\triangle P}$	0.054±0.001	0.039±0.003	0.034±0.004

Table 5.4: Gradient for the change in DIC ($\triangle$C) vs. change in nitrate ($\triangle$N) for the Drake Passage transect, as well as the y-intercept, correlation coefficient (R), $\overline{\triangle N}$, $\overline{\triangle C}$ and $\overline{\triangle P}$ for a) above the Mixed Layer Depth (ΔT > 0.2°C), b) below the Mixed Layer Depth. Hydrographic zones are labelled: Antarctic Zone (AZ), Polar Frontal Zone (PFZ) and Subantarctic Zone (SAZ). Uncertainties are given as standard deviations for the gradient and y-intercept, and standard errors for $\overline{\triangle N}$, $\overline{\triangle C}$ and $\overline{\triangle P}$.

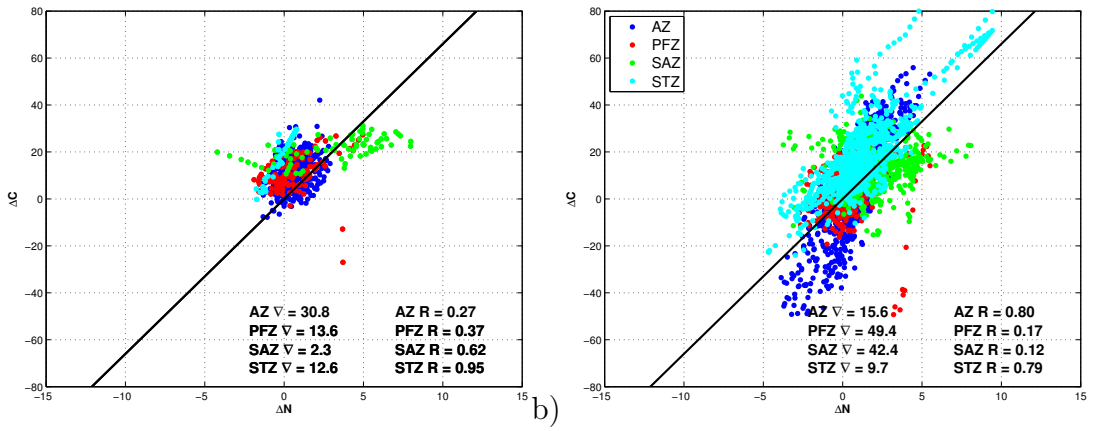

Figure 5.12: Ratio for change in DIC vs. change in nitrate ($\Delta C : \Delta N$) for the 30°E transect for a) above Mixed Layer Depth ($\Delta T > 0.2$°C), b) below Mixed Layer Depth. Gradient (∇) and correlation coefficients (R) for each hydrographic zone are also shown. Hydrographic zones are labelled: Antarctic Zone (AZ), Polar Frontal Zone (PFZ) and Subantarctic Zone (SAZ). The solid black line represents $R_{C:N}$ (= 6.6 : 1).

	Above MLD	AZ	PFZ	SAZ	STZ
	Gradient	30.8±5.2	13.6±3.2	2.3±0.3	12.6±0.6
	y-intercept	-9.3±4.4	2.5±3.0	14.3±0.8	21.0±0.3
a)	Correlation coefficient	0.27	0.37	0.62	0.95
	$\overline{\triangle N}$	0.66±0.35	0.59±0.69	2.98±0.57	-0.22±1.32
	$\overline{\triangle C}$	11.1±0.04	10.50±0.13	21.12±0.33	18.23±0.11
	$\overline{\triangle P}$	0.086±0.003	0.007±0.010	0.111±0.019	0.029±0.012
	Below MLD	AZ	PFZ	SAZ	STZ
	Gradient	15.6±0.4	49.4±13.0	42.4±14.8	9.7±0.3
	y-intercept	-7.2±0.9	-20.6±9.8	-60.6±19.8	6.5±0.5
b)	Correlation coefficient	0.80	0.17	0.12	0.79
	$\overline{\triangle N}$	0.52±0.53	0.53±0.43	1.74±0.38	1.23±0.56
	$\overline{\triangle C}$	0.94±0.04	5.54±0.05	13.27±0.07	18.53±0.07
	$\overline{\triangle P}$	0.041±0.003	0.005±0.003	-0.005±0.005	0.053±0.005

Table 5.5: Gradient for the change in DIC ($\triangle C$) vs. change in nitrate ($\triangle N$) for the 30°E transect, as well as the y-intercept, correlation coefficient (R), $\overline{\triangle N}$, $\overline{\triangle C}$ and $\overline{\triangle P}$ for a) above Mixed Layer Depth ($\Delta T > 0.2$°C), b) below Mixed Layer Depth. Hydrographic zones are labelled: Antarctic Zone (AZ), Polar Frontal Zone (PFZ), Subantarctic Zone (SAZ) and Subtropical Zone (STZ). Uncertainties are given as standard deviations for the gradient and y-intercept, and standard errors for $\overline{\triangle N}$, $\overline{\triangle C}$ and $\overline{\triangle P}$.

Drake Passage N:P and $\Delta C : \Delta N$ ratios Differences in the biology at the time of sampling find significant increases for both $\overline{\triangle N}$ and N : P for the majority of zones (Table 5.4a, b). $\overline{\triangle N}$ increase (1.52 to 1.91μmol kg^{-1}) and small $\overline{\triangle P}$ increase (0.034 to 0.054μmol kg^{-1}) in deep ocean zones are supportive of a nitrate increase above uncertainty limits, with a comparatively lower phosphate increase. Nitrate increase in excess of phosphate change, matches Hypothesis 1, potentially caused by either enhanced remineralisation, reduced denitrification or a change in the dominant phytoplankton species.

$\Delta C : \Delta N$ gradients for every hydrographic zone are far above the Redfield ratio, apart from the SAZ upper ocean, in contrast to N : P ratios near, or below the Redfield 16:1 ratio similar to Deutsch and Weber (2012)'s 14.5:1 estimate from Atlantic, Pacific and Indian Ocean GLODAP data. Higher correlation coefficient supports $\Delta C : \Delta N$ fits that are generally better in the deep ocean. $\overline{\triangle C}$ generally follows a south to north increasing trend for $\Delta C : \Delta N$ far above the Redfield ratio, both above and below MLD, despite uniform $\overline{\triangle N}$ increase, apart from the SAZ upper ocean. Therefore, this is supportive of excess $\overline{\triangle C}$ increase, above that typically supported by natural biological variation, leading to the conclusion that additional non-biological DIC input is likely to be anthropogenically caused.

The conclusion of upper ocean $\overline{\triangle C}$ increase corresponds directly to increased proximity to the enhanced CO_2 source, whilst deep waters are ventilated in the South Atlantic by the MOC (Sloyan and Rintoul, 2001b; Lumpkin and Speer, 2007; Meredith et al., 2011b). The conclusion for DIC increase in this study is in agreement with Gruber et al. (2009)'s assessment for a net CO_2 sink of anthropogenic CO_2 south of 44°S (Mikaloff Fletcher et al., 2006, 2007; Jacobson et al., 2007).

30°E N:P and $\Delta C : \Delta N$ ratios Generally, positive phosphate changes across 30°E, compares to nitrate increases in every zone except the data-sparse STZ upper ocean (Table 5.5). For the deep ocean, N : P increases between each occupation are primarily caused by N increase, rather than P change (Table 5.3c-d), corresponding with $\overline{\triangle C}$ increasing for each zone. $\Delta C : \Delta N$ conclusively in excess of the Redfield ratio for each zone, enables the conclusion that significant $\overline{\triangle C}$ increase dominates the increasing $\Delta C : \Delta N$. A mid-latitude $\overline{\triangle C}$ increase (e.g. PFZ upper ocean) is in agreement with enhanced CO_2 uptake (Mikaloff Fletcher et al., 2007; Gruber et al., 2009), whilst in the AZ-SAZ deep ocean, high $\Delta C : \Delta N$ is explained by MOC upwelling and outcropping of deep water masses (Speer et al., 2000; Meredith et al., 2011b) allowing along isopycnal CO_2 uptake prior to subduction (Sabine et al., 2004; Lovenduski et al., 2008; Gruber

et al., 2009). Low $\overline{\triangle C}$ for AZ deep ocean corresponds to a region dominated by old LCDW and likely contains low anthropogenically-sourced $\overline{\triangle C}$ change. Therefore in conclusion, $\overline{\triangle C}$ is positive for each zone and the overall $\triangle C$ increase signal remains, as excess $\overline{\triangle C}$ increase dominates $\Delta C : \Delta N$.

Additional stoichiometries ($R_{C:O_2}$, $R_{O_2:N}$, $R_{O_2:P}$) In addition to the excess $\overline{\triangle C}$ signal found from reviewing N : P and $\Delta C : \Delta N$ stoichiometries in the previous section, this section reviews additional stoichiometries to provide an indication of the extensiveness of the applicability of 'standard' stoichiometries, as given by Anderson and Sarmiento (1994). These stoichiometries are relevant both as independent assessments of Redfield ratio variability and also in subsequent calculation of anthropogenic carbon: $R_{C:O_2} = -117/170$ (-0.69), $R_{O_2:N} = -170/16$ (-10.625) and $R_{O_2:P} = -170/1$. $R_{C:O_2}$, $R_{O_2:N}$ and $R_{O_2:P}$ stoichiometries (Tables 5.6, 5.7 and 5.8) for each hydrographic zone along Drake Passage and 30°E are deduced using the same method as for $R_{N:P}$. $R_{C:O_2}$, $R_{O_2:N}$ and $R_{O_2:P}$ across all depths, occupy a range of stoichiometries between -1.78±0.06 to 1.37±0.11/1.37±0.30, -21.745±1.291 to 6.898±0.701 and -317.670±19.683 to 105.167±10.285, respectively.

The central tendency of these ratios across all zones and all transects is represented by the time-independent median (Table 5.9). Medians for $R_{C:O_2}$, $R_{O_2:N}$ and $R_{O_2:P}$ are all closer to zero within the upper ocean compared to the deep ocean. WW formation enhances O_2 concentration within the AZ upper ocean and further northwards (Figure 3.7) although WW O_2 maximum is associated with no nutrient signature. Nutrient depletion predominantly occurs within warmer water towards the north of each transect. Erosion of the WW O_2 maxima as it spreads northwards, and the southern limit of the nutrient depletion, creates a band of water with a positive correlation between O_2 and nutrient depletion, leading to more positive $R_{O_2:N}$ and $R_{O_2:P}$ ratios. $R_{O_2:N}$ and $R_{O_2:P}$ follow a general increasing trend from south to north across the transect. Upper ocean $R_{C:O_2}$ is affected by both C^{ant} uptake and WW ventilation. From the distribution of $R_{C:O_2}$ and associated interquartile range, it is difficult to infer a consistent deviation from the Redfield ratio.

Deep Ocean medians of $R_{O_2:N}$ and $R_{O_2:P}$ are closer to the Redfield ratio, compared to the upper ocean. Similar to the upper ocean, $R_{O_2:N}$ and $R_{O_2:P}$ become increasingly positive towards the north of the transects through the combination of erosion of the WW O_2 maxima and nutrient depletion. The proportion of the volume of the water column below MLD, with lower DIC concentration ($<2225 \mu mol\,kg^{-1}$) increases towards the north of each of the transect. Relatively high O_2 concentrations ($>220 \mu mol\,kg^{-1}$)

	$R_{C:O_2}$ Above MLD	AZ	PFZ	SAZ	STZ
a)	Drake Passage 1990	-0.09±0.18 (-15.3/170)	1.37±0.11 (232.9/170)	-0.52±2.36 (-88.4/170)	-
	Drake Passage 2009	-0.86±0.19 (-146.2/170)	1.05±0.07 (178.5/170)	1.37±0.30 (232.9/170)	-
	30°E 1996	-0.80±0.05 (-136.8/170)	-0.68±0.10 (-115.6/170)	-1.78±0.06 (-302.6/170)	-1.34±0.31 (-227.8/170)
	30°E 2008	-0.74±0.37 (-125.8/170)	1.08±0.31 (183.6/170)	-0.68±0.09 (-115.6/170)	1.01±0.17 (171.7/170)
	$R_{C:O_2}$ Below MLD	AZ	PFZ	SAZ	STZ
b)	Drake Passage 1990	-0.19±0.10 (-32.8/170)	-0.80±0.04 (136.0/170)	-1.29±0.06 (-219.3/170)	-
	Drake Passage 2009	-0.52±0.01 (-88.4/170)	-0.72±0.01 (-122.4/170)	-1.22±0.02 (-207.4/170)	-
	30°E 1996	-0.38±0.01 (-64.6/170)	-0.65±0.04 (-110.5/170)	-1.67±0.12 (-283.9/170)	-0.30±0.14 (-51.0/170)
	30°E 2008	-0.33±0.01 (-56.1/170)	-0.83±0.04 (-141.1/170)	-1.40±0.12 (-238.0/170)	-1.00±0.13 (-170/170)

Table 5.6: Redfield ratios $R_{C:O_2}$ for each hydrographic transect across Drake Passage and 30°E for each hydrographic zone, separated into the upper and deep ocean by the MLD. Standard Redfield ratios: $R_{C:O_2} = -117/170$ (-0.69).

through the northward persistence and along isopycnal subduction of the WW O_2 maxima are associated with increasingly lower DIC concentrations from south to north and explains the increasingly negative $R_{C:O_2}$ from the AZ to SAZ.

Summary This study finds that biologically-controlled $N:P$ ratios are in general agreement with typical Redfield values (De Baar et al. (1997) and Weber and Deutsch (2010)). $N:P$ ratios support a nitrate increase between each occupation of up to $2.46\pm0.21/2.79\pm0.46\mu$mol kg^{-1} at Drake Passage and 30°E, respectively, in addition to sectionwide $\Delta C:\Delta N$ gradient of up to 33.2 ± 3.5 and 49.4 ± 13.0 at Drake Passage and 30°E, respectively, clearly above the Redfield 6.6:1 ratio. $\overline{\triangle C}$ increases of, for example, $16.28\pm0.14\mu$mol kg^{-1} and $18.23\pm0.11\mu$mol kg^{-1} for the SAZ upper ocean, suggests $\overline{\triangle C}$ is in excess of typical biological differences, suggestive of anthropogenic CO_2, which is advected or mixed into the deep ocean to alter stoichiometries at all depths. Nitrate increases are observed along both transects throughout the water column, and help mask the magnitude of $\triangle C$, with anthropogenic CO_2 increase, hence greater than implied by $\Delta C:\Delta N$ increases.

c)

$R_{O_2:N}$ Above MLD	AZ	PFZ	SAZ	STZ
Drake Passage 1990	-1.33±13.53 (-21.3/16)	-5.37±2.00 (-85.9/16)	0.04±0.37 (0.6/16)	-
Drake Passage 2009	-6.56±1.11 (-105.0/16)	7.06±0.72 (113.0/16)	2.66±0.64 (42.5/16)	-
30°E 1996	-13.74±1.06 (-219.8/16)	-3.27±0.85 (-52.4/16)	-4.19±0.33 (-67.0/16)	-1.27±0.28 (-20.2/16)
30°E 2008	-2.11±0.52 (-33.8/16)	1.88±0.31 (30.0/16)	3.35±1.97 (53.6/16)	5.17±2.22 (82.7/16)

d)

$R_{O_2:N}$ Below MLD	AZ	PFZ	SAZ	STZ
Drake Passage 1990	-1.50±4.04 (-24.0/16)	-15.81±0.70 (-253.0/16)	-7.87±0.44 (-125.0/16)	-
Drake Passage 2009	-17.67±0.92 (-282.8/16)	-17.14±0.55 (-274.3/16)	-8.48±0.17 (-135.6/16)	-
30°E 1996	-13.99±1.39 (-223.8/16)	-6.02±0.53 (-96.4/16)	-3.19±0.18 (-51.0/16)	-0.30±0.10 (-4.8/16)
30°E 2008	-21.75±1.29 (-347.9/16)	-8.04±0.43 (-128.6/16)	-3.54±0.20 (-56.6/16)	-0.79±0.07 (-12.6±16)

Table 5.7: Redfield ratios $R_{O_2:N}$ for each hydrographic transect across Drake Passage and 30°E for each hydrographic zone, separated into the upper and deep ocean by the MLD. Standard Redfield ratio: $R_{O_2:N} = -170/16$ (-10.625).

e)

$R_{O_2:P}$ Above MLD	AZ	PFZ	SAZ	STZ
Drake Passage 1990	-186.4±233.8	-52.5±30.1	-9.6±6.0	-
Drake Passage 2009	-80.0±15.9	107.7±10.5	34.5±10.7	-
30°E 1996	-161.9±14.8	-66.1±12.3	-62.7±4.1	-17.1±3.4
30°E 2008	-25.5±7.5	15.0±4.9	51.3±30.5	60.8±18.5

f)

$R_{O_2:P}$ Below MLD	AZ	PFZ	SAZ	STZ
Drake Passage 1990	-109.0±43.7	-225.0±12.2	-120.6±6.2	-
Drake Passage 2009	-263.2±18.8	-284.0±10.3	-136.1±2.3	-
30°E 1996	-191.6±19.1	-85.8±8.2	-41.8±2.6	-5.9±1.4
30°E 2008	-317.7±19.7	-113.5±6.4	-53.7±3.1	-12.4±1.0

Table 5.8: Redfield ratios $R_{O_2:P}$ for each hydrographic transect across Drake Passage and 30°E for each hydrographic zone, separated into the upper and deep ocean by the MLD. Standard Redfield ratio: $R_{O_2:P} = -170/1$.

	Above MLD	Below MLD
$R_{C:O_2}$	-0.60±1.85 (-102.1/170)	-0.76±0.84 (-129.0/170)
$R_{O_2:N}$	-1.298±6.844 (-20.8/16)	-7.958±12.620 (-127.3/16)
$R_{O_2:P}$	-21.321±100.627	-117.055±171.800

Table 5.9: Median and interquartile range for each Redfield ratio across all zones and transects for above/below MLD. Standard Redfield ratios: $R_{C:O_2} = -117/170$ (-0.69), $R_{O_2:N} = -170/16$ (-10.625) and $R_{O_2:P} = -170/1$.

5.3 $\triangle C^*$ Anthropogenic Carbon (C^{ant})

5.3.1 Drake Passage

$\triangle C^*$ C^{ant} distribution calculated according to equations 4.9, 4.10, 4.11, 4.12, 4.14, and 4.26 across the Drake Passage 1990 occupation (Figure 5.13) reveal a C^{ant} transect maximum within the upper 200dbar. C^{ant} concentrations markedly shallow from north to south with $>20\mu mol\,kg^{-1}$ restricted to above 900dbar at the northern boundary. The $<10\mu mol\,kg^{-1}$ concentration band extends from ∼100dbar within UCDW near the Antarctic continent to ∼1200dbar at the northern boundary.

For 2009, C^{ant} penetrates deeper into the water column. A transect maximum of $C^{ant}>30\mu mol\,kg^{-1}$, is primarily within surface, SAMW and AAIW water masses. $C^{ant}>20\mu mol\,kg^{-1}$ has penetrated to ∼900dbar, north of ∼58.5°S, whilst the 10-20$\mu mol\,kg^{-1}$ range occupies a greater area beneath ∼1000dbar, north of ∼60°S. The $10\mu mol\,kg^{-1}$ isopleth well matches the $5\mu mol\,kg^{-1}$ in Figure 5.6b).

5.3.1.1 Biological component C^{bio} using Redfield ratios and in situ stoichiometric ratios: Drake Passage

In this section, C^{bio} is separated from C^{ant} for analysis (equation 4.8). Reasons for this are two-fold, firstly to interpret the influence of C^{bio} and its potential for causing enhanced C^{ant} and secondly reviewing the representativeness of the Redfield ratio by replacing them with the $R_{C:O_2}$ stoichiometries previously calculated in section 5.2.4.2, Table 5.6. Variations in stoichiometry have been previously suggested to be significant in North Atlantic C^{ant} estimates (Wanninkhof et al., 1999).

For the standard assumption of Redfield stoichiometries: $R_{C:O_2} = -117/170$ (-0.69), C^{bio} in 1990 and 2009 yields larger concentrations ($>100\mu mol\,kg^{-1}$) within the deep ocean and broadly corresponds to a high AOU, low oxygen concentration relationship (Figure 3.7). For 1990 in situ stoichiometries (Table 5.6), C^{bio} reaches $>200\mu mol\,kg^{-1}$ north of ∼58°S, below ∼1500dbar. Further south, concentrations decrease prior to

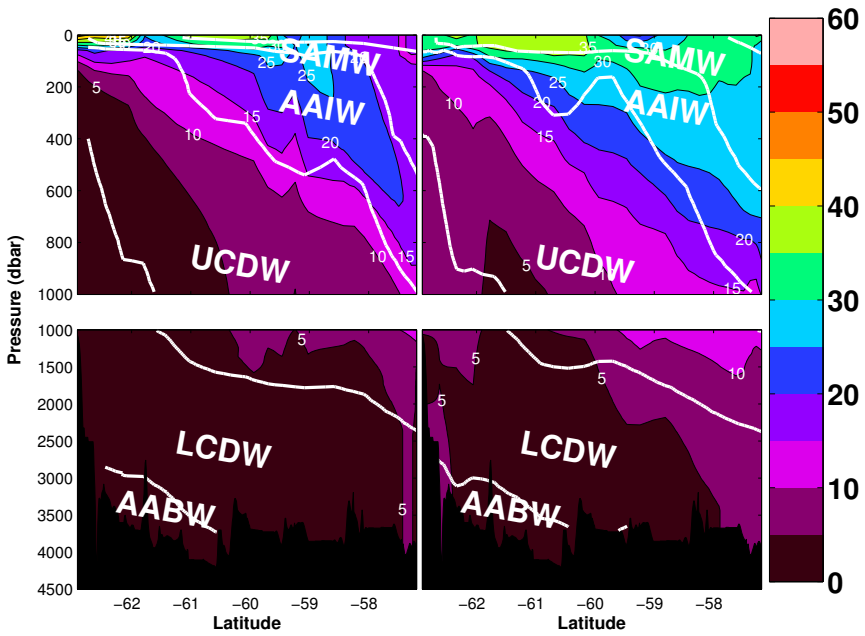

Figure 5.13: $\triangle C^*$-derived distribution across Drake Passage of C^{ant} for Left: 1990 and Right: 2009. Water masses are labelled following neutral density interfaces from Table 2.2. Neutral density interfaces are added for 2009 (solid lines) and 1990 (dashed lines). Units of μmol kg^{-1}.

a large area within the 120-140μmol kg^{-1} range across UCDW and LCDW between 59.5°S and 62°S. The 2009 in situ stoichiometry distribution more closely resembles that for Redfield stoichiometries with >140μmol kg^{-1} north of 58.5°S, below 1000dbar whilst the 120μmol kg^{-1} isopleth spans from 58°S to 62°S until a C^{bio} decrease south of 62°S. C^{bio} created using in situ stoichiometries (Table 5.6) therefore maintains a similar distribution, however, with maximum values typically in excess of 120μmol kg^{-1}, representing a far greater proportion of the water column.

5.3.2 30°E

The 30°E 1996 transect is directly comparable to Lo Monaco et al. (2005a)'s C^{ant} distributions. A similar pattern is observed (Figure 5.15a) with high C^{ant} concentrations (>30μmol kg^{-1}) predominately restricted to Surface and SAMW within the upper 1000dbar. As both Surface and SAMW outcrop north of ~55°S, higher C^{ant} (>30μmol kg^{-1}) is restricted to north of ~55°S. Close to the Antarctic continent, the 10-20μmol kg^{-1} concentration range extends throughout the water column corresponding to the southern limb of the Weddell Gyre, whilst further north, C^{ant} decreases to <10μmol kg^{-1} within the majority of the LCDW and AABW, particularly north of the

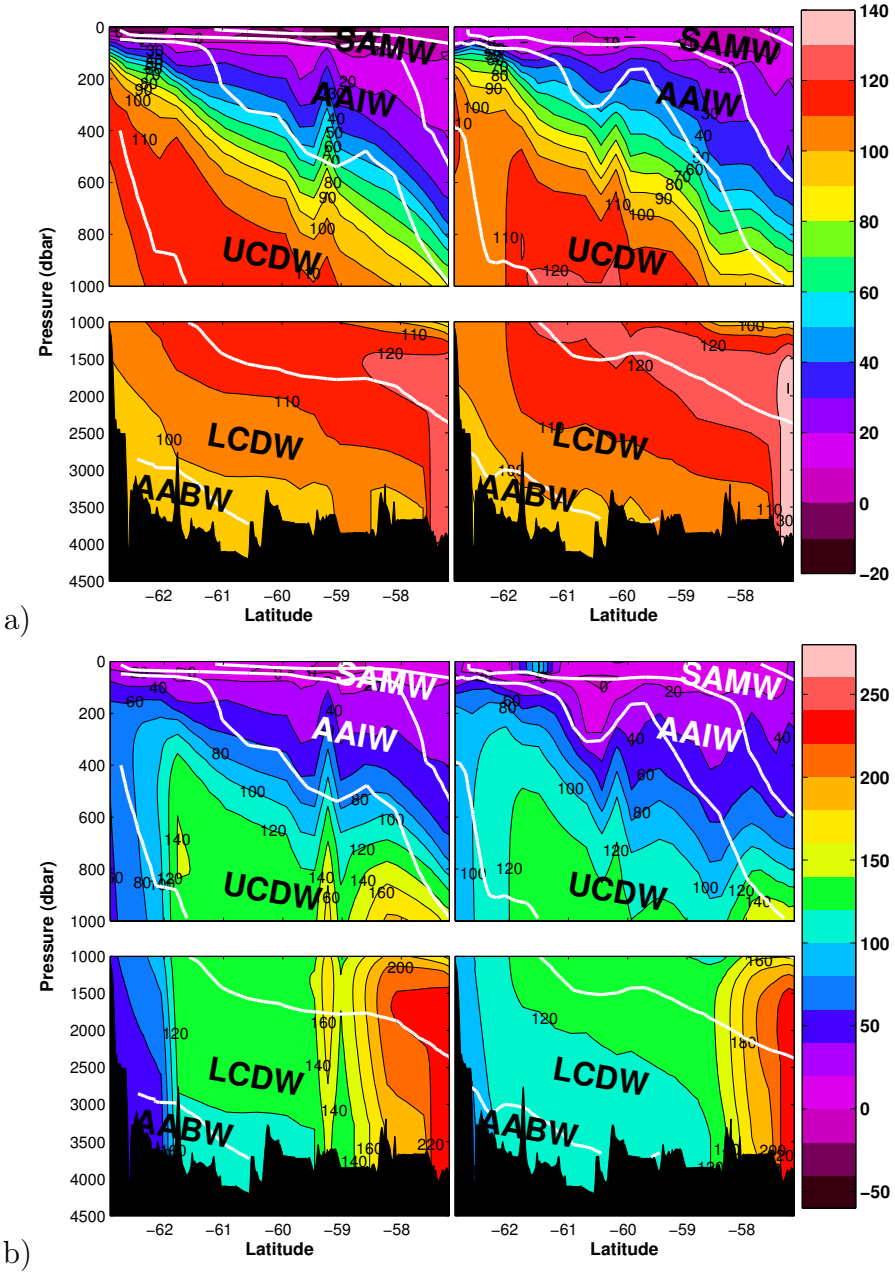

Figure 5.14: Distribution of the C^{bio} component of the ΔC^* calculation across Drake Passage, using a) Redfield ratios and b) in situ stoichiometric ratios for each hydrographic zone. For a) and b), Left: 1990 and Right: 2009. Units of μmol kg^{-1}.

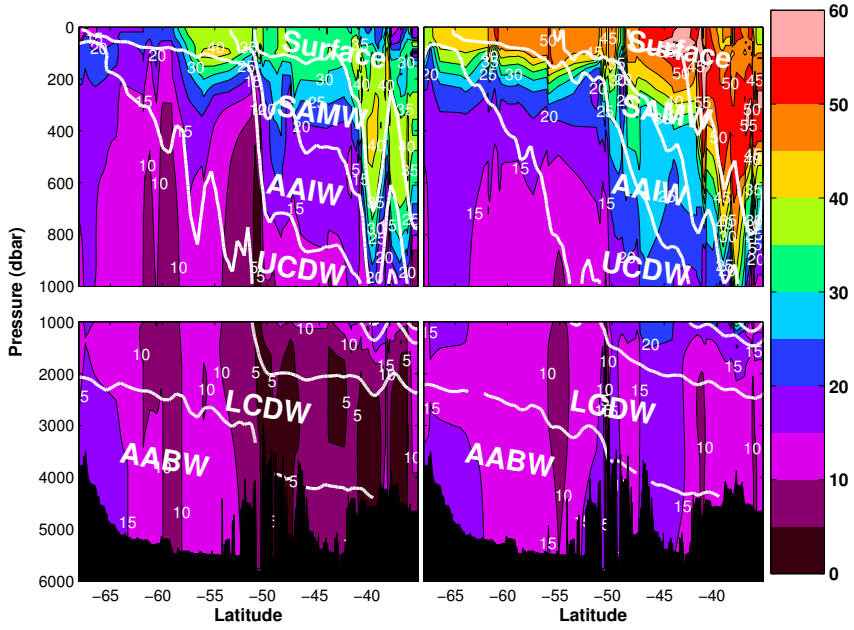

Figure 5.15: ΔC^*-derived distribution across 30°E of C^{ant} for Left: 1996 and Right: 2008. Water mass labels are added following the neutral density definitions from Table 2.2. Neutral density isopycnals are added for 2008 (solid lines) and 1996 (dashed lines). Units of μmol kg^{-1}.

PF, similar to Lo Monaco et al. (2005a).

Within the upper 1000dbar in 2008 (Figure 5.15b), higher C^{ant} (>40μmol kg^{-1}) pushes further southward within the upper 200dbar to the Antarctic continent with C^{ant} exceeding 50μmol kg^{-1} within the upper 200dbar between 40°S and 60°S and below 200dbar, north of 40°S within surface waters. C^{ant} >20μmol kg^{-1} is primarily restricted to surface, SAMW, AAIW and UCDW. In 2008, the extent of the <10μmol kg^{-1} water mass has shrunk into a few separate and smaller patches, with C^{ant} >10μmol kg^{-1} for the majority of UCDW, LCDW and AABW. C^{ant} >10μmol kg^{-1} for the deep ocean is at the upper end of the acceptable range with van Heuven et al. (2011) estimating ~9μmol kg^{-1} using TrOCA for warm deep water along 0°E, south of 55°S, however, this raises to ~16μmol kg^{-1} for AABW. Vázquez-Rodríguez et al. (2009b) suggests that Southern Ocean deep water C^{ant} estimates vary from negligible to up to one-third of surface water C^{ant} for a variety of C^{ant} methods (their Figure 4).

5.3.2.1 Biological component C^{bio} using Redfield ratios and in situ stoichiometric ratios: 30°E

The >100μmol kg^{-1} maxima dominates the 30°E 1996 Redfield ratio-derived C^{bio} distribution predominately within poorly-ventilated UCDW. Bottom waters maintain a con-

centration range of 60-90μmol kg^{-1}, whilst the section minima (<10μmol kg^{-1}) is within the upper 100dbar, within warm, salty Agulhas surface waters north of ∼40°S. For 2008, the >100μmol kg^{-1} maxima extends from the Agulhas shelf to near the Antarctic continent (∼67°S), whilst the >90μmol kg^{-1} isopleth traverses the section. The distribution broadly corresponds to the oxygen distribution (Figure 3.13), however, the distinctive Winter Water oxygen maxima is not associated with a clear C^{bio} minima.

For in situ stoichiometry (Table 5.6, Figure 5.16b), both the 1996 and 2008 distributions are dominated by the SAZ below mixed layer (∼200dbar) maxima (>160μmol kg^{-1}). The SAZ deep ocean C^{bio} corresponds to enhanced DIC and C^{ant} (>10μmol kg^{-1}) despite a lack of obvious ventilation (equation 4.7). Part of the deep ocean C^{ant} signal may therefore stem from an underestimate of the 30°E 2008 C^{bio} component using Redfield ratios yielding excess C^{ant} and related to variability within the water mass composition in this region. For both 1996 and 2008, $R_{C:O_2}$ from in situ stoichiometry is in excess of the Redfield ratio (-238.0 and -283.9 c.f. -170), corresponding with either an oxygen decrease, not observed in Figure 3.13, or a DIC increase, first hinted at in Figure 5.7a)-b) and 5.15. Variations in $R_{C:O_2}$ significantly affect the $R_{C:O_2}$AOU component of equation 4.7, and hence C^{ant} (Wanninkhof et al., 1999). Intrusion of DIC from south of the PF in 2008, and underestimation of C^{bio} contributes towards enhanced C^{ant} in Figure 5.15.

5.3.2.2 24°S

Along 24°S, only a single previous occupation of the transect in 2008 measured DIC, allowing calculation of C^{ant} only. This transect is free from the strong influence of the Antarctic Circumpolar Current and is largely uniform across the basin. Isopycnals shallow towards the east of the section, and this pattern is reflected by C^{ant}. High C^{ant} (>40μmol kg^{-1}) is exclusively within surface and SAMW broadly matching C^{ant} profiles for the 1995 Southern Subtropical Gyre dataset in Vázquez-Rodríguez et al. (2009b) (their Figure 4). Shallowing of the >20μmol kg^{-1} water mass from west to east follows the slope of the AAIW/UCDW interface. UCDW, LCDW and AABW have much lower concentrations (<20μmol kg^{-1}) with C^{ant} almost exclusively <10μmol kg^{-1} within LCDW and AABW.

5.4 Changes in Anthropogenic Carbon (C^{ant})

The following section describes the results from back-calculation methods (TrOCA, $\triangle C^{*}$) and extended Multiple Linear Regression (eMLR) for estimating anthropogenic

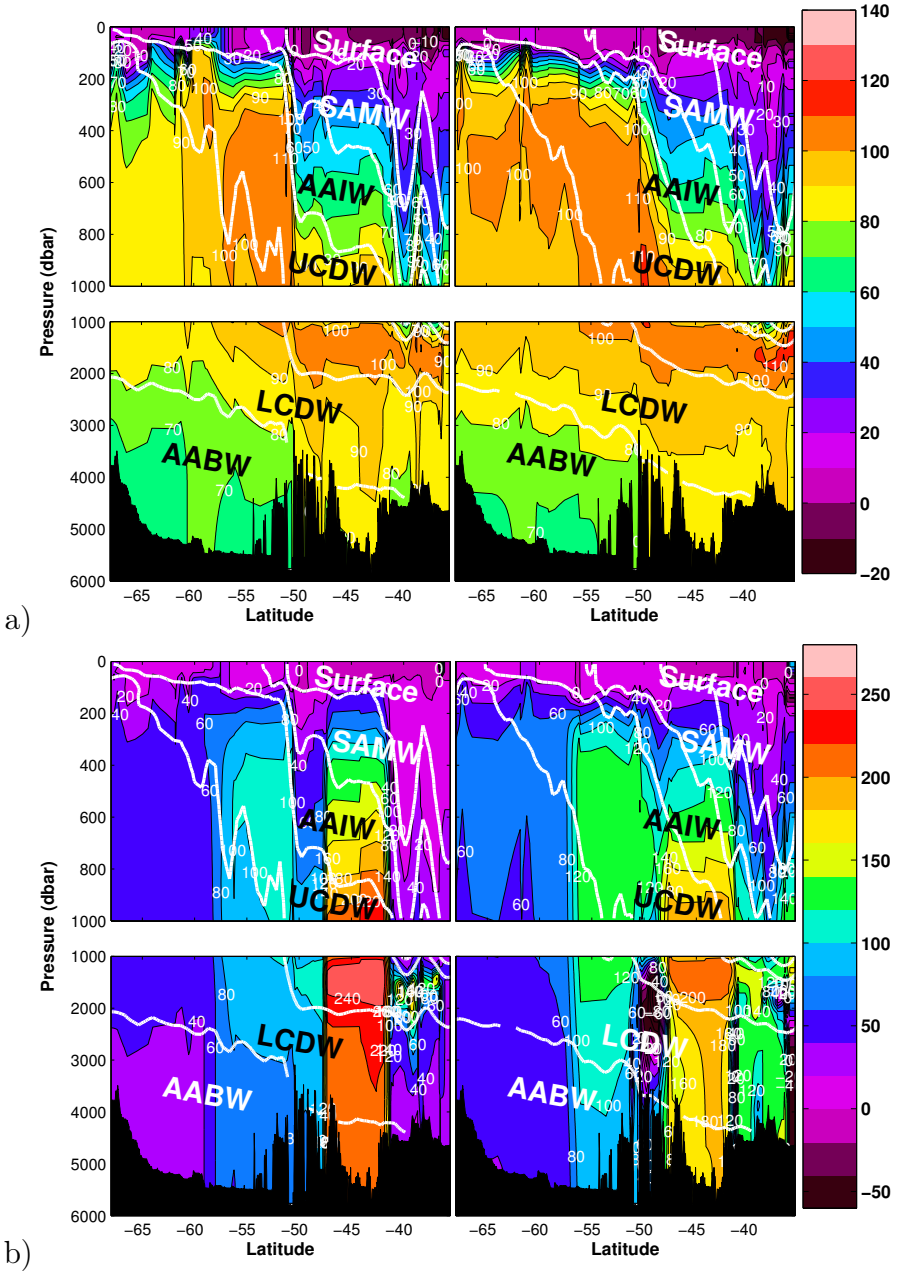

Figure 5.16: Distribution of the C^{bio} component of the ΔC^* calculation across 30°E, using a) Redfield ratios and b) in situ stoichiometric ratios for each hydrographic zone. For a) and b), Left: 1996 and Right: 2008. Units of μmol kg^{-1}.

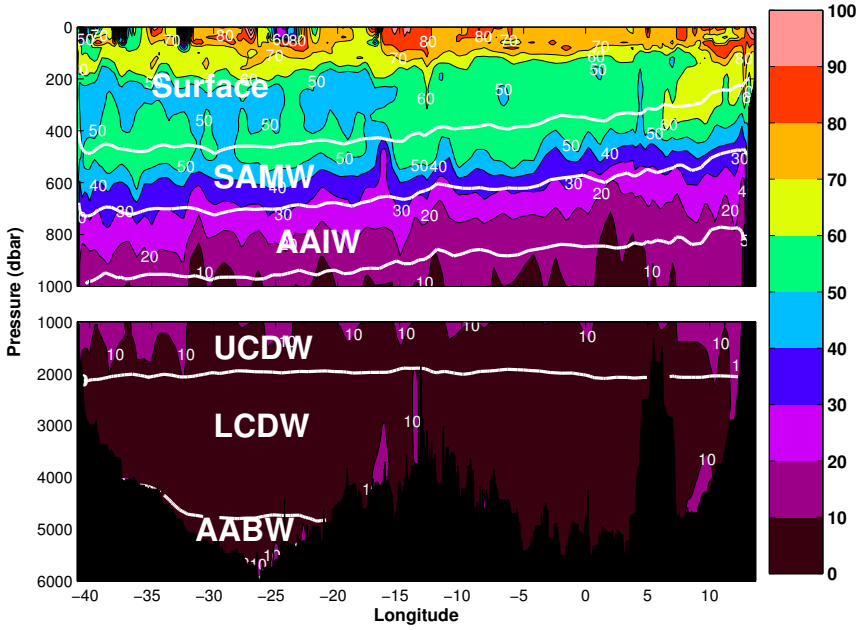

Figure 5.17: ΔC^*-derived distribution across 24°S of C^{ant}. Water masses labelled are added. Neutral density interfaces are added for 2009 (solid white lines). Units of μmol kg^{-1}.

CO_2 changes.

5.4.1 Back-calculation

5.4.1.1 Drake Passage

TrOCA estimates of $\triangle C^{ant}$ (equations 4.4 and 4.5, Figure 5.18a) yields similar features to the DIC residual differences (Figure 5.6b and 5.7b) and broadly similar to $\triangle C^*$ (Figure 5.18b). For Drake Passage, $\triangle C^{ant}$ increases across the majority of the section with $\triangle C^{ant}$ above 500dbar retaining some evidence for SAMW subduction and ventilation, north of the NPF. ΔC^{ant}>5μmol kg^{-1} is predominantly within the upper 1000dbar corresponding to Figure 5.7b) and recent subduction within SAMW, AAIW and upper UCDW. Small negative concentration patches are within the deep and bottom water, below ~2000dbar between the SPF and ~62°S, and between ~800-1500dbar, and 59.75°S and 60.5°S. For $\triangle C^*$, additional small negative patches are within ~50dbar of the surface affected by mixed layer variability.

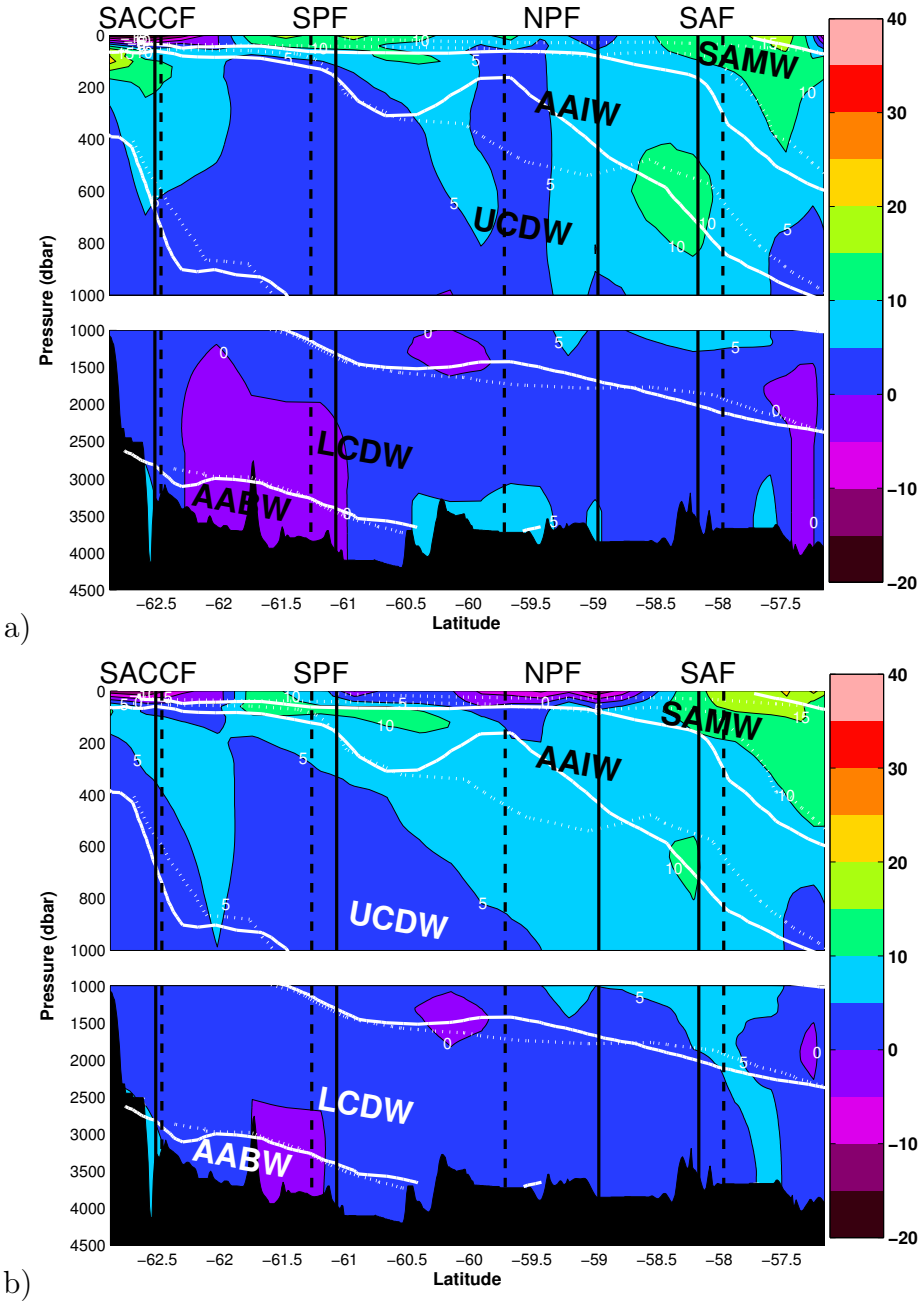

Figure 5.18: Distribution of $\triangle C^{ant}$ using the a) TrOCA and b) $\triangle C^{*}$ methodology across Drake Passage. $\triangle C^{ant}$ calculated from $C^{ant}_{2009} - C^{ant}_{1990}$. Water masses are labelled following neutral density interfaces from Table 2.2. Neutral density interfaces are added for 2009 (solid lines) and 1990 (dashed lines). The input values of θ, S, pressure, Alk, DIC and O_2 are quality-controlled fields (see Chapter 2). Units of μmol kg^{-1}.

5.4.2 30°E

For I6S for both TrOCA and $\triangle C^*$, high $\triangle C^{ant}$ exists throughout the water column, north of the Polar Front. Upper ocean $\triangle C^{ant}$ is readily explained through recent ventilation linked to deep water upwelling. Higher $\triangle C^{ant}$ within UCDW/LCDW/AABW north of PF is more difficult to explain given the longer renewal rate, for example, ∼100 year renewal rate for AABW in the Brazil Basin (Huang and Jin, 2002), and ∼1085 years for the global abyssal ocean (Orsi et al., 2001), compared to the shorter renewal rate of the upper ocean. DIC increases of $>10\mu mol\,kg^{-1}$ for much of the PF to STF water column (Figure 5.7) are linked to cross-frontal along isopycnal mixing, as described in section 5.2.1.2, and corresponds with differing water mass composition, rather than direct ventilation of these deep water masses. Northward progression of higher DIC concentrations is facilitated by a more diffusive Polar Front in 2008, compared to 1996 (Figure 5.1). South of the PF, $\triangle C^{ant}$ is predominantly within the $\sim\pm5\mu mol\,kg^{-1}$ uncertainty range with no evidence for higher $\triangle C^{ant}$ AABW from recent ventilation and formation. Negative concentrations, mostly $>$-5$\mu mol\,kg^{-1}$ occupy a greater area south of the ∼54°S for TrOCA than for $\triangle C^*$ and are generally below ∼200dbar and the Winter Water core. From Figure 5.7a)-b), no clear change of O_2 and TA concentrations appears to cause the negative concentrations.

5.4.2.1 TrOCA and $\triangle C^*$ Decadal C^{ant} Changes

Decadal changes of $\triangle C^{ant}$ for TrOCA and $\triangle C^*$ within each water mass along A21 and I6S (Tables 5.10-5.11) display greater changes along I6S with a clear trend for enhanced surface ocean $\triangle C^{ant}$ ($>10\mu mol\,kg^{-1}$), decreasing with depth. $\triangle C^{ant}$ along Drake Passage is potentially a lower estimate given the assumption for no alkalinity change. DIC accumulation in the deep ocean, between the PF and STF in I6S, within Figures 5.5b) and 5.18b), causes higher decadal variability in Table 5.10-5.11, with UCDW/LCDW/AABW changes an upper limit. Along Drake Passage, deep ocean $\triangle C^{ant}$ is almost uniformly positive yet within 0-5$\mu mol\,kg^{-1}$ change, suggesting a gradual accumulation within older, deep water masses. A weak reduction in $\triangle C^{ant}$ is observed for AABW, co-located with a weak negative signal for the DIC residual distributions (Figure 5.6b).

5.4.3 eMLR

Using the eMLR method (equations 4.28 and 4.29), $\triangle C^{ant}$ concentrations across Drake Passage (Figure 5.20) are enhanced ($>10\mu mol\,kg^{-1}$) within the upper 200dbar par-

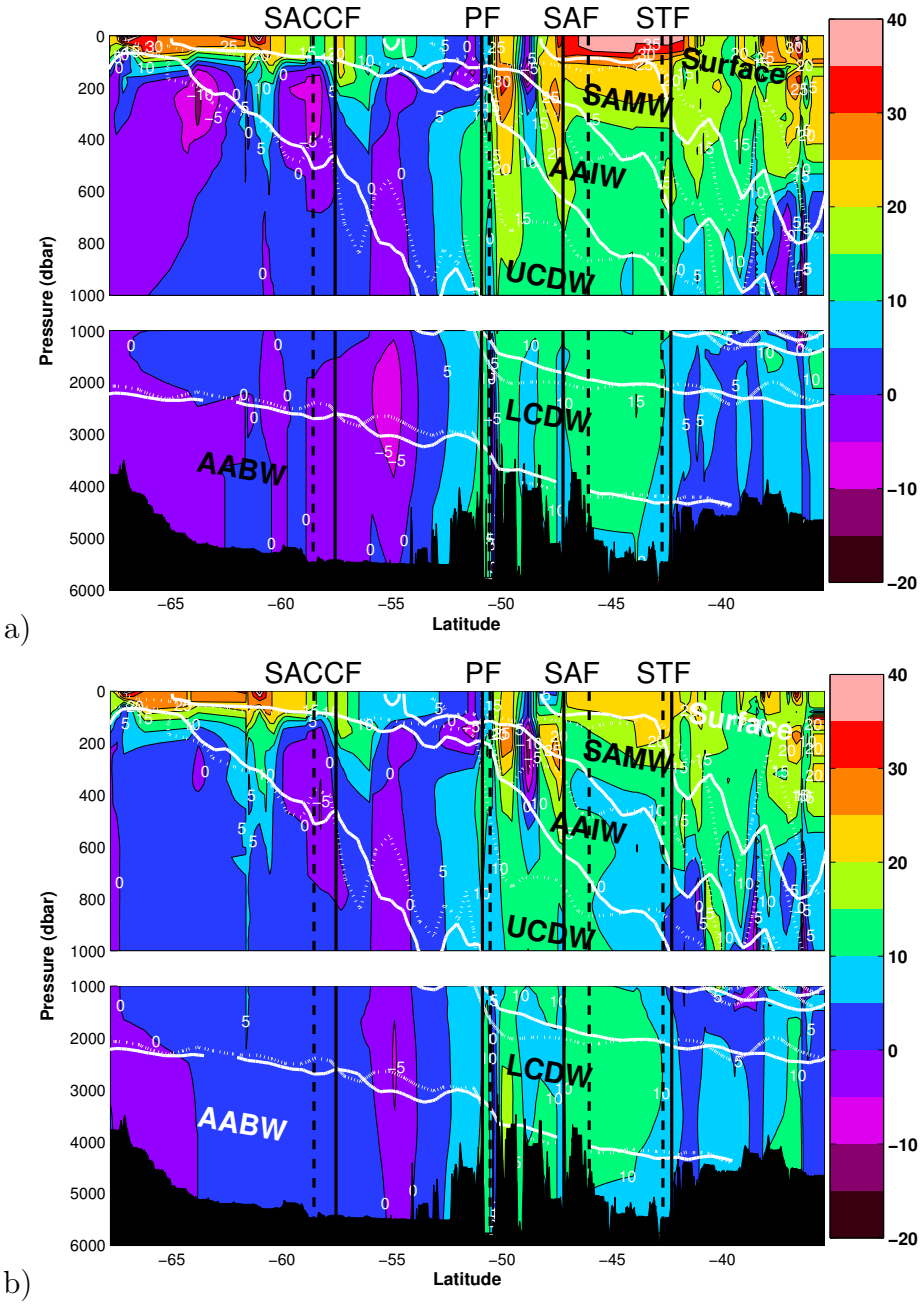

Figure 5.19: Distribution of $\triangle C^{ant}$ using the a) TrOCA and b) $\triangle C^*$ methodology across 30°E. $\triangle C^{ant}$ calculated from $C^{ant}_{2008} - C^{ant}_{1996}$. Water mass labels are added following the neutral density definitions from Table 2.2. Neutral density isopycnals are added for 2008 (solid lines) and 1996 (dashed lines). Units of μmol kg^{-1}.

a)

A21	All	SAZ	PFZ	AZ
Surface	5.9±0.3	5.9±0.3	*	*
SAMW	5.0±0.1	5.7±0.1	4.4±0.1	3.9±0.2
AAIW	3.7±0.1	3.5±0.1	4.3±0.1	3.2±0.1
UCDW	1.9±0.1	1.4±0.1	2.8±0.1	1.7±0.1
LCDW	1.0±0.1	1.2±0.1	1.3±0.1	1.0±0.1
AABW	-1.0±0.3	*	*	-1.0±0.3

b)

I6S	All	STZ	SAZ	PFZ	AZ
Surface	15.3±0.1	13.9±0.1	26.9±0.2	21.7±0.2	*
SAMW	10.8±0.2	8.7±0.2	15.3±0.3	13.6±0.4	0.8±0.3
AAIW	9.5±0.1	6.2±0.1	10.7±0.1	12.7±0.2	10.9±0.4
UCDW	6.9±0.1	5.9±0.1	9.5±0.1	9.3±0.1	4.8±0.2
LCDW	4.1±0.1	5.2±0.1	10.3±0.2	8.3±0.2	0.7±0.2
AABW	1.0±0.1	3.4±0.1	9.0±0.1	8.2±0.1	0.0±0.1

Table 5.10: Decadal variations of $\triangle C^{ant}$, calculated as an area-weighted mean, from TrOCA within each water mass: Surface, SAMW, AAIW, UCDW, LCDW and AABW along the a) A21 and b) I6S sections for all zones and each hydrographic zone: STZ, SAZ, PFZ and AZ. Standard error of the mean is also shown. Units of μmol kg^{-1} decade^{-1} .

a)

A21	All	SAZ	PFZ	AZ
Surface	8.1±0.2	8.1±0.2	*	*
SAMW	4.4±0.1	6.5±0.1	3.2±0.2	1.0±0.2
AAIW	3.4±0.1	3.6±0.1	4.1±0.1	3.8±0.1
UCDW	2.3±0.1	2.3±0.1	3.1±0.1	2.1±0.1
LCDW	1.2±0.1	2.0±0.1	1.2±0.1	1.0±0.1
AABW	0.7±0.3	*	*	0.7±0.3

b)

I6S	All	STZ	SAZ	PFZ	AZ
Surface	12.9±0.1	12.3±0.1	18.2±0.2	13.2±0.1	*
SAMW	9.1±0.1	8.1±0.1	11.2±0.3	11.4±0.3	1.3±0.2
AAIW	7.4±0.2	4.8±0.1	7.6±0.2	9.2±0.2	10.0±0.4
UCDW	6.0±0.1	3.9±0.1	9.3±0.1	8.3±0.1	5.0±0.2
LCDW	4.8±0.1	5.5±0.1	10.1±0.1	8.8±0.2	1.9±0.2
AABW	1.7±0.2	4.8±0.2	7.7±0.2	8.6±0.1	0.8±0.1

Table 5.11: Decadal variations of $\triangle C^{ant}$, calculated as an area-weighted mean, from $\triangle C^{*}$ within each water mass: Surface, SAMW, AAIW, UCDW, LCDW and AABW for a) A21 and b) I6S, for all zones and each hydrographic zone: STZ, SAZ, PFZ and AZ. Standard error of the mean is also shown. Units of μmol kg^{-1} decade^{-1} .

ticularly south of ∼58°S. The $>5\mu mol\,kg^{-1}$ isopleth corresponds with Winter Water subduction into SAMW and AAIW, in addition to further ventilation of the UCDW. The $>5\mu mol\,kg^{-1}$ isopleth deepens from above 200dbar at the Antarctic continent to ∼1500dbar between 57.5-60°S, well matching the $5\mu mol\,kg^{-1}$ isopleth in Figure 5.6b), and eventually to the seafloor north of 57.5°S. A relative minimum ($<5\mu mol\,kg^{-1}$) within the upper 1000dbar is predominately within UCDW close to the Antarctic continent. Deeper in the water column, an AABW and lower LCDW signal of $\Delta C^{ant}>5\mu mol\,kg^{-1}$ corresponds with recent AABW formation within the Weddell Sea. Overflow of Weddell Sea Deep Water (WSDW) into the Scotia Sea, and limited westward progression towards Drake Passage provides a $>5\mu mol\,kg^{-1}$ ΔC^{ant} maximum.

For 30°E, higher ΔC^{ant} corresponds with lighter water masses. Generally, cold water is capable of holding a greater concentration of DIC, however, Völker et al. (2002) suggests that a larger ΔC^{ant} signal is typically observed in warmer waters. Enhanced ΔC^{ant} concentrations correspond with higher temperatures with $\Delta C^{ant}>20\mu mol\,kg^{-1}$ within warm, salty westward-flowing Indian Ocean surface water within the STZ. The UCDW/LCDW interface follows a similar general trend compared to the $5\mu mol\,kg^{-1}$ isopleth in Figure 5.20b), at a shallower pressure. For lower LCDW, and AABW, ΔC^{ant} concentrations are 0-$5\mu mol\,kg^{-1}$, in contrast to Drake Passage observations. High AABW ΔC^{ant} caused by ventilation within the Weddell Sea appears insignificant at 30°E, despite a portion of Weddell Sea-formed AABW expected to reach 30°E.

In contrast to TrOCA, the eMLR signal is much smoother with no negative ΔC^{ant}, and is favoured in a number of studies (e.g. Brown et al. (2010); Wanninkhof et al. (2010); Peng and Wanninkhof (2010)). Brown et al. (2010) compared TrOCA with an eMLR analysis with much smoother results for eMLR (their Figure 3 and 10). Results from each method find broad correspondence within the Drake Passage upper ocean with enhanced ΔC^{ant} south of 60°S linked to WW ventilation and within the low positive ΔC^{ant} for UCDW and LCDW in both methods. The very limited positive AABW change in TrOCA is expanded by eMLR analysis.

For the 30°E section, similarities also include enhanced surface ocean ΔC^{ant}, whilst $\Delta C^{ant}>5\mu mol\,kg^{-1}$ isopleth is restricted to LCDW and above for eMLR. South of the PF, ΔC^{ant} is reduced with estimates $>5\mu mol\,kg^{-1}$ restricted to the upper 1500dbar. No negative ΔC^{ant} are within the eMLR-derived distribution with the lowest concentrations restricted primarily to LCDW/AABW. For TrOCA, small patches of negative ΔC^{ant} are dispersed throughout the water column, namely within UCDW, LCDW and AABW.

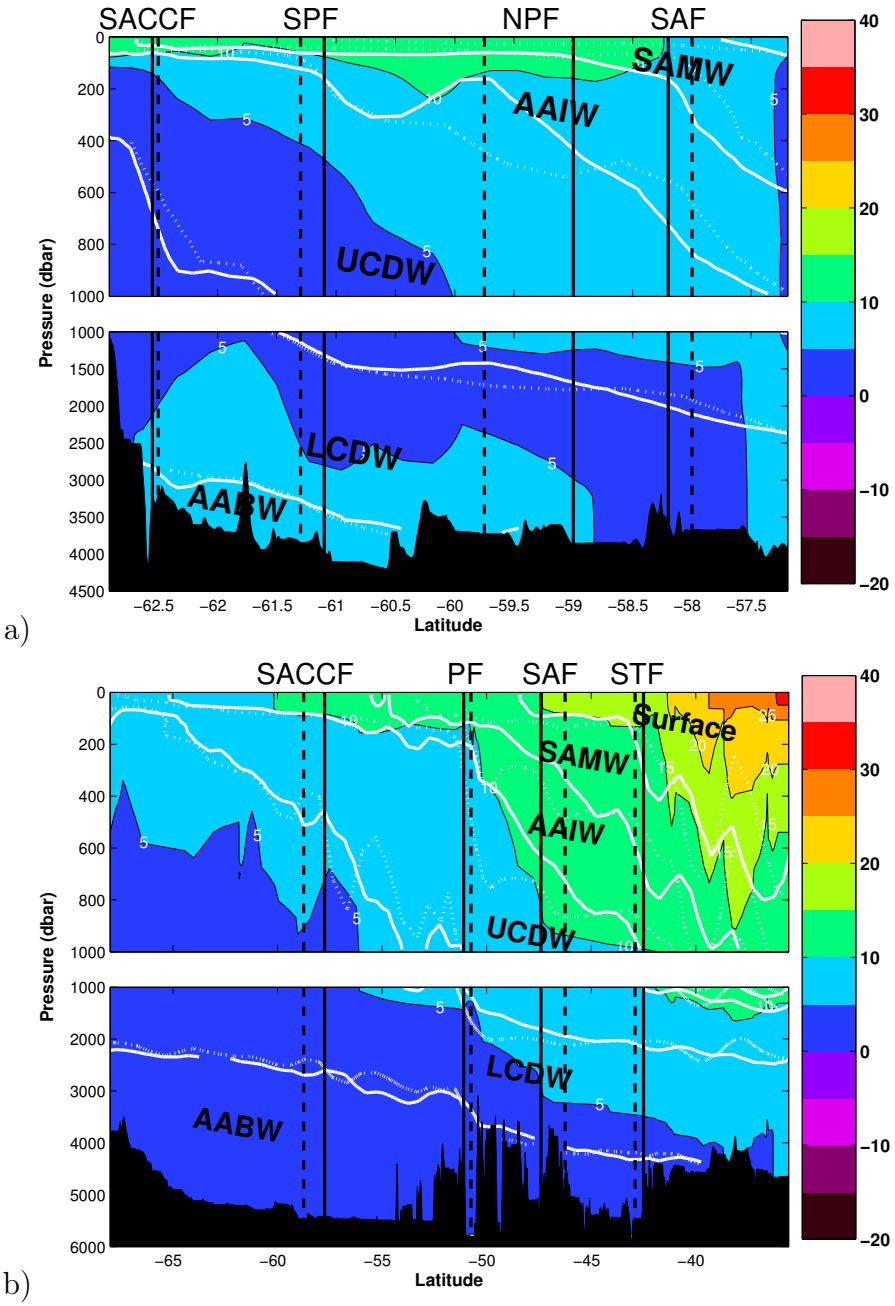

Figure 5.20: Distribution of $\triangle C^{ant}$ using the eMLR method. a) Drake Passage C^{ant} difference (A21 2009-A21 1990), b) 30°E C^{ant} difference (I6S 2008-I6S 1996). Units of μmol kg^{-1}.

a)

A21	All	SAZ	PFZ	AZ
Surface	3.7±0.1	3.7±0.1	*	*
SAMW	4.8±0.1	3.9±0.1	5.9±0.1	6.1±0.1
AAIW	4.6±0.1	3.8±0.1	4.9±0.1	5.2±0.1
UCDW	2.9±0.1	3.1±0.1	3.1±0.1	2.8±0.1
LCDW	2.6±0.1	2.7±0.1	2.8±0.1	2.7±0.1
AABW	3.4±0.1	*	*	3.4±0.1

b)

I6S	All	STZ	SAZ	PFZ	AZ
Surface	15.5±0.1	15.8±0.1	13.0±0.1	11.8±0.1	*
SAMW	11.1±0.1	11.5±0.1	11.2±0.1	10.0±0.1	9.4±0.1
AAIW	9.2±0.1	9.2±0.1	9.7±0.1	8.8±0.1	8.4±0.1
UCDW	6.7±0.1	6.7±0.1	7.2±0.1	6.1±0.1	6.1±0.1
LCDW	3.7±0.1	3.7±0.1	4.7±0.1	3.1±0.1	3.3±0.1
AABW	1.9±0.1	1.9±0.1	2.5±0.1	2.1±0.1	1.8±0.1

Table 5.12: Decadal variations of $\triangle C^{ant}$, calculated as an area-weighted mean, from uncorrected eMLR within each water mass: Surface, SAMW, AAIW, UCDW, LCDW and AABW along the a) A21 and b) I6S sections for all zones and each hydrographic zone: STZ, SAZ, PFZ and AZ. Standard error of the mean is also shown. Units of μmol kg^{-1} decade^{-1} .

5.4.3.1 eMLR Decadal C^{ant} Changes

Decadal changes using the eMLR method are listed in Table 5.12. Drake Passage shows the unusual profile of enhanced SAMW and AAIW decadal change compared to the surface ocean with higher AABW decadal change than expected (van Heuven et al., 2011). Comparable surface and AABW decadal changes is surprising. At 30°E, decadal changes show the expected pattern of enhanced upper ocean C^{ant} change caused by direct exchange with the atmosphere.

5.4.3.2 Corrections to eMLR ΔC^{ant}

This section so far has discussed the regression fit uncorrected for residuals in γ^n space. In this subsection, corrections are applied (equations 4.30 and 4.31), both sectionwide and per zone (Table 4.6). Along Drake Passage, sectionwide correction constrains the band of the DIC $>10\mu$mol kg^{-1} isopleth to correspond with subduction of the fresher recently ventilated water into the SAZ subsurface SAMW and AAIW providing a pathway for atmospheric CO_2 (Figure 5.21). The $>5\mu$mol kg^{-1} isopleth within the LCDW and AABW has reduced, however the remaining bulk of the UCDW $>5\mu$mol kg^{-1} is likely in excess of the real anthropogenic signal. Hydrographic zone corrections display a more confused picture with a decrease of AABW ΔC^{ant}, and an increase of ΔC^{ant}

	A21	All	SAZ	PFZ	AZ
a)	Surface	4.9±0.6	4.9±0.6	*	*
	SAMW	4.7±0.1	3.8±0.1	4.6±0.1	6.6±0.1
	AAIW	4.8±0.1	4.0±0.1	5.0±0.1	5.4±0.1
	UCDW	3.3±0.1	3.5±0.1	3.5±0.1	3.2±0.1
	LCDW	2.4±0.1	2.8±0.1	2.4±0.1	2.3±0.1
	AABW	2.4±0.1	*	*	2.4±0.1
	A21	All	SAZ	PFZ	AZ
b)	Surface	5.5±0.3	5.5±0.3	*	*
	SAMW	5.4±0.2	5.7±0.1	5.4±0.2	4.7±0.7
	AAIW	3.9±0.1	4.0±0.1	3.7±0.1	4.1±0.1
	UCDW	3.4±0.1	4.9±0.1	3.8±0.1	2.7±0.1
	LCDW	2.3±0.1	4.6±0.1	3.5±0.1	1.6±0.1
	AABW	0.6±0.1	*	*	0.6±0.1

Table 5.13: Decadal variations of $\triangle C^{ant}$, calculated as an area-weighted mean, from corrected eMLR within each water mass: Surface, SAMW, AAIW, UCDW, LCDW and AABW along the A21 for a) sectionwide and b) per zone section corrections, for all zones and each hydrographic zone: STZ, SAZ, PFZ and AZ. Standard error of the mean is also shown. Units of μmol kg^{-1} decade^{-1} .

throughout the water column north of the NPF. Within the upper 100dbar, both high ($>30\mu$mol kg^{-1}) and low ($<10\mu$mol kg^{-1}) alterations do not reflect expected corrections.

Decadal variations across Drake Passage reduce for AABW for both sectionwide and per zone corrections (Table 5.13). Per zone corrections cause a transition from larger decadal variability within the Antarctic Zone to larger decadal variability within the SAZ, resulting in an increase in decadal variations for Surface and SAMW, and a decrease in decadal variations for LCDW and AABW.

Along 30°E, sectionwide correction (Figure 5.22) only makes a small adjustment to ΔC^{ant} causing both a slight deepening of the 5μmol kg^{-1} isopleth, as well as erosion of the $>10\mu$mol kg^{-1} water mass within AAIW. The dominant pattern of higher ΔC^{ant} concentrations within warmer STZ upper water masses clearly remains. For the per zone correction (Figure 5.22), significant adjustments reduce the correlation between high ΔC^{ant} concentrations and γ^n isopycnals. North of the Subtropical Front, the 10μmol kg^{-1} isopleth shallows and extends southward to SAZ. High concentrations ($>20\mu$mol kg^{-1}) are within the upper 100dbar. North of the PF, the $>5\mu$mol kg^{-1} isopleth extends throughout the water column. South of the PF, the $>5\mu$mol kg^{-1} concentration area has greatly eroded, particularly within the UCDW and is restricted to AAIW and UCDW within the upper 100dbar. Deeper water is almost exclusively within the 0-5μmol kg^{-1} band, with a small patch of negative concentration within

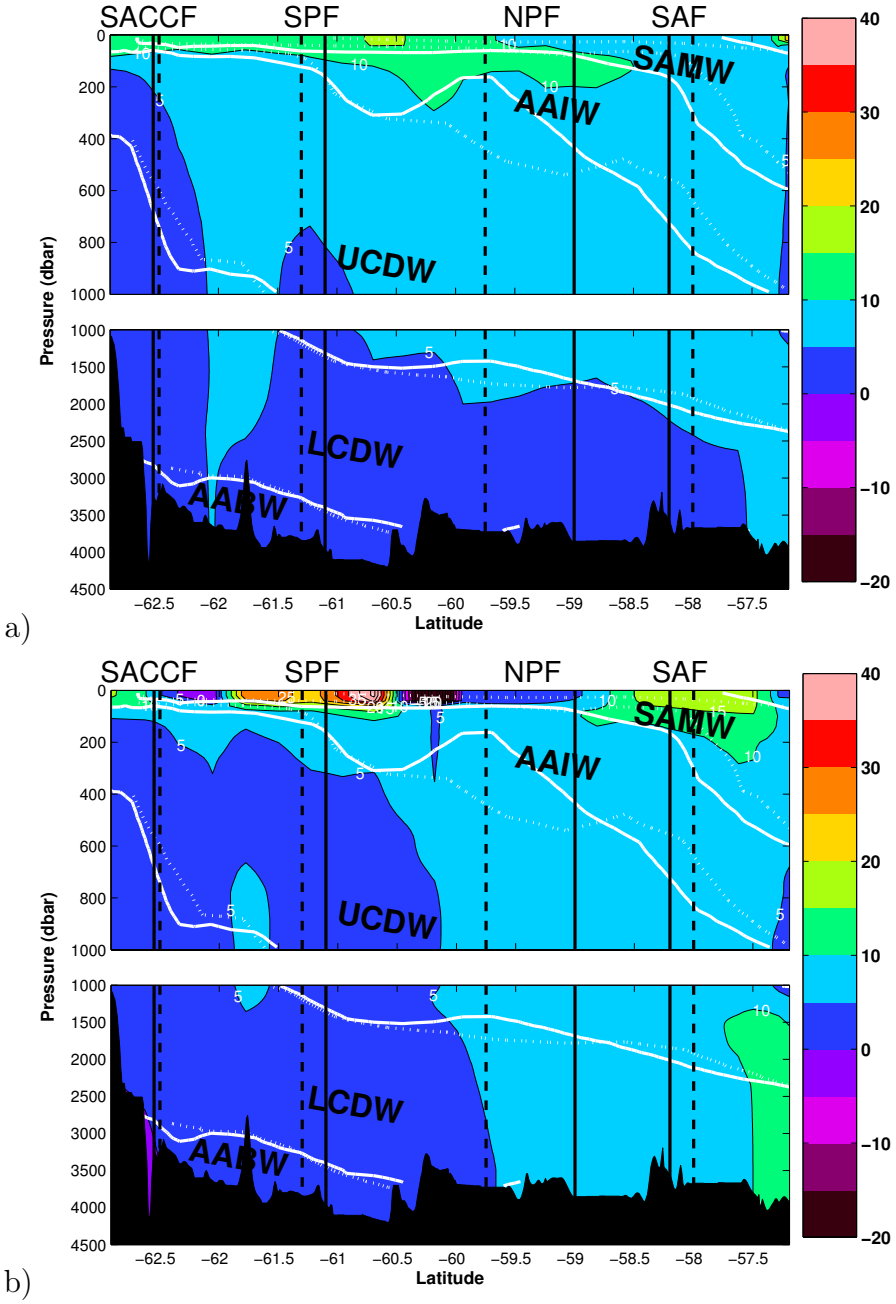

Figure 5.21: Distribution of $\triangle C^{ant}$ using the corrected eMLR method. Drake Passage C^{ant} difference (A21 2009-A21 1990) for a) sectionwide correction and b) per zone correction. Units of μmol kg^{-1}.

a)

I6S	All	STZ	SAZ	PFZ	AZ
Surface	16.4±0.1	16.6±0.1	15.2±0.1	13.8±0.1	*
SAMW	10.2±0.1	10.7±0.1	10.3±0.1	9.0±0.1	7.4±0.1
AAIW	7.8±0.1	8.2±0.1	7.9±0.1	7.6±0.1	7.0±0.1
UCDW	6.7±0.1	7.1±0.1	6.8±0.1	6.2±0.1	6.3±0.1
LCDW	4.0±0.1	5.0±0.1	4.4±0.1	3.4±0.1	3.6±0.1
AABW	2.4±0.1	2.7±0.1	2.4±0.1	2.2±0.1	2.4±0.1

b)

I6S	All	STZ	SAZ	PFZ	AZ
Surface	16.3±0.1	15.6±0.1	22.5±0.1	18.6±0.2	*
SAMW	11.3±0.1	10.4±0.1	13.8±0.2	11.1±0.1	10.9±0.3
AAIW	8.5±0.1	7.5±0.1	9.7±0.1	8.6±0.1	8.7±0.1
UCDW	6.7±0.1	6.9±0.1	8.7±0.1	9.0±0.1	3.5±0.1
LCDW	4.1±0.1	6.1±0.1	8.0±0.1	6.7±0.1	1.1±0.1
AABW	1.4±0.1	5.7±0.1	6.5±0.1	6.6±0.1	0.5±0.1

Table 5.14: Decadal variations of $\triangle C^{ant}$, calculated as an area-weighted mean, from eMLR within each water mass: Surface, SAMW, AAIW, UCDW, LCDW and AABW along the I6S for a) sectionwide and b) per zone section corrections, for all zones and each hydrographic zone: STZ, SAZ, PFZ and AZ. Standard error of the mean is also shown. Units of μmol kg^{-1} decade^{-1} .

AABW.

Decadal variations for sectionwide-corrected and per zone-corrected distributions shows variation particularly for surface and AABW (Table 5.13). An increase in surface decadal variation across 30°E (Table 5.14) for SAZ and PFZ corresponds with correction from apparent temperature dominance within the Figure 5.20 $\triangle C^{ant}$ distribution. Per zone corrections markedly increase AABW decadal change, particularly within STZ, SAZ and PFZ whilst decreasing AABW within the AZ.

5.5 Conclusion

This conclusion is structured to review the findings for both DIC and anthropogenic CO_2 analysis. All conclusions take into account that increased availability of anthropogenic CO_2 within the atmosphere leads to oceanic uptake of CO_2 into the upper ocean (Keeling et al., 2004). Dataset uncertainties govern the detail of the possible interpretations and limit their spatial and temporal applicability. Primarily the transects discussed in this Chapter reflect observations at the boundary of the South Atlantic Southern Ocean sector. Interpretations of the datasets beyond the boundary and into the interior of the South Atlantic are possible, yet the growth in uncertainties makes

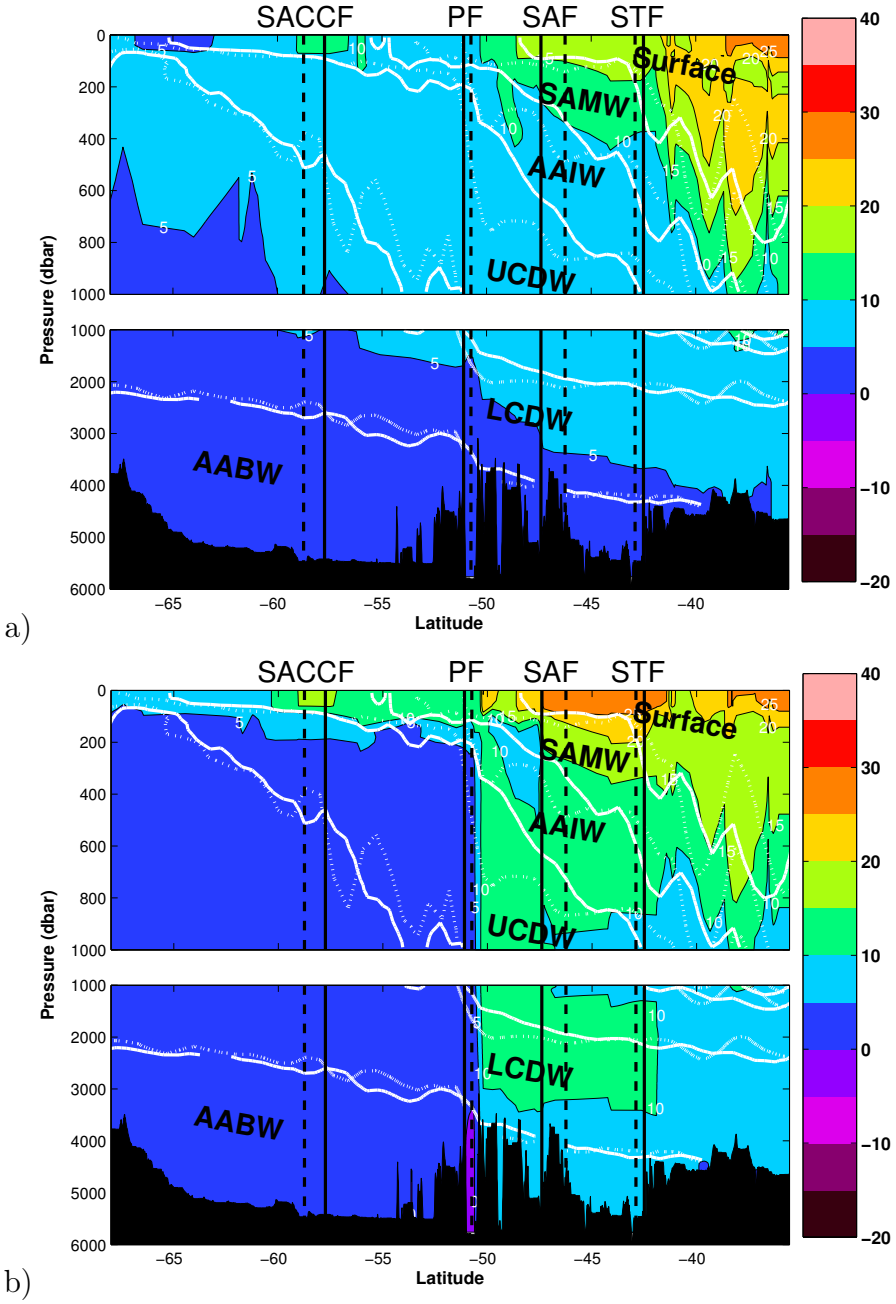

Figure 5.22: Distribution of $\triangle C^{ant}$ using the corrected eMLR method. 30°E C^{ant} difference (I6S 2008-I6S 1996) for a) sectionwide correction and b) per zone correction. Units of $\mu mol\,kg^{-1}$.

such extrapolations unwise, and hence this section will focus on the South Atlantic boundaries only.

5.5.1 DIC

This study has focussed on evaluating DIC increase along Drake Passage (1990-2009) and 30°E between South Africa and Antarctica (1996-2008). Direct comparison of the DIC distributions (section 5.2.1), and a comparison of the residuals generated by fitting the bottle data linearly interpolated onto a $0.01\gamma^n$ grid with a best fit line (section 5.2.2), are both methods aimed at limiting the interpolation applied to the measured datasets to help maintain dataset integrity, and remain close to the measured DIC values. An increase in DIC, in contrast to potential biological variability is compared in section 5.2.4.

5.5.1.1 DIC differences and DIC residual differences

Differencing of the DIC field and residual field (Figure 5.6, 5.7) generates a DIC increase through the majority of the water column across Drake Passage and 30°E. At Drake Passage, the most significant increases (ΔC>25μmol kg^{-1}) occur within the upper 600dbar, broadly related to subduction of SAMW, AAIW and within upper UCDW after recent ventilation upstream of Drake Passage, as well as recent ventilation of Winter Water within the Bellinghausen Sea. Decadal change of SAMW of 9.5$\pm$0.1/9.7$\pm$0.1μmol kg^{-1} decade^{-1} within SAZ gives an estimate of subsurface ventilation. At 30°E, a greater proportion of the transect has ΔC>5μmol kg^{-1}, particularly north of the Polar Front where comparatively stronger SAMW subsurface ventilation within the Agulhas regime (STZ), reaches 10.8$\pm$0.2/8.9$\pm$0.2μmol kg^{-1} decade^{-1} sectionwide. LCDW decadal change is generally significantly lower (i.e. <3μmol kg^{-1} decade^{-1}) outside of the 30°E PFZ/SAZ.

5.5.1.2 Redfield ratio

Differences in N : P at the time of sampling between two occupations of a transect reflects natural, biological variability. Across Drake Passage and 30°E, N : P ratios are generally at or below the Redfield ratio, giving a median of 12.7μmol kg^{-1} and 14.1μmol kg^{-1} for all zones within the mixed layer, respectively, and provides evidence for higher N : P in the more recent occupations. This is caused by nitrate increase of up to 1.91$\pm$0.50μmol kg^{-1} and 2.98$\pm$0.51μmol kg^{-1} across Drake Passage and 30°E whilst phosphate shows a mixed increasing/decreasing signal. ΔC : ΔN across both Drake

Passage and 30°E is in excess of the Redfield 6.6:1 ratio for the majority of hydrographic zones with a mixed layer mean for each transect, excluding the Drake Passage SAZ of 13.1±8.3μmol kg^{-1} and 14.8±6.1μmol kg^{-1}, respectively. ΔC : ΔN ratios exceeding the 6.6:1 ratio despite nitrate increase, conclusively suggests that DIC change is the source of the ΔC : ΔN increase. DIC increase in excess of that expected from biological cycling, corresponds with oceanic uptake of atmospheric anthropogenic CO_2 (Keeling et al., 1995, 2004).

5.5.2 Anthropogenic Carbon

This study has focussed on calculating ΔC^{ant} between occupations of a particular transect in different years. TrOCA and $\triangle C^*$ are both based on back-calculating C^{ant} by isolating the anthropogenic component from the DIC values measured today. Similarly to eMLR, these diagnostics inherently assume a constancy between present-day ocean circulation and biological activity, and those at pre-industrial times (Sabine and Tanhua, 2010). Yool et al. (2010) concluded C^{ant} calculated using TrOCA displayed excessive bias, whereas biases cancelled and reduced upon calculation of ΔC^{ant}. Therefore in this study, C^{ant} is only displayed for the $\triangle C^*$, which itself contains a number of uncertainties, as reviewed in Matsumoto and Gruber (2005), primarily relating to biases in the calculation of the water mass age and variability of C^{diseq} over time.

Evidence for anthropogenic carbon increase is observed at all depths and within all water masses. Firstly, discussion focusses on the back-calculation (TrOCA, $\triangle C^*$) distributions, which are similar across Drake Passage and 30°E, and are supportive of anthropogenic carbon input to the ocean through subduction and ventilation, particularly north of the PF. ΔC^{ant} is largest for upper ocean water masses, with sectionwide SAMW ventilation at Drake Passage estimated as 5.0±0.1/4.4±0.2μmol kg^{-1} decade^{-1} (TrOCA, $\triangle C^*$), compared to 10.8±0.2/9.1±0.1μmol kg^{-1} decade^{-1} (TrOCA, $\triangle C^*$) at 30°E, notably implying an increase at 30°E, double that at Drake Passage. Sectionwide CDW increases of 1.5±0.1/1.8±0.1μmol kg^{-1} decade^{-1} (TrOCA, $\triangle C^*$) along Drake Passage are more comparable to the 30°E Antarctic Zone decadal changes than the sectionwide CDW increase of 5.5±0.1/5.4±0.1μmol kg^{-1} decade^{-1} (TrOCA, $\triangle C^*$). Negative, or near-negative ΔC^{ant} signals of -1.0±0.2/0.7±0.3μmol kg^{-1} decade^{-1} are only observed for Drake Passage AABW.

eMLR distributions give a much smoother version of ΔC^{ant} and further provides evidence for anthropogenic carbon increase. Corrections to eMLR find the greatest correspondence to back-calculation estimations for the sectionwide correction along Drake Passage and the per-zone correction along 30°E, hence decadal changes from

each respective correction are discussed. eMLR is supportive of sectionwide SAMW ventilation of 4.7±0.1μmol kg^{-1} decade^{-1} at Drake Passage, compared to 11.3±0.1μmol kg^{-1} decade^{-1} at 30°E, with both estimates similar to back-calculations. CDW increases both at Drake Passage and 30°E by 2.9±0.1μmol kg^{-1} decade^{-1} and 5.4±0.1μmol kg^{-1} decade^{-1}, respectively.

van Heuven et al. (2011) also calculated decadal changes for C^{ant} along 0°E, south of 55°S, concluding a 1.2±0.6μmol kg^{-1} decade^{-1} for WSBW (S>34.6, θ<-0.7°C). Upon comparison with AABW along 30°E in this study, ΔC^{ant} changes within the AZ of 0.0±0.1/0.5±0.1/0.8±0.1μmol kg^{-1} decade^{-1} (TrOCA, eMLR, $\triangle C^*$) are all at the lower limit of van Heuven et al. (2011)'s estimate whilst sectionwide AABW ΔC^{ant} changes of 1.0±0.1/1.4±0.1/1.7±0.1μmol kg^{-1} decade^{-1} are in better agreement. Higher in the water column, this study finds an increasing C^{ant} trend, and in contrast to van Heuven et al. (2011)'s findings for negligible increasing C^{ant} in Weddell Sea Deep Water. Deep ocean changes are generally lowest in the LCDW, with the greatest changes within the anomalous PF to STF along 30°E with deep ocean changes outside of this latitude band likely to be more robust.

In conclusion, all methods support significant anthropogenic increase for surface, SAMW and AAIW water masses with the rate of increase at 30°E for SAMW, approximately double that at Drake Passage. This contrasts with similar rates of increase at Drake Passage and 30°E for residual differences and suggests that part of the variability signal is captured by changes in other ocean properties. CDW further supports consistent positive increase, above the negligible increase found by van Heuven et al. (2011). Few studies have so far quantified Southern Ocean ΔC^{ant}, and this study adds both estimates of decadal change for each water mass, and is the first study to comparatively estimate the ΔC^{ant} spatial distribution at the eastern and western boundaries of the Southern Ocean South Atlantic sector.

5.5.2.1 Adjusted C^{ant} field

High C^{ant} within the UCDW/LCDW/AABW between the PF and STF along 30°E can potentially be corrected for the natural variability signal suggested in section 5.2.1.2. DIC correction is therefore estimated between 42.9°S and 51°S by calculating the mean predicted DIC for each γ^n interval following Figure 5.9c) with the inclusion of AABW (Figure 5.23). The residual between each mean is shown in Table 5.15, and attributed to the natural variability between each occupation. Correction of the 2008 $\triangle C^*$ C^{ant} field in Figure 5.19a) yields 5.23b) and reduces the C^{ant} signal seen in the PF to STZ deep ocean to closer to 1996 values (Figure 5.19a). Decadal changes are clearly also reduced

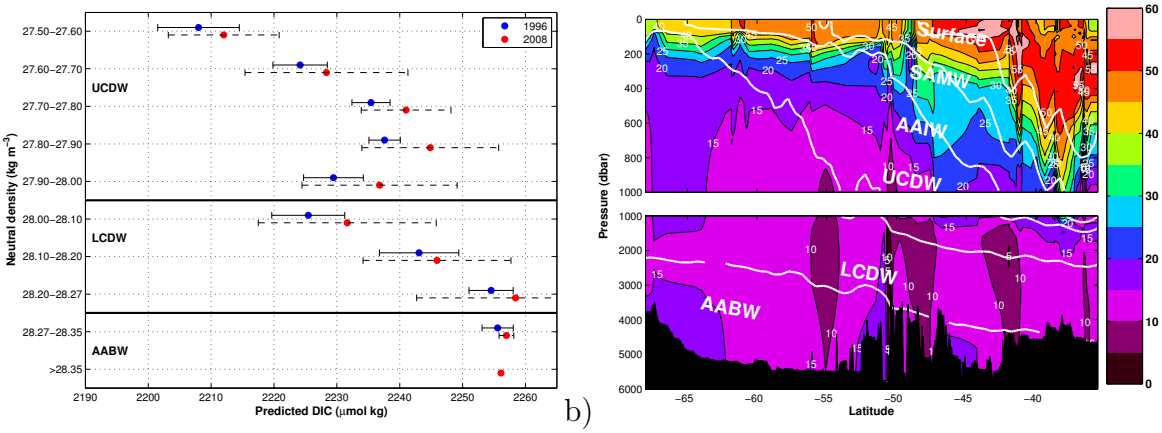

Figure 5.23: a) Mean and standard deviation for the predicted DIC. A dot defines the mean predicted DIC for the neutral density interval for 30°E between the PF and STF: 1996 (red) and 2008 (blue). Predicted DIC is calculated from a single regression equation for each water mass (UCDW/LCDW/AABW) and subsequently averaged into neutral density intervals. Water mass boundaries are shown for each deep water mass: UCDW, LCDW and AABW. b) C^{ant} distribution for comparison with Figure 5.19 for $\triangle C^*$, after subtraction of the estimated natural variability DIC signal between the PF and STF for UCDW/LCDW/AABW with values in Table 5.15a).

in Table 5.15b). In the following Chapter involving the construction of an inverse box model, this adjusted C^{ant} field will be applied given that the primary concern is regarding the C^{ant} inventory rather than the precise distribution.

5.5.3 Method Comparison: Comparison of ΔC^{ant} from TrOCA, $\triangle C^*$, and eMLR

TrOCA is the simplest method to apply, however, as reviewed by Yool et al. (2010) contains a number of biases in its calculation of C^{ant} leading to a ∼50% uncertainty, reducing to 7% for ΔC^{ant}. In this study, TrOCA estimates are robust in comparison to other estimates, and are useful in visualising ΔC^{ant}, given that none of the methods are 100% robust. The eMLR method is also relatively simple to apply, and relies upon deriving a statistical relationship between water mass properties measured at different years. eMLR is best applied to datasets with temporal separation of ∼10-20 years, given that for fewer years, the uncertainty will exceed the anthropogenic signal, whilst for a longer time period, the assumption for constancy of the other ocean properties becomes invalid.

The most complex method undertaken in this study is $\triangle C^*$, adjusted by the φC formulation, given that C^{ant} is calculated in addition to ΔC^{ant}. Breakdown of present

a)

Neutral density interval	DIC natural variability (μmol kg^{-1})
27.50-27.60	4.0
27.60-27.70	4.2
27.70-27.80	5.6
27.80-27.90	7.3
27.90-28.00	7.3
28.00-28.10	6.2
28.10-28.20	2.9
28.20-28.27	3.9
28.27-28.35	1.4
>28.35	*

b)

	SAZ	PFZ
UCDW	5.6±0.1	4.1±0.1
LCDW	6.3±0.1	6.0±0.1
AABW	5.8±0.2	6.3±0.1

Table 5.15: a) Difference in the mean predicted DIC calculated for each 30°E transect for the defined neutral density intervals, and attributed to natural variability. b) Decadal $\triangle C^*$ C^{ant} change in the UCDW/LCDW/AABW when the C^{ant} change attributed to natural variability, estimated in a) for each neutral density interval is removed. Units of μmol kg^{-1} decade^{-1}.

day DIC measurements into C^{bio}, C^{eqm}, C^{diseq} and C^{ant} components follows equation 4.6 and 4.12. A number of studies have undertaken analysis of $\triangle C^*$ across an entire ocean basin (e.g. Sabine et al. (1999, 2002); Lee et al. (2003)), and hence developed their own parameterisations for each component. Given that this study only makes use of transects at the boundary of the South Atlantic and that a substantial proportion of the water masses present in the South Atlantic are formed within other regions, parameterisations are only created in this study, where an alternative parameterisation is incompatible with the assumptions in this study. Parameterisations predominately follow the recent work of Pardo et al. (2011) (Indian/Pacific Oceans) and Vázquez-Rodríguez et al. (2012) (Atlantic Ocean). The decision on which parameterisation to use is based on sensitivity testing and the results of Lo Monaco et al. (2005a) and Vázquez-Rodríguez et al. (2009b). However, as previously noted in Chapter 4, different parameterisations make a substantial difference to the final C^{ant}, and hence all C^{ant} distributions are interpreted with caution. For ΔC^{ant}, much of the uncertainty cancels, with different parameterisations leading to similar ΔC^{ant}.

Therefore, in conclusion substantial uncertainties exist within C^{ant} estimates, when derived either from TrOCA (Yool et al., 2010), or using $\triangle C^*$. Parameterisations of both preformed alkalinity (equation 4.10) and C^{diseq} are subject to uncertainty and are particularly vulnerable given that Drake Passage and 30°E transects are at the boundary of the range of applicability for both parameterisations of Pardo et al. (2011)

and Vázquez-Rodríguez et al. (2012). C^{ant} uncertainties listed in Khatiwala et al. (2012) (their Table A1), for example $\pm 9 \mu mol\,kg^{-1}$ for $\triangle C^*$, serve as a lower bound to the uncertainty in this analysis. For ΔC^{ant} estimates using TrOCA and $\triangle C^*$, the associated uncertainties reduce and as each method displays a similar distribution, the reliability of each estimate is supported. eMLR distribution depends upon the 'correction' applied, with a sectionwide and per zone correction respectively preferred at Drake Passage and 30°E following a variety of refinements to the methodology suggested in e.g. Brown et al. (2010); Peng and Wanninkhof (2010); Wanninkhof et al. (2010); Park and Wanninkhof (2012). In conclusion for ΔC^{ant}, uncertainties for both TrOCA and $\triangle C^*$ are greatly reduced. For ease of application, the TrOCA method is preferred, as parameterisation of the preformed alkalinity is still required for ΔC^{ant} calculation using $\triangle C^*$. eMLR is also simple to apply, however, optimisation is likely dependent on the number of datapoints available, with which to construct a regression equation.

5.5.4 Future work

5.5.4.1 DIC Variability

Direct comparisons of DIC concentrations in this study, primarily make use of hydrographic transects across Drake Passage and 30°E. To better characterise the Southern Ocean DIC distribution, additional DIC measurements could be included all around the Antarctic continent, similar to the work of Williams (2007). This task is limited by the sparsity of Southern Ocean DIC measurements, with measurements made today, dependent on the availability of historic reliable DIC measurements, preferably making use of Certified Reference Materials (CRMs). The availability of in-situ DIC measurements using sensors and floats is still under development, however, continued advancement of sensor technology enables measurement platforms for carbon parameters to become a more realistic tool for future analysis.

5.5.4.2 Future work on TrOCA

Limitations of the applicability of the TrOCA method have been discussed in detail in Yool et al. (2010), with a ∼50% C^{ant} bias reducing to only a ∼7% bias through the cancelling of ΔC^{ant} uncertainties. This study found TrOCA provided a robust ΔC^{ant} estimate, comparable with $\triangle C^*$, and simple to apply. The concept of constructing a conservative parameter similar to TrOCA that better captures the variability of C^{ant} is an open challenge. Only a re-parameterisation of the TrOCA variable on a global scale, or the development of a TrOCA variable that is valid for specific locations, might be

capable of reducing the C^{ant} bias and improving ΔC^{ant}.

5.5.4.3 Future work on $\triangle C^*$

$\triangle C^*$ uncertainties have been previously reviewed in Matsumoto and Gruber (2005), and are discussed with reference to the Southern Ocean in van Heuven et al. (2011). This study has particularly followed the recent study within the Atlantic Ocean of Vázquez-Rodríguez et al. (2012) and focussed on carefully representing C^{diseq}, as described in section 4.3.2.5 using the parameterisations listed in Table 4.2 and eOMP for the deep ocean. Parameterisations of C^{diseq} are typically specific for a region or water mass, and any improvement in parameterisation is dependent on the quality of the predictor variables, e.g. nitrate, phosphate and silicate, and the representativeness of the local conditions to enable improvement of the C^{ant} estimate. For further comparison, alternative TA^o, C^{eqm} and C^{diseq} parameterisations from the literature e.g. Lee et al. (2003) could be applied and compared. The use of additional datasets within the Southern Ocean sector of the South Atlantic, for example, along the prime meridian (Hoppema et al., 2001; van Heuven et al., 2011) would help improve the representativeness of the parameterisations within the Southern Ocean.

van Heuven et al. (2011) also suggest the use of an age spectrum when determining water mass age from CFC estimates, with the biasing of age estimates discussed in Matsumoto and Gruber (2005). Difficulties arise for age estimates given that a given Source Water Type may be composed of water masses from different origins and therefore may have different ages. Hence favouring the parameterisations of Pardo et al. (2011), which make use of the Transit Time Distributions (TTD) method, in comparison to the parameterisation of Vázquez-Rodríguez et al. (2012) constructed using CFC water mass age estimates. Application of CFC age estimates has also been complicated in recent years through the observed plateau and decrease in atmospheric CFC (Figure 4.3). Therefore future work could include the calculation of water mass ages using additional available properties (e.g. $^3H - ^3He$, Sulphur Hexafluoride (SF6) or other transient tracers) for comparison.

5.5.4.4 Future work on eMLR

The 30°E section for uncorrected eMLR displays a high co-dependence with potential temperature. This study adds weight to the necessary use of a correction factor, similar to Brown et al. (2010) and Peng and Wanninkhof (2010) correcting for the residual created from $DIC^{measured} - DIC^{predicted}$ to improve eMLR accuracy. Application of the

eMLR technique in zones across the section, in a similar method to Peng and Wanninkhof (2010), is an alternative method to improve local ΔC^{ant} estimates.

Alternative corrections are preferred across each transect to improve the correspondence between eMLR and back-calculation methods with a single sectionwide correction across a large latitudinal/longitudinal range sub-optimum. In this study, ACC corrections adjust the 30°E ΔC^{ant} distribution to more closely correspond with back-calculation distributions whilst a sectionwide correction is preferred for Drake Passage. Further refinement of the method for other transects is required to assess whether a systematic method can be developed for calculating eMLR corrections.

Additional versions of the eMLR are suggested by Tanhua et al. (2007) and van Heuven et al. (2011) and warrant further examination, with both methods requiring reliable measurements of carbon parameters at decadal intervals. Further refinement for the eMLR technique has been considered, most recently by Thacker (2012), which rightly points out the vulnerability of the eMLR solution to a regression equation created over too large a spatial range, and the biasing effect that noise within the data might make to the conclusion. A rigorous review of the eMLR method as shown in Thacker (2012) is beyond the scope of this study, but presents an avenue for further research.

5.5.4.5 Summary

In conclusion, future work relies on continued hydrographic occupations to monitor DIC increase. DIC measurements in this study support the findings of Lo Monaco et al. (2005a,b) for an increase of DIC and anthropogenic CO_2 particularly within the surface, SAMW and AAIW, with a mean sectionwide estimate of SAMW ΔC^{ant} of $\sim$4.7μmol kg^{-1} decade^{-1} and $\sim$10.4μmol kg^{-1} decade^{-1} along Drake Passage and 30°E. This study is the first to quantify Drake Passage ΔC^{ant} and provides an update of Lo Monaco et al. (2005a)'s C^{ant} distributions, by creating a ΔC^{ant} distribution across the section. Future work is dependent on utilising existing historical datasets, which are vital for the construction of ΔC^{ant} including using the carefully constructed correction factors from GLODAP (Global Ocean Data Analysis Project), and CARINA (Carbon Dioxide in the Atlantic Ocean) to optimise estimates of ΔC^{ant}.

5.5.4.6 Key points

DIC has increased within the upper 1000dbar along Drake Passage and 30°E. Along both sections, DIC follows isopycnals to reach deeper into the water column at the

north of the section. Variability in the stoichiometric ratios indicate that the increases in DIC, can not solely be explained by changes in the biological cycling. Anthropogenic CO_2 distributions support the presence of C^{ant} and an increase in C^{ant} in Southern Ocean waters during the 1990's/2000's. C^{ant} greater than $5\mu mol\,kg^{-1}$ is predominately in the upper 1000dbar, although there is evidence for further increase within the deep ocean at the north of each section. A signal for enhanced deep ocean C^{ant} along 30°E is explained as being partially a result of natural variability in the mixing of deep water masses, which is not fully accounted for using the C^{ant} calculations methods.

The following Chapter will seek to develop an inverse box model for the South Atlantic Ocean for the purposes of investigating the circulation of volume, heat and salt. Additionally, C^{ant} from this Chapter will be synthesised into the inverse box model framework to quantify the fluxes of C^{ant} at the box boundaries.

Chapter 6

South Atlantic Ocean Inverse Box Model

6.1 Inverse Modelling

Since Wunsch (1978), the application of inverse modelling on both the global scale (Macdonald and Wunsch, 1996), and on regional scales (e.g. Wunsch (1978); Rintoul (1991); McDonagh and King (2005)) has improved estimates for the mean state of the ocean. This chapter will outline the inverse modelling theory, prior to applying the theory to the South Atlantic sector of the Southern Ocean for an update of the analysis by Fu (1981) and Rintoul (1991). Occupations of Drake Passage (repeat of WOCE A21) in 2009, Africa to Antarctica along 30°E (repeat of WOCE I6S) in 2008 and South America to Africa along 24°S in 2009 provide the data that will be used in this analysis. The decisions involved in the set-up and design of the model will be discussed.

6.1.1 Introduction and basic concepts

Inverse modelling has a range of computational, mathematical and statistical applications. For oceanographic and atmospheric purposes, inverse modelling commonly uses observed datasets as input. The aim of the inverse model is to adjust the 'known' values to obtain an adjusted dataset that is statistically consistent with appropriate constraints and, for oceanographic applications, better resembles the mean state of the ocean.

Present day observations throughout the global ocean are typically discrete measurements that are only reliable at the exact time and position of the measurement. Individual observations are therefore, prone to temporal and spatial bias based on the

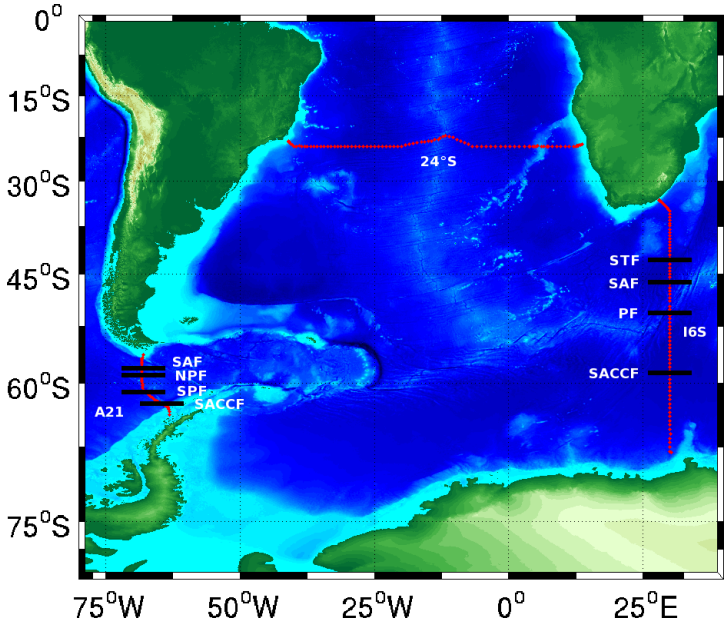

Figure 6.1: Map of hydrographic sections that form the boundary to the South Atlantic inverse box model. Sections are marked as A21 (Drake Passage), I6S (30°E) and across 24°S. Frontal boundaries are also marked following Table 3.3 and 3.6.

nature of the sampling pattern. Inverse modelling merges the initial observed datasets, with pre-existing high-quality measurements, such as, in situ Vema Channel observations as part of the Deep Basin Experiment (Hogg et al., 1996, 1999; Hogg and Owens, 1999), and high-quality estimates of the relevant local hydrographic circulation. Modern day synoptic measurements of the large-scale ocean climate rely on a combination of observation platforms including gliders, profiling floats (commonly referred to as Argo floats), remote sensing and intensive occupations and re-occupations of ocean transects. In recent years, through a combination of the WOCE (World Ocean Circulation Experiment) programme, CLIVAR (Climate Variability and Predictability) programme, GO-SHIP (Global Ocean Ship-based Hydrographic Investigations Program), and an ever-growing stock of Argo floats (>3500 in the ocean in May 2012), an improved synoptic profile has been possible of large-scale features on timescales ranging from seasonal to decadal. Information from any observation platform can provide valuable information to constrain the inverse model.

Inverse modelling is typically applied to a conceptual 'box' of hydrographic datasets. The increased availability of hydrographic datasets through the WOCE programme of previously poorly sampled regions, has allowed the study of a number of boxes and their large scale circulation. Examples of such inverse box analyses include: Wunsch (1978); Roemmich (1981); Naveira Garabato et al. (2003); McDonagh and King (2005);

Tsubouchi et al. (2012), extend from the Arctic to the Southern Ocean with this study aiming to build upon the work of previous authors.

Historically, inverse boxes created from the occupation of hydrographic transects have been limited to studying the lateral component of the flow of volume and thermohaline properties. Flux estimates are further improved by incorporating better characterisation of mixing and air-sea interactions in the ocean interior (McIntosh and Rintoul, 1997; Sloyan and Rintoul, 2001b,a). The inclusion of thermohaline properties from both hydrographic observations and the available heat and freshwater climatologies (discussed further in section 6.3.1.2) has the advantage of establishing values for the net effect of air-sea interaction on atmospheric heat flux, and precipitation and evaporation (Sloyan and Rintoul, 2001b,a). In addition, high quality measurements of chemical properties enable inverse model nutrient and carbon flux calculations, similar to Holfort et al. (1998) and Holfort and Siedler (2001) in the South Atlantic.

In this study, the methodology from pre-existing inverse box models will be applied to the South Atlantic box to constrain the lateral flow, mixing, air-sea interaction and Ekman flow terms. The initial field, and adjustments to the initial field creates a more robust picture of large-scale South Atlantic circulation that is thoroughly reviewed in later sections of this thesis. The novel feature of this inverse model is the inclusion of C^{ant} following from Chapters 4 and 5 to calculate inter-basin C^{ant} fluxes, previously limited to further north in the Atlantic (e.g. Holfort et al. (1998), Álvarez et al. (2003)).

6.2 Theory

The aim of constructing a South Atlantic box from three bounding hydrographic sections (Figure 6.1) is to calculate a balanced boxwide flow and this section describes the theoretical framework required. Station pairs along each hydrographic section bound a full depth water column. Layers of broadly homogeneous water are identified within the water column, in for example pressure or density space, to establish the section geometry. Station pairs and layer interfaces form a cross-sectional area, as exemplified by the cross-hatched area in Figure 6.2. Each cross-sectional area (e_i) enclosed by a station pair and a pair of layer interfaces is a component of the sectionwide geometry, and contributes towards the initial formulation of the inverse box model. For a single layer, hydrographic information is combined using the mathematical expression:

$$e_1 x_1 + e_2 x_2 + e_3 x_3 = y \tag{6.1}$$

where y is the volume transport, $e_{1,2,3}$ is the area for a single upper ocean layer

in Figure 6.2, and x is the geostrophic velocity. A single layer, along a single section comprised of four hydrographic stations is an idealised scenario, however is readily extended to a full depth water column containing multiple layers and multiple stations. Area coefficients (e_i) for each additional layer define the rows of a coefficient matrix **E**. Additional stations are included as additional terms ($e_i x_i$) on the left hand side of equation 6.1.

The aim of an inverse model is therefore to calculate the unknown velocities using hydrographic observations from well-sampled transects, such as Drake Passage (Meredith et al., 2011b), to constrain the inverse model final solution. For an initial estimate of the geostrophic current profile for a station pair, x in equation 6.1 represents the initial, unknown reference velocities, typically in the deep ocean. In this study, an initial field is firstly constructed using appropriate reference levels and reference level velocities (described in section 6.4.1) whilst x represents additional depth-independent adjustments to the initial geostrophic current profile.

The y component of equation 6.1 represents the imbalance between the initial volume transport estimate, and volume transport chosen as a constraint following equation:

$$y = \text{Constraint} - \text{Initial} \tag{6.2}$$

where for example, an initial 2Sv transport, constrained to 0Sv, results in a y=-2Sv imbalance. The role of the inverse model is therefore to adjust the initial solution by the imbalance to improve the representation of the individual hydrographic transect and the consistency of the boxwide circulation. For the idealised equation 6.1, the imbalance is given by y, whilst depth-independent velocities x, are the solved-for unknowns. In this study, an imbalance is calculated for each layer of the water column.

Equation 6.1 is generalised for multiple layers and multiple stations, with the additional inclusion of noise vector ε to account for errors:

$$\mathbf{Ex} + \varepsilon = \mathbf{y} \tag{6.3}$$

Where **x** is a vector of unknowns of size n x 1 (n rows, 1 column). The columns of the (m x n) coefficient matrix **E** represent section geometry. The resultant (m x 1) vector **y** contains the imbalance for each layer of the initial flow field, and hence, the values to which the system is to be constrained (McDonagh and King, 2005).

E contains the cross-sectional area between hydrographic station pairs. **x** contains the depth-independent velocity parameters to adjust the initial flow field according to the imbalances in **y**. The depth-independent velocities in **x** are the solution to

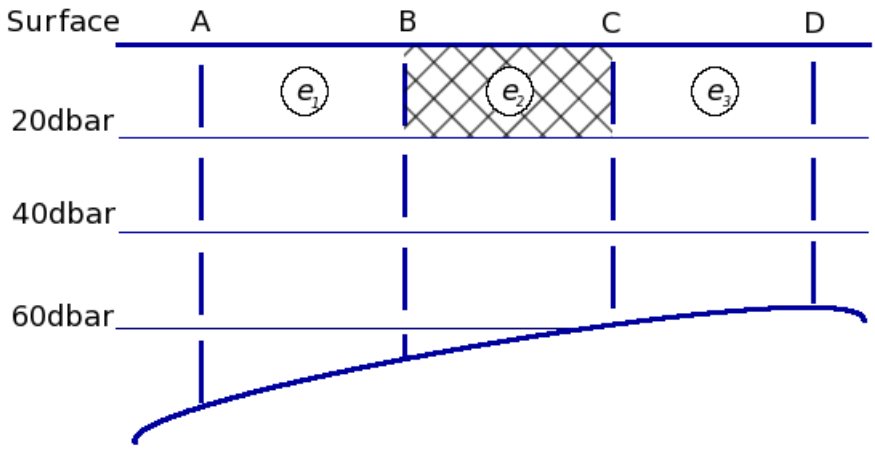

Figure 6.2: Example of the gridded area constructed by adjacent stations and layer interfaces. Vertical dashed lines indicate a CTD station, labelled as A, B, C and D; horizontal lines indicate the layer interface, given by pressure in this example. The curved line indicates the seafloor. The cross-hatched area between station pair B and C in the upper 20dbar exemplifies the area associated with a particular geostrophic velocity and transport. Each area within the upper 20dbar and bounded by a station pair is labelled by e_1, e_2 and e_3, respectively.

the inverse box model and addition of $\mathbf{x}$ to the initial field velocities yields the final solution. In this study, contributions to $\mathbf{x}$ are included from geostrophic, diapycnal, air-sea fluxes and Ekman transport terms on the South Atlantic boxwide ocean transport, later discussed in section 6.3.

For $\mathbf{E}$ in this study, neutral density interfaces separate the water column into layers (section 6.3.1.1). Each of the n columns of $\mathbf{E}$ represents a station pair, and each of the m rows represents layers within the water column, as defined by the modeller. Typically in oceanography problems, the coefficient matrix contains fewer rows (m) than columns (n), such that there are fewer equations that can be solved, compared with the number of $\mathbf{x}$ unknowns. This problem is therefore under-constrained ($n>m$), as in this study, the total n is equal to the total number of station pairs across Drake Passage, 30°E and 24°S.

6.2.1 Solving the system

Solutions of under-constrained inverse problems are solved in the literature using two main techniques: Singular Value Decomposition (SVD) and Gauss-Markov Estimators (GM). In this study, the method of Singular Value Decomposition (SVD) is chosen (Wunsch, 1996) although either technique should produce equivalent results. SVD decomposes the coefficient matrix $\mathbf{E}$, into three separate matrices given by:

$$\mathbf{E} = \mathbf{U}\mathbf{A}\mathbf{V}^{\mathbf{T}} \tag{6.4}$$

where $\mathbf{A}$ is a non-square $(m \times n)$ diagonal matrix with eigenvectors λ_i along the diagonal, $\mathbf{U}$ is a $m \times m$ matrix and $\mathbf{V}^T$ is a $n \times n$ matrix, with the T superscript indicating the transpose. If a diagonal matrix is non-square, then either some of the rows or columns will consist entirely of zeros, and not impact the solution. If k is taken as the number of nonvanishing singular values, then by limiting the size of the $\mathbf{U}$, $\mathbf{A}$ and $\mathbf{V}$ matrices, little information of value is lost from the solution:

$$\mathbf{E} = \mathbf{U}_k\mathbf{A}_k\mathbf{V}_k^{\mathbf{T}} \tag{6.5}$$

with $\mathbf{U}_k$ $(m \times k)$, $\mathbf{V}(n \times k)$ and $\mathbf{A}_k$ $(k \times k)$. Substitution of 6.5 into 6.3 gives:

$$\mathbf{U}_k\mathbf{A}_k\mathbf{V}_k^T\mathbf{x} + \mathbf{n} = \mathbf{y} \tag{6.6}$$

Following matrix manipulation, the unknown velocities can be solved for using:

$$\tilde{\mathbf{x}} = \mathbf{V}_k\mathbf{A}_k^{-1}\mathbf{U}_k^T\mathbf{y} \tag{6.7}$$

or more generally as:

$$\tilde{\mathbf{x}} = \mathbf{V}_k\mathbf{A}_k^{-1}\mathbf{U}_k^T\mathbf{y} + Q \tag{6.8}$$

with the noise expressed by substituting equation 6.7 into equation 6.6:

$$\tilde{\mathbf{n}} = (I - \mathbf{U}_k\mathbf{U}_k^T)\mathbf{y} \tag{6.9}$$

with the unknown velocity and noise results represented by $\tilde{\mathbf{x}}$ and $\tilde{\mathbf{n}}$, respectively, with I the identity matrix and Q the nullspace. The resulting $\tilde{\mathbf{x}}$ and $\tilde{\mathbf{n}}$ are dependent on the value of k chosen, with the number of singular values included within k commonly referred to as the solution 'rank'. Truncating the solution at k reduces the contribution of the solution covariance to the uncertainty, yet increases the nullspace contribution (Wunsch, 1996). A small k (i.e. low solution rank) reduces the dimensionality of the solution causing the unknown components to be solved using fewer singular values. A high solution rank indicates that more of the available information is used to reach a solution.

In practice, the solution rank chosen is a trade-off between characterising the solution as well as possible by fully solving all rows of the coefficient matrix, and the

inclusion of unnecessary equations with a high level of noise. At high solution rank, the errors and uncertainties within the initial field are magnified, resulting in a high and variable depth-independent velocity. At low solution rank, the solution is poorly parameterised and is outside the allowed uncertainty range, so is judged incorrect (Holfort et al., 1998). The optimum solution rank is chosen by limiting perturbations to the initial estimates of the unknown reference velocities to within one *apriori* standard deviation (further discussed in section 6.2.2 and 6.3.1.2, Figure 6.14), and limiting the residuals between the initial field and final solution for each layer, for each property, to within two *aposteriori* standard deviations (discussed in section 6.2.2, Figure 6.15).

6.2.2 Model Weighting

6.2.2.1 Row weighting

In order to better condition the pre-inversion matrix for solving for the unknown velocities, each row and each column of the $(m \times n)$ coefficient matrix $\mathbf{E}$ is weighted based on estimates of the previously known, '*apriori*' uncertainties within each of the individual components. The *apriori* uncertainties weight the influence of the different components prior to inversion. If the weighting on a single component is too small, it takes no part in the solution, whilst if a weighting is too large, the affected component will dominate the solution.

Solution weightings are applied following the guidelines of McDonagh and King (2005) and Tsubouchi et al. (2012). For row weighting, *apriori* uncertainties (ε_j) are estimated for each layer of the coefficient matrix. Ganachaud (2003b) determined from GCM (General Circulation Model) analysis that baroclinic variability is larger in the upper ocean than in the deep ocean. Therefore, upper ocean layers receive a higher *apriori* uncertainty, with the specific details for this analysis discussed in section 6.3.1.2.

For volume transport:

$$W_r = \frac{1}{\varepsilon_j} \tag{6.10}$$

whilst for property transports:

$$W_r = \frac{1}{2\eta_j^c \varepsilon_j} \tag{6.11}$$

where the standard deviation or property mean is given by η_j^c, whilst the factor of 2 (Ganachaud, 1999) is calculated from possible correlations between the zonally averaged and horizontal eddy components. Assuming that all errors are uncorrelated,

W_r $(m \times 1)$ is converted to a diagonal matrix $(W_r^{'})$ and premultiplied by the coefficient matrix, $\mathbf{E}$ and initial imbalance, $\mathbf{y}$ following:

$$W_r^{'}\mathbf{E}\mathbf{x} = W_r^{'}\mathbf{y} \tag{6.12}$$

6.2.2.2 Column weighting

The coefficient matrix station pairs are also column weighted, similarly using a specific *apriori* uncertainty for barotropic (ε_b), diapycnal (ε_w), air-sea (ε_q) and Ekman transport (ε_{Ek}) to create the corresponding column weights (W_c^b, W_c^ω, W_c^q, W_c^{Ek}) following Tsubouchi et al. (2012):

$$W_c^b = \left[\frac{\varepsilon_b}{A_j^{stn}}\right]^{\frac{1}{2}} \tag{6.13}$$

$$W_c^\omega = \left[\frac{\varepsilon_w}{A_j^{int}}\right]^{\frac{1}{2}} \tag{6.14}$$

$$W_c^q = \left[\frac{\varepsilon_q}{A_j^{surf}}\right]^{\frac{1}{2}} \tag{6.15}$$

$$W_c^{Ek} = \left[\frac{\varepsilon_{Ek}}{A_j^{Ek}}\right]^{\frac{1}{2}} \tag{6.16}$$

The area of each station pair is A_j^{stn}, the layer interface area for diapycnal transfer is A_j^{int}, ocean surface area for air-sea exchange is A_j^{surf} and the area between each station pair above the Ekman depth D_{Ek} is A_j^{Ek}. For application to the coefficient matrix, the W_c terms are concatenated and diagonalised, creating $W_c^{'}$. $W_c^{'}$ postmultiplies the coefficient matrix. The calculated $\mathbf{x}$ velocities are premultiplied by the column weights, post-inversion so that each variable is scaled by an estimate of its expected size. Column weighting is usually expressed as:

$$\left(\mathbf{E}^{'}W_c^{'}\right)\left((W_c^{'})^{-1}\mathbf{x}\right) = \mathbf{y}^{'} \tag{6.17}$$

where $\mathbf{E}^{'} = W_r^{'}\mathbf{E}$ and $\mathbf{y}^{'} = W_r^{'}\mathbf{y}$.

6.2.2.3 Weighting summary

Row and column weighting affects the preference with which the SVD solves a particular row of the coefficient matrix. Hence choosing an appropriate value for the *apriori* uncertainties requires careful sensitivity testing to the final solution. Additional information increases the skill with which the weightings are estimated, and helps guide the model solution.

Previous studies (e.g. Sloyan and Rintoul (2001b); Naveira Garabato et al. (2003); Jullion et al. (2010a); Tsubouchi et al. (2012)) have made use of data from hydrographic cruises, current meters and moorings to give an indication of the unknown velocities $\mathbf{x}$ and their uncertainties (e.g. Ganachaud (2003b)). In this study, the assumption is made that the $\mathbf{x}$ unknowns for barotropic velocities, diapycnal velocities, and velocity parameters relating to correction of air-sea interaction and Ekman adjustments are equal to zero. However, as described later in section 6.4, initial field reference velocities are applied prior to the inverse model calculation and hence $\mathbf{x}$ unknown velocities represent an additional depth-independent correction. Therefore, the row and column weightings must be carefully chosen to make sense in comparison to real ocean observations, and also give a qualitatively 'acceptable' final solution.

6.2.2.4 *Aposteriori* uncertainties

Aposteriori uncertainties take into account additional information from the coefficient matrix and the row and column weightings to provide an updated estimate of the *apriori* uncertainties. Prior covariance matrices (C_c, C_r) are constructed using the row and column weightings, following McIntosh and Rintoul (1997):

$$C_c = (W_c^{'})^2,\ C_r = (W_r^{'})^{-2} \tag{6.18}$$

before calculating the posterior covariance matrix C_{pc}, shown in:

$$C_{pc} = C_c - C_c\mathbf{E}^T\left(\mathbf{E}C_c\mathbf{E}^T + C_r\right)^{-1}\mathbf{E}C_c \tag{6.19}$$

with the resulting C_{pc} related to the *aposteriori* uncertainties in the column weightings (McIntosh and Rintoul, 1997), with posterior covariance matrix, C_{pr} related to row *aposteriori* uncertainties (Wunsch, 1996; McIntosh and Rintoul, 1997) by:

$$C_{pr} = \left\{I - \mathbf{E}C_c\mathbf{E}^T\left(\mathbf{E}C_c\mathbf{E}^T + C_r\right)^{-1}\right\} \times C_r\left\{I - \mathbf{E}C_c\mathbf{E}^T\left(\mathbf{E}C_c\mathbf{E}^T + C_r\right)^{-1}\right\} \tag{6.20}$$

with the square root of the diagonal component of each of the posterior covariance matrices, giving the *aposteriori* uncertainties for columns and rows respectively.

6.3 Model design

6.3.1 Geostrophic Flow

The first generation of oceanic inverse box models concentrated on representing the lateral flow, approximated as geostrophic, within the chosen box (e.g. Wunsch (1978); Rintoul (1991)). The geostrophic velocity (and transport) describes a steady-state flow based on the assumption of complete balance between the pressure gradient and the Coriolis force, where frictional terms are assumed negligible. Geostrophic velocities are therefore an approximation of the Navier-Stokes equation for fluid motion. This balance is displayed by the thermal wind equation:

$$f\frac{\partial(\rho v)}{\partial z} = -g\frac{\partial \rho}{\partial x} \tag{6.21}$$

where f is the Coriolis parameter ($f = 2\Omega sin\phi$, Ω is the rotation rate of the Earth, ϕ is latitude), ρ is seawater density, g is the gravitational acceleration, v is the geostrophic velocity and x and z are the horizontal and vertical coordinates, respectively. In the global ocean, in-situ density ρ can be readily calculated from salinity, temperature and pressure measurements, f, x and z are calculated based on knowledge of the measurement location to calculate the geostrophic velocity, v. Integrating equation 6.21 in the vertical from a depth z to z_0 gives an indefinite integral plus a constant of integration:

$$v(x,z) = -\frac{g}{f}\int_{z_o}^{z}\frac{1}{\rho}\frac{\partial \rho}{\partial x}dz + b(x,z_0) \equiv v_R + b \tag{6.22}$$

The baroclinic component (v_R) of the geostrophic velocity gives the relative velocity ($v_1 - v_{z_o}$) between two depths. For calculating the absolute baroclinic velocity, the depth z_0 is selected to give a $v_{z_o} \approx 0$. The baroclinic velocity is therefore calculated with reference to a known reference level (z_0) and a known reference velocity. Historically, oceanographers have worked to calculate a precise *level of no motion* for use in geostrophic flow calculations (Alderson and Cunningham, 1999; Donohue et al., 2001; Comas-Rodríguez et al., 2010), and can be defined by a depth, pressure, density or any other representative vertical coordinate. The constant of integration in equation 6.22 gives the depth-independent component (b) of the geostrophic velocity. Estimating

the barotropic flow contribution is a key source of uncertainty within any geostrophic velocity calculation.

Using hydrographic data, surfaces of constant density (isopycnals) are calculated from temperature, salinity and pressure. The density (ρ) and thus isopycnal slope ($^{\partial\rho}/_{\partial x}$) are required from at least two measurement stations in order to estimate a geostrophic (baroclinic) flow. For an inverse box model, the geostrophic velocity at a specific location provides only two dimensional information regarding ocean processes. As the ocean is a three-dimensional structure, the volume of water that flows between two measurement stations per second is estimated by:

$$V = \sum v(x,z) \times \triangle x \times \triangle z \tag{6.23}$$

The horizontal distance ($\triangle x$) between two measurement stations and the vertical distance ($\triangle z$) from the sea surface to the seafloor multiplied by the geostrophic velocity ($v(x,z)$) gives the volume transport (V) between two hydrographic stations. This allows estimates of the mass flow (ρV).

The concept of mass flow for any enclosed volume of ocean is a very powerful tool for an inverse box model. Conservation of mass and volume demands that if a mass of water flows into the box, then the same mass of water must leave the box. Mathematically, mass conservation (continuity of mass) is represented by:

$$\frac{1}{\rho}\frac{d\rho}{dt} + \left[\frac{\partial u}{\partial x} + \frac{\partial v}{\partial y} + \frac{\partial w}{\partial z}\right] = 0 \tag{6.24}$$

or, under the assumption of only very slow changes in seawater density with time, equivalent to volume conservation for an incompressible fluid:

$$\left[\frac{\partial u}{\partial x} + \frac{\partial v}{\partial y} + \frac{\partial w}{\partial z}\right] = 0 \tag{6.25}$$

with t the timescale for oceanographic processes, and u, v and w, the velocities in the x, y and z directions. Practically, volume conservation is applied to each layer of the initial field coefficient matrix.

Applying the continuity of mass (Equation 6.24) along with the geostrophic velocity (Equation 6.22), allows the volume transport (Equation 6.23), and more robustly the mass transport, to be written in a more rigorous form to account for observations at multiple depths and at multiple measurement stations:

$$\int_{x_1}^{x_2}\int_{z_1}^{z_2} \delta_i(v_{Rij} + b_{ij})\rho_{ij} dz dx = 0 \tag{6.26}$$

with the distance between the measurement stations (x) and the depth between each measurement (z) forming the cross-sectional area of the flow. ρ_i is the seawater density at each measurement point and δ_i is set to a value of +1 or -1 depending on whether the flow is into, or out of the box.

The discrete location of each hydrographic measurement in the horizontal and vertical in Equation 6.26 is equally represented by replacing the integrals with summations:

$$\sum_{i=1}^{n}\sum_{j=1}^{m} \delta_i L_i D_{ij}(v_{Rij} + b_i)\rho_{ij} = 0 \tag{6.27}$$

The distance between individual measurement stations is discretised as L_i with $i = 1...n$ representing the number of stations. The discretised vertical coordinate D_{ij} represents a local depth layer with the upper and lower layer boundary defined using either depth, pressure, density, potential density, neutral density, or any representative vertical coordinate. The distance between layer boundaries represents the layer thickness with $j = 1...m$ representing the number of layers (Jackett and McDougall, 1997). Neutral density is chosen for layer boundaries in this study.

The information from Equation 6.27 is fed into Equation 6.3. Considering geostrophic volume transport conservation only, **E** contains the cross sectional area ($L_i D_{ij}$) for each layer represented by a row in **E**, and each station pair, represented by a column in **E**. **y** denotes the transport imbalance for each layer of the inverse box, and **x** (1 x n) consists of unknown barotropic velocities (b_i) for each station pair.

Typically, the initial field contains an imbalance between volume inflow and outflow, hence Equation 6.27 $\neq 0$. For a specific layer, the imbalance $y(j)$ is the sum of the volume transport for each station pair for layer j plus the contribution of the mixing of mass and volume out of the density layer and the associated error n_{ij}. The magnitude of the unknown velocity for each station pair, i, is therefore determined by the magnitude of the initial imbalance.

The conservation of volume is not synonymous with the conservation of heat, salt or any other tracer. Take for consideration a volume transport balanced ocean box, with a volume transport of salty water from the north. If this is balanced by a fresh water flow to the south, then volume is conserved, however, excess salt has been added to the box. Salinity conservation is shown by:

$$\frac{dS}{dt} = \underbrace{-\left[u\frac{\partial S}{\partial x} + v\frac{\partial S}{\partial y} + w\frac{\partial S}{\partial z}\right]}_{advective} + \underbrace{\kappa_c\left[\frac{\partial^2 S}{\partial x^2} + \frac{\partial^2 S}{\partial y^2} + \frac{\partial^2 S}{\partial z^2}\right]}_{diffusive} \tag{6.28}$$

where the salinity within the enclosed ocean volume is given by S, and κ_c is the diffusivity of salt in water, and is dependent on the properties of the fluid (Gill, 1982). Equation 6.28 is composed of an advective term for the flow of salinity due to the water velocity, and a diffusive term due to a high-to-low concentration diffusion of molecules. Salinity in equation 6.28 can be directly substituted for an alternative tracer (C) whilst the conservation of tracer quantities (C_{ij}) is included by multiplying the left hand side of Equation 6.27. In the coefficient matrix, the conservation of any tracer, such as heat and salt, is readily included, as additional rows. In this study, unknown **x** velocities are calculated for layers representing volume, salinity, temperature and silicate imbalances and initialised as zero. Given the prior calculation of v_{z_o} velocities in the initial field, the **x** velocities represent additional depth-independent adjustments only.

6.3.1.1 Water Mass layer boundaries

Each transect is split into 21 neutral density (γ^n) layers (Jackett and McDougall, 1997). Neutral density water mass interfaces are extracted from Orsi et al. (1995, 1999); Heywood and King (2002) and Naveira Garabato et al. (2002b). The layers are subdivided into six water masses (Table 6.1).

6.3.1.2 Choice of *apriori* uncertainties for geostrophic flow

The *apriori* uncertainties, as shown in section 6.2.2, are required for each component of the inverse box model. Estimates for the geostrophic component are intended to weight values for the box boundary. Larger values are chosen from either property standard deviation or the property mean, and applied as the *apriori* uncertainty (ε_j) for each layer (section 6.2.2). Typically a property standard deviation is applied, however, the property mean is included to cope with excessively small standard deviation values, and to better weight higher temperature anomalies within the surface waters across the box. In this study, larger ε_j are applied to the upper ocean, in comparison to the deep ocean (Figure 6.3) following Ganachaud (2003b). Additionally, for the full depth transport around the box boundary, a small ε_j of 0.2Sv is applied to effectively constrain the system.

For the column weighting, *apriori* uncertainties are chosen to best balance the influence of each component of the coefficient matrix, **E**. *Apriori* uncertainty for the

Layer	Layer limits	Water Masses
1	γ^n<24	Surface Water
2	24<γ^n<25	
3	25<γ^n<26	
4	26<γ^n<26.80	
5	26.80<γ^n<26.90	Subantarctic Mode Water (SAMW)
6	26.90<γ^n<27.00	
7	27.00<γ^n<27.10	
8	27.10<γ^n<27.23	
9	27.23<γ^n<27.3	Antarctic Intermediate Water (AAIW)
10	27.3<γ^n<27.4	
11	27.4<γ^n<27.5	
12	27.5<γ^n<27.6	Upper Circumpolar Deep Water (UCDW)
13	27.6<γ^n<27.7	
14	27.7<γ^n<27.8	
15	27.8<γ^n27.9	
16	27.9<γ^n<28.0	
17	28.0<γ^n<28.1	Lower Circumpolar Deep Water (LCDW)
18	28.1<γ^n<28.2	
19	28.2<γ^n<28.27	
20	28.27<γ^n<28.35	Antarctic Bottom Water (AABW)
21	28.35<γ^n	

Table 6.1: Neutral density interfaces for each layer and corresponding water masses.

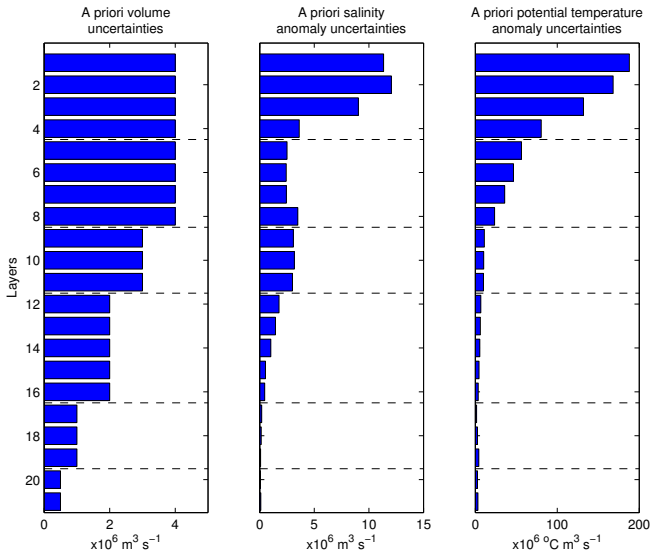

Figure 6.3: *apriori* volume, salinity anomaly and potential temperature anomaly uncertainties for each layer of the inverse box model, with units of Sv, Sv psu and Sv °C, respectively. (Sv=$10^6 \mathrm{m}^3\mathrm{s}^{-1}$)

geostrophic component is chosen as 1×10^{-2}, corresponding with Naveira Garabato et al. (2003), McDonagh and King (2005) and Jullion et al. (2010a). The *apriori* uncertainty is uniform for all station pairs across all transects.

6.3.2 Diapycnal Mixing

Following the founding work of Wunsch (1978), later generations of inverse models have attempted to include representations of the layer-to-layer flow across an isopycnal surface, or diapycnal mixing within their models (McIntosh and Rintoul, 1997; Sloyan and Rintoul, 2000; Ganachaud and Wunsch, 2000). Diapycnal mixing occurs for multiple reasons, for example, as a result of the vigorous interaction between the water column and topography, or as a result of significant upwelling (or downwelling) for the southern limb of the Atlantic Meridional Overturning Circulation (AMOC). On the large scale, balance between the pressure gradient and Coriolis force given by the geostrophic transport dominates the lateral flow of volume and other ocean properties. However, on a regional analysis, diapycnal mixing can provide a significant flow, into or out of a given layer especially in a region known for significant upwelling, such as the Southern Ocean.

Following McIntosh and Rintoul (1997), diapycnal velocities are calculated. In reality, diapycnal flux consists of both an advective component (w) from one layer to another, and a diffusive component (k_z) for a flux from a layer of high concentration to

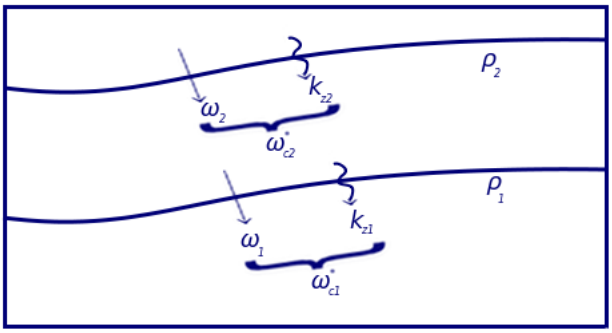

Figure 6.4: Simple schematic of diapycnal velocities in the ocean. Advective (ω_1, ω_2) and diffusive (k_{z1}, k_{z2}) velocities cross two isopycnal surfaces (ρ_1, ρ_2), expressed as the combined velocity (ω^*_{c1}, ω^*_{c2}). Each velocity component (ω, k) is independent. Isopycnal surfaces do not outcrop. Inspired by Speer (1997)'s Figure 1.

low concentration for each property (C), as shown for a simple schematic in Figure 6.4 (Speer, 1997; Speer et al., 2000). In Griffies et al. (2000), the diffusive component is regarded as an irreversible transfer of properties across isopycnals, whereas the advective component is driven by reversible stirring between density layers (Eckart, 1948). For this study, both advective and diffusive components are combined to form one diapycnal velocity (w^*_c) that is assigned for each layer interface (Sloyan and Rintoul, 2000).

Diapycnal flux gain or loss by each layer depends on the net contribution of the inflow/outflow across both the upper and lower isopycnal. Layer diapycnal volume flux is represented by:

$$V_{(z(\rho_2)-z(\rho_1))} = [Aw^*_c]_{z(\rho_2)} - [Aw^*_c]_{z(\rho_1)} \tag{6.29}$$

where A is the interface area for each layer and z (ρ) represents the depth, or pressure of the desired isopycnal. For the uppermost and deepest ocean layer, equation 6.29 is reduced to a single term to represent layer inflow/outflow. For the inverse box, diapycnal terms are included within **E** as the layer interface area for the upper and lower boundary within separate adjacent columns. The sign (positive into layer, negative out of the layer) is included. This is exemplified for an idealised four layer matrix construction for the **Ex** component:

$$\begin{pmatrix} A_1 & 0 & 0 \\ -A_1 & A_2 & 0 \\ 0 & -A_2 & A_3 \\ 0 & 0 & -A_3 \end{pmatrix} \begin{pmatrix} \omega^*_{c_1} \\ \omega^*_{c_2} \\ \omega^*_{c_3} \end{pmatrix} \tag{6.30}$$

where the ω^*_c components are additional unknowns in **x**. The upper row contains

a single area A_1 representing the single interface area between layer 1 and layer 2. Lower rows contain the upper and lower interface area. For property transports, the layer interface area is multiplied by the property mean ($A\bar{C}$). Therefore, separate ω_c^* components are calculated for mass, salinity and temperature following McIntosh and Rintoul (1997). In this study, all diapycnal fluxes ($V_{(z(\rho_2)-z(\rho_1))}$) were initialised to zero (McDonagh and King, 2005).

apriori uncertainties are dependent on pre-existing estimates of diapycnal velocities (ω) (e.g. Ledwell et al. (2011)). Estimates for the diapycnal and air-sea fluxes weight values that occupy the entire box area, and in particular the interface area and outcrop area for each of the neutral density layers within the box. The exact magnitude of the diapycnal flux has been a point of research since Munk (1966)'s initial inference of basinwide diapycnal diffusivity to be $1.3 \times 10^{-4}\mathrm{m}^2\mathrm{s}^{-1}$. Subsequent investigations have almost uniformly supported a mixing rate of order $1 \times 10^{-5}\mathrm{m}^2\mathrm{s}^{-1}$ (Toggweiler and Samuels, 1997; Webb and Suginohara, 2001). Ledwell et al. (2011) determine diapycnal diffusivities of $1.3\pm0.2 \times 10^{-5}\mathrm{m}^2\mathrm{s}^{-1}$ and $0.75\pm0.07 \times 10^{-5}\mathrm{m}^2\mathrm{s}^{-1}$ for a tracer release experiment, within the ACC, west of Drake Passage. Although the South Atlantic box contains regions of relatively enhanced mixing, such as for the rough Drake Passage topography and through the Scotia Sea (Heywood et al., 2002; Naveira Garabato et al., 2004), it is expected that a diapycnal diffusivity estimate of the order of $1 \times 10^{-5}\mathrm{m}^2\mathrm{s}^{-1}$ best represents current knowledge. As hinted at by Ledwell et al. (2011), and further reviewed in Marshall and Speer (2012), current estimates of diapycnal diffusivity are seemingly too small to support a dominant role for diapycnal fluxes within the upwelling of deep water in the Southern Ocean. Rather, upwelling predominantly occurs along isopycnal surfaces, mainly through wind and eddy processes (Wunsch, 1998; Olbers and Visbeck, 2005; Abernathey et al., 2011).

Therefore, *apriori* uncertainty for the diapycnal velocity is assigned as 10^{-5}, following from Orsi et al. (1999); Naveira Garabato et al. (2003) and recent observational estimates (e.g. Ledwell et al. (2011)) for a tentative estimate of an upper value for deep ocean diapycnal velocities.

6.3.3 Air-Sea induced diapycnal flux

Changes in surface seawater density across the global ocean varies significantly depending upon local surface processes such as evaporation, precipitation, or heat gain/loss. Isopycnal outcropping exposes a new density class to transformation to denser or lighter water. Water properties set during this surface transformation provide temperature and salinity signatures far from its buoyancy site.

Investigation of air-sea driven diapycnal flux dates from Walin (1982) and focuses on changes in buoyancy. Surface ocean temperature and salinity control surface density. Air-sea heat and freshwater fluxes at the surface cause density changes and changes to water column buoyancy. Surface density flux or buoyancy flux, B, is given by (e.g. Schmitt et al. (1989)):

$$B = \underbrace{{}^{\alpha H}/_{C_p}}_{Heat} - \underbrace{\rho\beta QS}_{Freshwater} \tag{6.31}$$

Heat flux is given by ${}^{\alpha H}/_{C_p}$ where α is the thermal expansion coefficient (units: 1/K), H is the air -sea heat flux for the outcropping area of the density class of interest, and C_p is the specific heat capacity (units: ${}^{Joules}/_{Kkg}$). Salt flux reflects freshwater gain/loss at the ocean surface through the hydrological cycle, given by $\rho\beta QS$, where β is the haline contraction coefficient, Q is the net freshwater flux for the outcropping area (units: $m\,s^{-1}$) and S is sea surface salinity. Buoyancy flux affects upper ocean stability, with surface warming and precipitation associated with stable conditions, and surface cooling and evaporation associated with unstable conditions. For an application of the buoyancy flux calculation, see Anitha et al. (2008).

Further application of the buoyancy flux principles of water mass transformation are developed in Schmitt et al. (1989); Speer and Tziperman (1992); Tziperman and Speer (1994); Sloyan and Rintoul (2001a,b), and applied directly to inverse box models in Naveira Garabato et al. (2003) and Jullion et al. (2010a). These applications calculate buoyancy flux across the outcropping area of a chosen density class and for an annual cycle T. Diapycnal volume flux induced by air-sea interaction is given by:

$$F_v = \int_T dt \int_{A_{\Delta\rho}} \left[\frac{1}{\Delta\rho} \left(\frac{\alpha H}{C_p} - \rho\beta QS \right) \right] dA \tag{6.32}$$

where ρ is the mean for the density class of interest ($\Delta\rho$) for in-situ density at the ocean surface, equivalent to potential density referenced to 0dbar, and $A_{\Delta\rho}$ is the outcropping area of $\Delta\rho$. A volume flux to lighter density gives a positive F_v.

In addition to the diapycnal volume flux associated with water mass transformation, the net air-sea flux is associated with the gain (loss) of heat and freshwater from (to) the atmosphere. The equations following Naveira Garabato et al. (2003) and Jullion et al. (2010a) are:

$$M_v = \int_T dt \int_A -Q\, dA \tag{6.33}$$

$$M_\theta = \int_T dt \int_A \frac{H}{C_p \rho} dA \tag{6.34}$$

with M_v the air-sea mass flux, as a result of the evaporation and precipitation of freshwater, and M_θ the air-sea heat flux, where A is the outcropping area of a layer of mean sea surface density ρ. Both M_v and M_θ are calculated for each layer, in contrast to F_v for each layer interface.

In the global ocean, air-sea interactions occur for every layer that outcrops to the atmosphere, including upwelled deep ocean water masses. For the inverse box in this study, the southern boundary is the Antarctic continent. In this region, MOC deep water mass upwelling occurs, in addition to Antarctic Bottom Water (AABW) formation along the Antarctic continent. All water masses defined in this study outcrop at the surface within the box.

To calculate the diapycnal volume flux, the outcropping area associated with each layer is added as extra columns to **E**, following the representation of **E** in equation 6.30. F_v, originally calculated for each layer interface is converted to give the net gain or loss for each layer. Coefficients for freshwater M_v and heat M_θ are included as additional columns in **E** for the salinity and temperature transport rows, respectively. The coefficients are the outcropping area for a layer of mean density (ρ) multiplied by the salinity of the freshwater input (0psu), or the mean layer temperature, respectively. The calculated air-sea interaction terms for volume (F_v), salinity (M_v) and heat (M_θ) are added to the **y** transport imbalances for each layer. Using the additional columns in **E**, additional unknowns equivalent to corrections to the air-sea induced volume transport are solved in **x**. *Apriori* uncertainties are estimated to be 50% of the initial estimate. Uncertainties arise from the uncertainty of the climatologies used to calculate heat and freshwater fluxes (section 6.4.4.2) as described in Lumpkin and Speer (2007).

6.3.4 Ekman transport

Ekman transport is a phenomena that affects atmosphere-to-ocean momentum transfer from the effects of winds only. Ekman transport is computed using:

$$V^{Ek} = \frac{A_{Ek}\tau}{f\rho} \tag{6.35}$$

where A_{Ek} is the area of the Ekman layer, f is the Coriolis parameter at the latitude of interest, ρ is the mean seawater density within the Ekman layer, and τ is the wind stress parallel to the hydrographic section. This study uses the analysis of

Bryden et al. (2011), which previously calculated Ekman transports along the section at 24°S based on NCEP wind stress (http://iridl.ldeo.columbia.edu/). Ekman transport is not calculated for the meridional sections, as within the Southern Ocean, zonal winds drive equatorward Ekman transport that is largely perpendicular to the meridional sections in this study (Toggweiler and Samuels, 1995; Lenn and Chereskin, 2009). As geostrophic circumpolar transport dominates, any cross-frontal Ekman transport is assumed negligible.

The Ekman transport acts as a lateral transport, in addition to the geostrophic transport discussed in subsection 6.3.1 and is calculated as a sectionwide estimate for each layer above the Ekman depth (D_{Ek}) for volume and additional properties. For volume transport, the Ekman transport is constructed as:

$$V_j^{Ek} = A_j v_j^{Ek} \tag{6.36}$$

for an Ekman velocity of v_{ij}^{Ek} within each layer, j, and an Ekman layer area, A_j. The area of each sectionwide layer above the D_{Ek}, estimated as 80dbar following Bryden et al. (2011), multiplied by the layer mean property ($\overline{C}$) for property transport, yields the Ekman coefficients for **E**, added as a single column. Application of Ekman transports has differed in the literature from a single unknown per transect (e.g. Ganachaud (2003a); McDonagh and King (2005)), to determining a single unknown per station pair (Naveira Garabato et al., 2003; Jullion et al., 2010a). Uncertainty with the Ekman transport from climatologies, limits the validity of explicitly including the Ekman transport for each station pair, and whether the resultant Ekman transport adjustments represent a true gain in information, hence this inverse model solves for a single unknown Ekman velocity in **x**. As the climatological data contains uncertainties which are difficult to quantify, an *apriori* uncertainty of 50% of the initial estimate is assigned.

6.3.5 Model Methodology

6.3.5.1 Property anomaly equations

Errors within the coefficient matrix are commonly assessed using the ratio of the largest to the smallest singular values, or 'condition number', that give a bound on the inaccuracy of the solved-for unknowns (McIntosh and Rintoul, 1997). Conditioning the coefficient matrix is therefore intended to reduce the errors, leading to the creation of property anomaly equations (Ganachaud, 1999).

Some properties, for example, salinity displays a far greater average value (e.g. 35)

compared to the estimated range of variability along a transect (e.g. 34-36 i.e. 2). Removing the average value, and focusing on the range of variability produces a better conditioned coefficient matrix. Calculating the 'average' value has been achieved using a number of different schemes in the literature, with Ganachaud (1999) creating anomalies by subtracting the mean property value from all the property values within each layer, in order to produce the most statistically robust property anomalies. The application of a separate mean value for each layer, however, creates adjacent layers with property values that are not directly comparable and leads to more complicated application of diapycnal processes. Hence in practice, inverse box modellers have favoured creating property anomalies by using a single boundary-wide 'average' value, applicable throughout the water column. This boundary-wide 'average' value is then either an approximated mean, for example 35 for salinity (Sloyan and Rintoul, 2001b), or the calculated mean for the box boundary (e.g. Jullion et al. (2010a); Tsubouchi et al. (2012)). In this study, the calculated mean for the box boundary of 34.767psu is applied.

Anomalies are applied for salinity and potential temperature, however not silicate, which as argued by Ganachaud (1999) displays a large concentration range between the surface and deep waters. This can create an apparent spurious source or sink of silica, hence non-anomaly equations for silica conservation are applied. After sensitivity testing, and to ensure the initial field full depth volume transport is well represented in the final solution, the initial imbalances $\mathbf{y}$ for full depth salinity anomaly and potential temperature anomaly transports are additionally weighted by a factor of 10, prior to applying the row and column weightings (section 6.2.2).

6.3.5.2 Layer Constraints

Barotropic, diapycnal, air-sea and Ekman components are included as additional columns in the coefficient matrix. For the barotropic component, the columns of $\mathbf{E}$ comprise the station pair area, and appropriately multiplied by the property anomaly for salinity and potential temperature respectively, and the original property value for silicate. Mass, salinity and potential temperature are constrained for each layer independently, as well as full-depth transport. Silicate is constrained for full depth only. The layer constraints for each property are listed in Table 6.2 and results in 67 $(22 \times 3 + 1)$ layers within the inverse model.

	Top-to-bottom	Within individual layers
Volume	yes	yes
Salinity	yes	yes
Potential Temperature	yes	yes
Silicate	yes	no

Table 6.2: Conservation constraints for the standard solution. Salinity and potential temperature anomalies are applied.

6.3.5.3 Summary

In summary, $\mathbf{x}$ velocities correspond with barotropic velocities, diapycnal velocities (w), air-sea flux velocity parameters (q) and Ekman velocities (v^{Ek}). Each column of $\mathbf{E}$ is associated with an unknown velocity in $\mathbf{x}$. As the initial field to be constructed in the following section, is a best initial circulation estimate using the available information, the perturbation from this estimate is evident in changes in $\mathbf{x}$. In this study, the inverse model is solving for 340 unknown reference velocities, resulting from Drake Passage (43 unknowns), 24°S (93 unknowns), 30°E (81 unknowns), as well diapycnal (60 unknowns), air-sea fluxes (62 unknowns) and Ekman fluxes (1 unknown).

6.4 Initial Field

The initial field is setup to give the best initial estimate for the South Atlantic and firstly tackles the *level of no motion* problem.

6.4.1 Level of No Motion (LNM)

Geostrophic velocities (Equation 6.22) are calculated as the relative velocity between two vertical coordinates. This calculation requires the specification of a *level of no motion* (LNM), $v = 0$ to compute the absolute velocity. The choice of this LNM, or 'reference level' is specific to each hydrographic cruise, and is dependent on the local hydrographic features. Common choices for reference level are at the ocean floor, where velocities are expected to reach a minimum, or between two distinctive water masses, where a level of $v = 0$ must exist for two flows in opposing directions. Direct velocity measurements provide the optimum method for selection of a LNM, however, they are often not available, or not judged to add a consistent level of skill to the calculation.

Drake Passage Multiple estimates for volume transport through Drake Passage exist from 124Sv referenced to in situ current meters (Nowlin et al., 1977) to estimates

of 154Sv and 136.6±7/129±7Sv from Firing et al. (2011) and Renault et al. (2011) for Lowered Acoustic Doppler Current Profiler (LADCP) derived reference levels. This compares with the canonical volume transport of 134±11Sv (Whitworth and Peterson, 1985). Meredith et al. (2011b) found the mean volume transport for 16 bottom-referenced hydrographic repeat sections across Drake Passage (136.7±6.9Sv), matching Cunningham et al. (2003). Given the interannual variability of the region (King & Jullion, in prep., Meredith et al. (2011b)), and the observed similarity between reference levels derived by LADCP and using a static reference level, the deepest common level between station pairs is applied as the reference level for my initial field, and captures the dominant baroclinic variability. A bottom triangle correction, described in section 6.4.2 is included.

Transect across at 24°S Southward flowing NADW across 24°S is balanced by northward flowing upper ocean water, and AABW particularly through Vema Channel towards the Brazil Basin (Hogg et al., 1999; McDonagh et al., 2002). The transition depth from southward to northward flow provides an ideal reference level at either upper water/NADW or NADW/AABW. Previous studies calculating South Atlantic transports have used a mixture of deepest common level (Holfort and Siedler, 2001), NADW/AABW transition (McDonagh and King, 2005) and upper waters/NADW (Bryden et al., 2011). For this study, an estimate of the zero velocity surface at a pressure of 1300dbar, as in Warren and Speer (1991) and Bryden et al. (2011) is applied.

Transect along 30°E The Agulhas regime, north of the Subtropical Front displays both an upper ocean circulation - Agulhas Current and Agulhas Return Current, as well, as an eastward flowing Agulhas Undercurrent (Beal and Bryden, 1999). An eastward undercurrent complicates the application of a static reference level, with a LADCP-referenced zero velocity estimate used in Beal and Bryden (1999). For simplicity, this study takes Bryden et al. (2005a) and Arhan et al. (2003) as a guide to selecting a reference level at 2000dbar from the African continent to 40°S, and a bottom reference level from 40°S to the STF (Arhan et al., 2003). Following the cautionary note of Park et al. (2001) with respect to the application of a mid-depth reference level, additional constraints are applied for the Agulhas regime as discussed in 6.4.3.

South of the STF, the dominant flow is eastward with no observed significant westward flow assumed across the section. Smaller velocities are expected in the deep ocean, explaining the 3500dbar reference level applied by Rintoul (1991). In this study,

Section	Reference Level
Drake Passage	Bottom
24°S	1300dbar
30°E Agulhas regime (North of 40°S)	2000dbar
30°E Agulhas regime (South of 40°S)	Bottom
30°E ACC regime	Bottom

Table 6.3: Reference levels for each of the box boundaries. The 30°E section has been split by the Subtropical Front (42.9°S) into an Agulhas and ACC regime.

a bottom-reference level is chosen following Park et al. (2001).

6.4.1.1 Summary of choice of LNM

The different reference levels are shown in Table 6.3 and Figure 6.5. Reference velocities at each reference level are shown in Figure 6.6. Drake Passage reference velocities generally show a $\pm 0.3 \mathrm{m\,s^{-1}}$ range with a single outlying reference velocity found in the shelf sea-deep ocean transition for two tightly spaced station pairs, and suggestive of a substantial on-slope feature. For 24°S, reference velocities are similarly generally within a $\pm 0.3 \mathrm{m\,s^{-1}}$, with a couple of reference velocities exceeding $\pm 0.5 \mathrm{m\,s^{-1}}$ near the western boundary. The Agulhas regime shows the largest observed reference velocities around the box boundary varying from positive to negative, highlighting the difficulty in selecting a static reference level that adequately characterises both the westward-flowing Agulhas Current and eastward-flowing Agulhas Return Current. The variability within the Agulhas regime decays away south of the Subtropical Front (42.9°S), remaining within $\pm 0.3 \mathrm{m\,s^{-1}}$ of zero velocity.

6.4.2 Bottom Triangle

Along Drake Passage and 30°E, as discussed in section 6.4.1, a bottom reference level is applied, or in practice corresponds to the Deepest Common Level (DCL) between two stations. A greater maximum depth at one station, in comparison to the adjacent station, means that a proportion of the flow within this 'bottom triangle' is lost. In order to better characterise the geostrophic transports, the bottom triangle is filled by nearest neighbour extrapolation from the DCL to the bottom.

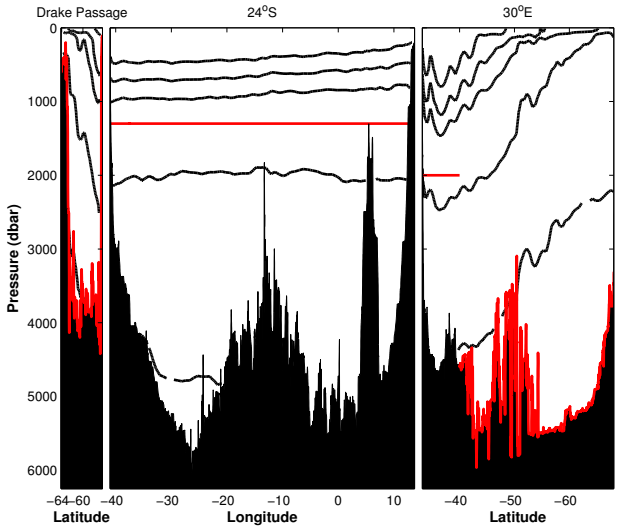

Figure 6.5: Reference levels (in red) around the box boundary consisting of Left Panel: Drake Passage (south to north), Central Panel: 24°S (west to east), Right Panel: 30°E (north to south). The black lines show the water mass limits, to be discussed in section 6.3.1.1.

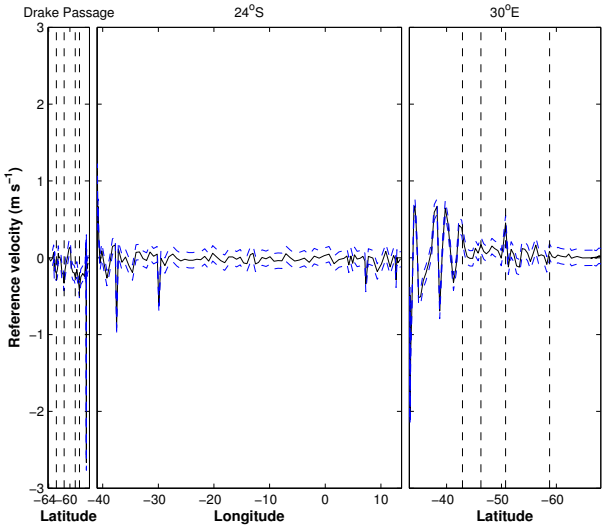

Figure 6.6: Initial field reference velocities (solid line) around the box boundary at the reference levels shown in Figure 6.5. Dashed lines show the *apriori* uncertainty (discussed further in 6.3.1.2). ACC fronts are added to the meridional sections. Along the Drake Passage transect from south to north: Southern Antarctic Circumpolar Current Front (SACCF), Southern Polar Front (SPF), Northern Polar Front (NPF) and Subantarctic Front (SAF), whilst along the 30°E section from north to south: Subtropical Front (STF), SAF, PF, SACCF. See Chapter 3 for front definitions.

6.4.3 Constraints

To better characterise the initial field, correction velocities are calculated for each constraint discussed below.

Drake Passage The only constraint across Drake Passage is a full-depth volume transport constraint of 136.7Sv (Cunningham et al., 2003; Meredith et al., 2011b).

24°S Following previous Brazil Basin studies as part of the Deep Basin Experiment, the bottom water constraint across 24°S is altered to 2°C isotherm. The 2°C isotherm definition includes AABW and the lower LCDW layers within Vema Channel and Hunter Channel. Bottom Water defined using the 2°C isotherm is given the acronym BW, to differentiate from AABW defined by γ^n>28.27. Northward BW flow estimates provide a constraint of 6.9Sv northward flow below the 2°C isotherm (Hogg et al., 1999; McDonagh et al., 2002). Within the eastern basin, a constraint is applied for zero net transport below the 2°C isotherm on the eastern side of Walvis Ridge (6°E) within the northern Cape Basin (McDonagh and King, 2005; Arhan et al., 2003).

For the upper ocean across 24°S, a southward, wind-driven estimate for the Ekman transport of 3.3Sv for the upper 80dbar must be included (Bryden et al., 2011). For the upper ocean of the western basin, the Brazil Current is constrained to 4.9Sv southward, west of 35°W, above 300dbar (Bryden et al., 2011). Finally, a sectionwide net salinity transport is applied for the assumption of salinity conservation between Bering Strait and 24°S, equal to the 26.0Sv psu Bering Strait salinity transport (Coachman and Aagaard, 1988).

30°E Net volume and/or property transports into the Atlantic Ocean, otherwise known as 'Agulhas leakage' has been a topic of intense debate (e.g. Gordon et al. (1992); McDonagh et al. (1999); Lutjeharms (2007); Beal et al. (2011)). In this study, north of the STF within the Agulhas regime, an Agulhas leakage term is estimated based on McDonagh et al. (1999) of 9Sv above the 3.5°C isotherm.

Across the boundary of the South Atlantic box, a constraint for zero net salinity divergence is included by summing together the salinity transport through the Agulhas regime, Drake Passage and across 24°S. The salinity transport outflow across the ACC regime is constrained to equal the inflow across the other three transects (Table 6.4). A small *apriori* uncertainty (0.2Sv) is applied to the full depth transport around the box boundary to ensure that this criteria is met, making use of well parameterised values for Drake Passage (Cunningham et al., 2003; Meredith et al., 2011b) and 24°S (Coachman

	Property	Vertical extent	Constraint
Drake Passage	Volume	Full depth	136.7Sv
24°S: Vema/Hunter Channel	Volume	$\theta < 2$°C	-6.9Sv
24°S: Brazil Current	Volume	Above 300dbar	4.9Sv
24°S: Cape Basin	Volume	$\theta < 2$°C	0Sv
24°S: Ekman transport	Volume	Above 80dbar	3.3Sv
24°S	Salinity	Full depth	26Sv psu
30°E: Agulhas regime	Volume	$\theta > 3.5$°C	9Sv
30°E: ACC regime	Salinity	Full depth	Boundary salinity transport

Table 6.4: Constraints applied to better parameterise the initial field for each of the sections along the box boundary. Positive (negative) values indicate a transport into (out of) the box. The boundary salinity transport refers to the net inflow of salinity transport across Drake Passage, 24°S and 30°E Agulhas regime combined to equal the net outflow of salinity transport through the ACC regime at 30°E.

	Velocity (ms^{-1}) (positive into box)
Drake Passage	-0.000398
24°S: Vema/Hunter Channel	0.0020
24°S: Brazil Current	-0.0095
24°S: Cape Basin	0.0058
24°S: Ekman transport	-0.0073
24°S	-0.000592
30°E: Agulhas regime	-0.0022
30°E: ACC regime	-0.0039

Table 6.5: Adjustments to the level of no motion to construct the initial geostrophic velocity field.

and Aagaard, 1988; Woodgate and Aagaard, 2005). Small uncertainty emphasises the zero salinity convergence constraint for the inverse box, rather than reflecting the actual uncertainty in the net full depth volume transport.

6.4.4 Initial geostrophic velocities and transports

Using the reference velocities (section 6.4.1) , and the constraints (section 6.4.3) applied to the initial geostrophic velocities, transports are estimated around the box boundary as shown in Figures 6.7, 6.8 and 6.9. This initial field is the input for the geostrophic velocity component of the inverse box model, and guides the inverse box model towards an optimal solution.

The initial field is characterised by zonal inflow through Drake Passage, particularly north of the Northern Polar Front with zonal frontal jets for both the Southern Polar

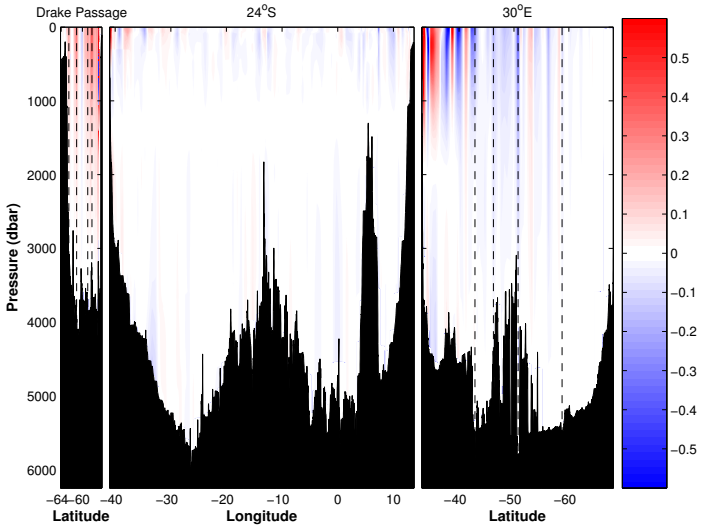

Figure 6.7: Initial geostrophic velocities (barotropic and baroclinic) around the box boundary. Red (blue) indicates flow into (out of) the box. The vertical dashed lines indicate frontal positions as defined in Chapter 3. Along the Drake Passage section from south to north: SACCF, SPF, NPF and SAF, whilst along the 30°E section from north to south: STF, SAF, PF, SACCF. Units of $\mathrm{m\,s^{-1}}$.

Front and SACCF. Along 24°S, the picture is more mixed and generally concentrated to the upper 1000dbar. Velocities associated with the southward NADW flow into the box are all $<0.05\mathrm{m\,s^{-1}}$.

For the 30°E section, Agulhas regime circulation consists predominantly of Agulhas Current box inflow north of ∼38°S. The return flow gives a more mixed signal with regions of inflow and outflow, within the upper 2000dbar, north of the STF. Within the ACC regime, the Polar Frontal Zone exhibits strong outflow within its zonal jet. South of the Polar Front, the strength of the geostrophic velocities decrease, with only small velocities observed south of the SACCF (58.75°S).

6.4.4.1 Diapycnal Mixing

For diapycnal property fluxes, a mean property value at the layer interface is required. The interface means for each property (S, θ) are generated using the WOCE Global Hydrographic Climatology (WGHC) by Gouretski and Koltermann (2004). WGHC data is on a 0.5° grid, and averaged along isopycnal surfaces. For the ocean interior, isopycnal averaging is preferable to isobaric averaging. The layer interface area for each of the neutral density interfaces in this study is constructed from the initial 45 levels from WGHC for each mapped property field. In this study, a diapycnal velocity is resolved for each layer interface, as a separate unknown for each property $[\omega_c^* = (\omega_m^*, \omega_s^*, \omega_t^*)]$

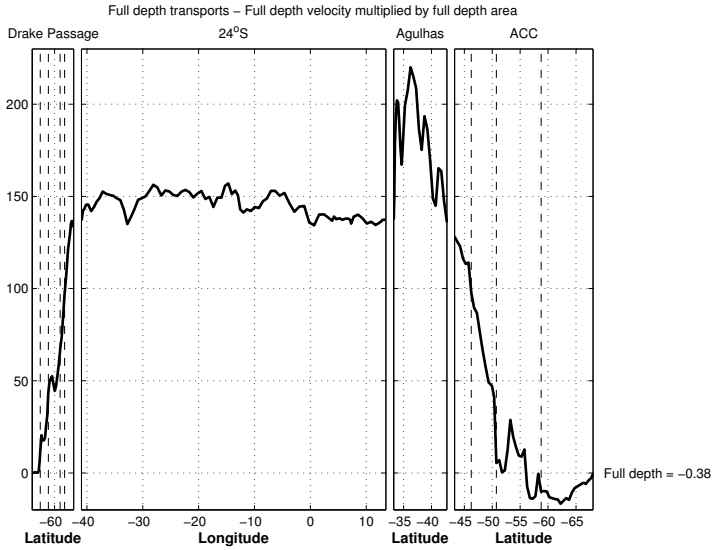

Figure 6.8: Cumulative transport of the initial geostrophic transport field around the box boundary. The cumulated total around the box boundary is shown. The 30°E section is separated into an Agulhas regime and ACC regime component. The vertical dashed lines indicate ACC frontal positions. Latitudes and longitudes are labelled as appropriate.

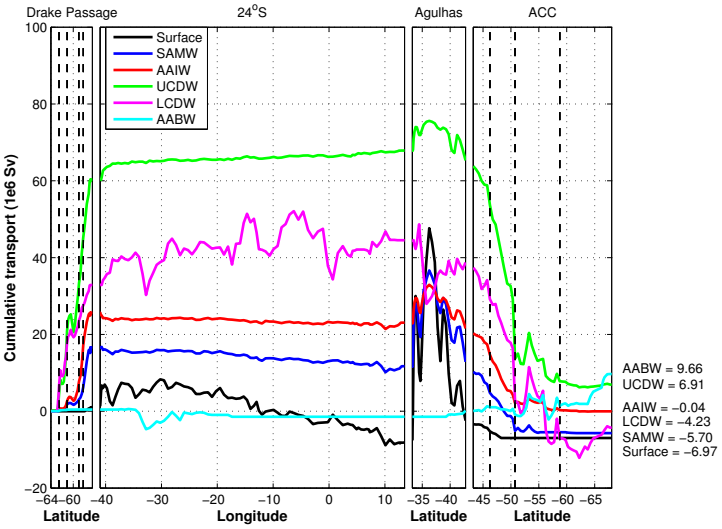

Figure 6.9: Cumulative transport of the initial geostrophic transport field around the box boundary for each water mass, with water masses defined according to Table 6.1. The cumulated total for each water mass is shown. Vertical dashed lines indicate the frontal positions according to Tables 3.3 and 3.6.

(mass, salinity, temperature (McIntosh and Rintoul, 1997)).

6.4.4.2 Air-sea induced diapycnal flux

Air-sea fluxes are explicitly included within the model using the descriptions from Schmitt et al. (1989); Speer and Tziperman (1992); Tziperman and Speer (1994); Sloyan and Rintoul (2001b); Naveira Garabato et al. (2003); Jullion et al. (2010a). Explicit inclusion of heat flux and freshwater flux terms for the entire surface area of the South Atlantic ocean is required for equation 6.32. Heat flux and freshwater flux to the atmosphere from the ocean is parameterised by equations 6.33 and 6.34. Heat flux terms are supplied by monthly-averaged estimates from the NOC (v2.0) climatology (Berry and Kent, 2009, 2011). The monthly average for the net heat flux is shown in Figure 6.10a). The net heat flux Q_{net} is the sum of the contributions from the latent (Q_H) and sensible heat flux (Q_E), and longwave flux (Q_{LW}) and shortwave flux (Q_{SW}) (Grist and Josey, 2003).

$$Q_{net} = Q_H + Q_E + Q_{LW} + Q_{SW} \tag{6.37}$$

The net heat flux is used to initialise the air-sea heat fluxes for each layer. As each layer is assumed to outcrop within the box, each layer must get a proportion of the net heat flux incident on the ocean surface. As the hydrographic sections are predominantly within austral summer, the mean of monthly averages for the January-February-March (JFM) period, is estimated as representative of the box. The mean heat flux for the JFM period is 65W m^{-2} (Figure 6.10) with an annual range from 129W m^{-2} in austral summer to -91W m^{-2} in austral winter.

Freshwater flux for equation 6.32 is parameterised based on the recommended climatologies from Schanze et al. (2010): Global Precipitation Climatology Project (GPCP) for precipitation (Adler et al., 2003), and Objectively Analysed Ocean-Atmosphere Flux (OAFlux) for evaporation (Yu and Weller, 2007; Yu et al., 2008). At each grid point, evaporation minus precipitation (E-P) is calculated using 2008 and 2009 estimates, before finding the box mean. Enhanced precipitation over the Southern Ocean sector of the South Atlantic (Figure 6.11) between 50°S and 60°S matches the general pattern for the global annual average of Figure 4 from Schanze et al. (2010). Enhanced precipitation persistence for the region throughout the year is shown in Figure 6.11. Freshwater flux caused by E-P is given by M_v, estimated as ∼mSv for the box. The effect of sea ice is not included and is likely relatively small (Ren et al., 2011), and smaller than the anticipated austral winter maximum. Care must be taken to ensure that comparable

units of mm^{-1} month or cm^{-1} year are used during the analysis.

In order to complete the calculation of the air-sea induced diapycnal flux, the density at the surface ρ, specific heat capacity at the surface C_p, thermal expansion coefficient α, and haline contraction coefficient β, require explicit calculation using sea surface properties. Monthly averaged surface temperature and salinity from *World Ocean Atlas* on a 1° grid (Boyer et al., 2005; Antonov et al., 2010; Locarini et al., 2010) supply the sea surface temperature (SST) and sea surface salinity (SSS), as well as estimates for the outcropping area for each neutral density layer. *World Ocean Atlas* is favoured due to the availability of monthly averaged sea surface properties given the magnitude of the variability in air-sea exchange over an annual cycle. Monthly properties for the JFM period are averaged, whilst the outcropping area is carefully scaled to match the total ocean surface area within the box.

Using *World Ocean Atlas* for the South Atlantic box, initial estimates of some deep ocean layers provided for no outcrop area within the region. As a tentative estimate, the outcropping area for all non-zero LCDW and AABW layers were averaged, and an average outcropping area for all LCDW and AABW was applied to ensure that air-sea interaction was possible for each water mass.

The resulting air-sea induced volume transport, freshwater flux and heat flux for the available layers and layer interfaces is shown in Figure 6.12. The diapycnal volume flux induced by air-sea interaction shown in Figure 6.12, is dominated by the heat flux, with a small freshwater contribution. The importance of heat flux is observed in Figure 6.10, in austral summer, as the ocean gains heat from the atmosphere. The increase in heat, increases the temperature of the surface layer converting exposed water masses to lighter densities. In austral winter, this process would be reversed with density gain of the exposed water masses, representing a decrease in water mass buoyancy.

6.4.4.3 Ekman transport

The southward flowing Ekman transport of 3.3Sv at 24°S reduces the magnitude of the northward flowing surface water mass transport, with model diagnosed adjustments required for box closure (Lux et al., 2001). At 26.5°N in the North Atlantic, Ekman transport fluctuations range between 7.9Sv southward and 16.3Sv northward (Cunningham et al., 2007). Ekman velocities are initialised by the contribution of the annual average 3.3Sv Ekman transport to the initial field imbalances ($\mathbf{y}$) following Bryden et al. (2011). Given Ekman transport variability, and the conclusion by Bryden et al. (2011), that their February-March Ekman transport estimate of 4.6Sv was anomalously high, an annual average is sufficient for avoiding additional uncertainty associated with

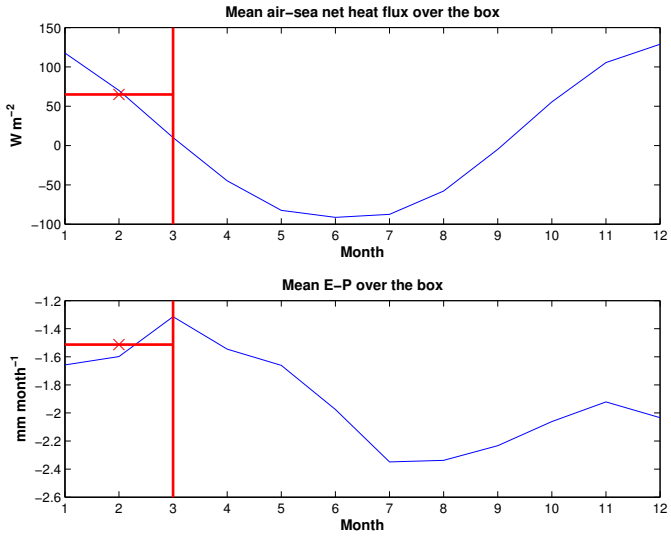

Figure 6.10: Upper Panel: Net heat flux per month over the box. The average for the JFM period is highlighted by a ×. Positive (negative) indicates heat flux into (out of) the ocean. Lower Panel: Net evaporation-precipitation in mm^{-1} month for the box, with the JFM average highlighted by a ×. Positive (negative) indicates a flux out of (into) the ocean.

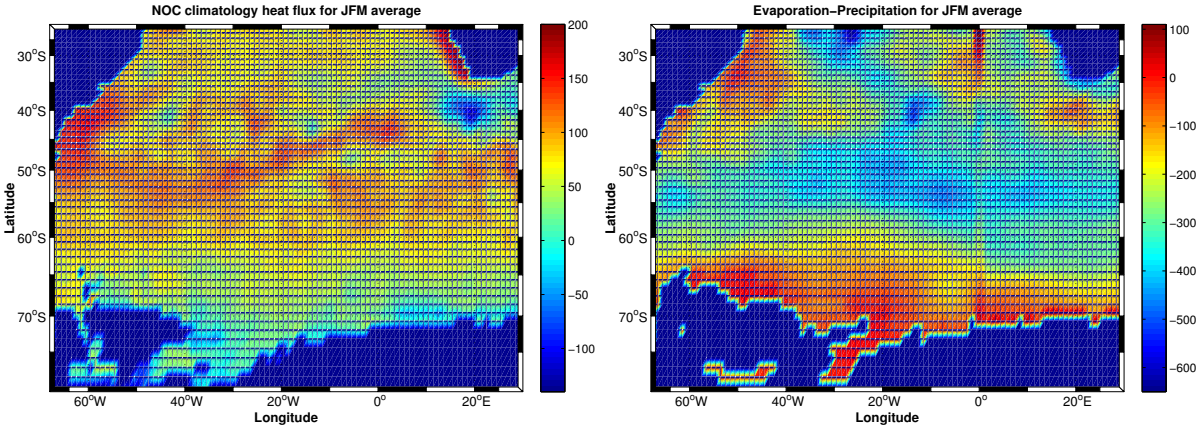

Figure 6.11: Left Panel: Ocean heat flux map of the South Atlantic sector of the Southern Ocean from NOC climatology. Right Panel: Evaporation-Precipitation for the South Atlantic sector of the Southern Ocean using Evaporation from the Objectively Analysed Ocean-Atmosphere Flux (OAFlux) and Precipitation from Global Precipitation Climatology Project (GPCP) recommended by Schanze et al. (2010).

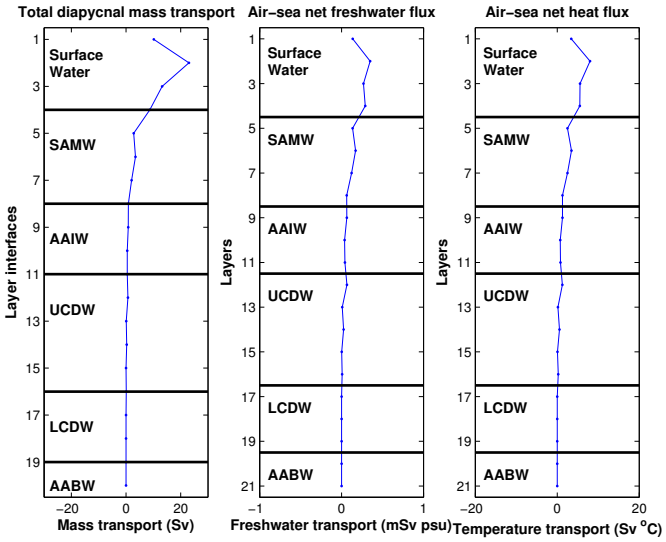

Figure 6.12: Left Panel: Diapycnal volume flux at the layer interface induced by air-sea interaction. The y-axis is labelled by the layer interface. Central Panel: Volume flux of freshwater from the atmosphere labelled for each layer and Right Panel: Heat flux from the atmosphere labelled for each layer.

seasonality. Using the Bryden et al. (2011) 3.3Sv estimate, Ekman transport is included for volume, salinity and temperature transports within a single column of the coefficient matrix, solving for a single unknown. The Ekman transport estimate is included at 24°S prior to inversion, and prior to constraining the salinity transport across 24°S to equal the Bering Strait inflow.

6.4.4.4 Additional constraints

Additional constraints, described in section 6.4.3, are included as additional rows in the **E** coefficient matrix. From Table 6.4, six constraints are applied for Drake Passage, Vema Channel, Cape Basin, Brazil Current, full depth along 24°S and the Agulhas regime along 30°E. The resultant imbalance vector **y** is initialised following equation 6.2. The 'Constraint' is equal to the constraint listed in Table 6.4. The 'Initial' is the initial value for the transports calculated from the initial field. **y** is therefore the imbalance between these two terms. In this study, the magnitude of **y** is small as the constraints listed in Table 6.4 are applied to constrain the initial field transports prior to applying to the inverse model. The Ekman transport listed in Table 6.4 is dealt with following section 6.4.4.3 in the inverse model.

6.4.4.5 Solution transports

Water mass properties are set by air-sea exchange at the surface, with additional interior ocean property changes attributable to mixing. This study aims to capture the mean state circulation, whilst acknowledging that natural fluctuations in hydrographic properties are inevitable (Naveira Garabato et al., 2009). In the following final solution, volume transports and transport-weighted properties: salinity, potential temperature, DIC, natural DIC and C^{ant} are calculated for each layer. Heat transport is calculated following Hall and Bryden (1982), representative of the mean flow rather than any southward heat flux through eddy transport. Natural DIC (C^{nat}) and C^{ant} are both taken from the $\triangle C^*$ analysis in Chapter 5, where natural DIC is DIC pre-industrialisation and refers to the linearised form of C^{eqm} from section 4.3.2.2, representative of atmosphere-ocean equilibrium at the 280ppm pre-industrial atmospheric CO_2 level. Along 30°E, the corrected version of the $\triangle C^*$ distribution (Figure 5.23) is applied to avoid the potential bias caused by excess C^{ant} in the deep ocean. All carbon parameters are refitted compared to Chapter 5 using least squares fitting to generate a distribution in pressure:latitude space. C^{ant} transport specifically is often reported in the literature as $\mathrm{Mmol\,s^{-1}}$ or $\mathrm{PgC\,yr^{-1}}$ with both units given in this study.

6.4.4.6 Summary

Sections 6.2-6.4 have dealt with the parameterisation of the inverse model initial field ranging from the initial hydrographic data to how this data is included in the inverse model, in order to generate a reliable solution. Care is taken to ensure the adjustments that the SVD makes to the initial field produces a mathematical solution from the infinite solution space that complies with the available constraints. The quality of the inverse solution is therefore highly dependent on the quality of the initial field, and for this reason careful consideration has been given to all aspects of the initial solution.

6.5 Final Solution

The chosen final solution is obtained by careful selection from the range of possible mathematical solutions after applying *apriori* and *aposteriori* uncertainties, as appropriate. Selecting the optimum rank for the SVD helps determine a representative solution (see section 6.2.1 for details) (McIntosh and Rintoul, 1997). Perturbations to the initial estimate, as a consequence of the asynchronicity of the hydrographic cruises are inevitable and are representative of the natural fluctuations within the ocean system,

as opposed to initial estimate inaccuracies.

6.5.1 The selected solution

6.5.1.1 Choice of solution rank

The solution rank is chosen after application of SVD to the row-weighted and column-weighted coefficient matrix. The rank of the solution (60 out of 73) is selected. The choice of rank is made at the point which the noise added by including additional rows negates the information gained. The co-dependency between ocean layers gives reason for selection of a solution rank below the full rank.

A first estimate of the relationship between the solution rank and the magnitude of the residual for this study is shown in Figure 6.13. Solution ranks $\sim>50$ are suitable solutions where the full depth salinity anomaly transport (Figure 6.13b), which is constrained to give a net salinity convergence within the box of zero, approaches zero. The volume full depth volume transport (Figure 6.13a) is equivalent to the freshwater divergence, and the stability of this value is demonstrated by a wide range of ranks within $\pm$1Sv. The exact rank is deduced by comparing Figures 6.13, 6.14 and 6.15. Depth independent velocities (Figure 6.14) are also compared to find a stable rank, where small changes in rank have only a small net effect on the solution. At low rank, the solution is little different to the initial field. At high rank, the conservation constraints are more closely satisfied with low residuals. The SVD creates each solution through the addition of an extra layer of information. For low rank solutions, deep ocean layers are solved first, as a result of the lower uncertainty for deep ocean transports (Figure 6.3). Ekman transports are restricted to the upper layers, hence only when the upper layers are included within the solution can the Ekman component of the solution be resolved.

Depth-independent velocities for the barotropic component of the solution, representing a modification to the initial velocity field (section 6.4), are shown in Figure 6.14. Barotropic velocities are generally within $\pm$0.5cm/s. The only observed velocities to exceed $\pm$0.9cm/s are in shallow water on the Chilean continental shelf south of Tierra del Fuego ($\sim$-1cm/s), at the eastern end of 24°S in $\sim$200dbar of water depth ($\sim$-1.2cm/s) on the Namibian shelf and at the western end of the 24°S section on the Brazilian continental shelf in $\sim$100dbar of water depth. Large velocities are observed at the northernmost station of the 30°E section in $\sim$200dbar of water depth on the Agulhas Bank yielding a large velocity ($\sim$-0.7cm/s), whilst the velocities spike in the deep ocean near the Antarctic continent ($\sim$0.7cm/s). Larger velocities in shallow water,

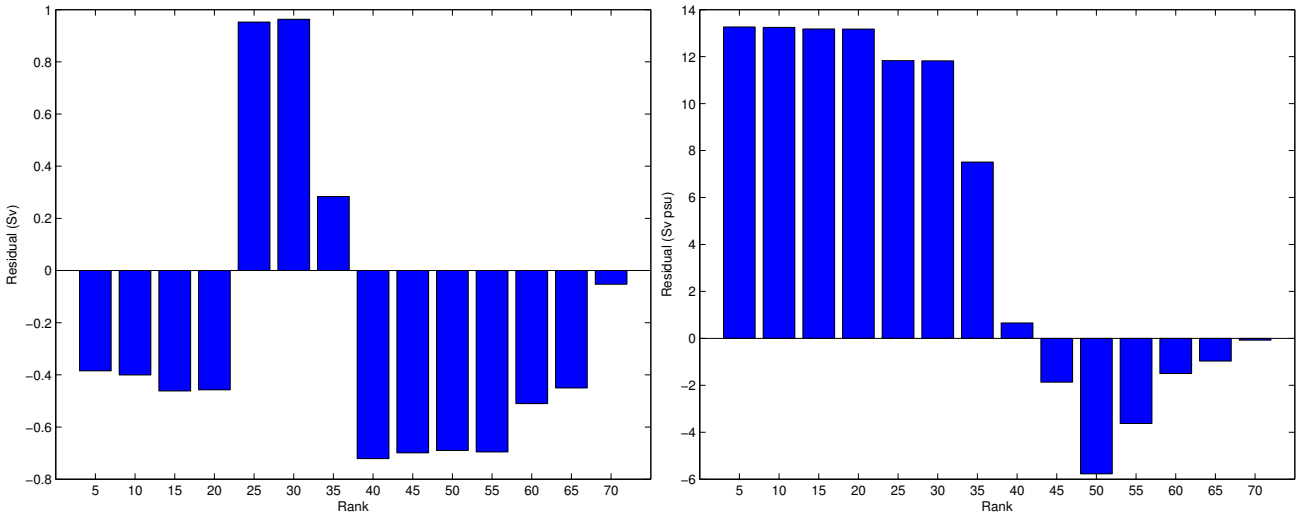

Figure 6.13: Residual of the full depth a) volume and b) salinity anomaly transport, calculated by subtracting the final solution imbalance and the initial field imbalance (equation 6.2), averaged for each 5 ranks.

close to the continental landmasses is considered a reasonable localised adjustment for each section. All adjustments off the continental shelves are within $\sim\pm 0.7$cm/s.

Final solution velocities Across Drake Passage, barotropic velocities cause a reduction in the South Atlantic box inflow (Figure 6.14). Across 30°E, outflow is decreased at the southern half of the ACC regime. Across 24°S, adjustments correspond with the specified constraints for the upper ocean Brazil Current (increasing inflow), bottom water flow through Vema Channel (increasing outflow) and for Cape Basin deep water (increasing inflow). Outside of these adjustments made to the constraints, little net adjustment is made to the reference velocity (columns 85-105).

After inversion, the difference between the initial field solution imbalance (equation 6.2) and the inverse model generated solution, calculated by multiplying the coefficient matrix and the depth-independent velocities in Figure 6.14, is compared in Figure 6.15. The residual imbalance is the difference between the initial and final solutions. Volume, salinity anomaly and potential temperature anomaly transport are well solved, with small residuals for layers across the water column.

Imbalance between the initial field and final solution full depth volume transports, following contributions by all velocity components (geostrophic, diapycnal, air-sea induced diapycnal and Ekman) yields -0.47Sv (c.f. -0.38Sv initial field geostrophic component only). For the individual layers within Figure 6.15, residual imbalances are satisfied within uncertainty for all layers with the exception of a slight excess imbalance for the

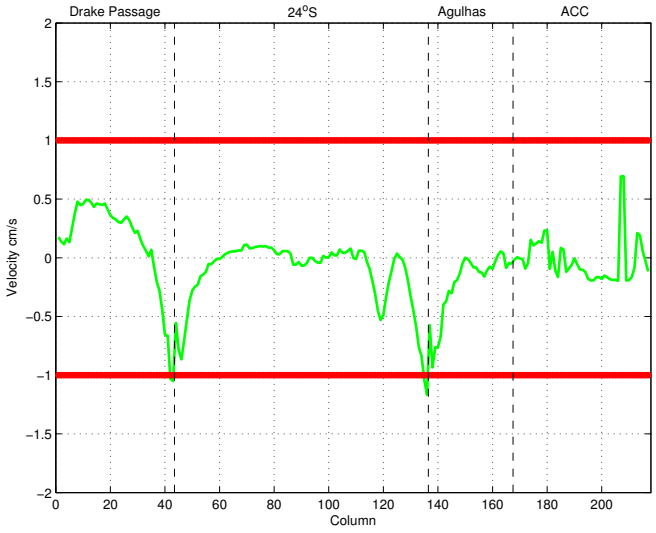

Figure 6.14: Depth-independent velocities for the barotropic component of the solution for a rank of 60 out of 73 around the box boundary. Positive (negative) velocities are box outflow (inflow). The columns represent the station pairs within the coefficient matrix **E**. The sections are combined following Drake Passage (south to north), 24°S (west to east) and 30°E (north to south), respectively.

bottom layer volume transport. This layer is present predominantly as a northward flow through Vema Channel, and a westward flow across 30°E, and is hypothesised to show a circulation pattern independent of overlying layers. The lack of co-dependency between this layer and all layers above, explain the larger residual for this layer. Larger residuals in the upper ocean for the salinity anomaly transport is explained by a greater baroclinic transport relative to the deep reference level (Ganachaud, 2003b; Jullion, 2008), and the influence of the air-sea freshwater flux.

Final geostrophic transport Geostrophic velocities of the solution after correction by the depth-independent, barotropic velocities are shown in Figure 6.16. The overall pattern of velocities shown in the initial field remains (Figure 6.7), with a strong inflow through Drake Passage and, a net negative velocity along 30°E south of the Subtropical Front. North of the Subtropical Front, positive and negative transports reflect the Agulhas Current inflow and Agulhas Return Current outflow.

Around the box boundary, the post-inversion full depth volume transport is compared to the initial field solution in Figure 6.17. Due to the large volume transports transecting Drake Passage (130-140Sv), the $<$0.5cm/s changes observed for the barotropic velocities across Drake Passage causes a reduction in the full depth volume transport of 8.3Sv (136.7Sv to 128.4Sv). Within the Agulhas regime, the large reference velocity

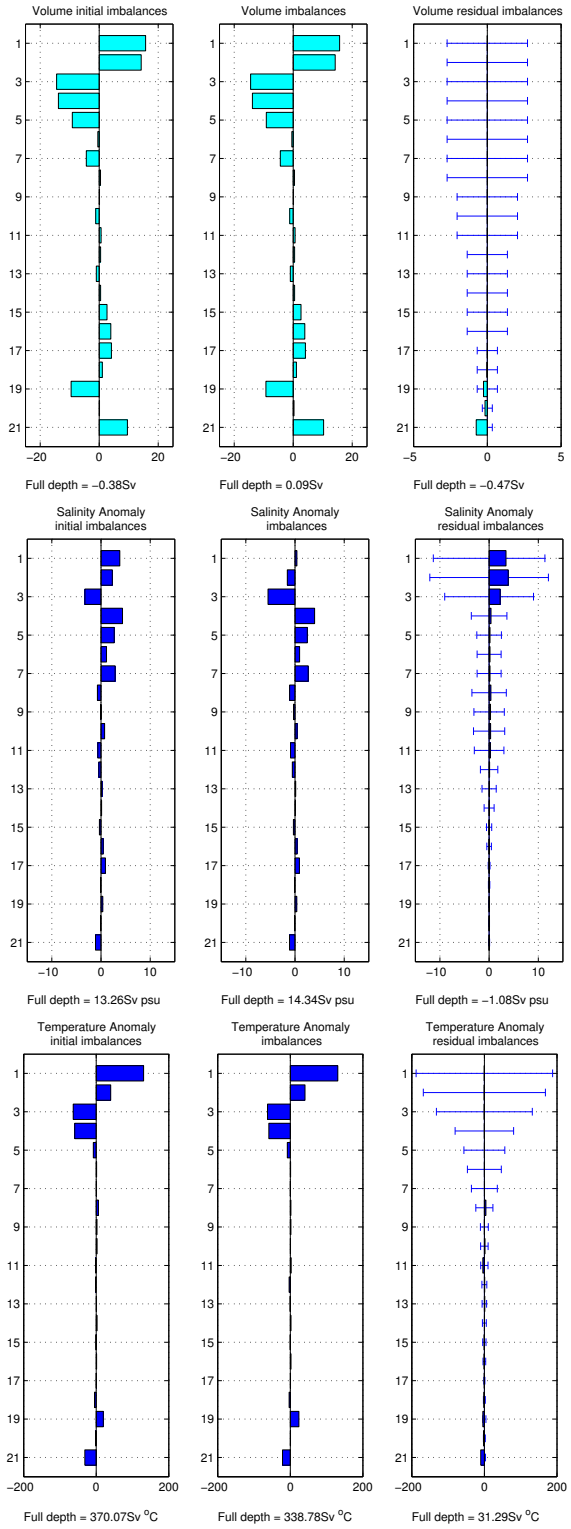

Figure 6.15: Initial field layer transports, final solution layer transports and the residual imbalance for Upper: Volume, Centre: Salinity anomaly and Lower: Potential temperature anomaly. Total layer transports or total residual imbalances are shown beneath each respective panel. Uncertainty estimates of two *aposteriori* standard deviations are shown. Positive (negative) transports represent box inflow (outflow).

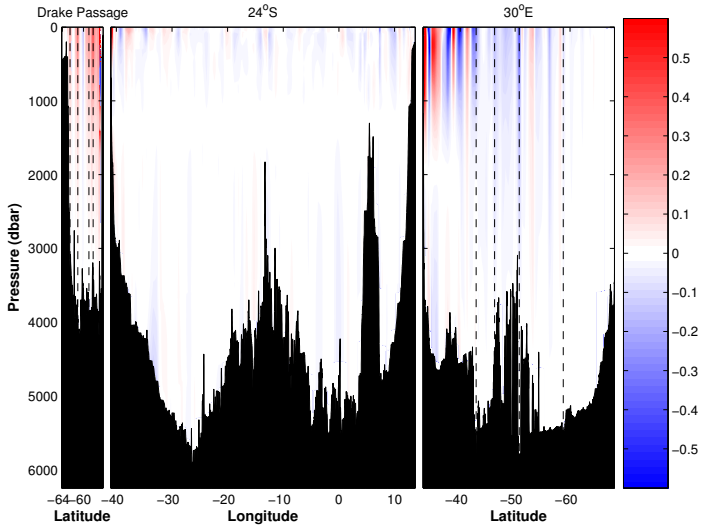

Figure 6.16: Solution geostrophic velocities (barotropic and baroclinic) around the box boundary. Into (out of) the box is shown by red (blue). The dashed lines indicate frontal positions as defined in Chapter 3. Along the Drake Passage section from south to north: SACCF, SPF, NPF and SAF, whilst along the 30°E section from north to south: STF, SAF, PF, SACCF.

along the Agulhas Bank acts to close the initial and final solution difference, giving a close correspondence between initial and final fields across 30°E with only minor variability observed south of ∼50°S.

Final solution freshwater influence Zero net salinity transport convergence is applied to the box. Excess volume transport represents the net freshwater input to, or output from, the box. The initial and final field variability south of 50°S is subject to uncertainty through the unquantified effect of sea ice and freshwater input or removal at the Antarctic continent. As observed in Figure 6.11 and suggested by previous analysis (e.g. Talley (2008)), the South Atlantic region is regarded as a region of net precipitation, therefore hypothesised to give a net freshwater divergence for the box. The solution agrees with this hypothesis, finding a net freshwater divergence of 0.30Sv, however, this may be variable on seasonal timescales.

In austral summer, sea ice formation temporarily stores freshwater within the South Atlantic, almost entirely contained within the Weddell Sea. In austral summer, sea ice contributes towards a near-surface freshening corresponding to a seasonal sea ice minimum around the Antarctic continent (Ren et al., 2011). In comparison, Weddell Sea sea ice extent reaches a maximum in austral winter and therefore, the effect of sea ice on the South Atlantic salinity budget is expected to be maximum in austral winter,

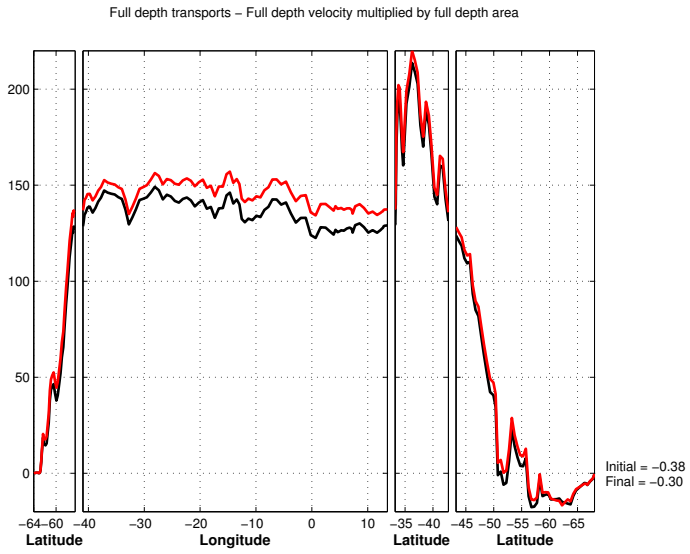

Figure 6.17: Cumulative full depth volume transport along the box boundary for the initial field (red) and the final solution (black). Positive (negative) transports represent box inflow (outflow). The total final solution volume transport is also marked.

increasing the freshwater convergence inside the South Atlantic box.

Final solution cumulative water mass transport Cumulative transport for each water mass around the box boundary indicates the net divergence/convergence for each water mass within the box (Figures 6.18 and 6.19, Table 6.6). To reiterate the water mass classifications from Chapter 2 and listed in Table 6.1, NADW is not shown as a separate water mass, and rather, is composed of lower UCDW and upper LCDW defined by $27.90 < \gamma^n < 28.10$. Lower baroclinic variability in the deep water masses gives lower *aposteriori* uncertainties with more robust divergences and convergences of deep water masses at the box boundary. The surface water mass is also impacted by the explicit inclusion of the Ekman component.

UCDW converges within the box, and is associated with upwelling by the southern limb of the Meridional Overturning Circulation, and a source water contribution to dense water formation at the Antarctic continent. LCDW divergence, which has notably increased within the final solution (Figure 6.19, Table 6.6) corresponds with greater outflow across 30°E (44.1Sv) compared to a weaker inflow (28.1Sv) through Drake Passage. Formation of dense water around the Antarctic continent contributes to AABW formation, but through diapycnal mixing also contributes to the lower layers of LCDW. The dilution of AABW properties through its northward transit towards the North Atlantic also increases LCDW, with boxwide AABW convergence primarily

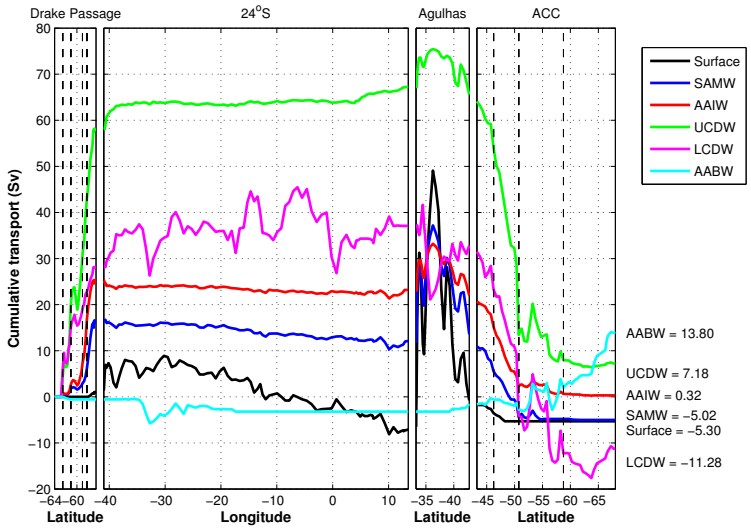

Figure 6.18: Cumulative transport along the box boundary for the final solution for each water mass, in comparison to Figure 6.9. Positive (negative) transports represent box inflow (outflow). The total cumulative transport for each water mass is shown. Vertical dashed lines indicating ACC fronts are marked.

counteracted by LCDW divergence. A complete description of LCDW is not possible without considering the westward LCDW and AABW flow across 30°E. Strong westward AABW flow south of ∼64°S is explained by the cyclonic Weddell Gyre (Naveira Garabato et al., 2002b), with the Weddell Gyre previously observed to extend eastward of 30°E (Park et al., 2001). This feature is further discussed in section 6.5.4.1. For this model, the South Atlantic box is a net importer of AABW across 30°E, particularly south of ∼64°S, with export occurring across 24°S.

The following sections will seek to examine the details of the inverse box solutions, focussing on the water masses mentioned above. At points, the NADW component ($27.90<\gamma^n<28.10$) will be displayed, in addition to UCDW ($27.50<\gamma^n<28.00$) and LCDW ($28.00<\gamma^n<28.23$), in particular for discussion of the 24°S section. The final solution is the theoretical optimal solution from the SVD analysis with uncertainties minimised, and hence represents a realistic interpretation of the mean ocean state within the South Atlantic region.

6.5.1.2 Additional constraints

A number of constraints are applied to flow features along the box boundary. The constraints are shown in Table 6.7. The final solution for Drake Passage shows a decrease in the full depth volume transport across the transect of 8.8±12.3Sv. However, the final solution is within the uncertainty estimate of the constraint and within the

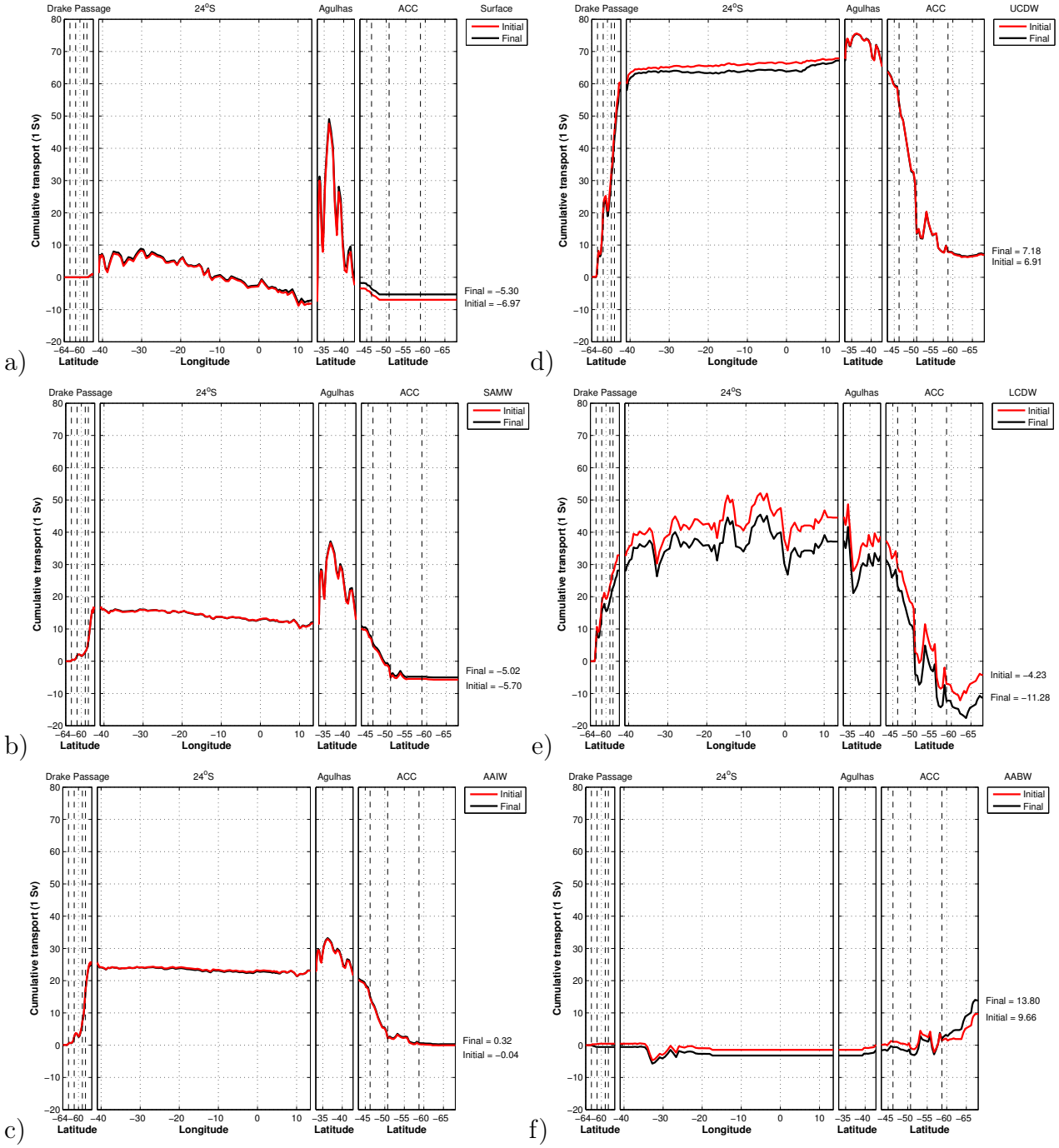

Figure 6.19: Initial (red) and final (black) cumulative transports along the box boundary for a) surface water, b) SAMW, c) AAIW, d) UCDW, e) LCDW and f) AABW (in Sv). Positive (negative) transports represent box inflow (outflow). Vertical dashed lines indicating ACC fronts are marked.

	Initial Solution (Sv)	Final Solution (Sv)
Surface	-7.0±4	-5.3±4
SAMW	-5.7±4	-5.0±4
AAIW	-0.0±3	0.3±3
UCDW	6.9±2	7.2±2
LCDW	-4.2±1	-11.3±1
AABW	9.7±0.5	13.8±0.5
Total	0.4±0.2	0.3±0.2

Table 6.6: Cumulated transports around the box boundary for both the initial and final solutions. Negative (positive) transport implies water mass divergence (convergence) for the box, and therefore water mass production (destruction). *aposteriori* uncertainties are shown.

likely observable range of volume transport through Drake Passage (King & Jullion, in prep., Meredith et al. (2011b) (their Figure 11), Renault et al. (2011)) therefore the solution is accepted.

At 24°S, the first constraint applies only a small adjustment to the current meter derived Vema/Hunter Channel bottom water flow from Hogg et al. (1999). This is consistent with a small amount of water mass exchange between the BW and the deep water above, between Vema Channel and 24°S. The second constraint is for the poorly resolved Brazil Current, as described in Bryden et al. (2011). Historical estimates of the Brazil Current volume transport along 23-24°S, range from 4.1Sv (Evans et al., 1983; Zemba, 1991) to 12.3Sv (Bryden et al., 2011) with the final solution of 5.8±0.1Sv falling within the historical range. Walvis Ridge gives the third constraint by acting as a sill to limit BW exchange between the northern Cape Basin and the eastern South Atlantic basin, initialised as 0±1Sv. The final solution shows insignificant adjustment, 0.2±0.1Sv southward, and is similar to the estimate of 0.1±0.5Sv of AABW southward flow from McDonagh and King (2005).

The full depth salinity transport solution at 24°S, closely matches the Bering Strait throughflow (Coachman and Aagaard, 1988; Woodgate and Aagaard, 2005) and follows the methodology of Holfort and Siedler (2001) for the quasi-zonal A10 WOCE section across at 30°S, who found a solution of 26.75±0.77Sv psu southward.

The contribution of westward volume transport, associated with Agulhas ring shedding (McDonagh et al., 1999; Dencausse et al., 2010a), to the South Atlantic is constrained using McDonagh et al. (1999). The final solution matches the constraint within uncertainties.

	Property	Vertical extent	Constraint	Solution
Drake Passage	Volume	Full depth	136.7±10Sv	128.4±8.3Sv
24°S: Vema/Hunter Channel	Volume	$\theta < 2$°C	-6.9±2Sv	-6.7±1.9Sv
24°S: Brazil Current	Volume	Above 300dbar	4.9±5Sv	5.8±0.1Sv
24°S: Cape Basin	Volume	$\theta < 2$°C	0±1Sv	0.2±0.1Sv
24°S	Salinity	Full depth	26±0.2Sv psu	25.8±0.2Sv psu
30°E: Agulhas regime	Volume	$\theta > 3.5$°C	9±3Sv	10.7±1.3Sv

Table 6.7: Details of the additional constraints applied to the model. Stated errors are the residual noise terms from the conservation equations. Positive (negative) transports are into (out of) the box.

6.5.2 Geostrophic velocity results by transect

6.5.2.1 Drake Passage

Volume transport Through Drake Passage (Figure (6.20)), UCDW dominates volume transport constituting almost half of the total volume transport (58.1 out of 128.4Sv). This compares well with the estimated UCDW volume transport observed in Cunningham et al. (2003) of 62.3Sv relative to the deepest common level. The contribution of the surface and AABW flows is negligible across the section (Figure 6.20, Table 6.8). The surface water mass is only observed north of the SAF with little associated transport, whilst AABW is prevented from reaching Drake Passage from the Weddell Gyre by the blocking effect of the Shackleton Fracture Zone (Cunningham et al., 2003) with only negligible westward transport observed.

Net inflow and outflow of each water mass (Table 6.1) is shown in Figure 6.21. Eastward flow dominates at all depths, apart from a net 0.6±0.5Sv westward flow for the AABW. The surface water mass is largely absent with the majority of the transport occurring between the densest SAMW γ^n layer (layer 8), and the densest LCDW layer (layer 19).

Each ACC front (SACCF, PF, SAF) that runs through Drake Passage acts as a pathway or 'jet' of enhanced volume transport with all fronts marked in Figure 6.20, and with fluctuations in the volume transport associated with each water mass (Table 6.8). The SACCF carries almost exclusively deep water masses with the flow equally split between UCDW and LCDW. The Polar Front is split into Northern and Southern limbs, with only a shallow cap of lighter water above the deep water masses at the Southern limb. LCDW dominance at the SPF switches to UCDW dominance at the NPF, with the NPF associated with only a small LCDW transport. The SAF predominantly carries SAMW, AAIW and UCDW.

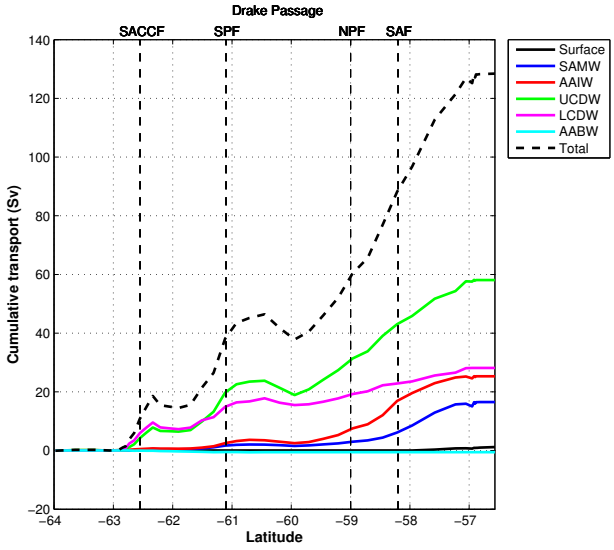

Figure 6.20: Cumulative volume transport across Drake Passage for each water mass (coloured lines), and the total volume transport (thick, dashed line). Positive (negative) transports represent box inflow (outflow). Thin, dashed vertical lines indicate ACC fronts.

Transport-weighted properties At Drake Passage, property fluctuations have been observed for the upper 100dbar (Sprintall, 2008) and other upper ocean water masses (SAMW, AAIW) (Naveira Garabato et al., 2009), however, no property trend has been observed in deep waters (Williams et al., 2006). Transport-weighted properties are therefore representative of the 2008/09 ocean, and not necessarily representative of the longer-term flow patterns.

Transport-weighted properties are calculated at Drake Passage for θ, salinity S, DIC and its natural component, and C^{ant} by dividing the property transport by the volume transport. Transport-weighted values are most meaningful for unidirectional flow, therefore only the eastward component of the flow is considered. The advantage of transport-weighted values over the statistical mean is that the property is weighted most heavily at the location of the transport maximum, and hence transport-weighted values are directly influenced by changes to the transport profile (Tillinger and Gordon, 2010). Transport-weighted properties follow typical profiles of TWθ and TWC^{ant} reaching a maxima for upper ocean waters, whilst TWS, TWDIC and TWC^{nat} are a relative minima. The differences between TWDIC and TWC^{nat} are more marked in the deep ocean, and caused by natural and biological variability rather than an entirely anthropogenic signal.

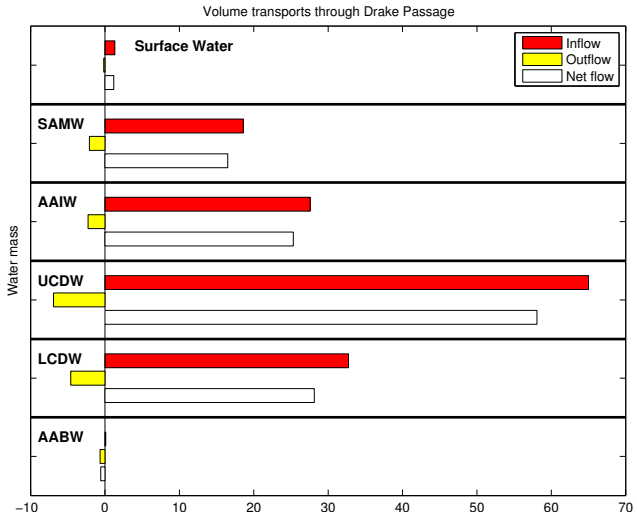

Figure 6.21: Volume transports in Sv for each inverse box water mass through Drake Passage. Inflow into the South Atlantic box is positive. Water mass boundaries are marked, and water masses labelled.

Water mass	Volume transport (Sv)	TWθ	TWS	TWDIC	TWC$^{\mathrm{nat}}$	TWC$^{\mathrm{ant}}$
Surface	1.2±4	7.23±0.07	33.975±0.020	2091.7±2.3	2059.0±0.7	26.9±0.6
SAMW	16.5±4	4.89±0.07	34.093±0.007	2134.9±1.3	2083.3±0.7	30.7±0.2
AAIW	25.3±3	3.08±0.06	34.131±0.006	2170.3±0.9	2107.7±0.6	26.8±0.3
UCDW	58.1±2	2.26±0.01	34.496±0.004	2242.7±0.6	2146.5±0.3	11.4±0.1
LCDW	28.1±1	1.36±0.01	34.719±0.001	2263.3±0.1	2177.2±0.2	4.8±0.1
AABW	-0.6±0.5	0.36±0.01	34.704±0.001	2263.5±0.1	2199.9±0.1	7.2±0.3
Total	128.4±10	2.55±0.01	34.423±0.003	2218.7±0.6	2137.4±0.5	15.4±0.1

Table 6.8: Total transport across Drake Passage for each water mass with *aposteriori* uncertainties. Transport-weighted (TW) mean values for potential temperature (θ), salinity S, DIC, C^{nat} and C^{ant} with standard error of the mean. For northward (southward) TW properties, all southward (northward) velocities are set to zero. TWθ and TWS have units of °C and psu, respectively whilst all other TW properties have units of $\mu\mathrm{mol\,kg}^{-1}$.

Water mass	Volume transport (Sv)
Surface	-8.2±4
SAMW	-4.4±4
AAIW	-2.1±3
UCDW	9.1±2
LCDW	9.0±1
AABW	-2.6±0.5
Total	0.7±0.3

Table 6.9: Total transport across 24°S for each water mass with *aposteriori* uncertainties. Positive (negative) values are into (out of) the box.

6.5.2.2 24°S

Atlantic Meridional Overturning Circulation is an area of ongoing research across the North Atlantic (for example, through the RAPID Climate Change programme). In the South Atlantic, the magnitude of the overturning has been estimated in a number of studies (e.g. Holfort and Siedler (2001); McDonagh and King (2005); Bryden et al. (2011)) using quasi-zonal hydrographic sections. The overturning circulation is characterised by southward-flowing deep water (North Atlantic Deep Water: NADW), and northward-flowing upper water masses. Upper water masses comprise, at least partly, of formerly deep waters which have upwelled south of the ACC, outcropped to the surface and been transported northwards, in order to compensate for southward flowing NADW. The magnitude, variability and predictability of this overturning are areas of current research (Cunningham et al., 2007; Drijfhout et al., 2011; Johns et al., 2011). Whereas the net mass transport across the 24°S section is expected to be small (∼1Sv), the 'overturning' is measured as the strength of the deep water flow. Across 24°S, Bryden et al. (2011) estimated a 21.5Sv overturning in 2009, compared with 16.5Sv in 1983.

Upper Ocean Circulation Focusing on the upper ocean across 24°S (Figure 6.22), starting from the western end, the Brazil Current transports surface water southward. Southward transport persists from the western boundary until ∼30°W. East of 30°W, the surface water mass shows a steady accumulation of northward flow of 14.9±4Sv. SAMW and AAIW both display a small northward transport, west of ∼38°W, corresponding to the Intermediate Western Boundary Current (IWBC), schematically represented in Schmid and Garzoli (2009). This northward transport plateaus between ∼38°W and ∼20°W with a net northward accumulation east of ∼20°W. Sectionwide transports for SAMW and AAIW are 4.4±4Sv and 2.2±3Sv northward (Table 6.9).

Water masses	Neutral density range (γ^n)	Volume transports from Sloyan and Rintoul (2001a) (Sv)	This study (Sv)
Surface/Thermocline (Layer 2-3)	24.0-26.0	3.3	1.3
SAMW (Layer 4-6)	26.0-27.0	6.3	9.7
AAIW(Layer 7-10)	27.0-27.4	4.5	3.9

Table 6.10: Volume transports across 24°S using neutral density definitions for water masses from Sloyan and Rintoul (2001b), inclusive of Ekman transport. The corresponding layer from this study and the neutral density range are shown (Table 6.1). Volume transports for each water mass from this study and Sloyan and Rintoul (2001a) (calculated from their Figure 6) are shown.

The pathway of upper ocean water through the South Atlantic has been subject to much debate (see section 6.6.4). Donners and Drijfhout (2004) reviewed the South Atlantic upper ocean circulation from existing inverse models. In Sloyan and Rintoul (2001a), a hydrographic section (SAVE2) running zonally between Brazil and Africa, and meridionally between 12-37°S acts to close the South Atlantic sector. For comparison to this study, neutral density layer boundaries are selected to match Sloyan and Rintoul (2001b)'s water mass definitions (Table 6.10). Smaller northward surface flow in this study is explained by the $\gamma^n = 24.0 - 26.0$ water mass substantially comprised of high temperature surface waters of the western South Atlantic basin, and as observed in Figure 6.22, this region shows southward surface flow. The combined northward transport within the surface/SAMW is 11.0Sv in this study, compared to 9.6Sv (Sloyan and Rintoul, 2001a). A slightly lower AAIW northward transport supports the broad agreement between the northward flow estimates in this study, and Sloyan and Rintoul (2001a).

Deep Ocean Circulation Focusing on deep water masses, UCDW and LCDW both show substantial southward-flowing volume transports, primarily representing southward NADW flow. UCDW steadily accumulates eastwards across the section, whilst LCDW flow varies substantially. East of the Mid-Atlantic Ridge (∼7°W), LCDW transports 11.7Sv northward between the Mid-Atlantic Ridge and Walvis Ridge (6°E). Northward flow on the eastern flank of the Mid-Atlantic Ridge is evidence for the closure of a deep water cyclonic flow within the Angola Basin (Warren and Speer, 1991; Stramma and England, 1999; Arhan et al., 2003; Hogg and Thurnherr, 2005). The southward extent of this deep water feature is unknown, yet schematically estimated by Arhan et al. (2003) to occupy the entire Angola Basin.

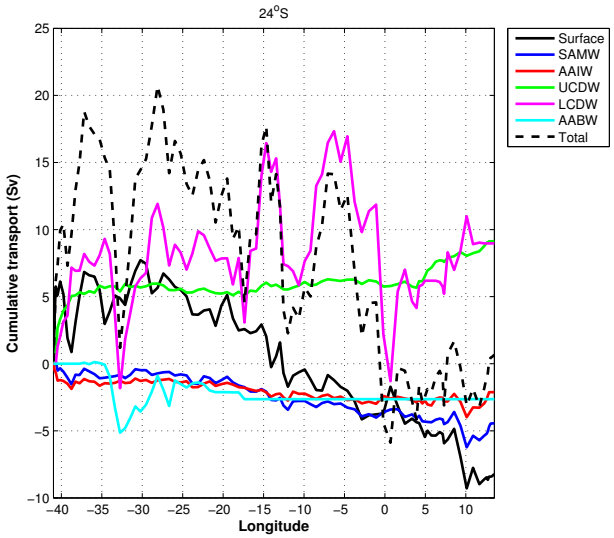

Figure 6.22: Cumulative volume transport across 24°S for each water mass, and the total volume transport constrained to Bering Strait salinity transport. Positive (negative) transports represent box inflow (outflow).

Deep water flow across 24°S is dominated by southward NADW flow defined by $27.9 < \gamma^n < 28.1$ (Meinen et al., 2012). NADW gives a net southward transport of 15.3Sv whilst capturing a portion of the same signature of zonal variability observed for LCDW (Figure 6.23), in comparison to the uniform UCDW transport. Zonal variability is partially related to interaction with topography, deep water gyre circulations (Arhan et al., 2003) and the possible existence of a zonal NADW pathway (Hogg and Thurnherr, 2005; van Sebille et al., 2012).

In the western basin, the Deep Western Boundary Current (DWBC) displays a clear signature of strong southward NADW flow (∼10Sv) west of 37°W along the South American continental shelf (Stramma and England, 1999; Garzoli and Matano, 2011). An overall southward transport trend is observed, west of the Mid-Atlantic Ridge (13°W).

Deep water gyre circulation within the Angola Basin, along the eastern flank of the Mid-Atlantic Ridge is also observed in Figure 6.23 showing two cyclonic gyre features within the eastern basin, from 13°W to 7°W and 2°W to 10°E. Each feature appears cyclonic, and is superimposed on the general trend of southward NADW flow across the basin. This could be linked to van Sebille et al. (2012)'s hypothesis, following from Arhan et al. (2003) and Hogg and Thurnherr (2005), for a zonal and possibly intermittent pathway for NADW, transporting 4Sv from the Deep Western Boundary Current to the Cape Basin.

Net northward AABW flow is confined to the western South Atlantic basin. AABW

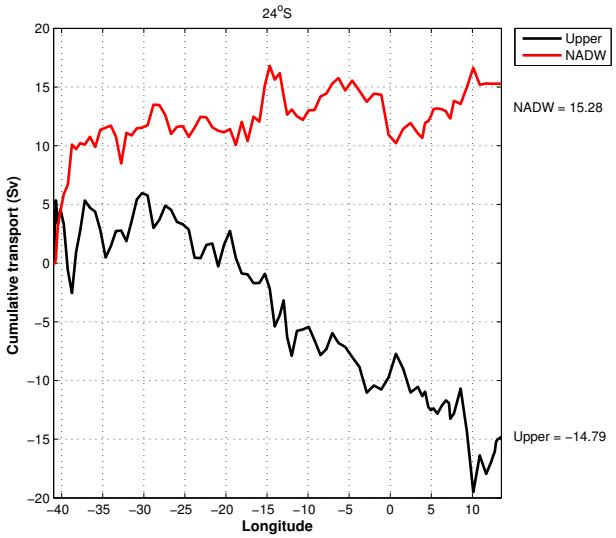

Figure 6.23: Cumulative NADW and 'Upper' ocean (Surface, SAMW, AAIW) transport across 24°S. Positive (negative) transports represent box inflow (outflow).

peaks at ∼5Sv prior to an apparent cyclonic feature between 33°W and 28°W, resulting in a net transport of 2.6Sv northward. Previous occurrences of AABW recirculation have been observed in the vicinity of Santos Plateau, west of Vema Channel (Hogg et al., 1999). It should be noted that the Vema/Hunter Channel BW constraint uses a more inclusive 2°C isotherm to define bottom water, rather than the γ^n>28.27 neutral density level, and therefore, a portion of the northward flowing Vema Channel bottom water contributes to LCDW northward flow. Constraining the BW northward flow below the 2°C isotherm to 6.9Sv northward follows in-situ BW measurements at Vema Channel (∼31°S) and Hunter Channel (∼34°S) by Hogg et al. (1999). Therefore, BW volume transport (defined by the 2°C isotherm) is assumed not to change significantly between ∼31-34°S and 24°S by diapycnal mixing into overlying waters. Walvis Ridge closes BW transport into and out of the Cape Basin to the north and west across 24°S. Bottom water circulation across 24°S within the Cape Basin is assumed to cancel through a cyclonic BW flow, hence Cape Basin shows no significant deep water flow. The cumulative transport across the section for each water mass is shown in Table 6.9, with a full depth transport of 0.7±0.3Sv southward.

Meridional and Overturning Circulation The meridional circulation across 24°S from the inverse solution corresponds well with the transport per unit depth profiles from Bryden et al. (2011) (their Figures 3 and 4). Separating the circulation into 21 γ^n layers yields 0.8±4Sv of southward flowing surface water (layers 1-2), as a re-

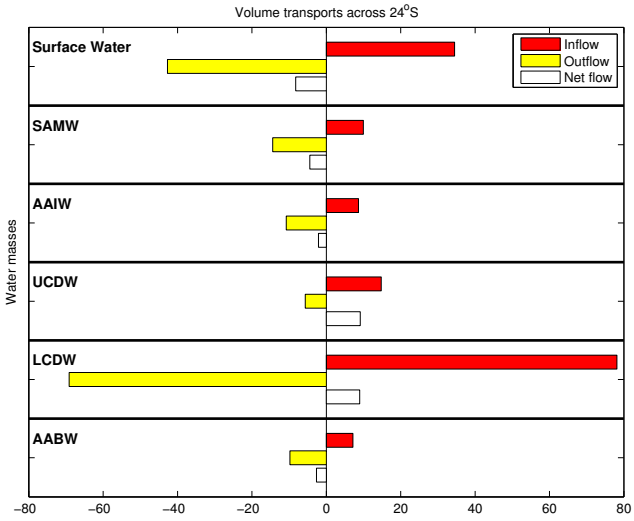

Figure 6.24: Volume transports for each inverse box model layer across 24°S. Inflow into the South Atlantic box is positive. Water mass boundaries are marked, and water masses labelled.

sult of the Ekman component of the solution, 15.8±3Sv northward upper ocean flow (layer 3-12), 20.2±2Sv southward deep water flow (layers 13-18) and 4.6±1Sv northward flow of lower LCDW/AABW (layers 19-21). The residual imbalance volume transport is 0.7±0.3Sv southward across 24°S. The strength of the meridional overturning circulation is estimated as the southward flow of 20.2Sv of deep water (primarily NADW). Previously, Bryden et al. (2011) calculated 21.5Sv and 16.5Sv from hydrographic occupations across 24°S, whilst estimates from elsewhere in the South Atlantic include across A10 (30°S) of 20±2Sv (McDonagh and King, 2005), 22.7Sv (Holfort and Siedler, 2001) and 23±3Sv (Ganachaud, 1999), an average of 17.9Sv from 17 hydrographic occupations across 35°S (Dong et al., 2009) and across A11 (nominally 45°S) of 21±2Sv (McDonagh and King, 2005), 21.7Sv (Holfort and Siedler, 2001) and 18±4Sv (Ganachaud, 1999). Mooring-derived North Atlantic overturning at 26°N estimate 18.7Sv at 1041m Cunningham et al. (2007) with more recent estimates of 18.5±4.9Sv (http://www.noc.soton.ac.uk/rapidmoc/).

The overturning is directly affected by the initial field constraints. The Brazil Current and Ekman transport constraints both add additional southward flow into the upper ocean, reducing the net northward flow within the surface ocean. The Vema/Hunter Channel bottom water constraint and Cape Basin constraint, increase northward flow of deep water across 24°S, thereby reducing the net southward flow, and hence reducing overturning. The overturning estimate therefore depends on the reliability of these constraints.

Source	Section	Freshwater (Sv)	Heat (PW)	Salt (Gg s^{-1} or Sv psu)
Rintoul (1991)	32°S	-	0.25PW	-
Lumpkin and Speer (2007)	32°S	-	0.60±0.08	-
Ganachaud (1999)	30°S	-	0.35±0.15	-
Holfort and Siedler (2001)	30°S	-0.51±0.02	0.29±0.05	-26.75±0.77
Ganachaud and Wunsch (2003)	30°S	-0.5±0.1	-	-26.7
McDonagh and King (2005)	30°S	-0.5±0.1	0.22±0.08	-26
Bryden et al. (2011)	24°S	-0.34/-0.29	0.7	-26
This Study	24°S	-0.7±0.3	0.40±0.08	-25.8±0.2

Table 6.11: Meridional property transport from inverse studies and empirical analysis across 24°S and 30S (WOCE A10), adapted from McDonagh and King (2005) and Williams (2007). A northward net flux is positive. Freshwater transport values follow McDonagh and King (2005). For heat transport, the meridional mass transport is set to zero.

A comparison of the meridional circulation with previous studies is shown in Table 6.11 (McDonagh and King, 2005). Sections across 24°S, 30°S and 32°S are included for comparison. As salinity is assumed to be conserved between Bering Strait and 24°S, the resulting mass transport is equivalent to a freshwater transport. The difference between 0.8Sv Bering Strait volume transport (Coachman and Aagaard, 1988; Woodgate and Aagaard, 2005) and 0.7Sv volume transport in this study across 24°S provides an indirect estimate of 0.1Sv of evaporation within the North Atlantic. Net evaporation is also supported by the previous studies (Table 6.11).

In summary, net water mass volume transports across 24°S (Figure 6.24) reveal that the largest inflow/outflows are within the surface water and LCDW. Net surface flow is northward, despite Ekman and Brazil Current transport constraints. SAMW and AAIW inflows/outflows are limited to ±15Sv, whilst UCDW and LCDW display a similar net flow, contributing to the southern limb of the MOC. AABW transport is small, and partially represents northward BW flow through Vema and Hunter Channel.

Heat, salinity and freshwater transport Previous estimates of heat transport across 24°S range from a 0.23PW southward flow (de las Heras and Schlitzer, 1999) to ∼1PW northward flow (Saunders and King, 1995). Table 6.11 shows previous estimates generated by inverse models, with the exception of Bryden et al. (2011) included for comparison. Piecuch and Ponte (2012) compare hydrographic estimates of meridional heat transport within the Atlantic Ocean with their mean state ocean estimates (ECCO) chosen as evolved and optimised solutions of the Massachusetts Institute of Technology

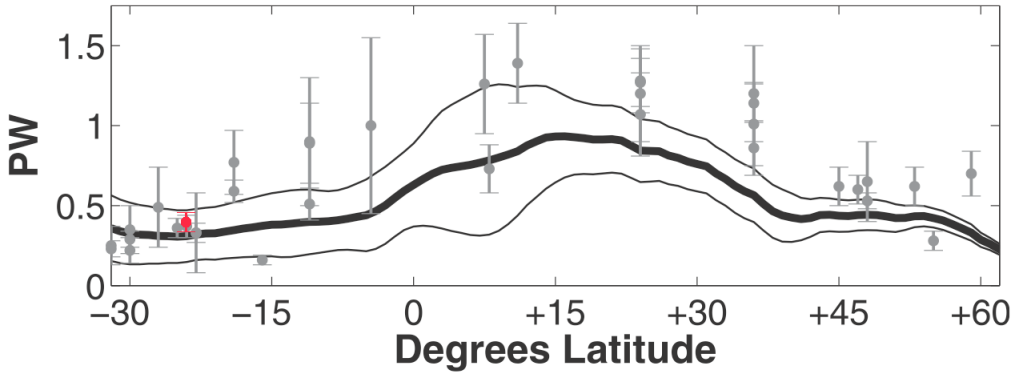

Figure 6.25: Meridional heat transport from Piecuch and Ponte (2012). The black solid thick line represents their average time-mean ECCO estimate, black solid thin lines represent the uncertainty interval as a standard deviation of the heat transport time series with the hydrographic estimates marked with the additional error bars (grey). The heat transport determined in this study is marked in red. See Piecuch and Ponte (2012) for the hydrographic estimates used.

general circulation model (MITgcm). Their estimates are shown in Figure 6.25 along with the estimate from this study (marked with a red point), calculated by adjusting the inverse model solution for zero net meridional mass transport. The estimate of 0.40±0.08PW in this study is within the band of anticipated heat transport across 24°S.

Equatorward flow is counter-intuitive for a equator-to-pole schematic of global heat transport and corresponds to southward flow of cold NADW into the South Atlantic Ocean at depth, and northward return flow of warmer upper ocean water masses. The analysis by Dong et al. (2009) shows close correlation between meridional overturning and heat transport, such that a 1Sv increase in the MOC yields a 0.05±0.01PW increase in northward heat transport. Barreiro et al. (2008) also obtained a 70% correlation between heat transport across 30°S and MOC intensity (Garzoli and Matano, 2011). The heat transport estimate of 0.40±0.08PW is within error bounds of the estimate of Holfort and Siedler (2001), which likewise apply a Bering Strait salinity transport constraint across a zonal section.

Total heat transport is separated into 'overturning' and 'gyre' components following the methods of Bryden and Imawaki (2001) and Bryden et al. (2011) (Table 6.12). The overturning component is sensitive to the initial field constraints (Table 6.4), particularly for the Ekman transport and Brazil Current, and the inverse model. The model increases the southward Brazil Current (west of 35°W) opposing the northward surface flow, decreases the northward bottom water (<2°C) flow, and limits the BW flow within

the Cape Basin. Overturning is strongly affected by the surface water, and the negative barotropic velocities applied to the western edge of the basin (Figure 6.14) help to increase the southward flow of the high temperature (>27°C) surface water. The gyre component of -0.12PW is within the estimates range from Bryden et al. (2011) with a slight decrease in the transport of the warm water northward, compared to Bryden et al. (2011)'s 2009 estimate.

For salinity transport, the overturning component of the circulation is similarly calculated, for comparison to Bryden et al. (2011) using the M_{ov} salt transport, in addition to the azonal component M_{az}. M_{ov} and M_{az} is calculated following Bryden and Imawaki (2001), Dijkstra (2007), Huisman et al. (2010) and Bryden et al. (2011)'s definition:

$$M_{ov} = -{}^{1}/_{\overline{\langle S \rangle}} \int \langle v \rangle \left(\langle S \rangle - \overline{\langle S \rangle} \right) L(z) dz \tag{6.38}$$

$$M_{az} = -{}^{1}/_{\overline{\langle S \rangle}} \int \int \left(v - \langle v \rangle - \overline{\langle v \rangle} \right) \left(S - \langle S \rangle - \overline{\langle S \rangle} \right) dx dz \tag{6.39}$$

where v is the northward velocity, S is salinity, L is zonal section width, z is depth, triangular brackets indicate zonal average and an overline represents vertical average. M_{ov} and M_{az} transports are effectively the freshwater transports associated with the overturning and gyre circulation components respectively. M_{ov} has been calculated in a number of studies (Dijkstra, 2007; Drijfhout et al., 2011; Huisman et al., 2010; Bryden et al., 2011) as an indicator of MOC circulation and stability. M_{ov} estimates (Table 6.12b) are similar to Bryden et al. (2011), in obtaining a net southward freshwater transport, supportive of freshwater input north of 24°S and acting to inhibit the MOC (Rahmstorf, 1996), whilst M_{az} supports a net northward freshwater transport associated with the horizontal or 'gyre' component (Bryden et al. (2011), their Table 2). Negative M_{ov} supports the theory for multiple equilibrium states for the MOC (Drijfhout et al., 2011; Cimatoribus et al., 2012), and Bryden et al. (2011) and Garzoli et al. (2013)'s observations. It should be noted however, that M_{ov}, similar to all the overturning calculations, is sensitive to the choice of Ekman transport and Brazil Current transport chosen in the initial field. Larger Ekman or Brazil Current transport constitutes a larger proportion of warm, salty surface water flowing southward opposing the net flow of the overturning circulation, and affecting the M_{ov} profile (Figure 6.26a). Therefore at this latitude, Ekman transport variability and interannual variability of the Brazil Current could see a temporary reversal of the M_{ov} sign.

The subtropical gyre drives the M_{az} component with southward (northward) flow

a)

	Overturning (PW)	Gyre (PW)	Total (PW)
This study	0.52	-0.12	0.40
Bryden et al. (2011) 2009 section	0.76	-0.07	0.68
Bryden et al. (2011) 1983 section	0.53	-0.14	0.38

b)

	Overturning (Sv psu)	M_{ov} (Sv)	M_{az} (Sv)
This study	3.3	-0.09	0.16
Bryden et al. (2011) 2009 section	4.6	-0.13	0.12
Bryden et al. (2011) 1983 section	3.3	-0.09	0.21

Table 6.12: a) Net heat flux across 24°S separated into overturning and gyre components. b) Overturning component of the salinity transport and associated M_{ov} and M_{az} transports. Positive (negative) transport is northwards (southwards).

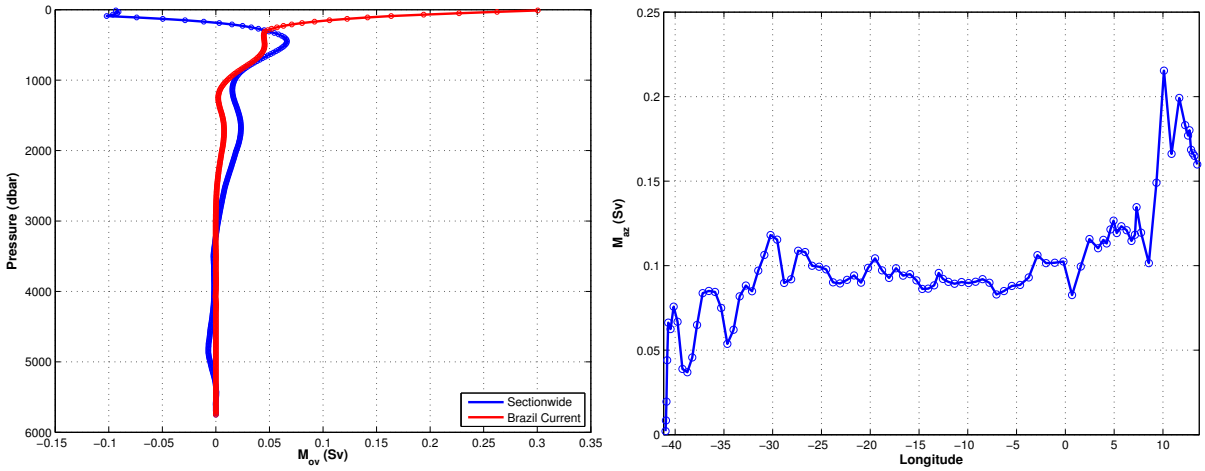

Figure 6.26: a) Cumulative M_{ov} as a function of pressure for the sectionwide M_{ov} (blue), and for west of 35°W, inclusive of the Brazil Current (red). Positive (negative) M_{ov} is northward (southward). b) Cumulative M_{az} as a function of latitude. Positive (negative) M_{az} is northward (southward).

in the western (eastern) side of the basin. Positive M_{az} in this study and Bryden et al. (2011), corresponds with the gyre transporting freshwater out of the South Atlantic box, and driven by the flow near the boundaries (Figure 6.26b). The importance of M_{az} is investigated by Cimatoribus et al. (2012), who suggest that an increase in the zonal salinity constrast across the South Atlantic increases M_{az}, and this is compensated by a decrease in M_{ov}. Changes in M_{az} could therefore dictate potential MOC shutdown.

Higher southward TWθ in Table 6.13 (fourth column), in comparison to northward TWθ corresponds to southward flow of the warmest surface waters along the section as part of the Brazil Current. Deeper water masses display a negligible difference between northward and southward TWθ. For full-depth transports, warmer temperature for the northward TWθ corresponds to northward return flow of the warmer, upper

Water mass	Northward transport (Sv)	Southward transport (Sv)	Northward TWθ	Southward TWθ	Northward TWS	Southward TWS
Surface	42.7±4	34.5±4	17.68±0.14	18.84±0.16	35.756±0.020	35.936±0.022
SAMW	14.4±4	10.0±4	8.66±0.06	8.64±0.07	34.670±0.007	34.674±0.007
AAIW	10.8±3	8.7±3	4.92±0.02	4.92±0.03	34.398±0.006	34.407±0.001
UCDW	5.7±2	14.8±2	3.37±0.06	3.40±0.01	34.694±0.004	34.762±0.003
LCDW	69.2±1	78.1±1	2.10±0.01	2.21±0.01	34.870±0.001	34.880±0.001
AABW	9.8±0.5	7.1±0.5	0.42±0.01	0.41±0.01	34.719±0.001	34.719±0.001
Total	153.1±0.3	152.5±0.3	7.01±0.05	6.42±0.05	35.033±0.003	35.047±0.003

Table 6.13: Northward and southward volume transport across 24°S for each water mass with uncertainties in Sv (Figure 6.24). Positive (negative) values are into (out of) the box. Transport-weighted (TW) mean θ and S for each water mass with standard error of the mean. For northward (southward) TWθ and S, all southward (northward) velocities are set to zero. TWθ has units of °C, and TWS is recorded in psu.

ocean. Transport-weighted salinities suggest higher salinity surface waters within the southward flowing Brazil Current surface waters, and relatively higher salinities within the southward flowing deep water, caused by the NADW salinity maxima.

Salinity, DIC, C^{nat} and C^{ant} Holfort et al. (1998) estimated a net southward DIC and natural/preindustrial DIC transport of 1.99±0.2Mmol s^{-1} and 2.26Mmol s^{-1} at 30°S. This compares to 2.31±0.2Mmol s^{-1} and 2.44±0.2Mmol s^{-1} in this study, with both studies including the net Bering Strait salinity transport (Lundberg and Haugan, 1996; Stoll et al., 1996; Holfort et al., 1998; Holfort and Siedler, 2001). Upon comparison with 1.63Mmol s^{-1} of Bering Strait northward flow (into Arctic) (Lundberg and Haugan, 1996), preindustrial North Atlantic divergence is higher in this study than Holfort et al. (1998). Divergence in the preindustrial North Atlantic basin is likely compensated by a combination of ocean inflow, air-sea transfer and riverine input.

Holfort et al. (1998) calculate a southward overturning DIC estimate of 34Mmol s^{-1} based on NADW southward flow (their Figure 4 for potential density interfaces of $36.82 < \sigma_2 < 37.04$). In this study, DIC and natural DIC southward overturning is 34.68Mmol s^{-1} and 33.72Mmol s^{-1} respectively, and hence supports 0.96Mmol s^{-1} greater southward DIC transport in 2008/09, compared to preindustrial times, and 0.28Mmol s^{-1} greater compared to Holfort et al. (1998). Hence, these results support the increase in DIC transport since the preindustrial period, in excess of depletion through air-sea interaction and biological processes.

This study finds total northward C^{ant} transport of 0.70Mmol s^{-1} (0.27 PgC yr^{-1}),

Water mass	Northward TWDIC	Southward TWDIC	Northward TWC^{nat}	Southward TWC^{nat}	Northward TWC^{ant}	Southward TWC^{ant}
Surface	2104.5±0.7	2102.8±1.1	2030.7±0.5	2028.4±0.5	59.3±0.3	57.1±0.4
SAMW	2167.7±0.6	2172.7±0.8	2070.0±0.4	2070.5±0.4	46.1±0.4	45.7±0.4
AAIW	2201.1±0.4	2204.8±0.5	2100.4±0.3	2100.9±0.3	21.7±0.3	21.2±0.3
UCDW	2204.3±0.3	2200.5±0.2	2123.7±0.1	2123.0±0.1	8.9±0.1	8.9±0.1
LCDW	2205.6±0.2	2202.3±0.2	2143.7±0.2	2140.7±0.2	4.0±0.1	4.7±0.1
AABW	2250.1±0.4	2249.1±0.4	2190.3±0.3	2189.8±0.3	6.3±0.1	4.8±0.1
Total	2177.6±0.3	2180.9±0.4	2105.4±0.4	2109.8±0.4	24.1±0.2	19.9±0.2

Table 6.14: Transport-weighted (TW) mean DIC, C^{nat} and C^{ant} for each water mass across 24°S with standard error of the mean. For northward (southward) TW properties, all southward (northward) velocities are set to zero. All TW properties have units of μmol kg^{-1}.

governed by northward transport of high C^{ant} surface water, and southward transport of C^{ant}-poor deep water with a C^{ant} overturning of 0.18Mmol s^{-1}. Northward C^{ant} transport is greater, compared to estimates of 0.43Mmol s^{-1} (0.16 PgC yr^{-1}) at 20°S by Holfort et al. (1998), 0.36Mmol s^{-1} (0.14 PgC yr^{-1}) and 0.46Mmol s^{-1} (0.18 PgC yr^{-1}) at 18°S and 31°S (Mikaloff Fletcher et al., 2006), when scaled to 1995, and 0.57Mmol s^{-1} (0.22 PgC yr^{-1}) and 0.26Mmol s^{-1} (0.10 PgC yr^{-1}) at 10°S and 30°S (Macdonald et al., 2003), respectively. The similarity in the northward upper ocean transport of 14.7Sv in this study, and ∼15Sv in Holfort et al. (1998), supports an increase in C^{ant} transport driven by increased C^{ant} in the surface water. Transport-weighted carbon properties are listed in Table 6.14. Upper ocean water masses hint at greater C^{ant} northward flow with a comparative 4.2±0.3μmol kg^{-1} increase of C^{ant} between northward and southward full-depth transports.

6.5.2.3 30°E

The meridional transect along 30°E represents the primary outflow of water from the South Atlantic box. This study has separated the 30°E section into an Agulhas regime and ACC regime using the Subtropical Front (42.9°S) as the hydrographical boundary. The northern part of the transect is dominated by the complex Agulhas circulation whilst the ACC regime shows the continuation of the strong eastward ACC transport, as observed through Drake Passage. Through traversing the South Atlantic Ocean, ACC properties are altered by interaction between the ACC and the upwelling limb of the MOC. Volume transport outflow across 30°E therefore primarily consists of Drake Passage volume transport plus any additional inflow into the South Atlantic box via

24°S and the Agulhas regime. Previous estimates of ACC regime transport include ∼160Sv (bottom-referenced at 30°E, Park et al. (2001)), ∼153Sv (bottom-referenced baroclinic at 0°E, Gladyshev et al. (2008)), and 147±0Sv (bottom referenced between 0°E and 30°E, Legeais et al. (2005)).

Agulhas regime From the African coast at the north of the section, total westward transport quickly accumulates to 65.7Sv, north of 34°S (Figure 6.27). This strong westward flow close to the continental slope corresponds with the schematic representation of Casal et al. (2009). Between ∼34-35°S, the net westward transport is interrupted by an eastward flow, before reaching a peak westward flow of 84.5Sv. Eastward flow likely corresponds to large cyclonic eddies within the region, as previously observed in Park et al. (2001) and diagnosed in the inverse model of Casal et al. (2009). Westward flow corresponds with the net Agulhas Current transport and compares with previous estimates from Bryden et al. (2005a) of 69.7Sv with a 21.5Sv standard deviation using a LADCP-referenced zero velocity surface, and 85Sv from Toole and Warren (1993) with the differences attributed to the differences in reference level. In this study, a single mid-depth reference level (2000dbar) is cautiously applied across the section from the continent to 40°S. A bottom reference level is applied south of 40°S, in response to the deepening topography at the northern flank of the Agulhas basin (Arhan et al., 2003), and is likely the cause of the difference between the Agulhas Current transport estimated in this study, compared to previous studies.

South of the peak westward flow, the Agulhas Return Current is attributed to the net eastward trend south of ∼36.25°S, with the return flow occupying a broader meridional extent compared with the Agulhas Current. North of the Subtropical Front, the Agulhas Return Current transport is estimated as 82.2Sv, extending between 36.25°S and 42.9°S. This gives a net volume transport for the Agulhas regime of 2.3Sv. The eastward flow from the Indian Ocean into the South Atlantic is commonly termed the 'Agulhas leakage', defined in this study as westward flow above the 3.5°C isotherm. Above 3.5°C, a 10.7Sv Agulhas leakage is detected (originally constrained to 9Sv), comparable with recent observations using subsurface floats and surface drifters of 15Sv (Richardson, 2007). The value of this inter-ocean exchange shows short-term variability, as well as, a suggested trend towards increasing Agulhas leakage of volume, heat and salt into the South Atlantic (Biastoch et al., 2009; Rouault et al., 2009).

The signature of the Agulhas Current and Return Current is observed within the upper ocean (surface, SAMW, AAIW) water masses, as well as weakly visible within UCDW and corresponds to a flattening of the deep water isotherms (Figure 6.28).

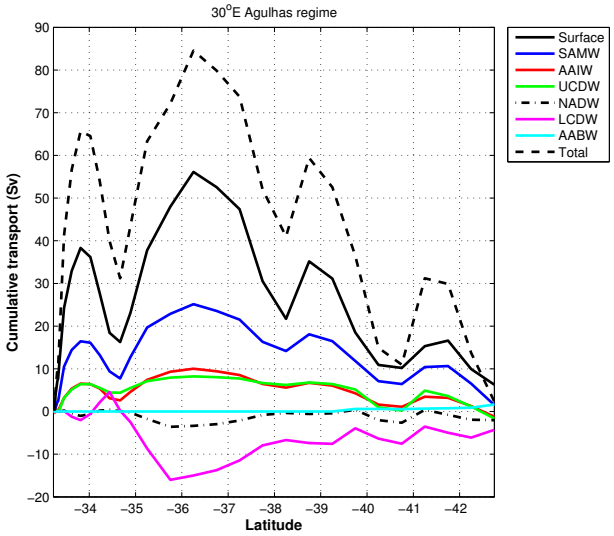

Figure 6.27: Cumulative volume transport across 30°E within the Agulhas regime (north of 42.7°S) for each water mass, and the total volume transport. NADW transport is added, computed from layers (16-17, Table 6.1) within the UCDW and LCDW water masses. Positive (negative) transports represent box inflow (outflow).

Within LCDW, substantial eastward flow is observed, whilst AABW is absent from the Transkei basin (north of ∼38°S). LCDW eastward flow is not the Agulhas Undercurrent (Beal and Bryden, 1999; Beal, 2009), which is primarily situated wedged against the African continental slope, and hence represents the eastward flow of NADW in the Indian Ocean. NADW ($27.90<\gamma^n<28.10$) is represented by enhanced salinity (>34.80), and is sourced from the Namib Col Current through the deep water channel in the Walvis Ridge, as well as a broad, weak zonal flow of NADW originating from the Deep Western Boundary Current (Arhan et al., 2003; van Sebille et al., 2012). North of 34°S, an eastward 1Sv NADW transport, compares with the ∼2.5Sv eastward NADW transport observed in Arhan et al. (2003) for a deep boundary current around southern Africa into the Natal Valley (McDonagh et al., 2008). A broader eastward flow is observed from ∼34-36°S, reaching 3.6Sv eastward, compared to 7Sv eastward in Arhan et al. (2003). In this study, continued stronger eastward flow is observed for the LCDW below the typical NADW density class. Cyclonic LCDW circulation, peaking at ∼35.7°S may be misleading, and instead may correspond to meandering of the deep water flow into the South Indian Ocean. For AABW, net westward flow is only observed for AABW (1.7Sv), south of 39°S within the deepening topography (>4000dbar) towards the northern flank of the Agulhas basin at ∼42.4°S.

Across the Agulhas regime (Figure 6.29), the surface water dominates the net full depth transport inflow. A small net inflow is observable for SAMW and AABW, with

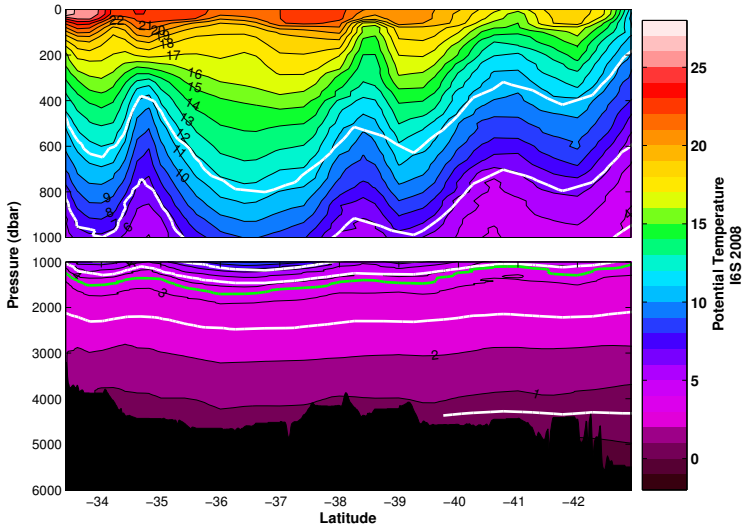

Figure 6.28: Potential temperature section of the Agulhas regime overlain with the neutral density isopycnal boundaries between each water mass (white lines), and the 3.5°C isotherm (green line).

Water mass	Volume transport (Sv)
Surface	6.3±4
SAMW	1.5±4
AAIW	-1.2±3
UCDW	-1.6±2
LCDW	-4.3±1
AABW	1.7±0.5
Total	2.3±2

Table 6.15: Total volume transport across the Agulhas regime of 30°E for each water mass with *aposteriori* uncertainties. Positive (negative) values are into (out of) the box.

outflow for AAIW, UCDW and LCDW. NADW yields a 3.6Sv eastward flow. Eastward flow through the Transkei basin is supported by Mantyla and Reid (1995) and Arhan et al. (2003) and the schematic of Schlüter and Uenzelmann-Neben (2008). On the northern flank of the Agulhas basin, AABW westward flow results from the pathway of AABW heading northwards from Enderby Basin (Figure 1.1) and across the saddle of the Southwest Indian Ridge (Kolla et al., 1976; Boswell and Smythe-Wright, 2002). The northward flow towards the Mozambique basin (Boswell and Smythe-Wright, 2002) bifurcates as it traverses the Agulhas basin and approaches the Agulhas plateau. One pathway continues northward, and a secondary pathway branches westward along the northern flank of the Agulhas basin into the Atlantic Ocean.

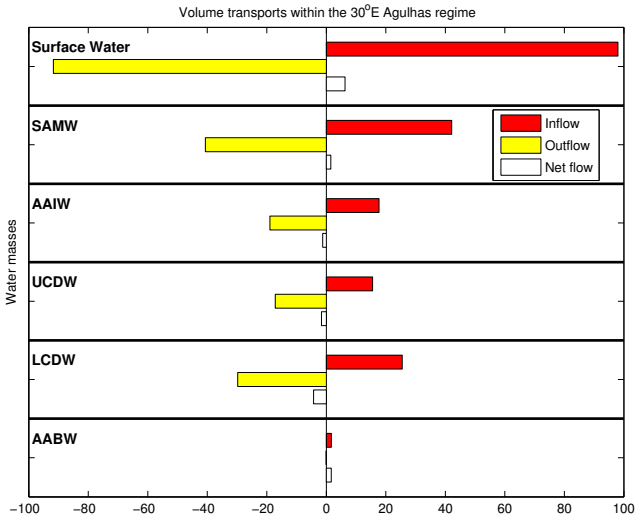

Figure 6.29: Volume transports for each inverse box model layer through the 30°E Agulhas regime. Inflow into the South Atlantic box is positive. Water mass boundaries are marked, and water masses labelled. Positive (negative) values are into (out of) the box.

Transport-weighted temperature, salinity, DIC, C^{nat} and C^{ant} Recent observations (Biastoch et al. (2009); Rouault et al. (2009)) have suggested a trend towards increasing Agulhas leakage, and the 10.7Sv and ∼400Sv psu leakage estimated in this study represents a mean estimate. The downstream effect of Agulhas leakage strengthening is an increase in higher salinity waters at 24°S. However, this observation is complicated by intensification of the Southern Hemisphere hydrological cycle (Curry et al., 2003), with both effects thought to be significant (McCarthy et al., 2011).

Agulhas regime volume transports are summarised in Table 6.16. Agulhas leakage volume transport reflects the model constraint. Transport-weighted temperatures (Table 6.17) further supports a leakage of heat into the South Atlantic, given that westward flowing surface, SAMW and AAIW water masses are warmer, compared to the eastward return flow. Westward flow is also saltier, however, an opposite pattern is observed for C^{ant}, with eastward flow containing higher C^{ant} and supplying the subtropical Indian Ocean with additional C^{ant}, supportive of the South Atlantic as a C^{ant} sink. The presence of C^{ant} is supported by the total increase in the eastward-flowing DIC compared to the pre-industrial C^{nat} estimate.

ACC regime South of the Subtropical Front, colder ACC water masses are observed. From Drake Passage, the ACC stretches meridionally from ∼56.5°S-64°S to ∼42.9°S-69°S at 30°E. Despite the greater meridional extent, volume transport is still associated

	Agulhas Current	Agulhas Return Current	Net flow	Agulhas leakage (>3.5°C)
Volume (Sv)	84.5	-82.2	2.3	10.7

Table 6.16: Model output for the Agulhas Current, Agulhas Return Current and the Agulhas leakage for volume transports within the Agulhas regime. The Agulhas leakage is defined as above the 3.5°C isotherm. (Mmol s^{-1}=1000kmol s^{-1}).

a)

	Westward Transport (Sv)	Eastward Transport (Sv)	Westward TWθ	Eastward TWθ	Westward TWS	Eastward TWS
Surface	98.2±4	92.0±4	16.45±0.20	15.80±0.16	35.377±0.008	35.338±0.011
SAMW	42.2±4	40.7±4	9.46±0.08	9.05±0.08	34.808±0.009	34.722±0.009
AAIW	17.7±3	18.9±3	5.67±0.06	5.23±0.05	34.521±0.005	34.441±0.005
UCDW	17.2±2	18.8±2	3.44±0.02	3.21±0.05	34.602±0.003	34.572±0.004
LCDW	25.9±1	30.2±1	1.58±0.01	1.54±0.02	34.788±0.001	34.782±0.001
AABW	1.7±0.5	0.1±0.5	0.38±0.01	-0.45±0.03	34.701±0.001	34.708±0.003
Total	203.0±2	200.7±2	10.92±0.10	10.10±0.09	35.037±0.005	34.973±0.005

b)

	Westward TWDIC	Eastward TWDIC	Westward TWC^{nat}	Eastward TWC^{nat}	Westward TWC^{ant}	Eastward TWC^{ant}
Surface	2083.8±2.0	2084.1±1.6	2029.7±1.3	2031.8±0.9	48.2±0.3	49.7±0.2
SAMW	2148.7±1.0	2146.1±1.0	2067.7±0.6	2068.0±0.6	29.2±0.6	35.6±0.7
AAIW	2201.9±1.0	2194.1±0.8	2102.8±0.7	2102.0±0.5	16.8±0.5	17.8±0.4
UCDW	2238.7±0.3	2231.6±0.3	2135.4±0.3	2134.7±0.3	16.5±0.1	16.3±0.1
LCDW	2234.7±0.2	2237.6±0.2	2164.0±0.4	2165.8±0.4	11.1±0.1	12.6±0.1
AABW	2254.8±0.4	2253.0±1.0	2194.8±0.4	2192.6±1.1	10.1±0.1	11.7±0.1
Total	2141.4±1.1	2144.0±1.0	2091.5±1.0	2075.6±0.9	33.8±0.3	35.1±0.3

Table 6.17: Eastward and westward transport-weighted (TW) mean θ, salinity S, DIC, C^{nat} and C^{ant} across the Agulhas regime for each water mass with standard error of the mean. For westward (eastward) TW properties, all eastward (westward) velocities are set to zero. TWθ and TWS have units of °C and psu, respectively, whilst all TW properties have units of μmol kg^{-1}.

with jets of enhanced transport at the ACC frontal positions. In this model, the transport across 30°E within the ACC regime is not specifically constrained, however, is included within the boxwide constraint for zero salinity convergence.

The previously mentioned estimates of ACC transport across 30°E of 147-160Sv (Park et al., 2001; Legeais et al., 2005; Gladyshev et al., 2008) are higher than the observed volume transport through Drake Passage (e.g. Cunningham et al. (2003)). For the South Atlantic box, this is understood primarily through the inflow of volume transport into the box through both Drake Passage and within the Agulhas regime. With a net inflow of 0.7Sv southward across 24°S, the ACC regime along 30°E is the exclusive region of net outflow for the South Atlantic box. The cumulative transport within the ACC regime (Figure 6.30) shows a net outflow for each water mass, apart from AABW. Surface, SAMW and AAIW outcrop at ∼48°S, ∼ 55°S and ∼ 64°S along the section.

Eastward flow dominates across the 30°E ACC regime (Figure 6.31). For upper ocean water masses, transport is almost entirely eastward, with westward flow ∼<5Sv for all surface, SAMW and AAIW layers with the largest eastward transport within LCDW. AABW displays the only net westward flow along the section, corresponding to the westward-flowing southern limb of the Weddell Gyre and Antarctic Slope Current, supported by observations within Svedrup (1940), Jacobs (1991), Schröder and Fahrbach (1999), Park et al. (2001), Meijers et al. (2010) and Cisewski et al. (2011), and further discussed in section 6.5.4.1.

For the SAF at 46.25°S, an increase in the full depth transport of ∼20Sv is associated with the front itself. Net accumulation of eastward full depth transport continues southward between the SAF and ∼50°S, north of the strong PF jet of ∼42Sv, primarily for UCDW and LCDW. The full depth volume transport of ∼133Sv north of 51°S dominates the sectionwide eastward flow.

The PF is located above the Southwest Indian (SWI) Ridge at ∼51°S. South of the PF, the SWI Ridge deepens and flattens into the Enderby Basin with an anticyclonic feature between ∼52.25-56.25°S spanning the UCDW, LCDW and AABW. The westward anticyclonic flow on the southern flank of the Southwest Indian Ridge is attributed to either an eddy, or an ACC meander.

The SACCF is responsible for a ∼9Sv eastward flow. South of the SACCF, transport variability is low with LCDW and AABW dominating the flow. For both LCDW and AABW south of ∼ 63.5°S, a westward flow is observed upon approaching the Antarctic continent, corresponding to the westward flowing Weddell Gyre southern limb and the Antarctic Slope Current (ASC). This is supported by evidence for AABW formation

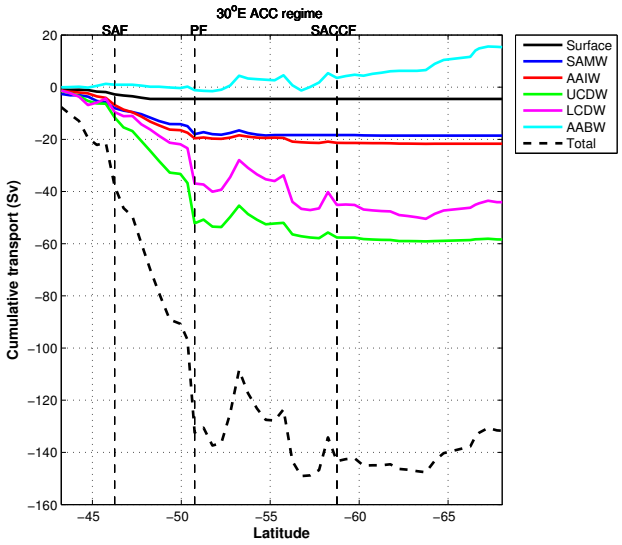

Figure 6.30: Cumulative volume transport across 30°E within the ACC regime for each water mass, and the total volume transport. Positive (negative) transports represent box inflow (outflow).

off Enderby Land (Jacobs and Georgi, 1977; Mantisi et al., 1991; Sloyan and Rintoul, 2001b), and particularly at the Cape Darnley polynya (Tamura et al., 2008; Kusahara et al., 2010; Ohshima et al., 2013).

Across the ACC regime, deep water masses (UCDW, LCDW) carry the greatest volume transport (Table 6.18), responsible for 102.5±2.2Sv of the eastward flow. Total eastward transport across the ACC regime of 131.7±10Sv, reflects the strong westward flow of AABW south of the SACCF. Total eastward transport across the ACC regime, north of the SACCF is 143.3Sv. For comparison with the previous literature, the combined flow across the Agulhas regime and ACC regime of 30°E must be added giving a net eastward flow of 129.4Sv. This is less than the previously mentioned estimates of 147-160Sv (Park et al., 2001; Legeais et al., 2005; Gladyshev et al., 2008), and much closer to the previously estimated volume transports through Drake Passage, which is a consequence of constraining the salinity transport around the box boundary. Previous estimates, as mentioned in Park et al. (2001), are dependent on the estimate for the westward Agulhas leakage, and particularly the reference level chosen within the Agulhas regime.

Transport-weighted temperature, salinity, DIC, C^{nat} and C^{ant} Only eastward transport-weighted properties are considered, to coincide with the direction of the majority of the flow. TW properties (Table 6.19) indicate particularly cold AABW along

Water mass	Volume transport (Sv)
Surface	-4.5±4
SAMW	-18.6±4
AAIW	-21.7±3
UCDW	-58.4±2
LCDW	-44.1±1
AABW	15.4±0.5
Total	-131.7±10

Table 6.18: Volume transport across 30°E ACC regime for each water mass with *apos-teriori* uncertainties. Positive (negative) values are into (out of) the box.

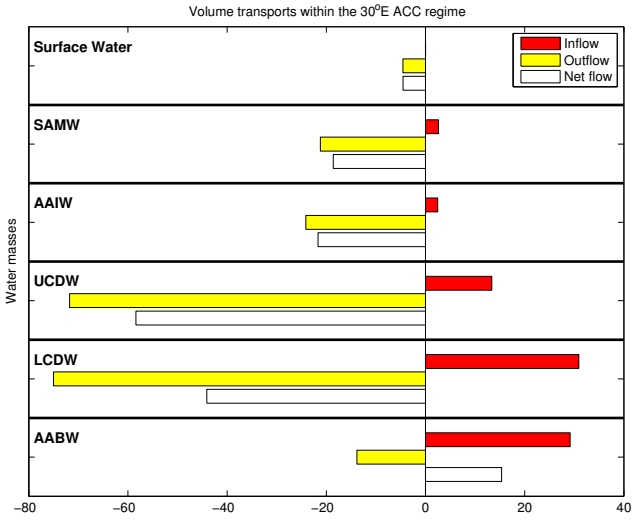

Figure 6.31: Volume transports for each inverse box model layer through 30°E ACC regime. Inflow into the South Atlantic box is positive. Water mass boundaries are marked, and water masses labelled.

	TWθ	TWS	TW DIC	TWC^{nat}	TW C^{ant}
Surface	7.58±0.24	33.973±0.038	2105.0±1.5	2055.3±1.3	50.0±0.5
SAMW	4.73±0.15	34.042±0.019	2136.3±1.1	2081.7±1.0	40.9±0.6
AAIW	2.91±0.06	34.129±0.008	2178.4±0.8	2110.7±0.7	31.8±0.5
UCDW	2.29±0.04	34.519±0.005	2237.5±0.4	2145.4±0.3	16.6±0.2
LCDW	1.29±0.01	34.731±0.001	2249.2±0.1	2174.0±0.3	10.3±0.1
AABW	-0.68±0.01	34.679±0.001	2254.5±0.1	2200.9±0.1	11.1±0.1
Total	2.16±0.02	34.503±0.001	2223.3±0.4	2147.4±0.4	18.8±0.1

Table 6.19: Transport-weighted (TW) mean θ, salinity S, DIC, C^{nat} and C^{ant} for each water mass across the 30°E ACC regime with standard error of the mean. For eastward TW properties, all westward velocities are set to zero. TWθ and TWS have units of °C and psu, respectively, whilst all TW properties have units of μmol kg^{-1}.

30°E whilst a salinity maxima is observed within LCDW caused by NADW influence. TWC^{ant} peaks in the surface and contributes, along with natural, biological variability to the differences between DIC and C^{nat}. The properties upon input to the South Atlantic at Drake Passage are compared to properties across the 30°E ACC regime later in section 6.19.

6.5.3 Geostrophic velocity results by water mass

6.5.3.1 Surface circulation

The model diagnoses a net northward flow of surface water of 8.2Sv across 24°S (Figure 6.32) and includes a 3.3Sv southward Ekman transport constraint in the initial field. Variability in Ekman transport estimates, for example, 3.69/3.06Sv at 23°S and 1.42/0.86Sv at 25°S from Holfort and Siedler (2001), directly affects net surface water flow. An additional small net outflow of 4.5Sv across the ACC regime is compensated by the 6.3Sv inflow of warm, salty Indian Ocean surface water through the Agulhas regime by Agulhas leakage. The box total yields a small net divergence of 5.3Sv.

6.5.3.2 Subantarctic Mode Water (SAMW) circulation

Across Drake Passage, SAMW is transported eastwards into the South Atlantic Ocean from its dominant formation site in the southeast Pacific Ocean (Aoki et al., 2007; Downes et al., 2009; Herraiz-Borreguero and Rintoul, 2010) feeding the salinity minimum layer of both SAMW and AAIW in the South Atlantic. The net 16.5Sv Drake Passage inflow, greater than Sloyan and Rintoul (2001a)'s 4.8Sv estimate, is mainly within the Subantarctic Zone.

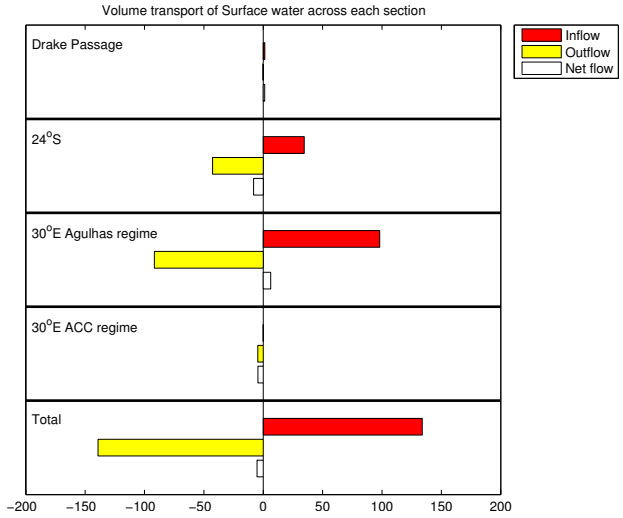

Figure 6.32: Surface water inflow, outflow and net flow from geostrophic volume transport in units of Sv for each section, and the total for the sections combined. The initial Ekman transport estimates across is included. Positive (negative) transports represent box inflow (outflow).

Transformation from SAMW, firstly occurs east of Drake Passage in the Scotia Sea; Naveira Garabato et al. (2003) diagnosed an excess of AAIW in the export, in principle supported by SAMW to AAIW conversion by upper ocean mixing (Herraiz-Borreguero and Rintoul, 2010). Transformation to SAMW likely occurs at the Brazil-Malvinas Confluence (Herraiz-Borreguero and Rintoul, 2010; Garzoli and Matano, 2011), through air-sea transformation (to be discussed in section 6.5.6), as suggested by Sloyan and Rintoul (2001a). Minimal inflow is observed through the Agulhas regime (1.5Sv). Outflow occurs both as the northward return flow of the meridional overturning circulation, and as the ACC throughflow at 30°E. The box total yields a net loss of 5.0Sv supporting observations of SAMW consumption in the South Atlantic. From the boundary-only evidence, a significant source of SAMW within the South Atlantic is not observed (Sloyan and Rintoul, 2001a).

6.5.3.3 Antarctic Intermediate Water (AAIW) circulation

Net eastward AAIW flow of 25.3Sv through Drake Passage is in agreement with the 27.9Sv flow calculated in Sloyan and Rintoul (2001a). AAIW inflow is primarily compensated by a net outflow across the 30°E ACC regime of 21.7Sv. Previous estimates of northward AAIW flow in the South Atlantic range between 2Sv at 35°S (800dbar to 1100dbar, Dong et al. (2009); Schmid and Garzoli (2009)), 2.8Sv at 35°S (800dbar to 1100dbar, Schmid and Garzoli (2009)), 3.1Sv at 25°S (γ^n=27.25-25.55, You et al.

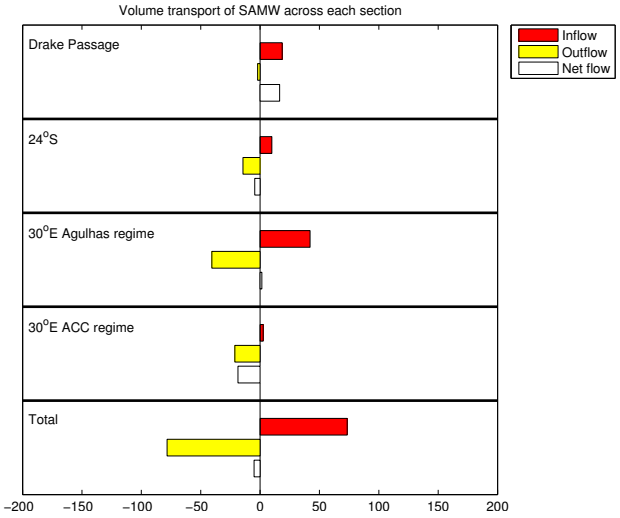

Figure 6.33: SAMW water inflow, outflow and net flow from geostrophic volume transport in units of Sv for each section, and the total for the sections combined. Positive (negative) transports represent box inflow (outflow).

(2003)), 3.8Sv at 30°S (σ_0=27.00-σ_1=32.00, Holfort and Siedler (2001)) and >10Sv at 30°S (σ_0=26.80-σ_2=36.75, de las Heras and Schlitzer (1999)). In this study, net northward AAIW flow of 2.1Sv is at the lower end of the previously estimated range. AAIW Agulhas regime outflow is significant in the context of discussion of *warm* and *cold* pathways, as discussed in Gordon et al. (1992) and Rintoul (1991), and many other following articles (see Garzoli and Matano (2011)), and will be discussed more fully in section 6.6.4.

6.5.3.4 Upper Circumpolar Deep Water (UCDW) circulation

UCDW comprises light NADW, in addition to other modified deep water masses. Net boxwide UCDW convergence is observed, with buoyancy gain transforming UCDW to lighter density classes. Net inflow through Drake Passage of 58.1Sv is nearly compensated at 30°E, by the Agulhas regime inflow and ACC regime outflow combined. Boxwide convergence of 7.2Sv therefore, is largely derived from southward flowing UCDW across 24°S, which upwells south of the ACC fronts to form upper ocean water masses (e.g. Sloyan and Rintoul (2001b)).

6.5.3.5 North Atlantic Deep Water (NADW) circulation

NADW is defined as 27.9<γ^n<28.1 and therefore exists within lower UCDW (27.5<γ^n<28.0) and upper LCDW (28.0<γ^n<28.27). Inflow is only at Drake Passage and 24°S. Across

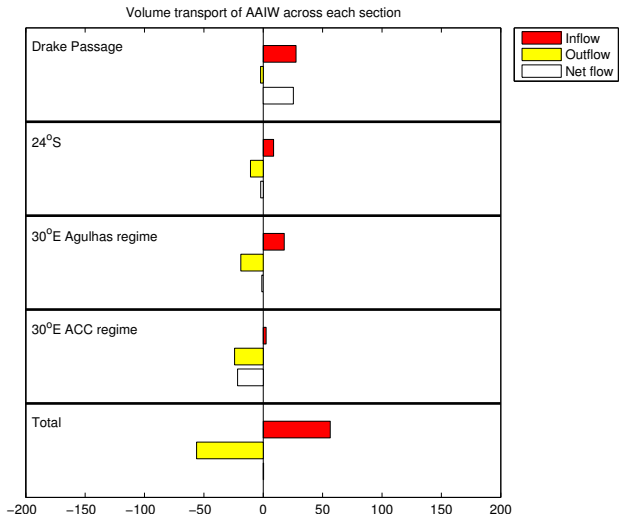

Figure 6.34: AAIW water inflow, outflow and net flow from geostrophic volume transport in units of Sv for each section, and the total for the sections combined. Positive (negative) transports represent box inflow (outflow).

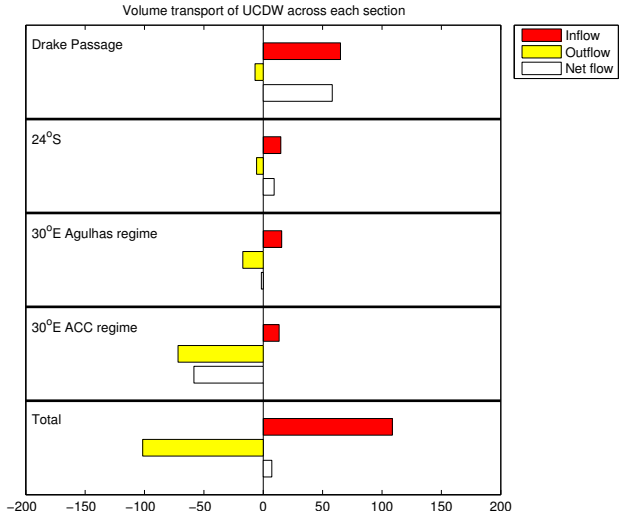

Figure 6.35: UCDW water inflow, outflow and net flow from geostrophic volume transport in units of Sv for each section, and the total for the sections combined. Positive (negative) transports represent box inflow (outflow).

24°S, inflow is 15.3Sv (Figure 6.36a) with a ∼10Sv contribution from the Deep Western Boundary Current and combines with the Drake Passage deep water inflow (30.1Sv). The 30°E ACC regime dominates outflow, in addition to a peak 3.6Sv eastward flow beneath the Agulhas Current (Figure 6.22) and a net broad return flow of 2.0Sv. The direction of the flow is in agreement with previous analyses (e.g. Arhan et al. (2003); Beal et al. (2006)) with Arhan et al. (2003) estimating ∼7Sv. South of the Agulhas regime, enhanced eastward flow is observed.

For the box total, the contribution of the Agulhas regime to the NADW escape route out of the Atlantic Ocean is still small, with the ACC regime favoured as the pathway for NADW to leave the Atlantic. NADW mixes with existing Southern Ocean deep water to form modified-NADW, which outflows across the 30°E ACC regime to yield a net convergence of 7.5Sv.

6.5.3.6 Lower Circumpolar Deep Water (LCDW) circulation

LCDW comprises the densest NADW, and additional denser water masses, partially derived from diapycnal mixing of AABW to a lighter density class. Abyssal mixing rates are particularly large over rough, Southern Ocean bottom topography (Heywood et al., 2002), with Naveira Garabato et al. (2003) suggesting a clear UCDW-LCDW boundary, with intense topographical mixing leading to re-distribution of volume and properties between LCDW and AABW.

Across Drake Passage, 24°S, and the Agulhas regime, net inflows of 28.1Sv, 9.0Sv and 4.3Sv are observed. Net outflow of 44.1Sv across the 30°E ACC regime leads to a net divergence of ∼11.3Sv (Figure 6.18). LCDW divergence within the box, contrasts to the net deep water convergence within Rintoul (1991). Excess outflow across the 30°E ACC regime is a consequence of AABW formation and subsequent entrainment into lighter water masses within the basin, supported by the AABW convergence and LCDW divergence in this model (Figure 6.18, section 6.5.4.1). Previous studies support significant abyssal mixing (Heywood et al., 2004; Naveira Garabato et al., 2004).

6.5.3.7 Antarctic Bottom Water (AABW) circulation

Total box AABW convergence of ∼13.8Sv is observed. Net flow of AABW across western Drake Passage is negligible as the Shackleton Fracture Zone inhibits AABW westward flow out of the Weddell Sea (Cunningham et al., 2003). Northward into the North Atlantic provides the major pathway for AABW export from the South Atlantic with a 2.6Sv northward flow accompanying the 0.6Sv export through Drake Passage.

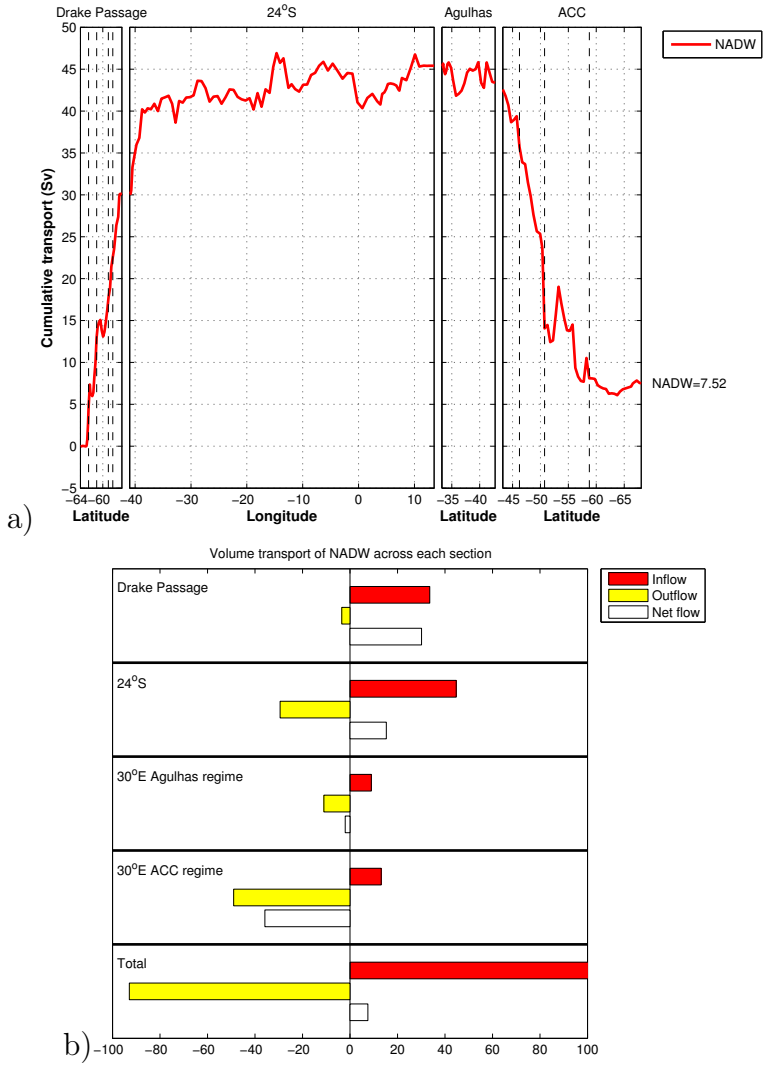

Figure 6.36: a) Cumulative transport of the NADW around the box boundary. Positive (negative) transports represent box inflow (outflow). Dashed vertical lines indicate the ACC front positions. NADW water inflow, outflow and net flow from b) geostrophic volume transport in units of Sv for each section, and the total for the sections combined. Positive (negative) transports represent box inflow (outflow).

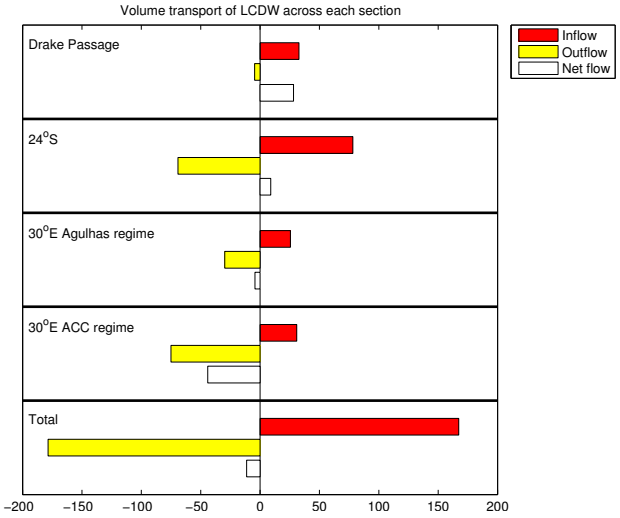

Figure 6.37: LCDW water inflow, outflow and net flow from geostrophic volume transport in units of Sv for each section, and the total for the sections combined. Positive (negative) transports represent box inflow (outflow).

Net inflow occurs across the 30°E regimes, with 1.7Sv Agulhas regime outflow confined to the northern flank of the Agulhas basin, with 15.4Sv inflow across the ACC regime.

6.5.4 Additional circulation features

6.5.4.1 Weddell Gyre circulation

Significant AABW formation east of 30°E is historically implied within the studies of e.g. Meredith et al. (2000) and Yabuki et al. (2006) by AABW signatures found downstream within the Weddell Gyre. Subsequent studies by Meijers et al. (2010) and Ohshima et al. (2013), have pinpointed the source of this AABW formation to the Cape Darnley polynya (65°-69°E). In this region, the intense and persistent sea ice production (Tamura et al., 2008; Kusahara et al., 2010) causes high salinity waters to form, adjacent to the shelf off Cape Darnley polynya, and subsequently sink along the continental slopes to form a type of AABW, termed Cape Darnley Bottom Water (CDBW) by Ohshima et al. (2013). CDBW is hypothesised to contribute ∼13-30% to Atlantic AABW production (Ohshima et al., 2013). CDBW deflects westward along the boundary of the Antarctic continent by the the Coriolis Force (Gill, 1973) and directly contributes to the southern limb of the Weddell Sea.

Westward flow is also seen within the Antarctic Slope Current (ASC), attributed to easterly winds along the Antarctic boundary (Svedrup, 1953; Mathiot et al., 2011), and exists separately to the more southerly Antarctic Coastal Current (ACoC). The ACoC

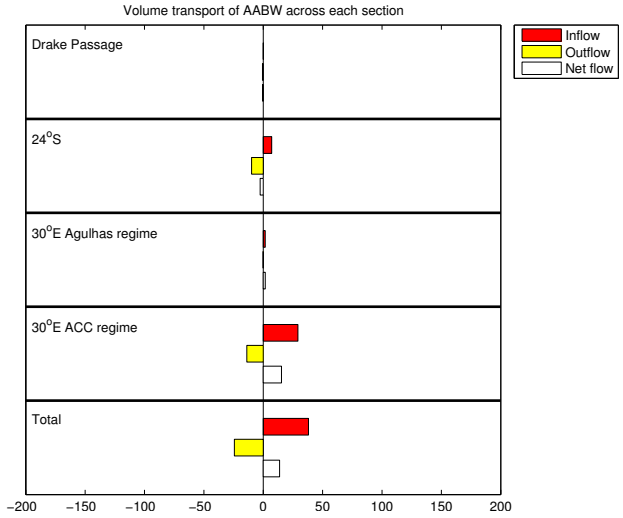

Figure 6.38: AABW water inflow, outflow and net flow from geostrophic volume transport in units of Sv for each section, and the total for the sections combined. Positive (negative) transports represent box inflow (outflow).

is not resolved in this study, as it exists closer to the Antarctic continent (Heywood et al., 2004).

The northern and southern limbs of the Weddell Gyre are delimited by a transition of thermohaline properties between 64.25°S and 65.25°S (Figure 6.39a). South of 65.25°S, θ/S profiles reveal Winter Water with a θ<-1.6°C and saltier than 34.2 signature. Within the transition zone, the Winter Water minima warms to θ>-1.5°C, whilst within the northern limb, the θ minima is uniformly at salinities fresher than 34.2. Within the AABW, high CFC-12 within the southern limb supports recent ventilation compared to the northern limb, east of 30°E, whilst transition zone stations merge with the northern limb. This signal is also observed for AOU profiles, which is also a traditional indicator of more recent ventilation. Greater and more recent AABW formation within the Cape Darnley polynya enables significant atmospheric exposure, whereas a portion of AABW formation within the Weddell Sea occurs near or potentially underneath the ice shelf, containing comparatively lower CFC-12.

Full depth cumulative transport for the southern limb, south of 64.25°S is 15.9±2.3Sv, largely comprised of LCDW (6.3±1Sv) and AABW (8.8±0.5Sv) within the Weddell Gyre southern limb, which continues westwards towards the Weddell Sea. Within the Weddell Sea, this deep water inflow is modified and subsequently exported northward, with wind-forcing thought to dominate this process (Jullion et al., 2010b; Gordon et al., 2010; Wang et al., 2012).

Westward transport of AABW through Drake Passage is strongly inhibited by the

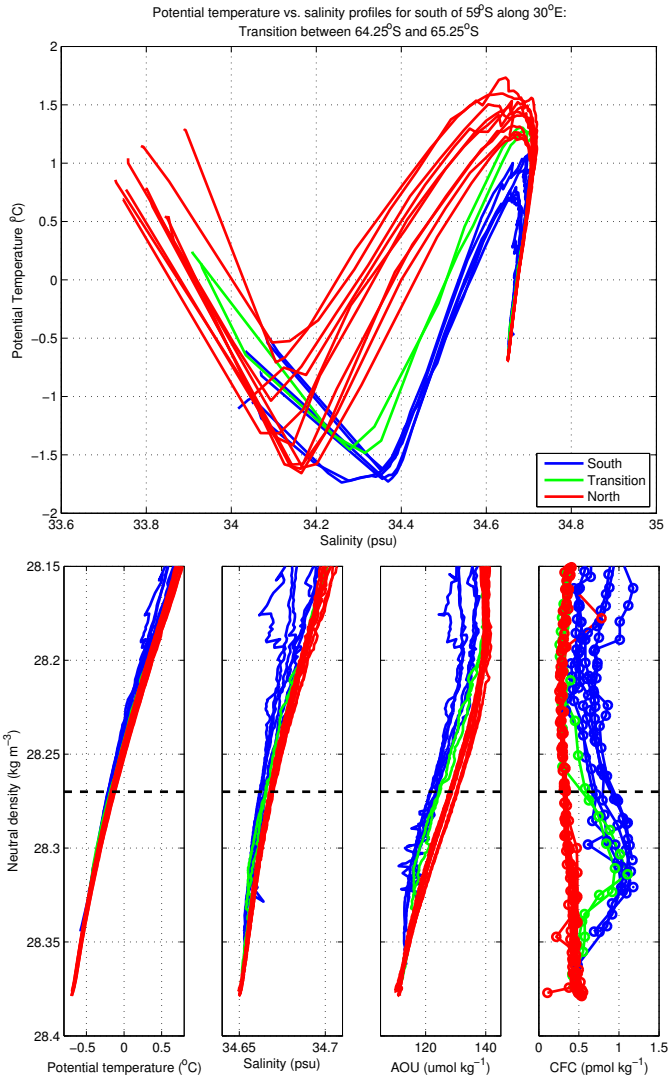

Figure 6.39: a) Potential temperature θ/Salinity S for the Weddell Gyre, south of 59°S. Northern (red), Transition (green) and Southern (blue) stations are demarcated at north of 64.25°S, between 64.25°S and 65.25°S, and south of 65.25°S, respectively. b) θ, S, AOU and CFC profiles versus neutral density for waters denser than 28.15. AABW, found at denser than 28.27, is marked by a dashed line.

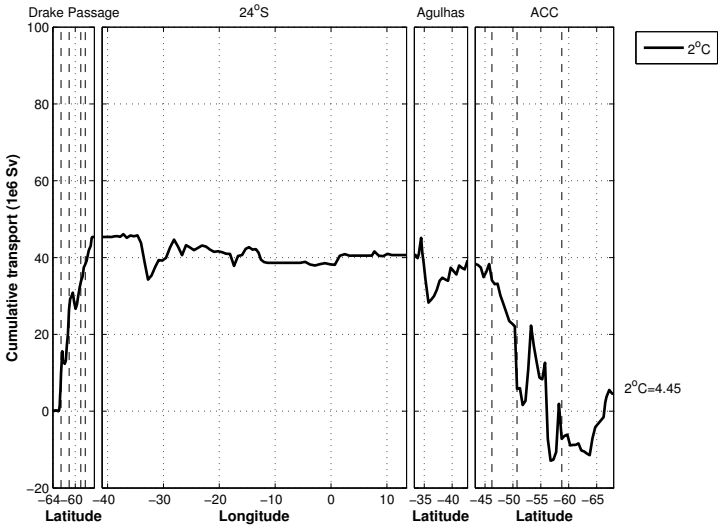

Figure 6.40: Cumulative transport below the 2°C isotherm along box boundary, referred to as Bottom Water (BW) in this thesis. Positive (negative) transports represent box inflow (outflow). The total transport <2°C is shown. Vertical dashed lines representing frontal positions are marked.

Shackleton Fracture Zone with the model diagnosing only a 0.6±0.5Sv westward AABW flow through Drake Passage, compared with total Weddell Sea AABW export estimates of 9.7±3.7Sv (Naveira Garabato et al., 2002b). Naveira Garabato et al. (2002b) suggested that AABW exits the Weddell Sea via the South Sandwich Abyssal Plain (Orsi et al., 1999) and over the South Scotia Ridge into the South Atlantic Ocean. Northward flow of bottom water within the western South Atlantic basin is restricted to the Vema and Hunter Channels. As AABW flows northwards, it warms and interacts with the overlying water mass (Figure 6.40, Hogg et al. (1999); McDonagh et al. (2002)), with the inverse model diagnosing a 6.7±2.2Sv northward flow (constrained to 6.9Sv), below the 2°C isotherm, west of the Mid-Atlantic Ridge. Partial recirculation, previously noted for AABW, has been previously observed as part of the Deep Basin Experiment (Hogg et al., 1999). East of the Mid-Atlantic Ridge (10°W), southward transport of BW, hypothesised as originating from overflow through the Romanche and Chain Fracture Zones is diagnosed as 2.2±1.1Sv, compared to mooring-derived estimates from Mercier and Speer (1998) of 1.22±0.25Sv below the 1.9°C isotherm.

Naveira Garabato et al. (2002b) also suggested a separate branch of the Weddell Sea AABW export forms the eastward-flowing northern limb of the Weddell Gyre. However in this study, the final solution maintains a westward flow across the anticipated meridional span of the gyre (Figure 6.17), suggesting a weak northern limb at the time of observation. As an alternative pathway, partial recirculation brings AABW east of

30°E into the Atlantic Ocean sector of the Southern Ocean prior to branching northwards towards the Indian Ocean. Haine et al. (1998), using CFC analysis, estimated a AABW volume transport of 0.8-1.6Sv follows this branch. From the inverse model, at 30°E westward AABW flow of 2.8±0.5Sv is observed between SACCF at ∼58.75°S and north of ∼64°S. This contrasts with the intuitively expected net eastward flow, as a result of outflow from the Weddell Gyre. Westward abyssal circulation between Africa and Antarctica has been previously observed in Reid (1989) and Gladyshev et al. (2008).

North of 57°S in the model, the signature of the hypothesised ACC meander between ∼52.25-56.25°S is evident. Locally, net westward AABW flow of 1.7±0.5Sv is conducive with an anticyclonic abyssal flow, constrained by the northern flank of the Southwest Indian Ridge (SWI) (∼50°S) to the south, and constrained to the north by the Agulhas Plateau. Eastward flow on the southern flank of the Southwest Indian Ridge is primarily connected to the overlying ACC meander, whilst possibly connecting to the cyclonic abyssal circulation observed by Gladyshev et al. (2008) within the Cape Basin, or the overall northeast flow of AABW from the Weddell Gyre towards the Southwest Indian Ocean basin. Read and Pollard (1999) and Boswell and Smythe-Wright (2002) showed that AABW flows from the Enderby Basin, over the saddle in the southwest Indian Ridge and into Agulhas Basin (Kolla et al., 1976) with Boswell and Smythe-Wright (2002) schematically indicating an eastward pathway.

In summary for this model, the dominant export of Weddell Sea AABW (9.7±3.7Sv Naveira Garabato et al. (2002b)) out of the South Atlantic sector of the Southern Ocean is by northward flow towards the North Atlantic with 6.7±2.2Sv observed through Vema Channel. The anticipated additional outflow across 30°E is hidden by the presence of the westward-flowing Weddell Gyre southern limb and Antarctic Slope Current (15.9±2.3Sv), and a suggested anticyclonic abyssal flow within the Agulhas basin.

6.5.4.2 ACC hydrographic zones and associated transports

ACC fronts separate eastward flow into hydrographic zones. Through the combined effect of the Meridional Overturning Circulation and the ACC, the South Atlantic is an active region for water mass transition between hydrographic zones. Following from the previous sections, Table 6.20a) shows the apparent increase of volume transport for the PFZ between Drake Passage and 30°E. Estimates of flow within a hydrographic zone have limited accuracy, given that the strongest flows are used as the boundary to each zone.

As an alternative, volume transports associated with each front are shown in Table

a)

	Drake Passage (Sv)	30°E ACC regime (Sv)
Subantarctic Zone	40.3	21.2
Polar Frontal Zone	50.1	111.2
Antarctic Zone	38.1	0.7

b)

	Drake Passage (Sv)	30°E ACC regime (Sv)
Subantarctic Front	61.3±6.8	67.9±6.8
Northern Polar Front	19.6	-
Southern Polar Front	31.9	-
Polar Front	51.5±5.5	41.7±6.8
Southern ACC Front	17.5±2.2	9.1±3.8

Table 6.20: Volume transports across Drake Passage and 30°E ACC regime split into a) hydrographic zones, and b) jets associated with each front. Latitudes used to define each frontal jet are at Drake Passage: SAF (57.1-58.7°S), NPF (58.7-59.5°S), SPF (60.5-61.9°S), SACCF (62.3-62.8°S) and 30°E: SAF (45.8-49.3°S), PF (50-50.8°S) and SACCF (58.3-58.8°S). The large SAF latitude range along 30°E captures the bulk of the large volume transport in the PFZ.

6.20b) following Renault et al. (2011). The volume transports for each front at Drake Passage and 30°E ACC are more comparable than for each zone. Comparable previous estimates for the transports associated with the SAF, PF and SACCF are given in Cunningham et al. (2003) as 53±10Sv, 57.5±5.7Sv and 9.3±2.4Sv and the first transect from Renault et al. (2011) as 59.8±2.8Sv, 57.2±2.8Sv and 10.9±1.6Sv. In this study, the Subantarctic Front transport is stronger, and the Polar Front transport is weaker than the previous estimates, with estimates heavily dependent on the choice of transition between SAF and PF transport. However, both estimates from this study fall within the associated error bounds. The SACCF is stronger than for previous estimates, with this difference a result of natural variability in the flow of CDW with UCDW and LCDW equally contributing towards the transport (Figure 6.20).

At 30°E, a significant transport is observed within the Polar Frontal Zone. Apportioning this transport to either the SAF or PF, results in a transport notably larger than that estimated from Park et al. (2001) of ∼25Sv (Table 6.20b). However, the PF has smaller transport than the ∼100Sv estimate in Park et al. (2001). This supports that the distribution of the transport between the SAF and PF is markedly different from Park et al. (2001) and reflects the variability that exists across this section with a more balanced spread of the volume transport observed in this study, using the 2008 30°E occupation.

6.5.4.3 Thermohaline and C^{ant} modification associated with ACC fronts

In addition to a volume transport, each front is associated with a salinity, temperature, DIC and C^{ant} transport. Transport-weighted salinity, potential temperature θ, DIC and C^{ant} are calculated, similar to Jullion (2008), Jullion et al. (2010a) and Vranes et al. (2002), by dividing the salinity, potential temperature, DIC and C^{ant} transports by the volume transport. These are calculated for each layer at each front. The ACC fronts extend across the South Atlantic Ocean with the frontal flow following an approximate streamline (Sokolov and Rintoul, 2009b). Differences between the salinity, θ, DIC and C^{ant} transport associated with a particular front along either meridional section of the box indicate cross-stream exchanges. In addition, the same technique is applied within the Agulhas regime for eastward and westward components of the flow.

Salinity, θ, DIC and C^{ant} divergences between the inflow and outflow of the frontal stream on different sides of the South Atlantic are calculated to see the effects on the transport caused by alterations in the thermohaline, DIC and C^{ant} properties. Initially, salinity, θ, DIC and C^{ant} transports will be biased by the net volume transport difference between the inflow and outflow. The effect of the volume transport is removed by scaling the thermohaline, DIC and C^{ant} transport inflows by the ratio of the mean volume transport for each layer ($\frac{V_{in}+V_{out}}{2}$), applied to the inflow and outflow thermohaline, DIC and C^{ant} volume transports (Jullion, 2008).

Subantarctic Front The SAF takes a meandering path within the South Atlantic. After flowing through Drake Passage, it partially follows the South American continent northwards towards the Brazil-Malvinas Confluence (Jullion et al., 2010a), before traversing eastwards to the north of South Georgia towards 30°E (Sokolov and Rintoul, 2009b). Firstly, looking at the potential temperature profile (Figure 6.41a), the upper ocean (surface, SAMW) has cooled ($\sim$ 1°C), corresponding with the upwelling of cooler deep water in the MOC southern limb. The upper ocean salinity profile shows a freshening across the basin for layer 9 and upwards, reaching a 0.19 freshening for layers 4 and 5. For deeper water masses, the outflow is observed to increase temperature slightly above the inflow by $\sim$0.3°C, as well as reaching a salinity > 34.7 and reducing DIC by $\sim 20 \mu mol\,kg^{-1}$. This is a signature of warmer, saline NADW, which has mixed with the existing Circumpolar Deep Water, in order to create a modified NADW outflow within the SAF at 30°E. The C^{ant} profile (Figure 6.41b) indicates a C^{ant} increase of 2.5-5.5$\mu mol\,kg^{-1}$ for UCDW/LCDW, reaching a 17-22$\mu mol\,kg^{-1}$ increase for layers 4 and 5. Warmer, saline NADW has a C^{ant} minima and lower DIC.

Salinity, temperature, DIC and C^{ant} divergence profiles support the salinity, poten-

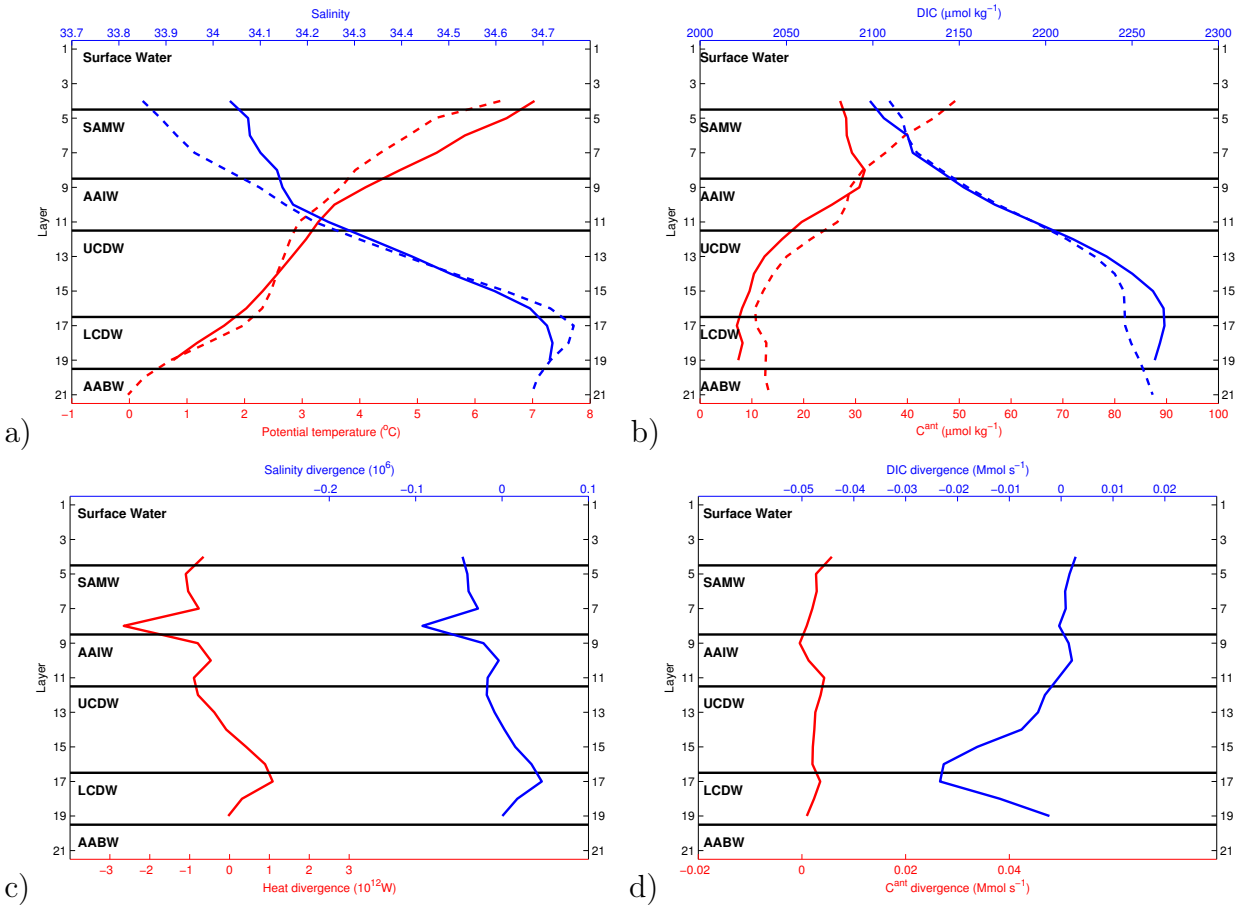

Figure 6.41: a) Volume transport-weighted salinity (blue) and potential temperature (red) and b) volume transport-weighted DIC (blue) and C^{ant} (red) for the SAF. Drake Passage inflow (solid line) and 30°E outflow (dashed line) are shown. c) Salinity divergence (blue) and heat divergence (red) and d) DIC divergence (blue) and C^{ant} divergence (red) within the SAF at Drake Passage and 30°E. Water mass boundaries are marked (solid black line), and water masses labelled.

tial temperature, DIC and C^{ant} observations with negative salinity and heat divergence and positive DIC and C^{ant} divergence for the upper ocean corresponding with a freshening, cooling and uptake of atmospheric C^{ant}. A peak in the positive salinity, heat and C^{ant}, and negative DIC divergence corresponds with the NADW signature. Net changes in salinity, temperature, DIC and C^{ant} transport, as a consequence of salinity, potential temperature, DIC and C^{ant} changes between the inflow and the outflow are -0.20×10^{12}kg s^{-1}, -7TW, -0.08Mmol s^{-1} and 0.03Mmol s^{-1}, respectively with the net effect of the upper ocean dominating salinity and potential temperature divergences.

Polar Front At Drake Passage, the Southern PF and Northern PF represent the shallower and deeper expression of the PF, respectively. For comparison with the Polar

Front observed at 30°E, a pseudo-PF at Drake Passage is created using thermohaline, DIC and C^{ant} properties from the surface, SAMW, AAIW and UCDW from NPF and LCDW and AABW from SPF. Profiles of salinity, potential temperature, DIC and C^{ant} at the Polar Front show a cooling (∼1°C), freshening (0.18), DIC increase (∼17μmol kg^{-1}) and C^{ant} increase (12-20μmol kg^{-1}) within SAMW. A cooling corresponds to upwelling of cold deep water to the surface, and a freshening to the outcrop of the cold, fresh Antarctic Surface Water (Rintoul et al., 2001). Within the intermediate water mass, Drake Passage displays a minima approaching 2°C, corresponding to northward progression of Winter Water (Naveira Garabato et al., 2009). The maxima observed within the UCDW inflow, is a continuum of the temperature profile, if the Winter Water was absent. For the deeper UCDW and LCDW, the slightly increased temperature associated with the outflow is attributed to NADW influence. At mid-depths, little difference is observed for salinity, with the NADW signature of higher salinity (>34.7) evident at the outflow, whilst below the NADW signature C^{ant} approaches a ∼0μmol kg^{-1} minima and DIC plateaus at 2261μmol kg^{-1} at Drake Passage. Recent AABW formation in the Weddell Sea and Cape Darnley polynya contributes to secondary C^{ant} maxima of ∼10μmol kg^{-1} for AABW at the outflow. Similar to the SAF, salinity, heat, DIC and C^{ant} divergences indicate that the changes in salinity, potential temperature and DIC within the South Atlantic basin have reduced the overall transports, whilst C^{ant} transports have increased, with the model diagnosing -0.14×10^{12}kg s^{-1}, -7TW, -0.09Mmol s^{-1} and 0.06Mmol s^{-1}, respectively. This is in spite of NADW heat and salt input.

Southern Antarctic Circumpolar Current Front Salinity, potential temperature, DIC and C^{ant} profiles for SACCF show the absence of a clear NADW signature. Within AAIW outcropping, a cooling of ∼0.6°C is observed. The inflow is thereby, observed to cool more sharply until the upper UCDW gives a 0.4°C warming, with an accompanying salinification of 0.03, DIC increase of 16μmol kg^{-1} and C^{ant} increase of up to 25.8μmol kg^{-1}. Evidence for an outflowing of warmer, saltier water within the upper deep ocean, suggests upwelling deep water has moved up the water column and gained C^{ant} primarily along isopycnal surfaces, before outcropping south of the SACCF. The salinity, heat, DIC and C^{ant} divergence indicates an increase in the respective transports of 0.01×10^{12}kg s^{-1}, 1TW, -0.02Mmol s^{-1} and 0.03Mmol s^{-1}.

Agulhas regime In addition to the ACC fronts, the Agulhas regime indicates an inflow and outflow of water across 30°E albeit with the majority of the outflowing

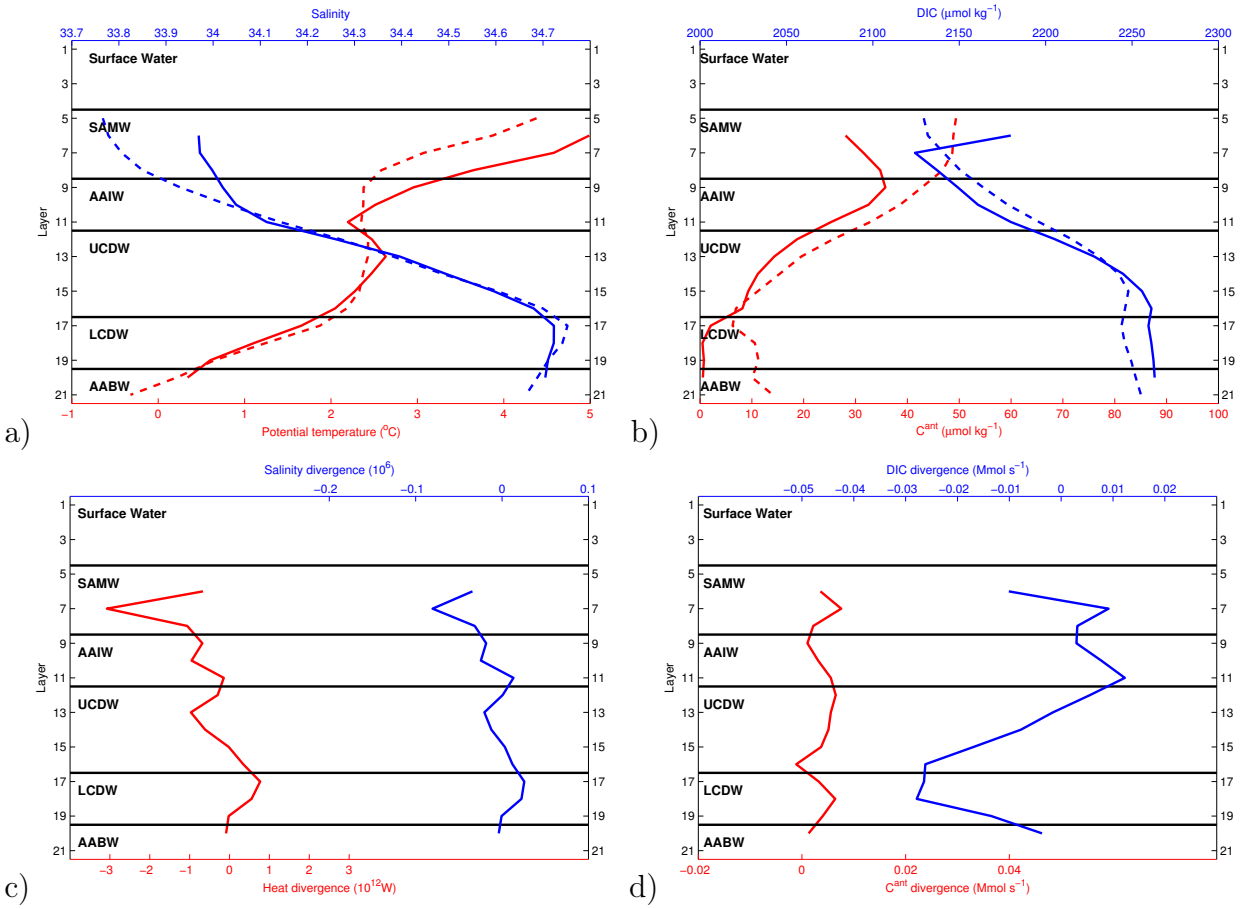

Figure 6.42: a) Volume transport-weighted salinity (blue) and potential temperature (red) and b) volume transport-weighted DIC (blue) and C^{ant} (red) for the PF. Drake Passage inflow (solid line) and 30°E outflow (dashed line) are shown. c) Salinity divergence (blue) and heat divergence (red) and d) DIC divergence (blue) and C^{ant} divergence (red) within the PF at Drake Passage and 30°E. Water mass boundaries are marked (solid black line), and water masses labelled.

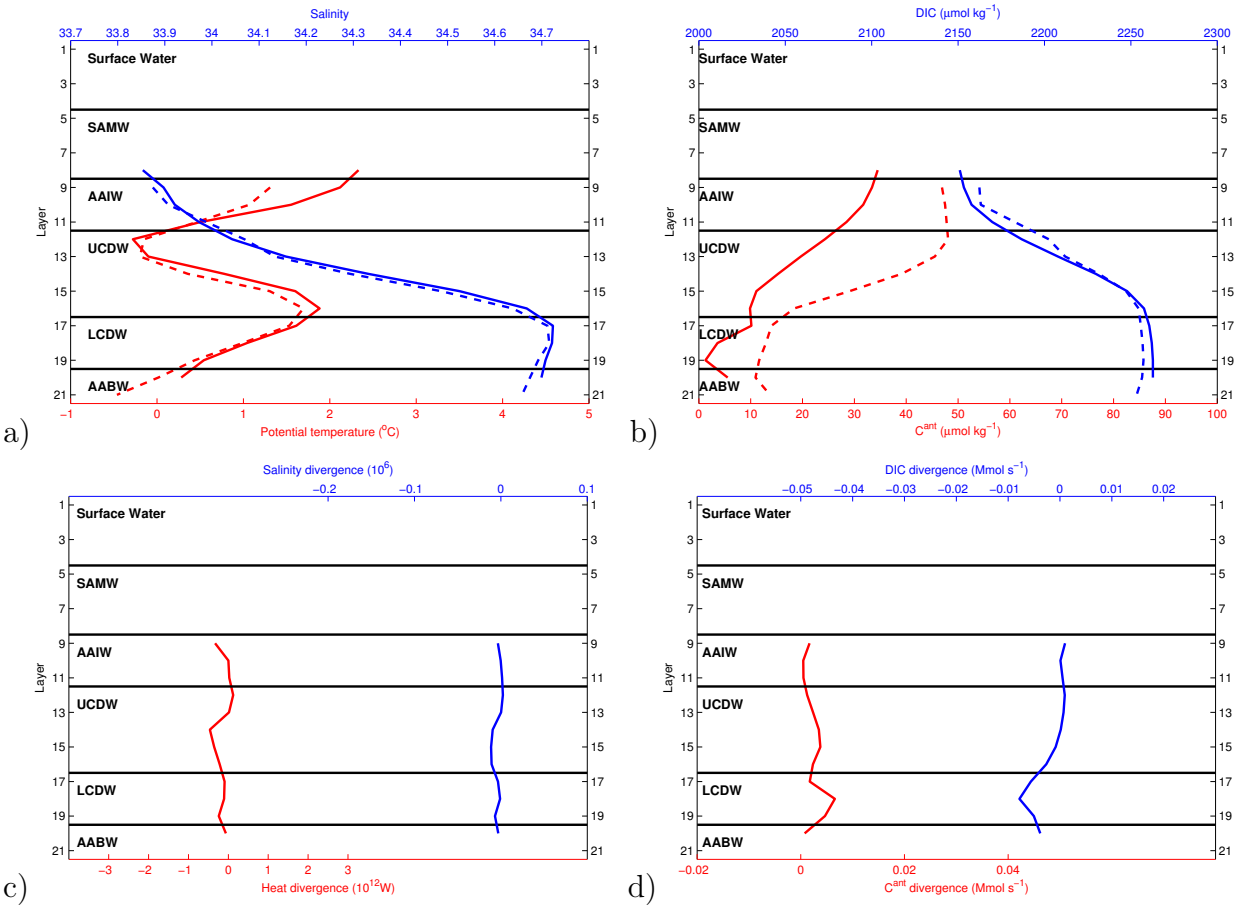

Figure 6.43: a) Volume transport-weighted salinity (blue) and potential temperature (red) and b) volume transport-weighted DIC (blue) and C^{ant} (red) for the SACCF. Drake Passage inflow (solid line) and 30°E outflow (dashed line) are shown. c) Salinity divergence (blue) and heat divergence (red) and d) DIC divergence (blue) and C^{ant} divergence (red) within the SACCF at Drake Passage and 30°E. Water mass boundaries are marked (solid black line), and water masses labelled.

	Salinity divergence ($\times 10^{12}$kg s^{-1})	Heat divergence (TW)	DIC divergence (Mmol s^{-1})	C^{ant} divergence (Mmol s^{-1})
SAF	-0.20	-6.96	-0.08	0.04
PF	-0.15	-6.92	-0.09	0.06
SACCF	0.01	0.96	-0.02	0.03
Agulhas	-1.14	-16.27	-0.04	0.03

Table 6.21: Salinity, heat, DIC and C^{ant} divergence for the major ACC fronts, and the Agulhas regime.

water returning in approximately the same direction as the inflowing water. For this assessment, the inflow and outflow between $\sim 35-38$°S are calculated. Within the upper ocean, temperature decreases slightly for the outflowing water at 0.4°C in the surface waters, rising to a 0.5°C decrease in the SAMW. Within the deep ocean, the temperature profiles display a tight coherency. For salinity and C^{ant}, a 0.13 and 7μmol kg^{-1} decrease for the uppermost surface water is observed, as well as a 0.1 decrease and 7-10μmol kg^{-1} increase throughout SAMW, whilst DIC differences reach 5μmol kg^{-1} within UCDW.

A negative salinity, heat and DIC divergence of -1.14×10^{12}kg s^{-1}, -16TW and -0.04Mmol s^{-1}, and positive C^{ant} divergence of 0.03Mmol s^{-1} respectively, indicates a loss of heat within the Agulhas system as warm, salty Indian Ocean waters reach further from their source, whilst downward mixing and isopycnal outcropping causes higher C^{ant} within the Return Current. This upstream analysis of the Agulhas regime, also supports the flux of warm and salty water into the Atlantic Ocean with the net loss of heat and salt attributed to Agulhas leakage. No clear NADW signature within the outflow is observed.

Salinity, heat, DIC and C^{ant} divergences are summarised in Table 6.21. The SAF and PF both exhibit an overall heat loss and freshening as their frontal streams traverse the basin. The Agulhas system also shows a net loss of heat and a freshening of the outflow, conducive with the loss of warm, salty upper ocean water into the South Atlantic through Agulhas leakage. Higher C^{ant} at 30°E upon comparison of Figure 5.13 and 5.23b) results in a positive net divergence for each ACC front, with net export of C^{ant} from the South Atlantic further supported in the Agulhas regime.

6.5.5 Diapycnal Mixing

Diapycnal velocities, in contrast to the geostrophic velocities are representative of the box interior, rather than at the box boundary. The only sizable diapycnal velocity

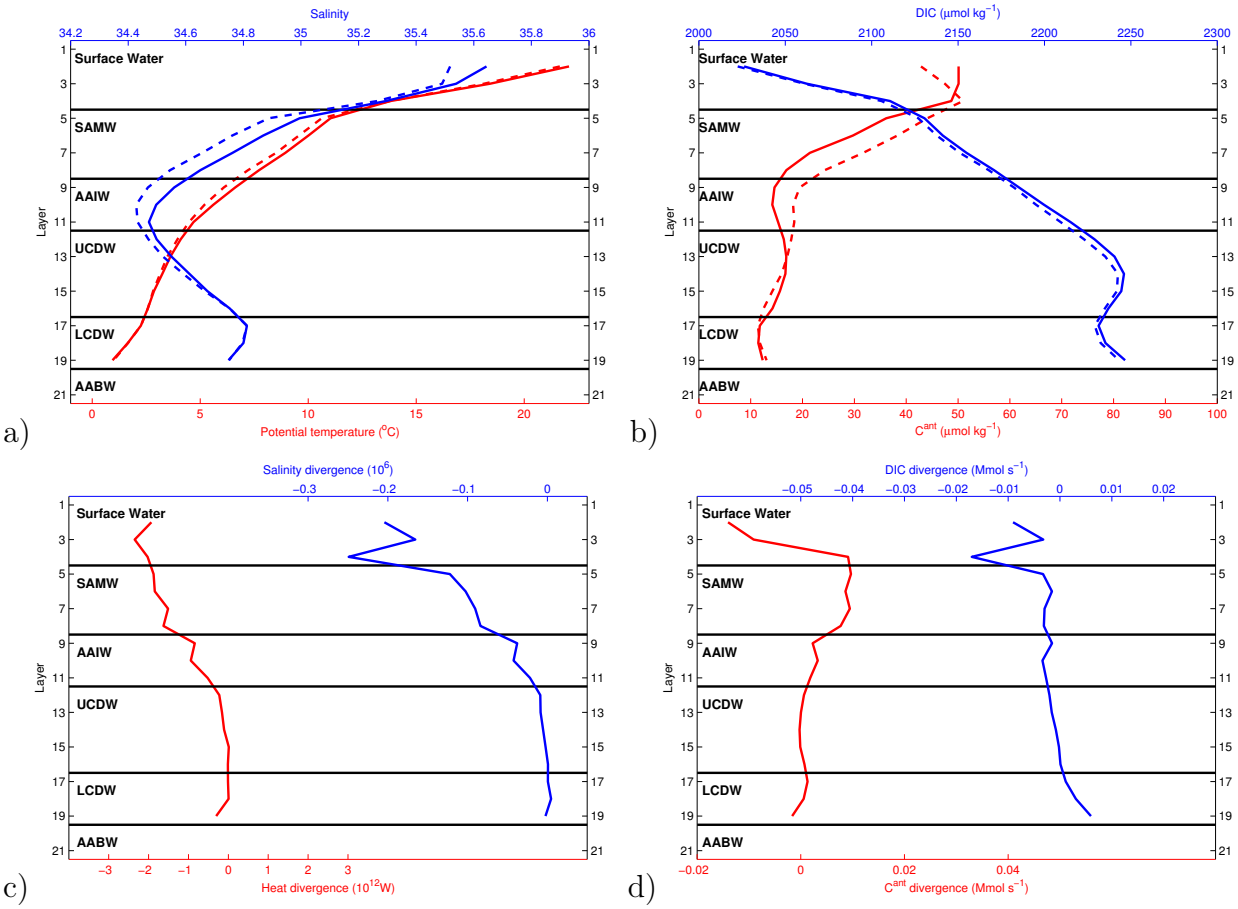

Figure 6.44: a) Volume transport-weighted salinity (blue) and potential temperature (red) and b) volume transport-weighted DIC (blue) and C^{ant} (red) for the currents within the Agulhas regime. Agulhas Current inflow (solid line) and Agulhas Return Current outflow (dashed line) are shown. c) Salinity divergence (blue) and heat divergence (red) and d) DIC divergence and C^{ant} divergence within the Agulhas regime. Water mass boundaries are marked (solid black line), and water masses labelled.

within the box interior is for the lower LCDW and the AABW (Figure 6.45), with upward velocities ($\sim 1.5 \times 10^{-5} \mathrm{m\,s^{-1}}$) matching the diapycnal velocity profile for the Southern Ocean Atlantic sector within Sloyan and Rintoul (2000), and close to previous observational estimates (e.g. Ledwell et al. (2011)). Upward volume transport (4.9-6.3Sv), contrasts with the downward heat transport observed from warmer, lower LCDW into colder AABW (Figure 6.47). In this region, Weddell Sea-formed AABW (WSDW/WSBW) is regarded as the coldest and most voluminous component of AABW (Orsi et al., 1999; Meredith et al., 2000; Gordon et al., 2010). AABW warming results in less extreme AABW, which is able to contribute towards AABW northward flow in the South Atlantic western basin, and ACC circulation.

Volume flux is most variable within LCDW with downward volume flux towards lower LCDW associated with upward heat flux (Figure 6.47). An upward heat flux is unexpected and results from the downward advective heat flux being lower than the upward diffusive flux. A small salt flux from NADW into lower LCDW and into upper UCDW is associated with the erosion of the salinity maximum (Figure 6.46). The small upward volume flux from NADW continues through the UCDW with an associated upward heat flux. Little volume or heat transport is observed within the upper layers, however, these layers see the greatest salinity flux.

Within SAMW and AAIW, a downward flux of salinity corresponds with a drawdown from the saltier, overlying thermocline and SAMW. The upward salinity flux to the surface layer reflects the fresher surface layer, as particularly observed within the ACC regime e.g. Figure 6.41a) for SAF, with an additional atmospheric freshwater input. Diapycnal mixing of salinity out of the SAMW is indicative of salty SAMW, and supports the suggestion by Sloyan and Rintoul (2000) that the origin of this salty SAMW corresponds to an inflow south of Africa bringing salty Indian Ocean water, as opposed to the fresher SAMW observed through Drake Passage. The fact that a similar downward transport is not observed for heat is curious and suggests that in the upper ocean in this model, heat transport is mainly along isopycnal surfaces.

Overall, the box interior estimates display similar characteristics to the analysis of Sloyan and Rintoul (2000), namely the downward heat flux into AABW and the salinification of AAIW. The results from this study, therefore, reaffirm the results from Sloyan and Rintoul (2000) for the Southern Ocean Atlantic sector and support in-situ observations of diapycnal mixing by giving no evidence for an enhanced mixing as large as 10^{-4}.

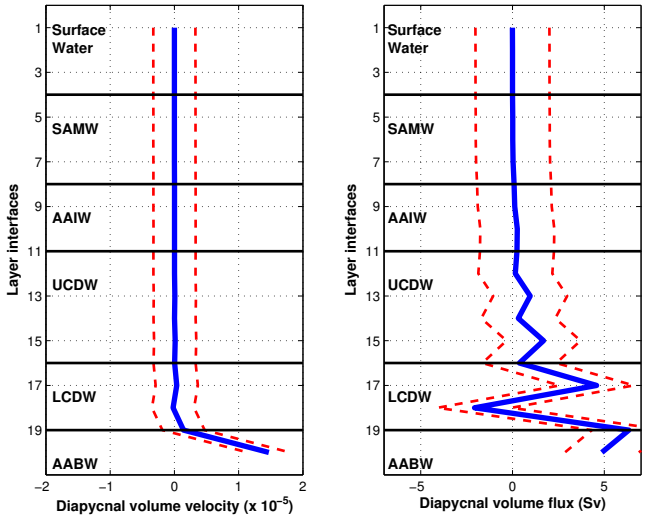

Figure 6.45: Diapycnal volume velocity ($\mathrm{m\,s^{-1}}$) and volume flux (Sv) across each layer boundary within the South Atlantic box. A positive (negative) velocity or transport represents an upward (downward) flow. The dashed lines represent one standard deviation. Water mass boundaries are marked (solid black line), and water masses labelled.

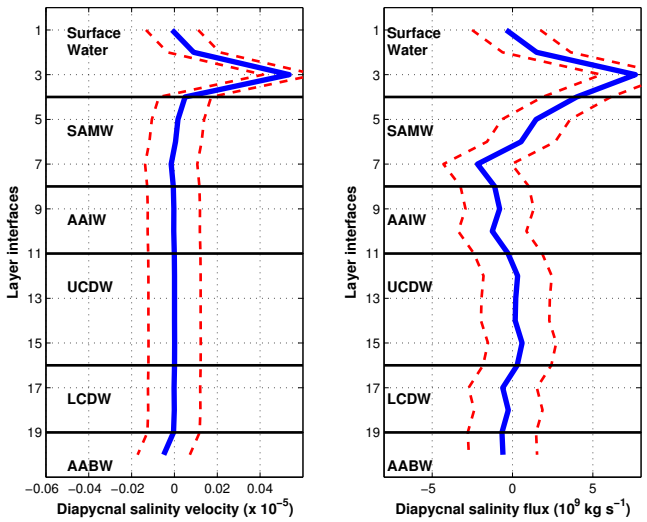

Figure 6.46: Diapycnal salinity velocity ($\mathrm{m\,s^{-1}}$) and salinity flux ($\mathrm{kg\,s^{-1}}$) across each layer boundary within the South Atlantic box. A positive (negative) velocity or transport represents an upward (downward) flow. The dashed lines represent one standard deviation. Water mass boundaries are marked (solid black line), and water masses labelled.

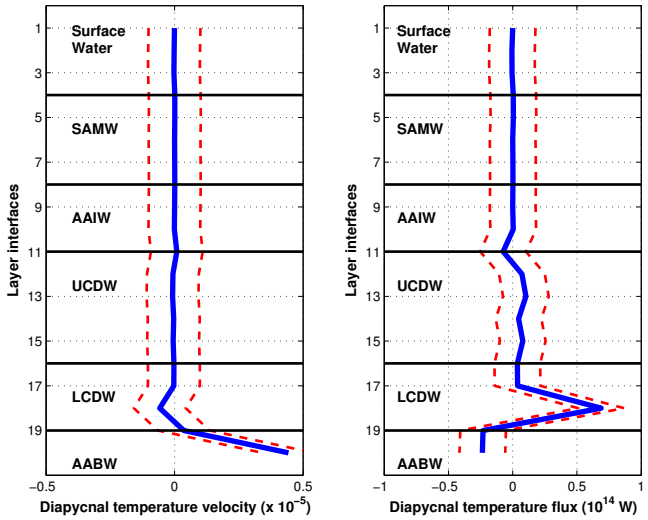

Figure 6.47: Diapycnal temperature velocity ($\mathrm{m\,s^{-1}}$) and temperature flux (W) across each layer boundary within the South Atlantic box. A positive (negative) velocity or transport represents an upward (downward) flow. The dashed lines represent one standard deviation. Water mass boundaries are marked (solid black line), and water masses labelled.

6.5.6 Air-sea interaction

Mixing induced by air-sea interaction, net air-sea freshwater flux and net air-sea heat flux is diagnosed for the interior of the inverse box. Solutions rely upon accurate estimates of the outcropping area within the box, as well as the temperature and salinity at the outcrop. In this model, all layers are expected to outcrop to facilitate AABW formation along the Antarctic continent. Difficulties with estimating the outcropping areas for isopycnals near the Antarctic continent, limit the accuracy of the deep ocean results.

Diapycnal volume flux induced by air-sea interaction is shown in Figure 6.48. An air-sea transformation of lighter surface water masses to denser surface waters and towards SAMW is observed, matching the observation of Sloyan and Rintoul (2001a). Their estimates of air-sea transformation for surface water (γ^n<26.0) to light SAMW (γ^n=26.0) of 14Sv, compare with the 14.6Sv transformation observed in this study to dense Surface water. This process is hypothesised to dominate within the southwest Atlantic region, in the vicinity of the energetic Malvinas Current as it approaches the Brazil-Malvinas Confluence (BMC). Cold and fresh surface water from Drake Passage is entrained by the SAF as it progresses northwards into the Argentine basin, and collides with warmer, salty Brazil Current surface water at the BMC. Warm and salty surface water overlying cold and fresh SAMW, enhances buoyancy flux. This contributes to-

wards the air-sea induced convergence of SAMW within the southwest Atlantic. Part of the newly formed dense Surface water/SAMW follows the South Atlantic Current zonally across the Atlantic, feeding the northward-flowing Benguela Current (Stramma and Peterson, 1990). Agulhas leakage contributes additional warm and salty water, towards the northward, meridional flow of warm, salty SAMW compensating NADW southward flow. Part of the newly formed SAMW continues to follow the SAF, contributing towards eastward SAMW flow within the ACC regime.

For AAIW, broad transformation towards lighter density water occurs through air-sea interactions. Convergence of dense Surface water/SAMW ($\sim$14.6Sv) is approximately compensated by the divergence of deep water masses: UCDW and upper LCDW ($\sim$15.2Sv). Sloyan and Rintoul (2001b) estimate a 34Sv air-sea induced flux of UCDW to AAIW for the Southern Ocean across all latitudes. In the Atlantic sector, the deep water divergence compares well with the 8Sv outcrop estimate for deep water from Sloyan and Rintoul (2001b). Upwelling of lighter deep water masses and transformation to SAMW/AAIW contributes towards the MOC southern limb. Outcropping of deep water masses within the Southern Ocean modifies the water mass properties through exposure to wind, heat and freshwater flux, modifying the buoyancy flux. For LCDW/AABW, little volume flux is observed, however, this is a consequence of the model parameterisation and the difficulty in estimating the proportion of outcropping area occupied near the ice edge, hence the deep ocean air-sea interaction volume fluxes are lower bound estimates.

Net freshwater flux into the South Atlantic contributes to the volume flux induced by air-sea interaction. The freshwater flux is shown in Figure 6.49 and reflects adjustments to the initial freshwater flux estimate, with a small associated flux predominately affecting the surface ocean. As described in Jullion et al. (2010a), the freshwater flux is difficult to estimate accurately given uncertainties in the upper ocean baroclinic variability (Ganachaud, 2003b; Naveira Garabato et al., 2003).

The surface ocean dominates the heat flux profile (Figure 6.50) due to higher surface layer temperatures within the subtropics, particularly in the western South Atlantic basin. Air-sea heat flux adjustments reach -0.53PW for the uppermost layer (Table 6.22), however, over the water column, a total net adjustment of -0.07PW is observed for the net air-sea heat flux input estimate of 2.15PW (65Wm^{-2} over the South Atlantic area). Therefore whilst the whole column adjustment is insignificant, the alterations for individual layers show a greater significance. The small overall adjustments suggest a good agreement between the climatological estimations from the NOC (v2.0) climatology and observations, despite an observed variability between the various heat flux

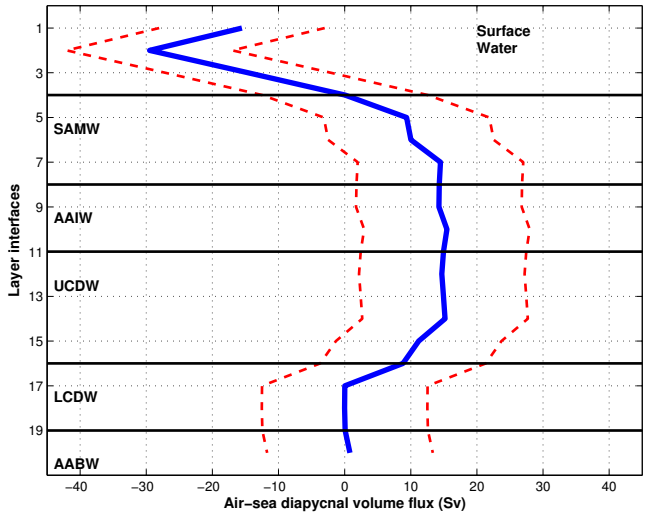

Figure 6.48: Diapycnal volume flux induced by air-sea interaction within the South Atlantic box. Positive (negative) values indicate a flux towards lighter (heavier) water masses. Water mass boundaries are marked (solid black line), and water masses labelled.

	Initial heat flux (PW) ($65\mathrm{Wm}^{-2} \times$ Area)	Adjustment heat flux (PW)
Layer 1	0.21	-0.53
Layer 2	0.48	-0.14
Layer 3	0.34	0.29
Layer 4	0.34	0.28
Total	2.15	-0.07

Table 6.22: Initial heat flux estimate and heat flux adjustment for surface water mass, and the whole water column.

climatology products (Liu et al., 2011).

6.5.7 Ekman

The model diagnoses Ekman transport adjustments, in addition to the Ekman transport applied across 24°S within the initial field. Ekman adjustments are assumed to be applied across the 24°S section. The total adjustment to the volume transport is 0.4Sv (Figure 6.51). Given the uncertainty within the NCEP wind stress (Brunke et al., 2011) used to derive the initial field Ekman transport, the additional transport associated with the Ekman adjustments is not assumed to be significant, however, it is significant within the context of this inverse model in ensuring a net salinity transport of ∼26Sv psu across 24°S.

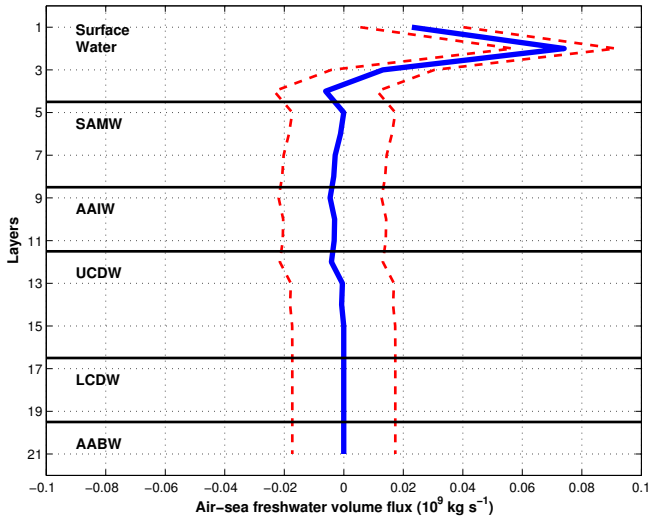

Figure 6.49: Diapycnal freshwater flux induced by air-sea interaction within the South Atlantic box. Positive (negative) values indicate a flux into (out of) the ocean. Water mass boundaries are marked (solid black line), and water masses labelled.

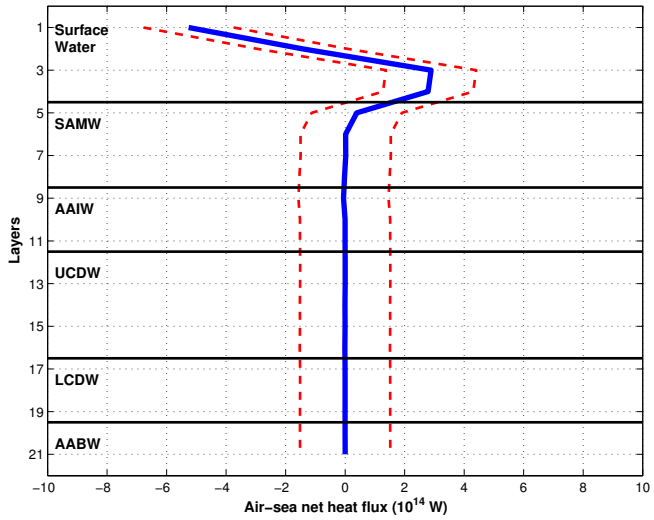

Figure 6.50: Diapycnal heat flux induced by air-sea interaction within the South Atlantic box. Positive (negative) values indicate a flux into (out of) the ocean. Water mass boundaries are marked (solid black line), and water masses labelled.

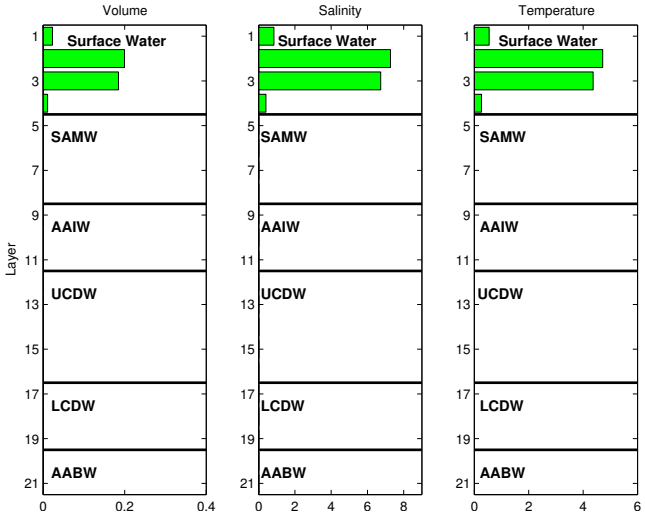

Figure 6.51: Left Panel: Ekman volume transport in Sv, Centre Panel: Ekman salinity transport in Sv psu, Right Panel: Ekman temperature transport in °C Sv . Positive (negative) transports represent box inflow (outflow). All transports are diagnosed using the inverse box model. Water masses and water mass boundaries are marked.

6.6 Conclusion

This chapter has focussed on the application of an inverse box model to the South Atlantic Ocean. Box boundaries are defined by Drake Passage in the west, 30°E in the east, 24°S in the north and the Antarctic continent to the south. The box, therefore spans from the subtropics into the Atlantic sector of the Southern Ocean. The water volume is separated in the vertical into 21 layers by 20 neutral density interfaces. Geostrophic, diapycnal, air-sea induced and Ekman components of the large-scale South Atlantic circulation have been reviewed.

The results for the box boundary volume transports are summarised in Figure 6.52 with the difference between the geostrophic transport inflow and outflow shown for each layer. Ekman transport adjustment within the surface water is small ∼0.4Sv. Net air-sea diapycnal transport is low within the surface waters whilst significantly contributing towards SAMW convergence, hypothesised to occur within the Argentine Basin and at the BMC. Residual SAMW imbalance of 9.3Sv is caused by a 14.2Sv SAMW convergence through air-sea induced interactions. AAIW residual imbalance of 1.1Sv contains little net diapycnal mixing, hence suggesting that AAIW properties remain relatively unchanged from their formation by the subduction of Winter Water within the Bellinghausen Sea (Naveira Garabato et al., 2009). Freshening observed in the Bellinghausen Sea, corresponds to a mixed freshening and salinification signal upstream in the South Atlantic (Arbic and Owens, 2001; Curry et al., 2003; McCarthy et al., 2011) through the

competition between freshening at formation and the salinification by Agulhas leakage into South Atlantic AAIW.

Large scale diapycnal flux of UCDW to lighter water masses is not observed. This supports the findings of Sloyan and Rintoul (2001a) for deep to intermediate water conversion in the Southern Ocean to occur along isopycnals, rather than supporting uniform interior upwelling from historical conceptual models (e.g Munk (1966); Gordon (1986)).

For UCDW, air-sea diapycnal flux divergence contributes to SAMW convergence, in accordance with dense water outcropping within the Southern Ocean. LCDW also contributes to SAMW convergence. Convergence of LCDW by interior diapycnal mixing corresponds to newly formed AABW mixing with overlying deep water, particularly over rough topography leading to both LCDW convergence and AABW divergence, consistent with Orsi et al. (1999). Formation of lighter AABW contributes towards northward bottom water flow ($<2°$C) within the Brazil Basin. Convergence for AABW around the box boundary is dependent upon uncertainties regarding the strength of the westward inflow of the Weddell Gyre southern limb and Antarctic Slope Current, and subsequent diapycnal upwelling within box. The sum of the residual imbalances for all water masses of $\sim$0.3Sv is representative of the uncertainty in the box closure.

Excess C^{ant} outflow from the box results in a net divergence for Surface, SAMW, AAIW, UCDW and LCDW. Net inflow of AABW reduces the total divergence to 1.55Mmol s^{-1}, and is supportive of C^{ant} absorption into the South Atlantic Ocean surface, and further discussed in sections 6.6.1 and 6.6.2.

6.6.1 Oceanic heat, freshwater and C^{ant} budget for the South Atlantic ACC

For the transects at Drake Passage and along 30°E across the ACC, a comparison of the transport-weighted properties reveals the difference in properties between South Atlantic entry and exit. Firstly, the temperature, salinity and C^{ant} differences between the mean properties at Drake Passage and south of Africa, south of the Subtropical Front, are calculated by subtracting the western section values from the eastern section values. Temperature differences are converted to heat transport by multiplying a Drake Passage/30°E mean volume transport, area-weighted density and area-weighted heat capacity, either for each water mass or for the full depth following Georgi and Toole (1982). Freshwater transports are calculated by dividing the salinity differences by the mean salinity, and multiplying by the mean volume transport, whilst C^{ant} transports are

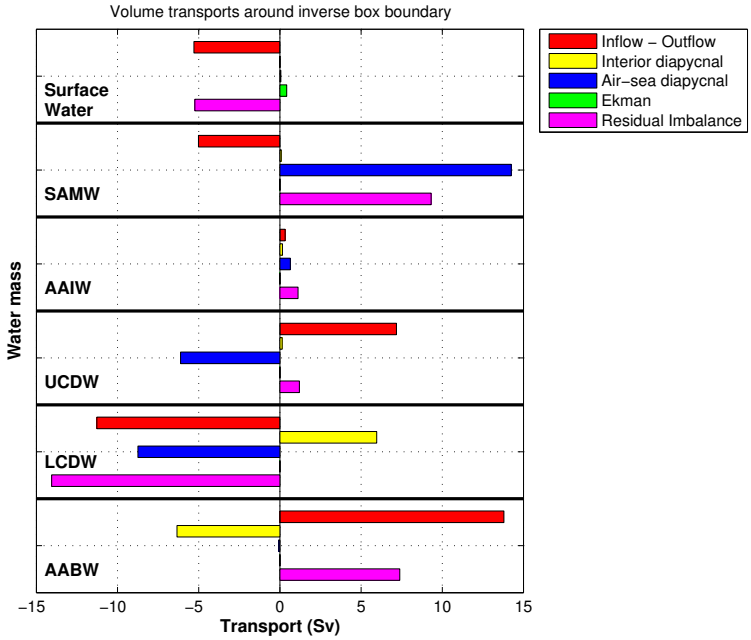

Figure 6.52: Volume budget for each layer showing the residual between the inflow and outflow for the geostrophic flow at the box boundary, interior diapycnal, air-sea diapycnal and Ekman adjustment components, as well as the residual imbalance. For each layer, the residual imbalance is the sum of the other components with the exception of the prior inclusion of the Ekman adjustment component within the geostrophic box boundary flows. Positive (negative) transports represent box inflow (outflow). Residual imbalance of $\sim$0.3Sv is representative of the uncertainty in the box closure. Each layer is separated by a thin, dashed line. Water mass boundaries are marked (solid black line), and water masses labelled.

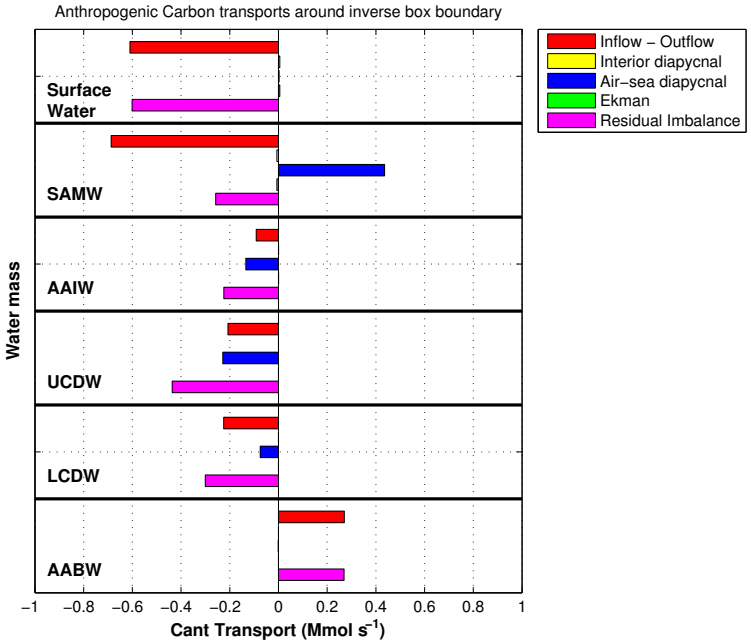

d)

Figure 6.53: C^{ant} budget for each layer showing the residual between the inflow and outflow for the geostrophic flow at the box boundary, interior diapycnal, air-sea diapycnal and Ekman adjustment components, as well as the residual imbalance. For each layer, the residual imbalance is the sum of the other components with the exception of the prior inclusion of the Ekman adjustment component within the geostrophic box boundary flows. Each layer is separated by a thin, dashed line. Water mass boundaries are marked (solid black line), and water masses labelled.

	$\triangle$T (°C)	$\triangle$S (psu)	$\triangle C^{ant}$ (μmol kg^{-1})	∇T(PW)	∇FW (Sv)	∇C^{ant} (Mmol s^{-1})
Surface	0.35 ±0.25	-0.002 ±0.043	23.1 ±0.8	0.0041 ±0.0064	-0.001 ±0.004	0.068 ±0.095
SAMW	-0.16 ±0.17	-0.051 ±0.020	10.2 ±0.6	-0.0115 ±0.0122	-0.026 ±0.012	0.181 ±0.043
AAIW	-0.17 ±0.08	-0.002 ±0.010	5.0 ±0.5	-0.0163 ±0.0084	-0.001 ±0.007	0.120 ±0.021
UCDW	0.03 ±0.02	0.023 ±0.006	5.2 ±0.2	0.0071 ±0.0053	0.039 ±0.011	0.309 ±0.017
LCDW	-0.07 ±0.01	0.012 ±0.001	5.5 ±0.1	-0.0103 ±0.0021	0.013 ±0.002	0.210 ±0.008
AABW	-1.04 ±0.01	-0.025 ±0.001	5.4 ±0.2	0.0337 ±0.0022	0.006 ±0.001	-0.032 ±0.003
Total	-0.39 ±0.03	0.080 ±0.003	3.5 ±0.1	-0.2064 ±0.0218	0.302 ±0.023	0.480 ±0.041

Table 6.23: Differences in transport-weighted temperatures ($\triangle$T), salinities ($\triangle$S) and C^{ant} ($\triangle C^{ant}$) and the net gain or loss of heat (∇T), freshwater (∇FW) and C^{ant} (∇C^{ant}) between the western and eastern boundary of the South Atlantic ACC.

estimated from C^{ant} differences and the mean volume transport. Uncertainty reflects the standard error of the mean added in quadrature, and is therefore a statistical uncertainty rather than being due to experimental uncertainty.

Across the Atlantic, the full depth ACC corresponds to a net heat loss of 0.2PW and a freshwater gain of 0.302Sv (Table 6.23). Heat loss matches the sign of the ocean-to-atmosphere heat flux applied in the initial field (Figure 6.10), and freshwater gain, primarily through precipitation, compares well with the available climatologies (Schanze et al., 2010) and approximately equal to the entire freshwater gain estimated for the box. C^{ant} gain, above the estimated uncertainty, matches previous studies in finding that the ACC region of the South Atlantic is a C^{ant} sink (Mikaloff Fletcher et al., 2006; Gruber et al., 2009).

For individual layers, the strongest signals for heat gain occur for surface water and AABW. For AABW however, temperature differences are calculated for eastward flow, whilst the bulk of AABW transport is westward. A gain of heat yet temperature decrease from west to east, equates to a net westward flow. Freshwater gain appears strongest within the deep water masses, and relates to the outcropping of salty NADW within UCDW and LCDW, and subsequent freshening through precipitation. A C^{ant} gain is observed for each water mass, apart from westward flowing AABW with 0.480±0.041Mmol s^{-1} (0.186±0.016PgC yr^{-1}) of C^{ant} gain for the full depth estimate.

6.6.2 C^{ant} storage

This Chapter has made use of the corrected C^{ant} field along 30°E (Figure 5.23b) to remove a portion of the anthropogenic signal attributed to natural variability. In this section only, the original $\triangle C^{*}$ C^{ant} field (Figure 5.15) is also included for comparison, to exemplify the excess divergence caused by the high deep ocean C^{ant} signal. The C^{ant} budget includes the Bering Strait salinity flux at 24°S, with higher C^{ant} transport for the northward flowing C^{ant}-rich surface water mass (Table 6.14). Full-depth net C^{ant} divergence supports C^{ant} absorption in the South Atlantic to acquire additional C^{ant}. An indirect estimate of the proportion of C^{ant} stored in the South Atlantic is computed following the methodology of Holfort et al. (1998), Álvarez et al. (2003) and Khatiwala et al. (2012). In general terms, storage of anthropogenic carbon within any ocean basin is given by the difference between box boundary transports and surface absorption. This is defined as correct in Álvarez et al. (2003), upon assumption that the following processes are compensatory: riverine input, production of organic carbon, burial into sediments and dissolution or burial of calcium carbonate in the sediments (Sarmiento et al., 1995; Stoll et al., 1996; Holfort and Siedler, 2001; Rosón et al., 2003).

In this inverse box model, diapycnal and air-sea induced diapycnal transfer results in zero net C^{ant} for the full depth C^{ant} budget (Figure 6.53). Geostrophic and Ekman effects therefore create the following equation:

$$\text{Storage} = F_{air-sea} + T_N + T_W + T_E \tag{6.40}$$

for the average air-sea CO_2 flux $F_{air-sea}$ and transports T_N, T_W and T_E across the northern, western and eastern boundaries of the inverse box. For C^{ant}, storage is represented by the temporal increase of C^{ant} throughout the water column, or mathematically by:

$$\text{Storage rate} = \frac{\mathrm{d}\int \mathrm{C}_{\mathrm{z}}^{\mathrm{ant}}\mathrm{dz}}{\mathrm{dt}} \tag{6.41}$$

where t is time and $\int \mathrm{C}_{\mathrm{z}}^{\mathrm{ant}}\mathrm{dz}$ is the accumulation of each anthropogenic CO_2 estimate at each depth level z (Álvarez et al., 2003). As datasets of high spatial resolution of DIC measurements are generally sparse, particularly in the Southern Ocean, an approximation for the magnitude of the anthropogenic CO_2 storage is calculated from the mean penetration depth (MPD) from Broecker et al. (1979):

$$\mathrm{MPD} = \frac{\int \mathrm{C}_{\mathrm{z}}^{\mathrm{ant}}\mathrm{dz}}{\mathrm{C}_{\mathrm{ml}}^{\mathrm{ant}}} \tag{6.42}$$

where C_z^{ant} and C_{ml}^{ant} are anthropogenic CO_2 estimates at depth, z and within the mixed layer, respectively. MPD is therefore the C^{ant} column inventory divided by C^{ant} from the mixed layer, and always yields a depth which is shallower than the actual depth to which the tracer penetrates (Peacock, 2004). Rearranging equation 6.42 and finding the temporal derivative gives an estimate of the anthropogenic CO_2 storage rate of equation 6.41 following Álvarez et al. (2003):

$$\text{Storage rate} = \frac{\mathrm{d}\int C_z^{ant}\mathrm{dz}}{\mathrm{dt}} = \text{MPD} \times \frac{\mathrm{d}C_{ml}^{ant}}{\mathrm{dt}} \tag{6.43}$$

where MPD is assumed to give a constant vertical profile with time, following the estimate by Gammon et al. (1982) that a conservative tracer requires $3 \times$ t years to reach a transient steady state. t therefore refers to the time since the influence of the industrial revolution ($\sim 1750 - 1800$) on the ocean.

In this study, the difference in C^{ant} between hydrographic occupations is the focus of Chapters 4 and 5, and the reader is urged to review these Chapters for clarity. In this study, $\triangle C_{ml}^{ant}$ is calculated using hydrographic sections only at the eastern and western boundaries of the inverse box by calculating the mean C^{ant} within the mixed layer for each occupation and finding the difference. The lack of DIC measurements at the northern boundary increases storage uncertainty. Using nomenclature from Chapter 5, storage rate is re-written as:

$$\text{Storage rate} = \text{MPD} \times \triangle C_{ml}^{ant} \times \rho_{ml} \tag{6.44}$$

where ρ_{ml} is the in-situ density within the mixed layer yielding storage rate with units of $\mathrm{mol\,m^{-2}\,yr^{-1}}$. Storage rate is therefore calculated using MPD estimates from Drake Passage and 30°E multiplied by the mean rate of C^{ant} increase in the mixed layer (Table 6.24). As listed in Table 6.24, MPD from Drake Passage and 30°E are notably shallower than 770m for the region between 10°S and 30°S (Holfort et al., 1998), and 790m at 24.5°N (Rosón et al., 2003).

Storage rates of $0.15\pm0.20\mathrm{mol\,m^{-2}\,yr^{-1}}$ along Drake Passage and $0.98\pm0.61\mathrm{mol\,m^{-2}\,yr^{-1}}$ along 30°E are comparable with previous South Atlantic estimates for storage rate (Table 6.25) and have been reviewed by Ríos et al. (2012) and Khatiwala et al. (2012). The Drake Passage estimate is the lowest storage rate, and reflects a shallower MPD and lower $\triangle C_{ml}^{ant}$ estimate within the Southern Ocean. In comparison, 30°E contains a greater proportion of subpolar and subtropical water, and thus has a storage rate that is within uncertainty of previous South Atlantic estimates.

For the South Atlantic box, the mean storage rate for Drake Passage and 30°E

	MPD (m) (Corrected)	MPD (m) (Uncorrected)	$\triangle C_{ml}^{ant}$ (μmol kg^{-1} yr^{-1})	ρ_{ml} (kg m^{-3})
Drake Passage	268.8		0.54	1027.0
30°E	624.3	653.3	1.52	1026.2
Mean	446.6	461.0	1.03	1026.6

Table 6.24: Mean Penetration Depth (MPD), mean $\triangle C_{ml}^{ant}$ (μmol kg^{-1}) within mixed layer and mean in-situ density ρ_{ml} (kg m^{-3}) within mixed layer for Drake Passage, 30°E, and a mean of both hydrographic sections. MPD is estimated to have a 20% uncertainty (Holfort et al., 1998), and a $\pm 0.5\mu$mol kg^{-1} $\triangle C_{ml}^{ant}$ uncertainty.

a)

Author	Storage rate (mol m^{-2} yr^{-1})
Murata et al. (2008)	0.6±0.1
Peng and Wanninkhof (2010)	0.83/0.35±0.3
Wanninkhof et al. (2010)	0.76
Ríos et al. (2012)	0.92±0.13
This study: Drake Passage	0.15±0.20
This study: 30°E (corrected)	0.98±0.61
This study: Mean (corrected)	0.47±0.29
This study: 30°E (uncorrected)	1.02±0.61
This study: Mean (uncorrected)	0.49±0.30

b)

	C^{ant} Transport (corrected) (Mmol s^{-1})	C^{ant} Transport (uncorrected) (Mmol s^{-1})
Drake Passage	2.07±0.84	
24°S	-0.70±0.41	
30°E: Agulhas	-0.20±0.18	-0.52±0.50
30°E: ACC	-2.72±1.11	-4.03±1.64
Total	-1.55±1.46	-3.18±1.92

Table 6.25: a) Comparison of C^{ant} storage rate (mol m^{-2} yr^{-1}) for the South Atlantic, and South Atlantic sector of the Southern Ocean (south of 15°S). b) C^{ant} transports at the box boundary in Mmol s^{-1} applying both the corrected and uncorrected $\triangle C^*$ C^{ant} distribution across 30°E. Uncertainties are calculated using the aposteriori volume transports and associated uncertainties and a C^{ant} uncertainty of 40% relative to a sectionwide C^{ant} area-weighted mean.

(Table 6.25) is integrated over the ocean surface area, estimated as $\sim 3.3 \times 10^{13} m^2$, yielding a basinwide C^{ant} storage of $0.47 Mmol\,s^{-1}$ ($0.19 \pm 0.12 PgC\,yr^{-1}$). The following C^{ant} storage is reported in $PgC\,yr^{-1}$ for ease of comparison with published values. The accuracy of basinwide C^{ant} storage is limited by the lack of a $\triangle C^{ant}_{ml}$ estimate at 24°S, however is comparable in magnitude to the estimate of $0.09 PgC\,yr^{-1}$ for the Atlantic between 31°S and 44°S, scaled to 1995 (Mikaloff Fletcher et al., 2006). Given an assumed basinwide increase in C^{ant} storage between 1995 and 2008-2009, and a 2008-2009 estimate of $\sim 0.19 PgC\,yr^{-1}$ south of 24°S, the region south of 44°S closer to the Antarctic continent is therefore hypothesised to store a maximum of $0.10 PgC\,yr^{-1}$. This estimate reflects one-third of the Southern Ocean-wide storage, south of 44°S, found in Gruber et al. (2009) of $0.32 \pm 0.23 PgC\,yr^{-1}$, and reflects the indirect calculation in this study, and limited dataset.

C^{ant} storage in addition to divergent fluxes at the box boundary (Figure 6.54) require a $0.79 \pm 0.58 PgC\,yr^{-1}$ ($2.04 \pm 1.50 Mmol\,s^{-1}$) air-sea input flux for the corrected C^{ant}. This is an upper bound on air-sea input flux for the South Atlantic, and far greater than the $0.19 PgC\,yr^{-1}$ implied for the ACC regime in section 6.6.1. It is also large in comparison to the estimated global CO_2 uptake of $2.2 \pm 0.25 PgC\,yr^{-1}$ (Mikaloff Fletcher et al., 2006), and more generally $\sim 2 PgC\,yr^{-1}$ from a range of oceanic and atmospheric observations, and ocean biogeochemistry models (Gruber et al. (2009); their Table 1). The requirement for a large air-sea input flux is primarily caused by the difference in C^{ant} fluxes at Drake Passage and 30°E. As observed for the C^{ant} distributions (Figures 5.13 and 5.23b) and the transport-weighted C^{ant} at the ACC fronts in section 6.5.4.3, Drake Passage deep ocean estimates are typically in the 0-10$\mu mol\,kg^{-1}$ range, compared to the 10-20$\mu mol\,kg^{-1}$ range at 30°E. The uncorrected C^{ant} from Figure 5.13 thus requires a $1.41 \pm 0.75 PgC\,yr^{-1}$ ($3.62 \pm 1.92 Mmol\,s^{-1}$) air-sea input flux, even further in excess of that implied from literature estimates. If, as part of a thought experiment, the difference between the C^{ant} air-sea flux within the ACC regime is assumed equal to $0.19 PgC\,yr^{-1}$ (Table 6.23), the required air-sea input flux to satisfy C^{ant} fluxes across the Agulhas and 24°S, and the C^{ant} storage reduces to $0.54 PgC\,yr^{-1}$, and therefore $0.73 PgC\,yr^{-1}$ of total air-sea input flux.

For an annual mean, Mikaloff Fletcher et al. (2006), and further analysed by Gruber et al. (2009), the Southern Ocean is the largest sink region of C^{ant} ($\sim > 0.70 PgC\,yr^{-1}$) with the South Atlantic between 18°S-44°S contributing a $\sim 0.1 PgC\,yr^{-1}$ C^{ant} uptake. C^{ant} air-sea input flux calculated from the divergent fluxes in this study, is only consistent with previous studies by Mikaloff Fletcher et al. (2006) and Gruber et al. (2009), if it is assumed that the Indian and Pacific sectors of the Southern Ocean are a net

source of C^{ant} to the atmosphere through reventilation (Sallée et al., 2012).

For fluxes at the box boundary, northward C^{ant} flux across 24°S, as discussed earlier is similar to previous estimates (Holfort et al., 1998; Macdonald et al., 2003; Mikaloff Fletcher et al., 2006). Therefore, the excess divergence found in this study is hypothesised as caused by excess outflow across 30°E, linked to the $\triangle C^*$ C^{ant} distribution (Figure 5.19a), and supported by the large adjustment found by correcting the deep ocean C^{ant} between the PF and STF for natural variability. The PF to STF is particularly vulnerable to C^{ant} anomalies given the large volume transports associated with each ACC front and hydrographic zone (Table 6.20). Khatiwala et al. (2012) describe a key difference between the 'ocean inversion' method for Ocean General Circulation Models (OGCMs), first applied in Gloor et al. (2003) and later in further depth in Mikaloff Fletcher et al. (2006, 2007); Gruber et al. (2009), Khatiwala et al. (2012), and C^{ant} flux estimates from ship transects. Hydrographic occupations are accurate for a single point in time, whilst the OGCMs method represent a transport integrated in time since the industrial revolution, and typically scaled to any selected year (e.g. 1995 in Mikaloff Fletcher et al. (2006)). Additionally, seasonal variability affects hydrographic fluxes (Wilkin et al., 1995) with Lachkar et al. (2009) suggesting that subtropical South Atlantic seasonal variability represents up to 20% of the annual mean transport of C^{ant}. The inverse model in this study, acts to create an 2008-2009 ocean mean such that the calculated divergence within the ACC is accurate at that time period, however, oceanic divergence, and hence the inferred air-sea input flux may differ from a transport integrated in time since the industrial revolution.

6.6.3 South Atlantic schematic circulation

The schematic circulation of geostrophic flow within the South Atlantic, for comparison to Rintoul (1991) is shown in Figure 6.55, firstly for upper ocean water masses, and secondly for deep ocean water masses. Conversion of AAIW to surface and SAMW occurs between Drake Passage and the ACC regime along 30°E. For LCDW, the increase between Drake Passage and 30°E is offset by the inflow of AABW, as part of the Weddell Gyre southern limb and Antarctic Slope Current. As there is no comparative AABW outflow within the box, the majority of the AABW upwells to lighter water masses, and this upwelled AABW is responsible for the increased LCDW transport across 30°E. These results support the observation by Rintoul (1991) that the South Atlantic box is a net formation region for deep water. However these results also suggest that the upwelling of AABW into Circumpolar Deep Water density classes is more significant than the intermediate to deep water conversion.

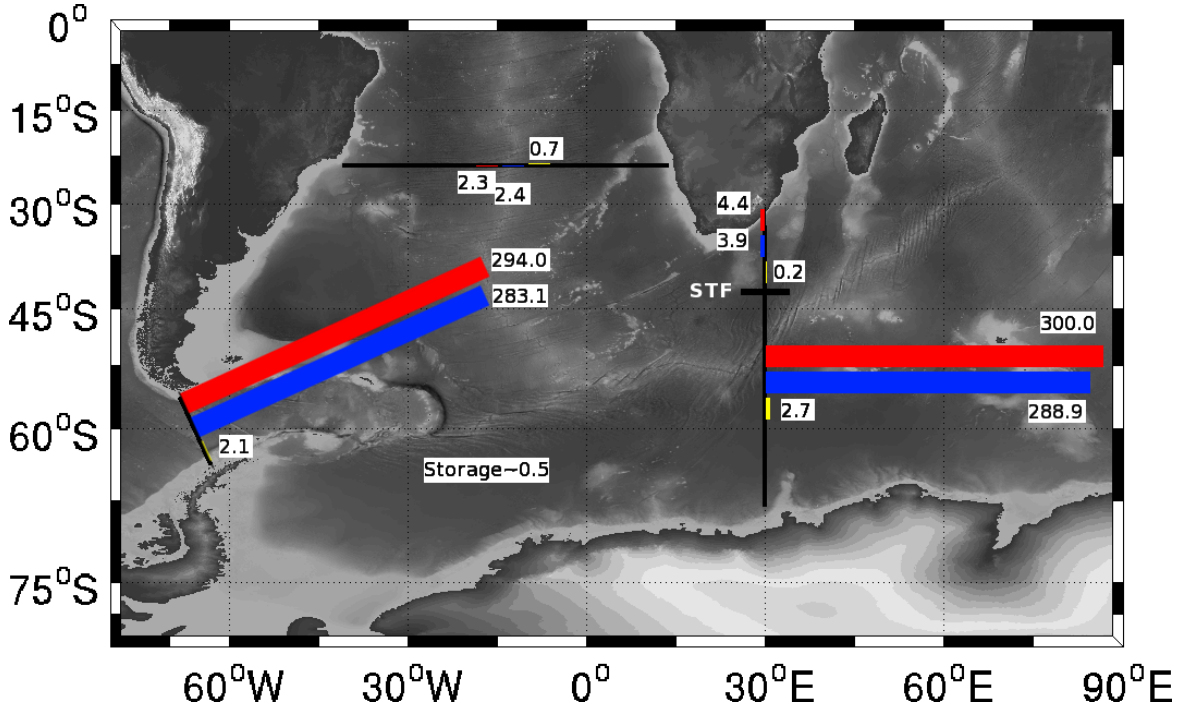

Figure 6.54: Schematic circulation for each component of carbon circulation within the inverse model solution: DIC (red), natural DIC (blue) and C^{ant} (yellow). The length of each bar is proportional to the net transport associated with each water mass. Numbers at the end of each bar give transports in $\mathrm{Mmol\,s^{-1}}$. C^{ant} bars are much shorter than either DIC or natural DIC, with the location of the number at the end of each bar, also indicating the direction of the flow. The interior storage term is also marked in $\mathrm{Mmol\,s^{-1}}$.

Within the subtropics, surface and SAMW inflows through the Agulhas regime are the major contribution of the warm water path to northward flow across 24°S. Agulhas upper water enters the South Atlantic and is entrained by the South Atlantic Current as it turns northwards at the African continent to form the Benguela Current. Transition of the Benguela Current from a boundary current to zonal flow towards the Brazilian coast is the pathway for Agulhas-sourced upper ocean water to cross northwards across 24°S. For deep water masses, southward flow across 24°S has a number of potential exit points. Approximately one-third of southward-flowing deep water exits within the Agulhas regime. The remainder flows into the Southern Ocean and contributes to both Circumpolar Deep Water, and the southern limb of the Meridional Overturning Circulation.

From Figure 6.56, the boxwide pathway of NADW can be hypothesised. If it is assumed that the Drake Passage inflow of water within the NADW density class traverses the ACC largely uninterrupted, a net 5.8Sv gain of NADW is from the 24°S southward flow. This gives a 7.8Sv flow across 30°E, out of the inflow of 15.3Sv across 24°S. Therefore, 7.5Sv of NADW is suggested to be upwelled to lighter water masses through a combination of diapycnal fluxes and air-sea induced diapycnal fluxes. This broadly matches the estimate of air-sea induced diapycnal fluxes of 7.3Sv from Figure 6.48 for NADW (layers 16, 17).

The inverse model of the South Atlantic of Rintoul (1991), categorised the layers by potential density into surface, intermediate, deep and bottom water masses. To best show the differences between this model and Rintoul's standard model, the inverse model applied in this study was re-run using the potential density (σ) isopycnals chosen by Rintoul to create 13 model layers. Therefore in this following section, surface is defined by layers 1-2, intermediate by layers 3-6, deep by layers 7-11, and bottom by layers 12-13. The intermediate water mass convergence within the Southern Ocean, as observed in Rintoul, is also observed in this study despite a greater intermediate transport exiting within the ACC regime along 30°E. This is caused by a larger inflow of intermediate water within the Agulhas regime. Greater net eastward flow of surface water in this study within the Agulhas regime is the most surprising feature and is caused by the $\sigma_0 = 26.80$ isopycnal deepening towards the south of the Agulhas regime and capturing a greater proportion of the Agulhas Return Current eastward flow. Eastward surface flow is compensated by westward intermediate water, leading to a net 5.4Sv westward flow. The net westward flow of bottom water across 30°E is thought to better represent the eastern closure of the Weddell Gyre, and the Antarctic Slope Current. It should be noted that this study includes diapycnal and air-sea interaction terms, which

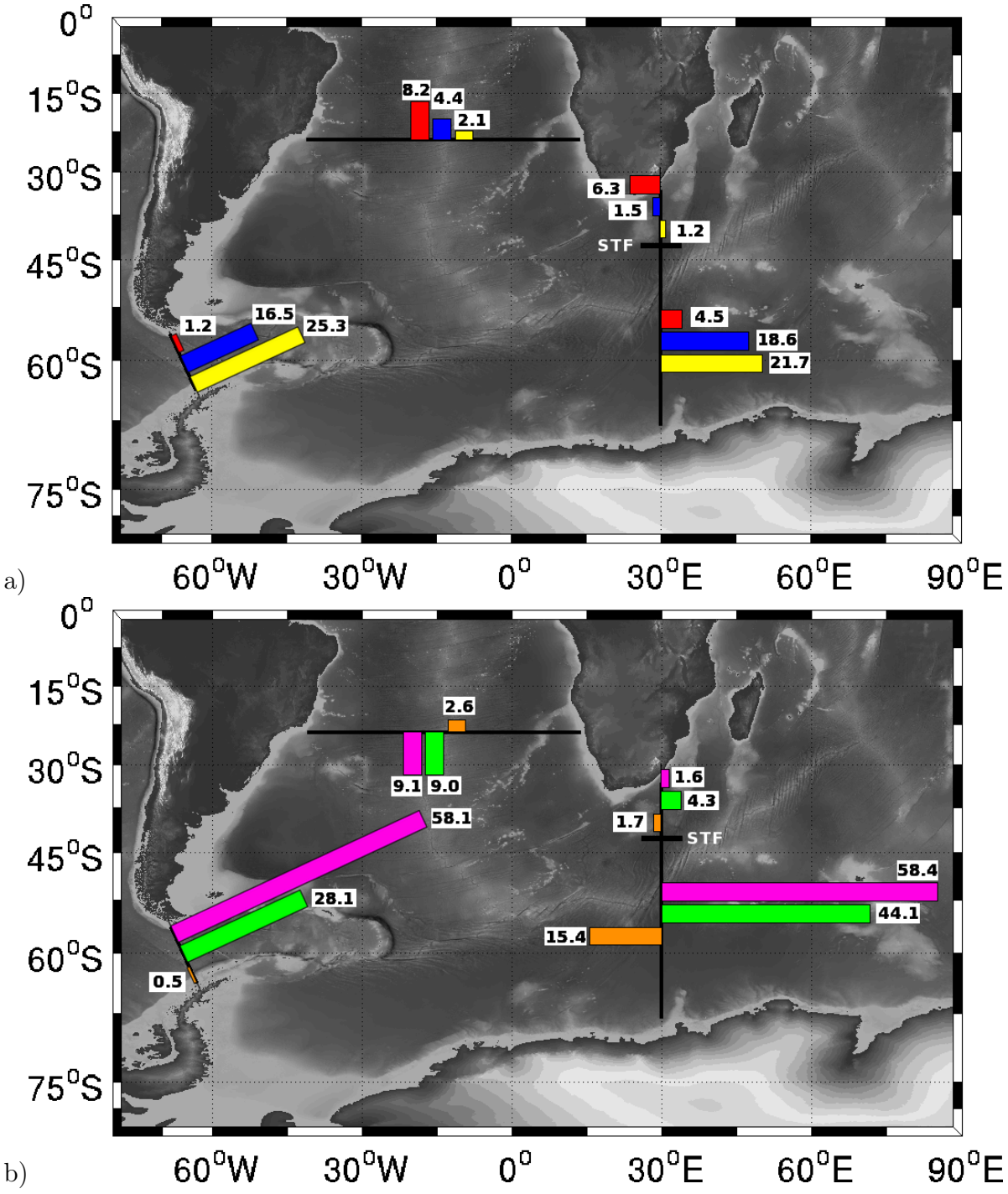

Figure 6.55: Schematic circulation for the inverse model solution. The length of each bar is proportional to the net transport associated with each water mass. Water masses shown are a) surface water (red), SAMW (blue), and AAIW (yellow) and b) UCDW (pink), LCDW (green) and AABW (orange). Numbers at the end of each bar give transports in Sv.

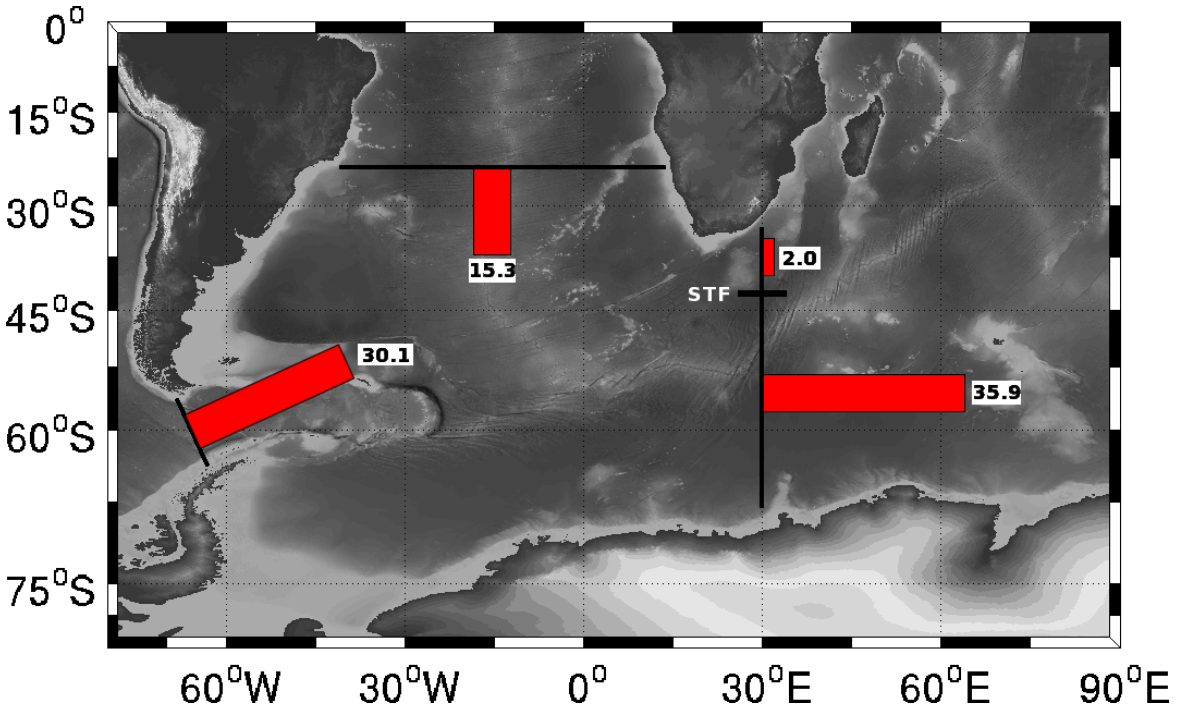

Figure 6.56: Schematic circulation for NADW from the inverse model solution. The length of each bar is proportional to the net transport. Numbers at the end of each bar give transports in Sv.

are significant for bottom water.

A major result from Rintoul's work was the apparent convergence of intermediate water, and divergence of deep water and bottom water. Both findings for intermediate and deep water are in agreement with this study. However, this study supports the conversion of intermediate water to both surface and deep water, whilst also supporting the conversion of bottom water to deep water, with diapycnal fluxes playing a significant role in this observation. Rintoul's further major result regarding the cold vs. warm pathway is discussed in the following section.

6.6.4 Cold versus warm water path

Gordon (1986) hypothesised that the southward NADW flow in the Atlantic is compensated by warm Indian Ocean thermocline water south of Africa. This study finds an Agulhas leakage above the 3.5°C isotherm of 10.7Sv (constrained to 9Sv). Therefore, contrasting with the findings of Rintoul (1991), this study finds a reasonable circulation pattern with the inclusion of a westward flux of warm water (>3.5°C), comparable with the 13Sv estimate of Gordon (1985). Rintoul (1991) suggests that the AAIW from Drake Passage is converted to surface water within the South Atlantic, and is the dom-

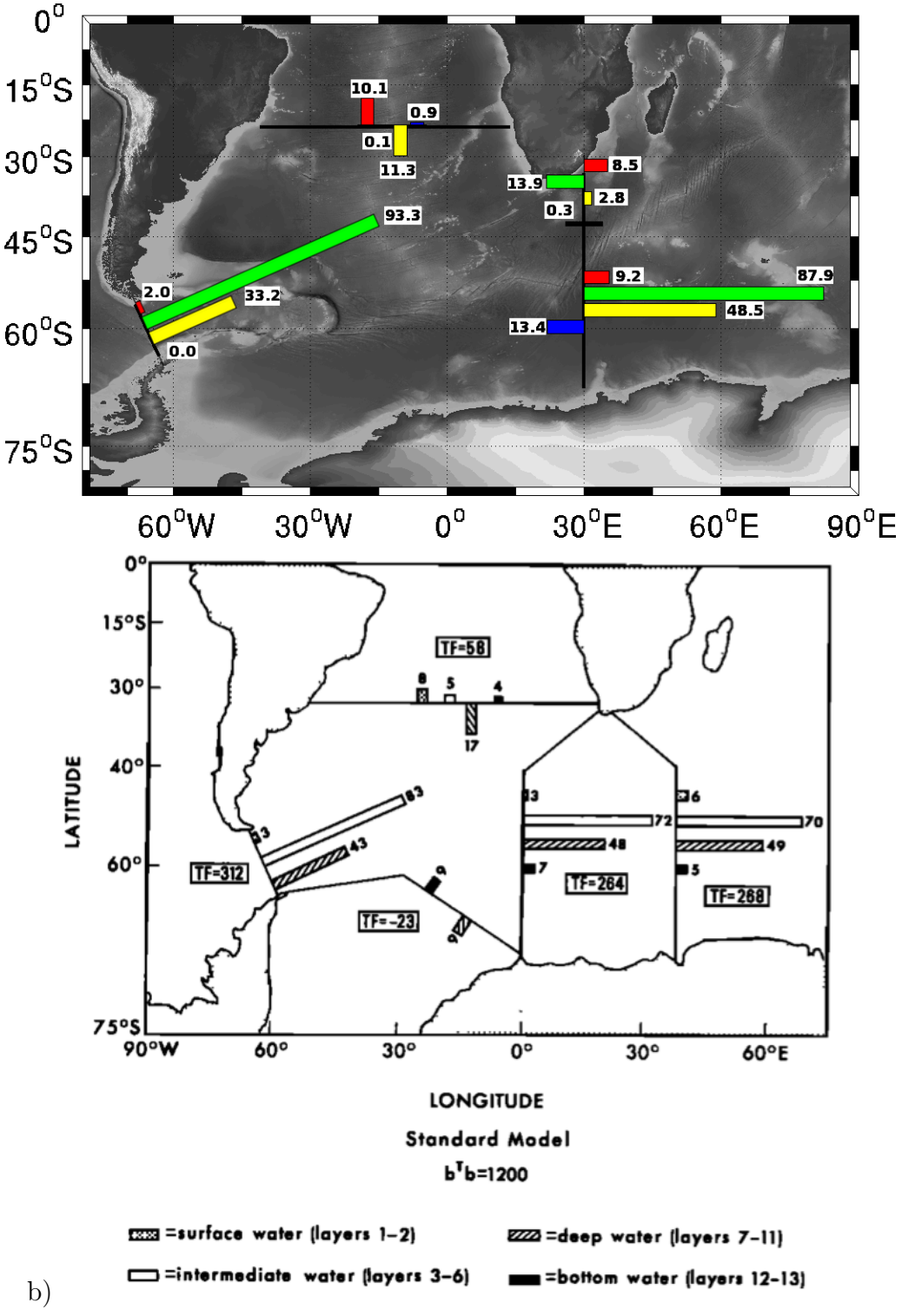

Figure 6.57: a) Schematic circulation for the inverse model solution using potential density water mass definitions to match Rintoul (1991). The length of each bar is proportional to the net transport associated with each water mass. Water masses shown are a) surface water (red), intermediate (green), deep (yellow) and bottom (blue). Numbers at the end of each bar give transports in Sv. b) Schematic circulation from Rintoul (1991) for the South Atlantic. The length of each bar is proportional to the net transport associated with each water mass. Numbers at the end of each bar give transports in Sv.

inant source of 24°S thermocline water, with 25.3Sv of AAIW found at Drake Passage in this study.

In this study, the net northward flow of upper ocean water is split between the surface water (8.2Sv), SAMW (4.4Sv) and AAIW (2.1Sv) with higher surface transport, suggesting a preference for warm water path involvement. Upper ocean flow is influenced by the mean value of the Benguela Current (∼13Sv, Garzoli et al. (1997)) with Garzoli and Matano (2011) suggesting that the source waters of this current can switch between cold-path dominated and warm-path dominated (section 1.2.4.9). Westward flow of the Agulhas Current is largely concentrated within the surface layer with some of this flow contributing to the Benguela Current, and thus the northward flow across 24°S. The decrease in surface water transport between the Agulhas regime and 24°S is partially attributed to the southward flowing Ekman transport.

The increase in the northward flow of SAMW and AAIW across 24°S compared to the westward flow of SAMW and AAIW across the Agulhas regime, indicates the cold water path with AAIW to SAMW conversion observed for air-sea interaction processes (Figure 6.48). As significant upwelling into the surface water mass is not observed from either diapycnal or air-sea interactions, it is unlikely that the inflow through Drake Passage is able to generate enough surface water. The results from this study therefore suggest a contribution from both warm and cold water paths with the surface waters dominated by inflow through the Agulhas regime. AAIW is dominated by a northward flow of SAMW and AAIW from Drake Passage via the BMC and South Atlantic Current, whilst SAMW is dominated by a combination of both paths.

6.6.5 Overturning freshwater transport (M_{ov})

Negative M_{ov} found in this study implies the overturning freshwater is exported from the North Atlantic into the South Atlantic Ocean, whilst salt is imported by the North Atlantic. The current set-up implies that freshwater transport acts to inhibit the thermally-driven MOC (Rahmstorf, 1996). A large freshwater perturbation by changes in the hydrological cycle or an increase in ice loss by, for example, melting of the Greenland Ice Sheet therefore could theoretically imply that the high latitude North Atlantic surface water could become too fresh to form NADW (section 1.2.3.5), and therefore cause MOC collapse.

The vertical M_{ov} profile in Figure 6.26a) suggests that the sign of M_{ov} is heavily dependent on the upper 450dbar, and therefore the northward flow of salty upper ocean water. A change of sign of M_{ov} could therefore be facilitated by either a freshening of the upper 450dbar, or an increase in the northward velocity, and therefore the northward

volume transport. Figure 6.58 shows the changes in M_{ov} profile for four experiments. Firstly, the salinity within the upper 450dbar is uniformly freshened until a 0.36psu freshening causes the sign of M_{ov} to reverse. Secondly, the salinity within the upper 300dbar, west of 35°W capturing the Brazil Current, is uniformly freshened with a 5psu freshening required for M_{ov} to reverse sign. Thirdly, a uniform volume transport is added to each datapoint above 450dbar sectionwide. An additional 4.6Sv of northward upper 450dbar transport is therefore required to force M_{ov} into a stable state. Fourthly, a uniform volume transport is added to each datapoint above 300dbar, west of 35°W, and therefore represents an adjustment to the Brazil Current. A 3.2Sv northward adjustment to the Brazil Current therefore reverses the sign of M_{ov}, and reduces the Brazil Current transport to 2.6Sv of southward flow. The uniform 5psu freshening of the Brazil Current required to reverse M_{ov} is unphysical. Given that the Brazil Current transport in this study is in agreement with Bryden et al. (2011) and Garzoli et al. (2013), only a lower bound estimate of the Brazil Current could correspond to a reversal of the M_{ov}, and hence, supports that M_{ov} is generally in a bistable state.

The response of M_{az} to these perturbations shows that sectionwide adjustments cause only minor adjustments to M_{az}. For the decrease in Brazil Current transports, M_{az} has responded by increasing the northward freshwater transport associated with the gyre. The Brazil Current salinity adjustment of 5psu within the upper 300dbar, west of 35°W, has caused a reversal in the direction of the subtropical gyre.

These model experiments are suggestive of the forcing that would be necessary for M_{ov} to indicate stable MOC, and confirms that M_{ov} is predominately negative, and supportive of MOC bistability. In reality, a blend of, for example, Brazil Current southward transport reduction and freshening could occur, but these experiments give an impression of the magnitude of the changes required within the upper 300/450dbar. The pattern of M_{az} response can therefore be extrapolated from Figure 6.58b) to the condition of increased M_{ov} through a freshwater perturbation in the North Atlantic. Sectionwide upper 450dbar adjustments cause only, a small M_{az} perturbation across the section. Increased Brazil Current southward transport would reduce M_{az}, whilst a salinification of the Brazil Current would likely cause a substantial increase in the northward M_{az} freshwater transport associated with the subtropical gyre supported by the numerical model results of Cimatoribus et al. (2012). This study calculated from in situ hydrographic observations in this study compares with previous studies reviewing M_{ov} stability from numerical model simulations e.g. Huisman et al. (2010); Drijfhout et al. (2011); Cimatoribus et al. (2012).

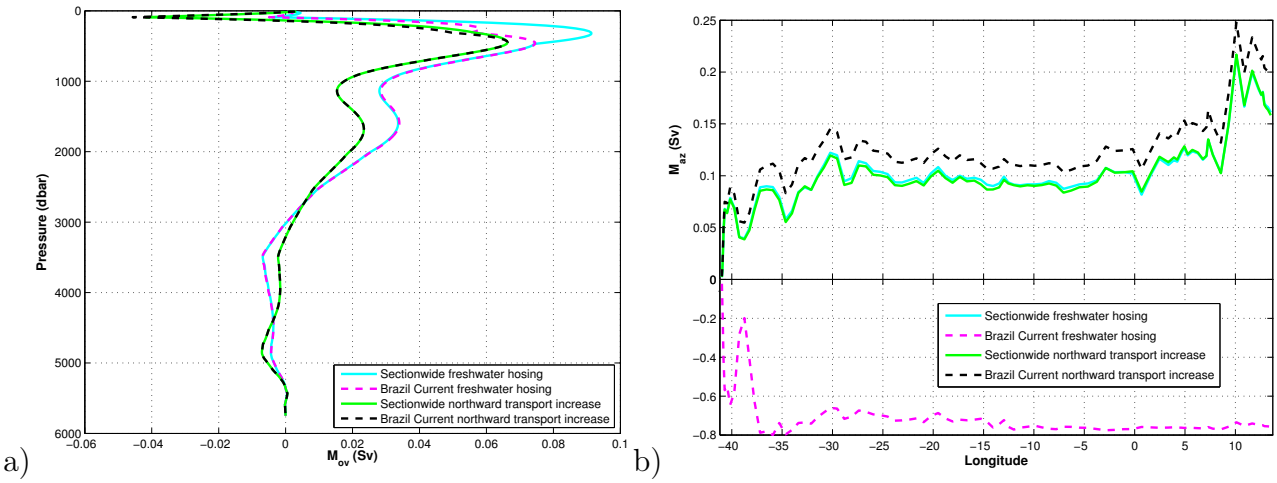

Figure 6.58: a) Cumulative vertical profile of M_{ov} for 1) sectionwide freshening of 0.36psu in the upper 450dbar, 2) freshening of 5psu in the upper 300dbar, west of 35°W, 3) sectionwide northward transport of 4.6Sv in the upper 450dbar and 4) northward transport of 3.2Sv in the upper 300dbar, west of 35°W. b) Cumulative zonal profile of M_{az} for experiments: 1), 2), 3) and 4).

6.6.6 Seasonal bias

Hydrographic sections in this study occurred in 2008/2009 austral summer, and as such the diagnosed fluxes are best representative of that time period. Variations in the large scale circulation across the ACC is partially dependent on the time periods of larger scale climatic variations (e.g. SAM/ENSO (Sallée et al., 2008)). Seasonality of SAM/ENSO is shown by Woodworth et al. (2004) to affect the bottom pressure and the ACC transport. However, the most direct effect of seasonality is the variation to temperature. A time series of transport estimates through Drake Passage (Meredith et al., 2011b, their Figure 11) demonstrates the variability in the transport-weighted mean temperature through Drake Passage. Their non-seasonally adjusted transport-weighted mean potential temperature for the 2009 Drake Passage occupation is consistent with the 2.55±0.01°C estimate for Drake Passage in this study (Table 6.8), whilst this is notably warmer in comparison to November-December hydrographic cruise occupations. A seasonal cycle of warming, primarily of the upper ocean, is therefore apparent through the austral summer. The month of the cruise is therefore significant for a consistent temperature and salinity comparison at the South Atlantic boundaries with the hydrographic sections in this study primarily occurring between February and early April.

Additionally, certain features included within the circulation show a seasonal cycle, for example AABW formation within the Weddell Sea, at Cape Darnley polynya or at

Prydz Bay (Fukamachi et al., 2000), which is more intense during the winter months. AABW production, as estimated by Williams et al. (2010b) off the coast of Adelie land, peaks in October whilst a warming and freshening causes a reduction during the summer months. During the austral summer months, there would therefore be a reduction in the potential for absorption of heat, freshwater or C^{ant} from the atmosphere, and penetration into the deep ocean.

At 30°E, the implications of a seasonal cycle of AABW formation east of 30°E, on AABW volume transport into the Weddell Sea are uncertain. Meredith et al. (2000) estimate that the apparent age for deep water within the Southern limb of the Weddell Gyre to be 18 years, and hence any temporal variations in production would be assumed to have been smoothed into the mean flow, with the 8.8Sv westward contribution of AABW to the Weddell Gyre southern limb, potentially comprised of water with an apparent age of ∼7 years, if Meredith et al. (2000)'s estimate is scaled to account for the reduced distance. Within the Weddell Sea, AABW production is hypothesised to lessen in austral summer, linked to surface wind forcing and larger scale climatic variations (Jullion et al., 2010b; Wang et al., 2012).

Greater sea ice coverage in austral winter would also have significant implications for the local freshwater budget, with the sea ice melt contributing significantly to a freshwater input at the end of the austral winter (Ren et al., 2011). An inverse box model using wintertime hydrographic sections would therefore have to include a sea ice term to account for this effect. However, given that a significant portion of the Weddell Sea, extending north of 60°S, is covered by sea ice during the wintertime, the total surface area for exchange of heat and C^{ant} would also decrease (Ren et al., 2011). Therefore in wintertime, saltier surface waters follows brine rejection, whilst reduced ocean surface area for heat and C^{ant} uptake, is offset by more active AABW formation.

One-time hydrographic sections are inherently attached with an uncertainty for comparison to a seasonal or annual mean, however, within the framework of the inverse box model, this is partially accounted for by the choice of hydrographic constraints. Air-sea fluxes are also chosen to coincide seasonally with the hydrographic sections. Therefore, this study is best representative of the South Atlantic circulation during austral summer.

6.6.7 Questions and future work

This work has provided a detailed analysis of the South Atlantic Ocean, inspired by the work of Rintoul (1991), and seeks to provide an updated model with DIC and C^{ant} included. The key findings in the model include:

- The observation of a significant 15.9Sv of westward Weddell Gyre return flow at 30°E linked to recent observations of substantial AABW formation within the Cape Darnley polynya (Ohshima et al., 2013).
- A Meridional Overturning Circulation of 20.2Sv with a net mass transport of 0.7±0.3Sv southward and M_{ov} of -0.09Sv (southward) across 24°S.
- An Agulhas leakage of 10.7±1.7Sv with a total eastward transport of Circumpolar Deep Water of 5.9±2.2Sv beneath the Agulhas Current system, north of the Subtropical Front.
- C^{ant} divergence within the South Atlantic box of -1.55±1.46Mmol s^{-1} caused by a C^{ant} air-sea uptake of 2.04±1.50Mmol s^{-1} (0.79±0.58PgC yr^{-1}).
- The shared influence of the cold and warm water path, through Agulhas-sourced surface water and Drake Passage-sourced AAIW.

This study has raised questions regarding the meridional variability of the overturning estimate. The RAPID project (http://www.noc.soton.ac.uk/rapidmoc/) has produced high-density overturning estimates in the North Atlantic at 24°N, however, the applicability of these estimates to other regions and, in particular the South Atlantic is reliant on the estimates from snapshot hydrographic cruises (e.g. Dong et al. (2009)). The implication of a South Atlantic monitoring system as advocated in Garzoli and Matano (2011), is to generate a more cohesive observational network across the Atlantic basin. Specific regions of interest include the Brazil Current, and particularly the meridional variability of the Brazil Current, and the zonal extent of the current particularly as the South Atlantic Current reaches the Brazilian coast, and bifurcates into the Brazil Current and the North Brazil Current. Further questions along 24°S regard the magnitude of the intermediate waters, which is significant for understanding the trade-off between the cold and warm pathways, and the sign of the M_{ov} transport, taken as an indicator of MOC stability.

Along 30°E, questions from the Agulhas regime including the magnitude of the eastward flow of deep water remain. The significance of this route as an escape path out of the South Atlantic from the Cape Basin is a topic of current research (van Sebille et al., 2012). Within the ACC regime, the strong, westward flow of AABW suggests both a net consumption of AABW within the South Atlantic box, and the existence of a strong source of AABW to the west of the South Atlantic box.

Improved diapycnal estimates for the initial field is also an area of possible improvement, with significant diapycnal fluxes especially within the bottom waters. This

is achievable through the continued improvement in hydrographic measurements both spatially and temporally, with the current DIMES (Diapycnal and Isopycnal Mixing Experiment in the Southern ocean) project seeking to address these issues using a range of floats, microstructure profiles, hydrographic observations and model output (Gille et al., 2007). The air-sea interactions have been shown to be significant in this study. The continued refinement of climatological data through longer time series, more reliable instruments and improved diagnostics will help produce more accurate estimates.

The conclusion of this future work, therefore relies on the necessity for the availability of continued observational data with improved temporal and spatial resolution helping to characterise South Atlantic circulation.

Chapter 7

Conclusion

The preceding Chapters have illustrated a study of the South Atlantic Ocean, focussing both on large-scale circulation, and on circulation-dependent DIC accumulation. Inter-basin exchange between Atlantic, Pacific and Indian Oceans is governed by interaction of major oceanic systems, principally, ACC, MOC and the Agulhas system. Variation in any of these systems has potential for basinwide consequences (e.g. Biastoch et al. (2008); Laurian and Drijfhout (2010); Marshall and Speer (2012)). This study follows Rintoul (1991)'s inverse box model of the South Atlantic with updated hydrography and the inclusion of additional carbon parameters: DIC, C^{nat}, C^{ant}, and feeds into other large-scale inverse models e.g. Ganachaud and Wunsch (2000); Sloyan and Rintoul (2000, 2001a,b). Several smaller-scale studies have themselves fed into this study to help improve the solution, including studies nominally between 30°S and 45°S (McDonagh and King, 2005), Southwestern Atlantic (Jullion et al., 2010a), Southeastern Atlantic (Arhan et al., 2003; Mercier et al., 2003), Agulhas Current (Casal et al., 2009), Scotia Sea (Naveira Garabato et al., 2003), and northern Weddell Sea (Franco et al., 2007).

This study provides an estimate for the geostrophic circulation at the boundaries of the South Atlantic. The inverse model combines hydrography datasets, complimented by climatologies where appropriate, to create a representative large-scale circulation. Subsequent diagnosis of inflow and outflow is separated both into water masses: Surface, SAMW, AAIW, UCDW, LCDW and AABW and for focussing on significant features, such as the ACC fronts, or Agulhas Current. Full depth salinity conservation is applied, with excess volume transport interpreted as freshwater flux at the surface. Volume transport and transport-weighted salinity, temperature, DIC, C^{nat} and C^{ant} fluxes are calculated at each boundary with interior diapycnal mixing and air-sea induced diapycnal transformations included. The inclusion of DIC, natural DIC and

C^{ant} connects with the thorough analysis of DIC and C^{ant} distributions in Chapters 4 and 5, with no previous study calculating carbon fluxes associated with South Atlantic interbasin exchange.

This study also calculates the distribution of both DIC and C^{ant} at the boundaries of the South Atlantic. ΔC^{ant} is calculated using the available repeat hydrographic occupations across Drake Passage and along 30°E using three separate methods: ΔC^*, TrOCA and eMLR. ΔC^* and TrOCA are both variations of the back-calculation method that focuses on calculating a value for pre-industrial DIC. eMLR is an alternative method that calculates a regression equation for C^{ant} change using other ocean properties. The only published study calculating $\triangle C^{ant}$ distribution across Drake Passage is limited to Chen (1982) for the upper 1000dbar. Calculations of 30°E $\triangle C^{ant}$ follow detailed studies by Lo Monaco et al. (2005a,b).

7.1 Distribution changes of Dissolved Inorganic Carbon and Anthropogenic Carbon ($\triangle C^{ant}$)

Three methods are applied to unpick evidence for DIC change, prior to focussing on the anthropogenic component. The most intuitive method is by direct comparison of DIC fields from two hydrographic occupations. Upstream ventilation of SAMW/AAIW and recent ventilation of WW near the Antarctic continent contributes to SAMW DIC increases of 9.5±0.1/10.8±0.2μmol kg^{-1} decade^{-1} across Drake Passage and 30°E for occupations in 1990/2009 and 1996/2008, respectively. Across Drake Passage, deep ocean increases are generally limited to 0-5μmol kg^{-1}, providing far greater structure compared to the previous distribution of Chen (1982) for the upper 1000dbar whilst increases along 30°E (1996-2008) are more uniformly >5μmol kg^{-1}. Additional calculation of changes in DIC residuals also support upper ocean ventilation along both Drake Passage and 30°E for SAMW increases of 9.7±0.1/8.9±0.2μmol kg^{-1} decade^{-1}, respectively. In the deep ocean, AABW suggests significant increases along Drake Passage (1.5±0.5μmol kg^{-1} decade^{-1}), whilst 30°E yields a negative signal (-1.1±0.3μmol kg^{-1} decade^{-1}).

A third method calculates stoichiometries above and below mixed layer depth, separated into hydrographic zones. Nitrate to phosphate ratio ($R_{N:P}$) reflects the biological signal. In this study, $R_{N:P}$ is generally at or below the Redfield ratio (16:1), with a section minimum typically within the low productivity Antarctic Zone upper ocean, corresponding with high inorganic nutrient concentrations and preference for nitrate uptake

(Whitehouse et al., 1995). $\triangle C : \triangle N$ exceed the Redfield ratio (6.6:1) for the majority of hydrographic zones, with a sectionwide average DIC increase below the mixed layer of 20.2±4.2/29.3±19.7μmol kg^{-1} for Drake Passage and 30°E, respectively, despite apparent co-incident nitrate increases of 1.76±1.08μmol kg^{-1} and 1.01±0.96μmol kg^{-1}. Excess $\triangle C : \triangle N$ therefore supports DIC changes in excess of biologically supported variations, supportive of C^{ant} increase along both South Atlantic sections.

C^{ant} distributions are broadly supported by Chen (1982) and Lo Monaco et al. (2005a). Distributions from back-calculation (TrOCA, $\triangle C^*$) methods clearly support C^{ant} increase by ventilation and subduction of SAMW and AAIW, particularly upstream of Drake Passage, contributing towards a SAMW sectionwide increase of 5.0±0.1/4.4±0.1μmol kg^{-1} decade^{-1} (TrOCA, $\triangle C^*$) . Further subduction of upper water masses upstream of 30°E ventilates the upper ocean particularly north of the PF leading to a sectionwide increase of 10.8±0.2/9.1±0.1μmol kg^{-1} decade^{-1}. A deep water C^{ant} signal within the SAZ and PFZ, without an obvious pathway given the longer renewal rate expected for deep water masses, is hypothesised as a combination of a true C^{ant} signal and the northward protrusion of natural DIC, and underestimation of the C^{bio} contribution. Removal of the natural variability of this deep ocean signal for $\triangle C^*$ reduces the C^{ant} signal.

Regression-derived distributions are notably smooth compared to back-calculation methods with two 'corrected' versions of the distributions calculated. SAMW and AAIW subduction is supported as a direct ventilation pathway, in addition to $\triangle C^{ant}$>20 μmol kg^{-1} within the actively ventilated STZ surface water mass. Greatest similarity with the back-calculation distribution is for sectionwide correction across Drake Passage, and per zone correction along 30°E. The selected corrections support a sectionwide SAMW increase of 4.7±0.1/11.3±0.1μmol kg^{-1} decade^{-1} for Drake Passage and 30°E, respectively. Combining all $\triangle C^{ant}$ calculation methods, $\triangle C^{ant}$ increase for all water masses and all hydrographic zones, ranges between -1.0 and 26.9μmol kg^{-1} decade^{-1}, predominately decreasing with depth, reaching a sectionwide and all method AABW average of 0.7±0.4/1.4±0.2μmol kg^{-1} decade^{-1} at Drake Passage and 30°E, respectively.

7.2 Circulation in the South Atlantic and synthesis of DIC and Anthropogenic Carbon ($\triangle C^{ant}$) estimates

The inversion estimate for South Atlantic circulation enables the diagnosis of a range of solution components, including diapycnal and air-sea induced transformation processes. The ACC is dominated by CDW flow across both Drake Passage and 30°E, and represents ∼66% of the flow across each section respectively. However, meridional ACC distribution varies from 50.1Sv through Drake Passage PFZ to 111.2Sv at 30°E. Larger eastward flow of LCDW (44.1Sv) at 30°E is moderated by a westward flow of AABW (15.4Sv), partially comprised of Cape Darnley Bottom Water (Ohshima et al., 2013), and contributes to the Weddell Gyre southern limb, supported by Meijers et al. (2010), and acts to close the Weddell Gyre.

The MOC is clearly represented by UCDW and LCDW southward flux across 24°S, predominately caused by 15.3Sv of NADW. MOC strength calculated from a deep water estimate is 20.2Sv, within the range of previous estimates (Ganachaud, 1999; Holfort and Siedler, 2001; McDonagh and King, 2005; Dong et al., 2009), and corresponds with M_{ov} of -0.09Sv. The upper MOC limb contributes 14.8Sv to the northward return flow, separated between Surface (8.2Sv), SAMW (4.4Sv) and AAIW (2.1Sv). The lower MOC limb contributes a 2.6Sv northward flow of AABW limited to the Brazil Basin. Bottom water defined by <2°C contributes a 6.7±2.2Sv northward flow west of the Mid-Atlantic Ridge. Negative M_{ov}, in agreement with previous hydrographic occupations but in contradiction to model estimates, suggests that the MOC is bistable, and at risk of collapse due to an excess freshwater perturbation in the North Atlantic.

Recent Agulhas regime studies have increasingly linked the region with variability in the wider climate and ocean circulation (Beal et al., 2011). Upper ocean leakage generated from the residual of westward-flowing Agulhas Current and eastward-flowing Agulhas Return Current is estimated as 7.8Sv for Surface and SAMW. Agulhas leakage defined by >3.5°C of 10.7±1.7Sv is comparable with a 15Sv estimate using subsurface floats and surface drifters (Richardson, 2007). AAIW, UCDW and LCDW flow eastward toward the Indian Ocean, and support the deep Agulhas regime as an escape pathway for NADW (2.0Sv) from the Atlantic Ocean DWBC.

Northward heat transport of 0.40±0.08PW across 24°S is within the range of previous estimates (Piecuch and Ponte, 2012), and broadly similar to Rintoul (1991)'s 0.25±0.12PW inverse model estimate. As observed in Rintoul (1991), to support the northward meridional heat flux across 24°S, more heat enters the basin at Drake Passage than exits south of Africa. Temperature differences between Drake Passage and

the 30°E ACC regime contribute up to 0.21±0.02PW to the northward flow.

Within the ACC, transport-weighted DIC supports a 4.6μmol kg^{-1} increase between the western and eastern South Atlantic ACC boundaries, primarily caused by surface uptake. Following Sabine et al. (2004), the Southern Ocean is typically a net sink of C^{ant}, whilst also exporting C^{ant} to neighbouring basins, and is confirmed by a C^{ant} divergence of 1.55±1.46Mmol s^{-1} (0.60±0.57PgC yr^{-1}) and a C^{ant} storage of 0.49±0.31Mmol s^{-1} (0.19±0.12PgC yr^{-1}). The estimated requirement for 2.04±1.50Mmol s^{-1} (0.79±0.58 PgC yr^{-1}) of air-sea input flux is high, compared to global estimates for a ∼2PgC yr^{-1} uptake flux (Gruber et al. (2009); their Table 1). Although a separate estimate based on the transport-weighted $\triangle C^{ant}$, suggests a lower 0.48±0.04Mmol s^{-1} (0.18±0.02PgC yr^{-1}) uptake flux for the ACC regime only. $\triangle C^{ant}$ increases in this study have supported a decadal increase at 30°E, almost double that at Drake Passage, and suggests that in recent decades the South Atlantic has been an increasing sink. Differences may also reflect a possible combination of reventilation in the Indian and Pacific Southern Ocean sectors (Sallée et al., 2012), and the single point in time measurements of the hydrographic occupations (Khatiwala et al., 2012), in comparison to the time-integrated estimates of Mikaloff Fletcher et al. (2006), Mikaloff Fletcher et al. (2007) and Gruber et al. (2009).

7.2.1 South Atlantic modification of water masses

UCDW (7.2Sv), AAIW (0.3Sv) and AABW (13.8Sv) are consumed within the South Atlantic, whilst Surface (5.3Sv), SAMW (5.0Sv) and LCDW (11.3Sv) are produced. Upwelling of UCDW, south of the ACC (Sloyan and Rintoul, 2001b), forms surface/SAMW that subsequently subducts into the subsurface upon exiting the South Atlantic at 24°S. The lower limb of the MOC causes upwelling of LCDW, partially comprised of lower NADW to facilitate AABW formation. However, the net LCDW divergence and AABW convergence supports a secondary mechanism for AABW upwelling into the LCDW density class. Net AABW export from the Weddell Sea is estimated by Naveira Garabato et al. (2002b) and Kerr et al. (2012) as 9.7±3.7Sv and 10.6±3.1Sv ($\gamma^n > 28.26$ kg m^{-3}), respectively, and not calculated explicitly in this study. This study finds that the majority of AABW is upwelled within the South Atlantic basin with a significant 6.3Sv AABW to LCDW diapycnal flux.

Inclusion of diapycnal and air-sea transformation are significant for water mass modification predominately for LCDW and AABW. These water masses interact directly with the rough topography on the ocean floor to initiate vertical mixing (e.g. Naveira Garabato et al. (2004)). In contrast, air-sea induced transformations are strongest within the upper ocean given the greater surface area for interaction. The effect of air-

sea transformation on the deep ocean is summarised as the ∼15.2Sv divergence of UCDW and LCDW.

7.2.2 Warm/Cold water pathways

Many studies have followed the work of Gordon (1986) in questioning the contribution of the westward flow within the Agulhas regime to the northward flowing limb of the MOC. The 'warm water' pathway from the Agulhas regime, contrasts with the 'cold water' pathway originating from Drake Passage.

This study constrains the Agulhas leakage transport to 10.7Sv from a 9Sv initial estimate (McDonagh et al., 1999), and suggests the joint involvement of both pathways in providing northward flowing upper ocean water. Agulhas leakage occurs mainly within the Surface water mass (6.3Sv) and contributes towards the 8.2Sv northward flow at 24°S. The northward-flowing Benguela Current contributes to a combined Surface, SAMW and AAIW transport of 14.8Sv across 24°S. AAIW, however, typically originates from Drake Passage via the cold water pathway to feed the northward flow of AAIW (2.1Sv), with no evidence for either the required Agulhas leakage or subsequent downwelling of westward flowing surface water. With limited upwelling by diapycnal or air-sea interaction, the cold water pathway predominantly contributes to the broad AAIW northward flow at 24°S. Northward flowing SAMW originates from a mix of the two pathways.

7.2.3 Overturning freshwater transports (M_{ov})

Southward overturning freshwater transport across 24°S, estimated to be 0.09Sv in terms of M_{ov}, is supportive of the theory of Dijkstra (2007) and Drijfhout et al. (2011), and the observations of Bryden et al. (2011) and Garzoli et al. (2013) that the M_{ov} acts to inhibit the MOC flow. Excess freshwater input in the North Atlantic, causing increased M_{ov}, could create surface water, which is too fresh to form NADW and cause MOC shutdown.

The direction of the M_{ov} is heavily dependent on the upper 450dbar, and therefore a perturbation in the upper waters is the most obvious method for perturbing the MOC. This study estimates that to shift the freshwater transport across 24°S to be northward, an extra 4.6Sv of sectionwide volume transport within the upper 450dbar would be required, compared to 3.2Sv when applied to the Brazil Current for the upper 300dbar, west of 35°W only. Sectionwide and Brazil Current salinity perturbations of 0.36psu and 5psu would also shift the freshwater transport (M_{ov}) to be northward. Therefore,

whilst changes in the volume transport could realistically see a temporary reversal of the sign of M_{ov} caused by, for example, a weakening of the Brazil Current transport, the large salinity perturbations required are unlikely without large-scale changes to the hydrological system. This study is the first assessment of these values using a hydrographic observation based model.

Perturbations to M_{ov}, also perturb M_{az}, with the salinity perturbations causing the largest response in M_{az}. Projections of MOC shutdown, based on changes in M_{ov} therefore require consideration of M_{az} to indicate how the circulation would change, if an MOC shutdown occurred.

7.3 Synthesis of marine biogeochemistry and physical oceanography

Combining C^{ant} estimates with an inverse box model framework for the South Atlantic is novel, and provides additional regional focus than provided by the global ocean inversion study of Mikaloff Fletcher et al. (2006). This work supports that the South Atlantic sector of the Southern Ocean is a major sink region for C^{ant}, and seasonally larger than that estimated by Mikaloff Fletcher et al. (2006). The northward C^{ant} transport of $0.70\pm0.41 \mathrm{Mmol\,s^{-1}}$ (0.27 ± 0.16 $\mathrm{PgC\,yr^{-1}}$) towards the North Atlantic is similar to Pérez et al. (2013)'s estimate of $0.25\pm0.05 \mathrm{PgC\,yr^{-1}}$ at 25°N, in addition to further net outflow of C^{ant} into the Indian Ocean. The estimates of C^{ant} transport are inherently dependent on the C^{ant} distribution, as described in Chapters 4 and 5, with excess C^{ant}, particularly in a frontal region, potentially leading to anomalous C^{ant} transports, with this study being the first to analyse changes in C^{ant} in recent decades for meridional hydrographic sections across the Southern Ocean.

This study therefore, provides precious additional information about the South Atlantic sector of the Southern Ocean, which was not previously known, such as estimates for boundary C^{ant} transports, overturning C^{ant} transport and the first inverse box-derived estimate for air-sea C^{ant} uptake. Furthermore, details regarding the South Atlantic circulation are also highlighted, for example, M_{ov} estimates for comparison to Bryden et al. (2011) and Garzoli et al. (2013), the size of the AABW residual transport and size of the eastward flowing Agulhas deep waters, are calculated in this model framework, and provide room for a number of further questions, related to the temporal accuracy of these results. For example, the rough topography within the South Atlantic contributes to diapycnal transfer, however, given the AABW inflow of 8.8Sv

associated with the Weddell Gyre southern limb, partial AABW reventilation leading to an anticipated ∼10Sv exiting the Weddell Sea (Naveira Garabato et al., 2002b; Kerr et al., 2012), therefore requires significant upwelling. This imbalance could be partially rectified by a strengthening of the Weddell Gyre northern limb, and hence requiring less vigorous upwelling.

This study therefore highlights outstanding issues, both within the calculation of C^{ant}, and more generally by determining changes in DIC, and furthermore with the details of the South Atlantic circulation. For C^{ant} calculations, the outstanding issues relate to the difficulties in representing water mass ventilation and a robust quantification for the saturation of a water parcel by C^{ant} upon ventilation. When a water parcel is at the surface, it is able to form an active relationship with the overlying atmosphere by both taking up and reventilating C^{ant} (Sallée et al., 2012). The saturation of a water parcel by C^{ant} is therefore a factor of both the length of exposure of the water parcel to the surface and the pre-ventilation saturation of the water parcel by DIC. The subsequent subduction of recently ventilated water is a pathway for C^{ant} into the ocean interior and is typically estimated using a water mass age estimate. Improved representation of C^{ant} air-sea interaction and the determining factors for CO_2 saturation would help develop a mechanistic understanding for C^{ant} subduction and accurately estimate C^{ant}, at least in recently ventilated waters, prior to significant ocean interior mixing. A synthesis between carbon biogeochemistry and physical oceanography is therefore, required to adequately quantify these processes.

7.4 Future work

This study supports the necessity for further observations of the mechanisms for WW formation near the Antarctic continent. WW is a clearly distinguishable water mass along both Drake Passage and 30°E that progresses northward to contribute towards subpolar water mass composition. The linkage between WW formed in the Bellinghausen Sea and downstream AAIW composition is a topic that requires further research following Naveira Garabato et al. (2009) and McCarthy et al. (2011, 2012). Current research supports an intensification of the hydrological cycle in connection with a freshening in AAIW formation sites in the South Atlantic (Curry et al., 2003; McCarthy et al., 2011), and similarly within the Indian and Pacific basins (Wong et al., 1999; Bindoff and McDougall, 2000). Whether a signal of the variability of WW driven by variability of large scale climate indices (ENSO/SAM), is evident at a remote location is a topic for further study using, for example, the available hydrographic data,

further field campaigns within the Bellinghausen Sea, or using the available models to track upstream WW trajectory.

Observational measurements of the strength of the Antarctic Slope Current are limited: 15.8±7.4Sv in Meijers et al. (2010), comparable to the Weddell Gyre southern limb estimate of 15.9±2.3Sv in this study, largely due to the challenging working environment and presence of sea ice close to the Antarctic continental shelf (Meijers et al., 2010). The southern limb is significant as a supply route for AABW to the Weddell Sea, by AABW typically formed in the Prydz Bay area (Jacobs and Georgi, 1977; Orsi et al., 1999; Yabuki et al., 2006; Meijers et al., 2010; Meredith et al., 2010) or at the Cape Darnley polynya (Tamura et al., 2008; Kusahara et al., 2010; Ohshima et al., 2013). Current research is keen to establish the volume of AABW to leave the Weddell Sea (Naveira Garabato et al., 2002b; Meredith et al., 2011a; Kerr et al., 2012) and possible changes to its composition. However, this study suggests the requirement for further hydrographic data to monitor the Weddell Sea AABW inflow, centered at ∼30°E. This project could follow a similar pattern to the Baseline Research on Oceanography, Krill and the Environment-West (BROKE-West) project described in Meijers et al. (2010) and Williams et al. (2010a). In addition, moorings similar to those used in Meredith et al. (2011a) would help to characterise the seasonality of the Weddell Gyre southern limb, given that AABW formation at the Cape Darnley polynya is thought to vary seasonally with sea ice formation (Meijers et al., 2010; Ohshima et al., 2013), and contributes to the seasonality of AABW inflow, and feeds into other studies focussed on bottom water seasonality within the Weddell Sea (Wang et al., 2012).

Anthropogenic Carbon calculations in this study have followed the commonly used $\triangle C^*$, TrOCA and eMLR methods for easier comparison to previous studies. A number of the most commonly applied methods for C^{ant} and $\triangle C^{ant}$ calculations are described in Sabine and Tanhua (2010), although additional methods also exist. An extension of the work in this study could therefore include the application of alternative methods. These methods would therefore include, in no particular order: Transit Time Distribution (TTD; Hall et al. (2002)), Time Series Residual (TSR; van Heuven et al. (2011)) and LM05 (Lo Monaco et al., 2005b). The principles of the TSR method are invoked in section 4.3.3.2 and 5.2.1.2. Methodology from the φC_T^o method described in Vázquez-Rodríguez (2008), Pérez et al. (2008) and Vázquez-Rodríguez et al. (2009a), is applied in this study following Pardo et al. (2011) and Vázquez-Rodríguez et al. (2012) as an improved parameterisation of $\triangle C^*$, rather than a separate method. Table 7.1 is therefore not an exhaustive list and other methods also exist for consideration. The reader is urged to refer to the papers listed in Table 7.1, as well as, Sabine and Tanhua

Method	Author	Advantages	Disadvantages
TTD	Hall et al. (2002)	DIC and biogeochemical data not required	Insensitive to changes in C^{bio}
TSR	van Heuven et al. (2011)	Insensitive to variable hydrography and biogeochemistry	Regression coefficients dependent on quality of measured parameters. Only previously applied to a 10 cruise dataset.
LM05	Lo Monaco et al. (2005b)	Relies on well-known oceanographic properties	Need to estimate preindustrial DIC, and air-sea disequilibrium

Table 7.1: Comparison of three methods, not used in this study, to determine ocean anthropogenic carbon C^{ant}: Transit Time Distribution (TTD), Time Series Residual (TSR) and LM05 (Lo Monaco et al., 2005b).

(2010) for further details.

In the North Atlantic, the Gulf Stream has been the subject of numerous hydrographic occupations, in-situ instrumentation, modelling studies and altimetry analysis (e.g. Halkin and Rossby, 1985; Mellor and Ezer, 1991; Smith et al., 2000; Bryden et al., 2005b), however, comparatively South Atlantic boundary currents have been far less studied. In the western basin, the Brazil Current has been the subject of a number of hydrographic surveys as described in Signorini (1978); Evans et al. (1983); Evans and Signorini (1985); Stramma (1989); Garfield (1990); Zemba (1991); Bryden et al. (2011), however, the lack of in-situ instrumentation has hindered determination of the Brazil Current strength and trajectory on shorter term timescales, as well as establishing a pattern of decadal variability. In-situ moorings, or alternatively Argo float profiles are desirable, as previously advocated in Bryden et al. (2011).

In the eastern basin, the Benguela Current has been previously studied as part of the Benguela Sources and Transports (BEST) project in 1992-1993 (Garzoli and Gordon, 1996; Garzoli et al., 1997, 1999). Despite the BEST project, questions remain regarding the Benguela Current composition and transport, particularly once Agulhas rings have diffused into the background field, and follow the topics mentioned by Garzoli and Matano (2011). Garzoli and Matano (2011), in particular, question Benguela Current composition variability and the downstream effect of variability between a cold and warm water pathway. As the offshore Ekman transport associated with Benguela Current causes upwelling and enhanced primary productivity along the Southwest African

coastline, the significance of variability of Benguela Current source water, and hence cold/warm water pathway variability, in the context of the fish populations and human coastal population, is an open question.

In addition to the upper ocean transfer of Indian Ocean water into the Cape Basin, the zonal deep water pathway from the Deep Western Boundary Current into the Cape Basin presents a mechanism for the direct connection between deep water formed in the North Atlantic and the Indian Ocean. van Sebille et al. (2012) draws together previous estimates from Speer et al. (1995), Zangenberg and Siedler (1998), Arhan et al. (2003) and Hogg and Thurnherr (2005) to hypothesise an intermittent eastward zonal deep water pathway. Walvis Ridge limits eastward flow of deep water from the eastern South Atlantic basin into the Cape Basin. Breaks in the ridge, such as at Namib Col (Speer et al., 1995), represent an ideal location for in-situ instruments. Observational evidence of van Sebille et al. (2012)'s model-derived hypothesis for a zonal deep water pathway is required.

The hydrographic occupations in this study occur during austral summer. In winter, the circulation may differ particularly in a freshwater context with, for example, sea ice accumulation in the Weddell Sea, and further around the Antarctic continent (Figure 7.1). Southern Ocean near-surface salinity typically experiences freshening in summer and salinification in winter (Ren et al., 2011), partially as a consequence of brine rejection. This inverse model does not include an explicit sea ice term, however, for a study closer to the Antarctic continent, for example, for a hypothesised inverse model near the Antarctic continental shelf as part of the BROKE-West project (Meijers et al., 2010; Williams et al., 2010a), sea ice should be explicitly calculated. This calculation could follow the work in the Arctic Ocean of Tsubouchi et al. (2012). For a wintertime inverse box model of the South Atlantic, explicitly including the contribution of sea ice in the model solution is advisable.

7.5 Concluding remarks

This study links together C^{ant} at the South Atlantic boundary and South Atlantic circulation. C^{ant} is divergent within the South Atlantic and requires an uptake flux of $0.79\text{PgC}\,\text{yr}^{-1}$ in order to maintain the $0.60\text{PgC}\,\text{yr}^{-1}$ divergence and additional $0.19\text{PgC}\,\text{yr}^{-1}$ C^{ant} storage within the basin. The uptake flux is reduced to $0.48\text{PgC}\,\text{yr}^{-1}$ for a separate method, considering the ACC regime only. Decadal C^{ant} increase supports SAMW increase at 30°E, approximately double that at Drake Passage. Northward flux of C^{ant}-rich upper ocean water via the MOC towards the North Atlantic and eastward flux

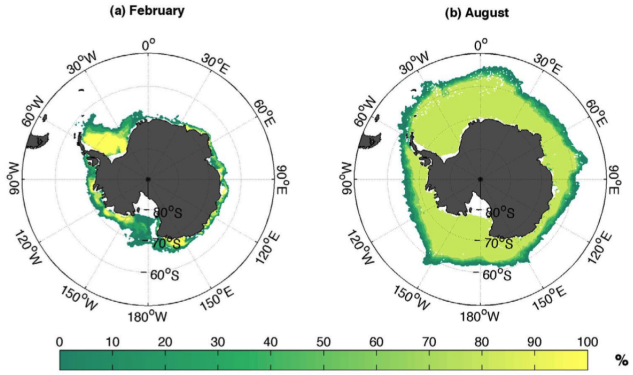

Figure 7.1: Sea ice concentration (%) from the mean of 5 years (2006-2010) of Argo data in a) February and b) August. Taken from Ren et al. (2011).

of recently ventilated upper ocean water into the Indian sector of the Southern Ocean confirm that the South Atlantic is a C^{ant} sink region, however, not a major storage region for C^{ant}, as C^{ant} is quickly flushed out.

Increases in DIC along the eastern and western boundary of the South Atlantic box are confirmed as anthropogenic in excess of an apparent small nitrate increase. Two back-calculation methods (TrOCA, $\triangle C^*$) and a separate extended multiple linear regression-based approach support C^{ant} increases along the eastern and western boundary of 10.4±0.2/4.7±0.2μmol kg^{-1} decade^{-1}, respectively for SAMW. Back-calculation methods typically show closer agreement, whilst eMLR representation is improved by a post-regression correction. C^{ant} increases are predominately within the upper ocean, and most closely correspond with regions of enhanced ventilation, for example, within the Agulhas regime, and within outcropping SAMW and AAIW in the Southern Ocean.

The inclusion of DIC, C^{nat} and C^{ant} within the inverse model of the South Atlantic is novel, and builds on the South Atlantic inverse model of Rintoul (1991). The inverse model solves for volume transport and transport-weighted properties around the box boundary built around a fundamental assumption for zero salinity convergence. This facilitates quantification of a mean steady state circulation that results in an estimate for MOC overturning of 20.2±2Sv and M_{ov} of -0.09Sv, in agreement with previous estimates, whilst carefully constraining a 10.7Sv Agulhas leakage. This study finds Agulhas leakage predominately within the Surface (6.3Sv) and SAMW (1.5Sv), as opposed to AAIW (1.2Sv eastward), supportive of the involvement of the warm water pathway in the MOC.

Near the Antarctic continent, this study has hypothesised the importance of the formation of WW, and its possible downstream signal. The connection of larger-scale atmospheric circulation features (ENSO, SAM; Naveira Garabato et al. (2009)) to WW

formation in the Bellinghausen Sea, and subsequent WW subduction to form AAIW is a subject for further study. This study emphasises the importance of WW formation on C^{ant} drawdown, as an important pathway for intermediate water ventilation. Also, the diagnosis of the Weddell Gyre southern limb of 15.9±2.3Sv within an inverse box model is new and likely partially comprised of recently ventilated and formed AABW at the Cape Darnley polynya (Tamura et al., 2008; Kusahara et al., 2010; Ohshima et al., 2013).

Finally, each component of this thesis, from biogeochemical aspects of the C^{ant} calculations to the quantification of overturning and mixing, builds a fuller picture of the complex South Atlantic circulation. The ACC, MOC and Agulhas systems are each significant, and responsible for influencing both oceanic and atmospheric climates over a large spatial range. This study therefore links with the existing body of work on South Atlantic circulation, as well as broader climate-related issues with the over-arching aim of furthering knowledge of a significant region of the world in the face of present-day and future climate change.

Bibliography

Abernathey, R., Marshall, J., Ferreira, D., 2011. The Dependence of Southern Ocean Meridional Overturning on Wind Stress. Journal of Physical Oceanography 41, 2261–2278.

Adler, R.F., Huffman, G.J., Chang, A., Ferraro, R., Xie, P.P., Janowiak, J., Rudolf, B., Schneider, U., Curtis, S., Bolvin, D., Gruber, A., Susskind, J., Arkin, P., Nelkin, E., 2003. The Version-2 Global Precipitation Climatology Project (GPCP) Monthly Precipitation Analysis (1979 - Present). Journal of Hydrometeorology 4, 1147–1167.

Alderson, S.G., Cunningham, S.A., 1999. Velocity Errors in Acoustic Doppler Current Profiler Measurements due to Platform Attitude Variations and Their Effect on Volume Transport Estimates. Journal of Atmospheric and Oceanic Technology 16, 96–106.

Allison, L.C., Johnson, H.L., Marshall, D.P., Munday, D.R., 2010. Where do winds drive the Antarctic Circumpolar Current? Geophysical Research Letters 37, L12605, doi:10.1029/2010GL043355.

Álvarez, M., Pérez, F.F., Bryden, H.L., Ríos, A.F., 2004. Physical and biogeochemical transports structure in the North Atlantic subpolar gyre. Journal of Geophysical Research 109, C03027, doi:10.1029/2003JC002015.

Álvarez, M., Ríos, A.F., Pérez, F.F., Bryden, H.L., Rosón, G., 2003. Transports and budgets of total inorganic carbon in the subpolar and temperate North Atlantic. Global Biogeochemical Cycles 17, 1–22.

Anderson, L.A., Sarmiento, J.L., 1994. Redfield ratios of remineralization determined by nutrient data analysis. Global Biogeochemical Cycles 8, 65–80.

Andrews, W.R.H., Hutchings, L., 1980. Upwelling in the Southern Benguela Current. Progress In Oceanography 9, 1–81.

Anitha, G., Ravichandran, M., Sayanna, R., 2008. Surface buoyancy flux in Bay of Bengal and Arabian Sea. Annales Geophysicae , 395–400.

Antonov, J.I., Seidov, D., Boyer, T.P., Locarini, R.A., Mishonov, A.V., Garcia, H.E., Baranova, O.K., Zweng, M.M., Johnson, D.R., 2010. World Ocean Atlas 2009, Volume 2: Salinity. Technical Report. S. Levitus, Ed. NOAA Atlas NESDIS 69, U.S. Government Printing Office. Washington, D.C.

Aoki, S., Bindoff, N.L., Church, J.A., 2005. Interdecadal water mass changes in the Southern Ocean between 30°E and 160°E. Geophysical Research Letters 32, L07607, doi:10.1029/2004GL022220.

Aoki, S., Hariyama, M., Mitsudera, H., Sasaki, H., Sasai, Y., 2007. Formation regions of Subantarctic Mode Water detected by OFES and Argo profiling floats. Geophysical Research Letters 34, L10606, doi:10.1029/2007GL029828.

Arbic, B., Owens, W., 2001. Climatic Warming of Atlantic Intermediate Waters. Journal of Climate 14, 4091–4108.

Arhan, M., Mercier, H., Park, Y.H., 2003. On the deep water circulation of the eastern South Atlantic Ocean. Deep Sea Research Part I: Oceanographic Research Papers 50, 889–916.

Armstrong, F.A.J., Stearns, C.R., Strickland, J.D.H., 1967. The measurement of upwelling and subsequent biological processes by means of the Technicon Autoanalyzer and associated equipment. Deep-Sea Research 14, 381–389.

Arntz, W.E., Gallardo, V.A., Gutiérrez, D., Isla, E., Levin, L.A., Mendo, J., Neira, C., Rowe, G.T., Tarazona, J., Wolff, M., 2006. El Niño and similar perturbation effects on the benthos of the Humboldt, California, and Benguela Current upwelling ecosystems. Advances in Geosciences 6, 243–265.

Arrigo, K.R., van Dijken, G., Long, M., 2008. Coastal Southern Ocean: A strong anthropogenic CO_2 sink. Geophysical Research Letters 35, L21602, doi:10.1029/2008GL035624.

Arrigo, K.R., Robinson, D.H., Worthen, D.L., Dunbar, R.B., DiTullio, G.R., VanWoert, M., Lizotte, M.P., 1999. Phytoplankton Community Structure and the Drawdown of Nutrients and CO_2 in the Southern Ocean. Science 283, 365–367.

Backeberg, B.C., Penven, P., Rouault, M., 2012. Impact of intensified Indian Ocean winds on mesoscale variability in the Agulhas system. Nature Climate Change 2, 608–612.

Baehr, J., Stroup, A., Marotzke, J., 2009. Testing concepts for continuous monitoring of the meridional overturning circulation in the South Atlantic. Ocean Modelling 29, 147–153.

Bailey, G.W., Chapman, P., 1991. Short-term variability during an anchor station study in the southern Benguela upwelling system : Chemical and physical oceanography. Progress In Oceanography 28, 9–37.

Banse, K., 1996. Low seasonality of low concentrations of surface chlorophyll in the Subantarctic water ring: underwater irradiance, iron, or grazing? Progress In Oceanography 37, 241–291.

Barbero, L., Boutin, J., Merlivat, L., Martin, N., Takahashi, T., Sutherland, S.C., Wanninkhof, R., 2011. Importance of water mass formation regions for the air-sea CO_2 flux estimate in the Southern Ocean. Global Biogeochemical Cycles 25, GB1005, doi:10.1029/2010GB003818.

Barreiro, M., Fedorov, A., Pacanowski, R., Philander, S.G., 2008. Abrupt Climate Changes: How Freshening of the Northern Atlantic Affects the Thermohaline and Wind-Driven Oceanic Circulations. Annual Review of Earth and Planetary Sciences 36, 33–58.

Bates, N., 2001. Interannual variability of oceanic CO_2 and biogeochemical properties in the Western North Atlantic subtropical gyre. Deep Sea Research Part II: Topical Studies in Oceanography 48, 1507–1528.

Beal, L.M., 2009. A Time Series of Agulhas Undercurrent Transport. Journal of Physical Oceanography 39, 2436–2450.

Beal, L.M., Bryden, H.L., 1997. Observations of an Agulhas Undercurrent. Deep Sea Research Part I: Oceanographic Research Papers 44, 1715–1724.

Beal, L.M., Bryden, H.L., 1999. The velocity and vorticity structure of the Agulhas Current at 32°S. Journal of Geophysical Research 104, 5151–5176.

Beal, L.M., Chereskin, T.K., Lenn, Y.D., Elipot, S., 2006. The Sources and Mixing Characteristics of the Agulhas Current. Journal of Physical Oceanography 36, 2060–2074.

Beal, L.M., De Ruijter, W.P.M., Biastoch, A., Zahn, R., 2011. On the role of the Agulhas system in ocean circulation and climate. Nature 472, 429–36.

Belkin, I.M., Gordon, A.L., 1996. Southern Ocean fronts from the Greenwich meridian to Tasmania. Journal of Geophysical Research 101, 3675–3696.

Bernard, C.Y., Dürr, H.H., Heinze, C., Segschneider, J., Maier-Reimer, E., 2011. Contribution of riverine nutrients to the silicon biogeochemistry of the global ocean - a model study. Biogeosciences 8, 551–564.

Bernard, C.Y., Laruelle, G.G., Slomp, C.P., Heinze, C., 2010. Impact of changes in river fluxes of silica on the global marine silicon cycle: a model comparison. Biogeosciences 7, 441–453.

Berner, R.A., 1990. Atmospheric Carbon Dioxide Levels Over Phanerozoic Time. Science 249, 1382–1386.

Bernhardt, H., Wilhelms, A., 1967. The continuous determination of low level iron, soluble phosphate and total phosphate with the AutoAnalyzer. Technicon Symposia I, 385–389.

Berry, D.I., Kent, E.C., 2009. A New Air-Sea Interaction Gridded Dataset from ICOADS With Uncertainty Estimates. Bulletin of the American Meteorological Society 90, 645.

Berry, D.I., Kent, E.C., 2011. Air-Sea fluxes from ICOADS: the construction of a new gridded dataset with uncertainty estimates. International Journal of Climatology 31, 987–1001.

Biastoch, A., Böning, C.W., Lutjeharms, J.R.E., 2008. Agulhas leakage dynamics affects decadal variability in Atlantic overturning circulation. Nature 456, 489–92.

Biastoch, A., Böning, C.W., Schwarzkopf, F.U., Lutjeharms, J.R.E., 2009. Increase in Agulhas leakage due to poleward shift of Southern Hemisphere westerlies. Nature 462, 495–8.

Bindoff, N., McDougall, T., 2000. Decadal Changes along an Indian Ocean Section at 32S and Their Interpretation. Journal of Physical Oceanography 30, 1207–1222.

Bindoff, N.L., Willebrand, J., Artale, V., Cazenave, A., Gregory, J., Gulev, S., Hanawa, K., Le Quéré, C., Levitus, S., Nojiri, Y., Shum, C.K., Talley, L.D., Unnikrishnan,

A., 2007. Observations: Oceanic Climate Change and Sea Level, in: Solomon, S., Qin, D., Manning, M., Chen, Z., Marquis, M., Averyt, K.B., Tignor, M., Miller, H. (Eds.), Climate Change 2007: The Physical Science Basis. Contribution of Working Group I to the Fourth Assessment Report of the Intergovernmental Panel on Climate Change. Cambridge University Press, Cambridge, United Kingdom and New York, NY, USA.

Bingham, R.J., Hughes, C.W., 2009. Signature of the Atlantic meridional overturning circulation in sea level along the east coast of North America. Geophysical Research Letters 36, L02603, doi:10.1029/2008GL036215.

Boebel, O., Rossby, T., Lutjeharms, J., Zenk, W., Barron, C., 2003. Path and variability of the Agulhas Return Current. Deep Sea Research Part II: Topical Studies in Oceanography 50, 35–56.

Böning, C.W., Dispert, A., Visbeck, M., Rintoul, S.R., Schwarzkopf, F.U., 2008. The response of the Antarctic Circumpolar Current to recent climate change. Nature Geoscience 1, 864–869.

Boswell, S.M., Smythe-Wright, D., 2002. The tracer signature of Antarctic Bottom Water and its spread in the Southwest Indian Ocean : Part I - CFC-derived translation rate and topographic control around the Southwest Indian Ridge and the Conrad Rise. Deep Sea Research Part I: Oceanographic Research Papers 49, 555–573.

Boyer, T., Levitus, S., Garcia, H., Locarnini, R.A., Stephens, C., Antonov, J., 2005. Objective analyses of annual, seasonal, and monthly temperature and salinity for the World Ocean on a 0.25° grid. International Journal of Climatology 25, 931–945.

Brandini, F.P., Boltovskoy, D., Piola, A., Kocmur, S., Röttgers, R., Abreu, P.C., Lopes, R.M., 2000. Multiannual trends in fronts and distribution of nutrients and chlorophyll in the southwestern Atlantic (30-62°S). Deep Sea Research Part I: Oceanographic Research Papers 47, 1015–1033.

Brea, S., Álvarez Salgado, X.A., Álvarez, M., Pérez, F.F., Mémery, L., Mercier, H., Messias, M.J., 2004. Nutrient mineralization rates and ratios in the eastern South Atlantic. Journal of Geophysical Research 109, C05030, doi:10.1029/2003JC002051.

Brewer, P.G., 1978. Direct observation of the oceanic CO_2 increase. Geophysical Research Letters 5, 997–1000.

Brewer, P.G., Wong, G.T.F., Bacon, M.P., Spencer, D.W., 1975. An Oceanic Calcium Problem. Earth and Planetary Science Letters 26, 81–87.

Broecker, W.S., 1974. "NO", A Conservative Water-Mass Tracer. Earth and Planetary Science Letters 23, 100–107.

Broecker, W.S., Peng, T.H., 1992. Interhemispheric transport of carbon dioxide by ocean circulation. Nature 356, 587–589.

Broecker, W.S., Takahashi, T., Simpson, H.J., Peng, T.H., 1979. Fate of Fossil Fuel Carbon Dioxide and the Global Carbon Budget. Science 206, 409–418.

Brown, P.J., Bakker, D.C.E., Schuster, U., Watson, A.J., 2010. Anthropogenic carbon accumulation in the subtropical North Atlantic. Journal of Geophysical Research 115, C04016, doi:10.1029/2008JC005043.

Brunke, M.A., Wang, Z., Zeng, X., Bosilovich, M., Shie, C.L., 2011. An Assessment of the Uncertainties in Ocean Surface Turbulent Fluxes in 11 Reanalysis, Satellite-Derived, and Combined Global Datasets. Journal of Climate 24, 5469–5493.

Bryden, H.L., Beal, L.M., Duncan, L.M., 2005a. Structure and Transport of the Agulhas Current and Its Temporal Variability. Journal of Oceanography 61, 479–492.

Bryden, H.L., Imawaki, S., 2001. Ocean heat transport, in: Siedler, G., Church, J., Gould, J. (Eds.), Ocean Circulation and Climate. Academic Press, pp. 455–474.

Bryden, H.L., King, B.A., McCarthy, G.D., 2011. South Atlantic overturning circulation at 24 ° S. Journal of Marine Research , 39–56.

Bryden, H.L., Longworth, H.R., Cunningham, S.A., 2005b. Slowing of the Atlantic meridional overturning circulation at 25 degrees N. Nature 438, 655–7.

Bryden, H.L., McDonagh, E.L., King, B.A., 2003. Changes in ocean water mass properties: oscillations or trends? Science 300, 2086–8.

Bullister, J.L., 2011. Atmospheric CFC-11, CFC-12, CFC-113, CCl4 and SF_6 Histories. `http://cdiac.ornl.gov/ftp/oceans/CFC_ATM_Hist/`. Accessed: 06/08/2012.

Byrne, D.A., Gordon, A.L., Haxby, W.F., 1995. Agulhas eddies: A Synoptic View Using Geosat ERM Data. Journal of Physical Oceanography 25, 902–917.

Cai, W., Cowan, T., Godfrey, S., Wijffels, S., 2010a. Simulations of Processes Associated with the Fast Warming Rate of the Southern Midlatitude Ocean. Journal of Climate 23, 197.

Cai, W., Shi, G., Cowan, T., Bi, D., Ribbe, J., 2005. The response of the Southern Annular Mode, the East Australian Current, and the southern mid-latitude ocean circulation to global warming. Geophysical Research Letters 32, L23706, doi:10.1029/2005GL024701.

Cai, W.J., Hu, X., Huang, W.J., Jiang, L.Q., Wang, Y., Peng, T.H., Zhang, X., 2010b. Alkalinity distribution in the western North Atlantic Ocean margins. Journal of Geophysical Research 115, 1–15.

Caldeira, K., Duffy, P., 2000. The role of the Southern Ocean in uptake and storage of anthropogenic carbon dioxide. Science 287, 620622.

Caldeira, K., Wickett, M., 2003. Anthropogenic carbon and ocean pH. Nature 425, 2003.

Callahan, J.E., 1972. Structure and circulation of deep-water in the Antarctic. Deep-Sea Research 19, 563–575.

Campos, E.J.D., Gonçalves, J.E., Ikeda, Y., 1995. Water mass characteristics and geostrophic circulation in the South Brazil Bight: Summer of 1991. Journal of Geophysical Research 100, 18537–18550.

Canadell, J.G., Le Quéré, C., Raupach, M.R., Field, C.B., Buitenhuis, E.T., Ciais, P., Conway, T.J., Gillett, N.P., Houghton, R.A., Marland, G., 2007. Contributions to accelerating atmospheric CO_2 growth from economic activity, carbon intensity, and efficiency of natural sinks. Proceedings of the National Academy of Sciences of the United States of America 104, 18866–70.

Cao, L., Eby, M., Ridgwell, A., Caldeira, K., Archer, D., Ishida, A., Joos, F., Matsumoto, K., Mikolajewicz, U., Mouchet, A., Orr, J.C., Plattner, G.K., Schlitzer, R., Tokos, K., Totterdell, I., Tschumi, T., Yamanaka, Y., Yool, A., 2009. The role of ocean transport in the uptake of anthropogenic CO_2. Biogeosciences 6, 375–390.

Carmack, E.C., Foster, T.D., 1975. On the flow of water out of the Weddell Sea. Deep-Sea Research 22, 711–724.

Carpenter, J.H., 1965. The Chesapeake Bay Institute Technique for the Winkler Dissolved Oxygen Method. Limnology and Oceanography 10, 141–143.

Casal, T.G.D., Beal, L.M., Lumpkin, R., Johns, W.E., 2009. Structure and downstream evolution of the Agulhas Current system during a quasi-synoptic survey in February-March 2003. Journal of Geophysical Research 114, C03001, doi:10.1029/2008JC004954.

Chapin, F.S., McFarland, J., McGuire, A.D., Euskirchen, E.S., Ruess, R.W., Kielland, K., 2009. The changing global carbon cycle: linking plant-soil carbon dynamics to global consequences. Journal of Ecology 97, 840–850.

Chen, C.T.A., 1982. On the distribution of anthropogenic CO_2 in the Atlantic and Southern oceans. Deep Sea Research Part A. Oceanographic Research Papers 29, 563–580.

Chen, G.T., Millero, F.J., 1979. Gradual increase of oceanic CO_2. Nature 277, 205–206.

Chen, W., Dong, B., Lu, R., 2010. Impact of the Atlantic Ocean on the multidecadal fluctuation of El Niño-Southern Oscillation-South Asian monsoon relationship in a coupled general circulation model. Journal of Geophysical Research 115, D17109, doi:10.1029/2009JD013596.

Chipman, D.W., Takahashi, T., Breger, D., Sutherland, S.C., 1991. Investigation of Carbon Dioxide in the South Atlantic and Northern Weddell Sea areas (WOCE Sections A-12 and A-21) during the Meteor Expedition 11/5, January-March, 1990. Technical Report. Lamont-Doherty Geological Observatory of Columbia University. Palisades, N.Y.

Church, J.A., White, N.J., 2006. A 20th century acceleration in global sea-level rise. Geophysical Research Letters 33, L01602, doi:10.1029/2005GL024826.

Church, J.A., White, N.J., Coleman, R., Lambeck, K., Mitrovica, J.X., 2004. Estimates of the Regional Distribution of Sea Level Rise over the 1950 - 2000 Period. Journal of Climate 17, 2609–2625.

Cimatoribus, A.A., Drijfhout, S.S., Toom, M., Dijkstra, H.A., 2012. Sensitivity of the Atlantic meridional overturning circulation to South Atlantic freshwater anomalies. Climate Dynamics 39, 2291–2306.

Cisewski, B., Strass, V.H., Leach, H., 2011. Circulation and transport of water masses in the Lazarev Sea, Antarctica, during summer and winter 2006. Deep Sea Research Part I: Oceanographic Research Papers 58, 186–199.

Coachman, L.K., Aagaard, K., 1988. Transports Through Bering Strait: Annual and Interannual Variability. Journal of Geophysical Research 93, 15535–15539.

Comas-Rodríguez, I., Hernández-Guerra, A., McDonagh, E.L., 2010. Referencing geostrophic velocities using ADCP data. Scientia Marina 74, 331–338.

Comiso, J.C., Mcclain, C.R., Sullivan, C.W., Ryan, J.P., Leonard, C.L., 1993. Coastal Zone Color Scanner Pigment Concentrations in the Southern Ocean and Relationships to Geophysical Surface Features. Journal of Geophysical Research 98, 2419–2451.

Crueger, T., Roeckner, E., Raddatz, T., Schnur, R., Wetzel, P., 2008. Ocean dynamics determine the response of oceanic CO_2 uptake to climate change. Climate Dynamics 31, 151–168.

Culberson, C.H., Huang, S., 1987. Automated amperometric oxygen titration. Deep Sea Research Part A. Oceanographic Research Papers 34, 875–880.

Culberson, C.H., Knapp, G., Stalcup, M., Williams, R.T., Zemylak, F., 1991. A comparison of methods for the determination of dissolved oxygen in seawater. Technical Report. WOCE Hydrographic Programme Office.

Cunningham, S.A., Alderson, S.G., King, B.A., Brandon, M.A., 2003. Transport and variability of the Antarctic Circumpolar Current in Drake Passage. Journal of Geophysical Research 108, 8084, doi:10.1029/2001JC001147.

Cunningham, S.A., Kanzow, T., Rayner, D., Baringer, M.O., Johns, W.E., Marotzke, J., Longworth, H.R., Grant, E.M., Hirschi, J.J.M., Beal, L.M., Meinen, C.S., Bryden, H.L., 2007. Temporal variability of the Atlantic meridional overturning circulation at 26.5°N. Science 317, 935–8.

Curry, R., Dickson, B., Yashayaev, I., 2003. A change in the freshwater balance of the Atlantic Ocean over the past four decades. Nature 426, 826–9.

Dai, A., Trenberth, K.E., 2002. Estimates of Freshwater Discharge from Continents : Latitudinal and Seasonal Variations. Journal of Hydrometeorology 3, 660–687.

De Baar, H.J.W., Vanleeuwe, M.A., Scharek, R., Goeyens, L., Bakker, K.M.J., Fritsche, P., 1997. Nutrient anomalies in Fragilariopsis kerguelensis blooms, iron deficiency and the nitrate/phosphate ratio (A. C. Redfield) of the Antarctic Ocean. Deep Sea Research Part II: Topical Studies in Oceanography 44, 229–260.

De Decker, A.H.B., 1970. Notes on an oxygen-depleted subsurface current off the west coast of South Africa. Investigational report Division of Sea Fisheries 84, 1–24.

Deacon, G.E.R., 1933. A general account of the hydrology of the South Atlantic Ocean. Discovery Reports 7, 171–238.

Deacon, G.E.R., 1937. The hydrology of the Southern Ocean. Discovery Reports 15, 1–24.

Dencausse, G., Arhan, M., Speich, S., 2010a. Routes of Agulhas rings in the south-eastern Cape Basin. Deep Sea Research Part I: Oceanographic Research Papers 57, 1406–1421.

Dencausse, G., Arhan, M., Speich, S., 2010b. Spatio-temporal characteristics of the Agulhas Current retroflection. Deep Sea Research Part I: Oceanographic Research Papers 57, 1392–1405.

Dengler, M., Schott, F.A., Eden, C., Brandt, P., Fischer, J., Zantopp, R.J., 2004. Break-up of the Atlantic deep western boundary current into eddies at 8 degrees S. Nature 432, 1018–20.

Denman, K., Brasseur, G., Chidthaisong, A., Ciais, P., Cox, P., Dickinson, R., Hauglustaine, D., Heinze, C., Holland, E., Jacob, D., Lohmann, U., Ramachandran, S., da Silva Dias, P., Wofsy, S., Zhang, X., 2007. Couplings Between Changes in the Climate System and Biogeochemistry, in: Solomon, S., Qin, D., Manning, M., Chen, Z., Marquis, M., Averyt, K., Tignor, M., Miller, H. (Eds.), Climate Change 2007: The Physical Science Basis. Contribution of Working Group I to the Fourth Assessment Report of the Intergovernmental Panel on Climate Change. Cambridge University Press, Cambridge, United Kingdom and New York, NY, USA.

Deutsch, C., Weber, T., 2012. Nutrient Ratios as a Tracer and Driver of Ocean Biogeochemistry. Annual Review of Marine Science 4, 113–141.

Dickson, A.G., 1994. Determination of dissolved oxygen in seawater by Winkler titration. Technical Report. WOCE operations manual.

Dickson, A.G., Afghan, J.D., Anderson, G.C., 2003. Reference materials for oceanic CO_2 analysis: a method for the certification of total alkalinity. Marine Chemistry 80, 185–197.

Dickson, A.G., Millero, F.J., 1987. A comparison of the equilibrium constants for the dissociation of carbonic acid in seawater media. Deep-Sea Research 34, 1733–1743.

Dickson, A.G., Sabine, C.L., Christian, J.R., 2007. Guide to best practices for ocean CO_2 measurements. PICES Special Publication 3, 1991.

Dijkstra, H.A., 2007. Characterization of the multiple equilibria regime in a global ocean model. Tellus A 59, 695–705.

Domingues, C.M., Church, J.A., White, N.J., Gleckler, P.J., Wijffels, S.E., Barker, P.M., Dunn, J.R., 2008. Improved estimates of upper-ocean warming and multi-decadal sea-level rise. Nature 453, 1090–3.

Doney, S., Hecht, M., 2002. Antarctic Bottom Water Formation and Deep-Water Chlorofluorocarbon Distributions in a Global Ocean Climate Model. Journal of Physical Oceanography 32, 1642–1666.

Doney, S.C., Fabry, V.J., Feely, R.A., Kleypas, J.A., 2009a. Ocean Acidification: The Other CO_2 Problem. Annual Review of Marine Science 1, 169–192.

Doney, S.C., Feely, R.A., Glover, D.M., Lindsay, K., Mahowald, N., Moore, J.K., Wanninkhof, R., 2009b. Mechanisms governing interannual variability in upper-ocean inorganic carbon system and air-sea CO_2 fluxes: Physical climate and atmospheric dust. Deep Sea Research Part II: Topical Studies in Oceanography 56, 640–655.

Dong, S., Garzoli, S., Baringer, M., Meinen, C., Goni, G., 2009. Interannual variations in the Atlantic meridional overturning circulation and its relationship with the net northward heat transport in the South Atlantic. Geophysical Research Letters 36, L20606, doi:10.1029/2009GL039356.

Donners, J., Drijfhout, S.S., 2004. The Lagrangian View of South Atlantic Interocean Exchange in a Global Ocean Model Compared with Inverse Model Results. Journal of Physical Oceanography , 1019–1035.

Donohue, K., Firing, E., Chen, S., 2001. Absolute geostrophic velocity within the Subantarctic Front. Journal of Geophysical Research 106, 19869–19882.

Dorrepaal, E., Toet, S., van Logtestijn, R.S.P., Swart, E., van de Weg, M.J., Callaghan, T.V., Aerts, R., 2009. Carbon respiration from subsurface peat accelerated by climate warming in the subarctic. Nature 460, 616–619.

Downes, S.M., Bindoff, N.L., Rintoul, S.R., 2009. Impacts of Climate Change on the Subduction of Mode and Intermediate Water Masses in the Southern Ocean. Journal of Climate 22, 3289.

Drijfhout, S.S., Weber, S.L., van der Swaluw, E., 2011. The stability of the MOC as diagnosed from model projections for pre-industrial, present and future climates. Climate Dynamics 37, 1575–1586.

Durack, P.J., Wijffels, S.E., 2010. Fifty-Year Trends in Global Ocean Salinities and Their Relationship to Broad-Scale Warming. Journal of Climate 23, 4342–4362.

Eckart, C., 1948. An analysis of the stirring and mixing processes in incompressible fluids. Journal of Marine Research VII, 265–275.

Emerson, S.R., Hodges, J.I., 2008. Chemical Oceanography and the Marine Carbon Cycle. Cambridge University Press, Cambridge.

Emery, W., 1977. Antarctic Polar Frontal Zone from Australia to the Drake Passage. Journal of Physical Oceanography 7, 811–822.

England, M.H., 1995. The Age of Water and Ventilation Timescales in a Global Ocean Model. Journal of Physical Oceanography 25, 2756–2777.

Etheridge, D.M., Steele, L.P., Langenfelds, R.L., Francey, R.J., Barnola, J.M., Morgan, V.I., 1996. Natural and anthropogenic changes in atmospheric CO_2 over the last 1000 years from air in Antarctic ice and firn. Journal of Geophysical Research 101, 4115–4128.

Evans, D.L., Signorini, S.R., 1985. Vertical Structure of the Brazil Current. Nature 315, 48–50.

Evans, D.L., Signorini, S.R., Miranda, L.B., 1983. A Note on the Transport of the Brazil Current. Journal of Physical Oceanography 13, 1732–1738.

Fahrbach, E., Rohardt, G., Scheele, N., Schröder, M., Strass, V., Wisotzki, A., 1995. Formation and discharge of deep and bottom water in the northwestern Weddell Sea. Journal of Marine Research 53, 515–538.

Falkowski, P.G., 2000. Rationalizing Elemental Ratios in Unicellular Algae. Journal of Phycology 6, 3–6.

Falkowski, P.G., 2012. The power of plankton. Nature 483, S17–S20.

Fennel, W., 1999. Theory of the Benguela Upwelling System. Journal of Physical Oceanography 29, 177–190.

Field, J.G., Shillington, F.A., 2006. Variability of the Benguela Current System, in: Robinson, A.R., Brink, K.H. (Eds.), The Sea, vol 14B: The Global Coastal Ocean: Interdisciplinary Regional Studies and Syntheses. Harvard University Press, Boston, MA, pp. 835–864.

Fine, R.A., 2011. Observations of CFCs and SF_6 as Ocean Tracers. Annual Review of Marine Science 3, 173–195.

Firing, Y.L., Chereskin, T.K., Mazloff, M.R., 2011. Vertical structure and transport of the Antarctic Circumpolar Current in Drake Passage from direct velocity observations. Journal of Geophysical Research 116, C08015, doi:10.1029/2011JC006999.

Fischer, J., Rhein, M., Schott, F., Stramma, L., 1996. Deep water masses and transports in the Vema Fracture Zone. Deep Sea Research Part I: Oceanographic Research Papers 43, 1067–1074.

Foldvik, A., Gammelsrød, T., Østerhus, S., Fahrbach, E., Rohardt, G., Schröder, M., Nicholls, K.W., Padman, L., Woodgate, R.A., 2004. Ice shelf water overflow and bottom water formation in the southern Weddell Sea. Journal of Geophysical Research 109, C02015, doi:10.1029/2003JC002008.

Foster, T.D., Carmack, E.C., 1976. Frontal zone mixing and Antarctic Bottom Water formation in the southern Weddell Sea. Deep-Sea Research 23, 301–317.

Fraga, F., Álvarez Salgado, X.A., 2005. On the variation of alkalinity during phytoplankton photosynthesis. Ciencias Marinas 31, 627–639.

Franco, B., Mata, M., Piola, A., Garcia, C., 2007. Northwestern Weddell Sea deep outflow into the Scotia Sea during the austral summers of 2000 and 2001 estimated by inverse methods. Deep Sea Research Part I: Oceanographic Research Papers 54, 1815–1840.

Friedlingstein, P., Houghton, R.A., Marland, G., Hackler, J., Boden, T.A., Conway, T.J., Canadell, J.G., Raupach, M.R., Ciais, P., Le Quéré, C., 2010. Update on CO_2 emissions. Nature Geoscience 3, 811–812.

Friedlingstein, P., Solomon, S., Plattner, G.K., Knutti, R., Ciais, P., Raupach, M.R., 2011. Long-term climate implications of twenty-first century options for carbon dioxide emission mitigation. Nature Climate Change 1, 457–461.

Friis, K., Körtzinger, A., Pätsch, J., Wallace, D., 2005. On the temporal increase of anthropogenic CO_2 in the subpolar North Atlantic. Deep Sea Research Part I: Oceanographic Research Papers 52, 681–698.

Fu, L.L., 1981. The General Circulation and Meridional Heat Transport of the Subtropical South Atlantic Determined by Inverse Methods. Journal of Physical Oceanography 11, 1171–1193.

Fukamachi, Y., Wakatsuchi, M., Taira, K., Kitagawa, S., Ushio, S., Takahashi, A., Oikawa, K., Furukawa, T., Yoritaka, H., Fukuchi, M., Yamanouchi, Y., 2000. Seasonal variability of bottom water properties off Adélie Land, Antarctica. Journal of Geophysical Research 105, 6531–6540.

Fyfe, J.C., Saenko, O.A., Zickfeld, K., Eby, M., Weaver, A.J., 2007. The Role of Poleward-Intensifying Winds on Southern Ocean Warming. Journal of Climate 20, 5391–5400.

Gammon, R.H., Cline, J., Wisegarver, D., 1982. Chlorofluoromethanes in the Northeast Pacific Ocean: Measured Vertical Distributions and Application as Transient Tracers of Upper and Ocean Mixing. Journal of Geophysical Research 87, 9441–9454.

Ganachaud, A., 2003a. Large-scale mass transports, water mass formation, and diffusivities estimated from World Ocean Circulation Experiment (WOCE) hydrographic data. Journal of Geophysical Research 108, 3213, doi:10.1029/2002JC001565.

Ganachaud, A., Wunsch, C., 2000. Improved estimates of global ocean circulation, heat transport and mixing from hydrographic data. Nature 408, 453–7.

Ganachaud, A., Wunsch, C., 2003. Large-Scale Ocean Heat and Freshwater Transports during the World Ocean Circulation Experiment. Journal of Climate 16, 696–705.

Ganachaud, A.S., 1999. Large Scale Oceanic Circulation and Fluxes of Freshwater, Heat, Nutrients and Oxygen. Ph.D. thesis. Massachusetts Institute of Technology/Woods Hole Oceanographic Institution Joint Program.

Ganachaud, A.S., 2003b. Error Budget of Inverse Box Models : The North Atlantic. Journal of Atmospheric and Oceanic Technology 20, 1641–1655.

Garfield, N.I., 1990. The Brazil Current at Subtropical Latitudes. Ph.D. thesis. University of Rhode Island, Providence.

Garzoli, S., Richardson, P., Duncombe Rae, C., Fratantoni, D., Goni, G.J., Roubicek, A., 1999. Three Agulhas rings observed during the Benguela current experiment. Journal of Geophysical Research 104, 20971–20985.

Garzoli, S.L., Baringer, M.O., Dong, S., Perez, R.C., Yao, Q., 2013. South Atlantic meridional fluxes. Deep Sea Research Part I: Oceanographic Research Papers 71, 21–32.

Garzoli, S.L., Garraffo, Z., 1989. Transports, frontal motions and eddies at the Brazil-Malvinas currents confluence. Deep Sea Research Part A. Oceanographic Research Papers 36, 681–703.

Garzoli, S.L., Goni, G.J., Mariano, A.J., Olson, D.B., 1997. Monitoring the upper southeastern Atlantic transports using altimeter data. Journal of Marine Research 55, 453–481.

Garzoli, S.L., Gordon, A.L., 1996. Origins and variability of the Benguela Current. Journal of Geophysical Research 101, 897–906.

Garzoli, S.L., Matano, R., 2011. The South Atlantic and the Atlantic Meridional Overturning Circulation. Deep Sea Research Part II: Topical Studies in Oceanography 58, 1837–1847.

Gebbie, G., Huybers, P., 2012. The Mean Age of Ocean Waters Inferred from Radiocarbon Observations: Sensitivity to Surface Sources and Accounting for Mixing Histories. Journal of Physical Oceanography 42, 291–305.

Georgi, D.T., Toole, J.M., 1982. The Antarctic Circumpolar Current and the oceanic heat and freshwater budgets. Journal of Marine Research 40, Supplement, 183–197.

Gill, A.E., 1973. Circulation and bottom water production in the Weddell Sea. Deep-Sea Research 20.

Gill, A.E., 1982. Atmospheric-Ocean Dynamics. Academic Press, London.

Gille, S.T., Speer, K.G., Ledwell, J.R., Naveira Garabato, A.C., 2007. Mixing and Stirring in the Southern Ocean. EOS 88, 382–383.

Gladyshev, S., Arhan, M., Sokov, A., Speich, S., 2008. A hydrographic section from South Africa to the southern limit of the Antarctic Circumpolar Current at the Greenwich meridian. Deep Sea Research Part I: Oceanographic Research Papers 55, 1284–1303.

Gleckler, P.J., Santer, B.D., Domingues, C.M., Pierce, D.W., Barnett, T.P., Church, J.A., Taylor, K.E., AchutaRao, K.M., Boyer, T.P., Ishii, M., Caldwell, P.M., 2012. Human-induced global ocean warming on multidecadal timescales. Nature Climate Change 2, 524–529.

Gloor, M., Gruber, N., Sarmiento, J., Sabine, C., Feely, R., Rodenbeck, C., 2003. A first estimate of present and preindustrial air-sea CO_2 flux patterns based on ocean interior carbon measurements and models. Geophysical Research Letters 30, L01010, doi:10.1029/2002GL015594.

Gloor, M., Sarmiento, J.L., Gruber, N., 2010. What can be learned about carbon cycle climate feedbacks from the CO_2 airborne fraction? Atmospheric Chemistry and Physics 10, 7739–7751.

Glover, D.M., Jenkins, W.J., Doney, S.C., 2002. Least Squares and regression techniques, goodness of fit and tests, non-linear least squares techniques. `http://w3eos.whoi.edu/12.747/notes/lect03/lectno03.html`. Accessed: 06/09/2012.

Goeyens, L., Tréguer, P., Baumann, M.E.M., Baeyens, W., Dehairs, F., 1995. The leading role of ammonium in the nitrogen uptake regime of the Southern Ocean marginal ice zones. Journal of Marine Systems 6, 345–361.

Goodkin, N.F., Levine, N.M., Doney, S.C., Wanninkhof, R., 2011. Impacts of temporal CO_2 and climate trends on the detection of ocean anthropogenic CO_2 accumulation. Global Biogeochemical Cycles 25, GB3023, doi:10.1029/2010GB004009.

Gordon, A.L., 1985. Indian-Atlantic Transfer of Thermocline Water at the Agulhas Retroflection. Science 227, 1030–1033.

Gordon, A.L., 1986. Interocean Exchange of Thermocline Water. Journal of Geophysical Research 91, 5037–5046.

Gordon, A.L., Greengrove, C.L., 1986. Geostrophic circulation of the Brazil-Falkland confluence. Deep-Sea Research 33, 573–585.

Gordon, A.L., Huber, B., McKee, D., Visbeck, M., 2010. A seasonal cycle in the export of bottom water from the Weddell Sea. Nature Geoscience 3, 551–556.

Gordon, A.L., Tchernia, P., 1972. Waters of the continental margin off Adélie coast, Antarctica, in: Hayes, D.E. (Ed.), Antarctic Oceanology II: The Australian-New Zealand Sector, Antarctic Research Series. American Geophysical Union, Washington, D.C., pp. 59–69.

Gordon, A.L., Weiss, R.F., Smethie, W.M., Warner, M.J., 1992. Thermocline and Intermediate Water Communication Between the South Atlantic and Indian Oceans. Journal of Geophysical Research 97, 7223–7240.

Gordon, L.I., Jennings, J.C., Ross, A.A., Krest, J.M., 1993. A Suggested Protocol for Continuous Flow Automated Analysis of Seawater Nutrients (Phosphate , Nitrate , Nitrite and Silicic Acid) in the WOCE Hydrographic Program and the Joint Global Ocean Fluxes Study. WOCE Operations Manual Part 3 , 1–55.

Gouretski, V., Jancke, K., 2000. Systematic errors as the cause for an apparent deep water property variability: global analysis of the WOCE and historical hydrographic data. Progress In Oceanography 48, 337–402.

Gouretski, V.V., Koltermann, K.P., 2004. WOCE Global Hydrographic climatology. Berichte des Bundesamtes fur Seeschiffahrt und Hydrographie Tech. Rep., 55.

Graham, R.M., de Boer, A.M., Heywood, K.J., Chapman, M.R., Stevens, D.P., 2012. Southern Ocean fronts: Controlled by wind or topography? Journal of Geophysical Research 117, C08018, doi:10.1029/2012JC007887.

Green, S.E., Sambrotto, R.N., 2006. Net community production in terms of C, N, P and Si in the Antarctic Circumpolar Current and its influence on regional water mass characteristics. Deep Sea Research Part I: Oceanographic Research Papers 53, 111–135.

Griffies, S.M., Pacanowski, R., Hallberg, R.W., 2000. Spurious Diapycnal Mixing Associated with Advection in a z-Coordinate Ocean Model. Monthly Weather Review 128, 538–564.

Grist, J.P., Josey, S.A., 2003. Inverse Analysis Adjustment of the SOC Air - Sea Flux Climatology Using Ocean Heat Transport Constraints. Journal of Climate 16, 3274–3295.

Gruber, N., Gloor, M., Mikaloff Fletcher, S.E., Doney, S., Dutkiewicz, S., Follows, M., Gerber, M., Jacobson, A.R., Joos, F., Lindsay, K., Menemenlis, D., Mouchet, A., Muller, S., Sarmiento, J.L., Takahashi, T., 2009. Oceanic sources, sinks, and transport of atmospheric CO_2. Global Biogeochemical Cycles 23, GB1005, doi:10.1029/2008GB003349.

Gruber, N., Sarmiento, J., Stocker, T., 1996. An improved method for detecting anthropogenic CO_2 in the oceans. Global Biogeochemical Cycles 10, 809–837.

Gruber, N., Sarmiento, J.L., 1997. Global patterns of marine nitrogen fixation and denitrification. Global Biogeochemical Cycles 11, 235–266.

Hahne, A., Volz, A., Ehhalt, D.H., Cosatto, H., Roether, W., Weiss, W., Kromer, B., 1978. Depth Profiles of Chlorofluoromethanes in the Norwegian Sea. Pure and Applied Geophysics 116, 575–582.

Haine, T.W.N., Watson, A.J., Liddicoat, M.I., Dickson, R.R., 1998. The flow of Antarctic bottom water to the southwest Indian Ocean estimated using CFCs. Journal of Geophysical Research 103, 27637–27653.

Halkin, D., Rossby, T., 1985. The Structure and Transport of the Gulf Stream at 73°W. Journal of Physical Oceanography 15, 1439–1452.

Hall, M.M., Bryden, H.L., 1982. Direct estimates and mechanisms of ocean heat transport. Deep-Sea Research 29, 339–359.

Hall, T.M., Haine, T.W.N., Waugh, D.W., 2002. Inferring the concentration of anthropogenic carbon in the ocean from tracers. Global Biogeochemical Cycles 16, GB1131, doi:10.1029/2001GB001835,.

Hall, T.M., Waugh, D.W., Haine, T.W.N., Robbins, P.E., Khatiwala, S., 2004. Estimates of anthropogenic carbon in the Indian Ocean with allowance for mixing and time-varying air-sea CO_2 disequilibrium. Global Biogeochemical Cycles 18, GB1031, doi:10.1029/2003GB002120.

Hammer, P.M., Hayes, J.M., 1978. Exploratory Analyses of Trichlorofluoromethane (F-11) in North Atlantic Water Columns. Geophysical Research Letters 5, 645–648.

Hanawa, K., Talley, L.D., 2001. Mode Waters, in: Siedler, G., Church, J.A., Gould, J. (Eds.), Ocean Circulation and Climate. Academic Press, pp. 373–386.

Hansell, D.A., Follows, M.J., 2008. Nitrogen in the Atlantic Ocean, in: Mulholland, M., Bronk, D., Capone, D., Carpenter, E. (Eds.), Nitrogen in the Marine Environment. Academic Press, pp. 597–630.

Hartin, C.A., Fine, R.A., Sloyan, B.M., Talley, L.D., Chereskin, T.K., Happell, J., 2011. Formation rates of Subantarctic mode water and Antarctic intermediate water within the South Pacific. Deep Sea Research Part I: Oceanographic Research Papers 58, 524–534.

Hauck, J., Hoppema, M., Bellerby, R.G.J., Völker, C., Wolf-Gladrow, D., 2010. Data-based estimation of anthropogenic carbon and acidification in the Weddell Sea on a decadal timescale. Journal of Geophysical Research 115, C03004, doi:10.1029/2009JC005479.

Hellmer, H.H., Kauker, F., Timmermann, R., Determann, J., Rae, J., 2012. Twenty-first-century warming of a large Antarctic ice-shelf cavity by a redirected coastal current. Nature 485, 225–8.

Helly, J.J., Levin, L.A., 2004. Global distribution of naturally occurring marine hypoxia on continental margins. Deep Sea Research Part I: Oceanographic Research Papers 51, 1159–1168.

Helm, K.P., Bindoff, N.L., Church, J.A., 2010. Changes in the global hydrological-cycle inferred from ocean salinity. Geophysical Research Letters 37, L18701, doi:10.1029/2010GL044222.

de las Heras, M.M., Schlitzer, R., 1999. On the importance of intermediate water flows for the global ocean overturning. Journal of Geophysical Research 104, 15515–15536.

Herraiz-Borreguero, L., Rintoul, S.R., 2010. Subantarctic mode water: distribution and circulation. Ocean Dynamics 61, 103–126.

van Heuven, S., Hoppema, M., Huhn, O., Slagter, H., de Baar, H., 2011. Direct observation of increasing CO_2 in the Weddell Gyre along the Prime Meridian during 1973-2008. Deep Sea Research Part II: Topical Studies in Oceanography 58, 2613–2635.

Heywood, K.J., King, B.A., 2002. Water masses and baroclinic transports in the South Atlantic and Southern oceans. Journal of Marine Research 60, 639–676.

Heywood, K.J., Naveira Garabato, A.C., Stevens, D.P., 2002. High mixing rates in the abyssal Southern Ocean. Nature 415, 1011–4.

Heywood, K.J., Naveira Garabato, A.C., Stevens, D.P., Muench, R.D., 2004. On the fate of the Antarctic Slope Front and the origin of the Weddell Front. Journal of Geophysical Research 109, C06021, doi:10.1029/2003JC002053.

Ho, T.Y., Quigg, A., Finkel, Z.V., Milligan, A.J., Wyman, K., Falkowski, P.G., Morel, F.M.M., 2003. The Elemental Composition of Some Marine Phytoplankton. Journal of Phycology 39, 1145–1159.

Hoegh-Guldberg, O., Mumby, P.J., Hooten, A.J., Steneck, R.S., Greenfield, P., Gomez, E., Harvell, C.D., Sale, P.F., Edwards, A.J., Caldeira, K., Knowlton, N., Eakin, C.M., Iglesias-Prieto, R., Muthiga, N., Bradbury, R.H., Dubi, A., Hatziolos, M.E., 2008. Change and Ocean Acidification. Science 318, 1737–1742.

Hogg, N., Owens, W.B., 1999. Direct measurement of the deep circulation within the Brazil Basin. Deep Sea Research Part II: Topical Studies in Oceanography 46, 335–353.

Hogg, N.G., Owens, W.B., Siedler, G., Zenk, W., 1996. Circulation in the Deep Brazil Basin, in: Wefer, G., Berger, W.H., Siedler, G., Webb, D. (Eds.), The South Atlantic: Present and Past Circulation. Springer, Berlin, pp. 249–260.

Hogg, N.G., Siedler, G., Zenk, W., 1999. Circulation and Variability at the Southern Boundary of the Brazil Basin. Journal of Physical Oceanography 29, 145–157.

Hogg, N.G., Thurnherr, A.M., 2005. A Zonal Pathway for NADW in the South Atlantic. Journal of Oceanography 61.

Holfort, J., Johnson, K., Schneider, B., Siedler, G., Wallace, D., 1998. Meridional transport of dissolved inorganic carbon. Global Biogeochemical Cycles 12, 479–499.

Holfort, J., Siedler, G., 2001. The Meridional Oceanic Transports of Heat and Nutrients in the South Atlantic. Journal of Physical Oceanography 31, 5–29.

Holley, S.E., Hydes, D.J., 1994. Procedures for the determination of dissolved oxygen in seawater. Technical Report. James Rennell Centre for Ocean Circulation.

Hoppema, M., Goeyens, L., 1999. Redfield behavior of carbon, nitrogen, and phosphorus depletions in Antarctic surface water. Limnology and Oceanography 44, 220–224.

Hoppema, M., Roether, W., Bellerby, R.G.J., de Baar, H.J.W., 2001. Direct measurements reveal insignificant storage of anthropogenic CO_2 in the Abyssal Weddell Sea. Geophysical Research Letters 28, 1747.

Hoppema, M., Velo, A., van Heuven, S., Tanhua, T., Key, R.M., Lin, X., Bakker, D.C.E., Perez, F.F., 2009. Consistency of cruise data of the CARINA database in the Atlantic sector of the Southern Ocean. Earth System Science Data , 63–75.

Hsu, K.J., Weissert, H.J., 1985. South Atlantic Paleoceanography. Cambridge University Press, Cambridge.

Hu, A., Meehl, G.A., Han, W., Yin, J., 2009. Transient response of the MOC and climate to potential melting of the Greenland Ice Sheet in the 21st century. Geophysical Research Letters 36, L10707, doi:10.1029/2009GL037998.

Huang, R.X., Jin, X., 2002. Deep Circulation in the South Atlantic Induced by Bottom-Intensified Mixing over the Midocean Ridge. Journal of Physical Oceanography 32, 1150–1164.

Huhn, O., Hellmer, H.H., Rhein, M., Rodehacke, C., Roether, W., Schodlok, M.P., Schröder, M., 2008. Evidence of deep- and bottom-water formation in the western Weddell Sea. Deep Sea Research Part II: Topical Studies in Oceanography 55, 1098–1116.

Huisman, S.E., den Toom, M., Dijkstra, H.A., Drijfhout, S., 2010. An Indicator of the Multiple Equilibria Regime of the Atlantic Meridional Overturning Circulation. Journal of Physical Oceanography 40, 551–567.

Ilyina, T., Zeebe, R.E., Maier-Reimer, E., Heinze, C., 2009. Early detection of ocean acidification effects on marine calcification. Global Biogeochemical Cycles 23, GB1008, doi:10.1029/2008GB003278.

Ishii, M., Kimoto, M., 2009. Reevaluation of Historical Ocean Heat Content Variations with Time-Varying XBT and MBT Depth Bias Corrections. Journal of Oceanography 65, 287–299.

Jackett, D.R., McDougall, T.J., 1997. A Neutral Density Variable for the World's Oceans. Journal of Physical Oceanography 27, 237–263.

Jacobs, S.S., 1991. On the nature and significance of the Antarctic Slope Front. Marine Chemistry 35, 9–24.

Jacobs, S.S., 2004. Bottom water production and its links with the thermohaline circulation. Antarctic Science 16, 427–437.

Jacobs, S.S., Amos, A.F., Bruchhausen, P.M., 1970. Ross Sea oceanography and Antarctic Bottom Water formation. Deep-Sea Research 17, 935–962.

Jacobs, S.S., Georgi, D.T., 1977. Observations on the southwest Indian/Atlantic Ocean. Deep-Sea Research 24, 43–84.

Jacobson, A.R., Mikaloff Fletcher, S.E., Gruber, N., Sarmiento, J.L., Gloor, M., 2007. A joint atmosphere-ocean inversion for surface fluxes of carbon dioxide: 2. Regional results. Global Biogeochemical Cycles 21, GB1020, doi:10.1029/2006GB002703.

Jansen, E., Overpeck, J., Briffa, K., Duplessy, J.C., Joos, F., Masson-Delmotte, V., Olago, D., Otto-Bliesner, B., Peltier, W., Rahmstorf, S., Ramesh, R., Raynaud, D., Rind, D., Solomina, O., Villalba, R., Zhang, D., 2007. Palaeoclimate, in: Solomon, S., Qin, D., Manning, M., Chen, Z., Marquis, M., Averyt, K., Tignor, M., Miller, H.L. (Eds.), Climate Change 2007: The Physical Science Basis. Contribution of Working Group I to the Fourth Assessment Report of the Intergovernmental Panel on Climate Change. Cambridge University Press, Cambridge, United Kingdom and New York, NY, USA.

Jenkins, W.J., 1987. 3H and 3He in the Beta Triangle: Observations of Gyre Ventilation and Oxygen Utilization Rates. Journal of Physical Oceanography 17, 763–783.

Johns, W.E., Baringer, M.O., Beal, L.M., Cunningham, S.A., Kanzow, T., Bryden, H.L., Hirschi, J.J.M., Marotzke, J., Meinen, C.S., Shaw, B., Curry, R., 2011. Continuous, Array-Based Estimates of Atlantic Ocean Heat Transport at 26.5°N. Journal of Climate 24, 2429–2449.

Johns, W.E., Beal, L.M., Baringer, M.O., Molina, J.R., Cunningham, S.A., Kanzow, T., Rayner, D., 2008. Variability of Shallow and Deep Western Boundary Currents off the Bahamas during 2004-05: Results from the 26°N RAPID-MOC Array. Journal of Physical Oceanography 38, 605–623.

Johnson, A., Biscaye, E., 1976. Abyssal Hydrography, Nephelometry, Currents, and Benthic Boundary Layer Structure in the Vema Channel. Journal of Geophysical Research 81, 5771–5786.

Johnson, G.C., 2008. Quantifying Antarctic Bottom Water and North Atlantic Deep Water volumes. Journal of Geophysical Research 113, C05027, doi:10.1029/2007JC004477.

Johnson, K.M., 1992. Operator's Manual: Single-Operator Multiparameter Metabolic Analyzer (SOMMA) for Total Carbon Dioxide (CT) with Coulometric Detection. Brookhaven National Laboratory, Brookhaven, N. Y. .

Johnson, K.M., King, A.E., Sieburth, J.M., 1985. Coulometric TCO_2 Analyses for Marine Studies; An Introduction. Marine Chemistry 16, 61–82.

Johnson, K.M., Sieburth, J.M., leB. Williams, P.J., Brändström, L., 1987. Coulometric Total Carbon Dioxide Analysis for Marine Studies: Automation and Calibration. Marine Chemistry 21, 117–133.

Johnson, K.M., Wills, K.D., Butler, D.B., Johnson, W.K., Wong, C.S., 1993. Coulometric total carbon dioxide analysis for marine studies : maximizing the performance of an automated gas extraction system and coulometric detector. Marine Chemistry 44, 167–187.

Jullion, L., 2008. Water mass modification in the Southwestern Atlantic. Ph.D. thesis. University of East Anglia.

Jullion, L., Heywood, K.J., Naveira Garabato, A.C., Stevens, D.P., 2010a. Circulation and Water Mass Modification in the Brazil-Malvinas Confluence. Journal of Physical Oceanography 40, 845–864.

Jullion, L., Jones, S.C., Naveira Garabato, A.C., Meredith, M.P., 2010b. Wind-controlled export of Antarctic Bottom Water from the Weddell Sea. Geophysical Research Letters 37, L09609, doi:10.1029/2010GL042822.

Kanamitsu, M., Ebisuzaki, W., Woollen, J., Yang, S.K., Hnilo, J.J., Fiorino, M., Potter, G.L., 2002. NCEP-DOE AMIP-II Reanalysis (R-2). Bulletin of the American Meteorological Society 83, 1631–1643.

Karl, D.M., Letelier, R.M., 2008. Nitrogen fixation-enhanced carbon sequestration in low nitrate, low chlorophyll seascapes. Marine Ecology Progress Series 364, 257–268.

Karstensen, J., Quadfasel, D., 2002. Water subducted into the Indian Ocean subtropical gyre. Deep Sea Research Part II: Topical Studies in Oceanography 49, 1441–1457.

Karstensen, J., Stramma, L., Visbeck, M., 2008. Oxygen minimum zones in the eastern tropical Atlantic and Pacific oceans. Progress in Oceanography 77, 331–350.

Karstensen, J., Tomczak, M., 1998. Age determination of mixed water masses using CFC and oxygen data. Journal of Geophysical Research 103, 18599–18609.

Kawakami, H., Honda, M.C., Wakita, M., Watanabe, S., 2007. Time-series observation of dissolved inorganic carbon and nutrients in the northwestern North Pacific. Journal of Oceanography 63, 967–982.

Keeling, C.D., 1960. The Concentration and Isotopic Abundances of Carbon Dioxide in the Atmosphere. Tellus , 199–203.

Keeling, C.D., Brix, H., Gruber, N., 2004. Seasonal and long-term dynamics of the upper ocean carbon cycle at Station ALOHA near Hawaii. Global Biogeochemical Cycles 18, GB4006, doi:10.1029/2004GB002227.

Keeling, C.D., Piper, S.C., Whorf, T.P., Keeling, R.F., 2011. Evolution of natural and anthropogenic fluxes of atmospheric CO_2 from 1957 to 2003. Tellus B 63, 1–22.

Keeling, C.D., Whorf, T.P., 1994. Atmospheric CO_2 records from sites in the SIO air sampling network, in: Boden, T.A., Kaiser, D.P., Sepanski, R.J., Stoss, F.W. (Eds.), Trends '93: A Compendium of Data on Global Change. ORNL/CDIAC-65, Carbon Dioxide Information Center, Oak Ridge National Laboratory, Oak Ridge, TN, pp. 16–26.

Keeling, C.D., Whorf, T.P., Wahlen, M., van der Plicht, J., 1995. Interannual extremes in the rate of rise of atmospheric carbon dioxide since 1980. Nature 375, 666–670.

Kerr, R., Heywood, K.J., Mata, M.M., Garcia, C.A.E., 2012. On the outflow of dense water from the Weddell and Ross Seas in OCCAM model. Ocean Science 8, 369–388.

Key, R.M., Kozyr, A., Sabine, C.L., Lee, K., Wanninkhof, R., Bullister, J.L., Feely, R.A., Millero, F.J., Mordy, C., Peng, T.H., 2004. A global ocean carbon climatology: Results from Global Data Analysis Project (GLODAP). Global Biogeochemical Cycles 18, GB4031, doi:10.1029/2004GB002247.

Khatiwala, S., Tanhua, T., Mikaloff Fletcher, S., Gerber, M., Doney, S.C., Graven, H.D., Gruber, N., McKinley, G.A., Murata, A., Ríos, A.F., Sabine, C.L., Sarmiento, J.L., 2012. Global ocean storage of anthropogenic carbon. Biogeosciences Discussions 9, 8931–8988.

Kheshgi, H.S., 1995. Sequestering atmospheric Carbon Dioxide by increasing ocean alkalinity. Energy 20, 915–922.

King, B.A., 2010. Cruise Report: Hydrographic sections across the Brazil Current and at 24°S in the Atlantic. Technical Report.

Kirkwood, D., 1996. Nutrients : Practical notes on their determination in sea water. ICES Techniques in marine environmental sciences , Copenhagen, International Council for the Explorat.

Kistler, R., Kalnay, E., Collins, W., Saha, S., White, G., Woollen, J., Chelliah, M., Ebisuzaki, W., Kanamitsu, M., Kousky, V., Dool, H.V.D., Jenne, R., Fiorino, M., 2001. The NCEP - NCAR 50-Year Reanalysis : Monthly Means CD-ROM and Documentation. Bulletin of the American Meteorological Society 82, 247–268.

Klatt, O., Fahrbach, E., Hoppema, M., Rohardt, G., 2005. The transport of the Weddell Gyre across the Prime Meridian. Deep Sea Research Part II: Topical Studies in Oceanography 52, 513–528.

Klinck, J.M., 1998. Heat and salt changes on the continental shelf west of the Antarctic Peninsula between January 1993 and January 1994 depth. Journal of Geophysical Research 103, 7617–7636.

Koeve, W., Kähler, P., 2010. Ocean science: Balancing ocean nitrogen. Nature Geoscience 3, 383–384.

Kolla, V., Sullivan, L., Streeter, S.S., Langseth, M.G., 1976. Spreading of Antarctic Bottom Water and its effects on the floor of the Indian Ocean inferred from Bottom-Water potential temperature, turbidity, sea-floor photography. Marine Geology 21, 171–189.

Körtzinger, A., Hedges, J.I., Quay, P.D., 2001. Redfield ratios revisited: Removing the biasing effect of anthropogenic CO_2. Limnology and Oceanography 46, 964–970.

Kuhlbrodt, T., Griesel, A., Montoya, M., Levermann, A., Hofmann, M., Rahmstorf, S., 2007. On the driving processes of the Atlantic Meridional Overturning Circulation. Reviews of Geophysics 45, 1–32.

Kusahara, K., Hasumi, H., Tamura, T., 2010. Modeling sea ice production and dense shelf water formation in coastal polynyas around East Antarctica. Journal of Geophysical Research 115, C10006, doi:10.1029/2010JC006133.

Lachkar, Z., Orr, J.C., Dutay, J.C., 2009. Seasonal and mesoscale variability of oceanic transport of anthropogenic CO_2. Biogeosciences 6, 2509–2523.

Ladd, C., Thompson, L., 2001. Water Mass Formation in an Isopycnal Model of the North Pacific. Journal of Physical Oceanography 31, 1517–1537.

Lal, R., 2003. Soil erosion and the global carbon budget. Environment International 29, 437–50.

Laruelle, G.G., Roubeix, V., Sferratore, A., Brodherr, B., Ciuffa, D., Conley, D.J., Dürr, H.H., Garnier, J., Lancelot, C., Le Thi Phuong, Q., Meunier, J.D., Meybeck, M., Michalopoulos, P., Moriceau, B., Ní Longphuirt, S., Loucaides, S., Papush, L., Presti, M., Ragueneau, O., Regnier, P., Saccone, L., Slomp, C.P., Spiteri, C., Van Cappellen, P., 2009. Anthropogenic perturbations of the silicon cycle at the global scale: Key role of the land-ocean transition. Global Biogeochemical Cycles 23, GB4031, doi:10.1029/2008GB003267.

Laurian, A., Drijfhout, S.S., 2010. Response of the South Atlantic circulation to an abrupt collapse of the Atlantic meridional overturning circulation. Climate Dynamics 37, 521–530.

Le Houérou, H.N., 1996. Climate change, drought and desertification. Journal of Arid Environments 34, 133–185.

Le Quéré, C., Raupach, M.R., Canadell, J.G., Marland, G., Bopp, L., Ciais, P., Conway, T.J., Doney, S.C., Feely, R.A., Foster, P., Friedlingstein, P., Gurney, K., Houghton, R.A., House, J.I., Huntingford, C., Levy, P.E., Lomas, M.R., Majkut, J., Metzl, N., Ometto, J.P., Peters, G.P., Prentice, I.C., Randerson, J.T., Running, S.W., Sarmiento, J.L., Schuster, U., Sitch, S., Takahashi, T., Viovy, N., van der Werf, G.R., Woodward, F.I., 2009. Trends in the sources and sinks of carbon dioxide. Nature Geoscience 2, 831–836.

Le Quéré, C., Rödenbeck, C., Buitenhuis, E.T., Conway, T.J., Langenfelds, R., Gomez, A., Labuschagne, C., Ramonet, M., Nakazawa, T., Metzl, N., Gillett, N., Heimann, M., 2007. Saturation of the southern ocean CO_2 sink due to recent climate change. Science 316, 1735–8.

Le Quéré, C., Takahashi, T., Buitenhuis, E.T., Rödenbeck, C., Sutherland, S.C., 2010. Impact of climate change and variability on the global oceanic sink of CO_2. Global Biogeochemical Cycles 24, GB4007, doi:10.1029/2009GB003599.

Ledwell, J., Montgomery, E., Polzin, K., St. Laurent LC, Schmitt, R., Toole, J., 2000. Evidence for enhanced mixing over rough topography in the abyssal ocean. Nature 403, 179–82.

Ledwell, J.R., St Laurent, L.C., Girton, J.B., Toole, J.M., 2011. Diapycnal Mixing in the Antarctic Circumpolar Current. Journal of Physical Oceanography 41, 241–246.

Lee, K., Choi, S.D., Park, G.H., Wanninkhof, R., Peng, T.H., Key, R.M., Sabine, C.L., Feely, R.A., Bullister, J.L., Millero, F.J., Kozyr, A., 2003. An updated anthropogenic CO_2 inventory in the Atlantic Ocean. Global Biogeochemical Cycles 17, GB1116, doi:10.1029/2003GB002067.

Lee, K., Tong, L.T., Millero, F.J., Sabine, C.L., Dickson, A.G., Goyet, C., Park, G.H., Wanninkhof, R., Feely, R.A., Key, R.M., 2006. Global relationships of total alkalinity with salinity and temperature in surface waters of the world's oceans. Geophysical Research Letters 33, L19605, doi:10.1029/2006GL027207.

Legeais, J.F., Speich, S., Arhan, M., Ansorge, I., Fahrbach, E., Garzoli, S., Klepikov, A., 2005. The baroclinic transport of the Antarctic Circumpolar Current south of Africa. Geophysical Research Letters 32, L24602, doi:10.1029/2005GL023271.

Lenn, Y.D., Chereskin, T.K., 2009. Observations of Ekman Currents in the Southern Ocean. Journal of Physical Oceanography 39, 768–779.

Levermann, A., Griesel, A., Hofmann, M., Montoya, M., Rahmstorf, S., 2005. Dynamic sea level changes following changes in the thermohaline circulation. Climate Dynamics 24, 347–354.

Levine, N.M., Doney, S.C., Wanninkhof, R., Lindsay, K., Fung, I.Y., 2008. Impact of ocean carbon system variability on the detection of temporal increases in anthropogenic CO_2. Journal of Geophysical Research 113, C03019, doi:10.1029/2007JC004153.

Levitus, S., Antonov, J.I., Boyer, T.P., Locarnini, R.A., Garcia, H.E., Mishonov, A.V., 2009. Global ocean heat content 1955-2008 in light of recently revealed instrumentation problems. Geophysical Research Letters 36, L07608, doi:10.1029/2008GL037155.

Lewis, E., Wallace, D.W.R., 1998. Program developed for CO_2 system calculations. Technical Report. Carbon Dioxide Information Analysis Center, Oak Ridge National Laboratory. Oak Ridge, Tennessee.

Limeburner, R., Whitehead, J., Cenedese, C., 2005. Variability of Antarctic bottom water flow into the North Atlantic. Deep Sea Research Part II: Topical Studies in Oceanography 52, 495–512.

Liu, J., Xiao, T., Chen, L., 2011. Intercomparisons of Air-Sea Heat Fluxes over the Southern Ocean. Journal of Climate 24, 1198–1211.

Lo Monaco, C., Álvarez, M., Key, R.M., Lin, X., Tanhua, T., Tilbrook, B., Bakker, D.C.E., van Heuven, S., Hoppema, M., Metzl, N., Ríos, A.F., Sabine, C.L., Velo, A., 2010. Assessing the internal consistency of the CARINA database in the Indian sector of the Southern Ocean. Earth System Science Data 2, 51–70.

Lo Monaco, C., Goyet, C., Metzl, N., Poisson, A., Touratier, F., 2005a. Distribution and inventory of anthropogenic CO_2 in the Southern Ocean: Comparison of three data-based methods. Journal of Geophysical Research 110, C09S02, doi:10.1029/2004JC002571.

Lo Monaco, C., Metzl, N., Poisson, A., Brunet, C., Schauer, B., 2005b. Anthropogenic CO_2 in the Southern Ocean: Distribution and inventory at the Indian-Atlantic boundary (World Ocean Circulation Experiment line I6). Journal of Geophysical Research 110, C06010, doi:10.1029/2004JC002643.

Locarini, R.A., Mishonov, A.V., Antonov, J.I., Boyer, T.P., Garcia, H.E., Baranova, O.K., Zweng, M.M., Johnson, D.R., 2010. World Ocean Atlas 2009, Volume 1: Temperature. Technical Report. S. Levitus, Ed. NOAA Atlas NESDIS 68, U.S. Government Printing Office. Washington, D.C.

Locarnini, R.A., Whitworth, T., Nowlin, W.D., 1993. The importance of the Scotia Sea on the outflow of Weddell Sea Deep Water. Journal of Marine Research 51, 135–153.

Lovenduski, N.S., Gruber, N., Doney, S.C., 2008. Toward a mechanistic understanding of the decadal trends in the Southern Ocean carbon sink. Global Biogeochemical Cycles 22, GB3016, doi:10.1029/2007GB003139.

Lovenduski, N.S., Ito, T., 2009. The future evolution of the Southern Ocean CO_2 sink. Journal of Marine Research 67, 597–617.

Luis, A.J., Pednekar, S.M., 2010. Hydrodynamics between Africa and Antarctica during Austral Summer 2008. Journal of Marine Systems 83, 45–57.

Lumpkin, R., Speer, K., 2007. Global Ocean Meridional Overturning. Journal of Physical Oceanography 37, 2550.

Lundberg, L., Haugan, P.M., 1996. A Nordic Seas-Arctic Ocean carbon budget from volume flows and inorganic carbon data. Global Biogeochemical Cycles 10, 493–510.

Lutjeharms, J., Ansorge, I., 2001. The Agulhas Return Current. Journal of Marine Systems 30, 115–138.

Lutjeharms, J.R.E., 2007. Three decades of research on the greater Agulhas Current. Ocean Science 3, 129–147.

Lutjeharms, J.R.E., van Ballegooyen, R.C., 1984. Topographic Control of the Agulhas Current System. Deep-Sea Research 31, 1321–1337.

Lutjeharms, J.R.E., van Ballegooyen, R.C., 1988. The Retroflection of the Agulhas Current. Journal of Physical Oceanography 18, 1570–1583.

Lux, M., Mercier, H., Arhan, M., 2001. Interhemispheric exchanges of mass and heat in the Atlantic Ocean in January-March 1993. Deep Sea Research Part I: Oceanographic Research Papers 48, 605–638.

Maamaatuaiahutapu, K., Garc, V., 1998. Transports of the Brazil and Malvinas Currents at their Confluence. Journal of Marine Research 56, 417–438.

Macdonald, A., Wunsch, C., 1996. An estimate of global ocean circulation and heat fluxes. Nature 382, 436–439.

Macdonald, A.M., Baringer, M.O., Wanninkhof, R., Lee, K., Wallace, D.W.R., 2003. A 1998-1992 comparison of inorganic carbon and its transport across 24.5°N in the Atlantic. Deep Sea Research Part II: Topical Studies in Oceanography 50, 3041–3064.

Mantisi, F., Beauverger, C., Poisson, A., Metzl, N., 1991. Chlorofluoromethanes in the western Indian sector of the Southern Ocean and their relations with geochemical tracers. Marine Chemistry 35, 151–167.

Mantyla, A.W., Reid, J.L., 1983. Abyssal characteristics of the World Ocean waters. Deep-Sea Research 30, 805–833.

Mantyla, A.W., Reid, J.L., 1995. On the origins of deep and bottom waters of the Indian Ocean. Journal of Geophysical Research 100, 2417–2439.

Marinov, I., Gnanadesikan, A., Toggweiler, J.R., Sarmiento, J.L., 2006. The Southern Ocean biogeochemical divide. Nature 441, 964–7.

Marshall, J., Speer, K., 2012. Closure of the meridional overturning circulation through Southern Ocean upwelling. Nature Geoscience 5, 171–180.

Martin, J.H., Fitzwater, S.E., Gordon, R.M., 1990. Iron deficiency limits phytoplankton growth in Antarctic waters. Global Biogeochemical Cycles 4, 5–12.

Martin, J.H., Knauer, G.A., Karl, D.M., Broenkow, W.W., 1987. VERTEX: carbon cycling in the northeast Pacific. Deep-Sea Research 34, 267–285.

Matano, R.P., Simionato, C.G., de Ruijter, W.P., van Leeuween, P.J., Strub, P.T., Chelton, D.B., Schlax, M.G., 1998. Seasonal variability in the Agulhas Retroflection region. Geophysical Research Letters 25, 4361–4364.

Mathiot, P., Goosse, H., Fichefet, T., Barnier, B., Gallée, H., 2011. Modelling the seasonal variability of the Antarctic Slope Current. Ocean Science 7, 455–470.

Matsumoto, K., Gruber, N., 2005. How accurate is the estimation of anthropogenic carbon in the ocean? An evaluation of the Δ C * method. Global Biogeochemical Cycles 19, GB3014, doi:10.1029/2004GB002397.

McCarthy, G., McDonagh, E., King, B., 2011. Decadal Variability of Thermocline and Intermediate Waters at 24°S in the South Atlantic. Journal of Physical Oceanography 41, 157–165.

McCarthy, G.D., King, B.A., Cipollini, P., McDonagh, E.L., Blundell, J.R., Biastoch, A., 2012. On the sub-decadal variability of South Atlantic Antarctic Intermediate Water. Geophysical Research Letters 39, L10605, doi:10.1029/2012GL051270.

McCartney, M., 1977. Subantarctic Mode Water, in: Angel, M. (Ed.), A Voyage of Discovery: George Deacon 70th Anniversary Volume. Pergamon, pp. 103–119.

McCartney, M., Bennett, S., Woodgate-Jones, M., 1991. Eastward Flow through the Mid-Atlantic Ridge at 11°N and Its Influence on the Abyss of the Eastern Basin. Journal of Physical Oceanography 21, 1089–1121.

McDonagh, E., Arhan, M., Heywood, K., 2002. On the circulation of bottom water in the region of the Vema Channel. Deep Sea Research Part I: Oceanographic Research Papers 49, 1119–1139.

McDonagh, E., Bryden, H., King, B., Sanders, R., 2008. The circulation of the Indian Ocean at 32°S. Progress In Oceanography 79, 20–36.

McDonagh, E.L., 2009. Cruise Report: Hydrographic sections of Drake Passage. Technical Report.

McDonagh, E.L., Bryden, H.L., King, B.A., Sanders, R.J., Cunningham, S.A., Marsh, R., 2005. Decadal Changes in the South Indian Ocean Thermocline. Journal of Climate 18, 1575–1590.

McDonagh, E.L., Heywood, K.J., Meredith, M.P., 1999. On the structure, paths, and fluxes associated with Agulhas rings. Journal of Geophysical Research 104, 7–20.

McDonagh, E.L., King, B.A., 2005. Oceanic Fluxes in the South Atlantic. Journal of Physical Oceanography 35, 109.

McIntosh, P., Rintoul, S., 1997. Do Box Inverse Models Work? Journal of Physical Oceanography 27, 291–308.

McNeil, B., Metzl, N., Key, R., Matear, R., Corbiere, A., 2007. An empirical estimate of the Southern Ocean air-sea CO_2 flux. Global Biogeochemical Cycles 21, GB3011, doi:10.1029/2007GB002991.

Mehrbach, C., Culberson, C.H., Hawley, J.E., Pytkowicz, R.M., 1973. Measurement of apparent dissociation constants of carbonic acid in seawater at atmospheric pressure. Limnology and Oceanography 18, 897–907.

Meijers, A.J.S., Klocker, A., Bindoff, N.L., Williams, G.D., Marsland, S.J., 2010. The circulation and water masses of the Antarctic shelf and continental slope between 30 and 80°E. Deep Sea Research Part II: Topical Studies in Oceanography 57, 723–737.

Meinen, C.S., Piola, A.R., Perez, R.C., Garzoli, S.L., 2012. Deep Western Boundary Current transport variability in the South Atlantic: preliminary results from a pilot array at 34.5° S. Ocean Science 8, 1041–1054.

Mellor, G.L., Ezer, T., 1991. A Gulf Stream Model and Altimetry Assimilation Scheme. Journal of Geophysical Research 96, 8779–8795.

Mercier, H., Arhan, M., Lutjeharms, J., 2003. Upper-layer circulation in the eastern Equatorial and South Atlantic Ocean in January-March 1995. Deep Sea Research Part I: Oceanographic Research Papers 50, 863–887.

Mercier, H., Morin, P., 1997. Hydrography of the Romanche and Chain Fracture Zones. Journal of Geophysical Research 102, 10373–10389.

Mercier, H., Speer, K.G., 1998. Transport of Bottom Water in the Romanche Fracture Zone and the Chain Fracture Zone. Journal of Physical Oceanography 4, 779–790.

Meredith, M., King, J., 2005. Rapid climate change in the ocean west of the Antarctic Peninsula during the second half of the 20th century. Geophysical Research Letters 32, L19604, doi:10.1029/2005GL024042.

Meredith, M.P., 2013. Oceanography: Replenishing the abyss. Nature Geoscience 6, 166–167.

Meredith, M.P., Gordon, A.L., Naveira Garabato, A.C., Abrahamsen, E.P., Huber, B.A., Jullion, L., Venables, H.J., 2011a. Synchronous intensification and warming of Antarctic Bottom Water outflow from the Weddell Gyre. Geophysical Research Letters 38, L03603, doi:10.1029/2010GL046265.

Meredith, M.P., Locarnini, A., Van Scoy, K.A., Watson, A.J., Heywood, K.J., King, B.A., 2000. On the sources of Weddell Gyre Antarctic Bottom Water. Journal of Geophysical Research 105, 1093–1104.

Meredith, M.P., Wallace, M.I., Stammerjohn, S.E., Renfrew, I.A., Clarke, A., Venables, H.J., Shoosmith, D.R., Souster, T., Leng, M.J., 2010. Changes in the freshwater composition of the upper ocean west of the Antarctic Peninsula during the first decade of the 21st century. Progress In Oceanography 87, 127–143.

Meredith, M.P., Woodworth, P.L., Chereskin, T.K., Marshall, D.P., Allison, L.C., Bigg, G.R., Donohue, K., Heywood, K.J., Hughes, C.W., Hibbert, A., Hogg, A.M., Johnson, H.L., Jullion, L., King, B.A., Leach, H., Lenn, Y.D., Morales Maqueda, M.A., Munday, D.R., Naveira Garabato, A.C., Provost, C., Sallée, J.B., Sprintall, J., 2011b. Sustained monitoring of the Southern Ocean at Drake Passage: Past achievements and future priorities. Reviews of Geophysics 49, 1–36.

Metzl, N., 2009. Decadal increase of oceanic carbon dioxide in Southern Indian Ocean surface waters (1991-2007). Deep Sea Research Part II: Topical Studies in Oceanography 56, 607–619.

Mikaloff Fletcher, S.E., Gruber, N., Jacobson, A.R., Doney, S.C., Dutkiewicz, S., Gerber, M., Follows, M., Joos, F., Lindsay, K., Menemenlis, D., Mouchet, A.,

Müller, S.A., Sarmiento, J.L., 2006. Inverse estimates of anthropogenic CO_2 uptake, transport, and storage by the ocean. Global Biogeochemical Cycles 20, GB2002, doi:10.1029/2005GB002530.

Mikaloff Fletcher, S.E., Gruber, N., Jacobson, A.R., Gloor, M., Doney, S.C., Dutkiewicz, S., Gerber, M., Follows, M., Joos, F., Lindsay, K., Menemenlis, D., Mouchet, A., Müller, S.A., Sarmiento, J.L., 2007. Inverse estimates of the oceanic sources and sinks of natural CO_2 and the implied oceanic carbon transport. Global Biogeochemical Cycles 21, GB1010, doi:10.1029/2006GB002751.

Millero, F.J., 2000. The Carbonate System in Marine Environments, in: Gianguzza, A., Pelizetti, E., Sammartono, S. (Eds.), Chemical Processes in Marine Environments. Springer-Verlag, Berlin Heidelberg, Germany, pp. 9–37.

Millero, F.J., 2007. The marine inorganic carbon cycle. Chemical Reviews 107, 308–41.

Mills, M.M., Arrigo, K.R., 2010. Magnitude of oceanic nitrogen fixation influenced by the nutrient uptake ratio of phytoplankton. Nature Geoscience 3, 412–416.

Mintrop, L., 2004. VINDTA, Versatile instrument for the Determination of Titration Alkalinity. Manual for versions 3S and 3C. Version 2.0. MARine ANalytics and DAta (MARIANDA), Kiel, Germany , 45.

Moffat, C., Owens, B., Beardsley, R.C., 2009. On the characteristics of Circumpolar Deep Water intrusions to the west Antarctic Peninsula Continental Shelf. Journal of Geophysical Research 114, C05017, doi:10.1029/2008JC004955.

Molinelli, E.J., 1981. The Antarctic Influence on Antarctic Intermediate Water. Journal of Marine Research 39, 267–293.

Moore, J.K., Abbott, M.R., 2000. Phytoplankton chlorophyll distributions and primary production in the Southern Ocean. Journal of Geophysical Research 105, 28709–28722.

Munk, W.H., 1966. Abyssal recipes. Deep-Sea Research 13, 707–730.

Murata, A., Kumamoto, Y., Sasaki, K., Watanabe, S., Fukasawa, M., 2008. Decadal increases of anthropogenic CO_2 in the subtropical South Atlantic Ocean along 30°S. Journal of Geophysical Research 113, C06007, doi:10.1029/2007JC004424.

Murata, A., Kumamoto, Y., Sasaki, K., Watanabe, S., Fukasawa, M., 2010. Decadal increases in anthropogenic CO_2 along 20°S in the South Indian Ocean. Journal of Geophysical Research 115, C12055, doi:10.1029/2010JC006250.

Murata, A., Kumamoto, Y., Watanabe, S., Fukasawa, M., 2007. Decadal increases of anthropogenic CO_2 in the South Pacific subtropical ocean along 32°S. Journal of Geophysical Research 112, C05033, doi:10.1029/2005JC003405.

Naveira Garabato, A., Heywood, K., Stevens, D., 2002a. Modification and pathways of Southern Ocean Deep Waters in the Scotia Sea. Deep Sea Research Part I: Oceanographic Research Papers 49, 681–705.

Naveira Garabato, A.C., Ferrari, R., Polzin, K.L., 2011. Eddy stirring in the Southern Ocean. Journal of Geophysical Research 116, C09019.

Naveira Garabato, A.C., Jullion, L., Stevens, D.P., Heywood, K.J., King, B.A., 2009. Variability of Subantarctic Mode Water and Antarctic Intermediate Water in the Drake Passage during the Late-Twentieth and Early-Twenty-First Centuries. Journal of Climate 22, 3661.

Naveira Garabato, A.C., McDonagh, E.L., Stevens, D.P., Heywood, K.J., Sanders, R.J., 2002b. On the export of Antarctic Bottom Water from the Weddell Sea. Deep Sea Research Part II: Topical Studies in Oceanography 49, 10.

Naveira Garabato, A.C., Polzin, K.L., King, B.A., Heywood, K.J., Visbeck, M., 2004. Widespread intense turbulent mixing in the Southern Ocean. Science 303, 210–3.

Naveira Garabato, A.C., Stevens, D.P., Heywood, K.J., 2003. Water mass conversion, fluxes, and mixing in the Scotia Sea diagnosed by an inverse model. Journal of Physical Oceanography 33, 2565–2587.

Nelson, D.M., Treguer, P., Brzezinski, M.A., Leynaert, A., Quéguiner, B., 1995. Production and dissolution of biogenic silica in the ocean: Revised global estimates, comparison with regional data and relationship to biogenic sedimentation. Global Biogeochemical Cycles 9, 359–372.

Nelson, G., Hutchings, L., 1983. The Benguela upwelling area. Progress in Oceanography 12, 333–356.

Nowlin, W.D., Clifford, M., 1982. The kinematic and thermohaline zonation of the Antarctic Circumpolar Current at Drake Passage. Journal of Marine Research 40, 481–507.

Nowlin, W.D., Whitworth, T., Pillsbury, R.D., 1977. Structure and Transport of the Antarctic Circumpolar Current at Drake Passage from Short-Term Measurements. Journal of Physical Oceanography 7, 788–802.

Ohshima, K.I., Fukamachi, Y., Williams, G.D., Nihashi, S., Roquet, F., Kitade, Y., Tamura, T., Hirano, D., Herraiz-Borreguero, L., Field, I., Hindell, M., Aoki, S., Wakatsuchi, M., 2013. Antarctic Bottom Water production by intense sea-ice formation in the Cape Darnley polynya. Nature Geoscience 6, 235–240.

Olbers, D., Visbeck, M., 2005. A model of the zonally averaged stratification and overturning in the Southern Ocean. Journal of Physical Oceanography 35, 1190–1205.

Oliveira, L.R., Piola, A.R., Mata, M.M., Soares, I.D., 2009. Brazil Current surface circulation and energetics observed from drifting buoys. Journal of Geophysical Research 114, C10006, doi:10.1029/2008JC004900.

Orr, J.C., Fabry, V.J., Aumont, O., Bopp, L., Doney, S.C., Feely, R.a., Gnanadesikan, A., Gruber, N., Ishida, A., Joos, F., Key, R.M., Lindsay, K., Maier-Reimer, E., Matear, R., Monfray, P., Mouchet, A., Najjar, R.G., Plattner, G.K., Rodgers, K.B., Sabine, C.L., Sarmiento, J.L., Schlitzer, R., Slater, R.D., Totterdell, I.J., Weirig, M.F., Yamanaka, Y., Yool, A., 2005. Anthropogenic ocean acidification over the twenty-first century and its impact on calcifying organisms. Nature 437, 681–6.

Orsi, A.H., Jacobs, S.S., Gordon, A.L., Visbeck, M., 2001. Cooling and ventilating the Abyssal Ocean. Geophysical Research Letters 28, 2923.

Orsi, A.H., Johnson, G.C., Bullister, J.L., 1999. Circulation, mixing, and production of Antarctic Bottom Water. Progress in Oceanography 43, 55–109.

Orsi, A.H., Nowlin, W.D., Whitworth, T., 1993. On the circulation and stratification of the Weddell Gyre. Deep Sea Research Part I: Oceanographic Research Papers 41, 169–203.

Orsi, A.H., Whitworth, T., Nowlin, W.D., 1995. On the meridional extent and fronts of the Antarctic Circumpolar Current. Deep Sea Research Part I: Oceanographic Research Papers 42, 641–673.

Pardo, P.C., Vázquez-Rodríguez, M., Pérez, F.F., Rios, A.F., 2011. CO_2 air-sea disequilibrium and preformed alkalinity in the Pacific and Indian oceans calculated from subsurface layer data. Journal of Marine Systems 84, 67–77.

Park, G.H., Wanninkhof, R., 2012. A large increase of the CO_2 sink in the western tropical North Atlantic from 2002 to 2009. Journal of Geophysical Research 117, C08029, doi:10.1029/2011JC007803.

Park, Y.H., Charriaud, E., Craneguy, P., Kartavtseff, A., 2001. Fronts, transport, and Weddell Gyre at 30°E between Africa and Antarctica. Journal of Geophysical Research 106, 2857–2879.

Park, Y.H., Charriaud, E., Fieux, M., 1998. Thermohaline structure of the Antarctic Surface Water/Winter Water in the Indian sector of the Southern Ocean. Journal of Marine Systems 17, 5–23.

Park, Y.H., Gamberoni, L., Charriaud, E., 1993. Frontal Structure, Water Masses, and Circulation in the Crozet Basin Crozet Basin. Journal of Geophysical Research 98, 12361–12385.

Patra, P.K., Maksyutov, S., Ishizawa, M., Nakazawa, T., Takahashi, T., Ukita, J., 2005. Interannual and decadal changes in the sea-air CO_2 flux from atmospheric CO_2 inverse modeling. Global Biogeochemical Cycles 19, GB4013, doi:10.1029/2004GB002257.

Peacock, S., 2004. Debate over the ocean bomb radiocarbon sink: Closing the gap. Global Biogeochemical Cycles 18, GB2022, doi:10.1029/2003GB002211.

Peng, T., Wanninkhof, R., Feely, R., 2003. Increase of anthropogenic CO_2 in the Pacific Ocean over the last two decades. Deep Sea Research Part II: Topical Studies in Oceanography 50, 3065–3082.

Peng, T.H., Wanninkhof, R., 2010. Increase in anthropogenic CO_2 in the Atlantic Ocean in the last two decades. Deep Sea Research Part I: Oceanographic Research Papers 57, 755–770.

Perez, F.F., Alvarez, M., Aida, F.R., 2002. Improvements on the back-calculation technique for estimating anthropogenic CO_2. Deep Sea Research Part I: Oceanographic Research Papers 49, 859–875.

Pérez, F.F., Mercier, H., Vázquez-Rodríguez, M., Lherminier, P., Velo, A., Pardo, P.C., Rosón, G., Ríos, A.F., 2013. Atlantic Ocean CO_2 uptake reduced by weakening of the meridional overturning circulation. Nature Geoscience 6, 146–152.

Pérez, F.F., Vázquez-Rodríguez, M., Louarn, E., Padín, X.A., Mercier, H., Ríos, A.F., 2008. Temporal variability of the anthropogenic CO_2 storage in the Irminger Sea. Biogeosciences 5, 1669–1679.

Peterson, R.G., 1992. The boundary currents in the western Argentine Basin. Deep Sea Research Part A. Oceanographic Research Papers 39, 623–644.

Peterson, R.G., Stramma, L., 1991. Upper-level circulation in the South Atlantic Ocean. Progress In Oceanography 26, 1–73.

Peterson, R.G., Whitworth, T., 1989. The subantarctic and polar fronts in relation to deep water masses through the southwestern Atlantic. Journal of Geophysical Research 94, 10817.

Piecuch, C.G., Ponte, R.M., 2012. Importance of Circulation Changes to Atlantic Heat Storage Rates on Seasonal and Interannual Time Scales. Journal of Climate 25, 350–362.

Piola, A.R., Gordon, A.L., 1989. Intermediate waters in the southwest South Atlantic. Deep-Sea Research 36, 1–16.

Poisson, A., Metzl, N., Brunet, C., 1996. Cruise Report: I6S 1996. Technical Report.

Pollard, R., Tréguer, P., Read, J., 2006. Quantifying nutrient supply to the Southern Ocean. Journal of Geophysical Research 111, C05011, doi:10.1029/2005JC003076.

Polzin, K., Toole, J., Ledwell, J., Schmitt, R., 1997. Spatial Variability of Turbulent Mixing in the Abyssal Ocean. Science 276, 93–6.

Pondaven, P., Ragueneau, O., Tréguer, P., Hauvespre, A., Dezileau, L., Reyss, J.L., 2000. Resolving the 'opal paradox' in the Southern Ocean. Nature 405, 168–72.

Poole, R., Tomczak, M., 1999. Optimum multiparameter analysis of the water mass structure in the Atlantic Ocean thermocline. Deep Sea Research Part I: Oceanographic Research Papers 46, 1895–1921.

Prezelin, B.B., Hofmann, E.E., Mengelt, C., Klinck, J.M., 2000. The linkage between Upper Circumpolar Deep Water (UCDW) and phytoplankton assemblages on the west Antarctic Peninsula continental shelf. Journal of Marine Research 58, 165–202.

Prinn, R.G., Weiss, R.F., Fraser, P.J., Simmonds, P.G., Cunnold, D.M., Alyea, F.N., O'Doherty, S., Salameh, P., Miller, B.R., Huang, J., Wang, R.H.J., Hartley, D.E., Harth, C., Steele, L.P., Sturrock, G., Midgley, P.M., McCulloch, A., 2000. A history of chemically and radiatively important gases in air deduced from ALE/GAGE/AGAGE. Journal of Geophysical Research 105, 17751–17792.

Provost, C., Escoffier, C., Maamaatuaiahutapu, K., Kartavtseff, A., Gargon, V., 1999. Subtropical mode waters in the South Atlantic Ocean. Journal of Geophysical Research 104, 21033–21049.

Quartly, G.D., Kyte, E.A., Srokosz, M.A., Tsimplis, M.N., 2007. An intercomparison of global oceanic precipitation climatologies. Journal of Geophysical Research 112, D10121, doi:10.1029/2006JD007810.

Quigg, A., Finkel, Z.V., Irwin, A.J., Rosenthal, Y., Ho, T.Y., Reinfelder, J.R., Schofield, O., Morel, F.M.M., Falkowski, P.G., 2003. The evolutionary inheritance of elemental stoichiometry in marine phytoplankton. Nature 425, 291–294.

Rahmstorf, S., 1996. On the freshwater forcing and transport of the Atlantic thermohaline circulation. Climate Dynamics 12, 799–811.

Raven, J.A., Falkowski, P.G., 1999. Oceanic sinks for atmospheric CO_2. Plant, Cell and Environment 22, 741–755.

Raymond, P.A., Cole, J.J., 2003. Increase in the Export of Alkalinity from North America's Largest River. Science 301, 88–91.

Read, J.F., Pollard, R.T., 1999. Deep inflow into the Mozambique Basin. Journal of Geophysical Research 104, 3075–3090.

Redfield, A.C., Ketchum, B.H., Richards, F.A., 1963. The influence of organisms on the composition of sea-water. Interscience, New York.

Reid, J., Nowlin, W., Patzert, W., 1977. On the Characteristics and Circulation of the Southwestern Atlantic Ocean. Journal of Physical Oceanography 7, 62–91.

Reid, J.L., 1989. On the total geostrophic circulation of the South Atlantic Ocean : Flow patterns, tracers, and transports. Progress In Oceanography 23, 149–244.

Reiss, C., Hewes, C., Holm-Hansen, O., 2009. Influence of atmospheric teleconnections and Upper Circumpolar Deep Water on phytoplankton biomass around Elephant Island, Antarctica. Marine Ecology Progress Series 377, 51–62.

Ren, L., Speer, K., Chassignet, E.P., 2011. The mixed layer salinity budget and sea ice in the Southern Ocean. Journal of Geophysical Research 116, C08031, doi:10.1029/2010JC006634.

Renault, A., Provost, C., Sennéchael, N., Barré, N., Kartavtseff, A., 2011. Two full-depth velocity sections in the Drake Passage in 2006 - Transport estimates. Deep Sea Research Part II: Topical Studies in Oceanography 58, 2572–2591.

Rhein, M., Stramma, L., Krahmann, G., 1998. The spreading of Antarctic bottom water in the tropical Atlantic. Deep Sea Research Part I: Oceanographic Research Papers 45, 507–527.

Richardson, P.L., 2007. Agulhas leakage into the Atlantic estimated with subsurface floats and surface drifters. Deep Sea Research Part I: Oceanographic Research Papers 54, 1361–1389.

Rienecker, M.M., Suarez, M.J., Gelaro, R., Todling, R., Bacmeister, J., Liu, E., Bosilovich, M.G., Schubert, S.D., Takacs, L., Kim, G.K., Bloom, S., Chen, J., Collins, D., Conaty, A., da Silva, A., Gu, W., Joiner, J., Koster, R.D., Lucchesi, R., Molod, A., Owens, T., Pawson, S., Pegion, P., Redder, C.R., Reichle, R., Robertson, F.R., Ruddick, A.G., Sienkiewicz, M., Woollen, J., 2011. MERRA: NASA's Modern-Era Retrospective Analysis for Research and Applications. Journal of Climate 24, 3624–3648.

Rintoul, S., Bullister, J., 1999. A late winter hydrographic section from Tasmania to Antarctica. Deep Sea Research Part I: Oceanographic Research Papers 46, 1417–1454.

Rintoul, S.R., 1991. South Atlantic Interbasin Exchange. Journal of Geophysical Research 96, 2675–2692.

Rintoul, S.R., 1998. On the origin and influence of Adélie Land Bottom Water, in: Jacobs, S.S., Weiss, R.F. (Eds.), Ocean, Ice, and Atmosphere: Interactions at the Antarctic Continental Margin, Antarctic Research Series. American Geophysical Union, Washington, D.C., pp. 151–171.

Rintoul, S.R., Donguy, J.R., Roemmich, D.H., 1997. Seasonal evolution of upper ocean thermal structure between Tasmania and Antarctica. Deep Sea Research Part I: Oceanographic Research Papers 44, 1185–1202.

Rintoul, S.R., Hughes, C.W., Olbers, D., 2001. The Antarctic Circumpolar Current System, in: Siedler, G., Church, J., Gould, J. (Eds.), Ocean Circulation and Climate. Academic Press, pp. 271–302.

Rintoul, S.R., Solokov, S., 2001. Baroclinic transport variability of the Antarctic Circumpolar Current south of Australia (WOCE repeat section SR3). Journal of Geophysical Research 106, 2815–2832.

Ríos, A., Velo, A., Pardo, P., Hoppema, M., Pérez, F., 2012. An update of anthropogenic CO_2 storage rates in the western South Atlantic basin and the role of Antarctic Bottom Water. Journal of Marine Systems 94, 197–203.

Ríos, A.F., Vázquez-Rodríguez, M., Padin, X.A., Pérez, F.F., 2010. Anthropogenic carbon dioxide in the South Atlantic western basin. Journal of Marine Systems 83, 38–44.

Robinson, I., 2004. Measuring the Oceans from Space: The Principles and Methods of Satellite Oceanography.

Roden, G.I., 1986. Thermohaline fronts and baroclinic flow in the Argentine basin during the austral spring of 1984. Journal of Geophysical Research 91, 5075.

Roemmich, D., 1981. Estimation of Meridional Heat Flux in the North Atlantic by Inverse Methods. Journal of Physical Oceanography 10, 1972–1983.

Roether, W., Klein, B., Kozyr, A., Gaslightwala, A.F., Patrick, R.G., Van Woy, R., Millard, R., Mantyla, A., Jennings, J.C., 1990. Cruise Report: Cruise Narrative for A21, S04A and SR02. Technical Report.

Roether, W., Schlitzer, R., Putzka, A., Beining, P., Bulsiewicz, K., Rohardt, G., Delahoyde, F., 1993. A Chlorofluoromethane and Hydrographic Section Scross Drake Passage: Deep Water Ventilation and Meridional Property Transport. Journal of Geophysical Research 98, 14423–14435.

Rosón, G., Ríos, A.F., Pérez, F.F., Lavín, A., Bryden, H.L., 2003. Carbon distribution, fluxes, and budgets in the subtropical North Atlantic Ocean (24.5°N). Journal of Geophysical Research 108, 3144, doi:10.1029/1999JC000047.

Rouault, M., Penven, P., Pohl, B., 2009. Warming in the Agulhas Current system since the 1980's. Geophysical Research Letters 36, L12602, doi:10.1029/2009GL037987.

Roy, T., Bopp, L., Gehlen, M., Schneider, B., Cadule, P., Frölicher, T.L., Segschneider, J., Tjiputra, J., Heinze, C., Joos, F., 2011. Regional Impacts of Climate Change and Atmospheric CO_2 on Future Ocean Carbon Uptake: A Multimodel Linear Feedback Analysis. Journal of Climate 24, 2300–2318.

Rubin, S.I., 2003. Carbon and nutrient cycling in the upper water column across the Polar Frontal Zone and Antarctic Circumpolar Current along 170°W. Global Biogeochemical Cycles 17, GB1087, doi:10.1029/2002GB001900.

Sabine, C.L., Feely, R.A., Gruber, N., Key, R.M., Lee, K., Bullister, J.L., Wong, C.S., Wanninkhof, R., Wallace, D.W.R., Tilbrook, B., Millero, F.J., Peng, T.H., Kozyr, A., Ono, T., Rios, A.F., 2004. The oceanic sink for anthropogenic CO_2. Science 305, 367–71.

Sabine, C.L., Feely, R.A., Key, R.M., Bullister, J.L., Millero, F.J., Lee, K., Peng, T.H., Tilbrook, B., Ono, T., Wong, C.S., 2002. Distribution of anthropogenic CO_2 in the Pacific Ocean. Global Biogeochemical Cycles 16, GB1083, doi:10.1029/2001GB001639.

Sabine, C.L., Key, R.M., Johnson, K.M., Millero, F.J., Poisson, A., Sarmiento, J.L., Wallace, D.W.R., Winn, C.D., 1999. Anthropogenic CO_2 inventory of the Indian Ocean. Global Biogeochemical Cycles 13, 179–198.

Sabine, C.L., Tanhua, T., 2010. Estimation of Anthropogenic CO_2 Inventories in the Ocean. Annual Review of Marine Science 2, 175–198.

Sallée, J.B., Matear, R.J., Rintoul, S.R., Lenton, A., 2012. Localized subduction of anthropogenic carbon dioxide in the Southern Hemisphere oceans. Nature Geoscience 5, 579–584.

Sallée, J.B., Speer, K., Morrow, R., 2008. Response of the Antarctic Circumpolar Current to Atmospheric Variability. Journal of Climate 21, 3020.

Sallée, J.B., Speer, K., Rintoul, S., Wijffels, S., 2010a. Southern Ocean Thermocline Ventilation. Journal of Physical Oceanography 40, 509.

Sallée, J.B., Speer, K.G., Rintoul, S.R., 2010b. Zonally asymmetric response of the Southern Ocean mixed-layer depth to the Southern Annular Mode. Nature Geoscience 3, 273–279.

Sallée, J.B., Wienders, N., Speer, K., Morrow, R., 2006. Formation of subantarctic mode water in the southeastern Indian Ocean. Ocean Dynamics 56, 525–542.

Saraceno, M., Provost, C., Piola, A.R., Bava, J., Gagliardini, A., 2004. Brazil Malvinas Frontal System as seen from 9 years of advanced very high resolution radiometer data. Journal of Geophysical Research 109, C05027, doi:10.1029/2003JC002127.

Sarmiento, J.L., Gruber, N., 2006. Ocean Biogeochemical Dynamics. Princeton University Press, United States of America.

Sarmiento, J.L., Murnane, R., Le Quéré, C., 1995. Air-sea CO_2 transfer and the carbon budget of the North Atlantic. Philosophical Transactions Biological Sciences 348, 211–219.

Saunders, P.M., King, B.A., 1995. Oceanic Fluxes on the WOCE A11 section. Journal of Physical Oceanography 25, 1942–1958.

Schanze, J.J., Schmitt, R.W., Yu, L.L., 2010. The global oceanic freshwater cycle: A state-of-the-art quantification. Journal of Marine Research 68, 569–595.

Schlesinger, W.H., Reynolds, J.F., Cunningham, G.L., Huenneke, L.F., Jarrell, W.M., Virginia, R.A., Whitford, W.G., 1990. Biological Feedbacks in Global Desertification. Science 247, 1043–1048.

Schlüter, P., Uenzelmann-Neben, G., 2008. Indications for bottom current activity since Eocene times: The climate and ocean gateway archive of the Transkei Basin, South Africa. Global and Planetary Change 60, 416–428.

Schmid, C., Garzoli, S.L., 2009. New observations of the spreading and variability of the Antarctic Intermediate Water in the Atlantic. Journal of Marine Research 67, 815–843.

Schmidtko, S., Johnson, G.C., 2012. Multidecadal Warming and Shoaling of Antarctic Intermediate Water. Journal of Climate 25, 207–221.

Schmitt, R.W., Bogden, P.S., Dorman, C.E., 1989. Evaporation Minus Precipitation and Density Fluxes in the North Atlantic. Journal of Physical Oceanography 19, 1208–1221.

Schmittner, A., 2005. Decline of the marine ecosystem caused by a reduction in the Atlantic overturning circulation. Nature 434, 628–633.

Schmitz, W.J., McCartney, M.S., 1993. On the North Atlantic Circulation. Reviews of Geophysics 31, 29–49.

Schott, F.A., Dengler, M., Zantopp, R., Stramma, L., Fischer, J., Brandt, P., 2005. The Shallow and Deep Western Boundary Circulation of the South Atlantic at 5 ° - 11 ° S. Journal of Physical Oceanography 35, 2031–2053.

Schröder, M., Fahrbach, E., 1999. On the structure and the transport of the eastern Weddell Gyre. Deep Sea Research Part II: Topical Studies in Oceanography 46, 501–527.

Schroeder, M., Fahrbach, E., Hoppema, M., Rohardt, G., Wisotzki, A., 2004. Decadal-scale variations of water mass properties in the deep Weddell Sea. Ocean Dynamics 54, 77–91.

van Sebille, E., Johns, W.E., Beal, L.M., 2012. Does the vorticity flux from Agulhas rings control the zonal pathway of NADW across the South Atlantic? Journal of Geophysical Research 117, C05037, doi:10.1029/2011JC007684.

Shannon, L.V., 1985. The Benguela ecosystem part I. Evolution of the Benguela, physical features and processes. Oceanography and Marine Biology: an Annual Review 23, 105–182.

Shannon, L.V., Nelson, G., 1996. The Benguela: Large scale features and processes and system variability, in: Wefer, G. (Ed.), The South Atlantic: Present and Past Circulation. Springer-Verlag, pp. 163–210.

Shillington, F.A., 1998. The Benguela upwelling system off southwestern Africa, in: Robinson, A.R., Brink, K.H. (Eds.), The Sea, vol 11: The Global Coastal Ocean: Interdisciplinary Regional Studies and Syntheses. Harvard University Press, Boston, MA, pp. 583–604.

Sievers, A., Emery, J., 1978. Variability of the Antarctic Polar Frontal Zone in the Drake Passage - Summer 1976-1977. Journal of Geophysical Research 83, 3010–3022.

Sievers, H.A., Nowlin, W.D., 1984. The Stratification and Water Masses at Drake Passage. Journal of Geophysical Research 89, 10489–10514.

Sigman, D.M., Altabet, M.A., McCorkle, D.C., Francois, R., Fischer, G., 2000. The δ15N of nitrate in the Southern Ocean: Nitrogen cycling and circulation in the ocean interior. Journal of Geophysical Research 105, 19599–19614.

Signorini, S.R., 1978. On the circulation and the volume transport of the Brazil Current between the Cape of Sào Tomé and Guanabara Bay. Deep-Sea Research 25, 481–490.

Sloyan, B.M., Rintoul, S.R., 2000. Estimates of Area-Averaged Diapycnal Fluxes from Basin-Scale Budgets. Journal of Physical Oceanography 30, 2320–2341.

Sloyan, B.M., Rintoul, S.R., 2001a. Circulation, Renewal, and Modification of Antarctic Mode and Intermediate Water. Journal of Physical Oceanography 31, 1005–1030.

Sloyan, B.M., Rintoul, S.R., 2001b. The Southern Ocean Limb of the Global Deep Overturning Circulation. Journal of Physical Oceanography 31, 143–173.

Smethie, W.M., 1993. Tracing the thermohaline circulation in the western North Atlantic using chlorofluorocarbons. Progress In Oceanography 31, 51–99.

Smith, R.D., Maltrud, M.E., Bryan, F.O., Hecht, M.W., 2000. Numerical Simulation of the North Atlantic Ocean at 1/10°. Journal of Physical Oceanography 30, 1532–1561.

Smith, W.H.F., Sandwell, D.T., 1997. Global Sea Floor Topography from Satellite Altimetry and Ship Depth Soundings. Science 277, 1956–1962.

Smythe-Wright, D., Chapman, P., Rae, C., Shannon, L., Boswell, S., 1998. Characteristics of the South Atlantic subtropical frontal zone between 15°W and 5°E. Deep Sea Research Part I: Oceanographic Research Papers 45, 167–192.

Sokolov, S., Rintoul, S., 2007. Multiple Jets of the Antarctic Circumpolar Current South of Australia. Journal of Physical Oceanography 37, 1394.

Sokolov, S., Rintoul, S.R., 2002. Structure of Southern Ocean fronts at 140°E. Journal of Marine Systems 37, 151–184.

Sokolov, S., Rintoul, S.R., 2009a. Circumpolar structure and distribution of the Antarctic Circumpolar Current fronts: 1. Mean circumpolar paths. Journal of Geophysical Research 114, C11018, doi:10.1029/2008JC005108.

Sokolov, S., Rintoul, S.R., 2009b. Circumpolar structure and distribution of the Antarctic Circumpolar Current fronts: 2. Variability and relationship to sea surface height. Journal of Geophysical Research 114, C11019, doi:10.1029/2008JC005248.

Spadone, A., Provost, C., 2009. Variations in the Malvinas Current volume transport since October 1992. Journal of Geophysical Research 114, 1–21.

Sparrow, M.D., Heywood, K.J., Brown, J., 1996. Current structure of the South Indian Ocean. Journal of Geophysical Research 101, 6377–6391.

Speer, K., Rintoul, S.R., Sloyan, B., 2000. The Diabatic Deacon Cell. Journal of Physical Oceanography 30, 3212–3222.

Speer, K., Tziperman, E., 1992. Rates of Water Mass Formation in the North Atlantic Ocean. Journal of Physical Oceanography 22, 93–104.

Speer, K.G., 1997. A note on average cross-isopycnal mixing in the North Atlantic ocean. Deep Sea Research Part I: Oceanographic Research Papers 44, 1981–1990.

Speer, K.G., Dittmar, T., 2008. Cruise Report: I06S 2009. Technical Report.

Speer, K.G., Siedler, G., Talley, L., 1995. The Namib Col Current. Deep Sea Research Part I: Oceanographic Research Papers 42, 1933–1950.

Speer, K.G., Zenk, W., 1993. The Flow of Antarctic Bottom Water into the Brazil Basin. Journal of Physical Oceanography 23, 2667–2682.

Spence, P., Fyfe, J.C., Montenegro, A., Weaver, A.J., 2010. Southern Ocean Response to Strengthening Winds in an Eddy-Permitting Global Climate Model. Journal of Climate 23, 5332–5343.

Sprintall, J., 2008. Long-term trends and interannual variability of temperature in Drake Passage. Progress In Oceanography 77, 316–330.

Stephens, J.C., Marshall, D.P., 2000. Dynamical Pathways of Antarctic Bottom Water in the Atlantic. Journal of Physical Oceanography 30, 622–640.

Stephenson, G.R., Gille, S.T., Sprintall, J., 2012. Seasonal variability of upper ocean heat content in Drake Passage. Journal of Geophysical Research 117, C04019, doi:10.1029/2011JC007772.

Stewart, R.H., 2008. Introduction to Physical Oceanography. `http://oceanworld.tamu.edu/resources/ocng_textbook/contents.html`. Accessed: 19/12/2012.

Stoll, M., van Aken, H., de Baar, H., de Boer, C., 1996. Meridional carbon dioxide transport in the northern North Atlantic. Marine Chemistry 55, 205–216.

Stommel, H., 1948. The Westward Intensification of Wind-Driven Ocean Currents. Transactions, American Geophysical Union 29, 202–206.

Stramma, L., 1989. The Brazil current transport south of 23°S. Deep Sea Research Part A. Oceanographic Research Papers 36, 639–646.

Stramma, L., England, M., 1999. On the water masses and mean circulation of the South Atlantic Ocean. Journal of Geophysical Research 104, 20863–20883.

Stramma, L., Peterson, R., 1990. The South Atlantic Current. Journal of Physical Oceanography 20, 846–859.

Stuiver, M., Quay, P.D., Ostlund, H.G., 1983. Abyssal Water Carbon-14 Distribution and the Age of the World Oceans. Science 219, 849–851.

Sudre, J., Garçon, V., Provost, C., Sennéchael, N., Huhn, O., Lacombe, M., 2011. Short-term variations of deep water masses in Drake Passage revealed by a multiparametric analysis of the ANT-XXIII/3 bottle data. Deep Sea Research Part II: Topical Studies in Oceanography 58, 2592–2612.

Sullivan, C.W., Arrigo, K.R., McClain, C.R., Comiso, J.C., Firestone, J., 1993. Distributions of Phytoplankton Blooms in the Southern Ocean. Science 262, 1832–1837.

Svedrup, H.U., 1940. Hydrology: British, Australian, New Zealand Antarctic Research Expedition 1929-31, Series A, 3(2). Technical Report.

Svedrup, H.U., 1953. The currents off the coast of Queen Maud Land. Norsk Geografisk Tidesskrift 14, 239–249.

Swart, S., Chang, N., Fauchereau, N., Joubert, W., Lucas, M., Mtshali, T., Roychoudhury, A., Tagliabue, A., Thomalla, S., Waldron, H., Monteiro, P.M., 2012. Southern Ocean Seasonal Cycle Experiment 2012: Seasonal scale climate and carbon cycle links. South African Journal of Science 108, 3–5.

Swart, S., Speich, S., Ansorge, I.J., Goni, G.J., Gladyshev, S., Lutjeharms, J.R.E., 2008. Transport and variability of the Antarctic Circumpolar Current south of Africa. Journal of Geophysical Research 113, C09014, doi:10.1029/2007JC004223.

Taft, B.A., 1963. Distribution of salinity and dissolved oxygen on surfaces of uniform potential specific volume in the South Atlantic, South Pacific and Indian Oceans. Journal of Marine Research 21, 129–145.

Takahashi, T., Broecker, W.S., Langer, S., 1985. Redfield ratio based on chemical data from isopycnal surfaces. Journal of Geophysical Research 90, 6907–6924.

Takahashi, T., Sutherland, S., Wanninkhof, R., Sweeney, C., Feely, R., Chipman, D., Hales, B., Friederich, G., Chavez, F., Sabine, C., Watson, A., Bakker, D., Schuster, U., Metzl, N., Yoshikawa-Inoue, H., Ishii, M., Midorikawa, T., Nojiri, Y., Kortzinger, A., Steinhoff, T., Hoppema, M., Olafsson, J., Arnarson, T., Tilbrook, B., Johannessen, T., Olsen, A., Bellerby, R., Wong, C., Delille, B., Bates, N., de Baar, H.,

2009. Climatological mean and decadal change in surface ocean pCO_2, and net sea-air CO_2 flux over the global oceans. Deep Sea Research Part II: Topical Studies in Oceanography 56, 554–577.

Talley, L., 2008. Freshwater transport estimates and the global overturning circulation: Shallow, deep and throughflow components. Progress In Oceanography 78, 257–303.

Talley, L.D., 1996. The South Atlantic: Present and Past Circulation. Springer-Verlag.

Talley, L.D., Pickard, G.L., Emery, W.J., Swift, J.H., 2011. Descriptive Physical Oceanography An Introduction. Academic Press, London. sixth edition.

Tamura, T., Ohshima, K.I., Nihashi, S., 2008. Mapping of sea ice production for Antarctic coastal polynyas. Geophysical Research Letters 35, L07606, doi:10.1029/2007GL032903.

Tanhua, T., Körtzinger, A., Friis, K., Waugh, D.W., Wallace, D.W.R., 2007. An estimate of anthropogenic CO_2 inventory from decadal changes in oceanic carbon content. Proceedings of the National Academy of Sciences of the United States of America 104, 3037–42.

Thacker, W.C., 2012. Regression-based estimates of the rate of accumulation of anthropogenic CO_2 in the ocean: A fresh look. Marine Chemistry 132-133, 44–55.

Thomas, E.R., Marshall, G.J., McConnell, J.R., 2008. A doubling in snow accumulation in the western Antarctic Peninsula since 1850. Geophysical Research Letters 35, L01706, doi:10.1029/2007GL032529.

Thomas, H., Friederike Prowe, A.E., van Heuven, S., Bozec, Y., de Baar, H.J.W., Schiettecatte, L.S., Suykens, K., Koné, M., Borges, A.V., Lima, I.D., Doney, S.C., 2007. Rapid decline of the CO_2 buffering capacity in the North Sea and implications for the North Atlantic Ocean. Global Biogeochemical Cycles 21, GB4001, doi:10.1029/2006GB002825.

Thorpe, S.E., Heywood, K.J., Brandon, M.A., Stevens, D.P., 2002. Variability of the southern Antarctic Circumpolar Current front north of South Georgia. Journal of Marine Systems 37, 87–105.

Tillinger, D., Gordon, A., 2010. Transport weighted temperature and internal energy transport of the Indonesian throughflow. Dynamics of Atmospheres and Oceans 50, 224–232.

Timmermann, A., An, S.I., Krebs, U., Goosse, H., 2005. ENSO Suppression due to Weakening of the North Atlantic Thermohaline Circulation. Journal of Climate 18, 3122–3139.

Timmermann, A., Okumura, Y., An, S.I., Clement, A., Dong, B., Guilyardi, E., Hu, A., Jungclaus, J.H., Renold, M., Stocker, T.F., Stouffer, R.J., Sutton, R., Xie, S.P., Yin, J., 2007. The Influence of a Weakening of the Atlantic Meridional Overturning Circulation on ENSO. Journal of Climate 20, 4899–4919.

Toggweiler, J.R., Samuels, B., 1995. Effect of Drake Passage on the global thermohaline. Deep Sea Research Part I: Oceanographic Research Papers 42, 477–500.

Toggweiler, J.R., Samuels, B., 1997. On the Ocean's Large-Scale Circulation near the Limit of No Vertical Mixing. Journal of Physical Oceanography 28, 1832–1852.

Tomczak, M., 1981. A multi-parameter extension of temperature / salinity diagram techniques for the analysis of non-isopycnal mixing. Progress In Oceanography 10, 147–171.

Tomczak, M., Large, D.G.B., 1989. Optimum Multiparameter Analysis of Mixing in the Thermocline of the Eastern Indian Ocean. Journal of Geophysical Research 94, 16141–16149.

Toole, J.M., McDougall, T.J., 2001. Mixing and Stirring in the Ocean Interior, in: Siedler, G., Church, J., Gould, J. (Eds.), Ocean Circulation and Climate. Academic Press, London, pp. 337–355.

Toole, J.M., Schmitt, R.W., Polzin, K.L., 1994. Estimates of diapycnal mixing in the abyssal ocean. Science 264, 1120–3.

Toole, J.M., Warren, B.A., 1993. A hydrographic section across the subtropical South Indian Ocean. Deep Sea Research Part I: Oceanographic Research Papers 40, 1973–2019.

Touratier, F., Azouzi, L., Goyet, C., 2007. CFC-11, Delta14 C and 3 H tracers as a means to assess anthropogenic CO_2 concentrations in the ocean. Tellus B 59, 318–325.

Touratier, F., Goyet, C., 2004a. Applying the new TrOCA approach to assess the distribution of anthropogenic CO_2 in the Atlantic Ocean. Journal of Marine Systems 46, 181–197.

Touratier, F., Goyet, C., 2004b. Definition, properties, and Atlantic Ocean distribution of the new tracer TrOCA. Journal of Marine Systems 46, 169–179.

Tréguer, P., Jacques, G., 1992. Dynamics of nutrients and phytoplankton, and fluxes of carbon, nitrogen and silicon in the Antarctic Ocean. Polar Biology 12, 149–162.

Tréguer, P., Nelson, D.M., Van Bennekom, A.J., Demaster, D.J., Leynaert, A., Quéguiner, B., 1995. The Silica Balance in the World Ocean: A Reestimate. Science 268, 375–379.

Tréguer, P., Van Bennekom, A.J., 1991. The annual production of biogenic silica in the Antarctic Ocean. Marine Chemistry 35, 477–487.

Tréguer, P.J., De La Rocha, C.L., 2012. The World Ocean Silica Cycle. Annual review of marine science , 1–25.

Trenberth, K., Jones, P., Ambenje, P., Bojariu, R., Easterling, D., Klein Tank, A., Parker, D., Rahimzadeh, F., Renwick, J.A., Rusticucci, M., Soden, B., Zhai, P., 2007. Observations: Surface and Atmospheric Climate, in: Solomon, S., Qin, D., Manning, M., Chen, Z., Marquis, M., Averyt, K.B., Tignor, M., Miller, H.L. (Eds.), Climate Change 2007: The Physical Science Basis. Contribution of Working Group I to the Fourth Assessment Report of the Intergovernmental Panel on Climate Change. Cambridge University Press, Cambridge, United Kingdom and New York, NY, USA.

Tsubouchi, T., Bacon, S., Naveira Garabato, A.C., Aksenov, Y., Laxon, S.W., Fahrbach, E., Beszczynska-Moller, A., Hansen, E., Lee, C.M., Ingvaldsen, R.B., 2012. The Arctic Ocean in summer: boundary fluxes and water mass transformations. Journal of Geophysical Research 117, C01024, doi:10.1029/2011JC007174.

Turner, J., Colwell, S.R., Marshall, G.J., Lachlan-Cope, T.A., Carleton, A.M., Jones, P.D., Lagun, V., Reid, P.A., Iagovkina, S., 2005. Antarctic climate change during the last 50 years. International Journal of Climatology 25, 279–294.

Tziperman, E., Speer, K., 1994. A study of water mass transformation in the Mediterranean Sea : analysis of climatological data and a simple three-box model. Dynamics of Atmospheres and Oceans 21, 53–82.

Uppala, S.M., Kållberg, P.W., Simmons, A.J., Andrae, U., Da Costa Bechtold, V., Fiorino, M., Gibson, J.K., Haseler, J., Hernandez, A., Kelly, G.A., Li, X., Onogi, K., Saarinen, S., Sokka, N., Allan, R.P., Andersson, E., Arpe, K., Balmaseda, M.A.,

Beljaars, A.C.M., Van De Berg, L., Bidlot, J., Bormann, N., Caires, S., Chevallier, F., Dethof, A., Dragosavac, M., Fisher, M., Fuentes, M., Hagemann, S., Hólm, E., Hoskins, B.J., Isaksen, L., Janssen, P.A.E.M., Jenne, R., McNally, A.P., Mahfouf, J.F., Morcrette, J.J., Rayner, N.A., Saunders, R.W., Simon, P., Sterl, A., Trenberth, K.E., Untch, A., Vasiljevic, D., Viterbo, P., Woollen, J., 2005. The ERA-40 reanalysis. Quarterly Journal of the Royal Meteorological Society 131, 2961–3012.

Vázquez-Rodríguez, M., 2008. Reconstructing preformed properties and air-sea CO_2 disequilibria for water masses in the Atlantic from subsurface data: An application in anthropogenic carbon determination. Technical Report. Universidade de Vigo.

Vázquez-Rodríguez, M., Padin, X., Pardo, P., Ríos, A., Pérez, F., 2012. The subsurface layer reference to calculate preformed alkalinity and air-sea CO_2 disequilibrium in the Atlantic Ocean. Journal of Marine Systems 94, 52–63.

Vázquez-Rodríguez, M., Padin, X.A., Ríos, A.F., Bellerby, R.G.J., Pérez, F.F., 2009a. An upgraded carbon-based method to estimate the anthropogenic fraction of dissolved CO_2 in the Atlantic Ocean. Biogeosciences Discussions 6, 4527–4571.

Vázquez-Rodríguez, M., Touratier, F., Lo Monaco, C., Waugh, D.W., Padin, X.A., Bellerby, R.G.J., Goyet, C., Metzl, N., Ríos, A.F., Pérez, F.F., 2009b. Anthropogenic carbon distributions in the Atlantic Ocean: data-based estimates from the Arctic to the Antarctic. Biogeosciences 6, 439–451.

Vellinga, M., Wood, R.A., 2002. Global Climatic Impacts of a Collapse of the Atlantic Thermohaline Circulation. Climatic Change 54, 251–267.

Vivier, F., Provost, C., 1999. Direct velocity measurements in the Malvinas Current component and filaments. Journal of Geophysical Research 104, 21083–21103.

Völker, C., Wallace, D.W.R., Wolf-Gladrow, D.A., 2002. On the role of heat fluxes in the uptake of anthropogenic carbon in the North Atlantic. Global Biogeochemical Cycles 16, GB1138, doi:10.1029/2002GB001897.

Vranes, K., Gordon, A.L., Ffield, A., 2002. The heat transport of the Indonesian Throughflow and implications for the Indian Ocean heat budget. Deep Sea Research Part II: Topical Studies in Oceanography 49, 1391–1410.

Wakeham, S.G., 2000. Organic Matter Preservation in the Ocean: Lipid Behaviour from Plankton to Sediments, in: Gianguzza, A., Pelizzetti, E., Sammartano, S. (Eds.), Chemical Processes in Marine Environments. Springer-Verlag, Berlin, pp. 127–139.

Wakeham, S.G., Lee, C., 1993. Production, transport, and alteration of particulate organic matter, in: Engel, M.H., Macko, S.A. (Eds.), Organic geochemistry: Principles and applications. Plenum Press, New York, pp. 145–169.

Wakita, M., Watanabe, S., Murata, A., Tsurushima, N., Honda, M., 2010. Decadal change of dissolved inorganic carbon in the subarctic western North Pacific Ocean. Tellus B 62, 608–620.

Walin, G., 1982. On the relation between sea-surface heat flow and thermal circulation in the ocean. Tellus 34, 187–195.

Walker, S.J., Weiss, R.F., Salameh, P.K., 2000. Reconstructed histories of the annual mean atmospheric mole fractions for the halocarbons CFC-11, CFC-12, CFC-113 and carbon tetrachloride. Journal of Geophysical Research 105, 14285–14296.

Wallace, D.W.R., 1995. Monitoring global ocean carbon inventories. Technical Report. Texas A&M University, College Station Texas. OOSDP Background Report.

Wang, Q., Danilov, S., Fahrbach, E., Schröter, J., Jung, T., 2012. On the impact of wind forcing on the seasonal variability of Weddell Sea Bottom Water transport. Geophysical Research Letters 39, L06603, doi:10.1029/2012GL051198.

Wanninkhof, R., Doney, S.C., Bullister, J.L., Levine, N.M., Warner, M., Gruber, N., 2010. Detecting anthropogenic CO_2 changes in the interior Atlantic Ocean between 1989 and 2005. Journal of Geophysical Research 115, C11028, doi:10.1029/2010JC006251.

Wanninkhof, R., Doney, S.C., Peng, T.H., Bullister, J.L., Lee, K., Feely, R.A., 1999. Comparison of methods to determine the anthropogenic CO_2 invasion into the Atlantic Ocean. Tellus 51B, 511–530.

Wanninkhof, R., Peng, T.H., Huss, B., Sabine, C.L., Lee, K., 2003. Comparison of inorganic carbon system parameters measured in the Atlantic Ocean from 1990 to 1998 and recommended adjustments. ORNL/CDIAC-140 Carbon Dioxide Information Analysis Center , 43.

Warner, M.J., Weiss, R.F., 1985. Solubilities of chlorofluorocarbons 11 and 12 in water and seawater. Deep Sea Research Part A. Oceanographic Research Papers 32, 1485–1497.

Warren, B.A., Speer, K.G., 1991. Deep Circulation in the Eastern South-Atlantic Ocean. Deep Sea Research Part A. Oceanographic Research Papers 38, S281–S322.

Webb, D.J., Suginohara, N., 2001. Vertical mixing in the ocean. Nature 409, 37.

Weber, T.S., Deutsch, C., 2010. Ocean nutrient ratios governed by plankton biogeography. Nature 467, 550–554.

Weppernig, R., Schlosser, P., Khatiwala, S., Fairbanks, R.G., 1996. Isotope data from Ice Station Weddell: Implications for deep water formation in the Weddell Sea. Journal of Geophysical Research 101, 25723.

White, W.B., Annis, J., 2004. Influence of the Antarctic Circumpolar Wave on El Niño and its multidecadal changes from 1950 to 2001. Journal of Geophysical Research 109, C06019, doi:10.1029/2002JC001666.

White, W.B., Peterson, R.G., 1996. An Antarctic circumpolar wave in surface pressure, wind, temperature and sea-ice extent. Nature 380, 699–702.

Whitehouse, M.J., Priddle, J., Woodward, E.M.S., 1995. Spatial variability of inorganic nutrients in the marginal ice zone of the Bellingshausen Sea during the Austral spring. Deep Sea Research Part II: Topical Studies in Oceanography 42, 1047–1058.

Whitworth, T., Nowlin, W., 1987. Water Masses and Currents of the Southern Ocean at the Greenwich Meridian. Journal of Geophysical Research 92, 6462–6476.

Whitworth, T., Orsi, A.H., Kim, S.J., Nowlin, W.D., Locarini, R.A., 1998. Water masses and mixing near the Antarctic Slope Front, in: Jacobs, S.S., Weiss, R.F. (Eds.), Ocean, Ice, and Atmosphere: Interactions at the Antarctic Continental Margin, Antarctic Research Series. American Geophysical Union, Washington, D.C., pp. 1–27.

Whitworth, T., Peterson, R.G., 1985. Volume Transport of the Antarctic Circumpolar Current from Bottom Pressure Measurements. Journal of Physical Oceanography 15, 810–816.

Wilkin, J.L., Mansbridge, J.V., Godfrey, J.S., 1995. Pacific Ocean Heat Transport at 24°N in a High-Resolution Global Model. Journal of Physical Oceanography 25, 2204–2214.

Williams, A., Bacon, S., Cunningham, S., 2006. Variability of the Lower Circumpolar Deep Water in Drake Passage 1926-2004. Geophysical Research Letters 33, L03603, doi:10.1029/2005GL024226.

Williams, A.P., 2007. Antarctic Climate: Ocean fluxes and variability. Ph.D. thesis. University of Southampton.

Williams, G., Nicol, S., Aoki, S., Meijers, A., Bindoff, N., Iijima, Y., Marsland, S., Klocker, A., 2010a. Surface oceanography of BROKE-West, along the Antarctic margin of the south-west Indian Ocean (30-80°E). Deep Sea Research Part II: Topical Studies in Oceanography 57, 738–757.

Williams, G.D., Aoki, S., Jacobs, S.S., Rintoul, S.R., Tamura, T., Bindoff, N.L., 2010b. Antarctic Bottom Water from the Adélie and George V Land coast, East Antarctica (140-149°E). Journal of Geophysical Research 115, C04027.

Williams, R.G., Follows, M.J., 2011. Ocean Dynamics and the Carbon Cycle. Cambridge University Press, Cambridge.

Wilson, J.D., Barker, S., Ridgwell, A., 2012. Assessment of the spatial variability in particulate organic matter and mineral sinking fluxes in the ocean interior: Implications for the ballast hypothesis. Global Biogeochemical Cycles 26, GB4011, doi:10.1029/2012GB004398.

Wong, A.P.S., Bindoff, N.L., Church, J.A., 1999. Large-scale freshening of intermediate waters in the Pacific and Indian oceans. Nature 400, 440–443.

Woodgate, R.A., Aagaard, K., 2005. Revising the Bering Strait freshwater flux into the Arctic Ocean. Geophysical Research Letters 32, L02602, doi:10.1029/2004GL021747.

Woodworth, P.L., Meredith, M., Hughes, C.W., Stepanov, V., 2004. Changes in the ocean transport through Drake Passage during the 1980s and 1990s, forced by changes in the Southern Annular Mode. Geophysical Research Letters 31, L21305, doi:10.1029/2004GL021169.

Wu, L., Jing, Z., Riser, S., Visbeck, M., 2011. Seasonal and spatial variations of Southern Ocean diapycnal mixing from Argo profiling floats. Nature Geoscience 4, 363–366.

Wu, L., Li, C., Yang, C., Xie, S.P., 2008. Global Teleconnections in Response to a Shutdown of the Atlantic Meridional Overturning Circulation. Journal of Climate 21, 3002–3019.

Wunsch, C., 1978. The North Atlantic general circulation west of 50°W determined by inverse methods. Reviews of Geophysics 16, 583–620.

Wunsch, C., 1996. The Ocean Circulation Inverse Problem. Cambridge University Press.

Wunsch, C., 1998. The Work Done by the Wind on the Oceanic General Circulation. Journal of Physical Oceanography 28, 2332–2340.

Wust, G., 1935. The Stratosphere of the Atlantic Ocean. Scientific results of the German Atlantic Expedition of the Research Vessel 'Meteor' 1925-27. Technical Report. (English translation, W. J. Emery, Amerind, New Delhi, 1978).

Xie, P., Arkin, P.A., 1997. Global Precipitation : A 17-Year Monthly Analysis Based on Gauge Observations , Satellite Estimates , and Numerical Model Outputs. Bulletin of the American Meteorological Society 78, 2539–2558.

Yabuki, T., Suga, T., Hanawa, K., Matsuoka, K., Kiwada, H., Watanabe, T., 2006. Possible Source of the Antarctic Bottom Water in the Prydz Bay Region. Journal of Oceanography 62, 649–655.

Yool, A., Oschlies, A., Nurser, A.J.G., Gruber, N., 2010. A model-based assessment of the TrOCA approach for estimating anthropogenic carbon in the ocean. Biogeosciences 7, 723–751.

You, Y., Lutjeharms, J.R.E., Boebel, O., de Ruijter, W.P.M., 2003. Quantification of the interocean exchange of intermediate water masses around southern Africa. Deep Sea Research Part II: Topical Studies in Oceanography 50, 197–228.

You, Y., Tomczak, M., 1993. Thermocline circulation and ventilation in the Indian Ocean derived from water mass analysis. Deep-Sea Research 40, 13–56.

Yu, L., Jin, X., Weller, R.A., 2008. Multidecade Global Flux Datasets from the Objectively Analyzed Air-sea Fluxes (OAFlux) Project : Latent and Sensible Heat Fluxes, Ocean Evaporation, and Related Surface Meteorological Variables. Technical Report January. Woods Hole Oceanographic Institution.

Yu, L., Weller, R., 2007. Objectively Analyzed Air-Sea Heat Fluxes for the Global Ice-Free Oceans (1981-2005). Bulletin of the American Meteorological Society 88, 527–539.

Yuan, X., Martinson, D.G., Dong, Z., 2004. Upper ocean thermohaline structure and its temporal variability in the southeast Indian Ocean. Deep Sea Research Part I: Oceanographic Research Papers 51, 333–347.

Zangenberg, N., Siedler, G., 1998. Path of the North Atlantic Deep Water in the Brazil Basin. Journal of Geophysical Research 103, 5419–5428.

Zemba, J.C., 1991. The Structure and Transport of the Brazil Current between 27° and 36° South. Ph.D. thesis.

Zenk, W., Morozov, E., 2007. Decadal warming of the coldest Antarctic Bottom Water flow through the Vema Channel. Geophysical Research Letters 34, L14607, doi:10.1029/2007GL030340.

Zenk, W., Siedler, G., Lenz, B., Hogg, N.G., 1999. Antarctic Bottom Water Flow through the Hunter Channel. Journal of Physical Oceanography 29, 2785–2801.

Zenk, W., Visbeck, M., 2012. Structure and evolution of the abyssal jet in the Vema Channel of the South Atlantic. Deep Sea Research Part II: Topical Studies in Oceanography , 1–17.

Zickfeld, K., Eby, M., Weaver, A.J., 2008. Carbon-cycle feedbacks of changes in the Atlantic meridional overturning circulation under future atmospheric CO_2. Global Biogeochemical Cycles 22, GB4011, doi:10.1029/2012GB004398.

Zika, J.D., Sloyan, B.M., McDougall, T.J., 2009. Diagnosing the Southern Ocean Overturning from Tracer Fields. Journal of Physical Oceanography 39, 2926–2940.